UNIVERSITÉ DE LORRAINE | BIBLIOTHÈQUES UNIVERSITAIRES

AVERTISSEMENT

Ce document est le fruit d'un long travail approuvé par le jury de soutenance et mis à disposition de l'ensemble de la communauté universitaire élargie.

Il est soumis à la propriété intellectuelle de l'auteur. Ceci implique une obligation de citation et de référencement lors de l'utilisation de ce document.

D'autre part, toute contrefaçon, plagiat, reproduction illicite encourt une poursuite pénale.

Contact bibliothèque : ddoc-theses-contact@univ-lorraine.fr
(Cette adresse ne permet pas de contacter les auteurs)

LIENS

Code de la Propriété Intellectuelle. articles L 122. 4
Code de la Propriété Intellectuelle. articles L 335.2- L 335.10
http://www.cfcopies.com/V2/leg/leg_droi.php
http://www.culture.gouv.fr/culture/infos-pratiques/droits/protection.htm

Ecole Doctorale Sciences et Ingénierie des Molécules Produits Procédés et Énergie

Thèse de doctorat

Screening, Separation and Identification of Metal-Chelating Peptides in Protein Hydrolysates - Valorization of Proteins Extracted from fish scales of Red Tilapia and Sunflower meal By-products

Criblage, séparation et identification de peptides chélateurs de métaux dans des hydrolysats de protéines - Valorisation de protéines extraites à partir de co-produits: écaille de poisson Tilapia rouge et farine de tournesol

Présentée et soutenue publiquement pour l'obtention du titre de

DOCTEUR DE L'UNIVERSITÉ DE LORRAINE

Mention : Procédés Biotechnologiques

par

Jairo Andrés CAMAÑO ECHAVARRÍA

Le 16 Décembre 2024

Devant le jury composé de :

Rapporteurs:	Mme Loubna FIRDAOUS	Maître de Conférence HDR, Université de Lille
	M. Rotimi ALUKO	Professeur, Université de Manitoba, Canada
Examinateurs:	M. Kenji SATO	Professeur, Université de Kyoto, Japon
Président du jury	M. Chibuike UDENIGWE	Professeur, Université de Ottawa, Canada
Membre invité:	M. Ludovic MAILLARD	Maître de Conférences-HDR, Université de Montpellier
Co-encadrante de thèse:	Mme Katalin SELMECZI	Maître de Conférences-HDR, Université de Lorraine
Directrice de thèse:	Mme Laetitia CANABADY-ROCHELLE	Chargée de recherche CNRS, HDR, LRGP, Nancy

Dedicated to GOD and my family.

To my father and systers who made this possible.

To my beloved Mom "Nelly ECHAVARRÍA" (R.I.P)

Abstract

Metal-chelating peptides (**MCPs**) are compounds that interact with metal ions and form peptide-metal complexes. Considering such ability of peptides and the numerous roles of metals in biological processes, many studies have demonstrated that these MCPs provide positive health outcomes. In recent years, due to the current concern for environmental issues from agro-industrial waste, there is a growing interest to use emerging proteins from agro-industrial by-products. Therefore, this work investigated the use of red Tilapia scale and sunflower meal by-products as potential protein sources for the production of biofunctional hydrolysates containing MCPs using single and sequential enzymatic treatments, by setting up several screening, separation, *in vitro* characterization techniques up to peptide identification. In addition, this PhD work presents the effect of Cu^{2+} coordination on the production of food peptide-derived biomaterials endowed with *in vivo* antioxidant properties. First, Tilapia scale gelatin (**TSG**) and sunflower meal protein isolate (**SMPI**) were extracted. Then, enzymatic hydrolysis treatments were used to produce protein hydrolysates (TSG, Alcalase® and Alcalase® followed by Flavourzyme®; SMPI, Protamex® and Protamex® followed by Flavourzyme®). Regarding TSG, the whole and ≤ 1 kDa fraction hydrolysates obtained using Alcalase® offered an effective strategy to obtain small-sized Fe^{2+}-chelating peptides, with suitable ABTS scavenging and ACE inhibitory activities. The LC-MS/MS analysis confirmed the presence of peptide sequences with Asp, Glu, Ser, Lys and Arg, which might offer potentially metal-chelating and antioxidant properties of TSG hydrolysates. Meanwhile, in all investigated SMPI hydrolysates, several peptide sequences, identified by LC-MS/MS, evidenced the presence of His at different position from C- and N-termini. The most interesting Ni^{2+}/Cu^{2+}-chelating sequences were characterized by their "ATCUN" motif (*i.e.,* WL**H**). Furthermore, our work provided for the first time the self-assembly pattern of TSG and SMPI hydrolysates through Cu^{2+} coordination and the investigation of their *in vivo* antioxidant property by Cu^{2+}-induced oxidative stress using the *Caenorhabditis elegans* as a model organism. The physico-chemical characterization of these self-assembled peptides by various analysis (ThT, ANS, DLS, TEM and rheological data) revealed that upon Cu^{2+} coordination, tunable self-assembled bioactive peptide-based nanostructures endowed with improved mechanical properties were generated in both types of hydrolysates. Moreover, the MCPs present in hydrolysate produced with a single enzymatic treatment (TSG, Alc; SMPI, ≤ 1 kDa Prot) significantly reduced the endogenous ROS levels through Cu^{2+} coordination, which finally extended the lifespan of *C. elegans*. These results are extremely promising on the production of MCPs from agro-industrial by-products-derived proteins for food, nutraceutical, and biomedical applications.

Keywords: Bioeconomy, by-products, Metal-chelating peptides, antioxidant activity, self-assembled peptides, peptide-derived biomaterials, *Caenorhabditis elegans*.

Résumé

Les peptides chélateurs de métaux (**PCMs**) sont des peptides qui interagissent avec les ions métalliques et forment des complexes peptide-métal. Compte tenu de cette biofonctionalité et de nombreux rôles des métaux dans les processus biologiques, diverses études ont montré que ces PCMs ont des effets positifs sur la santé. Ces dernières années, en raison de préoccupations environnementales, l'utilisation de protéines émergentes issues de co-produits agro-industriels a suscité un intérêt croissant. Par conséquent, cette thèse avait pour objectif d'étudier l'utilisation d'écailles de poisson (Tilapia rouge) et de tourteau de tournesol comme sources potentielles de protéines pour produire des d'hydrolysats biofonctionnels contenant ces PCMs. Différents traitements enzymatiques ont été étudiés et les hydrolysats obtenus ont été analysés à l'aide de techniques de criblage, de séparation, de caractérisation *in vitro* jusqu'à l'identification des peptides chélateurs de métaux. De plus, l'effet de la coordination du Cu^{2+} par des peptides - dérivés d'hydrolysats peptidiques - a été étudiée en vue de produire des biomatériaux dotés de propriétés antioxydantes *in vivo*.

Tout d'abord, la gélatine présente dans les écailles de tilapia (**TSG**) et l'isolat de protéines issu de tourteau de tournesol (**SMPI**) ont été extraits. Ensuite, différents traitements enzymatiques ont été réalisés afin de produire des hydrolysats peptidiques (TSG, Alcalase® et Alcalase® suivi de Flavourzyme® ; SMPI, Protamex® et Protamex® suivi de Flavourzyme®). Pour le TSG, les hydrolysats et leurs fractions ≤ 1 kDa, obtenus à l'aide de l'Alcalase®, ont permis d'obtenir des peptides chélateurs de Fe^{2+} de petite taille, ayant des activités de piégeage de l'ABTS et d'inhibition de l'ECA adéquates. L'analyse LC-MS/MS a confirmé la présence de séquences peptidiques qui pourraient offrir des propriétés chélatrices de métaux et antioxydantes des hydrolysats de TSG. Par ailleurs, dans tous les hydrolysats de SMPI, plusieurs séquences peptidiques, identifiées par LC-MS/MS, ont mis en évidence la présence de résidus His. Les séquences chélatrices de Ni^{2+} /Cu^{2+} les plus intéressantes ont été caractérisées par leur motif "ATCUN" (*i.e.,* **WLH**). En outre, cette thèse a étudié pour la première fois, l'auto-assemblage de peptides présents dans des hydrolysats de TSG et de SMPI, induit par coordination avec le Cu^{2+}, et leur propriété antioxydante a été étudié *in vivo* en utilisant *Caenorhabditis elegans*. Ces peptides auto-assemblés - générés à partir des deux types d'hydrolysats - ont été caractérisés par diverses analyses (ThT, ANS, DLS, TEM et données rhéologiques). Ces nanostructures auto-assemblées à base de peptides bioactifs ont montré des propriétés mécaniques améliorées. De plus, les PCMs présents dans l'hydrolysat produit avec un seul traitement enzymatique (TSG, Alc ; SMPI, ≤ 1 kDa Prot) ont significativement réduit les niveaux de ROS endogènes grâce à la coordination de Cu^{2+}, prolongeant ainsi la durée de vie de *C. elegans*. Ces résultats, extrêmement prometteurs pour la production de PCMs à partir de protéines extraites de co-produits agro-industriels, permettent d'envisager des applications alimentaires, nutraceutiques et biomédicales.

Mots-clés : Bioéconomie, co-produits, peptides chélateurs de métaux, activité antioxydante, peptides auto-assemblés, biomatériaux dérivés de peptides, *Caenorhabditis elegans*.

Acknowledgements

We would like to thank the Directors of the LRGP, Laurent FALK and Marie-Odile SIMONNOT.

Firs, I would like to thank my supervisor Dr **Laetitia CANABADY-ROCHELLE** (senior research scientist, HDR, CNRS, LRGP) for giving me the opportunity to pursue this Ph.D. program, for her guidance, understanding, encouragement and constant support throughout my PhD. Being a part of Laetitia's team has been a great honor. She is an honest, trustful and understanding person who has inspired me to pursue my goals over the past four years at Laboratory of Chemical Reactions and Process Engineering (LRGP).

My special thanks to the other members of my thesis committee, my co-supervisor Dr **Katalin SELMECZI** (Associate Professor, HDR, L2CM) who has helped me with ideas, useful suggestions and assistance during my PhD. She has provided me with scientific insight several times, particularly in peptide-metal interaction. Professor Dr **Chibuike UDENIGWE** who gave me the opportunity to do the international internship in his lab at the School of Nutrition Science of University of Ottawa, Canada. He has provided me with scientific insight in peptide self-assembly, and he has been always a wonderful resource of professional advices and encouragements.

I would also like to express my sincere gratitude to all the people at all the laboratories and platforms used to carry out this work (LRGP, LCPM, L2A, L2CM, LIBIO; platforms: SAMPL, ASIA & PASM and PhotoNS) for their support and collaboration to this work.

I gratefully acknowledge Dr **Jean-Michel GIRARDET** (Research Engineer) for providing the access to switchSENSE® technology, Dr **Sandrine BOSCHI-MULLER** (Professor at University of Lorraine) for her scientific discussions, **Steve PONTVIANNE** (Assistant Engineer) and Dr **Cédric PARIS** (Research Engineer) for providing help and making it possible use the HPLC and MS/MS instrumentation for this work, respectively. I am extremely grateful to Dr **Céline CAKIR-KIEFER** and **Christelle MATHÉ** (Associate Proffesor at University of Lorraine) for their contribution in this project, especially her expertise in SDS-PAGE technique. I also want to express gratitude to French Engineer **Philippe ARNOUX** for his kindness, assistance, experience and immeasurable help in explaining any equipment that I needed to use at LRGP. A special thanks to the PhD candidates **Raliat ABIOYE** and **Samanta SARAHÍ** for their help regarding peptide self-assembly and *in vivo* antioxidant assays at University of Ottawa.

I would like to acknowledge the member of my individual monitoring committee (CSI) **Dr Loïc STEFAN** (Research scientist at CNRS) and **Dr Franziska LEDERER** (Professor at Helmholtz-Zentrum, Germany), who provided me good suggestions and feedback during my PhD.

I express my gratitude to Dr **Loubna FIRDAOUS** (Associate Professor, University of Lille, France), Dr **Rotimi ALUKO** (Professor at University of Manitoba, Canada) for accepting to review my PhD thesis. I would also thank the other examiners of my PhD thesis Dr **Kenji SATO** (Professor at University of Kyoto, Japan), Dr **Chibuike UDENIGWE** (Professor at University of Ottawa, Canada) and Dr **Ludovic MAILLARD** (Associate Professor at University of Montpellier, France).

I also want to express my sincere appreciation to my bachelor and master degree supervisor in Colombia, **Dr José Edgar ZAPATA** (Professor at University of Antioquia, Colombia) for his guidance and encouragement throughout my research journey. My roots as a researcher come from Pr. José Edgar.

I am immensely thankful to the French government. This PhD cannot be proceeded further without the financial support from the ANR JCJC MELISSA (2020-2024) and the "Impact Biomolecules" project of the "Lorraine Université d'Excellence "(Investissements d'avenir–ANR project number 15-004), notably with the project Doctor Explore and Achieve More (DrEAM 9) that financially supported my doctoral mobility at University of Ottawa.

I would also like to thank all my lab mates, my friends all around the world for their unwavering support and cherished memories, especially my true friends **Sebastian GAVIRIA, Morgane MOINARD** and **Rachel IRANKUNDA**, with whom I have shared all the ups and downs of my PhD and who have given me support, encouragement and friendship.

Finally, a great and deep thanks goes to my family in Colombia especially my father (**Jairo CAMAÑO**), sisters (**Lidis CAMAÑO** and **Gloira CAMAÑO**) for their continuous love, prayers and support all the way during my university life. They always heard me out and encouraged me even through the roughest of days- this is for all of you!

"The important thing is not to stop questioning. Curiosity has its own reason for existing."
Albert Einstein

"The only way to do great work is to love what you do."
Steve Jobs

Table of contents

Abstract 5

Acknowledgements 7

Table of contents 9

List of figures 13

List of tables 20

List of appendices 22

List of abbreviations 25

Resumé de la thèse en Français 28

General introduction 42

Chapter 1. State of the art 46

1.1 Introduction 47

1.2 Metal-chelating peptides 48

1.2.1. Definition 48

1.2.2. Presence of Metal-chelating peptides in nature 49

1.2.3. Productions of MCPs by proteolysis 51

1.3 Food, pharmaceutical and cosmetic applications 57

1.3.1 Nutraceutical and food applications 57

1.3.2 Pharmaceutical applications 57

1.3.3 Cosmetic applications 59

1.4 Screening methodologies of MCPs 59

1.4.1 Surface plasmon resonance 59

1.4.2 Screening based on fluorometry 61

1.4.3 Screening based on UV-visible spectrophotometry 65

1.4.4 Ion selective electrode 69

1.4.5 Screening using other methodologies 70

1.4.6 Screening of MCPs coupled to their identification 71

1.5 Separation of MCPs 74

1.5.1 Immobilized metal ion affinity chromatography 74

1.5.2 Separation coupled to peptide identification using IMAC-MS/MS 74

1.5.3 Simulation of IMAC separation from SPR data 75

1.6 Chemical interaction between peptide and metal ions 76

1.6.1 Fourier-transform infrared spectroscopy 76

1.6.2 Isothermal titration calorimetry 79

1.7 Conlusions 83

Chapter 2. Optimization of Gelatin Extraction from Red Tilapia Scales using a Fractional Factorial Experimental Design and Evaluation of Physico-chemical and Viscoelastic Properties 84

2.1. Introduction 85

2.2. Materials and Methods 86
2.2.1. Chemicals and reagents 86
2.2.2. Gelatin extraction from Tilapia scales 87
2.2.3. Responses investigated 89
2.2.4. Physico-chemical characterization 91
2.2.5. Rheological properties 92

2.3. Results and discussion 93
2.3.1 Effect of the studied parameters on gelation extraction 93
2.3.2 Statistical evaluation of operating conditions 96
2.3.3 Responses optimization 97
2.3.4 Physico-chemical characterization 98
2.3.5 Rheology properties 103

2.4. Conclusions 105

Chapter 3. Gelatin Hydrolysates of Red Tilapia (Oreochromis spp.) Scale By-products: Investigation of Metal-Chelating Properties and their related Bioactivities 106

3.1 Introduction 107

3.2 Materials and methods 109
3.2.1 Chemicals and equipments 109
3.2.2 Gelatin extraction from Tilapia scales 109
3.2.3 Proteolysis 110
3.2.4 Physico-chemical characterization 110
3.2.5 Screening of MCPs in Tilapia hydrolysates using switchSENSE® technology 112
3.2.6 Biofunctional characterization 113
3.2.7 Mass spectrometry identification and sequence analysis 114
3.2.8 Statistical analysis 115

3.3 Results and discussion 116
3.3.1 Physical-chemical characterization of the TSG hydrolysates 116
3.3.2 Screening of MCPs in Tilapia hydrolysates using switchSENSE® technology 122
3.3.3 Biofunctional characterization of Tilapia hydrolysates 125
3.3.4 Peptide identification by LC-MS/MS 131

3.4 Conclusions 134

Chapter 4. Identification of Ni^{2+}-binding Peptides in Sunflower Meal Protein Hydrolysate for Deeper Understanding of Peptide-Metal Interactions 135

4.1 Introduction 136

4.2 Materials and methods 138
4.2.1 Chemicals 138
4.2.2 Synthetic peptides investigated 138
4.2.3 Metal-binding peptides investigated in hydrolysate 140
4.2.4 Peptide-metal interaction 143
4.2.5 Statistical analysis 145

4.3 Results and discussions 146
4.3.1 Investigation of Ni^{2+}-binding peptides in IMAC-Ni^{2+} 146
4.3.2 Peptide-metal interaction 157

4.4 Conclusions 168

Chapter 5. Sunflower Metal-Chelating Peptides derived from Sunflower Meal Protein: Preparation, Isolation and Antioxidant Properties 169

5.1 Introduction 170

5.2 Materials and methods 171

5.2.1 Chemicals and equipments 171
5.2.2 Production of sunflower meal protein isolate 172
5.2.3 Enzymatic hydrolysis 173
5.2.4 Physico-chemical characterization 173
5.2.5 Metal-chelating peptide characterization 175
5.2.6 Statistical analysis 179

5.3 Results and discussions 180

5.3.1 Physico-chemical characterization of protein hydrolysates 180
5.3.2 Characterization of MCPs in SMPI hydrolysates 184

5.4 Conclusions 196

Chapter 6. Tuning Peptide Self-Assembly Patterns in Tilapia Scale Gelatin Hydrolysates through Cu^{2+} Coordination: Characterization, Identification and Antioxidant Evaluation 199

6.1 Introduction 200

6.2 Materials and methods 201

6.2.1 Chemicals and reagents 201
6.2.2 Preparation of protein hydrolysate from Tilapia scale 202
6.2.3 Investigation of peptide-Cu^{2+} interaction 203
6.2.4 Peptide self-assembly characterization 206
6.2.5 Assessment of antioxidant activity in C. elegans *in vivo* model 208
6.2.6 Statistical analysis 210

6.3 Results and discussion 211

6.3.1 Cu^{2+} coordination properties 211
6.3.2 Physico-chemical characterization of self-assembled peptides 218
6.3.3 Antioxidant activity in C. elegans *in vivo* model 224

6.4 Conclusions 227

Chapter 7. Effect of Cu^{2+} Coordination on Peptide Self-Assembly, Mechanical Properties, and Bioactivity of Peptide Hydrolysates Obtained from Sunflower Meal Protein Isolate. 229

7.1 Introduction 230

7.2 Materials and methods 231

7.2.1 Chemicals and reagents 231
7.2.2 Preparation of protein hydrolysate from sunflower meal 232
7.2.3 Investigation of peptide-Cu^{2+} interaction 233
7.2.4 Peptide self-assembly characterization 236
7.2.5 Assessment of antioxidant activity in C. elegans *in vivo* model 238
7.2.6 Statistical analysis 240

7.3 Results and discussion 241

7.3.1 Cu^{2+} coordination properties 241
7.3.2 Physico-chemical characterization of self-assembled peptides 249
7.3.3 Antioxidant activity in C. elegans *in vivo* model 258

7.4 Conclusions 262

General conclusion and perspectives *263*

PhD outcomes *268*

References *273*

Appendices *303*

List of figures

Figure 0.1. Structure de la thèse. 41

Figure 0.2. Thesis overview 45

Figure 1.1. Metal ion (M^{n+}) coordination thorough several functional groups present in peptides. Upper part illustrates the formation of peptide-metal complexes by peptides without chelating sidechains R. (A) metal coordination through amino and carbonyl termini; (B) tripeptide complexing metal ions through amino and carboxyl termini. Lower part shows some examples of metal coordination through chelating functional groups present in sidechains; (C) His-containing peptides (imidazole group), (D) Cys-containing peptides (thiol group) and (E) Asp-containing peptides (carboxylate group). 50

Figure 1.2. Strategy for the preparation, separation, purification, and identification of MCPs present in hydrolysates produced from food source protein. 53

Figure 1.3. Schematic illustration of the stepwise detection of metal-chelating peptides using surface plasmon resonance. (A) A beam of polarized light incidents on the gold film surface, at an angle producing total internal reflection. Beyond a critical angle, the beam is completely reflected back out through the prism. The changes in the optical properties of the film gold surface due to the binding of analyte (Metal-chelating peptides, MCP) to ligand (NTA-Ni^{2+} on dextran) will affect the resonance angle. (B) The change in the intensity with resonance angle induced by the adsorption of a monolayer of small molecules. (C) Real-time SPR sensorgram of peptide-metal interaction which provides information about binding interactions. (D) Sorption isotherm used to obtain affinity constants. 61

Figure 1.4. Description of the switchSENSE® methodology applied to study of peptide-metal interaction. (A) Schematic representation of hybridization of single-strand DNA nanolever (ssDNA) with a complementary-strand DNA nanolever (cDNA) that contents NTA. Binding of nickel (Ni^{2+}) ions results in fluorescence quenching due to the proximity of the metal ions to the fluorophore (quenching effect). Fluorescence intensity is increased when the fluorophore is discarded from the quenching nickel surface due to metal-chelating peptides bind to nickel metal ions. (B) The measuring of the association and dissociation of metal-chelating peptide (MCP) and immobilized nickel ions is shown. The kinetic (k_{on}, k_{off}) and affinity constant (K_D) of the peptide-metal interaction are determined by real-time measurement. (C) Dynamic mode. 62

Figure 1.5. Schematic image representing the metal-chelating peptide detection based on a CLSM approach. (A) detection of peptide-metal complex formation. Free metal ions interact with fluorescence indicator, increasing the signal intensity, whereas, in the peptide-metal complex, there is a reduction in such an intensity. (B, C) Schematic illustration of the interaction between the fluorescence indicator and metal ion on surface. In presence of metal-chelating peptides, fluorescence signal decreases, allowing to study binding kinetics of peptide and metal ions in real time. 64

Figure 1.6. Chemical reactions involved in metal-chelation test. M: metal ion; MCP: metal-chelating peptides; L: ligand..... 66

Figure 1.7. Overall scheme of isothermal titration calorimetry. A, B) principle of isothermal titration calorimetry. C, D) basics of ITC experiments. From Microcal ITC systems (Malvern Panalytical, Malvern, United Kingdom)..... 81

Figure 2.1. Tilapia scales gelatin extraction process set up in this study with fractional factorial experimental design approach using ultrapure water. Adapted from Chen et al., (2019). 88

Figure 2.2. Percentage of contribution of single factors and two-factor interactions effects on investigated responses..... 95

Figure 2.3. 2D contour plots of responses. (A) crude protein content CPC (%) as a function of solvent-to-solid ratio and extraction time; (B) free amino groups content (FAG, mmol Eq Glycine/g) and (C) protein extraction yield PEY (%) as a function of solvent-to-solid ratio and temperature. 97

Figure 2.4. Physico-chemical characterization of gelatin extracts (A) SDS-PAGE (12.5 %) profile of the red Tilapia scales flour (TSF) and the ten gelatin extracts from Tilapia scales. Numbers define the coded level of FFD. Lane "M" represents a pre-stained molecular weight marker (ref: 26619, Thermo Scientific™, Vilnius, Lithuania), γ: γ-chain; β: β-chain; α_1: α_1-chain; α_2: α_2-chain; LMWA: low molecular weight aggregates, Opt: optimal gelatin. (B) Amount of molecular weight constituents of gelatin extracts obtained by densitometric analysis of SDS-PAGE gels. (C) α_1/α_2 ratio of gelatin extracts. 100

Figure 2.5. MS Amino acids composition of red tilapia scale gelatin obtained in optimal conditions (g/100 g of gelatin), (A) Individual AA content, (B) AA gathered as class. 102

Figure 2.6. Rheological properties of the most interesting gelatin extracts (Run 1, 8, 9 and optimal run). (A) gelling and (B) melting temperatures; (C) and (D) elastic (G') and loss (G'') moduli, respectively. 104

Figure 3.1. Relation between metal-chelating activity and other important biofunctional properties investigated in this study (antioxidant and antihypertensive activities) reported from the literature (Cushman & Cheung, 1971; Canabady-Rochelle *et al.,* 2018). 108
Figure 3.2. Molecular weight distribution of protein marker, Tilapia scale flour (TSF), Tilapia scale gelatin (TSG) and Tilapia scale gelatin hydrolysates. (A) SDS-PAGE patterns of protein marker, TSF, TSG and TSG hydrolysates. (B) and (C) Size exclusion chromatography profile of Tilapia scale gelatin hydrolysates. 118
Figure 3.3. Kinetic study between metal-chelating peptides present in TSG hydrolysates and nickel ions using switchSENSE® technology. A, C, E, G**)** association rate (k_{on}) of binding kinetic studies of metal-chelating peptides of Alc, Alc+Flav, ≤ 1 kDa Alc, ≤ 1 kDa Alc+Flav gelatin hydrolysates interacting with Ni^{2+}, respectively. B, D, F and H) dissociation rate (k_{off}) of binding kinetic studies of metal-chelating peptides of Alc, Alc+Flav, ≤ 1 kDa Alc, ≤ 1 kDa Alc+Flav gelatin hydrolysates interacting with Ni^{2+}, respectively. Alc: Alcalase® hydrolysate, Alc+Flav: Alcalase® followed by Flavourzyme®; ≤ 1 kDa: ultrafiltrated hydrolysate. 123
Figure 3.4. SwitchSENSE® measurements in static and dynamic modes of TSG hydrolysates. (A) average observed constant rate (k_{obs}) of TSG hydrolysates with respective standard deviations. (B) changes in the local fluorophore environment (ΔF) of free-nickel references spots and samples spots for Alc, Alc+Flav, ≤ 1 kDa Alc and ≤ 1 kDa Alc+Flav TSG hydrolysates, respectively (static mode). (C) size index changes (ΔSI) of NTA, NTA-Ni^{2+} and NTA-Ni^{2+}-MCPs present in TSG hydrolysates determined by sizing analysis (dynamic mode)..... 125
Figure 3.5. Results obtained from the LC-MS/MS identification of peptides present in Tilapia scale hydrolysates. (A) number of peptides identified (B) peptide length distribution, (C-D) AA composition. 131
Figure 3.6. MS/MS spectra for the parent ions of peptides present in Tilapia scale hydrolysates. Alc: (A) GPAGPL, (B) SGPPVPGPIGPM; Alc+Flav: (C) GPPVPGPIGPM, (D) GPVGMPGAR; ≤ 1 kDa Alc: (E) GPAGPR, (F) PGAPGR; ≤ 1 kDa Alc+Flav: (G) GPAGPL, (H) PGA. 133
Figure 4.1. Chemical structures of pure peptides studied by IMAC, switchSENSE®, UV-visible spectroscopy, and CD techniques. (A, B, C) His-containing peptides without proline (group I), (E, F, G, H) His-containing peptides with proline (group II), (D, I, J) No His-containing peptides, and (K) positive Ni^{2+}-binding peptide (6His peptide). (L) schematic representation of ATCUN peptide-metal (M^{n+}) complex. Imidazole, indole and thiol groups could play a role in the Ni^{2+}-binding properties (circle). 139

Figure 4.2. Retention times (min) of pure peptides studied with HisTrap IMAC-Ni^{2+}. Values are expresses as the mean ± standard deviation of three independent determination. Different letters indicate significant differences (*p-value* < 0.05)..... 147
Figure 4.3. Study of peptide-Ni^{2+} interaction in SMPI hydrolysates using immobilized metal ion affinity chromatography (IMAC). (A-D) The isolation of Ni^{2+}-binding peptides of SMPI hydrolysates. 148
Figure 4.4. Ni^{2+}-binding peptides present in SMPI hydrolysates identified by the LC-MS/MS. (A-B) Effect of sequential enzymatic treatment and 1 kDa ultrafiltration on the number of Ni^{2+}-binding peptides identified in F2 fractions. (C) Peptide length profile of identified peptides. (D) AA frequency of Ni^{2+}-binding peptides identified. 151
Figure 4.5. Part I. Sequenced mass spectra of twelve different Ni^{2+}-binding peptides structures obtained from SMPI hydrolysates and processes by MaxQuant software. ATCUN motif-containing peptides identified: (A) LL**H**VT, (B) WL**H**, (C) SP**H** and (D) SP**HW**TIN 154
Figure 4.5. Part II. Sequenced mass spectra of twelve different Ni^{2+}-binding peptides structures obtained from SMPI hydrolysates and processes by MaxQuant software. His-containing peptide with His residue placed at second position from N and C-termini: (E) A**H**NLLY, (F) S**H**TVVY, (G) GAV**HW**, (H) GVDFIR**H**R. 155
Figure 4.5. Part III. Sequenced mass spectra of twelve different Ni^{2+}-binding peptides structures obtained from SMPI hydrolysates and processes by MaxQuant software. His-containing peptide with His residue placed at first position from N and C-termini: (I) **H**A**W**, (J) **H**NDGNTELVVVVF, (K) DFIR**H**, (L) SEVF**H**. 156
Figure 4.6. Study of the interaction of synthetic peptides and SMPI hydrolysates with nickel ions using switchSENSE® technology. 159
Figure 4.7. UV-visible and CD measurements of the peptide-Ni^{2+} interaction of pure peptides. (A-B) Pep11.**W**L**H**NDTE; (C-D) Pep13.FATCIAR**H**; (E-F) Pep21.**HHHHHH**..... 164
Figure 4.8. UV-visible and CD measurements of the SMPI hydrolysates (A-B) Prot; (C-D) Prot+Flav; (E-F) ≤ 1 kDa Prot; (G-H) ≤ 1 kDa Prot+Flav..... 165
Figure 4.9. Schematic representation of the 4N coordination mode of ATCUN peptide identified in Prot hydrolysates (WL**H**). This peptide motif WL**H** is present in two synthetic studied in the present work (Pep1.**W**L**H**NDGN, 2.**W**L**H**NDGNTE). 167
Figure 5.1. Molecular weight distribution of protein and peptides hydrolysates from SMPI. (A) SDS-PAGE profile (12.5 %) of sunflower meal, sunflower meal protein isolate, and whole

protein hydrolysates (Prot and Pro). (B) and (C) size exclusion chromatographic profile of sunflower meal protein isolate hydrolysates and their ≤ 1 kDa fractions. 183
Figure 5.2. (A) The process for generating reactive oxygen species (ROS) *via* the Fenton reaction cycle involves molecular oxygen and ascorbate in the presence of copper and iron ions. (B-C) The inhibition of Cu^{2+}/Fe^{3+}-induced ROS production by chelating copper assessed by measuring ascorbate absorbance intensity at 265 nm. 185
Figure 5.3. Antioxidant activities of Prot, Prot+Flav, ≤ 1 kDa Prot and ≤ 1 kDa Prot+Flav hydrolysates. Fe^{2+}-chelating activity (A), ABTS radical scavenging activity (C), and reducing power ability (E) as a function of hydrolysate concentration. Half efficient concentration EC_{50} (mg/mL) values determined for Fe^{2+}-chelating (B), ABTS radical scavenging (D), and reducing power activities (F). 189
Figure 5.4. The fractionation of Cu^{2+}-chelating peptides of sunflower meal protein isolate hydrolysates obtained by different enzymatic treatments. The unbounding (injection phase) and bound peptides (elution phase) present in Prot (A), Prot+Flav (B), ≤ 1 kDa Prot (C) and ≤ 1 kDa Prot+Flav (D). 191
Figure 5.5. Results obtained from the MS/MS identification of peptides present in sunflower meal protein isolate hydrolysates. (A) Number of peptides identified in F1, F2 and F3 fraction in whole and ≤ 1 kDa fraction hydrolysates. (B) and (C) amino acid composition of Cu^{2+}-chelating peptides identified in the F2 fractions of all the hydrolysates. 193
Figure 5.6. Sequenced mass spectra of eight different Cu^{2+}-chelating peptides structures obtained from sunflower meal protein isolate hydrolysates and processes by MaxQuant software. (A) **H**NDGNTELVVVVF (F2: Prot+Flav), (B) **H**VDQETASKL (F2: Prot), (C) SP**H**WTIN (F2: all the hydrolysates), (D) WV**H**NDGNAE (Prot) containing His residue in the first and third position from amino terminus. (E) ALFSP**H** (F3: Prot and ≤ 1 kDa Prot) (F) FSP**H** (F2: Prot+Flav) (G) GTA**H**WL (F3: Prot), (H) SEVF**H**VD (F2: Prot and Prot+Flav) containing His residue in the first and third position from carboxylate terminus. 195
Figure 6.1. Uv-visible and CD measurements of the peptide-Cu^{2+} interaction of different TSG hydrolysates. (A-B) Alc, (C-D) Alc+Flav, (E-F) ≤ 1 kDa Alc, (G-H) ≤ 1 kDa Alc+Flav. (I-J) Proposed modes of coordination for the copper chelating peptides present in the TSG hydrolysates based on CD data (adapted from Osz et al., 2002 and Sóvágó et al., 2012). 212
Figure 6.2. Cu^{2+}-chelating ability of different TSG hydrolysates determined with pyrocatechol violet assay. (A) Chelating ability as function of hydrolysate concentration. (B) EC_{50} values

expressed as the quantity (mg/mL) of hydrolysate that is required to chelated 50 % of Cu^{2+}. 214

Figure 6.3. Nano-LC-MS/MS identification of peptide sequences present in different TSG hydrolysates. (A) number of peptides identified, (B) percentage of lengths of identified peptides, (C) distribution of amino acid (AA) residues of identified peptides, (D) percentage of AA residue group types, (E) distribution of peptides isoelectric point (pI), and (F) distribution of hydropathicity GRAVY index. 217

Figure 6.4. Thioflavin T (ThT) intensity, surface hydrophobicity (S_o), particle size, polydispersity index (PDI) and particle size distribution of different TSG hydrolysates upon the Cu^{2+} complexation. (A) Thioflavin T (ThT) assay, (B) Surface hydrophobicity (S_o), (C) average particle size, (D-G) particle size distribution and (H) PDI values. 219

Figure 6.5. Effect of Cu^{2+} complexation on mechanical strength and viscoelastic behaviour study by amplitude sweeps and frequency sweeps measurements of different TSG hydrolysates. (A-D) amplitude sweeps, (E-H) frequency sweeps. G' and G'' are the elastic modulus and loss modulus, respectively. 222

Figure 6.6. Transmission electron microscopy (TEM) of TSG hydrolysates (only Alc+Flav and ≤ 1 kDa Alc) with and without Cu^{2+} ions..... 223

Figure 6.7. Alleviation of oxidative stress by EDTA, Alc, Alc+Flav, ≤ 1 kDa Alc and ≤ 1 kDa Alc+Flav hydrolysates in oxidation-damaged *C. elegans.* (A) Effects of Cu^{2+} coordination by EDTA and peptides present in TSG hydrolysates on ROS level in Cu^{2+}-exposed nematodes. L3-stage nematodes were treated with and without samples treatment (negative control nematodes) for 24 h at 22 ± 2 °C, and then exposed to 1 mM Cu^{2+} sulphate for another 12 h. (B)-(G) Representative images of Cu^{2+}-exposed L3-stage nematodes untreated control (only with Cu^{2+}), EDTA, Alc, Alc+Flav, ≤ 1 kDa Alc and ≤ 1 kDa Alc+Flav-treated groups captured by an Axiocam 506 camera. 226

Figure 7.1. UV-visible and CD measurements of the peptide-Cu^{2+} interaction of different SMPI hydrolysates. (A-B) Prot, (C-D) Prot+Flav, (E-F) ≤ 1 kDa Prot, (G-H) ≤ 1 kDa Prot+Flav. 243

Figure 7.2. Cu^{2+}-chelating ability of different SMPI hydrolysates determined with pyrocatechol violet assay. (A) Chelating ability as function of hydrolysate concentration. (B) EC_{50} values expressed as the quantity (mg/mL) of hydrolysate required to chelate 50 % of Cu^{2+}. 244

Figure 7.3. Part I. nano-LC-MS/MS identification of peptide sequences present in different SMPI hydrolysates. (A) total number of peptides identified, (B-C) ATCUN peptide sequences

identified in complex with Cu^{2+} ions by 4N coordination mode. (D) percentage of lengths of all identified peptides. 246
Figure 7.3. Part II, (E) distribution of amino acid (AA) residues of total identified peptides, (F) percentage of AA residue group types, (G) distribution of peptides isoelectric point (pI), and (H) distribution of hydropathicity GRAVY index. 247
Figure 7.4. Thioflavin T (ThT) intensity, surface hydrophobicity (S_o), particle size, polydispersity index (PDI) and particle size distribution of different SMPI hydrolysates upon the Cu^{2+} complexation. (A) Thioflavin T (ThT) assay, (B) Surface hydrophobicity (S_o), (C) average particle size, (D-G) particle size distribution and (H) PDI values. 251
Figure 7.5. Transmission electron microscopy (TEM) of whole SMPI hydrolysates (Prot and Prot+Flav) with and without Cu^{2+} ions. 254
Figure 7.6. Effect of Cu^{2+} complexation on mechanical strength and viscoelastic behaviour study by amplitude sweeps and frequency sweeps measurements of different SMPI hydrolysates. (A-D) amplitude sweeps, (E-H) frequency sweeps. G′ and G′′ are the elastic modulus and loss modulus, respectively. 256
Figure 7.7. Alleviation of oxidative stress by EDTA, Prot, Prot+Flav, ≤ 1 kDa Prot and ≤ 1 kDa Prot+Flav hydrolysates in oxidation-damaged *C. elegans.* (A) ROS level in Cu^{2+}-exposed nematodes. (B-G) L3-stage nematodes were treated with and without samples treatment (control nematodes) for 24 h at 22 ± 2 °C, and then exposed to 1 mM Cu^{2+} (200 µL) for another 12 h. 261

List of tables

Tabla 1.1. Metal-chelating peptides reported from different food protein sources. NA: not applied 52

Table 1.2. Biological relevance and deficiency symptoms of essential metal elements to the human body. 58

Table 1.3. Summary of assays used for determining iron and copper chelating activity of food protein hydrolysates. 67

Table 1.4. Overview of the absorption wavenumbers of the chemical groups associated to protein/peptides reported in literature. 78

Table 1.5. FTIR and UV-visible used for understanding of peptide-metal interaction. 79

Table 1.6. Thermodynamic parameters of reported peptide-metal interaction studies. n.s: no studied 82

Table 2.1. Responses of 2^{4-1} fractional factorial design for Tilapia scales gelatin extraction: crude protein content (%), free amino groups content (mmol Eq G/g) and protein extraction yield (%). Run 9-11: central points. 89

Table 2.2. Predicted and experimental values of crude protein content, free amino groups content and protein extraction yield obtained for Tilapia scales gelatin extracts. 98

Table 3.1. Peptide concentration of Tilapia scale flour (TSF), Tilapia scale gelatin (TSG) and Tilapia scale gelatin hydrolysates. 119

Table 3.2. Amino acids (AA) composition of TSG and its hydrolysates (g/100 g) given by amino acid and by amino acid class (hydrophobic, positively charged, negatively charged, aromatic, sulfur containing, essential and branch chain AA). 121

Table 3.3. Biofunctional properties of Tilapia scale gelatin hydrolysates and positive controls. 126

Table 4.1. Ni^{2+}-binding peptides identified from the F2 (elution phase) SMPI hydrolysates using IMAC-Ni^{2+} separation followed by LC-MS/MS analysis. 140

Table 4.2. Ni^{2+}-binding peptides identified from the F2 (elution phase) SMPI hydrolysates using IMAC-Ni^{2+} separation followed by LC-MS/MS analysis. 150

Table 4.3. Spectroscopic data for the peptide-Ni^{2+} complexes at 1:1 metal-to-ligand ratio at pH 7.4. 163

Table 5.1. The degree of hydrolysis (DH) and peptide concentration of hydrolysates prepared by different enzymatic treatments determined by OPA assay. 181
Table 5.2. Cu^{2+}-chelating peptides identified from the F2-F3 sunflower meal protein isolate hydrolysates fractions using IMAC- Cu^{2+} separation followed by LC-MS/MS analysis. 192
Table 6.1. Spectroscopic data for the peptide-Ni^{2+} complexes at 1:1 metal-to-ligand ratio at physiological pH 7.4. 213
Table 6.2. Potential Cu^{2+}-chelating peptides containing either His or Met residues obtained from nano-LC-MS/MS analysis. 216
Table 6.3. Effects of Cu^{2+} coordination by EDTA and peptides present in TSG hydrolysates on the lifespan-extension of Cu^{2+}-exposed nematodes. 225
Table 7.1. Spectroscopic data for the peptide-Cu^{2+} complexes at 1:4 metal-to-ligand ratio at physiological pH 7.4. 244
Table 7.2. Potential Cu^{2+}-chelating peptides containing His and Cys residues obtained from nano-LC-MS/MS analysis. 248
Table 7.3. Effects of Cu^{2+} coordination by EDTA and peptides present in SMPI hydrolysates on the lifespan-extension of Cu^{2+}-exposed nematodes. 259

List of appendices

Appendix 2.1. The employed design (FFD 2^{4-1}) fits a first-order polynomial model (Sepian et al., 2019) (Equation. (1)).....303

Appendix 2.2. Steps carried out in rheology experiments with their respective conditions 304

Appendix 2.3. Pareto charts for CPC (A), FAG content (B) and PEY (C). A: Solvent-to-solid ratio; B: extraction time; C: temperature; D: ultrasound time; FAG: free amino groups; PEY: protein extraction yield. CPC: crude protein content. Orange bars: positive effects. Blue bars: negative effects. Higher bars: higher impact on the response.....305

Appendix 2.4. ANOVA analysis of fractional experimental design of gelatin protein extraction on the three investigated responses.....307

Appendix 2.5. Multiple regression modelling.....308

Appendix 2.6. CD spectra of gelatin extracts prepared using different extraction conditions. 309

Appendix 2.7. Rheological properties of the most interesting gelatin extracts (Run 1, 8, 9 and optimal run). (a, c, e, g) Changes in the elastic (G') and loss (G'') moduli during cooling (50 to 10 °C) for run 1, run 8, run 9 and optimal one, respectively. (b, d, f, h) Changes in the elastic (G') and loss (G'') moduli during heating (10 to 50 °C) for run 1, run 9, optimal run and run 8, respectively (I and j). 310

Appendix 2.8. Changes in the phase angle during cooling (50-10 °C) and heating (10-50 °C), respectively. 311

Appendix 3.1. CAS numbers of chemicals and reagents. 312

Appendix 3.2. Tilapia scale gelatin extraction process set up in this study. 313

Appendix 3.3. Composition of stacking and separation gels used in SDS-PAGE experiments. 314

Appendix 3.4. Size Exclusion Chromatography 315

Appendix 3.5. Amino acid composition.....316

Appendix 3.6. Protein data base used for peptide identification 317

Appendix 3.7. Parameters of database searches used for peptide identification 318

Appendix 3.8. MaxQuant™ identification successfully carried out on a synthetic mixture containing 8 peptides at 1 mM: MS/MS spectra show y ions (red peak), b ions (blue peaks),

and ions resulting from loss of water or ammonia of b and y ions (orange peaks). A) GHR, (B) GHRGFSGL, (C) KGHR, (D) KGHRGF, (E) GHRGF, (F) KHV, (G) RGMKGH, (H) RGMKGHR. 319
Appendix 3.9. Biofunctional properties of red Tilapia scale gelatin hydrolysates. (A) iron-chelating activity, (B) ABTS scavenging activity, (C) ACE inhibition activity. 320
Appendix 3.10. Antimicrobial activity 321
Appendix 3.11. Antimicrobial activity of sodium benzoate, whole Tilapia scale gelatin hydrolysates, and their 1 kDa fractions. 322
Appendix 3.12. MS Peptides sequences identified from Alc, Alc+Flav, ≤ 1 kDa Alc and ≤ 1 kDa Alc+Flav hydrolysates. 326
Appendix 4.1. 11S globulin seed storage protein G3, 55.687 kDa, 493 amino acids. 330
Appendix 4.2. The peptide concentration and degree of hydrolysis (DH) of hydrolysates prepared by different enzymatic treatments determined by OPA assay. 331
Appendix 4.3. Protein data base used for peptide identification from *Helianthus annuus* (Common sunflower). 332
Appendix 4.4. Parameters of database searches used for peptide identification. 333
Appendix 4.5. Sequenced mass spectra of metal-binding peptides structures from a synthetic peptides hydrolysate composed of 8 pure peptides obtained from 11S globulin seed storage protein G3 (P19084) and processes by MaxQuant software. (A) AIPTGTA**H,** (B) FATCIAR**H**, (C) KFPILE**H**, (D) KFPILE**H**L, (E) KFPILE**H**LR, (F) WL**H**NDGN, (G) WL**H**NDGNTE and (H) **W**VSFKTN. 334
Appendix 4.6. Unbound peptides sequences identified from Prot, Prot+Flav, ≤ 1 kDa Prot and ≤ 1 kDa Prot+Flav hydrolysates. 335
Appendix 4.7. Kinetic study between metal-binding peptides and nickel ions using switchSENSE® technology. (A-K**)** association rate (k_{on}) of binding kinetic studies of pure metal-chelating peptides. 340
Appendix 4.8. Kinetic study between metal-binding peptides present in SMPI hydrolysates and nickel ions using switchSENSE® technology. (A-D**)** association rate (k_{on}) of binding kinetic studies of metal- binding peptides. 341
Appendix 5.1. Peptides sequences identified from the F1 fractions (unbounding peptides) of sunflower meal protein hydrolysates fractions using IMAC-Cu^{2+} separation followed by LC-MS/MS analysis. 342

Appendix 6.1. The peptide concentration and degree of hydrolysis (DH) of hydrolysates prepared by different enzymatic treatments determined by OPA assay. 348
Appendix 6.2. Peptides sequences identified from ≤ 1 kDa fractions of Tilapia scale gelatin hydrolysates using nano-LC-MS/MS analysis. 349
Appendix 6.3. Effects of Cu^{2+} coordination by EDTA and peptides present in TSG hydrolysates on the lifespan-extension of Cu^{2+}-exposed nematodes. 352
Appendix 7.1. Peptides sequences identified from ≤ 1 kDa fractios of sunflower meal protein hydrolysates using nano-LC-MS/MS analysis. 353
Appendix 7.2. His and Cys-contanig peptides sequences identified from ≤ 1 kDa fractios of sunflower meal protein hydrolysates using nano-LC-MS/MS analysis. 366
Appendix 7.3. Sequenced mass spectra of six different ATCUN-binding peptides structures obtained from SMPI hydrolysates and processes by MaxQuant software. (A) AV**H**WTY, (B) KG**H**LQPN, (C) NE**H**KLPIL, (D) QY**H**PGQQ, (E) SE**H**IQGQ, (F) VD**H**ETAE. 369
Appendix 7.4. Effects of Cu^{2+} coordination by EDTA and peptides present in SMPI hydrolysates on the lifespan-extension of Cu^{2+}-exposed nematodes. 370

List of abbreviations

AA: Amino acid
AAA: Aromatic amino acids
AAE: Ascorbic acid equivalent
ACE: Angiotensin I-converting enzyme
Adeq Precision: Adequate precision
Alc: Alcalase®
Alc+Flav: Alcalase® followed by Flavourzyme®
ANOVA: Analysis of variance
ANS: 8-anilino-1-naphthalenenesulfonic acid
$AscH^-$: Ascorbate
ATCUN: Amino terminal Cu(II) and Ni(II)-binding
ECT: EDTA complexing titration
BAPs: Bioactive peptides
BCAA: Branched chain amino acids
CD: Circular dichroism spectroscopy
cDNA-NTA: Second complementary strand
C. elegans: *Caenorhabditis elegans*
CLSM: Confocal laser scanning microscopy
cp: Crossover point
CPC: Crude protein content
CV: Column volumes
CT: Charge transfer transition
DCF: 2',7'-dichlorofluorescin diacetate
d-d transition: d level to another d level
DFO: Desferrioxamine
DH: Degree of hydrolysis
D_H : Hydrodynamic diameter
DLS: Dynamic light scattering
d.m: Dry matter
DR: Dynamic response
ΔDR: Relative changes in DR
EAA: Essential amino acids
EC_{50}: Half maximal effective concentration
EDTA: Ethylenediaminetetraacetic acid
ESI: Electrospray ionization
FAAS: Flame atomic absorption spectrophotometry
FAG: Free amino group content
FAO: Food and Agriculture Organization
FFD: Fractional factorial design
Flav: Flavourzyme®
FAPGG: N-[3- (2-Furyl) acryloyl]-Phe-Gly-Gly
FTIR: Fourier-transform infrared spectroscopy

ΔF: Relative changes in fluorescence
G1: First generation
G2: Second generation
G3: Third generation
G': Elastic modulus
G'': Loss modulus
GPC: Gel permeation chromatography
GRAVY: Grand average of hydropathicity
HAA: Hydrophobic amino acids
HSAB: Hard and Soft Acid Bases
IC_{50}: Half inhibitory concentration
IDA: Iminodiacetic acid
IEC: Ion exchange chromatography
IMC: Imidazole concentration
ISE: Ion selective electrode
IMAC: Immobilized metal-ion affinity chromatography
ITC: Isothermal titration calorimetry
K_A: Affinity constant
K_D: Dissociation constant
k_{obs}: Observed rate kinetic constant
k_{Off}: Dissociation kinetic constant
k_{On}: Association kinetic constant
LMWA: Low molecular weight aggregates
M: Protein marker
MCPs: Metal-chelating peptides
MS: Mass spectrometry
MS/MS: Tandem mass spectrometry
MW: Molecular weight
MWCO: Molecular weight cut-off
MTs: Metallothioneins
NCAA: Negatively charged amino acids
NGM: Nematode growth medium
NTA: Nitriloacetic acid
OPA: *o*-phthalaldehyde
***o*-CPC:** *Ortho*-cresolphthalein complexone
PCAA: Positively charged amino acids
PCs: Phytochelatins
PDA: Photodiode array detector
PEG: Polyethyleneglycol
PDI: Polydispersity index
Pep1: WLHNDGN
Pep2: WLHNDGNTE
Pep3: FATCIARH
Pep4: WVSFKTN

Pep5: AIPTGTAH
Pep6: KFPILEH
Pep7: KFPILEHL
Pep8: KFPILEHLR
Pep9: GNPQ
Pep10: LLAF
Pep11: HHHHHH
PEY: Protein extraction yield
pI: Isoelectric point
PV: Pyrocatechol violet
qsf: Quantity sufficient for
REF: Reference electrode
R_{max}: Maximal response
ROS: Reactive oxygen specie
RP-HPLC: Reverse phase high performance liquid chromatography
RT: Retention time
SCAA: Sulfuric contanining amino acids
SD: Standard deviation
SDS-PAGE: Sodium dodecyl sulfate polyacrylamide gel electrophoresis
ssDNA: Single strand DNA
SEC: Size exclusion chromatography
SM: Sunflower meal
SMPI: Sunflower meal protein isolate
SPR: Surface plasmon resonance
ΔSI: Binding size index
TCA: Trichloroacetic acid
TEAC: Trolox equivalent antioxidant capacity
TEM: Transmission electron microscopy
ThT: Thioflavin T
Trolox: 6-hydroxy-2,5,7,8-tetramethylchroman-2-carboxylic acid
TSF: Tilapia scale flour
TSG: Tilapia scale gelatin
TSGH: Tilapia scale gelatin hydrolysate
UF: Ultrafiltration
UV-vis: Ultraviolet-visible spectroscopy
≤ 1 kDa: Ultrafiltrated hydrolysate

Resumé de la thèse en Français

1. Contexte sociétal et objectif de cette thèse

L'aquaculture et l'agriculture contribuent largement à la production alimentaire mondiale. Cependant, ces industries génèrent de grandes quantités de déchets, qui sont souvent rejetés sans aucun traitement, ce qui entraîne des problèmes environnementaux (Singh et al., 2019).

L'aquaculture est l'une des industries à la croissance la plus rapide dans la production alimentaire mondiale, fournissant une source importante de protéines pour l'alimentation humaine. Selon FAO, (2024) la production aquacole a été estimée à plus de 223,2 millions de tonnes en 2022, dont 50 à 70 % considérés comme des déchets. De même, environ 1,3 milliard de tonnes de déchets sont générés chaque année au cours de la transformation des ressources agricoles (Greses et al., 2020). La communauté scientifique s'intéresse donc de plus en plus à la recherche d'utilisations alternatives pour les co-produits agro-industriels, afin de les valoriser et de réduire leur impact environnemental.

Les écailles de poisson tilapia rouge (*Oreochromis spp.)* et le tourteau de tournesol sont des co-produits de l'industrie agroalimentaire. Le tilapia est le troisième poisson d'élevage le plus répandu au monde (Ngo et al., 2010). Pourtant, dans les usines de transformation du poisson, les écailles, l'un des principaux déchets de la transformation du poisson, sont souvent rejetées lors de la récupération des filets de poisson (Weng & Wu, 2015). À ce jour, environ 50 000 tonnes de d'écailles sont produites chaque année dans le monde entier, au cours de la transformation des poissons (Wang et al., 2020). Principalement composées de protéines de collagène (30-50%) et de minéraux tel que l'hydroxyapatite (Ca_5 $(PO)_{43}$ OH) (30-40 %), les écailles de poisson constituent un co-produit d'intérêt, notamment pour l'extraction de gélatine (Lin et al., 2020). D'autre part, le tournesol (*Helianthus annuus* L.) est le troisième oléagineux le plus produit au monde, après le soja et le colza, avec une production totale de 53.5 millions de tonnes en 2019 (Náthia-Neves & Alonso, 2022). Après l'extraction d'huile issue de graines de tournesol, le tourteau résiduel contient environ 30 à 50% de protéines, avec une production mondiale de 22,3 tonnes en 2019-2020 (Efthymiou et al., 2021).

En raison de leur teneur élevée en protéines, diverses alternatives ont été explorées au cours des dernières décennies afin d'utiliser ces co-produits agro-industriels, notamment en tant

qu'aliments pour bétail, agents fertilisants, production d'ensilage, ainsi que divers produits cosmétiques, sanitaires, vétérinaires, médicinaux, fonctionnels ou nutraceutiques (Chalamaiah et al., 2019 ; Villamil et al., 2017). Parmi les produits médicinaux ou fonctionnels, les peptides bioactifs (**PBA**) obtenus à partir de l'hydrolyse de protéines sont des composés biologiques, naturellement cryptés dans la séquence de protéines sous une forme inactive et libérés lors de la protéolyse. Aujourd'hui, ces peptides suscitent un intérêt du fait leurs nombreuses activités biologiques et fonctionnelles rapportées dans la littérature, telles que les propriétés antioxydantes, immunomodulatrices, antihypertensives, anticancéreuses, anti-inflammatoires, antimicrobiennes, hypo-cholestérolémiques, antidiabétiques et de chélation des métaux (Liu et al., 2020). Les peptides fonctionnels et bioactifs sont dérivés soit de matrices d'origine animale (*e.g.,* le lait, les œufs, la viande et le poisson), soit de végétaux tels que le soja, le blé et de nombreuses autres légumineuses (Lorenzo et al., 2018). Dans une stratégie de bioéconomie, les sources de protéines provenant de co-produits végétaux et agro-industriels suscitent actuellement un engouement (Hadnadjev et al., 2017). En effet, ces co-produits présentent un intérêt énorme pour la production de peptides biofonctionnels et bioactifs - tels que les peptides chélateurs de métaux (**PCM**) - en raison de leur teneur élevée en protéines et de leur valeur ajoutée potentielle élevée après protéolyse (Tonolo et al., 2024).

Plusieurs études ont rapporté la découverte de peptides bioactifs à partir de protéines d'écailles de poisson telles que le poisson-lait (Huang et al., 2018), la carpe herbivore (Chen et al., 2019), la bonite à ventre rayé (Qiu et al., 2019) et la sole (Viji et al., 2019). De même, diverses protéines d'origine végétale ont été rapportées, parmi lesquelles les protéines de colza (Xie et al., 2015), de noix (Lv et al., 2017) ou encore de graines de chia (Latha et al., 2021). Néanmoins, à ce jour, peu de données sont disponibles dans la littérature en ce qui concerne la production de PCMs à partir d'hydrolysats de protéines, obtenus soit à partir de gélatine extraite d'écailles de tilapia rouge ou de protéines extraites de tourteau de tournesol. De plus, à la connaissance de l'auteur, peu de choses sont connues dans la littérature concernant l'utilisation de l'hydrolyse enzymatique séquentielle pour produire des PCMs à partir de la gélatine de poisson ou de protéines extraites de tourteau de tournesol, notamment en utilisant l'Alcalase®/ la Protamex® suivie de la Flavourzyme®. Étant donné que l'Alcalase® et la Protamex® sont des endopeptidases censées améliorer l'action ultérieure de la

Flavourzyme® (mélange enzymatique d'endo et exopeptidases) en augmentant le nombre de sites N-terminaux, nous avons émis l'hypothèse qu'un traitement enzymatique séquentiel (Alcalase®/Protamex® suivi de Flavourzyme®) pourrait améliorer les propriétés biofonctionnelles des hydrolysats dérivés de co-produits agro-industriels. De plus, malgré un grand nombre d'études concernant l'induction de l'auto-assemblage de peptides de synthèse lors de la coordination d'ions métalliques, l'intérêt que présente la coordination du Cu^{2+} pour générer des biomatériaux supramoléculaires bioactifs à partir de peptides auto-assemblés d'origine alimentaire (**SAPs**) n'a pas encore été exploité à ce jour. Ainsi, dans une stratégie de bioéconomie, l'objectif global de ce travail de thèse a été d'étudier l'utilisation de co-produits tels que les écaille de poisson (tilapia rouge) et le tourteau de tournesol comme sources potentielles de protéines afin de produire des PCMs multifonctionnels, via des traitements enzymatiques simples ou séquentiels, en mettant en place plusieurs techniques de criblage, de séparation et de caractérisation *in vitro*. De plus, ce travail de thèse s'est intéressé à l'effet de la coordination du Cu^{2+} sur la production de biomatériaux à base de peptides auto-assemblés, d'origine alimentaire, et dotés de propriétés antioxydantes *in vivo*.

2. Approche scientifique

Cette thèse de doctorat a étudié le potentiel que présentent les co-produits tels que les écailles de tilapia et le tourteau de tournesol afin de produire des PCMs. Ce travail de thèse a été divisé en trois sections et sept chapitres (Fig. 0.1). Dans un premier temps, une revue bibliographique a été rédigée concernant le criblage, la séparation et l'identification de peptides chélateurs de métaux (PCMs) pour des applications nutritionnelles, cosmétiques et pharmaceutiques (**chapitre 1**; Camaño Echavarría et al., 2024). La deuxième section s'est concentrée sur l'utilisation de co-produits tels que les écailles de tilapia et le tourteau de tournesol comme sources de protéines pour la production ultérieure de PCMs. Dans une première sous-section (2.1), nous avons exploré l'optimisation de l'extraction de la gélatine, une protéine extraite de des écailles de poisson tilapia (**chapitre 2**) et l'utilisation potentielle de cette protéine afin de produire des PCMs par protéolyse (**chapitre 3**). Parallèlement, dans la sous-section 2.2, l'utilisation de tourteau de tournesol a été étudiée afin de produire des PCMs. Ainsi, dans les **chapitres 4** et **5**, les hydrolysats de protéines – produits à partir de protéines extraites de tourteau de tournesol - ont été caractérisés puis fractionnés par chromatographie IMAC (IMAC-Ni^{2+} et Cu^{2+}) ; cette étape a été suivie d'une identification de

séquences peptidiques par analyse LC-MS/MS. Par la suite, la section 3 (**chapitres 6 et 7**) a cherché à exploiter à la fois la biofonctionnalité/bioactivité des hydrolysats protéiques (hydrolysat de gélatine et de protéines de tournesol) et les propriétés d'auto-assemblage de ces hydrolysats peptides. Pour atteindre cet objectif, la coordination du Cu^{2+} a été étudiée comme une approche non conventionnelle afin de générer diverses nanostructures auto-assemblées bioactives, à base de peptides, et dotées de propriétés mécaniques améliorées. Enfin, la conclusion générale reprenant les principaux résultats de cette thèse, ainsi que les perspectives à court et à long terme ont été présentées.

3. Principaux résultats

3.1. Les peptides chélateurs de métaux dans la littérature

Les peptides chélateurs de métaux, qui forment des complexes de coordination métal-peptide avec divers ions métalliques, peuvent être utilisés comme ingrédients biofonctionnels, notamment pour améliorer la santé humaine et prévenir certaines maladies. Le **chapitre 1** (revue bibliographique) présente les connaissances récentes sur les peptides chélateurs de métaux d'origine alimentaire, les stratégies mises en œuvre pour leur découverte, leur étude et leur identification. Après avoir établi les propriétés générales des peptides chélateurs de métaux, leur production à partir de différentes sources de protéines alimentaires ainsi que leurs applications potentielles ont été examinées et discutées, en particulier dans les domaines de la nutrition, de la cosmétique et de la pharmaceutique. De plus, cette revue bibliographique a donné un aperçu des progrès réalisés au cours des dernières décennies dans la découverte de peptides chélateurs de métaux obtenus par hydrolyse de protéines d'origine alimentaire, et en abordant les différentes méthodologies permettant leur criblage, leur séparation et leur identification. En outre, cet état de l'art sur le sujet a mis l'accent sur les techniques utilisées pour évaluer l'interaction peptide-métal, permettant de mieux comprendre les paramètres physico-chimiques et thermodynamiques associés à la formation de complexes de coordination peptide-métal, ainsi que les résidus d'acides aminés spécifiques impliqués dans la coordination des métaux.

3.2. Valorisation des écailles de poisson tilapia

Bien que de nombreux co-produits agro-industriels aient été signalés comme sources de protéines pour la production de PCMs à partir d'hydrolysats de protéines, à ce jour, peu de données bibliographiques portent sur l'utilisation de gélatine extraite à partir d'écailles de

tilapia rouge. L'obtention d'un isolat de protéines (> 85 % en masse) est fondamentale pour produire des PCMs à partir d'hydrolysats de protéines, ces protéines étant elles-mêmes extraites à partir de co-produits agro-industriels. En effet, les propriétés de l'hydrolysat protéique résultant, contenant des PCMs potentiels, dépendront principalement de la pureté de la protéine utilisée lors de l'hydrolyse et de sa séquence en acides aminés. Ainsi, après avoir compris les principes fondamentaux de la production de MCPs (**chapitre 1)**, le procédé d'extraction des protéines de gélatine à partir d'écailles de tilapia (**TSG**) a été optimisé à l'aide d'une méthodologie de plan factoriel fractionnaire dans le **chapitre 2**. L'effet du rapport solvant-solide (A), du temps d'extraction (B), de la température (C) et du temps d'utilisation des ultrasons (D) a été étudié sur la teneur en protéines extraites (**CPC**) et en groupes d'acides aminés libres (**FAG**) ainsi que sur le rendement d'extraction des protéines (**PEY**). En outre, les extraits de TSG les plus intéressants ont été étudiés par SDS-PAGE et par rhéométrie afin de déterminer, respectivement, leur profile protéique et leurs propriétés viscoélastiques. La teneur en protéines extraites (CPC) a légèrement varié entre 95,4 et 99,2% en fonction de facteurs étudiés, correspondant ainsi au CPC d'un isolat de protéines (> 85 %). Selon le procédé utilisé lors de l'extraction de la gélatine, la teneur en FAG variait entre 0,23 et 0,31 mmol Eq G/g et était fortement influencée par la température (C) et le temps d'extraction (B). Nous avons mis en évidence que lors d'un procédé hydrothermique, le collagène présent dans la farine d'écailles de poisson tilapia rouge était partiellement hydrolysé en gélatine, conduisant à une augmentation de la teneur en FAG. Bien que l'hydrolyse du collagène puisse également être augmentée par des ultrasons, nos résultats n'ont montré qu'une légère amélioration de la teneur en FAG (sans et avec ultrasons : 0,28 et 0,31 mmol Eq G/g, respectivement). Quel que soit le procédé utilisé pour l'extraction de la gélatine, le rendement d'extraction en protéines (**PEY**), exprimé en g de protéines extraites/100 g de protéines présentes dans la farine d'écailles de Tilapia, a varié de 31,9 à 48,5 %. En effet, le rendement d'extraction en protéines a augmenté avec le rapport solvant/solide, étant donné qu'une augmentation du substrat (rapports inférieurs) a entraîné une augmentation de la viscosité, ralentissant ainsi les transferts de masse et de chaleur, nécessaires à l'extraction de protéines. L'optimisation du procédé a montré que les réponses maximales de la teneur en FAG et du PEY étaient obtenues pour un rapport solvant-solide fixé à 10 mL/g, une durée d'extraction de 3 h et une température de 85 °C sans ultrasons, tandis que la teneur en protéines brutes restait élevée. De plus, le profil optimal en électrophorèse (SDS-PAGE) de la gélatine était

similaire à celui du collagène standard de type I, largement rapporté dans les co-produits issus de la transformation du poisson, avec des chaînes β et α comme composants principaux. Ces chaînes β et α ont fourni des propriétés physico-chimiques et viscoélastiques appropriées, rendant la gélatine extraite à partir des écailles de tilapia rouge adaptée pour des applications alimentaires et pharmaceutiques ou encore pour la production de peptides bioactifs.

Compte tenu des propriétés physico-chimiques intéressantes de l'isolat de gélatine obtenu à partir d'écailles de tilapia rouge (en particulier la teneur en protéines et la quantité de groupes aminés libres) et du peu de données concernant son utilisation pour la production d'hydrolysats protéiques à l'aide d'enzymes, notre attention s'est ensuite portée sur la production d'hydrolysats de gélatine. Ainsi, l'objectif du **chapitre 3** a été d'utiliser la gélatine - protéine extraite des écailles du tilapia rouge (*Oreochromis spp*.) - pour produire un hydrolysat protéique, contenant potentiellement des peptides chélateurs de métaux, et d'étudier les propriétés biofonctionnelles et bioactives de ces hydrolysats. La gélatine a été soumise à trois traitements enzymatiques (Alcalase®, Flavourzyme®, ou Alcalase® suivi de Flavourzyme®) afin d'étudier les propriétés biofonctionnelles des hydrolysats en fonction de leurs propriétés physico-chimiques. Ensuite, les deux hydrolysats présentant le plus d'intérêt, générés soit par un seul traitement enzymatique (**Alc**), soit par un traitement enzymatique séquentiel (**Alc+Flav**), ont été ultrafiltrés sur une membrane ayant un seuil de coupure de 1 kDa. L'hydrolysat Alc+Flav a montré un degré d'hydrolyse plus élevé (**DH** : 29,74 ± 1,29 %) que l'Alc (19,70 ± 1,08 %). A noter que l'Alcalase® est une endopeptidase caractérisée par une très large spécificité dans le clivage des peptides alors que le Flavourzyme® est un mélange de huit endo et exopeptidases produites par *Aspergillus oryzae*. Dans notre étude, les endopeptidases contenues dans l'Alcalase® ont augmenté le nombre de sites N-terminaux disponibles dans l'hydrolysat de TSG, favorisant ainsi l'activité protéolytique ultérieure des exopeptidases présentes dans la Flavourzyme®. Par conséquent, l'hydrolysat de TSG traité préalablement par l'Alcalase® a constitué un substrat favorable. L'hydrolysat traité de manière séquentielle, caractérisé par un grand nombre de peptides de petite taille, a montré la plus grande capacité de liaison aux métaux (Ni^{2+}) par l'analyse switchSENSE®. Sa capacité de chélation des métaux a été associée à des propriétés antioxydantes élevées (piégeage des radicaux libres et pouvoir réducteur). Après ultrafiltration sur une membrane de 1 kDa, les deux fractions inférieures à 1 kDa on présenté des propriétés de chélation du Fe^{2+} plus élevées que les hydrolysats entiers

correspondants. Les deux hydrolysats entiers et leurs ultrafiltrats respectifs ont montré une activité inhibitrice de l'enzyme de conversion de l'angiotensine I (ACE) dans la gamme rapportée pour les hydrolysats de peptides d'origine alimentaire. La fraction d'hydrolysat ≤ 1 kDa produite par l'Alcalase® a permis d'obtenir des peptides chélateurs de Fe^{2+} de petite taille, avec une activité inhibitrice de l'ACE appropriée. En outre, la fraction d'hydrolysat obtenue par un traitement séquentiel (*i.e.*, Alcalase® suivi de Flavourzyme®) ≤ 1 kDa a produit de manière efficace des peptides chélateurs de Ni^{2+} de petite taille, dotés de propriétés antioxydantes. L'analyse LC-ESI-MS/MS a confirmé la présence de séquences peptidiques contenant les résidus Asp, Glu, Ser, Lys et Arg, qui pourraient offrir des propriétés chélatrices de métaux et antioxydantes.

3.3. Valorisation de tourteau de tournesol

Afin d'approfondir les concepts introduits précédemment pour la production de peptides biologiquement actifs à partir d'hydrolysats de protéines dérivés de co-produits, nous avons également exploré la valorisation des tourteaux de tournesol (**SM**) en tant que source potentielle de protéines pour la production d'hydrolysats protéiques, contenant potentiellement des PCMs. Bien que des données de la littérature aient montré la capacité des hydrolysats de protéines extraites de tourteau de tournesol à chélater les ions métalliques, il n'existe qu'une compréhension limitée des séquences peptidiques impliquées dans ces phénomènes et de la manière dont le mécanisme de complexation des métaux par les peptides se produit. Etant donné que de nombreuses études se sont déjà concentrées sur l'optimisation de l'extraction de protéines à partir de tourteau de tournesol, le **chapitre 4** a directement approfondi le criblage de ces peptides biofonctionnels cibles, à partir d'hydrolysats obtenus à partir d'isolat de protéines extraites de tourteau de tournesol (**SMPI**). Dans ce contexte, nous nous sommes intéressés plus particulièrement aux peptides chélateurs de nickel. Avec de nombreux effets physiologiques sur les organismes vivants, le nickel peut induire un stress oxydatif en raison de la participation du couple redox Ni^{2+}/Ni^{3+} dans les réactions de Fenton/Haber-Weiss. Ainsi, en complexant le Ni^{2+}, les PCMs pourraient prévenir les maladies chroniques associées aux dommages oxydatifs. Ainsi, dans le **chapitre 4**, l'objectif a été d'étudier la capacité des hydrolysats de SMPI et de dix peptides synthétiques (potentiellement présents dans les protéines de tournesol) à former des liaisons avec le Ni^{2+}. Pour cela, le switchSENSE® et l'IMAC, ont été utilisées afin de cribler/séparer la présence de

PCM dans les hydrolysats ; par la suite, la spectroscopie UV-vis et le dichroïsme circulaire ont permis de décrire les modes de coordination et les sites de liaison possibles. Tout d'abord, un isolat de protéines de tournesol a été obtenu par extraction à l'aide d'une précipitation au point isoélectrique. Ensuite, deux traitements enzymatiques (Protamex®, **Prot** ; et Protamex® suivi de Flavourzyme® **Prot+Flav**) ont été appliqués afin de produire deux hydrolysats entiers et leur fraction ≤ 1 kDa, obtenue suite à une étape d'ultrafiltration. Comme pour les peptides purs contenant de l'His, la capacité de liaison au Ni^{2+} de tous les hydrolysats était presque identique en IMAC-Ni^{2+} (temps de rétention similaire). L'analyse LC-ESI-MS/MS des fractions enrichies de peptides liant le Ni^{2+} a révélé que parmi tous les hydrolysats étudiés, plusieurs séquences peptidiques contenaient des résidus His, localisés à différentes positions par rapport aux extrémités N- et C- terminales. Néanmoins, les séquences de liaison au Ni^{2+} les plus intéressantes étaient caractérisées par leur motif "ATCUN" (*i.e.,* WL**H** et LL**H**VT). De plus, les études réalisées à l'aide du switchSENSE® ont montré que la capacité à lier le Ni^{2+} des peptides issus du tournesol ne dépendait pas seulement de la présence en résidus His, mais également de leur position au sein de la chaîne polypeptidique ainsi que de la présence de proline, suggérant que les hydrolysats Prot présentaient la capacité la plus élevée de se lier au Ni^{2+}. Les données en spectroscopie UV-vis et CD ont confirmé que les peptides issus de tournesol se liaient au Ni^{2+} par l'intermédiaire de l'azote de la chaîne latérale de l'imidazole des résidus His et des liaisons amides déprotonées, indiquant des géométries octaédriques et plan-carrées des complexes formés. Les peptides contenant des résidus His mais dépourvus de proline pourraient constituer une stratégie appropriée pour produire des peptides chélateurs de métaux à partir de tourteau de tournesol, les motifs les plus prometteurs étant LL**H**VT et WL**H**.

Après avoir démontré le potentiel du tourteau de tournesol pour produire des peptides chélateurs de Ni^{2+} (**chapitre 4**), le **chapitre 5** a eu pour objectif de décrire les propriétés physico-chimiques et la large gamme d'activités antioxydantes liées aux propriétés de complexation de métaux des hydrolysats produits à partir de SMPIDeux traitements enzymatiques (Protamex®, **Prot**; et Protamex® suivi de Flavourzyme* , **Prot+Flav**) ont été appliqués sur l'isolat de protéines de tournesol afin de produire des hydrolysats entiers et leur fraction ≤ 1 kDa. Les propriétés physicochimiques de ces différents hydrolysats (entiers ou ultrafiltrés) ont été caractérisées. Diverses analyses ont été effectuées, notamment la

quantification à l'OPA, la détermination de profils peptidiques en SDS-PAGE et par la chromatographie d'exclusion de taille (**SEC**), les tests d'ascorbate (Cu^{2+}/Fe^{3+}), la chélation du Fe^{2+}, le piégeage du radical ABTS et les tests de pouvoir réducteur. En outre, sur la base de nombreuses similitudes déjà décrites entre les processus de complexation des ions Ni^{2+} et Cu^{2+}, les peptides chélateurs de Cu^{2+} présents dans les hydrolysats de SMP ont été fractionnés à l'aide de IMAC-Cu^{2+}. Les peptides présents dans les fractions collectées ont ensuite été identifiés par spectrométrie de masse (LC-MS/MS) afin d'établir une relation entre leur séquence et leurs propriétés antioxydantes liées à leurs capacités à complexer les métaux. Lors du traitement séquentiel, une grande quantité de liaisons peptidiques a été coupée, libérant principalement des peptides de petite taille. Les hydrolysats Prot obtenus ont montré les propriétés les plus élevées, à la fois en ce qui concerne la chélation du Fe^{2+}, l'inhibition de la production d'espèces réactives de l'oxygène (**ROS**) induite par le Cu^{2+} et les activités de piégeage de l'ABTS. En outre, l'hydrolyse séquentielle a amélioré la capacité à inhiber la production de ROS induite par le Fe^{3+} ainsi que le pouvoir réducteur. Toutes les séquences peptidiques identifiées par LC-MS/MS à partir des fractions retenues en IMAC-Cu^{2+} contenaient au moins un résidu histidine, jouant un rôle crucial dans la liaison avec le Cu^{2+}. En outre, Asp, Glu et Arg ont été identifiés comme d'autres résidus d'acides aminés potentialisant les propriétés chélatrices de métaux et antioxydantes des hydrolysats étudiés.

3.4. Combinaison de la bioactivité et des propriétés d'auto-assemblage des peptides

Outre leurs propriétés biofonctionnelles, les peptides d'origine alimentaire peuvent s'auto-assembler en nanostructures organisées, grâce à un processus spontané et réversible, ce qui leur confère un potentiel d'utilisation élevé, dans un large éventail d'applications nutraceutiques, cosmétiques et biomédicales.

Aujourd'hui, la combinaison de la bioactivité et des propriétés d'autoassemblage des peptides d'origine alimentaire est devenue un sujet d'actualité en recherche en vue de développer de nouveaux nanomatériaux biofonctionnels. En particulier, la coordination des ions métalliques constitue une approche novatrice pour ajuster l'auto-assemblage de peptides afin de produire des biomatériaux à base de peptides et dotés de fonctions biologiques potentielles liées à la présence de ces peptides. Toutefois, à ce jour, cette approche n'a pas été exploitée avec des hydrolysats produits à partir de protéines d'origine alimentaire. Par conséquent, suite aux conclusions du **chapitre 3** - démontrant le potentiel des peptides présents dans les hydrolysats

de TSG pour coordinner les ions métalliques -, le **chapitre 6** a évalué l'effet de la coordination des ions métalliques pour induire l'auto-assemblage de peptides et étudier leurs propriétés antioxydantes *in viv*o, chez *Caenorhabditis elegans,* en tant qu'organisme modèle. Deux traitements enzymatiques (Alcalase®, **Alc** ; et Alcalase® suivi de Flavourzyme®, **Alc+Flav**) ont été utilisés afin de préparer des hydrolysats entiers et leur fraction ≤ 1 kDa suite à une étape d'ultrafiltration. La capacité des hydrolysats à former des complexes peptide-Cu^{2+} a été démontrée par spectroscopies UV-visible, dichroïsme circulaire, dosage du pyrocatéchol et nano-LC-MS/MS, tandis que la transformation structurale du modèle d'auto-assemblage des peptides induite par la coordination du Cu^{2+} a été révélée par fluorescence (à l'aide de la thioflavine T (**ThT**) et de l'ANS), par diffusion dynamique de la lumière (**DLS**) et par microscopie électronique à transmission (**TEM**). Enfin, l'activité antioxydante des peptides auto-assemblés a été déterminée *in vivo* par l'étude du stress oxydatif induit par le Cu^{2+} en utilisant *Caenorhabditis elegans* comme organisme modèle. Lors de la coordination avec le Cu^{2+}, l'intensité de la fluorescence ThT et l'hydrophobicité de surface de tous les hydrolysats de TSG ont diminué, suggérant une dégradation des structures des feuillets β et la formation d'agrégats amorphes. Les études rhéologiques ont confirmé que les propriétés structurales et mécaniques des assemblages supramoléculaires résultants pouvaient être ajustées après ajout d'ions Cu^{2+}. En outre, grâce aux propriétés de chélation du Cu^{2+}et celles d'auto-assemblage induit par le Cu^{2+}, les peptides présents dans l'hydrolysat de TSG produit avec Alcalase® ont réduit de manière significative les niveaux de ROS endogènes, par coordination de Cu^{2+}, prolongeant ainsi la durée de vie de *C. elegans*. Ces résultats ont permis de mieux comprendre l'effet de la coordination du Cu^{2+} sur la progression de l'auto-assemblage des peptides et sur les phénomènes d'oxydation induite par le Cu^{2+} chez les vers *C. elegans*, ainsi que certaines perspectives pour les peptides auto-assemblés d'origine alimentaire dans les applications en biomatériaux et en nutraceutique.

Suite à notre discussion sur le potentiel élevé des tourteaux de tournesol pour la production de MCPs, comme démontré dans les **chapitres 4** et **5**, et suite au **chapitre 6** sur les peptides bioactifs auto-assemblés à partir d'hydrolysats de protéines alimentaires, nous avons également étudié l'effet de la coordination du Cu^{2+} avec les peptides sur leur auto-assemblage et leurs propriétés antioxydantes *in vivo* des hydrolysats issus de tourteaux en utilisant le stress oxydatif induit par Cu^{2+} chez *Caenorhabditis elegans*. Deux traitements enzymatiques

(Protamex®, **Prot** ; et Protamex® suivi de Flavourzyme®, **Prot+Flav**) ont été appliqués afin de produire des hydrolysats entiers et leur fraction ≤ 1 kDa. La caractérisation physicochimique de ces peptides auto-assemblés (**SAP**) par diverses analyses (ThT, ANS, DLS, TEM et données rhéologiques) a révélé que la coordination du Cu^{2+} par les peptides générait des nanostructures auto-assemblées à base de peptides, dotées de propriétés physico-chimiques et mécaniques améliorées.

Les résultats ont suggéré que la taille, la forme, les propriétés physico-chimiques et mécaniques des structures auto-assemblées résultantes ne dépendaient pas seulement du nombre de ligands de liaison de Cu^{2+} mais aussi de la géométrie de la liaison de coordination et des affinités de liaison Cu^{2+}-ligand, différentes parmi les hydrolysats étudiés. L'étude de l'activité antioxydante *in vivo* a révélé une activité biologique distincte du Prot ≤ 1 kDa contenant des séquences peptidiques capables de coordination le Cu^{2+} avec le motif ATCUN (*i.e.,* KGHLQPN). Cette étude représente une stratégie réalisable pour explorer la coordination du Cu^{2+} pour la formation de matériaux dérivés de peptides alimentaires, via des peptides contenant des résidus His et des Cys, et peut servir de base à des applications en biomatériaux supramoléculaires chélatant le Cu^{2+}, y compris des systèmes d'administration de médicaments injectables, des matériaux structurants et des produits nutraceutiques fonctionnels.

4. Perspectives

Sur la base des résultats obtenus dans les **chapitres 2** et **3**, le co-produit constitué d'écailles de tilapia rouge présente un grand potentiel de valorisation, notamment pour la production de peptides chélateurs de métaux. Dans une perspective à court terme, les recherches futures devraient se concentrer sur la mise à l'échelle des procédés d'extraction de protéines et de production d'hydrolysat et sur l'effet de la montée en échelle sur les propriétés biofonctionnelles de l'hydrolysat de gélatine. Premièrement, en ce qui concerne la montée en échelle du procédés, les conditions optimales d'extraction de la gélatine déterminées au **chapitre 2** pourraient être adaptées à un réacteur à plus grande échelle (réacteur pilote d'une capacité de 5 à 10 L) afin de produire de la gélatine dans un volume plus important. Deuxièmement, étant donné le potentiel de l'hydrolysat de gélatine ≤ 1 kDa Alc (**chapitre 3**), il serait intéressant d'augmenter la production de ce premier hydrolysat en utilisant un réacteur pilote suivi d'un procédés d'ultrafiltration à flux tangentiel et d'une membrane ayant un seuil de coupure fixé à 1 kDa. Après la montée en échelle des procédés d'hydrolyse et

d'ultrafiltration, la caractérisation de cet hydrolysat obtenu à l'échelle pilote permettrait de déterminer si cet hydrolysat initial a conservé ses propriétés biofonctionnelles et bioactives lors de la mise à l'échelle. Au cours de la mise à l'échelle de ce procédé, il conviendra d'appliquer et d'étudier des méthodes d'optimisation pour trouver les conditions d'exploitation optimales (*i.e.,* méthodologie de surfaces de réponse). Outre la confirmation des propriétés biofonctionnelles des séquences peptidiques chélatrices de métaux, certaines séquences peptidiques chélatrices de métaux identifiées à partir d'hydrolysats de gélatine pourraient être synthétisées par SPPS et caractérisées pour leur activité chélatrice de métaux et leurs bioactivités liées à la chélation de métaux afin d'avoir une connaissance plus fine des mécanismes de complexation.

Dans une perspective à long terme, les travaux futurs pourraient s'intéresser aux réacteurs membranaires enzymatiques. Le réacteur enzymatique à membrane est basé sur le couplage d'une réaction enzymatique avec un processus de séparation par membrane. Cette technologie pourrait constituer une approche intéressante pour surmonter les inconvénients liés à l'utilisation d'un réacteur discontinu classique (réacteur en batch) dans la pratique industrielle, en améliorant à la fois la productivité, les coûts d'exploitation, l'activité enzymatique, etc.

D'autre part, l'utilisation de tourteaux de tournesol comme source de protéines pour produire des peptides chélateurs Ni^{2+}/Cu^{2+} (**chapitres 4** et **5**) s'est également avérée être une ressource intéressante. Ainsi, des recherches plus approfondies sur l'étude de l'interaction peptide-métal en utilisant d'autres techniques telles que l'infra-rouge à transformée de Fourier et la calorimétrie de titration isotherme peuvent être utiles pour comprendre en profondeur les mécanismes de coordination des peptides purs avec les ions métalliques. En outre, la simulation par dynamique moléculaire et par docking moléculaire des complexes peptide-métal en tant qu'approches théoriques devrait être effectuée pour mieux comprendre l'interaction des peptides avec différents ions métalliques avant les évaluations *in vitro* des peptides. La combinaison de toutes ces analyses fournira des informations sur la description de l'interaction à l'échelle moléculaire, la conformation structurale, les énergies d'interaction, les sites de chélation et les mécanismes de chélation possibles. En raison de la présence du motif ATCUN, les peptides chélateurs de Ni^{2+}/Cu^{2+} identifiés à partir d'hydrolysats issus de de tourteau de tournesol, ayant un résidu His en troisième position à partir de l'extrémité aminée

(c'est-à-dire LL**H**VT et WL**H**), pourraient avoir une meilleure stabilité dans le complexe peptide-Cu^{2+} formé. Ils pourraient donc avoir un effet bénéfique sur la santé et une valeur nutritionnelle intéressante pour les produits alimentaires en améliorant la biodisponibilité des minéraux. Ces séquences peptidiques pourraient être synthétisées afin d'évaluer leur capacité à prolonger la durée de conservation des formulations alimentaires, notamment en retardant la dégradation oxydative induite par les métaux dans les systèmes d'émulsion, par exemple. La biodisponibilité et la stabilité des peptides chélateurs de métaux pourraient également être étudiées dans des modèles animaux et humains afin de valider leur potentiel *in vivo*.

Enfin, comme décrit dans les **chapitres 6** et **7**, l'utilisation de la coordination du Cu^{2+} comme approche non conventionnelle permettant d'induire l'auto-assemblage des peptides, a généré diverses nanostructures. Ces nanotructures, à base de peptides bioactifs auto-assemblés, provenant d'hydrolysats issus d'écailles de tilapia, ou de tourteau de tournesol, ont montré des propriétés mécaniques améliorées. Cependant, pour mieux comprendre comment certains paramètres (comme par exemple le nombre de peptides liant le Cu^{2+}, la géométrie de la liaison de coordination et les affinités de liaison peptide-Cu^{2+}) affectent le modèle d'auto-assemblage des nanostructures résultantes, les peptides identifiés comme étant plus intéressants (*i.e.,* AV**HW**TY, **C**R**W**ISF et GPSGPRGPAGP**H**) devraient faire l'objet d'un examen plus approfondi. Ainsi, l'effet du rapport métal/peptide pourrait être étudié sur le modèle d'auto-assemblage afin de déterminer les conditions appropriées pour améliorer les structures des biomatériaux supramoléculaires obtenus, en fonction des propriétés requises. Enfin, d'autres études pourraient être consacrées à la recherche de la biostabilité et de la biocompatibilité des peptides auto-assemblés d'origine alimentaire dans des modèles cellulaires ainsi qu'à leurs applications finales en tant que systèmes d'administration de médicaments injectables, matériaux structurants pour l'ingénierie tissulaire, matériaux mous auto-gélifiants, agents thérapeutiques et produits nutraceutiques fonctionnels.

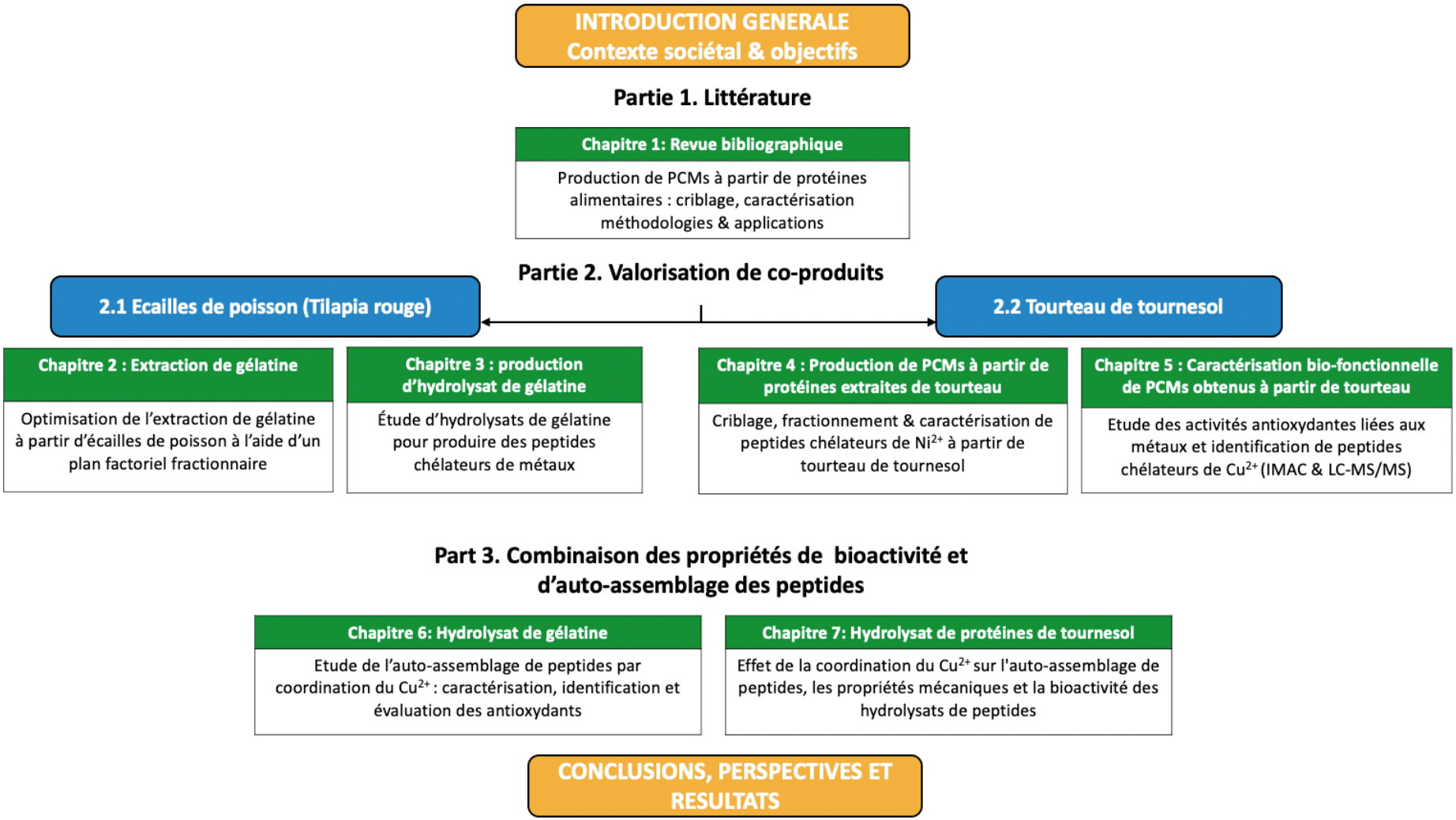

Figure 0.1. Structure de la thèse.

General introduction

Aquaculture and agriculture are major contributors to global food production. However, these industries generate large amounts of waste, which is often discarded without any treatment, leading to environmental problems (Singh et al., 2019). Aquaculture is among the fastest-growing industries in global food production, providing a significant source of protein for human diets. According to the FAO, (2024), aquaculture production was estimated to exceed 223.2 million tons in 2022, with 50-70 % considered as waste. Similarly, in agriculture, it is estimated that 1.3 billion tons of waste are generated annually during processing (Greses et al., 2020). This has led to a growing interest from the scientific community to explore alternative uses for agro-industrial by-products, promoting their valorization and reducing the environmental impact caused by their disposal.

Red Tilapia (*Oreochromis* spp.) scales and sunflower meal are by-products of agro-industries. Tilapia is the third most widely farmed fish worldwide (Ngo et al., 2010). Yet, in fish factories, the scales, one of the main fish processing wastes, are often discarded during the filet processing (Weng & Wu, 2015). To date, approximately 50 000 tons of wastes are produced per year worldwide during the de-scaling processing (Wang et al., 2020). Mainly composed of collagen protein (30-50 %) and minerals as hydroxyapatite ($Ca_5(PO_4)_3OH$) (30-40 %), fish scales by-product is of great interest for gelatin extraction (Lin et al., 2020). On the other hand, sunflower (*Helianthus annuus* L.) is the third most produced oilseed in the world, after soybean and rapeseed, with a total production of 53.5 million tons in 2019 (Náthia-Neves & Alonso, 2022). After oil extraction from sunflower seeds, the remaining meal residue contains approximately 30-50% proteins, and its global production was 22.3 tons in 2019-2020 (Efthymiou et al., 2021).

Due to their high protein content, various alternatives for the utilisation of these agro-industrial waste have been explored in recent decades, notably as animal feed, fertilizer agents, silage production, as well as cosmetic, sanitary, veterinary, medicinal, functional or nutraceutical products (Chalamaiah et al., 2019; Villamil et al., 2017). Among medicinal or functional products, bioactive peptides (**BAPs**) obtained from protein hydrolysis, are biological compounds, naturally encrypted within protein sequence under an inactive form and released upon proteolysis. Nowadays, these peptides have gained great interest due to their numerous biological and biofunctional activities reported in the literature such as antioxidant,

immunomodulatory, antihypertensive, anticancer, anti-inflammatory, antimicrobial, hypo-cholesterolemic, antidiabetic and metal-chelating properties (Liu et al., 2020). Functional and bioactive peptides, such as metal-chelating peptides (**MCPs**), are derived either from matrices of animal origin (*e.g.,* milk, eggs, meat and fish), or from vegetable such as soybeans, wheat, and many other legumes (Lorenzo et al., 2018). In a bioeconomy strategy, the protein sources from plant and agro-industrial by-products have currently gained significant interest (Hadnadjev et al., 2017). This presents tremendous potential for the production of MCPs due to their high protein content and their potential high-added value after proteolysis (Tonolo et al., 2024).

Several studies reported the discovery of bioactive peptides from fish scale protein such as milkfish (Huang et al., 2018), grass carp (Chen et al., 2019), skipjack tuna (Qiu et al., 2019), and sole (Viji et al., 2019). Similarly, various plant-based proteins have been reported among them rapeseed (Xie et al., 2015), defatted walnut flake (Lv et al., 2017) and chia seed (Latha et al., 2021). Nevertheless, to date, there is little data available in the literature on the productions of MCPs from red Tilapia scale gelatin and sunflower meal by-products protein hydrolysates. Moreover, to the author's knowledge, there is a lack of evidence about the use of sequential enzymatic hydrolysis to produce MCPs on fish gelatin protein and sunflower meal protein using Alcalase® followed by Flavourzyme® and Protamex® followed by Flavourzyme® treatments, respectively. Since Alcalase® and Protamex® (endopeptidases) are expected to improve the subsequent action of Flavourzyme® (endo and exopeptidases) by increasing the number of N-terminal sites, we hypothesized that a sequential enzymatic treatment (Alcalase®/Protamex® and then Flavourzyme®) could therefore improve the biofunctional properties of hydrolysates derived from agro-industrial by-products. Additionally, despite a large number of studies on the induction of peptide self-assembly through metal ion coordination in synthetic peptides, the potential of Cu^{2+} coordination to generate bioactive supramolecular biomaterial from food-derived self-assembled peptides (**SAPs**) has not yet been exploited to date. Thus, in a bioeconomy strategy, the overall aim of this PhD work was to investigate the use of red Tilapia scale and sunflower meal by-products as potential protein sources for the production of multifunctional MCPs using single and sequential enzymatic treatments, by setting up several screening, separation and *in vitro* characterization techniques. In addition, this PhD work presents the effect of Cu^{2+} coordination on the productions of food-derived SAP biomaterials endowed with *in vivo* antioxidant properties.

This PhD thesis describes the potential of Tilapia scale and sunflower meal by-products for producing MCPs. This PhD work was divided into three sections with seven chapters (Fig. 0.2). It began with a **review** of the current literature about screening, separation and identification of metal-chelating peptides for nutritional, cosmetic and pharmaceutical applications (**Chapter 1**; Camaño Echavarría et al., 2024). The second section focused on the use of Tilapia scale and sunflower meal by-product as protein sources for the productions of MCPs. Therefore, this section is divided into two subsections 2.1 and 2.2. The subsection 2.1 explored the optimization of Tilapia scale gelatin extraction (**Chapter 2**) and its potential to be used as a protein source to produce MCPs (**Chapter 3**). Meanwhile, the use of sunflower meal to produce MCPs was investigated on the subsection 2.2 with the subsequent **Chapters 4** and **5**, which included IMAC-Ni^{2+} and Cu^{2+} separation followed by LC-MS/MS analysis and biofunctional characterization of sunflower meal protein hydrolysates. Moving forward with the combination of bioactivity and self-assembly properties of protein hydrolysates, the last section 3 (**Chapter 6** and **7**) introduced the use of Cu^{2+} coordination as a nonconventional approach to generate various tunable self-assembled bioactive peptide-based nanostructures, endowed with improved mechanical properties and produced from Tilapia scale and sunflower meal by-products protein hydrolysates, respectively. Finally, general conclusions of the main findings, short- and long-term perspectives and the outcomes of this thesis were presented.

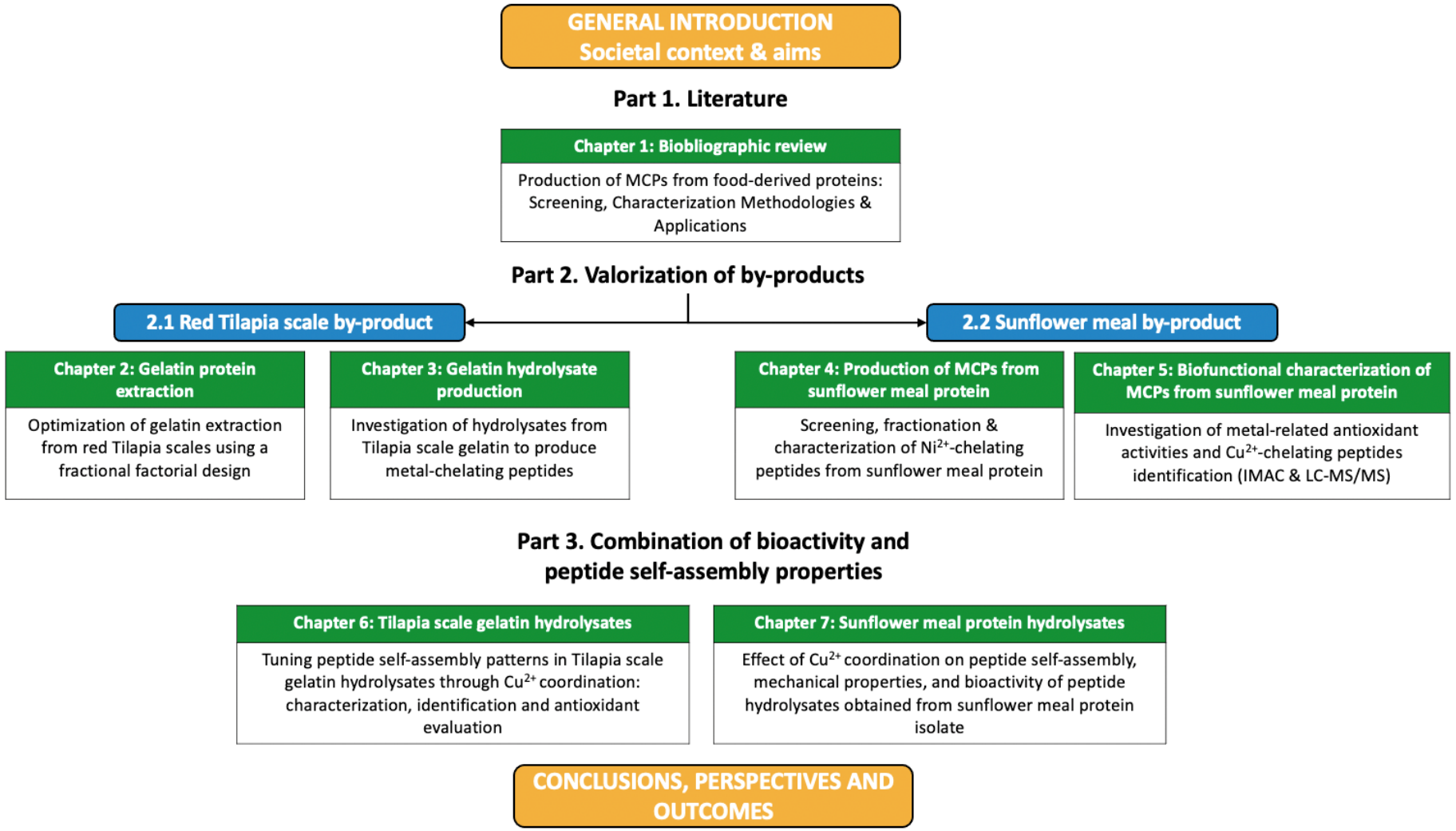

Figure 0.2. Thesis overview

Chapter 1. State of the art

Having established the environmental problematic of agro-industrial by-products over the past few decades, and how it has led to their use as protein sources, this **Chapter 1** is a review on conventional and novel alternatives for screening metal-chelating peptides (**MCPs**) in food-derived protein hydrolysates. The aim of this review was to provide a state-of-the-art of the recent advances in MCPs derived from protein hydrolysates, and to provide an overview of the various strategies used for their production, screening, separation, characterization, identification, and potential applications as functional ingredients in the nutritional, cosmetic, or pharmaceutical fields.

This Chapter has already been published in the journal *Food & Function* as:

Camaño Echavarría, J. A., El Hajj, S., Irankunda, R., Selmeczi, K., Paris, C., Udenigwe, C. C., & Canabady-Rochelle, L. L. S. (2024). Screening, Separation and Identification of Metal-Chelating Peptides for Nutrition, Cosmetic and Pharmaceutical Applications. *Food & Function*, *15*(15), 3300-3326. https://doi.org/10.1039/d3fo05765h

1.1 Introduction

Bioactive peptides (**BAPs**) are biological compounds, naturally encrypted within protein sequences in their inactive form and can be released upon proteolysis. Nowadays, these peptides have been attracting increasing attention due to their ease of preparation and wide variety of biological and biofunctional activities, such as antioxidant, immunomodulatory, antihypertensive, anticancer, anti-inflammatory, antimicrobial, hypocholesterolemic, antidiabetic, opioid-like, and metal-chelation (Chalamaiah et al., 2019; Liu et al., 2020). Functional and bioactive peptides, like metal-chelating peptides (**MCPs**), have been widely explored over the last two decades towards the discovery of new biomolecules for nutritional, cosmetic and pharmaceutical applications because of the role of metal ions in several biological processes.

MCPs are biofunctional peptides that interact with metal ions and forming peptide-metal complexes. Considering such ability of peptides and the numerous roles of metals in biological processes, many studies in the literature have demonstrated that these MCPs provide positive health outcomes. For instance, due to the complexation with various metals (such as divalent ions Ca^{2+}, Zn^{2+}, Fe^{2+} and Cu^{2+}) endowed with important biological functions, MCPs promote better stability, absorption, and bioavailability of these minerals (Guo et al., 2015; Wang et al., 2012); thus they can eventually be used as nutraceutical compounds for mitigating mineral deficiency and related health problems and overcome the drawbacks of mineral supplement salts in the market. Besides, angiotensin-converting enzyme (ACE) is a Zn^{2+}-dependent enzyme involved in hypertension, with zinc ion playing an important role in the active site. It has been reported that the binding of peptides to Zn^{2+} might move the zinc ion away from the active site, resulting in a change in the conformation of the active site and eventually ACE inhibition (Ni et al., 2012). Thus, MCPs capable of binding the zinc cofactor could potentially possess ACE inhibitory activity and be used as antihypertensive compounds (Olalere et al., 2023). MCPs can also act as indirect antioxidants while complexing transition metal ions (*i.e.,* Fe^{2+} and Cu^{2+}) (Canabady-Rochelle et al., 2018), preventing oxidative damage and related chronic disease conditions (Nwachukwu & Aluko, 2019). Indeed, free Fe^{2+} and Cu^{2+} can generate reactive oxygen species (ROS) *via* the Fenton and Haber-Weiss reactions. These ROS are responsible for radical chain reaction, inducing biomolecules damages and, thus, degenerative, neurological, cardiovascular, and cancer diseases (Gaetke & Chow, 2003).

In the global context of food protein-derived hydrolysates, MCPs are produced either from matrices of animal origin (*e.g.,* milk, eggs, meat and fish), or from vegetable sources, such as soybeans, wheat, and many other legumes and cereals (Lorenzo et al., 2018). However, in recent years, several studies on the production of MCPs have emphasized on the use of agro-industrial by-products as protein sources of BAPs due to low environmental impacts of their production, high protein content, and potentially high-added value after by-products valorisation (Hadnadjev et al., 2017). Once the protein source is selected, MCPs can be released from their protein precursors by *in vitro* hydrolysis (enzymatic, fermentative) or by gastrointestinal digestion (Bamdad et al., 2011; Megías et al., 2008). Then, following the classic empirical approach, hydrolysates are processed based on their structural and physico-chemical properties (Udenigwe & Aluko, 2012). Separation and purification techniques generally used for MCPs discovery are ultrafiltration (**UF**), gel filtration chromatography (**GPC**), reverse phase high-performance liquid chromatography (**RP-HPLC**), immobilized metal-ion affinity chromatography (**IMAC**), and ion-exchange chromatography (**IEC**). Finally, the MCPs can be identified by mass spectrometry (Guo et al., 2014). In recent years, the literature regarding MCPs production using such approach has increased. However, these techniques might cause drawbacks: they are expensive, time and reagent consuming. To the author's knowledge, there is a lack of review papers that focus on conventional and novel alternatives for screening MCPs in food protein hydrolysates. Therefore, this review aimed to provide a comprehensive discussion on the most recent progress regarding MCPs derived from food protein hydrolysates, presenting an overview of the multiple strategies applied for their production, characterization, identification and their potential applications as functional ingredients in nutrition, cosmetic or pharmaceutical fields.

1.2 Metal-chelating peptides

1.2.1. Definition

Bioactive peptides are naturally encrypted within protein sequence under an inactive form and released upon hydrolysis (Le Gouic et al., 2018). Nowadays, these peptides have gained significant interest due to their numerous biological and biofunctional activities, *e.g.,* antioxidant, immunomodulatory, antihypertensive, anticancer, anti-inflammatory, antimicrobial, hypo-cholesterolemic, antidiabetic, opioid-like, and metal-chelating properties

(Chalamaiah et al., 2019; Liu et al., 2020). More specifically, metal-chelating peptides (MCPs) are functional peptides able to form complexes *via* peptide-metal interactions involving coordination bonds (Caetano-Silva et al., 2021). Their metal-chelating properties are associated with their primary sequence and notably their backbone structural diversity, which contains both carboxyl and amino groups (**Figure 1.1A,B**,Bassan & Marchesan, 2023), in addition to the diverse side chains of amino acids (**AA**) residues (**Figure 1.1C,D,E**, Bassan & Marchesan, 2023 ;Sun et al., 2020). The reaction between AA and metals is a Lewis acid-base reaction following the HSAB theory (**HSAB** for Hard and Soft Acid and Bases). This theory ranks ligands (Lewis bases) and metals (Lewis acids) as hard, intermediate or soft and states that the formed complexes between soft acid and soft base or between hard acid and hard base have better stability (Irankunda et al., 2022). Among all 20 AA, histidine, cysteine, aspartic acid, and glutamic acid have the highest metal-chelating ability (**Figure 1.1C,D,E**, Bassan & Marchesan, 2023 ;Fortunato & Mba, 2021) Their respective functional groups (imidazole, thiol, and carboxylate) can coordinate the metal ion. Thus, the metal-chelating capacity of biofunctional peptides strongly depends on the presence and the number of these AA residues in their sequence.

1.2.2. Presence of Metal-chelating peptides in nature

Metal-chelating peptides are naturally present in living organisms (plants, animals, microorganisms, and human body) for several defensive roles (El Hajj, 2021). Due to the presence of excess heavy metals (*i.e,* As^{3+}, Pb^{2+}, Hg^{2+}, Co^{2+}, Cd^{2+}, Cu^{2+}, Ni^{2+}, Zn^{2+}) in leaves and roots, plants induce the synthesis of metal-binding proteins or peptides and the formation of complexes with metals as the main detoxification mechanism (Prasad, 2004). Plants produce a range of metal-chelating ligands, named metallothioneins (**MTs**) and phytochelatins (**PCs**) (Ahmad et al., 2019). Rich in cysteines, MTs produced by plant are the class II MTs (**MT-IIs**), which differ from the mammalian MT-I in the location and number of cysteine (Rauser, 1999). Derived from the tripeptide glutathione (GSH), and produced within the cytosol, PCs (cysteine- and glutathione-rich compounds) exist in numerous varieties of plants, which grow in high and low metal concentrations environments (Merlos, 2014). Besides, PCs have been identified in algae, fungi, microorganisms, and animals, and MCPs can be extracted from these sources (Ahmad et al., 2019).

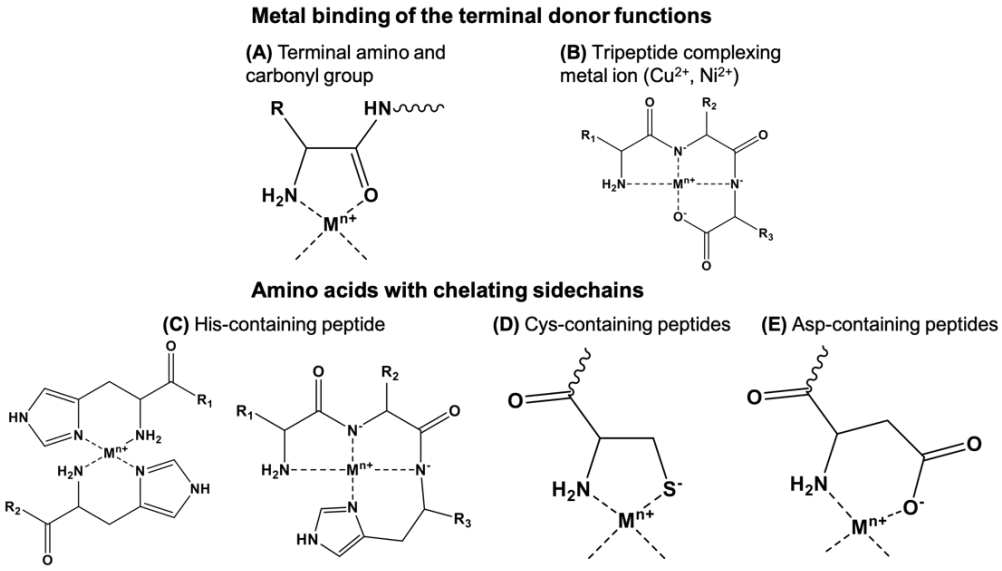

Figure 1.1. Metal ion (M^{n+}) coordination thorough several functional groups present in peptides. Upper part illustrates the formation of peptide-metal complexes by peptides without chelating sidechains R. (A) metal coordination through amino and carbonyl termini; (B) tripeptide complexing metal ions through amino and carboxyl termini. Lower part shows some examples of metal coordination through chelating functional groups present in sidechains; (C) His-containing peptides (imidazole group), (D) Cys-containing peptides (thiol group) and (E) Asp-containing peptides (carboxylate group).

Microbial communities and mineral have interacted for eons. Indeed, wherever minerals are located, there exist microbial communities (Gilbert, 2014). Similar to plants, bacteria and higher organisms have developed resistance mechanisms to toxic metals, mainly by binding proteins such as MTs or PCs (Mejáre, 2001). Various metal-binding proteins secreted by bacteria and yeast have been studied for decades. In a study, researchers identified the first prokaryotic MT in a few cyanobacterial strains of the genus *Synechococcus* (Ji, 1995). Currently, expression of MTs on the surface of different bacterial genera like *Escherichia, Bacillus, Mycobacterium, Paenibacillus, Alcaligenes, Acidovorax, Rhodococcus* and *Pseudomonas,* have been widely reported (Mejáre, 2001; Sharma et al., 2021). Yet, expressed on *E. coli* surface, metal-binding peptides containing histidine or cysteine, are characterized by a higher affinity, selectivity and specificity than metal-binding proteins (Mejáre, 2001).

Based on genetic engineering, microorganisms can be modified to express a particular peptide on its outer surface (Dunbar, 2017). In bioremediation strategies, genetically modified microorganisms could be used to remove metal from contaminated water and waste streams

(Mejáre, 2001). Moreover, in mineral exploration, bacteria that bind particular metals are used as highly-sensitive metal detectors (Dunbar, 2017). Although some of the natural approach discussed above could contribute to MCPs production, the heterologous expression of native and/or genetically modified peptides is still challenging.

1.2.3. Productions of MCPs by proteolysis

1.2.3.1 Protein hydrolysis

To date, numerous studies have reported other approaches to produce MCPs, such as food protein hydrolysis (Guo et al., 2014; Sun et al., 2020; Udechukwu et al., 2016; Walters et al., 2018) with the potential of food-derived protein to obtain MCPs either from animal origin (*e.g.,* milk, eggs, meat and fish), or from vegetable sources such as soybeans, wheat, and many other legumes and cereals (Lorenzo et al., 2018). The plant source has attracted the interest of scientists due to the current controversy over the consumption of animal proteins, despite their high nutritional value (Hadnadjev et al., 2017). Likewise, high-protein by-products from agro-industrial processes, such as wheat germ (Zhu et al., 2015), sunflower cake (Megías et al., 2008), soybean cake (Bao et al., 2008; Lv et al., 2013), Pacific cod fish bone (Zhang et al., 2019) and Tilapia skin (Lin et al., 2021) can be valorized by proteolysis to generate high value-added products (Hou et al., 2017; Udenigwe & Aluko, 2012). **Table 1.1** summarizes some MCPs sequences already identified from hydrolysates produced from various food source.

Generally, the empirical approach used to produce MCPs from food protein sources is carried out as described in **Figure 1.2** (Guo et al., 2014; Sun et al., 2020). First, a suitable protein source is identified, and subsequently submitted to proteolysis (Li-Chan, 2015). Then, the raw hydrolysates undergo separation and purification processes based on a peptide-metal interaction to isolate the targeted metal-chelating peptides (Caetano-Silva et al., 2021; Sun et al., 2020). Finally, biofunctional evaluations, identification and synthesis of the most promising sequences is required to validate the metal-chelating properties of identified sequences (Daroit & Brandelli, 2021).

Tabla 1.1. Metal-chelating peptides reported from different food protein sources. NA: not applied

Protein source	Substrate used	Metal	Fractionation/Purification	Sequence	Ref.
Animal	Egg protein	Iron	MWCO: 5 kDa. GPC, RP-HPLC	DKLPGFGDS	Palika et al., (2015)
	Egg white		NA	DHTKE	Sun et al., (2017)
	Casein		MWCO: 3 kDa. GPC, RP-HPLC	EDVPSER, HKEMPFPK, NMAINPSK, AVPYPQR	Miao et al., (2019)
	Cheese milk		MWCO: 3 kDa. RP-HPLC	VAPFPQ	Timon et al., (2019)
	Duck egg white		RP-HPLC	PVEE, RSS	Li et al., (2019)
	Whey protein		MWCO: 3, 5, 10 kDa. RP-HPLC	VRTPEVDDE, VLDTDYK, VEELKPTPEGDLEI	Athira et al., (2021)
	Bovine serum		MWCO: 3, 5, 10 kDa. RP-HPLC	DNLPNPEDRKNYE	Choi et al., (2012)
	Whey protein	Calcium	NA	GY	Zhao et al., (2014)
			MWCO: 1, 5 kDa. RP-HPLC	EE, EY	Huang et al., (2015)
	Porcine blood plasm		MWCO: 3 kDa. RP-HPLC	VSGVEDVN	Seung & Kyung, (2009)
	Auxis thazard		MWCO: 5 kDa. GPC, RP-HPLC	EPAH	Chen et al., (2019)
	Egg		MWCO: 2 kDa. RP-HPLC	DEEENDQVK	Zhang et al., (2021)
Aquatic	Pacific cod skin gelatin	Iron	GPC, RP-HPLC	GPAGPHGPPGKDGR AGPHGPPGKDGR	Wu et al., (2017)
	Acetes japonicus		MWCO: 30, 10, 1 kDa. RP-HPLC	DADSVNFPVHGL FKVGQGNTPILK	Vo et al., (2020)
	Tilapia muscle	Calcium	GPC	WEWLHYW	Charoenphun et al., (2012)
	Antarctic krill		GPC, RP-HPLC	VLGYIQIR	Hou et al., (2018)
	Oyster protein	Zinc	IMAC, RP-HPLC	HLRQEEKEEVTV, GSLK,	Chen et al., (2013)
			MWCO: 3 kDa. RP-HPLC	GAVEDLERVK, VVGDDIAWLR	Wang et al., (2021)
	Rye secalin		NA	CQV, QCA	Udechukwu et al., (2017)
Plant	Barley	Iron	NA	SVNVPLY	Eckert et al., (2016)
	Walnut flake		GPC, RP-HPLC	LAGNPDDEFRPQ VEDELVAVV	Lv et al., (2017)
	Mung bean		MWCO: 30, 10, 5 kDa. GPC, RP-HPLC	PAIDL, LLGIL, AIVIL, LLLG, HADAD	Budseekoad et al., (2018)
	Sea cucumber		RP-HPLC	No identified	Sun, Cui, Jin, et al., (2017)
	Peony seed		RP-HPLC	SMRKPPG	Zhang et al., (2019)
	Sesame meal	Zinc	IMAC, RP-HPLC	SM, LAN, IAN, RKR, RQR	Wang et al., (2012)
	Rapeseed		IMAC, RP-HPLC	AR, NSM, GKR, EPSH	Xie et al., (2015)
	Soybean		MWCO: 10, 3 kDa. IMAC, RP-HPLC	DEGEQPRPFPFP	Lv et al., (2013)
	Wheat germ	Calcium	MWCO: 3, 1 kDa. RP-HPLC	FVDVT	Wang et al., (2018)
	Sea cucumber		RP-HPLC	NDEELNK	Cui et al., (2018)
Agro-industrial by-products	Alaska pollock skin	Iron, Copper	GPC, IMAC, RP-HPLC	SCH	Guo et al., (2013)
			GPC, IMAC, RP-HPLC	GPAGPHGPPG	Guo et al., (2015)
	Tilapia skin		IMAC-RP-HPLC	PFRMY, RGFTGM	Song et al., (2023)
	Scad by-products	Iron	MWCO: 10, 5, 3 kDa, GPC, IMAC, RP-HPLC	QKGTYDDYVEGL	Jiang et al., (2019)
	Tilapia skin collagen		GPC, IMAC, RP-HPLC	GPAGPAGEK, DGPSGPKGDR	Lin et al., (2021)
	Shrimp byproduct		MWCO: 5, 1 kDa. RP-HPLC	TCH	Huang et al., (2010)
	Tilapia scales	Calcium	RP-HPLC	NGNNGEAGKIG	Chen et al., (2014)
	Pacific cod bone		RP-HPLC	KGDPGLSPGK	Zhang et al., (2019)
	Tilapia bone collagen		GPC, RP-HPLC	GPAGPHGPVG, FDHIVY, YQEPVIAPKL	Liao et al., (2020)

1.2.3.2 Parameters involving the production of MCPs

For MCPs production, several criteria are considered for an adequate selection of the protein source such as the use of (i) matrices from agro-industrial by-products rich in proteins, (ii) with specific peptide sequences or AA residues of particular pharmacological or medicinal interest (Udenigwe & Aluko, 2012). Indeed, the protein selection is one of the most important variable in MCPs production, since the AA sequence plays a crucial role in the metal-chelating capacity of the peptides, which depends on the parent protein (Guo et al., 2014). Once the protein source is selected, MCPs can be released from their protein precursors by *in vitro* protein hydrolysis (Bamdad et al., 2011; Megías et al., 2008). Endogenous and exogenous proteolytic enzymes and microorganisms are commonly used for releasing MCPs from proteins (Lorenzo et al., 2018; Sun et al., 2020). Enzymatic proteolysis, widely used in the food industry for decades (Daroit & Brandelli, 2021), is carried out using proteolytic enzymes, either pure (*e.g.,* trypsin, papain, chymotrypsin) or in complex mixtures (*e.g.,* Alcalase®, Protamex®, Flavourzyme®, Neutrase®). Besides, fermentation approach is usually performed using different microorganisms, particularly GRAS microbial strains (generally recognized as safe, *e.g.,* lactic acid bacteria) (Chalamaiah et al., 2019).

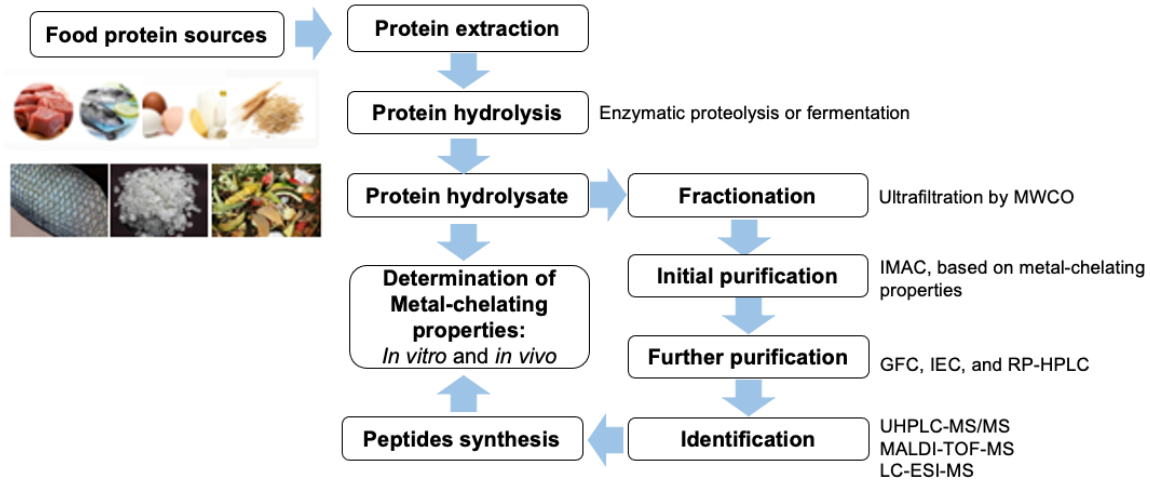

Figure 1.2. Strategy for the preparation, separation, purification, and identification of MCPs present in hydrolysates produced from food source protein.

MWCO: molecular weight cut off; IMAC: immobilized metal-ion affinity chromatography; HPLC: high performance liquid chromatography; RP-HPLC: reversed phase high performance liquid chromatography; GPC: gel filtration chromatography; IEC: ion exchange chromatography; UHPLC-MS/MS: ultra-high performance liquid chromatography-tandem mass spectrometry. MALDI-TOF-MS: matrix-assisted laser desorption/ionization time-of-flight mass spectrometry. LC-ESI-MS: liquid chromatography-electrospray ionization mass spectrometry.

The proteases used in food hydrolysis present specific cleavage sites in a protein substrate. For instance, pure enzymes such as trypsin and papain specifically cleave the peptide bonds at the C-terminal side of lysine and arginine residues and at the hydrophobic regions, respectively (Bing et al., 2024; Wang et al., 2021). Meanwhile, enzymes in complex mixtures, such as Alcalase® (having a broad specificity, and involving the carboxyl groups, W, E, M, F, Y and K in the cleavage sites (Bing et al., 2024; Wang et al., 2021), Flavourzyme® (cleaving the peptide bonds between L and P or between two P residues), Neutrase® (notably cleaving between L and F at the C-terminus), and Protamex® have been reported with an extensively broad specificity (Bing et al., 2024). Thus, upon proteolysis, thousands of peptides can be produced with potential antioxidant, anti-hypertensive, metal chelating, antidiabetic, anti-inflammatory and antimicrobial activities (Liu et al., 2022). However, in terms of MCPs production, more metal-chelating peptides were present in food protein hydrolysates produced by enzymes in complex mixtures compared to pure enzyme treatments, due to their extensively broad specificity. For instance, Alcalase® has been reported as an excellent alternative for producing MCPs from food protein. Several studies have shown that Fe^{2+}, Zn^{2+} and Ca^{2+}-chelating peptides in protein hydrolysates obtained using Alcalase® present better chelating profile than those generated by papain or trypsin (Chai et al., 2015) In addition, Alcalase® can also be used in a combined way with other proteases to generate more MCPs (Tacias-Pascacio et al., 2020).

Despite their efficiency to hydrolyze proteins and release MCPs, both production approaches impact the peptide profile differently (Lorenzo et al., 2018). Compared to microorganisms, enzymatic hydrolysis is more controllable as the proteases have specific cleavage sites on proteins, thus releasing specific peptides sequences constituting of various AA of interest (Lorenzo et al., 2018). Moreover, this process is generally recognized as efficient, safe, quick, and relatively inexpensive (Nwachukwu & Aluko, 2019). In enzymatic proteolysis processes, multiple aspects are taken into consideration, since the biofunctional characteristics of the MCPs obtained depend on various factors, such as the enzyme specificity, the process conditions (i.e., pH, temperature, time), the enzyme/substrate ratio, and the degree of hydrolysis. Depending on the protein source used and the proteolysis process parameters, various peptide sequences are obtained, endowed with various physico-chemical properties (Tu et al., 2018).

Thus, the appropriate parameters for conducting enzymatic hydrolysis must be selected based not only on literature, but also on enzyme specifications. For instance, the experimental conditions employed to produce peptides endowed with high metal-chelating properties derived from food protein hydrolysates using enzymes such as Alcalase®, papain, trypsin, Neutrase®, Flavourzyme® and Protamex® is reported in the work of Zhao et al., (2012), Tacias-Pascacio et al., (2020), Wang et al., (2021), Liu et al., (2022) and (Ren et al., 2023).

1.2.3.3 Fractionation of hydrolysates

After proteolysis, a sequential fractionation is generally carried out to concentrate the bioactive fractions (Daroit & Brandelli, 2021). The ultrafiltration (UF) process separates peptides according to their size using different molecular weight cut-off (**MWCO**) membranes, generally comprised within 0.1 and 100 kDa for MCPs fractionation (**Table 1.1**). Peptide fractions below 3 kDa exhibit higher chelating activity compared to larger fractions (> 3 kDa) (Boukil et al., 2018). Indeed, low molecular weight peptides were reported for their better metal-chelating properties than the larger ones with peptide less than 10 AA residues often considered as the most interesting ones in terms of bioactivity for nutraceutical and health applications (Guo et al., 2014; Li et al., 2017; Sun et al., 2020; Wen et al., 2020). Thus, di- and tripeptides are the most recommended ones for binding and delivering minerals, due to their higher aqueous solubility compared to larger peptides (Sun et al., 2020; Vo et al., 2020).

1.2.3.4 Separation, purification and identification

Once the desired MW is obtained, MCPs are generally purified by using a combination of chromatographic techniques based on different separation principles.

1.2.3.4.1 IMAC

The immobilized metal-ion affinity chromatography is a preliminary step of MCPs separation (Guo et al., 2014). IMAC is based on the affinity of some peculiar AA residues of proteins or peptides for some transition metal ions (*e.g.,* Zn^{2+}, Cu^{2+}, Ni^{2+} or Co^{2+}) immobilized onto a complexing ligand that is grafted onto the chromatographic solid phase. These divalent ions are often used for protein purification due to their ability to coordinate the electron donating

atoms of some AA residues accessible at the protein surface (Mooney et al., 2011). After IMAC, other liquid chromatography techniques are used as intermediate stages of purification as described hereafter.

1.2.3.4.2 GPC

In gel permeation chromatography GPC, the molecules access the porous matrix differently according to their size and are eluted in decreasing order of size (O'Fagain et al., 2011). GPC enables the determination of MW distribution of MCPs previously captured with IMAC. Several studies have used GPC for the fractionation of hydrolysates from different food sources (Guo et al., 2013; Torres-Fuentes et al., 2011; Xie et al., 2015).

1.2.3.4.3 IEC

Ion exchange chromatography is based on ionic interactions between targeted biomolecules and the opposite surface charges on the ionic resin (Jungbauer & Hahn, 2009). MCPs were purified from porcine blood plasma and black pomfret viscera protein hydrolysates using an anion-exchange column, respectively (Jai et al., 2011; Seung & Kyung, 2009). Some sequences of MCPs were identified in these protein sources, prior to amino acids sequencing using LC/ESI tandem mass spectrometry and PepSeq *de novo* sequencing algorithm.

1.2.3.4.4 RP-HPLC

Reverse phase high performance liquid chromatography is based on the hydrophobic interaction between protein/peptides and the hydrophobic stationary phase, mainly C18 column. In RP-HPLC, the bound peptides are eluted by adding organic solvents to the mobile phase. Nowadays, the number of RP-HPLC applications in peptide purification has rapidly expanded usually selected as the last purification step. In MCPs purification approach, RP-HPLC is rather used as a preparative technique, before MCPs sequence identification by MS (**Figure 1.2**) (Andjelković et al., 2017).

1.2.3.4.5 MS identification

Finally, irrespective of the purification step (IMAC, GPC, IEC, and/or RP-HPLC), the mass and the sequence of the isolated MCPs can be identified by mass spectrometry (**MS**) and tandem mass spectrometry (**MS/MS**), respectively (Caetano-Silva et al., 2021; Sun et al., 2020). For instance, the IEC and ESI-MS complementary approach was applied to MCPs present in

protein hydrolysates obtained from marine fish skin: Horse mackerel and croaker (Jai et al., 2011) and Alaska pollock skin (Guo et al., 2013), providing the AA sequences of an hexapeptide (NHRYDR), decapeptide (GNRGFACRHA), and tripeptide (SCH) responsible of high iron-chelating properties, respectively.

1.3 Food, pharmaceutical and cosmetic applications

1.3.1 Nutraceutical and food applications

As natural and functional ingredients derived from food-based biomolecules, metal-chelating peptides have shown an increasing interest in food system applications notably as mineral-based supplements and food additives (Wen et al., 2020). In the formulation of mineral-based supplements, MCPs can promote better stability, absorption, and bioavailability of various metal ions (Ca^{2+}, Zn^{2+}, Fe^{2+} and Cu^{2+}) with important functions in the human body (Guo et al., 2015; Wang et al., 2012). Indeed, used as food-derived nutritional supplements, MCPs are one of the most common nutraceutical strategies to reduce the risk of mineral deficiencies (Guo et al., 2014). Sun et al., (2016) and Udechukwu et al., (2016) reviewed the calcium and zinc-chelating peptides obtained from various food proteins, among them soybean (DEGEQPRPFPFP, Lv et al., 2013) and rapeseed (AR, NSM, GKR, EPSH, Xie et al., 2015), for improving calcium and zinc bioavailability, respectively.

On the other hand, MCPs can act as indirect antioxidant while complexing transition metal ions (*i.e.,* Fe^{2+} and Cu^{2+}) responsible for food system oxidation. Thus, MCPs can prevent lipid peroxidation that negatively affects shelf-life of lipid-based products (Wen et al., 2020). MCPs have been supplemented in food (Sun et al., 2020) as additives in meat system (Sarbon et al., 2018), linoleic acid system, cooked pork patties, and fish oil-water emulsions, such as mayonnaise, to inhibit lipid oxidation (Wen et al., 2020).

1.3.2 Pharmaceutical applications

Minerals (*i.e.,* Ca^{2+}, Zn^{2+}, $Fe^{2+/3+}$, Cu^{2+}) possess a wide variety of biological functions. As essential elements in biological systems, they are involved in storage and transport functions and are required for metalloenzymes. Their dietary deficiency or excess could lead to numerous diseases affecting many organs in the body (**Table 1.2**). Thus, the dietary intake of

these metals should be well controlled. Upon aging, the dysregulation in metal ion homeostasis can disrupt many physiological functions, particularly in the central nervous system, causing neurodegenerative diseases, such as Alzheimer and Parkinson diseases. Elevated levels of iron, copper, and zinc promote oxidative events in the brain and increase the aggregation of β-amyloid proteins, involved in plaque formation in Alzheimer patients' brain. Besides, these metal ions might contribute in carcinogenesis (Chen et al., 2019). The iron excess in the body supplies tumors in hepatocellular carcinoma and lung cancer (Kowdley, 2004; Valko et al., 2006) while cobalt sulphate would increase proliferative lesion in respiratory tracks of mice, leading to alveolar/bronchiolar neoplasms (Bucher et al., 1999). Therefore, understanding the biochemical relationships between biometals and chronic diseases provides various novel therapeutic interventions involving MCPs (Pokusa & Kralova Trancikova, 2017).

Table 1.2. Biological relevance and deficiency symptoms of essential metal elements to the human body.

Metal ion	Biological relevance	Deficiency symptoms	Excess symptoms	Ref.
Iron	Oxygen transport and utilization, DNA synthesis, electron transport, substrate for haemoglobin production.	Anemia, immune system disorders.	Hemochromatosis: Joint pain, abdominal, pain, fatigue, weakness.	(Crichton & Ward, 2003; Fraga, 2005; Kim et al., 2012; Zoroddu et al., 2019)
Copper	Electron donor for enzymatic reactions, electron transporter (copper enzyme cytochrome c oxidase), participation in the formation of connective tissue, as collagen and keratin.	Artery weakness, liver disorder, secondary anemia.	Cu toxicity, associated with liver damage. Acute Cu intoxication leads to gastrointestinal effects, abdominal pain, cramps, nausea, diarrhea, and vomiting.	(Fraga, 2005; Kim et al., 2012; Luza & C, 1996; Prohaska & Gybina, 2004; Zoroddu et al., 2019)
Zinc	Enzymatic action of more than 300 proteins: carbonic anhydrase, superoxide dismutase, alkaline phosphatase, etc.	Skin damage, stunted growth, retarded sexual maturation, alopecia, diarrhoea and eczematous skin rash.	Zn toxicity, associated with low Cu status, altered Fe function, reduced immune function, and reduced levels of high-density lipoprotein (HDL).	(Chesters & Will, 1981; Fraga, 2005; Guo et al., 2013; Kim et al., 2012; Maret, 2013; Zoroddu et al., 2019)
Calcium	Cofactor for numerous enzymes, major component of bone and teeth, intracellular functions as a messenger in cascade signaling reactions.	Retarded skeletal growth, hypocalcemia, risk of osteoporosis.	Osteoporosis (weakening of the bones), kidney stones, kidney failure, abnormal heart rhythm.	(Brini et al., 2013; Kim et al., 2012; Shenkin, 2008; Zoroddu et al., 2019)

1.3.3 Cosmetic applications

In recent years, the cosmetic industry has shown an increased interest toward the use of peptides as cosmetical ingredients (Ledwon et al., 2021), being recognized as the next generation of cosmeticals (Apone et al., 2019; Malerich & Berson, 2014). Various mechanisms exist for peptides with cosmetic application, and specifically metal carrier peptides such as metal-chelating peptides (Errante et al., 2020).

Skin is one of the main organs in our body (Tobin, 2006). Upon aging, skin tends to become dry, and is affected by a lack of elasticity, inducing lines and wrinkles appearance. Among many skin aging factors (UV-light exposition, malnutrition, smoking, etc), heavy metals (Pb^{2+}, Cd^{2+}, Zn^{2+}, Hg^{2+}, As^{3+}, Cu^{2+}, Ni^{2+}, Fe^{2+}) constitute a serious threat for skin health (Zhao et al., 2021). Skin is generally the most exposed organ to heavy metal stress and thus the most damaged by metal-induced toxic effects (Tito et al., 2011). Metals such as Ni^{2+} can negatively affect the growth, proliferation and gene expression of cultured keratinocytes, a human epidermal cell line. Also, Ni^{2+} activates collagenases, enzymes responsible of collagen degradation in the skin (Cammarota et al., 2006), which induces loss of its fitness and elasticity (Tito et al., 2011). Inversely, copper has beneficial effects for the skin and is required for wound healing (Malerich & Berson, 2014). Thus, peptide-copper complexes enhance the synthesis of extracellular matrix proteins in the skin, such as collagen I. Notably, bioactive peptides employed in cosmetic applications are mainly produced by chemical synthesis or enzymatic proteolysis (Apone et al., 2019).

1.4 Screening methodologies of MCPs

1.4.1 Surface plasmon resonance

Surface plasmon resonance (**SPR**) is a real time, rapid and label-free technology used to study biomolecular interactions, notably the binding of small molecules to purified protein (Wang & Zhou, 2018). SPR measures the refractive index changes caused by the interaction of biomolecules with the surface of SPR biosensors (Zhou et al., 2019). More details about the SPR principle are reported in El Hajj, (2021) (**Figure 1.3**).

Numerous sensor chips are used in SPR, depending on the molecular interaction of interest. For studying the affinities and kinetics of molecular interaction between histidine (His)-tagged

proteins/peptides and metal ion, nitriloacetic acid (**NTA**) is commonly used to immobilize metal ions (Drescher et al., 2018). NTA can form chelates with divalent metal cations (*e.g.,* Cu^{2+}, Ni^{2+}, Zn^{2+}, Co^{2+}) through four coordination sites of M^{2+}, while two coordination sites on the metal ion remain free to interact with specific AA of proteins/peptides, notably imidazole rings of histidine residue (Qu et al., 2020). NTA-Ni^{2+} sensor chips were used in SPR to investigate the binding mechanism of His-tagged peptides (Knecht et al., 2009); the thermodynamic and kinetic data of the peptides, including oligohistidines and mixed oligohistidines/oligoalanines, demonstrated that the hexahistidine tag has the highest affinity. Another SPR application involved the screening of MCPs in commercial protein hydrolysates (Canabady-Rochelle et al., 2018). The most interesting hydrolysates were determined in terms of metal-chelation properties, which correlated with their antioxidant properties. More recently, in our team, El Hajj et al., (2023) employed SPR to evaluate the metal-chelating activity of soy and pea protein hydrolysates. Results revealed that the hydrolysates obtained by sequential treatments using Flavourzyme® as exopeptidases exhibited the highest metal-chelating properties.

Over the past decades, several applications of SPR have been developed with high sensitivity and selectivity. SPR using NTA-Ni^{2+} chip is the most common approach for studies on metal-chelating peptides. Conversely, SPR focuses on detection of metal ion circulating in solution to evaluate the metal-chelating properties of immobilized peptides (Daniyal et al., 2018). By this approach, Cu^{2+} (Ocka et al., 2001) Cd^{2+} (May May & Russell, 2003) Zn^{2+} and Ni^{2+} (Kim et al., 2012; Wu & Lin, 2005) were detected. A high-resolution differential SPR sensor was built for the accurate real-time measurement and quantification of metal ions while coating the sensing surface with peptides (*e.g.,* GGH, HHHHHH), enabling the selective detection of Cu^{2+} and Ni^{2+} (Forzani et al., 2005). Similarly, a sensitive SPR method was set for Hg^{2+} detection in aqueous media, exhibiting excellent selectivity over Pb^{2+}, $Cd^{2+,}$ Mg^{2+}, Ca^{2+}, Cu^{2+}, Zn^{2+}, Fe^{2+}, and Fe^{3+} (Wang et al., 2010).

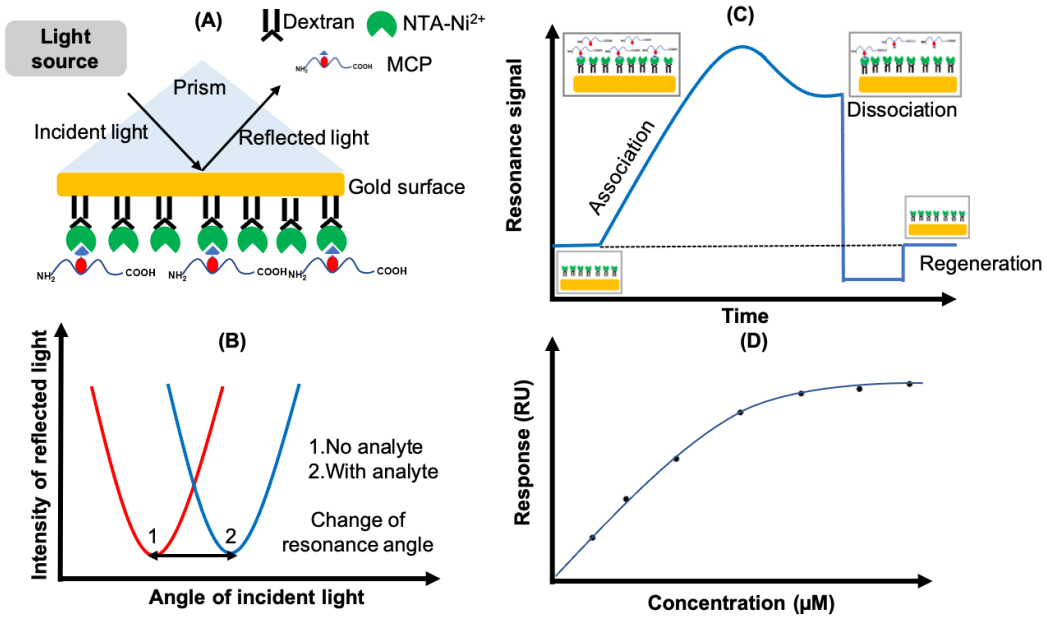

Figure 1.3. Schematic illustration of the stepwise detection of metal-chelating peptides using surface plasmon resonance. (A) A beam of polarized light incidents on the gold film surface, at an angle producing total internal reflection. Beyond a critical angle, the beam is completely reflected back out through the prism. The changes in the optical properties of the film gold surface due to the binding of analyte (Metal-chelating peptides, MCP) to ligand (NTA-Ni^{2+} on dextran) will affect the resonance angle. (B) The change in the intensity with resonance angle induced by the adsorption of a monolayer of small molecules. (C) Real-time SPR sensorgram of peptide-metal interaction which provides information about binding interactions. (D) Sorption isotherm used to obtain affinity constants.

1.4.2 Screening based on fluorometry

1.4.2.1 Biochip-based technology switchSENSE®

The switchSENSE®, a biophysical technology, works with electrically actuated DNA nanolevers on chip-based gold microelectrodes. In this technology, double stranded DNA nanolevers are tethered on a chip, electrically actuated in order to oscillate at high frequencies by alternating the voltage across the gold surface (Knecht et al., 2009). While one single strand DNA (**ssDNA**) is functionalized with a fluorophore, the second complementary strand (**cDNA-NTA**) is grafted with a capture molecule, *i.e.*, NTA, onto which Ni^{2+} is loaded in excess and immobilized (Knecht et al., 2009). When the analyte in solution (*e.g.,* peptide) flows across the surface, the interaction occurring between the biomolecules and the surface-tethered ligands (*e.g.* metal ion) is analyzed (**Figure 1.4**, biosensors, 2021).

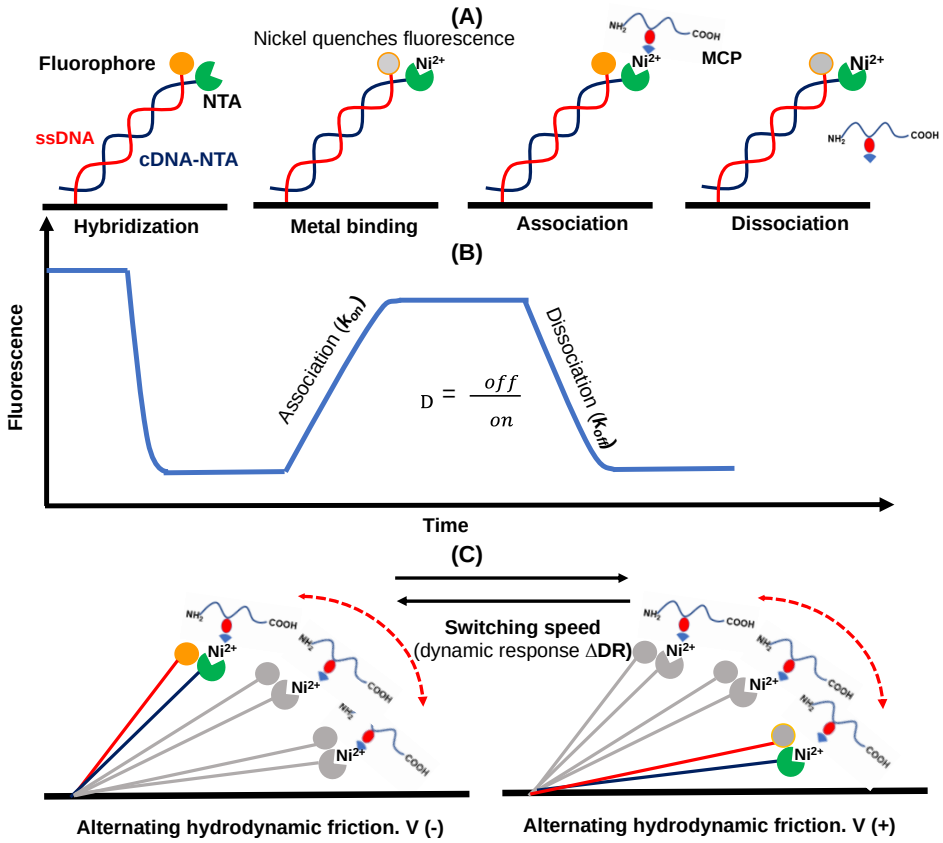

Figure 1.4. Description of the switchSENSE® methodology applied to study of peptide-metal interaction. (A) Schematic representation of hybridization of single-strand DNA nanolever (ssDNA) with a complementary-strand DNA nanolever (cDNA) that contents NTA. Binding of nickel (Ni^{2+}) ions results in fluorescence quenching due to the proximity of the metal ions to the fluorophore (quenching effect). Fluorescence intensity is increased when the fluorophore is discarded from the quenching nickel surface due to metal-chelating peptides bind to nickel metal ions. (B) The measuring of the association and dissociation of metal-chelating peptide (MCP) and immobilized nickel ions is shown. The kinetic (k_{on}, k_{off}) and affinity constant (K_D) of the peptide-metal interaction are determined by real-time measurement. (C) Dynamic mode.

Application of an alternating voltage to electrode induces a switching of the nanolevers that becomes slower upon metal-chelating peptide binding. Upon analyte binding, the hydrodynamic friction of the nanolevers and their movement are affected. Dynamic response (ΔDR) estimated by the time resolved fluorescence intensity changes, typically of the upward motion of the DNA. Following the evolution of the DR signal allows the determination of unspecific binding onto the DNA double strands.

The switchSENSE® technology was successfully applied to investigate protein/peptide interactions with different types of binding partners, notably proteins, peptides or other small molecules (Clery et al., 2017; El Hajj et al., 2021). Nickel ion has a quenching effect on the

fluorescent probe, thus, upon binding of protein/MCPs, the fluorescence intensity is restored (**Figure 1.4A, 1.4B**). Similarly, in another study, a switchSENSE® assay was developed to characterize the kinetics of ion-dependent aptamer (single-stranded DNA oligonucleotides, designed to bind tightly to their target) folding and protein binding (Ponzo et al., 2019). Subjecting the immobilized aptamers to K^+, NH_4^+, Na^+, and Li^+, the signal strongly decreased as a result of efficient ion binding. Recently in our team, the presence of MCPs in soy and tilapia protein hydrolysates using switchSENSE® technology was reported (El Hajj et al., 2021). The observed rate kinetic constants (k_{obs}) highlighted an association of the peptides with the immobilized Ni^{2+}. Yet, dissociation rate constants (k_{off}), and consequently the affinity parameter (K_D), could not be determined. Hence, switchSENSE® technology is promising in measuring the affinity and kinetics of protein/peptide-metal interaction, especially as an alternative method for screening MCPs in protein hydrolysate.

1.4.2.2 Confocal laser scanning microscopy

Confocal laser scanning microscopy (**CLSM**), a modern imaging technique currently considered as an essential tool in biological research (Huebner et al., 2013) enables the visualization and interpretation of microstructures with a high quasi-microscopic resolution and depth selectivity. Compatible with 3D live imaging, CSLM enables access to dynamic cellular and molecular processes. The image obtained from the focal plane only (noises removed optically) is acquired point by point under localized laser excitation. CLSM detects the fluorescence emitted by excited molecules present in a sample after their laser beam irradiation (Jekle & Becker, 2015). The excitation and the emission spectra being obtained at the excitation and the emission wavelengths of the fluorochrome, respectively (Canette & Briandet, 2014).

To screen MCPs, in real-time imaging mode, CLSM can monitor the kinetics of physical, chemical, and biological processes. The fluorescent ligands binding to other components can be visualized, allowing interaction studies between biomolecules. Metal-binding studies are based on a fluorescence enhancement/quenching of a fluorescent indicator. This so-called probe binds to the metal ion, and alters the fluorescence intensity detected (Dean et al., 2012). The principle of following the interaction of a biomolecule (*e.g.,* MCPs) with metal ions based on fluorescence-based indicator displacement assays using CSLM is shown in **Figure**

1.5A, 1.5B and **1.5C**. The method involves (i) the contact between the fluorescent indicator and the surface (*i.e.,* metal ion), where it binds reversibly (fluorescence enhancement), and (ii) the addition of a competitive molecule (*i.e.,* peptides) at increasing concentration to observe its ability to displace the fluorescent indicator. This second step induces a fluorescent quenching upon the indicator release from the surface into solution due to the binding of the investigated molecule onto the surface.

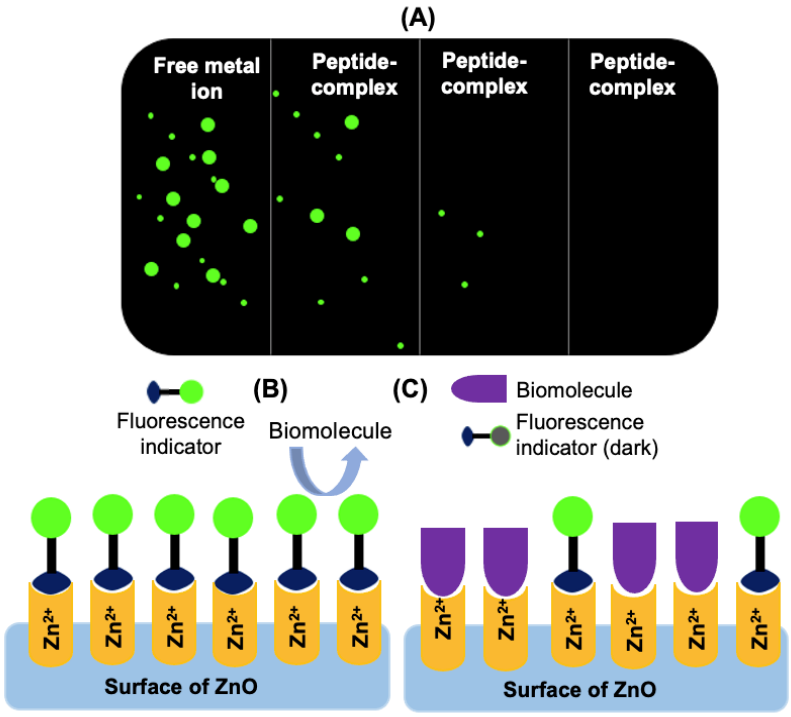

Figure 1.5. Schematic image representing the metal-chelating peptide detection based on a CLSM approach. (A) detection of peptide-metal complex formation. Free metal ions interact with fluorescence indicator, increasing the signal intensity, whereas, in the peptide-metal complex, there is a reduction in such an intensity. (B, C) Schematic illustration of the interaction between the fluorescence indicator and metal ion on surface. In presence of metal-chelating peptides, fluorescence signal decreases, allowing to study binding kinetics of peptide and metal ions in real time.

Recently, Cui et al., (2018) observed the dynamic structural changes of a peptide-calcium complex (NDEELNK–Ca^{2+}) by CSLM during gastrointestinal digestion using a fluorescent probe Fluo-3 AM to label free Ca^{2+}. Upon acidification during *in vitro* gastric digestion (pH 2), Ca^{2+} was released from the complex, showing a high fluorescence intensity. During the terminal

phase of intestinal digestion (pH 7.5), the fluorescence disappeared due to a possible self-aggregation of the peptide−Ca^{2+} complex. In a study by Michaelis and coworkers (Michaelis et al., 2019), amino acids, polyamine, and drugs were screened for their affinities for material surfaces by an indicator displacement assays using CLSM. The competitive binding between a fluorescent probe and the targeted analyte (AA residues: alanine, histidine, aspartic acid, proline, serine, cysteine, and leucine) was observed for a given interaction site (silica and zinc oxide surfaces) and binding affinity parameters were determined with respective surfaces using PDMPO and FluoZin-1 as fluorescent probes. Likewise, Muller et al., (2020) used CLSM for copper detection using a fluorescent peptide (ATCUN-like peptide 5/6-FAM-Dap-β-Ala-His) to selectively bind Cu^{2+}. Upon Cu^{2+} binding, the fluorescence of the peptide sensor was quenched, permitting the indirect detection of Cu^{2+} in solution. Hence, the determination of metal ion by fluorescence quenching observed by CLSM could be useful to study quantitatively the peptide-metal ion interactions.

Many sensitive fluorescent probes highly specific for metal ions (*e.g.,* Fe^{3+}, Fe^{2+}, Cu^{2+}, Zn^{2+}) were used for their detection, notably to explore neuronal metal homeostasis and metal-related physiological processes (Hao et al., 2013). Besides, probes targeting toxic metals (*e.g.,* Pb^{2+}, Hg^{2+}, Cd^{2+}, Ag^{+}, Au^{3+}, and Pt^{2+}) were reported in cellular toxicity studies (Zhang et al., 2011). Johnson et al., (2018) used a metal-specific fluorescent probe (Leadmium™ Green AM) for visualizing and quantifying the bacterial Cd^{2+} biosorption, highlighting CSLM as a powerful tool for quantifying the metal distribution in complex realistic environments. To date, CLSM has shown a high potential in the study of free metal ions and their behaviour using a fluorescent probe. Nevertheless, its use in metal-binding peptides evaluation is scarce. Thus, the metal-chelating capacity of peptides using CSLM needs to be further investigated.

1.4.3 Screening based on UV-visible spectrophotometry

1.4.3.1 Iron-chelation test

The iron-chelating activity (Fe^{2+}) is a colorimetric assay followed by UV-visible spectrophotometry, based on the use of reagents such as ferrozine (3-(2-pyridyl)-5,6-diphenyl-1,2,4-triazine-*p*,*p*'-disulfonic acid monosodium salt hydrate) or *o*-phenanthroline (Carter, 1971; Lee & Song, 2009). Ferrozine assay, based on changes in the absorbance spectrum of the stable [Fe^{2+}-(Ferrozine)$_3$] complex (λ_{max} = 562 nm, log*b* = 15.70) (Smith et al.,

2021) in the presence of an investigated sample (**Figure 1.6**), is commonly performed to determine metal-chelating capacity of a peptide hydrolysate (Canabady-Rochelle et al., 2015; Guo et al., 2014). In comparison, *o*-phenanthroline method is based on the formation of a [Fe^{2+}-(*o*-phen)$_3$] complex (λ_{max} = 510 nm, logβ = 20.69) (Alexander et al., 1977). In both tests, the iron-chelating capacity of an investigated sample is related to an absorbance decrease associated to the decrease of colored complexes formed, in the presence of MCPs (Sun et al., 2020). **Table 1.3** summarizes the metal-chelating investigation on protein hydrolysates, highlighting the protein source, method, enzyme used in proteolysis and main found values.

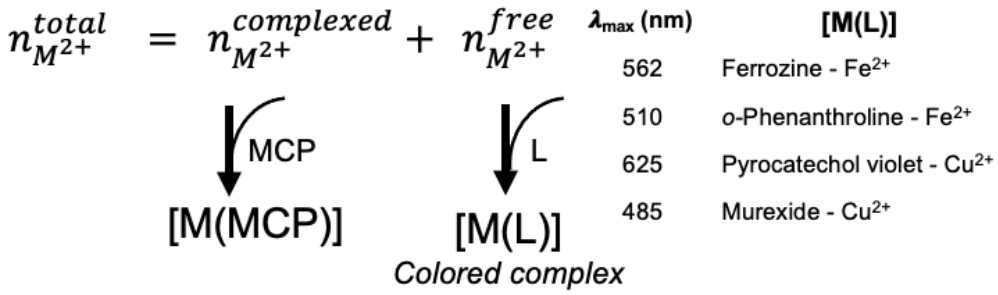

Figure 1.6. Chemical reactions involved in metal-chelation test. M: metal ion; MCP: metal-chelating peptides; L: ligand.

1.4.3.2 Copper-chelation test

The copper-chelating activity (Cu^{2+}) of a hydrolysate is determined similarly by colorimetric assays, either using pyrocatechol violet (**PV**) or murexide reagents (**Table 1.3**). The Cu^{2+}-chelation with pyrocatechol violet - the most commonly used method (Guo et al., 2014)- is based on the absorbance changes followed at λ_{max} = 625 nm attributed to the [(Cu^{2+})(PV)$_3$] complex (**Figure 1.6**) (Yadav & Zelder, 2021).

Upon complexation of copper (Cu^{2+}) by the investigated metal chelating peptide, the concentration of [M(MCP)] complex present in the assay increases, which leads a decrease in absorbance of [(Cu^{2+})(PV)$_3$] complex (**Figure 1.6**) (logβ = 10.08) (Yadav & Zelder, 2021). In other studies, the copper-chelating activity of MCPs was determined using murexide as color indicator (**Figure 1.6**) (Canabady-Rochelle et al., 2018; El Hajj et al., 2021), however, a weak stability complex (λ_{max} = 485 nm, logβ = 4.36) (Shamsipur et al., 1989) is formed between murexide and a small amounts of copper (Cu^{2+}) present in the solution.

Table 1.3. Summary of assays used for determining iron and copper chelating activity of food protein hydrolysates.

Protein source	Enzyme treatment (experimental conditions)	Chelation test	Metal-chelating properties	Ref.
Barley seed	Alcalase® (pH: 8, 50 °C), Flavourzyme® (pH: 7, 50 °C) and Pepsin (pH: 2, 37 °C)		39–73%	Bamdad et al., (2011)
African Yam bean seed	Alcalase® (pH: 9, 50 °C)		60%	Ajibola et al., (2011)
Peony seed dreg	Alcalase® (pH: 10, 55 °C)	Fe^{2+}: Ferrozine at 1 mg/mL	5-60%	Zhang et al., (2019)
Casein protein	Trypsin (pH: not specified, 50 °C)		20-30%	Miao et al., (2019)
Pacific cod skin gelatin	Trypsin (pH: 7.5, 37 °C), Alcalase® (pH: 8, 55 °C) and Flavourzyme® (pH: 7, 50 °C)		12-58%	Wu et al., (2017)
Chickpea protein	Pepsin (pH: 2.5, 37 °C) and Pancreatin (pH: 7.5, 37 °C)	Fe^{2+}: Ferrozine at 0.4 mg/mL	40%	Torres-Fuentes et al., (2011)
Alaska pollock skin	Trypsin (pH: 8, 50 °C) and Flavourzyme® (pH: 7, 50 °C)		67%	Guo et al., (2013)
Soybean protein	Trypsin (pH: 8, 37 °C)	Fe^{2+}: Ferrozine at 0.8 mg/mL	18.47 µg/mg	Zhang et al., (2012)
Mung beans proteins	Papain, Alcalase® and Neutrase® (pH: 10, 45 °C)	Fe^{2+}: Ferrozine at 10 µg/mL	60 µg/mg	Zhang et al., (2021)
	Alcalase® (pH: 8,60 °C), Neutrase®, Protamex®, Flavourzyme® and Papain (pH: 7, 50 °C)	Fe^{2+}: Ferrozine (0.2-1 mg/mL)	EC_{50}: 0.22-0.55 mg/mL	Liu et al., (2022)
Lentinus edodes protein	Alcalase® (pH: 8,60 °C), Protamex® (pH: 7, 50 °C), Trypsin (pH: 7, 50 °C), Papain (pH: 7, 50 °C) and Neutrase® (pH: 7, 50 °C)	Fe^{2+}: Ferrozine (1-5 mg/mL)	24.67 g/100 g	Bing et al., (2024)
Tree peony proteins	Alcalase® (pH: 8,60 °C), Neutrase®, Papain, Protamex® and Flavourzyme® (pH: 7, 50 °C)	Fe^{2+}: Ferrozine	EC_{50}: 0.99- 2.70 mg/mL	Wang et al., (2021)
Rice bran protein	Alcalase® (pH: 8, 60 °C), Neutrase®, Pepsin, Chymotrypsin and Trypsin (pH: 7, 50 °C)	Fe^{2+}: Ferrozine (0.1-25 mg/mL)	EC_{50}: 2.27 mg/mL	Ren et al., (2023)
Porcine blood plasma	Flavourzyme® (pH: 7, 50 °C)	Fe^{2+}: *o*-phenanthroline	0.40 mM	Lee & Song, (2009)
Mung beans	Alcalase®, Flavourzyme® (pH: 8, 50 °C), Trypsin, Pancreatin (pH: 7, 37 °C), Pepsin (pH: 2, 37 °C)		19.24 mg/g	Budseekoad et al., (2018)
Chickpea protein	Pepsin (pH: 2.5, 37 °C) and Pancreatin (pH: 7.5, 37 °C)	Cu^{2+}: Pyrocatechol violet	27-45%	Torres-Fuentes et al., (2011)
Bean protein			35-50%	Carrasco-Castilla et al., (2012)
Alaska pollock skin	Trypsin (pH: 8, 50 °C)		0.12-0.72 µmol/µmol	Guo et al., (2015)
Rice bran albumin	Papain (pH: 8, 37 °C)		EC_{50}: 0.62 mg/mL	Kubglomsong et al., (2018)
Salmon by-product	Alcalase® (pH: 7.5, 55 °C), Neutrase® (pH: 8, 55 °C), Protamex® (pH: 6.5, 55 °C) and Flavourzyme® (pH: 7, 50 °C)		6-12 mg/g	Vo & Pham, (2020)
Chia seed	Pepsin (pH: 2), Pancreatin (pH: 7) (Temperatures: 30, 37, 45°C)		40-75%	Latha et al., (2021)
Soy, wheat and rice	Commercial hydrolysates		60-80%	Canabady-Rochelle et al., (2018)
Fish (greater weever)	Trypsin (pH: 8, 37 °C) and Alcalase® (pH: 8, 50 °C)	Cu^{2+}: Murexide	71.4%	Kula et al., (2020)
Soybean	Alcalase®(pH: 8, 55 °C), Protamex®, Flavourzyme® (pH: 7, 55 °C)		60-70%	El Hajj et al., (2021)
Barley grain	Trypsin (pH: 7.4, 37 °C)		77%	Tok et al., (2020)

Upon the copper (Cu^{2+}) complexation by MCPs, the amount of free Cu^{2+} is followed by a decrease in absorbance of the [(Cu^{2+})(murexide)] complex, allowing to estimate the chelation capacity of peptides.

The iron chelation tests cited previously and the copper chelation test with PV are based on the use of stoichiometric amounts of ligand that form moderately stable complexes with metal ions. These conditions where competition takes place between assay ligand and MCPs are the most suitable for evaluating the metal ion chelation capacity of MCPs from food-derived protein hydrolysates.

There are many alternatives to report the metal-chelating ability of MCPs (**Table 1.3**), however to determine whether food protein hydrolysates possess suitable metal-chelating properties, comparison with a positive control becomes necessary. Glutathione, composed of glutamate, cysteine, and glycine (γ-Glu-Cys-Gly), displays remarkable metal-chelating properties due to its thiol group (-SH), which plays a crucial role in defending the body against metal-induced oxidative stress (Jozefczak et al., 2012). The metal-chelating ability of glutathione, determined by a Fe^{2+}-chelating assay and expressed as the half maximal effective concentration (EC_{50}), was found to be 1.82 mg/mL (Liu et al., 2022). Consequently, peptides derived from food protein hydrolysates characterized by lower EC_{50} values than glutathione, are potential candidates as promising MCPs. A few examples of food-derived MCPs with low and high metal-chelating properties are displayed in **Table 1.3**.

1.4.3.3 Other chelation assays

Colorimetric methods are also used for determining the chelating activities for other metals, such as Zn^{2+}, Ca^{2+} and Gd^{3+}. Zinc-chelating activity is determined by the 4-(2-pyridylazo) resorcinol assay where the free Zn^{2+} and 4-(2-pyridylazo) resorcinol (PAR) reagent form a red-colored complex (λ_{max} = 500 nm) (Sun et al., 2020). The Zn^{2+}-chelating capacity of whey and sea cucumber-derived peptides was investigated using this approach (Liu et al., 2019; Udechukwu et al., 2018). Likewise, Ca^{2+}-chelating capacity was measured by a colorimetric assay using the *ortho*-cresolphthalein complexone (*o*-CPC) method (Katsoulos et al., 2020; Kumar & Gill, 2018). Calcium ions bind to the *o*-CPC reagent, forming a red-violet complex, which absorbs at 570 nm (Gitelman, 1967; Sun et al., 2020). First, the samples are dissolved

in Ca^{2+}-binding phosphate buffer (20 mM, pH 7.8) with $CaCl_2$ (5 mM) to form peptide-Ca^{2+} complex. Then, the mixture is stirred at 37 °C for 60 min and the solution is centrifuged (4000 rpm, 20 min) to remove the insoluble calcium phosphate salt (Zhao et al., 2014). As a result, the Ca^{2+} content in the supernatant, complexed with the peptide is determined using *o*-CPC reagent. The Ca^{2+}-chelating properties of a variety of whey and bovine serum-derived peptide were characterized by this method (Argade & Ahlawat, 2021; Choi et al., 2012; Huang et al., 2015; Zhao et al., 2014).

1.4.4 Ion selective electrode

During the past decades, metal ions have been detected by ion selective electrodes (**ISE**) due to their low cost, simplicity, low detection limits, and good selectivity (Inamuddin & Alam, 2008) ISE is a potentiometry technique widely used to study environmental analytes *e.g.,* trace metals, phosphate, nitrite, nitrate, etc. (De Marco et al., 2007). The metal ion concentration (*e.g.,* Fe^{2+}, Zn^{2+}, Ca^{2+}, Cu^{2+}, Pb^{2+}) is determined based on an electrochemical sensor, which measures electronic signals (electric potential Φ) using a voltmeter and converts it into the concentration of a particular ion in bulk solutions (Aroua et al., 2008). ISE requires the use of a reference electrode to electrochemically determine the concentration of target ions in various chemical environments (Tang et al., 2018).

To evaluate metal-chelating properties of proteins, hydrolysates or peptides using ISE, the free metal ion content is usually determined before and after adding samples. Potentiometry was successfully used to measure the free calcium ion in relation to the Ca-binding properties of various proteins and hydrolysates, *e.g.,* soy proteins (Kroll, 1984), skim milk protein (Canabady-Rochelle et al., 2007), soy protein hydrolysate (Canabady-Rochelle et al., 2009), Tilapia protein hydrolysates (Charoenphun et al., 2012), and mung bean protein hydrolysates (Budseekoad et al., 2018). For this purpose, Ca^{2+}-protein/hydrolysate complex was formed at pH 7.8, which precipitates from the solution. By measuring the calcium content in the supernatant using the pH/ION meter, and based on the Ca-ion mass balance, the mass of bound calcium and hence the calcium-binding capacity was determined.

1.4.5 Screening using other methodologies

Alternative techniques can be used to determine the metal-chelating properties of food proteins and peptides. Examples include flame atomic absorption spectrophotometry (**FAAS**) and complexometric titration (Sun et al., 2020).

In FAAS, the sample is introduced into the atom cell, where metal ions in solution are converted into the atomic state by means of flame. Then, analyte atoms absorb the energy (light) at a specific wavelength, proportional to their concentration in the cell. From the amount of absorbed light, the concentration of the metal in solution is calculated (Hill & Fisher, 2017). Metal-chelating properties are determined using FAAS based on the knowledge of the initial metal ion amount and by measuring the remaining free metal ion amount upon peptide-metal complexation. Zinc-chelating capacities of yak casein hydrolysate (Wang et al., 2011), and sea cucumber-derived synthetic peptides (Liu et al., 2019) were evaluated using FAAS. Similarly, Chen et al., (2014), Hou et al., (2018), Zhang et al., (2019), Malison et al., (2021), investigated the calcium-chelating peptides from various hydrolysates from Tilapia scale, Antarctic krill protein, Pacific cod bone protein, and chicken foot broth byproduct respectively.

In EDTA complexing titration (**ECT**), EDTA is titrated into the solution obtained after peptide-metal complex reaction to bind the free metal ion, and thus indirectly determine the amount of complexed metal (Xie et al., 2015). In ECT, the formation of a colored complex indicates the titration end point, which depends on the metal ion indicator. Some metal ion indicators, their mechanism of action, chemical properties, and specific conditions to be used (*i.e,* pH, metal ions detected, color transition) have been briefly discussed (Burgot, 2012). For example, the color indicator mixture of xylenol orange and hexamethylenetetramine switches from purple to yellow (equivalence point) once the remaining free metal ion is complexed by EDTA (Barge et al., 2006). Wang et al., (2012) evaluated the zinc and iron-chelating capacity of sesame protein hydrolysate by EDTA complexing titration (Wang et al., 2012). Recently, the zinc-chelating peptides were also determined from mung bean protein hydrolysates by ECT (Fu et al., 2019). Similarly, the Gd^{3+}-chelating capacity can be estimated by the amount of free Gd^{3+} quantification using ECT in the presence of xylenol orange indicator (Barge et al., 2006).

1.4.6 Screening of MCPs coupled to their identification

1.4.6.1 Differential analysis by mass spectrometry

Mass spectrometry (**MS**) was used during the last decades to discover and identify MCPs (Tu et al., 2018). In this approach, proteins/peptides must be generally separated prior to MS analysis (León et al., 2018). Liquid chromatographic coupled to MS (**LC-MS**) provided simple and effective approaches. The most commonly used techniques for MCPs identification include liquid chromatography-electrospray ionization mass spectrometry (**LC-ESI-MS**), ultra-high performance liquid chromatography-tandem mass spectrometry (**UHPLC-MS/MS**), and matrix-assisted laser desorption/ionization time-of-flight mass spectrometry (**MALDI-TOF-MS**) (Sun et al., 2020).

Many MCPs sequences were evidenced using this approach in various protein hydrolysates produced from soybean (Lv et al., 2013), Tilapia scales (Chen et al., 2014), wheat germ (Zhu et al., 2015), Pacific cod skin gelatin (Wu et al., 2017), and scad fish (*Decapterus maruadsi*) by-product (Jiang et al., 2019). Yet, these multistep methods are time-consuming and costly. To address these drawbacks, our team recently developed a rapid and direct screening of Fe^{2+}-chelating peptides in protein hydrolysates based on a differential LC-HRMS (high resolution mass spectrometry) analysis of mass spectra (Paris et al., 2021). The proof of concept was validated on tryptic casein hydrolysate using ion pair IP-RPLC-ESI-HRMS. The presence of MCPs was validated by a mass difference of 53.919 m.u. between the mass spectral peak of iron-peptide complex and the one of free uncomplexed peptide. Besides, the relative abundance of each complex was used to compare the peptide chelating performance.

1.4.6.2 Screening coupled to peptide identification "in silico"

Bioinformatic strategy (*in silico* analysis) can simulate protein hydrolysis, and predict peptide bioactivity from known primary protein sequences (Daroit & Brandelli, 2021). This emerging approach gives quick information about the potential protein source for producing MCPs, as well as the potential biofunctional activities of protein fragments, including metal-chelating capacity (Ca^{2+}, Cu^{2+}, Fe^{3+}, Mg^{2+}, Mn^{2+}, Zn^{2+}) (Lu et al., 2012; Remko et al., 2011). This could be done prior to conducting experimental approaches, which requires isolation and purification process than can be expensive and time consuming. Additionally, *in silico* approach allows to

obtain complementary information about the safety of MCPs sequences obtained from experimental data.

Nowadays, a large number of databases and bioinformatics tools are available and focus specifically on bioactive peptides (Daroit & Brandelli, 2021), among them StraPep (information about experimental structure, location of disulfide bonds and secondary structure, Wang et al., 2018), FeptideDB (predicts the potential of cleaved peptides to identify new ACE inhibitors, Panyayai et al., 2019), SpirPep (in *silico* digestion of protein, classification of peptides by bioactivity, Anekthanakul et al., 2018), PlantPepDB (experimentally validated plant-derived peptides database, Das et al., 2020), BIOPEP-UWM (presence of bioactive fragments in protein sequences, providing information on proteases that release particular peptides, Minkiewicz et al., 2019), MBPD (specific data base for milk bioactive peptides and peptidomic data analysis, Nielsen et al., 2017), and PeptideLocator (machine learning algorithm to provide information on bioactive peptides prediction within protein sequences, Mooney et al., 2013). Additionally, the *in silico* approach enables the prediction of the metal-chelating potential of sequences by estimating the percentage of metal-binding residues (H+C, D+E) over the total number of AA residues (Lu et al., 2012; Remko et al., 2011).

On the other hand, substantial scientific evidences have shown that toxic peptides may be generated upon the protein isolation, protein pretreatment, proteolysis and the metal-chelating peptides preparation. These peptides could present for example hepatotoxicity, which is associated to the deficient protein synthesis and cell necrosis due to the inhibition of RNA polymerase (Liu et al., 2020). Gupta et al., (2013) developed ToxinPred tool, a unique *in silico* method used to predict toxicity of peptides, which can provide useful information previous to MCPs preparation. Indeed, certain amino acid residues like Cys and His (involved in metal-chelating properties) together with Asn and Pro were often found in toxic peptides. Recently, three zinc-chelating peptides sequences (TGLL, YILIK, FDEE) obtained from coconut cake globulin hydrolysates were analyzed using ToxinPred and In silico predicted as non toxic; however *in vitro* and *in vivo* toxicity studies on these peptides are needed (Zheng et al., 2023). Besides, the allergenicity profile of peptides plays also an important role in MCPs processing to ensure their safety for human consumption (Singh et al., 2023). Thus, several *in silico* tools can be used to predict the potentially allergenic metal-chelating peptides such as Allergome (http://www.allergome.org/), Allergen FP (http://www.ddg-pharmfac.net/AllergenFP) and

WHO/IUIS (http://www.allergen.org/) (Liu et al., 2020; Singh et al., 2023). Despite the use of these powerful bioinformatic tools to provide an overview of MCPs safety, little attention has to be paid to study the toxicity and allergenicity of novel metal-chelating peptides in clinical assays.

Furthermore, molecular docking is another *in silic*o approach used to study metal-chelating properties of peptides and to understand the peptide-metal interaction (Meng et al., 2021). The behavior of metals in the binding site of target proteins/peptide can be characterized to elucidate fundamental biochemical processes (Roy et al., 2015). In Yiannikouris et al., (2009), the molecular mechanisms of the peptide-Cu^{2+} interaction was investigated using Silicon Graphics computers equipped with Accelrys packages. More recently, Wang et al., (2021) used molecular docking to predict interactions between hydrophobic peptides from oyster protein hydrolysates and zinc ions. All peptides had at least one chelating amino acid residue, with D and E the most frequent ones involved in zinc chelation.

In another approach (Auwal et al., 2019), the MCPs effect was investigated on the deactivation of zinc-dependent enzymes, such as angiotensin I-converting enzyme (ACE). The ACE inhibition is a key therapeutic approach for controlling high blood pressure; thus, the molecular mechanism of Zn^{2+}-chelating peptides interaction with Zn^{2+} present on ACE active site was explored *in silico*, Zn^{2+} being crucial for the enzyme activity. Hence, Jimsheena & Gowda, (2011), Pan et al., (2013) and Jia et al., (2015) evaluated by molecular docking the ACE inhibition by peptides derived from arachin, whey protein and silkworm pupa (*Bombyx mori*) protein hydrolysates, respectively, where the direct Zn^{2+} coordination by peptide at the ACE active site plays a significant role in ACE inactivation. The mechanism of two Zn^{2+}-chelating peptides (RALP and WYT) was reported on ACE inhibition and involved their C-terminal carboxylic oxygen (Gunalan et al., 2020). Similarly, Auwal et al., (2019) predicted by molecular docking the binding mode of five metal-chelating peptides from stone fish (*Actinopyga lecanora*) hydrolysates with ACE.

1.5 Separation of MCPs

1.5.1 Immobilized metal ion affinity chromatography

The immobilized metal ion affinity chromatography has been considered as the first stage in the purification of MCPs (Guo et al., 2014). Characterized by a high sensitivity, selectivity, binding capacity and recovery rates, IMAC is the most widely used chromatography for isolating MCPs (Sun et al., 2020). This separation technique is based on the affinity of some amino acid residues of peptides or proteins for transient metal ions (*e.g.,* Zn^{2+}, Cu^{2+}, Ni^{2+} or Co^{2+}) immobilized onto a complexing ligand (*e.g.,* NTA, Iminodiacetic acid IDA), the latter being grafted onto the chromatographic solid phase.

As metal ion, Ni^{2+} is widely used due to its affinity for exposed side chains of histidine residues, in some cases found at the N- or C-terminus (Block et al., 2009; Chikha et al., 2002). Guo et al., (2015) investigated the purification of MCPs from Alaska pollock skin collagen hydrolysate, using IMAC resins charged with various metal ions (M^{2+}: Ca^{2+}, Zn^{2+}, Fe^{2+} and Cu^{2+}) immobilized onto the chromatographic phase *via* IDA complexing agent. Various profiles of peptides were separated on each IMAC-M^{2+} columns, indicating a different MCPs composition according to the immobilized metal ion. In other studies, the Zn^{2+}-chelating peptides were purified using IMAC-Zn^{2+} in sesame (Wang et al., 2012), oyster (Chen et al., 2013) and rapeseed protein hydrolysates (Xie et al., 2015). Similarly, De la Hoz et al., (2014), Lv et al., (2013) and Lv et al., (2017) separated in IMAC the Fe^{3+}-chelating peptides present in sugar cane yeast, soybean defatted, and walnut flake protein hydrolysates, respectively.

1.5.2 Separation coupled to peptide identification using IMAC-MS/MS

In the empirical approach, once MCPs are enriched by IMAC, further purification is carried out by RP-HPLC, followed by a subsequent tandem mass spectrometry (MS/MS) analysis for their identification. Indeed, in MS/MS experiments, the second mass analyzer is used to generate sequence information, in addition to the molecular weight information generated in the first MS experiment (Borch & Roepstorff, 2010). Currently, numerous studies evaluated the offline IMAC-MS/MS approach for detecting MCPs in protein hydrolysates targeting various metal ions such as Zn^{2+} (Udechukwu et al., 2021; Wang et al., 2012; Zhu et al., 2015) ,Ca^{2+} (Guo et al., 2015; Lv et al., 2013), Fe^{3+} (Lv et al., 2013; Lv et al., 2017), Cu^{2+} (Guo et al., 2015), or Fe^{2+} (Guo et al., 2015; Guo et al., 2013; Lin et al., 2021). Nevertheless, this method

is laborious since desalting step is required before MS/MS analysis (Wang et al., 2006). To overcome this constraint, some studies directly separated and identified MCPs by IMAC-MS online coupling. Hence, phosphopeptides produced from β-casein by the enzymatic hydrolysis with trypsin were identified using online IMAC/ESI/MS (Nuwaysir & T., 1993), with a sufficient sensitivity to detect peptides at the picomolar level. Besides, sample losses were lower compared to offline approach. Similarly, an automated online IMAC-capillary RP-HPLC-ESI-MS/MS platform was used by Wang et al., (2006). Phosphopeptides, well-known MCPs, were eluted from IMAC column, then directly trapped on the C18 precolumn and analysed by LC-ESI-MS/MS. This developed platform was highly sensitive, for detecting phosphopeptides. Although online IMAC-MS/MS technology has been used for the identification of phosphopeptides, achieving high sensitivity, practicability, and feasibility remains a challenge.

In addition to former chromatographic techniques, SPR could also be used to separate and directly identify MCPs when coupled to online MS system. Borch & Roepstorff, (2010) reported the capture of 6-His-tagged proteins by SPR, using NTA-Ni^{2+} derivatized sensorchips, followed by their elution and their MS identification.

1.5.3 Simulation of IMAC separation from SPR data

Chromatography modelling and simulation can be used to predict the separation of MCPs in IMAC (Irankunda et al., 2022). It allows the prediction of peptide concentration profile as a function of time for given operating parameters. Chromatography modelling can be performed using a transport dispersive model, which describes the phenomenon that occurs in a chromatography column, like mass transfer, assuming that adsorption occurred at constant temperature, radial homogeneity and lumped coefficients for axial dispersion and mass transfer resistances (Le Gouic et al., 2018; Ng et al., 2012). A crucial step in chromatography modelling consists of finding Langmuir sorption isotherm parameters (q_{max}, the maximal binding capacity, and K_A, the affinity constant) that can be used as input data for MCPs separation simulation. Indeed, the sorption isotherm gives information about the equilibrium between the concentration of the peptide in the mobile phase (eluant) and the stationary phase (chromatography phase) at a constant temperature. Several methods are used to obtain sorption isotherm, like adsorption-desorption, frontal analysis, perturbation *etc.*, but they require a series of experiments and high amount of sample and buffers (Seidel-

Morgenstern, 2004). Therefore, biosensors-based techniques are promising alternatives to obtain sorption isotherm parameters due to their high sensitivity, the use of small quantity of sample and buffers, and their efficacy to screen MCPs in protein hydrolysates (Canabady-Rochelle et al., 2018). In addition, there is analogy between IMAC and SPR since both technologies are based on peptide-metal ion interactions and present some similarities: the same metal can be chosen for immobilization (*e.g.,* Ni^{2+}) and the same complexing agent like NTA can be used, supported by the matrix in both technologies (Irankunda et al., 2022). This analogy between both techniques may lead to efficient prediction of MCPs separation in IMAC using sorption isotherm parameters obtained by SPR (Irankunda et al., 2024).

To perform MCPs separation simulation, pdepe solver (Matlab) could be used. Parameters from SPR (maximal response (R_{max}) and the dissociation constant (K_D) are transposed to IMAC in order to obtain input data (q_{max}, the maximal binding capacity and K_A, the affinity constant) usable for IMAC simulation. Finally, the output data is the profile of peptide concentration as a function of time, from which the simulated retention time of a peptide is obtained, as reported in the proof of concept established by Muhr and colleagues (Muhr et al., 2020). On the other hand, experiments are done in IMAC, and experimental retention time is compared with the simulated retention time in order to validate the chromatography modelling. More recently, in our team, Irankunda et al., (2024) deciphered the peptide-metal interaction involved in IMAC and SPR technology of 22 peptides. The finding indicated that most of the studied peptides with a high retention time in IMAC also exhibited a high affinity in SPR, which agreed with Muhr and colleagues (Muhr et al., 2020).

1.6 Chemical interaction between peptide and metal ions

1.6.1 Fourier-transform infrared spectroscopy

Fourier-transform infrared spectroscopy (**FTIR**) gives information about the chemical composition and conformational structure of food components (Gómez-Guillén et al., 2010). This technique is extremely useful to investigate the protein/peptide structure: it provides a wealth of information on structure and environment of the protein/peptide backbone and of the amino acid side chains (Barth, 2000). FTIR is based on the increase in the amplitude of bond vibrations following the absorption of infrared energy at a frequency corresponding to the frequency of the bond's natural vibration. The vibrational-rotational bands occur between

4000 and 400 cm^{-1}, and the wavenumber of absorption depends on the relative masses of the atoms, force constants of the bonds and the geometry of atoms (Silverstein et al., 2005).

In MCPs research, FTIR has been used to find relevant information for understanding peptide-metal complexation (Wu et al., 2020). To study this complexation, FTIR commonly investigate two spectra related to the metal-chelating peptides alone and the peptide-metal complex. By comparing the absorption bands, the specific groups involved in the peptide-metal ion interaction can be identified. For instance, changes in the characteristic IR absorption bands of carboxylate, amine, and amide groups in the hydrolysate/peptide spectra may reflect the interaction of metal ions with these organic ligand groups containing C=O, C-N and N-H bonds (Sun et al., 2017). In the FTIR spectrum, proteins and peptides are usually distinguished from other compounds due to the characteristic spectral features localised in two major spectral regions *i.e.,* Amide I and Amide II, related to the peptide bonds (**Table 1.4**) (Athira et al., 2021). Upon a peptide-metal ion interaction, these group bands are shifted to a different wavenumber (Dn ~10-30 cm^{-1}) with some variation in the peak intensity as observed in the spectrum of the metal-peptide complex (Nie et al., 2014). Hence, the wavelength shift of infrared absorption peak of characteristic groups indicates their involvement in metal ion chelation and is used to determine the type of active group coordinated to the metal ion. Some examples in literature of the most reported chemical groups in protein/peptides associated with metal ion complexation are summarised in **Table 1.5**.

Likewise, a Ca^{2+}-chelating peptide (DPAH) purified from tuna fish (*Auxis thazard*) protein hydrolysate was characterized by FTIR (Chen et al., 2019), showing that the Ca^{2+} binding sites involve the carboxylic group of Glu, and the carboxylic group and the amide group of the C-terminal His. Regarding iron-complex, Huang et al., (2011), Wang et al., (2011), and Wu et al., (2017) investigated the possible binding mode of iron-chelating peptides from shrimp processing by-products, yak casein and Pacific cod skin gelatin hydrolysates, respectively. FTIR data revealed that all the peptides bind with ferrous ions through the amino and carboxylate terminal groups and the amide bond of the peptide backbone as well as the amino (C-N) and imine (C=N) of the arginine side chain. Recently, sea cucumber-derived synthetic peptides involved in zinc-chelation were investigated by FTIR, and the carboxyl groups were found to be the primary binding sites for zinc ion (Liu et al., 2019).

Table 1.4. Overview of the absorption wavenumbers of the chemical groups associated to protein/peptides reported in literature.

Amide group	Functional group	Absorption wavenumber (cm^{-1})	Assignments	Ref.
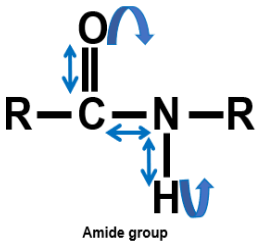 Amide group	Amide A	~3400-3300	N-H stretching vibration	Barth, (2007)
	Amide B	~3100		
	Amide I	~1700-1600	C=O stretching vibration (80%) C-N stretching vibration (10%) C-H bending vibration (10%)	(Barth, 2007; Y. Zhang et al., 2021; Zhou et al., 2012)
	Amide II	~1600-1500	N-H bending vibration (60%) C-N stretching vibration (40%)	
	Amide III	~1400-1200	C-N stretching vibration (30%) N-H bending vibration (30%) C=O stretching vibration (20%) and other (20%)	(Barth, 2007; Meng et al., 2021)
	Carboxylate	~1400	COO^-	Chen et al., (2013)
	Carbonyl	~1600	C=O	Wang et al., (2021)
	C-H, N-H, C=O	~800-400	C-H, C=O and N-H bending vibrations	Wang et al., (2014)
	Sulfhydryl	~2551	S-H vibrations	(Barth, 2000; Barth, 2007)

Currently, FTIR has been used to study peptide-metal ion interaction on both whole hydrolysates and peptide fractions from soybean protein using Ca^{2+}, Fe^{2+} and Zn^{2+} (Kong et al., 2021). Zhao, *et al.,* (2014) studied the calcium-chelating capacity of a peptide (GY) isolated from whey protein hydrolysate and found that the oxygen atoms of the carboxyl group and the nitrogen atoms of the amine group are coordinated to calcium ion.

Note that FTIR is usually carried out after analysis by UV-vis spectroscopy (Wu et al., 2020). Once the presence of peptide-metal interaction is confirmed by UV-vis, FTIR is performed in order to have deeper information. **Table 1.5** summarizes the FTIR use in some MCPs studies to date. Meng *et al.* (2021) investigated the properties of Tilapia skin collagen peptide to chelate zinc ion from different sources (*i.e.,* zinc sulfate or lactate) using FTIR and UV-vis analysis. Substantial differences were observed in the infrared and UV-vis spectra of the two peptide-zinc complexes, indicating that various zinc sources could influence the metal-ligand interactions and the types of amino acid residues involved in chelation.

Table 1.5. FTIR and UV-visible used for understanding of peptide-metal interaction.

Source of peptides	Metal ion	Techniques of Analysis	Investigated complex	Finding	Ref.
Soybean protein	Calcium	FTIR	Hydrolysate-Ca	Amino nitrogen atoms and oxygen atoms in the carboxyl group involved in complexation	Bao et al., (2008)
Whey protein			GY-Ca		Zhao et al., (2014)
Tuna fish			EPAH		Chen et al., (2019)
Wheat germ protein		UV-visible and FITR	KGDPGLSPGK-Ca		Liu et al., (2013)
Antarctic krill			Hydrolysate-Ca		Hou et al., (2018)
Pacific cod bone			VLGYIQIR-Ca		Zhang et al., (2019)
Oyster protein	Zinc	UV-visible and FTIR	HLRQEEKE EVTVGSLK-Zn and 24 hydrophobic peptides	Carboxyl, carbonyl and amino: main chelating sites for peptides to zinc ions	(Chen et al., 2013; Wang et al., 2021)
Sesame protein			SM-Zn and NCS-Zn	Imino nitrogen, carboxyl oxygen, hydroxyl oxygen, sulfhydryl sulphur and oxygen of the peptide bond in both peptides involved in coordination with Zn^{2+}	Wang et al., (2014)
Sea cucumber protein			WLTPTYPQ-Zn, AATGVMPLDM-Zn, and AAYCATKFA-Zn	Carboxylic groups of peptides primarily involved in zinc chelation	Liu et al., (2019)
Coconut cake			FDEE-Zn	Amide bond, carboxyl group: main binding sites for zinc ions	Zheng et al., (2023)
Whey protein			Hydrolysates-Zn	The carboxylate anion of peptide C-terminal, D and E side chains, and the hydroxyl group of S and T residues involved in zinc chelation.	Udechukwu et al., (2018)
Sea cucumber protein	Iron	UV-visible and FTIR	Hydrolysate-Fe	Iron-binding sites corresponded primarily to carboxyl oxygen and amino nitrogen atoms, c-terminal, glutamic acid, and aspartic acid residues	Sun et al., (2017)
Whey protein					Fan, et al., (2023)
Tilapia skin collagen					Athira et al., (2021)
					Lin et al., (2021)
Whey protein			Hydrolysate-Fe and WPI-Fe	Complexation given by carboxyl group of side chains of D and E residues	Caetano-Silva et al., (2017)
Walnut		FTIR	Hydrolysate-Fe	Carboxyl, carbonyl, and amino groups involved in the process of chelating ferrous ions	Fan et al., (2023)
Mung bean protein			Hydrolysate-Fe	Iron chelating site related to the carboxylic acid group in the peptide chains (C-terminal carboxyl group and E residue in peptide chains)	Zhang et al., (2021)
Soybean protein	Calcium, zinc and iron	FTIR	Hydrolysate-Ca, Zn, Fe	Complexation of metal ions by peptides principally *via* the carboxyl oxygen and amino nitrogen atoms	Kong et al., (2021)

1.6.2 Isothermal titration calorimetry

Isothermal titration calorimetry (**ITC**) has been applied to study of a wide range of biomolecular interactions, especially metal-protein/peptide interactions (El Hajj, 2021; Li et al., 2013). ITC enables the determination of the thermodynamic parameters such as the dissociation constant (K_D), the reaction stoichiometry (n), the enthalpy (ΔH), and the entropy change (ΔS) associated with biomolecular interactions. All these parameters are determined in one experiment by direct measurement of the heat released or absorbed upon the

association of a ligand with metals (El Hajj, 2021). The ITC contains two identical cells kept at thermal equilibrium (ΔT=0) throughout the experiment. One cell is filled with water or buffer solution, while the other, the sample cell, is filled with one component involved in the interaction. These experiments involve the measurement of the heat energy as a function of time that must be added to the sample cell to maintain zero temperature difference between the two cells. Once the second component of the interaction is injected into the sample cell in a series of aliquots, an enthalpic change occurs. According to this enthalpy change, the interaction can be either endothermic (ΔH>0) or exothermic (ΔH<0) (Ladbury & Chowdhry, 1996).

In ITC experiments, the peptide is first put into the sample cell, then titration is performed by injecting the titrant solution (*i.e.,* metal ion solutions) into the sample cell (**Figure 1.7A**). The ITC data relate the power (µcal/s or W) output/input required to maintain the sample cell at the experimental temperature as a function of time (**Figure 1.7B**). Then, the heat involved per injection is determined by integrating the peaks with respect to time (**Figure 1.7C**), and subsequently plotted against the molar ratio of the peptide: metal ion (**Figure 1.7D**). The latter plot constitutes the binding isotherms, from which the thermodynamic parameters of the interaction (K_D, n, ΔH, and ΔS) are obtained by appropriate fitting with binding models (Eckert et al., 2016; Nielsen et al., 2003). An appropriate fit of experimental data (**Figure 1.7D**, binding titration curve) can determine whether there is one or more classes of metal-binding sites, independent or not, hence involving cooperativity phenomenon (El Hajj, 2021).

ITC has been widely applied to determine the thermodynamics of several peptide-metal interactions. In general, studies report the thermodynamic parameters (ΔH, ΔS, n, K_A) and how they can explain the complexation phenomena. **Table 1.6** provides a summary of the peptide-metal interaction by ITC to date. The negative ΔG (Gibbs free energy change, calculated from ΔG = ΔH-TΔS) values imply that the complexation occurs spontaneously (Eckert et al., 2016). The positive ΔS values are related to entropically favored complexation reactions, meaning that upon ligand binding some phenomena, such as solvent re-organization, release of tightly bound water, or conformational changes of peptide side-chains, could occur (Zeng et al., 2011). On the other hand, the K_A parameter refers to the binding constant between the metal ion and peptide, while the n value indicates the number of binding sites on the peptide chain.

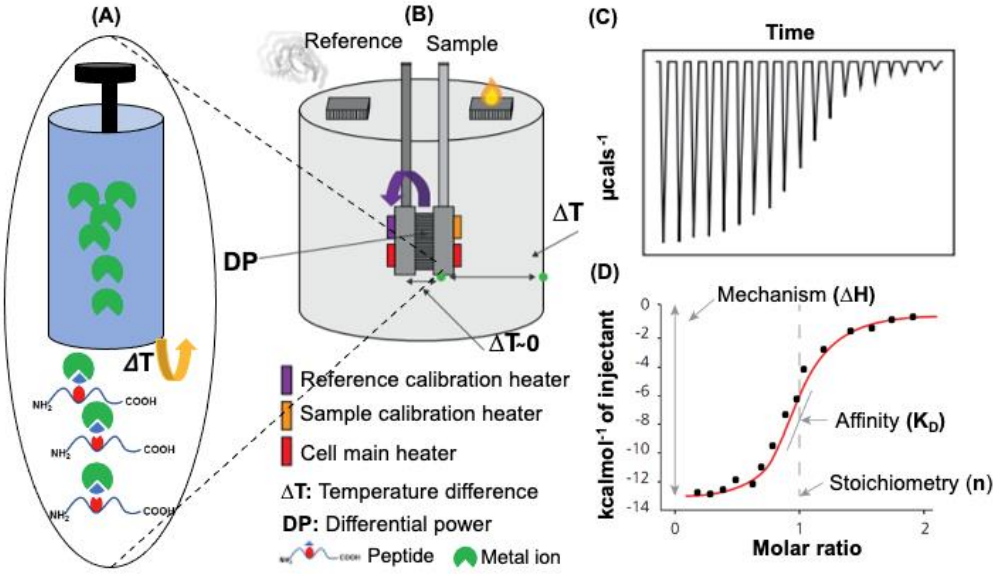

Figure 1.7. Overall scheme of isothermal titration calorimetry. A, B) principle of isothermal titration calorimetry. C, D) basics of ITC experiments. From Microcal ITC systems (Malvern Panalytical, Malvern, United Kingdom).

Previously, Canabady-Rochelle and colleagues used ITC to study the complexation between calcium and soy/milk protein, and hydrolyzed soy protein, respectively (Canabady-Rochelle et al., 2009, 2010). Result showed that the calcium-peptide interaction was endothermic (ΔH>0) in nature and was fitted by a one-site binding model for both systems. Yet, unhydrolyzed soy proteins bound more Ca^{2+} than hydrolyzed soy proteins (~52 and ~2 mg of Ca/g of proteins, respectively). This could be due to the fact that soy protein hydrolysis involves modification in protein structure that impacts on the Ca-binding sites, leading to unfavorable Ca^{2+} complexation with the target amino acids (Canabady-Rochelle et al., 2009). More recently, Cui and colleagues investigated the interaction between calcium and a heptapeptide (NDEELNK) obtained from sea cucumber ovum by ITC (Cui et al., 2018). The binding was an exothermic reaction (negative ΔH values and ΔG<0), revealing that the binding reaction occurred spontaneously. Also, one molecule of Ca^{2+} bound one molecule of the peptide (stoichiometry value, n = 0.87). Similarly, Liao et al., (2019) investigated the calcium complexation by the VLPVPQK peptide from casein hydrolysate; binding reaction occurred spontaneously (ΔG<0) and the stoichiometry revealed that the peptide contains more than 3 calcium-binding sites (n = 3.86).

Besides calcium-peptide complexation, other divalent metal ions have been studied by ITC, notably the binding of Mg^{2+}, Zn^{2+}, and Cu^{2+} with 1–25 β-caseinophosphopeptide (Zidane et al., 2012). The authors highlighted that the titration of phosphopeptide with metal ions yielded endothermic binding isotherms (ΔH>0), and one mole of the peptide bound two moles of Mg^{2+} or Zn^{2+} (pH 8, 37 °C).

Also, they demonstrated that the low binding affinity constants for these metal ions could facilitate the release of metals in the intestinal tract. In contrast, the peptide did not bind Cu^{2+} at pH 8, which might be because non-phosphorylated residues are likely more suitable candidates for binding (i.e., histidine).

Table 1.6. Thermodynamic parameters of reported peptide-metal interaction studies. n.s: no studied

Peptide	Metal ion	Thermodynamic parameters				Ref.
		ΔH (kJ/mol)	ΔS (J/mol.K)	n (sites)	K_A (M^{-1})	
Bacitracin	Zn^{2+}	2.5 ± 0.1	17.24	1	74.36	Qi et al., (2008)
	Co^{2+}	0.8 ± 0.1	13.37	1	214	
	Cu^{2+}	0.9 ± 0.1	20.66	1	6.4×10^3	
	Ni^{2+}	0.9 ± 0.1	17.62	0.5	1.4×10^3	
CPP β-CN(1–25)4P	Ca^{2+}	7.8 ± 1.4	95.8	2.2 ± 0.3	4.9×10^3	Zidane et al., (2012)
	Mg^{2+}	7.5 ± 2.5	96.2	1.6 ± 0.5	5.9×10^3	
	Zn^{2+}	27.4 ± 1.0	165.7	2.2 ± 0.1	11.2×10^3	
SVNVPLY	Fe^{2+}	7.40	112.81	2	6.5×10^{-8}	Eckert et al., (2016)
DHTKE		5.4 ± 0.9	80.22	2.1 ± 0.2	1.4×10^5	(Sun, Cui, Jin, et al., 2017)
NDEELNK	Ca^{2+}	25.3 ± 0.5	16.7	0.8 ± 0.01	3.7×10^4	Cui et al., (2018)
VLPVPQK		5.6 ± 2.8	50.2	3.8 ± 0.9	3.7×10^3	Liao et al., (2019)
GAG	Cu^{2+}	14.6 ± 0.6	37.1 ± 0.6	n.s	8.70×10^3	Makowska et al., (2019)
GDG		8.7 ± 0.1	42.6 ± 0.1		8.70×10^5	
GKG		14.2 ± 0.7	36.7 ± 0.8		8.70×10^3	
GHG		12.7 ± 0.6	28.4 ± 1.5		1.6×10^7	

Makowska et al., (2019) contributed to a better understanding of the coordination mode of Cu^{2+} in the GXG complexes with free terminal groups while studying the interactions of Cu^{2+} with GAG, GDG, GKG, and GHG peptides by ITC. The Cu^{2+}-peptide bonds strongly depended on the donor atoms involved in coordination, since differences were observed between all binding parameters of the tripeptides. The complex Cu^{2+}-GHG, which involves Cu-N (imidazole of His) bond showed more covalent character compared to any of the other complex studied (**Table 1.6**).

Concerning iron complexation, Sun et al., (2017) studied the binding process of DHTKE pentapeptide from egg white hydrolysates and Fe^{2+} by ITC. The exothermic binding isotherms indicated a spontaneous peptide-Fe^{2+} complexation ($\Delta H<0$, $\Delta G<0$). DHTKE contained two functional iron chelating sites (n=2). Similarly, Eckert et al., (2016) found two iron-binding sites in SVNVPLY heptapeptide from barley protein hydrolysate. Meanwhile, Schonberger et al., (2021) investigated ten gallium-binding synthetic peptides as a tool for the sustainable treatment of industrial waste streams. The thermodynamic parameters for the interaction of studied peptides with gallium were determined by ITC, explaining possible binding mechanisms.

1.7 Conclusions

Due to the ability of peptides to complex metal ions by many functional groups, food-derived MCPs obtained by enzymatic proteolysis show tremendous potential as biofunctional ingredients and additives for nutrition, cosmetic and pharmaceutical applications. Indeed, they can enhance the bioaccessibility and bioavailability of minerals, preventing metal-induced oxidation, and reducing the risk of metal-related diseases. Previous studies have established a broad variety of food protein sources, including by-product-derived proteins, as substrates for the production of novel MCPs with a high added-value. In addition, a wide range of reported methodologies facilitate the production, characterization, and identification of MCPs.

Furthermore, emerging methodologies for screening MCPs, such as SPR, switchSENSE®, CLSM and ISE, have been reported by a few studies. Indeed, these techniques could also be used to obtain quick and in-depth information about the potential of food-protein hydrolysates for MCPs production. This review has provided a comprehensive and concise analysis of the current state of art of food-derived MCPs over the past decades, focusing on their production, characterization, identification, and understanding of the peptide-metal interaction, which is one of the most important aspects towards the design and development of MCPs. Moreover, further studies associated with clinical assays, industrial application, biological efficacy, sensory profile, toxicity, allergenicity of metal-chelating peptides derived from food proteins hydrolysates are required to validate their potential application and ensure their safety for human consumption in the market.

Chapter 2. Optimization of Gelatin Extraction from Red Tilapia Scales using a Fractional Factorial Experimental Design and Evaluation of Physico-chemical and Viscoelastic Properties

Although many agro-industrial by-products have been reported as protein sources for the production of Metal-Chelating Peptides (MCPs) from protein hydrolysates, to date there is little literature data about the use gelatin from red Tilapia scales by-product. Obtaining a protein isolate is fundamental to produce MCPs from protein hydrolysates produced from agro-industrial by-products. Indeed, the properties of the resulting hydrolysate, containing potential metal-chelating peptides, will mainly depend on the purity of the native protein and its amino acid sequence. Thus, after understanding the fundamental principles about the productions of MCPs outlined in **Chapter 1**, this **Chapter 2** explores the optimization of gelatin extraction process from red Tilapia scales using a fractional factorial design methodology in order to produce gelatin protein with the most suitable properties for bioactive peptides production or for pharmaceutical application.

This Chapter will be submitted to the journal *Food* as:

Camaño*, J.A., Nekka, A., Arnoux, P., Mathe, C., Cakir-Kiefer, C., Stefan, L., Paris, C., Selmeczi, K., Zapata, J.E., Canabady-Rochelle*, L. Optimization of Gelatin Extraction from Red Tilapia Scales and Evaluation of its Physico-chemical and Viscoelastic Properties.

2.1. Introduction

Nowadays, aquaculture has resulted in a rapid increase in fish production with 223.2 million tons produced in 2022 (FAO, 2024).This growth is accompanied by numerous amounts of wastes (50-70 % of the total fresh fish weight) (Villamil et al., 2017), which significantly impact the environment (Martínez-Alvarez et al., 2015). Tilapia (*Oreochromis* spp.) is the third most widely cultured fish worldwide (Ngo et al., 2010). Yet, in fish factories, the scales, one of the main fish processing wastes, are often discarded during the filet processing (Weng & Wu, 2015). To date, approximately 50,000 tons of wastes are produced per year worldwide during the de-scaling processing, which pollutes the environment (Wang et al., 2020). Mainly composed of collagen protein (30-50 %) and minerals as hydroxyapatite ($Ca_5(PO_4)_3OH$) (30-40 %), fish scales by-products are of great interest for gelatin extraction (Lin et al., 2020). Indeed, once extracted, gelatin could be marked as high added-value product, while solving a recurrent problem of waste disposal (Kasankala et al., 2007).

Gelatin, a fibrous protein obtained from collagen heat denaturation (Caruso et al., 2020), has numerous applications (Wangtueai & Noomhorm, 2009). For instance, this protein is widely used in the pharmaceutical field (200,000 tons in the last decades, Alipal et al., 2021), in addition to food, cosmetic and packaging industries, due its excellent functional and biological properties (Viji et al., 2019). Besides, gelatin is often used in biotechnology and biomedicine (Huang, et al., 2018), notably for culture medium, tissue engineering and bone substitutes (Al-Nimry et al., 2021). Gelatin can be produced from various sources, notably the pig skin and bovine hide (Tu et al., 2015). However, other sources are sought for various reasons i.e., the outbreak of mad cow disease or Bovine Spongiform Encephalopathy but also due to its unacceptability for some religions when produced from cattle and/or pigs (Kasankala et al., 2007). Thus, new gelatin resources have been explored, notably fish by-products (*i.e.,* fish skin, fin, bone and scale), rich in collagen (Zhang et al., 2019).

Collagen is commonly converted into gelatin by a four-step process (Wangtueai & Noomhorm, 2009): demineralization of scales, washing, extraction, and drying. To ensure an efficient gelatin extraction, this common process has to be optimized to obtain the maximum yield of gelatin with the required physical (*i.e.,* molecular weight distribution, solubility, gelling and melting temperatures, and viscosity) and chemical properties (*i.e.,* crude protein content, amino acid composition, and degree of hydrolysis) (Montero & Acosta, 2020). Both

yield and quality of gelatin depend on the extraction conditions used during the collagen treatment (Kasankala et al., 2007). Thus, several parameters should be evaluated to achieve optimal gelatin extraction process from fish by-products. One-factor-at-a-time method is often used in product/process studies. Yet, this approach lacks investigation into interaction effects, resulting in time-consuming and potentially unreliable for determining optimal conditions.

Experimental design, crucial in various scientific and industrial fields, provides meaningful insights for product and process development (Rezende et al., 2018). The exploration of optimal conditions for protein extraction increased the use of statistical tools like factorial design, which assesses multiple factors and their interactions simultaneously (Montero & Acosta, 2020). While a complete factorial design is costly and time-consuming (Salleh et al., 2015), fractional factorial design (**FFD**) provides an effective optimization tool that reduces the number of experiments without compromising accuracy. FFD focuses on significant main effects and two-factor interactions while neglecting higher order interactions, making it a valuable tool for optimizing protein extraction processes with fewer experiments (Heiberger & Holland, 2015).

To the author's knowledge, the gelatin extraction process from red Tilapia scales has never been optimized to date using FFD. Therefore, this study aims to determine the optimal conditions for gelatin extraction from red Tilapia scales using this former approach while studying the effects of four factors (*i.e.,* the solvent-to-solid ratio, the extraction time, the temperature, and the ultrasound time) on three investigated responses (*i.e*., the crude protein content, the free amino groups content and the protein extraction yield). In addition, this study presents the physico-chemical characterization of the most interesting gelatin extracts obtained, by SDS-PAGE profile and circular dichroism as well as their viscoelastic properties.

2.2. Materials and Methods

2.2.1. Chemicals and reagents

Chemicals and reagents were provided by Sigma–Aldrich (St Louis, MO, USA): 37 % hydrochloric acid (HCl), 97 % sulphuric acid (H_2SO_4), *o*-Phthalaldehyde (OPA), glycine, *N,N*-

dimethyl-2-mercaptoethyl ammonium, sodium tetraborate decahydrate, sodium dodecyl sulfate and sodium carbonate. The NaOH anhydrous pellets, potassium sulfate and hydrogen peroxide 30 % (w/v) were purchased from VWR International (Atlanta, USA). Boric acid and methyl red were provided by Merck (Darmstadt, Germany). All reagents used in this study were analytical grade.

2.2.2. Gelatin extraction from Tilapia scales

2.2.2.1. Scales collection and preparation

Red Tilapia (*Oreochromis* spp.) scales were supplied by El Gaitero SAS (Sopetrán, Colombia). The Tilapia scales flour (**TSF**) was prepared according to the literature (Sierra-Lopera & Zapata-Montoya, 2021; Tu et al., 2015) with slight modifications. In brief, scales were washed three times with distilled water to remove the surface-adhering impurities. Then, they were dried by a convective oven (50 °C, 24 h; Thermo Scientific™, Waltham, USA) and ground with liquid nitrogen using a cutting mill (Retsch SM 300, Éragny, France) equipped with a 2 mm sieve (Restch, Éragny, France).

2.2.2.2. Gelatin extraction process

The gelatin was extracted from the Tilapia scales flour according to the process described in **Figure 2.1**. First, a demineralization step was carried out similarly to a published method (Chen et al., 2019). The Tilapia scales were decalcified using 0.4 M HCl solution. Then, the demineralized scales were washed with ultrapure water (18.2 $MW.cm^{-1}$ at 25 °C). The gelatin was then extracted from demineralized scales using a hydrothermal extraction. The extraction was carried out using a 250 mL thermostatic beaker connected to a water flow and a thermostat (Haake, Karlsruhe, Germany). The demineralized scales were dissolved in water at different solvent-to-solid ratios, for different extraction time and temperature conditions according to a fractional factorial design (FFD) (**Table 2.1**). Then, the mixture was transferred into a 500-mL beaker, and cooled down until reaching room temperature. When required, the mixture was then submitted to ultrasounds (Bandelin sonopuls hd 2070, Berlin, Germany) at a 20 kHz frequency and 70 W of power for 0 or 60 min. To remove the solid residues, the extracting solutions were ultracentrifuged (Eppendorf AG, Hamburg, Germany). The collected

supernatants containing the gelatin were dried at 50 °C using a convective oven for 24 h (Memmert GmbH & Co. KG, Saxony, Germany). Finally, the dried gelatin samples were ground for 30 seconds using a basic mill (Moulinex, Alençon, France) and stored at −20 °C until further analysis.

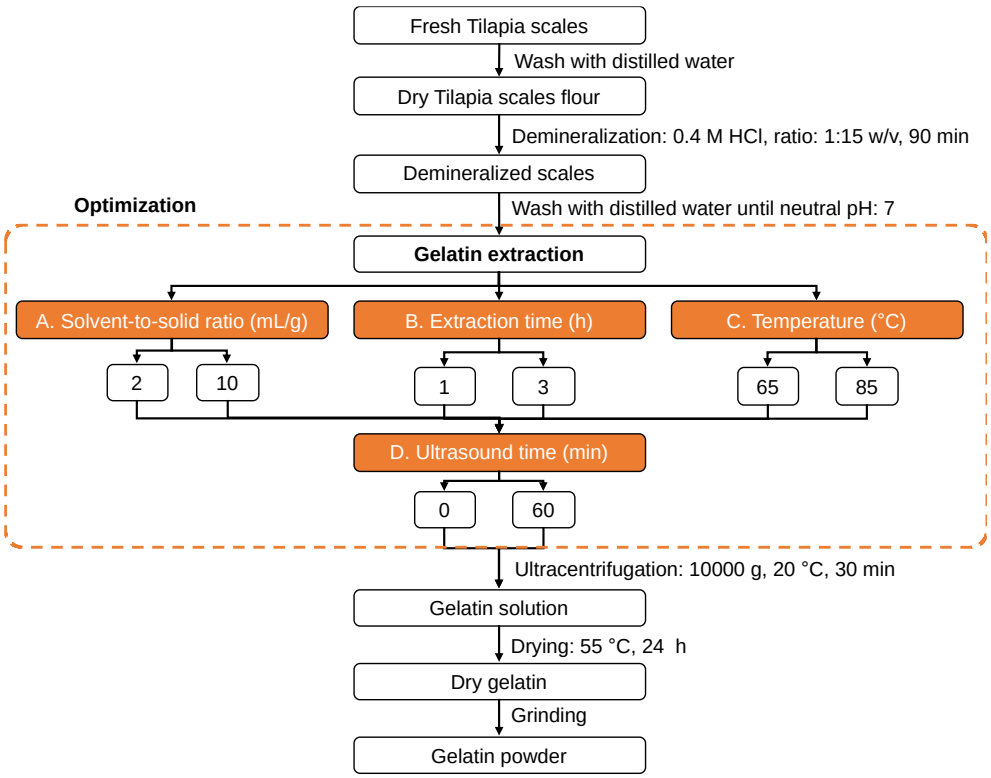

Figure 2.1. Tilapia scales gelatin extraction process set up in this study with fractional factorial experimental design approach using ultrapure water. Adapted from Chen et al., (2019).

2.2.2.3. Fractional factorial design

To optimize the extraction conditions of gelatin from Tilapia scales, a 2^{4-1} FFD was used. In a resolution IV FFD, 4 factors (A, B, C, D) are investigated, where the main effects do not consider the third order interactions and above, since insignificant (Rezende et al., 2018). In this design, the fraction generator "I", equal to "ABCD", is applied to obtain the factorial fraction (factor D obtained by multiplying ABC, **Table 2.1**). The 2^{4-1} FFD applied here is commonly used to minimize the number of experiments to run without sacrificing its accuracy (Salleh et al., 2015).

Table 2.1. Responses of 2^{4-1} fractional factorial design for Tilapia scales gelatin extraction: crude protein content (%), free amino groups content (mmol Eq G/g) and protein extraction yield (%). Run 9-11: central points.

Run	Design matrix								Reponses		
	Code factors				Uncoded factors				CPC	FAG	PEY
	A	B	C	D	A (mL/g)	B (h)	C (°C)	D (min)	%	mmol Eq G/g	%
TSF									45.2 ± 0.8	0.01 ± 0.004	
1	-1	-1	-1	-1	2	1	65	0	99.2 ± 0.9	0.23 ± 0.004	37.6 ± 0.1
2	+1	-1	-1	+1	10	1	65	60	96.9 ± 0.3	0.23 ± 0.01	41.3 ± 0.1
3	-1	+1	-1	+1	2	3	65	60	96.7 ± 0.4	0.25 ± 0.02	37.3 ± 0.1
4	+1	+1	-1	-1	10	3	65	0	97.2 ± 0.2	0.24 ± 0.02	38.7 ± 0.1
5	-1	-1	+1	+1	2	1	85	60	98.2 ± 1.3	0.26 ± 0.02	38.8 ± 0.4
6	+1	-1	+1	-1	10	1	85	0	95.4 ± 0.8	0.28 ± 0.03	48.5 ± 0.4
7	-1	+1	+1	-1	2	3	85	0	97.6 ± 0.8	0.28 ± 0.03	31.9 ± 0.2
8	+1	+1	+1	+1	10	3	85	60	97.1 ± 0.7	0.31 ± 0.04	47.2 ± 0.3
9	0	0	0	0	6	2	75	30	96.9 ± 1.5	0.26 ± 0.02	39.1 ± 0.7
10	0	0	0	0	6	2	75	30	96.7 ± 0.8	0.27 ± 0.02	39.7 ± 0.4
11	0	0	0	0	6	2	75	30	95.6 ± 0.7	0.26 ± 0.02	41.2 ± 0.1

The following 4 factors were all studied at two levels ('low' -1 or 'high' +1): the solvent-to-solid ratio (A, 2 or 10 mL/g), the extraction time (B, 1 or 3 h), the temperature (C, 65 or 85 °C) and the ultrasound time (D, 0 or 60 min). For estimating pure error and increasing the probability of detecting significant factors, three repetitions at the central point (runs 9, 10 and 11) were added to the experimental design matrix, leading to eleven experimental runs on total**.**

After carrying out this FFD, the effect of these 4 factors was investigated for each extracted gelatin sample, on the 3 followed responses: the crude protein content (CPC, %), the free amino groups content (FAG, mmol Eq Glycine/g) and the protein extraction yield (PEY, %), all being important for gelatin production of high productivity and quality (Montero & Acosta, 2020). Each analysis was repeated to present data as mean ± standard deviation.

2.2.3. Responses investigated

2.2.3.1 Crude protein content

The crude protein content (CPC) was determined by Kjeldahl (AOAC 954.01; AOAC, 2000). First, TSF and the 8 gelatin extracts were digested inside a START D Microwave Digestion System (Milestone, Milan, Italy) and the total nitrogen content was determined using a PRO-

NITRO M Kjeldahl distiller (Selecta, Barcelona, Spain). CPC was estimated using a nitrogen-to-protein conversion factor (F*p*) of 5.95 as reported for fish scales (Huang et al., 2016).

2.2.3.2 Free amino group content

The free amino groups (FAG) content was determined by OPA quantification similarly to Canabady-Rochelle et al., (2018). Briefly, the FAG determination in each sample was performed by mixing 200 µL of the OPA reagent with 20 µL of sample or standard solution, prepared at 1 mg/mL in ultrapure water. The 96-well microplates (Nunclon^{TM} delta surface, Thermo scientific, Roskilde, Demark) were used for spectroscopic measurements. The absorbance value was measured in quintuple at 340 nm using a spectrophotometer MRX Multiskan Go (ThermoFicher Scientificm, Vantaa, Finland) equipped with a microplate reader. A calibration curve was performed with glycine diluted in ultrapure water (0-5 mM). Results were expressed as mmol equivalent glycine per gram of sample (mmol Eq G/ g).

2.2.3.3 Protein extraction yield

The protein extraction yield (PEY, %) of each extracted sample, expressed by g crude protein extracted/100 g crude protein in TSF used, was estimated by the protein mass present in each gelatin extract divided by the total crude protein mass present in Tilapia scales flour for the same sample (Equation 1) **(Zhang et al., 2019)**.

$$PEY\ (\%) = \left\lfloor \frac{M_{TSG}\ x\ P_{TSG}}{M_{TSF}\ x\ P_{TSF}} \right\rfloor X\ 100 \qquad (1)$$

Where M_{TSG} is the mass (g) of Tilapia scales gelatin (TSG) obtained after extraction, M_{TSF} is the mass (g) of Tilapia scales flour (TSF) used for extraction, and P_{TSG} and P_{TSF} are the crude protein content (%) of Tilapia scales gelatin and Tilapia scales flour, respectively.

2.2.3.4 Statistical analysis

After experimental extraction, the 3 investigated responses were integrated into the experimental design to investigate the effects of the principal factors and their interactions on the responses, and determine which effects are statistically significant. All statistical analyses were performed at a significance level of 0.05 (*p-value* < 0.05). The responses were

analyzed using the Design Expert 11 statistical software (Stat-Ease Inc, Minneapolis, USA). It enabled to determine initially their contribution percentages for each factor and their interactions in order to preselect which ones are relevant. Then, these latter ones were confirmed by ANOVA (Sepian et al., 2019). From ANOVA, a relationship between the predicted responses and the investigated factors were obtained using a first-order polynomial model (**Appendix 2.1**).

2.2.4. Physico-chemical characterization

2.2.4.1 SDS-PAGE profile

The molecular weight profile of TSF, 8 gelatin extracts (run 1-8 in FFD), 1 sample at central point (run 9) and the optimal run (10 mL/g, 3 h, 85 °C) was investigated by sodium dodecyl sulfate polyacrylamide gel electrophoresis (SDS-PAGE) according to the method reported by Tu et al., (2015), using a Mini-Protean tetra cell electrophoresis system (Bio-Rad Laboratories, Hercules, USA). The samples were prepared at 20 mg/mL in ultrapure water. Then, the solubilized protein solutions were dissolved at a ratio of 1:4 (v/v) with sample buffer (0.5 M Tris-HCl, pH 6.8, containing 10 % (w/v) SDS, 50 % (v/v) glycerol, and 0.05 % (w/v) bromophenol blue with 0.5 % (w/v) 2-mercaptoethanol). These mixtures were heated at 100 °C for 5 min to denature proteins. Then, 10 µL of each sample (*i.e.,* containing 40 µg of protein) or solution of molecular weight maker (range: 10 – 250 kDa; Catalog N°: 26619, Thermo Scientific™, Vilnius, Lithuania) were loaded onto the polyacrylamide gel, made of a 12.5 % separation gel and a 5 % stacking gel (Tu et al., 2015). The electrophoresis was conducted at a voltage of 120 V for 15 min and then, 180 V for 1 h. After electrophoresis, the gel was stained for 1 h with a solution containing 0.1 % (w/v) Coomassie blue R-250 (Sigma-Aldrich, Oakville, Canada), 7.5 % (v/v) acetic acid and 5 % (v/v) ethanol. Subsequently, the gel was destained with a solution containing 30 % (v/v) ethanol and 7.5 % (v/v) acetic acid for 1 h. Finally, densitometric analysis of Coomassie blue-stained gels was carried out using GelAnalyzer 19.1 (www.gelanalyzer.com) to quantify the relative amount of gelatin components (α_1, α_2 β and γ chains) and its low molecular weight aggregates (**LMWA**).

2.2.4.2 Circular dichroism spectroscopy

Circular dichroism (**CD**) spectra of the 10 gelatin extracts (9 gelatin extracts and optimal run) were recorded from 185 to 260 nm at 0.5 nm intervals using a MOS-450 CD spectrometer (Bio-Logic Science Instruments, France). Samples were prepared at 0.2 mg/mL in 0.1 M acetic acid, and transferred into a 2 mm-pathlength cuvette for analysis (at 25 °C as in Chen et al., 2022).

2.2.4.3 Amino acid analysis

The amino acid composition was only carried out for the optimal Tilapia scales gelatin sample obtained by FFD using a UHPLC system (Thermo Fisher Scientific) set on-line with an Orbitrap ID-X Tribrid mass spectrometer (Thermo Fisher Scientific), equipped with an atmospheric pressure ionization interface. First, the sample was subjected to a complete acid hydrolysis (6 N HCl, 130 °C, 24 h) and then, dried at 65 °C under vacuum (Huang et al., 2016). Finally, 5 µL sample solution (1 g/L in ultrapure water) were injected and separated on C18 Alltima reverse phase column (150×2.1mm, 5 µm; Grace/Alltech, Darmstadt, Germany) equipped with a C18 Alltima pre-column (7.5×2.1 mm, 5 µm) at 10°C.

2.2.5. Rheological properties

Rheology measurements were performed for the most interesting gelatin extracts solely using an AR2000 rheometer (TA Instruments, New Castle, DE) operating in oscillatory mode, equipped with a Peltier plate temperature control and a Couette geometry immersed inside the sample (Giraud et al., 2020). Gelatin samples were prepared at 6.67% (w/v) in ultrapure water and heated up using an oil bath (60 °C, 20 min), allowing a complete dissolution. Then, the samples were transferred to the rheometer (T = 60 °C) and the following sequence of measurements were carried out. The steps and experimental conditions used are displayed in supplementary data (**Appendix 1.2**). All the measurements were repeated a minimum of three times. Collected data were treated using Origin 2023 (OriginLab Corporation), and fitted as sigmoid functions to extract the gelling and melting temperatures values, corresponding to the inflection point of the curve.

2.3. Results and discussion

2.3.1 Effect of the studied parameters on gelation extraction

2.3.1.1 Crude protein content

The effect of the solvent-to-solid ratio (A), extraction time (B), temperature (C) and ultrasound time (D) was investigated on gelatin extraction using a FFD. The responses CPC, FAG content and PEY are presented for each extract in **Table 2.1**.

The CPC varies slightly between 95.4 and 99.2 % as a function of the investigated factors and is in agreement with the CPC in a protein isolate (> 85 %). Whatever the treatment, the gelatin extracts obtained show similar and even higher protein concentration compared to the literature. Zhang et al., (2019) reported similar protein values (97.8 %) in gelatin extract obtained from Tilapia scales using a hydrothermal treatment (ratio 1:2 w/v, 135 °C for 90 min). Besides, for temperature comprised between 65-85 °C, protein values were determined at 87 %, 84 %, and 88 % for gelatin extracts obtained from grass carp skin (Kasankala et al., 2007), bighead carp scales (Wangtueai & Noomhorm, 2009), and lizardfish scales (Tu et al., 2015), respectively. Thus, the protein extraction set up here on red Tilapia scales flour is an efficient process: the gelatin obtained is above 95 % of CPC for all the extracts and the mineral fraction - notably hydroxyapatite – may be mainly removed by the demineralization process. Additionally, these experimental responses were analyzed by contribution percentage of each factor and their respective interactions (**Figure 2.2A**), and Pareto charts analysis (**Appendix 2.3**).

The contribution percentage of each single factor and their two-factor interactions are presented in **Figure 2.2**. For CPC, when all 4 factors are compared individually, the solvent-to-solid ratio (A) shows the highest percentage of contribution (33.6 %), while the two factors interaction AB (*i.e.*, solvent-to-solid ratio with extraction time) shows the highest percentage of contribution at 31.6 %.

Although various involved factors have a different effect on the CPC, all the levels of factors have the potential to produce a protein isolate from red Tilapia scales gelatin, maintaining a suitable crude protein content for gelatin production (95-99 %).

2.3.1.2 Free amino group content

According to the gelatin extraction process applied, the free amino groups (FAG) content varies between 0.23 and 0.31 mmol Eq G/g (**Table 2.1**). The FAG content of all gelatin extracts is higher (> 0.2 mmol Eq G/g) than that of TSF (0.012 ± 0.004 mmol Eq G/g) due to the natural hydrolysis of collagen upon protein extraction. This is in agreement with Nagarajan et al., (2012), who evidenced that upon hydrothermal process, collagen present in Tilapia scales flour was partially hydrolyzed into gelatin, leading to an increased FAG content. Besides, the highest FAG content is reached after 60 min (70 W) of ultrasounds (0.31 mmol Eq G/g), probably due to the large shear forces generated from cavitation, breaking inter and intramolecular bonds of collagen (Chandrapala et al., 2011). Although the hydrolysis of collagen can be increased by ultrasounds, our results only show a slight improvement in FAG content (without and with ultrasound: 0.28 and 0.31 mmol Eq G/g, respectively).

The FAG content determined in our gelatin extracts is similar to the value reported by Tu et al., (2015) (0.17 - 0.20 mmol Eq L-leucine/g), who observed the highest degradations with ultrasound carried out at 200 W at 60 °C for 1-3 h.

According to the contribution percentage of each single factor and their two-factor interactions (**Figure 2.2**)**,** the FAG content is highly affected by the temperature (C) and the extraction time (B), which show the highest contribution (70.8 %, and 17.1 %, respectively). Regarding the interactions, the solvent-to-solid ratio with temperature (AC) shows the highest percentage of contribution at 7.3 %.

Our results are in accordance with the study of Tu and co-authors (Tu et al., 2015), who reported that the gelatin extraction from bighead carp scales led to a FAG content increase for longer extraction times. Likewise, Zhang et al., (2019) found that higher temperatures increased the FAG content.

2.3.1.3 Protein extraction yield

Whatever the gelatin extraction process applied, the protein extraction yield (PEY), expressed by g crude protein extracted/100 g crude protein in Tilapia scales flour used, varies from 31.9-48.5 % (**Table 2.1**). The gelatin extracted at 85 °C (runs: 6 and 8) have significantly higher extraction yields as compared to those extracted at 65 °C in similar conditions (runs: 2 and 4).

Similar to our study, Huang et al., (2016) evidenced that the high temperatures used during the extraction process decomposes the matrix of Tilapia scales and weakens the tight linkage between collagen and hydroxyapatite, leading to the solvent penetration and the PEY increase. Several studies suggested that PEY of gelatin does not only depend on the CPC of the fish scales but also on fish species, fish parts, biological conditions (*i.e.,* length, weight) and extraction procedures used (Upasen et al., 2019).

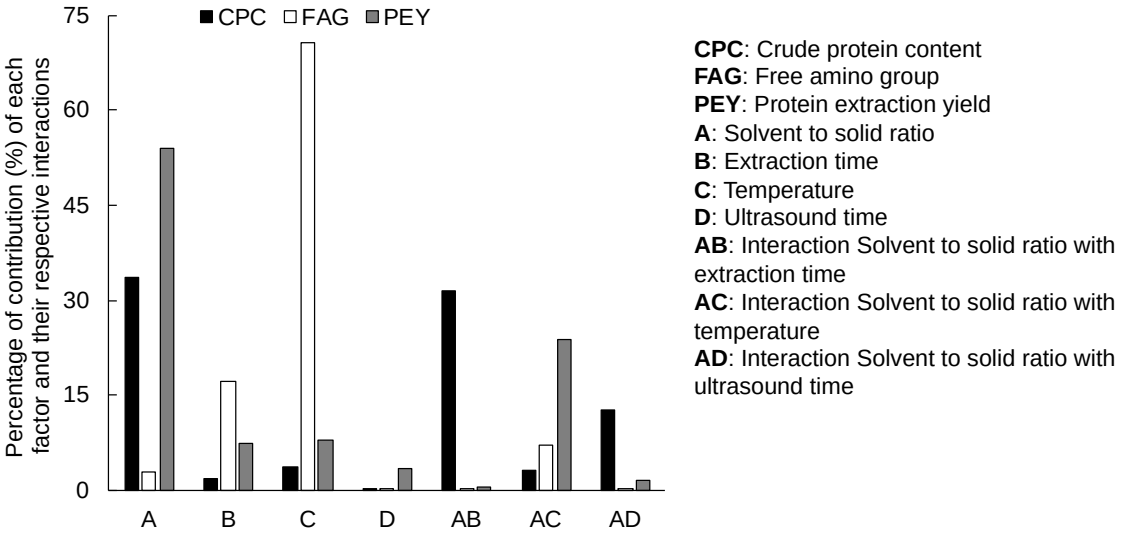

Figure 2.2. Percentage of contribution of single factors and two-factor interactions effects on investigated responses.

In **Figure 2.2**, the solvent-to-solid ratio (A) has the highest effect on the protein extraction yield (54 %), followed by the interaction solvent-to-solid ratio with temperature (AC, 23.7 %), the temperature (C, 7.9 %) and the extraction time (B, 7.4 %). Our results are in agreement with the literature: the PEY increases with the solvent-to-solid ratio, since a substrate increase (lower ratios) causes a viscosity increase, thus slowing down the mass and the heat transfers required for protein extraction, until preventing them (Xue et al., 2015; Y. Zhang et al., 2019).

Besides, higher temperatures (C) release higher gelatin content, enhancing the protein extraction yield. Similar results were reported by Zhang et al., (2019) and Huang et al., (2016) who extracted gelatin from Tilapia scales by hydrothermal treatment at 85-135 °C for 15-120 min, without previous demineralization. According to these former authors, the collagen-hydroxyapatite crosslinking was destructed upon high-temperature treatment, enhancing the gelatin extraction.

2.3.2 Statistical evaluation of operating conditions

2.3.2.1 Mutiple regression modeling

From ANOVA data (**Appendix 2.4**), the multiple regression modeling enables to plot the linear relationship between the factors (A, B, C and D) and their interactions with the investigated responses (CPC, FAG, and PEY). It allows to predict responses outcome given the level of factors. ANOVA data (**Appendix 2.4**) provides three statistically significant models (*p-value* < 0.05) corresponding to the CPC, FAG content and PEY. Based on this result, the simplest statistical models are built for these three responses, respectively, from significant single factors and their interactions (*p-value* < 0.05; Equations (3)**,** (4) and (5)). Note that in these first-order polynomial models, the negative or positive coefficients correspond to positive or negative effects, with a value proportional to the observed coded effect.

$$CPC\ (\%) = 97.07 - 0.65A + 0.63AB \quad (3)$$

$$FAG\ content\ (mmol\ EqG/g) = 0.26 + 4.47x10^{-3}A + 0.01B + 0.02C + 7.04x10^{-3}AC \quad (4)$$

$$PEY\ (\%) = 40.12 + 3.75A + 1.43C + 2.49AC \quad (5)$$

With CPC: crude protein content; FAG: free amino groups; PEY: protein extraction yield; A: solvent-to-solid ratio; B: extraction time; C: temperature; AB, AC and AD: corresponding two factor interactions.

In order to evaluate the quality of fit in the obtained models, the regression coefficients (R^2 and adjusted R^2), lack of fit and adequate precision (**Adeq precision**) of the resulting models were determined **(Appendix 2.5**). For FAG content and PEY models, the values of R^2 and adjusted R^2 are close to 1, indicating a good fitting since higher than 0.90. Thus, these two models could explain more than 90% of variability of the experimental responses. On the contrary, for CPC, although the model was significant, the R^2 coefficients are lower than 0.9 (0.69 and 0.82), explaining just 60-80 % variability of this response. Similarly, the lack of fit and Adeq precision analysis suggest that FAG and PEY models present higher reliability than CPC one. Therefore, the results of these statistical parameters indicate that the FAG content and PEY models only could be suitable to predict the responses and to optimize the gelatin extraction from red Tilapia scales.

2.3.2.2 Response surfaces

Based on ANOVA and modeling results, the 2D contour plots were obtained using the Design Expert statistical software in order to observe the potential interaction effects between two factors. Only one interaction has a statistically significant effect for each response (**Figure 2.3A**, **2.3B** and **2.3C**). For each of these panels, the interaction between two factors is presented, setting the other two factors constant. The **Figure 2.3A** shows the effects of the solvent-to-solid ratio (A) and extraction time (B) on the CPC, at 65 °C and without ultrasounds. For low values of solvent-to-solid ratio and extraction time, the crude protein content increases slightly (red color). The effects of the solvent-to-solid ratio (A) and temperature (C) were investigated on FAG content (**Figure 2.3B**) and PEY (**Figure 2.3C**), both with extraction time set constant at 3 h and without ultrasounds. For high values of solvent-to-solid ratio and temperature, both FAG content and PEY increase (red color). Indeed, more collagen is turned into gelatin as a consequence of high temperatures in agreement with Zhang et al., (2019).

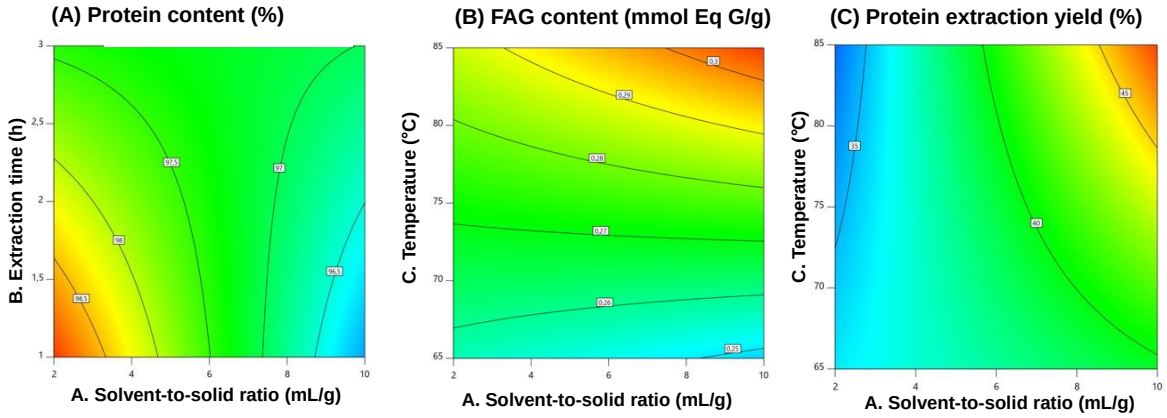

Figure 2.3. 2D contour plots of responses. (A) crude protein content CPC (%) as a function of solvent-to-solid ratio and extraction time; (B) free amino groups content (FAG, mmol Eq Glycine/g) and (C) protein extraction yield PEY (%) as a function of solvent-to-solid ratio and temperature.

Factors set constant: 65 °C and 0 min of ultrasound time for crude protein content; 3 h of extraction time and 0 min ultrasound time both for FAG and PEY.

2.3.3 Responses optimization

The multiple response optimization aims to define factor conditions that would maximize FAG content (0.31 mmol Eq G/g) and PEY (48.5 %), while keeping the CPC suitable for protein

isolates (95-99 %). Indeed, the optimal extraction conditions are obtained by the desirability function of design Expert statistical software, similarly to Montero & Acosta, (2020). To reach this goal, the conditions for gelatin extraction must be: 10 mL/g of solvent-to-solid ratio, 3 h of extraction time, 85 °C of temperature and no ultrasounds. Finally, to validate the three models and the reproducibility of the optimum, the predicted response values obtained by the various models (Equations (3), (4) and (5)) were checked experimentally using same optimum extraction conditions (optimal run: 10 mL/g, 3 h, 85 °C, 0 min). For this latter extract and for all investigated responses, the experimental and predicted values were compared using the relative error (%). For each analyzed response, the relative error is less than 10%, thus the predicted values are consistent with the experimental ones, demonstrating the efficiency and the adequacy of the simplified models (**Table 2.2**). Thus, the models are quite reliable especially for predicting FAG content and PEY of gelatin obtained from red Tilapia scales. Besides, the CPC model can be considered acceptable despite its low fit.

Table 2.2. Predicted and experimental values of crude protein content, free amino groups content and protein extraction yield obtained for Tilapia scales gelatin extracts.

Reponses	Predicted value	95 % CI low*	95 % CI high**	Experimental value	% Relative error***
CPC (%)	96.2	95.6	97.7	95.9 ± 0.4	0.2
FAG (mmol Eq G/g)	0.31	0.30	0.30	0.29 ± 0.003	6.9
PEY (%)	46.5	41.3	51.6	42.8 ± 0.2	8.7

Solvent-to-solid ratio: 10 mL/g; extraction time: 3 h; temperature: 85 °C, ultrasound time: 0 min; CPC: Crude protein content FAG: Free amino group; PEY: Protein extraction yield; CI: Confidence Interval; * 95% CI low: Lower limit of the 95% CI (experimental value); ** 95% CI high: Upper limit of the 95% CI (experimental value); ***Relative error estimated by making the absolute value of subtraction of the measured value by the real value, divided by the real value, and then multiply by 100%.

2.3.4 Physico-chemical characterization

2.3.4.1 SDS-PAGE profile

To observe the presence of gelatin components under different hydrothermal extraction condition, SDS-PAGE profile was obtained. **Figure 2.4A** shows the molecular weight of TSF and gelatin extracts. Overall, the TSF and gelatin extract presents different bands, which consist of the following chains: α, α_1 (~120 kDa) and α_2 (~130 kDa), and their cross-linked β

chain (~190 kDa) and γ chain (~330 kDa) (**Figure 2.4A**), belonging to gelatin components as previously reported (Chen et al., 2016). This electrophoretic pattern is similar to that of standard type I collagen, widely reported in fish processing by-products (Huang et al., 2016; Thuy et al., 2014).

Based on the densitometric analysis of the gel, quantitative data of the gelatin components (α_1, α_2, β and γ chains) and LMWA (<100 kDa) are shown in **Figure 2.4B**. Notably, in all the gelatin extracts, the bands intensity of low molecular weight aggregates (i.e., LMWA <100 kDa) increases compared to TSF (**Figure 2.4B**). This band intensity increase is associated to collagen hydrolysis into gelatin upon thermal extraction process, leading to a higher presence of smaller gelatin component due to the cleavage of inter-chain covalent crosslinks (Karim & Bhat, 2009). Moreover, gelatin extracted with higher extraction temperature (85 °C; run 5,6,7,8) present a lower band intensity of the γ, β and α chains than those produced with lower extraction temperature (65°C; run 1,2,3,4); similar results were reported in gelatin extraction from splendid squid skin (Sinthusamran et al., 2014).

The major components of gelatin, γ, β and α chains are present in all the gelatin extracts (**Figure 2.4A** and **2.4B**), except in the run 8, where γ and β chains are strongly degraded, and the relative amount of LMWA increases notably. These results are in agreement with the OPA quantification since smaller protein fragments production is related to higher FAG content. With the highest FAG content (**Table 2.1**; 0.31 mmol Eq G/g), the run 8 evidences that the highest solvent-to-solid ratio (A: 10 mL/g), extraction time (B: 3 h) and temperature (C: 85 °C) improve the degree of collagen hydrolysis in agreement with literature (Tu et al., 2015; Zhang et al., 2019). Likewise, the use of ultrasounds induces a higher degradation of γ, β and α-chains of collagen. Indeed, this aggressive treatment increases the hydrolysis of collagen-derived constituents due to the large shear force generated from cavitation phenomenon, breaking inter and intramolecular cross-links between collagen and remaining hydroxyapatite. Similar to our SDS-PAGE results, Tu et al., (2015) showed by FAG quantification that ultrasounds concomitantly increase small-sized protein production during gelatin extraction. However, according to the experimental design results, this increase does not have any significant effects on studied responses (CPC, FAG, PEY) in the range of investigated factors.

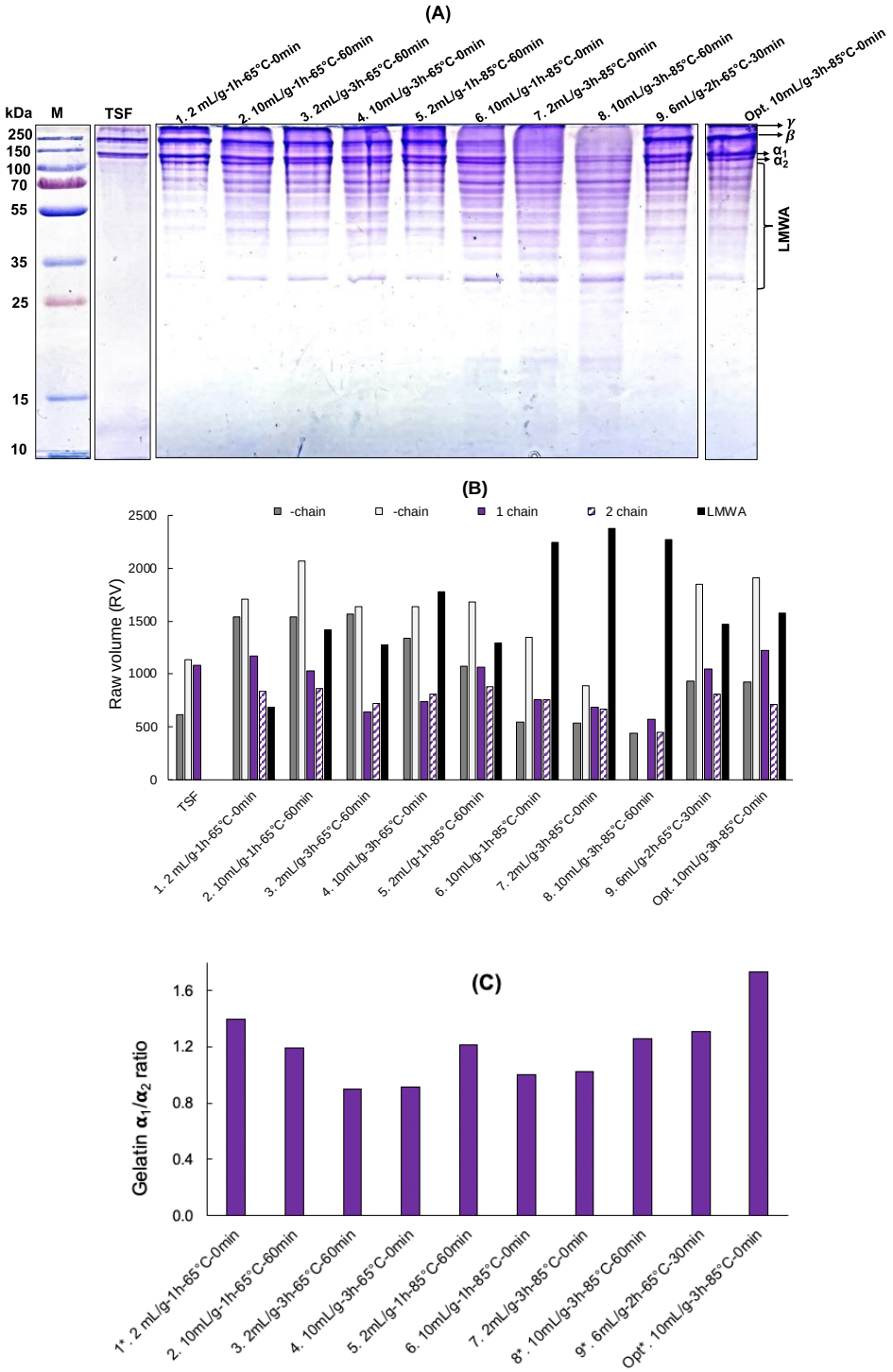

Figure 2.4. Physico-chemical characterization of gelatin extracts (A) SDS-PAGE (12.5 %) profile of the red Tilapia scales flour (TSF) and the ten gelatin extracts from Tilapia scales. Numbers define the coded level of FFD. Lane "M" represents a pre-stained molecular weight marker (ref: 26619, Thermo Scientific™, Vilnius, Lithuania), γ: γ-chain; β: β-chain; α_1: α_1-chain; α_2: α_2-chain; LMWA: low molecular weight aggregates, Opt: optimal gelatin. (B) Amount of molecular weight constituents of gelatin extracts obtained by densitometric analysis of SDS-PAGE gels. (C) α_1/α_2 ratio of gelatin extracts.

On the other hand, it was demonstrated that functional properties of gelatin can be affected by the molecular weight distribution, notably the α_1/ α_2 chain ratio. Based on densitometric analysis of the gel, α_1/α_2 chain ratios were estimated (**Figure 2.4C**). The α_1/α_2 ratio of gelatin extracts obtained by different condition ranges between 0.9-1.7, highlighting that the optimal gelatin, run 1, 8 and the central point (run 9) exhibit the highest values with 1.7, 1.4, 1.3 and 1.3, respectively. These values are similar to those found in other fish processing by-products (cod and hake skin gelatin, α_1/ α_2 ratio: ~1, Gómez-Guillén et al., 2010), and closer to the characteristics of type I collagen (α_1/ α_2 ratio: ~2). In relation to α_1/ α_2 ratio, these four gelatin extracts (run 1, 8, 9 and optimal run) obtained with different extraction conditions may have some interesting dynamic viscoelastic properties, which play an important role in gelatin applications, thus these properties were further investigated.

2.3.4.2 Circular dichroism spectra

The CD analysis is widely used to observe protein secondary structure. The CD signatures (**Appendix 2.6**) of all the gelatin extracts exhibit a similar behavior with a negative peak at 196-200 nm with slight variations in ellipticity values. This suggests that triple-helix structure of collagen is destroyed upon the gelatin thermal extraction process, and that the protein structure of gelatin extracts is characterized by random coils (Karim & Bhat, 2009). Indeed, native collagen triple-helix structure is generally observed with a positive peak at 220-230 nm, and a negative peak at around 200 nm, but once partial thermal hydrolysis occurs, the positive peak disappears due to the disruption of the covalent crosslink present in collagen. Similar to our study, the CD spectra of commercial cold-water fish gelatin, bovine bone gelatin (Zhang et al., 2020) and Nile Tilapia skin gelatin (Chen et al., 2022) exhibited random coils structure, generally found in denatured collagen (Tan & Chang, 2018).

2.3.4.3 Amino acids analysis

Amino acids (AA) profile was assessed only for red Tilapia scales gelatin obtained in the optimal condition (10 mL/g, 3 h, 85 °C, 0 min) (**Figure 2.5**), both as individual AA residues content (**Figure 2.5A**) and gathered as class of AA (*i.e.*, hydrophobic, positively charged, negatively charged, aromatic, branched chain and essential AA (**Figure 2.5B**). High levels of

glycine, glutamic acid, alanine, proline, and arginine are found, whereas methionine, tyrosine and lysine had the lowest levels.

Similar AA profile was found in type I collagen, the main collagen present in gelatin from fish scales (Nagai et al., 2004). The AA profile of the obtained optimal gelatin is quite similar to the one observed by Zhang et al., (2019) and Weng & Wu, (2015) who worked on Tilapia scales gelatin, from *Oreochromis niloticus* and Tilapia *zillii*, respectively. Similarly, Nagai et al., (2004) evidenced those AA as the most abundant ones in collagen obtained from three types of fish scales (sardine, red sea bream, japanese sea bass). Thanks to its high content of essential amino acids (*i.e.,* tryptophan, lysine, histidine, phenylalanine, leucine, isoleucine, methionine, valine, threonine), Tilapia scales gelatin shows interesting nutritional applications (Sierra-Lopera & Zapata-Montoya, 2021). Besides, acidic, negatively charged (glutamic and aspartic acids), hydrophobic AA (proline and alanine) and positively charged AA (arginine, histidine, lysine) composition, widen the applications of Tilapia scales gelatin to cosmetic, food and medicine (Zhang et al., 2019).

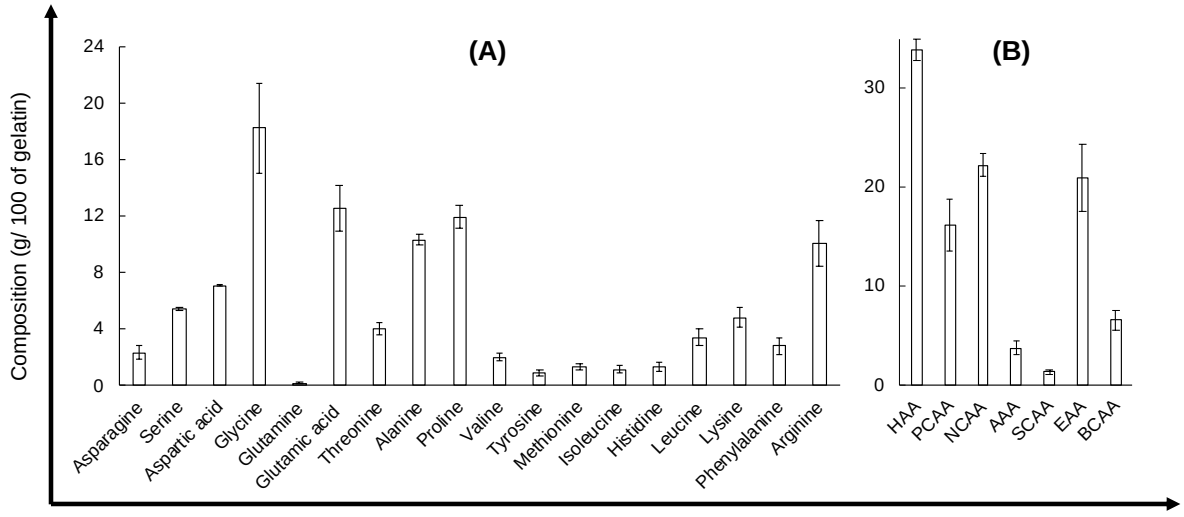

Figure 2.5. MS Amino acids composition of red tilapia scale gelatin obtained in optimal conditions (g/100 g of gelatin), (A) Individual AA content, (B) AA gathered as class.

AAA: Aromatic amino acids= Phe, Trp, Tyr; NCAA: Negatively charged amino acids= Asp, Glu, Asn, Gln; PCAA: Positively charged amino acids= Arg, His, Lys; HAA: Total Hydrophobic amino acids= Ala, Val, Ile, Leu, Tyr, Phe, Trp, Pro, Met and Cys; SCAA: Sulphur containing amino acids= Met and Cys; EAA: Essential amino acids= Trp, Lys, His, Phe, Leu, Ile, Met, Val, Thr; BCAA: Branched chain amino acids= Ile; Leu, Val.

2.3.5 Rheology properties

Gelatin from Tilapia scales with the most interesting properties in terms of molecular weight distribution (α_1/ α_2 ratio) (run 1, 8, 9 and optimal run) were characterized by rheology to assess their dynamic viscoelastic properties, since this is one of the most remarkably characteristic of gelatins to be used in food and pharmaceutical industries (Karim & Bhat, 2009). The elastic (G') and the loss (G'') moduli and the phase angle during colling (from 50 to 10 °C) and heating (from 10 to 50 °C) steps and the following of the thermal transition measured by the change in the phase angle of the different gelatin extracts were plotted (**Appendix 2.7** and **2.8**, respectively). Then, characteristic gelling (13.5-19.8 °C) and melting (21.8-27.2 °C) temperatures were obtained at the inflection point of the sharp decrease of the phase angle (**Figure 2.6A-B**.).

Gelatin obtained by run 1 (2 mL/g, 1 h, 65 °C, 60 min) and optimal run (10 mL/g, 3 h, 85 °C, 0 min) exhibit the best gelling and melting capacity, showing the highest G' and G'' (**Figure 2.6C-D**) with not statistically significant differences (*p-value* ≥ 0.05), followed by run 9 (6 mL/g, 2 h, 75 °C, 30 min) and 8 (10 mL/g, 3 h, 85 °C, 60 min). The viscoelastic properties are notably affected by the physico-chemical properties of gelatin such as molecular weight distribution profile, amount of γ, β components and α_1/ α_2 ratio. In fact, α_1-chain interacts better with the other constituent chains of gelatin that form the gel than α_2-chain does (Karim & Bhat, 2009). Sample 1 (2 mL/g, 1 h, 65 °C, 60 min) and optimal sample (Opt: 10 mL/g, 3 h, 85 °C, 0 min) are characterized by the highest α_1/ α_2 ratio (**Figure 2.4C**), which may explain their high gelling and melting temperatures.

The gelling temperatures (run 1, 19.8 °C and optimal run, 18 °C) are in the same range than other studies on gelatin fish skin from cod and hake (11-13 °C, Gómez-Guillen et al., 2002), grass carp (19.5 °C, Kasankala et al., 2007), tuna (19 °C, Montero & Acosta, 2020), rohu (18.52 °C) and common carp (17.9 °C) (Ninan et al., 2011) chemical (18.03 °C) and fermentation (18.33 °C) gelatins from Nile Tilapia skin (Chen et al., 2022). Similarly, the melting temperatures of run 1 (27.2 °C) and optimal run (25.8 °C) were higher than those of squid gelatin (20 °C, Gómez-Guillen et al., 2002) and similar than those of gelatin from Tuna skin (25.6 °C, Montero & Acosta, 2020), Bighead carp scales (27.7 °C, Tu et al., 2015) and slightly lower than those of gelatin fish skin from Nile Tilapia (28.8-29.9 °C, Chen et al., 2022), rohu

(29.27 °C) and common carp (28.13 °C) (Ninan et al., 2011). Even though there is no statistically significant effect of ultrasound on studied response variables, the SDS-PAGE profile analysis shows noticeable differences regarding the amount of γ, β, α- chains of the different gelatin extract when ultrasound was used, which does influence on the gelling and melting temperatures. The higher content of LMWA, associated to a high degradation of gelatin components (mainly β, α-chains) in run 8 (10 mL/g, 3 h, 85 °C, 60 min), could explain the lowest viscoelastic properties in this gelatin. This is in agreement with Gómez-Guillen et al., (2002), who reported that squid skin gelatin offered low gelling temperature due to the higher amount of LMWA compared to other fish skin gelatins. Hence, to obtain gelatin endowed with high viscoelastic properties from red Tilapia scale for its further use in food and pharmaceutical applications, extensive degradation of gelatin components must be avoided.

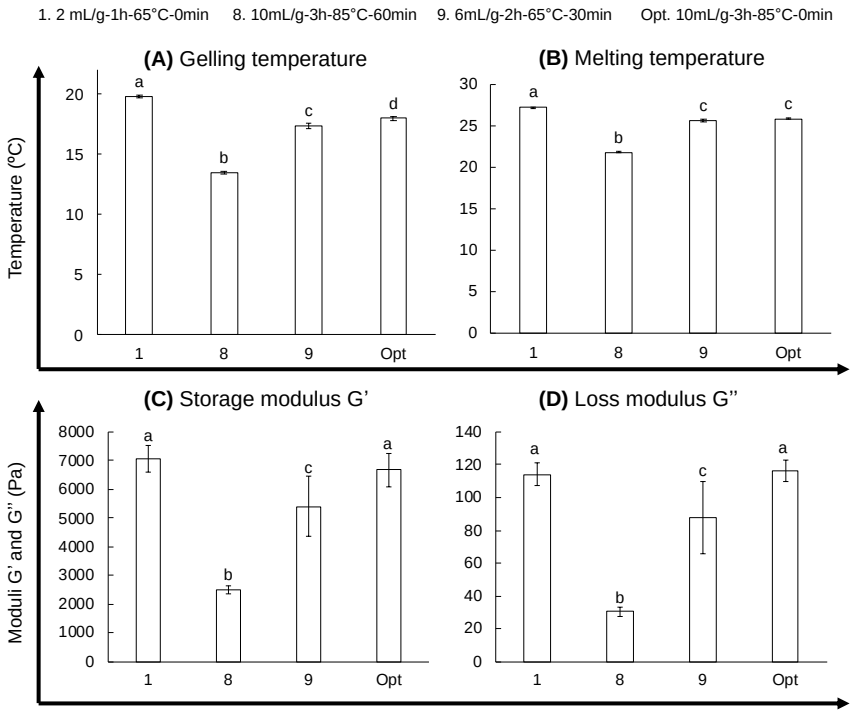

Figure 2.6. Rheological properties of the most interesting gelatin extracts (Run 1, 8, 9 and optimal run). (A) gelling and (B) melting temperatures; (C) and (D) elastic (G') and loss (G'') moduli, respectively.

2.4. Conclusions

Red tilapia scales can be valorized through gelatin extraction. To the author's knowledge, the gelatin extraction process from the red Tilapia scales has never been optimized to date. The application of the FFD for gelatin extraction process enabled to assess the impact of numerous parameters on responses *i.e*., crude protein content, free amino group content and protein extraction yield. This approach optimizes results while minimizing the number of experiments required. The crude protein content, high for all extraction experiments (> 95 %), is suitable for protein isolates. During the gelatin extraction from Tilapia scales, the solvent-to-solid ratio and the interaction of the solvent-to-solid ratio with temperature have the most significant effect on FAG content and PEY. Two reliable statistical models based on FFD were developed and used for the optimization of these responses. The optimization solution for multiple responses shows that a solvent-to-solid ratio of 10 mL/g, extraction time of 3 h, and temperature of 85 °C without ultrasounds, provide the maximal responses of FAG content and PEY, while crude protein content remained high. More, viscoelastic properties analysis revealed that run 1 (2 mL/g, 1 h, 65 °C, 60 min) and optimal run exhibit (10 mL/g, 3 h, 85 °C, 0 min) the highest gelling and melting capacities, in agreement with SDS-PAGE. Taken together, the optimal gelatin includes both the most optimized response in term of CPC, FAG, PEY, but also exhibits a molecular weight distribution profile that highlights β, α-chains as major components. These former chains provide appropriate viscoelastic properties, making gelatin from red Tilapia scales suitable for food and pharmaceutical application or bioactive peptides production due to its content of β, α-chains and LMWA.

Chapter 3. Gelatin Hydrolysates of Red Tilapia (*Oreochromis* spp.) Scale By-products: Investigation of Metal-Chelating Properties and their related Bioactivities

Considering the interesting physico-chemical properties of the gelatin isolate obtained from red Tilapia scales (i.e., protein content and amount of free amino groups) and the lack of evidence for its use in the production of protein hydrolysates using enzymes, our attention is now focused on the production of gelatin hydrolysates following on from **Chapter 2** above. Thus, this **Chapter 3** focuses on the potential of Tilapia scale gelatin to produce protein hydrolysates endowed with metal-chelating properties and their metal-related bioactivities through the use of single and sequential enzymatic treatments.

This Chapter will be submitted to the *Journal of Agricultural and Food Chemistry* as:

Camaño*, J.A., Irankunda, R., Arnoux, P., Girardat, J.M., Cakir-Kiefer, C., Risler, A., Stefan, L., Paris, C., Zapata, J.E., Selmeczi, K., Canabady-Rochelle*, L. Gelatin Hydrolysates of Red Tilapia (Oreochromis spp.) Scale By-products: Investigation of Metal-Chelating Properties and their related Bioactivities.

3.1 Introduction

Over the last ten years, aquaculture has dramatically increased due to the rapid human population growth, reaching a production of 223.2 million tons in 2022, 62.6 % of which contributes to capture fisheries (FAO, 2024). About 50-70 % of the total fresh fish weight are wastes, leading to significant adverse impact on the environment (Sierra-Lopera & Zapata-Montoya, 2021). Tilapia is the third most widely cultured fish worldwide: with 6 million tons in 2020, its production is expected to reach 7.3 million tons by 2030 (Munguti et al., 2022). Thus, red Tilapia manufacturing produces large quantities of wastes, especially scales, often discarded during the filet processing. Composed of collagen (30-50 %) and mainly hydroxyapatite ($Ca_5(PO_4)_3OH$) (30-40 %), fish scales present a great interest for gelatin production. This fibrous proteins obtained from the heat denaturation of collagen has numerous applications in food, pharmaceutical and cosmetic industries, thanks to its excellent functional and biological properties (Viji et al., 2019).

In the past two decades, a growing interest has emerged in the valorization of food-protein sources to produce hydrolysates containing bioactive and biofunctional peptides. Encrypted within the primary sequence of parent proteins, these target peptides released during protein hydrolysis or gastrointestinal digestion have been reported for their antioxidant, antihypertensive, anti-cancer, anti-inflammatory, antimicrobial, antidiabetic and metal-chelating activities (Wen et al., 2020). In an ecological transition and bioeconomy development context, researches have shifted their focus from traditional raw proteins to by-product-derived proteins.

These peptides, endowed with metal-chelating capacity, have been highlighted for their related bioactivity such as antioxidant (Viji et al., 2019) and anti-hypertensive properties (Zhang et al., 2019) (**Figure 3.1**). Indeed, metal-chelating peptides can act as indirect antioxidants while complexing transition metal ions such as Fe^{2+} and Cu^{2+} and thus, would prevent oxidative damage-related chronic diseases (Canabady-Rochelle et al., 2018). Besides, angiotensin-converting enzyme (**ACE**), a Zn^{2+}-dependent enzyme, is involved in hypertension. The Zn^{2+}-chelating peptides could move the zinc ion away from the ACE active site, modifying its conformation and eventually inactivating ACE (Lin et al., 2023).

Despite the huge production of red Tilapia scale by-product (up to 50000 tons worldwide per year), there is no literature reporting the production of gelatin hydrolysate from this specific fish source and by-product. Besides, to the author's knowledge, there is a lack of evidence about the use of sequential enzymatic hydrolysis on fish gelatin protein using Alcalase® followed by Flavourzyme®. As endopeptidase, Alcalase® is widely used in fish by-products hydrolysis, whereas, Flavourzyme®, composed of both endo and exopeptidases produced from *Aspergillus oryzae*, is recognized for its exopeptidase activity (Zhang et al., 2019). Since Alcalase® is expected to improve the subsequent action of Flavourzyme® by increasing the number of N-terminal sites, a sequential enzymatic treatment (Alcalase® and then Flavourzyme®) could therefore improve the biofunctional properties of red Tilapia scale gelatin hydrolysates. Therefore, this work aimed to evaluate the efficiency of different enzymatic treatments and 1 kDa ultrafiltration on metal-chelating, antioxidant, ACE-inhibitory activities of red Tilapia scale gelatin hydrolysate, as well as to identify the peptide sequences present.

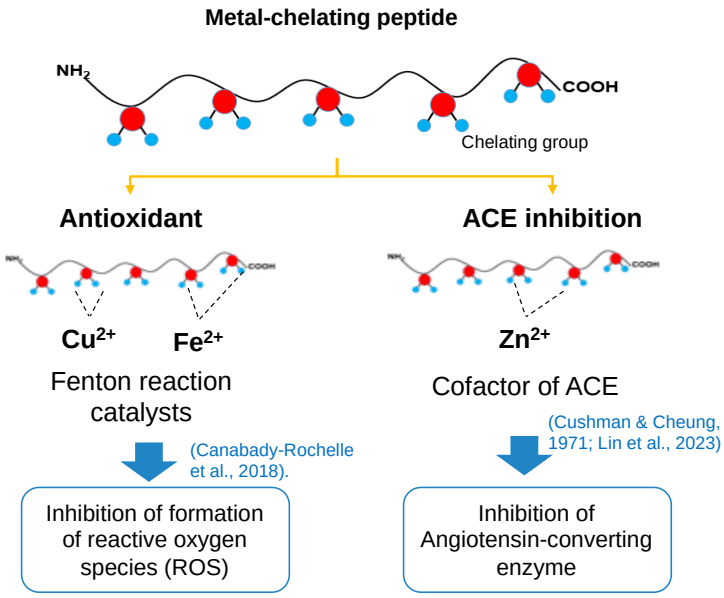

Figure 3.1. Relation between metal-chelating activity and other important biofunctional properties investigated in this study (antioxidant and antihypertensive activities) reported from the literature (Cushman & Cheung, 1971; Canabady-Rochelle *et al.,* 2018).

3.2 Materials and methods

3.2.1 Chemicals and equipments

Several chemicals were provided by Sigma–Aldrich (St Louis, MO, USA): 37 % hydrochloric acid (HCl), 97 % sulfuric acid (H_2SO_4), ammonium bicarbonate, *O*-Phthalaldehyde (**OPA**), N,N-dimethyl-2-mercaptoethyl ammonium, sodium tetraborate, sodium dodecyl sulfate, glycine, ethylenediaminetetraacetic acid (Na_2**EDTA**, $\cdot 2H_2O$), carnosine, 3-(2-Pyridyl)-5,6-diphenyl-1,2,4-triazine-p,p'-disulfonic acid monosodium salt hydrate 97 % (ferrozine), ferrous chloride solution (**$FeCl_2$**), murexide, copper sulfate (**$CuSO_4$**), hexamine, 2,2'-azinobis (3-ethylbenzothiazoline-6-sulfonic acid) diammonium salt (**ABTS**), 6-hydroxy-2,5,7,8-tetramethylchroman-2-carboxylic acid (**Trolox®**), potassium persulfate, potassium ferricyanide, trichloroacetic acid (**TCA**), ferric chloride (**$FeCl_3$**), iron(III) ferrocyanide $Fe_4[Fe(CN)_6]_3$ (Prussian blue), ascorbic acid, N-[3- (2-Furyl) acryloyl]-Phe-Gly-Gly (**FAPGG**), angiotensin converting enzyme, Alcalase® (≥ 2.4 Alcalase® Units (AU)/g) and Flavourzyme® (≥ 500 U/g) enzymes. Other analytical grade chemicals (potassium sulfate, sodium phosphate monobasic-NaH_2PO_4, sodium phosphate dibasic-Na_2HPO_4) were purchased from VWR International (Atlanta, USA) (CAS numbers in **Appendix 3.1**).

All the spectrophotometric measurements were performed using a spectrophotometer MRX Multiskan Go (ThermoFicher Scientific, Vantaa, Finland) equipped with a microplate reader and 96-well microplates (NunclonTM delta surface, Thermo scientific, Roskilde, Denmark).

3.2.2 Gelatin extraction from Tilapia scales

Red Tilapia (*Oreochromis* spp.) scales were supplied by El Gaitero SAS (Sopetrán, Colombia). The Tilapia scale flour (**TSF**) prepared according to Chen et al., (2019) and submitted to bromatological analysis contained 39.6 ± 0.56 % crude proteins, 3.4 ± 0.07 % fat, and 51.7 ± 1.9 % ash (mineral fraction, mainly hydroxyapatite) in the dry matter (AOAC, 2000). The protein extraction process involved TSF demineralization followed by a hydrothermal extraction using ultrapure water (**Appendix 3.2**). First, the demineralization process was performed similarly to Chen et al., (2019). The demineralized TSF was washed with ultrapure water (18.2 MΩ .cm at 25 °C) until reaching pH 7.0. Then, the gelatin protein was extracted from demineralized TSF at 50 % (w/v) using ultrapure water under stirring for 3 h at 65 °C (Wangtueai & Noomhorm, 2009). After protein extraction, the Tilapia scale gelatin (**TSG**) containing 98.8 % of proteins was stored at – 20 °C until further use.

3.2.3 Proteolysis

The gelatin protein extracted from Tilapia scales was hydrolyzed using three different enzymatic treatments: Alcalase® alone (**Alc**), Flavourzyme® alone (**Flav**) or a sequential treatment using Alcalase® followed by Flavourzyme® (**Alc+Flav**).

For each proteolysis experiment, TSG powder (5 g) was dissolved in 250 mL of ammonium bicarbonate buffer solution (50 mM) using a 1 % (w/w) enzyme-to-substrate ratio (**E:S**) with the following conditions: 55 °C, pH 8 for Alcalase® and pH 7 for Flavourzyme®, respectively. After proteolysis, the corresponding protease was heat inactivated (95 °C, 15 min). In the sequential treatment, Alcalase® was inactivated just before Flavourzyme® treatment. Then, the solutions were centrifuged (10000 *g,* 15 min, 25 °C) for removing enzymes. Finally, the supernatants were lyophilized (LABCONCO, Kansas City, USA) and stored at −20 °C for further analysis.

The two most interesting hydrolysates (Alc and Alc+Flav) were further fractionated by membrane ultrafiltration using an ultrafiltration stirred cell 47-mm system (XFUF04701; Millipore, Molsheim, France) under magnetic stirring and pressure of 5 bar of nitrogen. The ultrafiltration unit was first equipped with a molecular weight cut-off membrane of 10 kDa (Millipore, Billerica, USA), conditioned according to the specification, before ultrafiltration. Each hydrolysate (200 mL; 20 mg/mL in ultrapure water) was passed through the membrane; then, the permeate was ultrafiltrated onto a 1-kDa cut-off membrane (Millipore, Billerica, USA). The resulting ultrafiltrates (≤ 1 kDa fractions) were lyophilized and stored at −20°C until further used.

3.2.4 Physico-chemical characterization

3.2.4.1 OPA quantification and degree of hydrolysis

The degree of hydrolysis (**DH**, %) of whole hydrolysates (*i.e.,* Alc, Flav and Alc+Flav) and the peptide concentration of ≤ 1 kDa hydrolysates (Alc and Alc+Flav, the most interesting ones, expressed as mmol equivalent of primary amine groups per gram of hydrolysate (mmol eq. NH_2/g), were determined by *o*-Phthalaldehyde (**OPA**) for microplate by spectrophotometry (Canabady-Rochelle et al., 2018). The DH of whole hydrolysates (Alc, Flav, Alc+Flav) was expressed as the ratio of free amino groups present in the hydrolysate to the total amino

groups present in the sample obtained after complete acid digestion of Tilapia scales gelatin (10 mg of gelatin in 10 mL of 6 M HCl at 130 °C, 24 h in oven). For DH calculation (Equation. 1), the peptide bonds of gelatin protein were assumed to be all cleaved after acid digestion:

$$\text{Degree of Hydrolysis (\%)} = \left[\frac{\text{NH}_2\,\text{x} - \text{NH}_2\,0}{\text{NH}_2\,\text{T} - \text{NH}_2 0}\right] \text{x } 100 \qquad (1)$$

Where: NH_2X and NH_20 are the number of free-NH_2 groups after and before enzymatic hydrolysis, respectively, and NH_2T, the total NH_2 determined after complete acid hydrolysis.

3.2.4.2 Molecular weight distribution

The molecular weight (**MW**) of TSF, TSG and its hydrolysates was investigated by two complementary techniques: sodium dodecyl sulfate polyacrylamide gel electrophoresis (**SDS-PAGE**) and peptide size (size exclusion chromatography, **SEC**).

SDS-PAGE. The MW distribution of TSF, TSG and whole gelatin hydrolysates was investigated by SDS-PAGE (Tu et al., 2015). The samples were prepared at 20 mg/mL in ultrapure water; the polyacrylamide gel consisted of a 7.5 % separation gel and a 5% stacking gel (**Appendix 3.3**).

Size Exclusion Chromatography. The MW distribution of the whole hydrolysates (Alc and Alc+Flav) and their ≤ 1 kDa ultrafiltrates was determined by SEC using a 515 HPLC pump (Waters, Milford, MA, USA), a degazer and a RID 10-A Shimadzu detector as reported in (El Hajj et al., 2023) (**Appendix 3.4**).

3.2.4.3 Amino acids composition

In order to quantify the amino acids (**AA**) composition of TSG and its hydrolysates (Alc, Alc+Flav and their respective ultrafiltrates), the samples were subjected first to a complete acid hydrolysis (10 mg in 10 mL of 6 M HCl, 130 °C, 2 h in microwave) using a microwave digestion system (Microwave Start D Milestone, Milan, Italy) (Rutherfurd & Gilani, 2009). Then, the completely hydrolyzed sample was dried at 65 °C under vacuum. After hydrolysis, the quantitative analysis of AA of samples was carried out on a UHPLC-MS system (ThermoFisher Scientific, San Jose, CA, USA) connected to a photodiode array detector and a LTQ^{XL} mass spectrometer equipped with an atmospheric pressure ionization interface

operating in electrospray positive mode (**ESI$^+$**) as reported in El Hajj et al., (2023) (**Appendix 3.5**).

3.2.5 Screening of MCPs in Tilapia hydrolysates using switchSENSE® technology

The interactions between peptides present in TSG hydrolysates and nickel ions (Ni^{2+}) were investigated using a biosensor analyzer DRX (switchSENSE® Dynamic Biosensors GmbH, Planegg, Germany). This technology can be used in static and in dynamic modes as reported in Muller-Landau & Varela, (2021). Experiments were conducted according to the method initiated by El Hajj et al., (2021) with some modifications. Briefly, an electrically switchable DNA chip designated as MPC-48-2-R1-S, incorporated tris-nitrilotriacetic acid and Cy5 dye as a fluorescent probe. The chip comprised six electrode-related spots, with two serving as reference points and the remaining four designated as sample spots, each functionalized with Ni^{2+}-chelating DNA nanolevers. Tilapia scale gelatin hydrolysates and ultrafiltrates were prepared at 50, 100, and 200 µM eq. NH_2 (according to OPA assay) using T40 buffer (*i.e.,* 10 mM Tris-HCl, 40 mM NaCl, and 0.05 % v/v Tween 20 at pH 7.4). Then, the sample solutions were injected into the microfluidic device at a flow rate of 30 µL/min for a 4-min association phase, followed by the injection of T40 buffer at 50 µL/min for a 4 min dissociation phase to release the analytes. After each investigated concentration, Ni^{2+} ions were removed using 100 mM EDTA, followed by a Ni^{2+} rebinding phase before examining another concentration. A buffer blank was analyzed to correct all kinetic experiments for non-specific interactions (static mode measurements).

Between the association and dissociation phases in static mode measurements, the flow was paused to perform the dynamic mode measurement, which evaluate the specificity of the peptide-metal interaction and analyze the size of the peptide bound to Ni^{2+}. The hydrodynamic diameter (**D_H**) is typically determined in the case of proteins immobilized on the nanolevers; in our study, due to the absence of any protein, the variation in D_H calculated between Ni^{2+} only, and Ni^{2+} carrying metal-chelating peptides (**MCPs**) corresponded rather to a binding size index (**ΔSI**).

The analysis of the different curves was performed using the switchANALYSIS® software from Dynamic Biosensors using non-linear fitting of single exponential functions. Each kinetic

experiment was performed twice with different sample preparations and the ΔSI values represent the average of eight measurements.

3.2.6 Biofunctional characterization

3.2.6.1 Antioxidant tests

Fe^{2+}-chelating activity. The capacity of TSG hydrolysates to chelate Fe^{2+} was determined similarly to Canabady-Rochelle et al., (2015) by measuring the formation of the Fe^{2+}-ferrozine complex (λ_{max} = 562 nm). Two positive controls (EDTA, 0.04-5 mg/mL and carnosine, 0-10 mg/mL) were investigated. The iron-chelating activity of gelatin hydrolysates was calculated according to Equation (2).

$$\text{Iron chelating activity } (\%) = \left[\frac{A_0 - A_s}{A_o}\right] X\ 100 \qquad (2)$$

where A_0 is the absorbance of the control (without sample), and A_s is the absorbance either of the sample or of the positive control (EDTA or carnosine). The results were expressed as the half maximal effective concentration (**EC_{50}**), *i.e.,* the hydrolysate concentration required for 50 % of iron chelation.

Radical scavenging activity. The ABTS radical scavenging activity was carried out similarly to Canabady-Rochelle et al., (2015). Trolox® (positive control; 0-120 µM) was used for calibration. In the meantime, the samples were prepared at various concentrations (0-1 mg/mL) in the 4 mM phosphate buffer. Carnosine was also used for comparison at the same concentrations. The ABTS radical solution was diluted in phosphate buffer (4 mM, pH 7.4) to reach an initial absorbance value of 0.70 ± 0.02 at 734 nm. The ABTS radical scavenging activity was calculated by Equation (3).

$$\text{ABTS Radical scavenging } (\%) = \left[\frac{A_0 - A_s}{A_o}\right] X100 \qquad (3)$$

where A_0 represents the initial absorbance of $ABTS^{\cdot+}$ radical solution (without samples), and A_s indicates the absorbance of the remaining radical (with samples). The EC_{50} was determined as hydrolysate/positive control concentration required for scavenging 50 % of ABTS radical.

Reducing power. It was determined similarly to Canabady-Rochelle et al., (2015) in reference to ascorbic acid as positive control. Ascorbic acid (calibration curve from 0 to 0.1 mg/mL), carnosine and hydrolysate solutions (investigated concentration: 1 mg/mL) were prepared in phosphate buffer (0.2 M, pH 6.6). The absorbance was determined at 700 nm after 10 min of incubation at 25 °C. The ability of gelatin hydrolysates to reduce Fe^{3+} to Fe^{2+} was expressed in micromoles of ascorbic acid equivalent per gram of sample (µmol AAE/g).

3.2.6.2 ACE inhibitory activity

The ability of gelatin hydrolysates to inhibit the ACE activity was evaluated *in vitro* using N-[3-(2-furyl) acryloyl]-Phe-Gly-Gly (FAPGG) substrate (Estévez et al., 2020). Briefly, hydrolysate solutions were prepared at various concentrations (0-5 mg/mL) in 50 mM Tris-HCl buffer containing 300 mM NaCl, pH 7.5. Each sample solution (10 µL) was mixed with 10 µL of ACE (final activity of 0.25 U/mL according to the specification). Then, 150 µL of 0.5 mM FAPGG (preheated at 37 °C for 15 min) was added. The absorbance was measured every minute at a wavelength of 340 nm for 30 min at 37 °C. The ACE activity was expressed as the rate of hydrolysis of FAPGG substrate (ΔA/min). Hence, the ACE inhibition activity (%) was calculated according to Equation (4):

$$\text{ACE inhibition (\%)} = \left[\frac{\Delta A_{/\text{min}}(\text{blank}) - \Delta A_{/\text{min}}(\text{sample})}{\Delta A_{/\text{min}}(\text{blank})}\right] \text{X } 100 \qquad (4)$$

Where $\Delta A_{/\text{min}}$ (blank) is ACE activity without hydrolysate (volume of hydrolysate solution replaced by Tris-HCl buffer), and $\Delta A_{/\text{min}}$ (sample) is ACE activity in the presence of hydrolysate.

Results were reported as the half maximal inhibitory concentration (IC_{50}) of hydrolysate leading to 50 % ACE inhibition activity.

3.2.7 Mass spectrometry identification and sequence analysis

3.2.7.1 LC-MS/MS analysis

To identify the peptide sequences present in the produced hydrolysates, the samples (1 mg/mL) were analysed on a Thermo Scientific UHPLC-HRMS system composed of a Vanquish Flex™ liquid chromatography unit coupled to a photodiode array detector (PDA) and an

Orbitrap ID-X™ Tribrid™ high-resolution mass spectrometer operating in electrospray ionization mode (ESI) as in Dos Santos Morais et al., (2020).

3.2.7.2 Peptide sequences identification

The Thermo Xcalibur raw data resulting from LC-MS/MS analysis of gelatin hydrolysates were processed using MaxQuant™ proteomics software (version 2.4.13.0) to automatically elucidate the amino acid sequences of the hydrolysis peptides (Tyanova et al., 2016). The peptide search was conducted using a restricted collagen (*Oreochromis niloticus*) proteins data base containing 30 entries obtained from UniProtKB (https://www.uniprot.org/, accessed on 27 January 2024, **Appendix 3.6**). The parameters of database search were adjusted as previously published (Boachie et al., 2022; Yu et al., 2024) (**Appendix 3.7**). Before applying this automated procedure to the Tilapia gelatin hydrolysate samples, a preliminary test was conducted on a mixture of 8 synthetic peptides from type I collagen (G9M6I5, *Oreochromis niloticus*), *i.e.,* GHR, GHRGFSGL, KGHR, KGHRGF, GHRGF, KHV, RGMKGH, RGMKGHR (1 mM each) in order to validate it. All the 8 peptides were identified (**Appendix 3.8**).

3.2.8 Statistical analysis

To evaluate the effect of enzymatic treatments and 1-kDa ultrafiltration process on physical-chemical and biofunctional properties of hydrolysates, results were statistically analyzed by one-way analysis of variance (ANOVA). All the measurements of OPA quantification and biofunctional properties (Ni^{2+} binding ability, Fe^{2+}-chelating, radical scavenging, and reducing and ACE inhibitory activities) were triplicated and data presented as means ± standard deviation. Significant differences between means of samples were determined by Fisher's multiple range test. Differences at *p-value* < 0.05 were considered significant. Statistical calculations were conducted using the software Statgraphics centurion XVI version 16.1.03 (Statgraphics Technologies Inc, Virginia, USA).

3.3 Results and discussion

3.3.1 Physical-chemical characterization of the TSG hydrolysates

3.3.1.1 Determination of the degree of hydrolys

Three different TSG hydrolysates were produced: Alc, Flav, and Alc+Flav. For each hydrolysate, the effect of enzymatic treatment was evaluated on their physico-chemical and biofunctional properties.

The DH parameter can only be measured before ultrafiltration. The Alc+Flav hydrolysate shows the highest DH (29.74 ± 1.29 %), followed by Alc (19.70 ± 1.08 %), and Flav alone (4.35 ± 0.43 %). The DH of gelatin hydrolysates is significatively different (*p-value* < 0.05) as a function of the enzymatic treatment. The Alcalase® is an endopeptidase characterized by a very broad specificity in peptide cleavage. In our study, Alc shows higher DH (19.7 %) compared to Zhang et al., (2019) and Sierra-Lopera & Zapata-Montoya, (2021), who evidenced DH values of 12.9 % and 16.7 %, respectively, for the same resource and similar enzymatic treatment. Besides, Flavourzyme® is a mixture of eight endo and exopeptidases produced by *Aspergillus oryzae* (Huang et al., 2018). In our study, Flavourzyme® alone shows lower proteolytic activity than Alcalase® towards TSG, which demonstrates a lower affinity between the endopeptidases contained in Flavourzyme® and TSG compared to Alcalase® alone, in agreement with the literature (Nchienzia et al., 2010). Yet, a high activity is found for Flavourzyme® used as exopeptidase, since the DH obtained in the sequential hydrolysis of TSG is 10 % higher: 19.70 % and 29.74 % for Alc and Alc+Flav, respectively.

Hence, endopeptidases contained in Alcalase® increase the number of N-terminal sites available in TSG hydrolysate, then promoting the proteolytic activity of exopeptidases present in Flavourzyme®. Therefore, the TSG Alcalase® hydrolysate is a favorable substrate for Flavourzyme® as reported previously (Nchienzia et al., 2010).

3.3.1.2 Peptide profile

SDS-PAGE. The MW distribution of TSF, TSG and the three gelatin whole hydrolysates were investigated by SDS-PAGE (**Figure 3.2A**). First, the unhydrolyzed TSF profile shows 4 bands: one superior to 250 kDa with low intensity, another around 180 kDa, and two more inferior to 150 kDa, which correspond to cross-linked chains of type I collagen, γ, β, α_2 and α_1 chains,

respectively. These bands are characteristic of the type I collagen, present in fish scales (Huang et al., 2018). Then, for the TSG, the bands intensity is higher than in TSF, showing a smear with higher coloration. Other bands located at lower MWs (25-100 kDa) are also observed and indicated by an arrow (**Figure 3.2A**). These bands are associated to the collagen hydrolysis upon gelatin heating during extraction, with α- and β-chains gradually degraded into protein fragments and peptides. Our results are in agreement with Qiu et al., (2019) who previously observed that type I collagen from skipjack tuna (*Katsuwonus pelamis*) scales showed α_1, α_2 and β bands, further degraded into smaller fragments during gelatin extraction.

Concerning gelatin hydrolysates, upon Alc and Alc+Flav treatments, all bands found in TSG disappear, meaning a high degradation of peptide bonds. Several peptide fragments might be produced below 10 kDa, but are not observed due to the SDS–PAGE resolution limit (10-250 kDa). Inversely, the Flav treatment shows larger peptide fragments, with a profile similar to the native protein (TSG) between (25-100 kDa). These results are in agreement with the DH determination in the corresponding samples: the higher the DH, the lower band intensity in the corresponding hydrolysate. From both DH determination and SDS-PAGE, Alc and Alc+Flav treatments are the most efficient ones on red Tilapia scale gelatin, highlighting the high affinity of Alcalase® for this protein, and the noteworthy exopeptidase activity of Flavourzyme® upon sequential treatment. According to the literature, the peptides less than 10 AA residues being often considered as the most interesting ones in terms of bioactivity for further nutraceutical and health applications (Wen et al., 2020), thus, the Flav hydrolysate was discarded for further experiments. Hence, the Alc and Alc+Flav hydrolysates solely were further ultrafiltrated through a 1-kDa cutoff ultrafiltration membrane and their respective ultrafiltrates were characterized for their physico-chemical and biofunctional properties.

Size-Exclusion Chromatography. The whole hydrolysates (Alc and Alc+Flav) and their respective ultrafiltrates were analyzed by SEC (**Figure 3.2B**). For the whole hydrolysates, the MWs are mainly distributed between 0.2 and 3 kDa (90 % area of peaks). On the other hand, as expected after a 1 kDa ultrafiltration, the ≤ 1 kDa Alc and ≤ 1 kDa Alc+Flav hydrolysates mainly present a MW distribution between 0.2 and 1 kDa (**Figure 3.2B,C**). Area of peaks in < 0.2 kDa corresponds to free AA (the mean MW of an AA being considered within 100-140 Da). Thus, Alc and Alc+ Flav are able to produce free AA according to **Figure 3.2C**, yet in a lower way for Alc alone. Our results are in agreement with Huang et al., (2018), who reported that

the production of free AA after using Alcalase® and Flavourzyme® enzymes. Hydrolysate produced by Alc+Flav has higher number of small-sized peptides than hydrolysates produced by a single Alcalase® treatment whether or not an ultrafiltration process applied, which is related to the sequential Flavourzyme® exopeptidase activity.

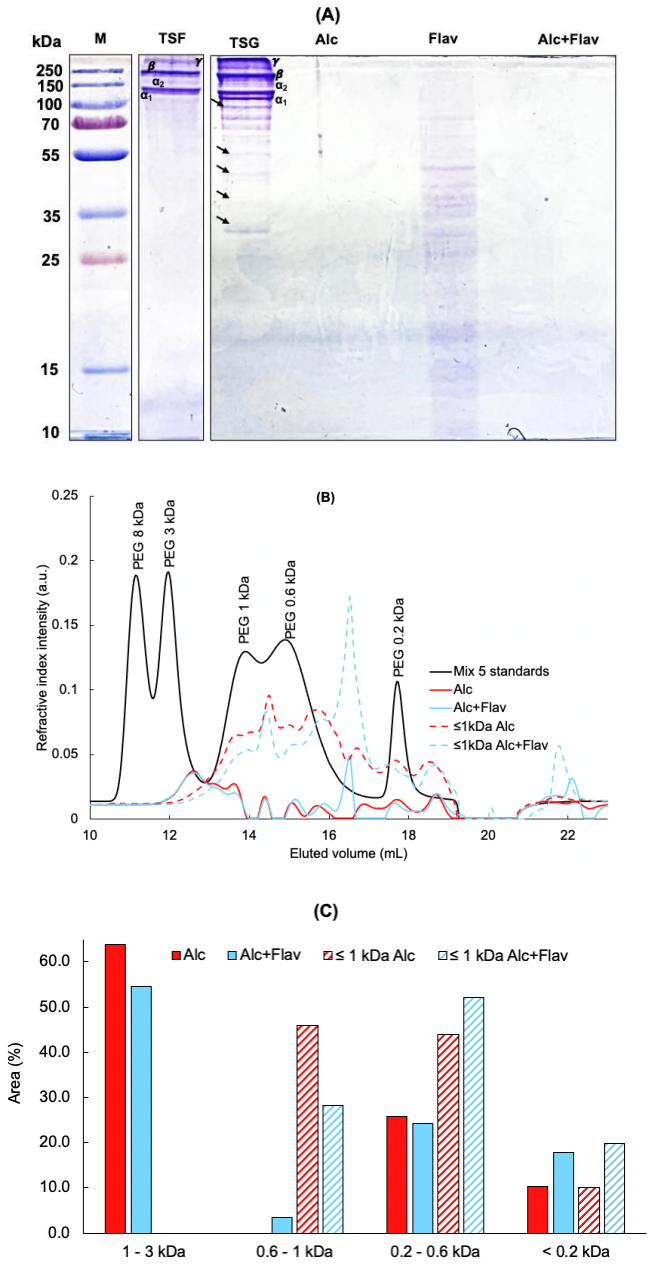

Figure 3.2. Molecular weight distribution of protein marker, Tilapia scale flour (TSF), Tilapia scale gelatin (TSG) and Tilapia scale gelatin hydrolysates. (A) SDS-PAGE patterns of protein marker, TSF, TSG and TSG hydrolysates. (B) and (C) Size exclusion chromatography profile of Tilapia scale gelatin hydrolysates.

Alc: Alcalase® hydrolysate; Alc+Flav: Alcalase® followed by Flavourzyme® hydrolysate. M: Marker; TSF: Tilapia scale flour; TSG: Tilapia scale gelatin, Alc: Alcalase® hydrolysate; Flav: Flavourzyme® hydrolysate, Alc+Flav: Alcalase® followed by Flavourzyme®; ≤ 1 kDa: ultrafiltrated hydrolysate; PEG: Polyethylene glycol.

SEC data are in agreement with the DH and SDS-PAGE results, since protein degrades into polypeptides down to smaller peptides as a result of enzymatic treatment. Hence, TSG Alc+Flav hydrolysates may present a high potential of biological activity due to their small-sized peptide content.

3.3.1.3 Peptide quantification

The peptide molar concentration was investigated using OPA quantification and expressed as mmol eq. NH_2 of TSF, TSG, whole and ≤ 1 kDa gelatin hydrolysates per gram of sample (**Table 3.1**). The flour (TSF) shows the lowest peptide concentration, due to collagen tightly linked to hydroxyapatite (Zhang et al., 2019). Then, upon the gelatin extraction by hydrothermal process, the peptide molar concentration increases for gelatin (TSG) compared with TSF. Indeed, collagen present in TSF is partially hydrolysed during gelatin extraction, releasing small protein fragments.

Table 3.1. Peptide concentration of Tilapia scale flour (TSF), Tilapia scale gelatin (TSG) and Tilapia scale gelatin hydrolysates.

Samples	mmol eq. NH_2/g
TSF	0.01 ± 0.004^{a}
TSG	0.26 ± 0.01^{b}
Alc	1.44 ± 0.06^{c}
Alc+Flav	2.02 ± 0.08^{d}
≤ 1 kDa Alc	1.79 ± 0.07^{e}
≤ 1 kDa Alc + Flav	2.93 ± 0.10^{f}

Alc: Alcalase® hydrolysate, Alc+Flav: Alcalase® followed by Flavourzyme®; ≤ 1 kDa: ultrafiltrated hydrolysate. Values are mean ± SD (n = 5). Values with different letters within the same column indicate significant differences (*p-value* < 0.05).

Finally, once gelatin hydrolysed by Alc and Alc+Flav, the peptide molar concentration is notably increased, indicating the increase of NH_2 terminus and thus, higher peptide or free amino group concentration. As found for DH, the Alc hydrolysis leads to a high number of small-sized peptides, as previously reported (Viji et al., 2019; Wen et al., 2020). For whole hydrolysates and their respective ≤ 1 kDa fractions, the peptide molar concentration is always

higher in Alc+Flav hydrolysates than in Alc hydrolysate. More, compared to the whole hydrolysates, the ≤ 1 kDa ultrafiltrates present higher peptide molar concentration for a same sample mass, in agreement with the enrichment of small-sized peptides after ultrafiltration (24 and 45 % increase for Alc and Alc+Flav, respectively).

3.3.1.4 Amino acids composition

Bioactivity properties of peptides present in food-protein hydrolysates are notably influenced by their amino acid composition. The AA profile of TSG and its hydrolysates (whole and ≤ 1-kDa hydrolysates) are shown in **Table 2**. The AA profiles are presented**,** both as individual AA residues content and gathered as class of AA (*i.e*., hydrophobic, positively charged, negatively charged, aromatic, branched chain and essential AA). Generally, slight differences are found in the AA composition of whole Alc and Alc+Flav hydrolysates, due to the fact that both hydrolysates are obtained from the same native protein (TSG).

High levels of glycine, glutamic acid, alanine, proline, and arginine are observed, whereas methionine, tyrosine and lysine have the lowest levels. Similar AA profiles are reported for type I collagen, *i.e.,* the main collagen present in fish scales derived from various species (sardine, red sea bream, japanese sea bass) (Nagai et al., 2004). The AA profile of TSG hydrolysates obtained is quite similar to the one observed by Zhang et al., (2019) for Tilapia scale (*Oreochromis niloticus)*.

Regarding the ≤ 1 kDa hydrolysates (Alc and Alc+Flav), the composition is similar for most of high concentrated AA (*i.e.,* glycine, alanine, proline, and arginine). The glutamic acid residue is the only one presenting a significative difference (*p-value* <0.05), with a slightly higher concentration value in Alc than in Alc+Flav (11.89 g/100 g versus 9.69 g/100 g, respectively). Thus, despite the 1 kDa ultrafiltration, hydrolysates tend to maintain the proportion of the five main AA (including glutamic acid), at ratios similar to those initially calculated for the TSG protein from its sequence knowledge. Moreover, AA composition gathered as class of AA reveals the presence of high content of hydrophobic and charged AA, especially, arginine, proline, glutamic acid and alanine, which widens the applications of TSG to cosmetic, food, and medicine (Zhang et al., 2019). In addition, thanks to its high content of essential AA (EAA)

(**Table 3.2**), TSG hydrolysates obtained in our study present interesting nutritional applications.

Table 3.2. Amino acids (AA) composition of TSG and its hydrolysates (g/100 g) given by amino acid and by amino acid class (hydrophobic, positively charged, negatively charged, aromatic, sulfur containing, essential and branched chain AA).

Amino acid	Concentration (g/ 100 g sample)				
	Gelatin	Alc	Alc+Flav	≤ 1 kDa Alc	≤ 1 kDa Alc+Flav
Asparagine	2.04 ± 0.37^{ab}	2.33 ± 0.46^{b}	2.25 ± 0.44^{b}	1.53 ± 0.53^{bc}	1.20 ± 0.26^{c}
Serine	4.73 ± 0.50^{a}	5.93 ± 0.14^{b}	5.85 ± 0.22^{bc}	5.54 ± 0.30^{c}	5.34 ± 0.30^{c}
Aspartic acid	6.38 ± 0.66^{a}	7.70 ± 0.12^{b}	7.56 ± 0.32^{b}	5.5 ± 054^{ac}	4.63 ± 0.55^{c}
Glycine	16.73 ± 2.94^{a}	18.84 ± 3.20^{a}	19.18 ± 3.25^{a}	19.25 ± 3.42^{a}	21.99 ± 3.96^{a}
Glutamine	0.12 ± 0.03^{a}	0.17 ± 0.04^{a}	0.16 ± 0.04^{a}	0.13 ± 0.03^{a}	0.12 ± 0.03^{a}
Glutamic acid	11.06 ± 0.44^{a}	11.65 ± 0.61^{a}	11.65 ± 0.46^{a}	11.89 ± 0.67^{a}	9.69 ± 0.46^{b}
Threonine	3.82 ± 0.45^{a}	4.12 ± 0.41^{a}	4.11 ± 0.42^{a}	4.11 ± 0.41^{a}	3.77 ± 0.38^{a}
Alanine	9.66 ± 0.60^{a}	11.20 ± 0.47^{a}	11.03 ± 0.46^{a}	12.56 ± 0.70^{a}	14.58 ± 1.06^{a}
Proline	11.3 ± 1.05^{a}	12.36 ± 0.76^{a}	12.37 ± 0.91^{a}	11.14 ± 0.65^{a}	10.93 ± 0.65^{a}
Valine	2.86 ± 0.19^{ab}	2.00 ± 0.35^{b}	2.23 ± 39^{bc}	2.61 ± 0.36^{abc}	3.07 ± 0.55^{a}
Tyrosine	1.05 ± 0.15^{ab}	0.87 ± 0.14^{b}	0.84 ± 15^{b}	1.16 ± 0.19^{a}	1.10 ± 0.16^{ab}
Methionine	1.38 ± 0.21^{ab}	1.29 ± 0.25^{ab}	1.06 ± 21.23^{b}	1.67 ± 0.29^{a}	1.31 ± 0.17^{c}
Isoleucine	1.96 ± 0.29^{a}	1.04 ± 0.22^{b}	1.14 ± 0.23^{b}	1.39 ± 0.25^{b}	0.98 ± 0.19^{b}
Histidine	1.58 ± 0.34^{a}	1.13 ± 0.25^{a}	1.14 ± 0.27^{a}	1.43 ± 0.34^{a}	1.29 ± 0.26^{a}
Leucine	4.45 ± 0.35^{a}	3.08 ± 0.51^{b}	3.11 ± 0.47^{bc}	3.95 ± 0.45^{ac}	3.72 ± 0.50^{ac}
Lysine	5.69 ± 0.58^{a}	4.22 ± 0.65^{b}	4.25 ± 0.63^{b}	3.41. ± 0.57^{ac}	3.58 ± 0.58^{abc}
Phenylalanine	3.63 ± 0.41^{a}	2.51 ± 0.48^{b}	2.54 ± 0.42^{b}	3.01 ± 0.45^{ab}	2.88 ± 0.40^{ab}
Arginine	11.48 ± 1.61^{a}	9.48 ± 1.44^{a}	9.44 ± 1.40^{a}	9.66 ± 1.38^{a}	11.06 ± 1.37^{a}
HAA	36.33 ± 0.50^{a}	34.38 ± 0.53^{b}	34.36 ± 0.84^{b}	37.51 ± 0.76^{a}	37.28 ± 1.01^{a}
PCAA	18.76 ± 2.49^{a}	14.84 ± 2.33^{ab}	14.85 ± 2.31^{ab}	14.5 ± 2. 28^{b}	15.94 ± 2.20^{ab}
NCAA	19.6 ± 0.81^{ac}	21.86 ± 0.20^{b}	21.62 ± 0.26^{b}	19.06 ± 0.31^{c}	15.65 ± 1.17^{ac}
AAA	4.68 ± 0.55^{ab}	3.38 ± 0.61^{b}	3.39 ± 0.55^{b}	4.17 ± 0.64^{ab}	3.99 ± 0.55^{ab}
SCAA	1.38 ± 0.21^{ab}	1.29 ± 0.25^{ab}	1.06 ± 0.21^{b}	1.67 ± 0.29^{a}	1.31 ± 0.17^{c}
EAA	25.41 ± 2.81^{a}	19.42 ± 3.11^{b}	19.63 ± 3.05^{b}	21.59 ± 3.11^{ab}	19.32 ± 2.86^{ab}
BCAA	9.29 ± 0.82^{a}	6.13 ± 0.86^{b}	6.49 ± 0.91^{bc}	7.96 ± 0.95^{ac}	7.77 ± 0.90^{ac}

Values are mean ± SD (n = 3). Values with different letters within the same column indicate significant differences (*p-value* < 0.05). Alc: Alcalase® hydrolysate, Alc+Flav: Alcalase® followed by Flavourzyme®; ≤ 1 kDa: ultrafiltrated hydrolysate. AAA: Aromatic amino acids= Phe, Trp, Tyr; NCAA: Negatively charged amino acids= Asp, Glu, Asn, Gln; PCAA: Positively charged amino acids= Arg, His, Lys; HAA: Total Hydrophobic amino acids= Ala, Val, Ile, Leu, Tyr, Phe, Trp, Pro, Met and Cys; SCAA: Sulphur containing amino acids= Met and Cys; EAA: Essential amino acids= Trp, Lys, His, Phe, Leu, Ile, Met, Val, Thr; BCAA: Branched chain amino acids= Ile; Leu, Val.

3.3.2 Screening of MCPs in Tilapia hydrolysates using switchSENSE® technology

3.3.2.1 Static mode

The ability of TSG hydrolysates (whole and ultrafiltrated samples) was evaluated by real-time molecular interaction analysis using the switchSENSE® technology. For each hydrolysate, three different concentrations were introduced into the microfluidic device.

Figure 3.3 illustrates the kinetic study of the interaction TSG hydrolysates and the immobilized Ni^{2+} ions. During the association phase, a significant increase in fluorescence is observed in all hydrolysates until reaching equilibrium (**Figure 3.3A, 3.3C, 3.3E,** and **3.3G** for Alc, Alc+Flav, ≤ 1 kDa Alc, and ≤ 1 kDa Alc+Flav, respectively). This fluorescence enhancement indicates the presence of MCPs in gelatin hydrolysates that can bind to Ni^{2+} ions. As a result, the fluorescent probe is no longer quenched by Ni^{2+} ions due to steric hindrance caused by the MCPs.

Regarding the dissociation phase, which was only studied for the highest concentration of hydrolysates at 200 µM eq. NH_2 (the dissociation rate does not depend on the analyte concentration), fluorescence readily decreases for all the hydrolysates (**Figure 3.3B, 3.3D,** and **3.3F, 3.3H** for Alc, Alc+Flav, ≤ 1 kDa Alc, and ≤ 1 kDa Alc+Flav, respectively). This decrease can be attributed to the MCPs release, leading to the disappearance of steric hindrance previously associated with their binding to Ni^{2+} ions. Note that all hydrolysates exhibit a similar rapid dissociation phase suggesting similar diffusion patterns upon dissociation.

In order to determine the association rate (k_{on}) and dissociation rate (k_{off}) constants, as well as the dissociation constant at equilibrium ($K_D=k_{off}/k_{on}$), global fitting of the resulting association and dissociation curves for all hydrolysates is necessary. Nevertheless, in our study, no dissociation rate (k_{off}) could be obtained using any models, probably due to the rapid dissociation observed. Indeed, it could also be related to the fact that dissociation does not occur with the period of time of dissociation of the experiment, therefore, the K_D values could not be determined with accuracy as previously reported (El Hajj et al., 2021). Instead, observed rate constant was calculated ($k_{obs}= k_{on}. C + k_{off}$), which depends on the hydrolysates concentration (C) (**Figure 3.4A)**. The k_{obs} values obtained provide information about how fast the binding reaction occurs. Results for the whole hydrolysates indicate that the MCPs present in Alc might bind to Ni^{2+} faster than those obtained by the sequential treatment (Alc+Flav), whereas among the 1 kDa fractions, the ≤ 1 kDa Alc+Flav exhibits the fastest

binding to Ni^{2+} ions. Moreover, Alc+Flav hydrolysates (both whole and ≤ 1 kDa fraction) display similar k_{obs} (*p-value* ≥ 0.05), suggesting that the molecular weight distribution of their respective Ni^{2+}-chelating peptides is similar due to a well-achieved hydrolysis using two proteases.

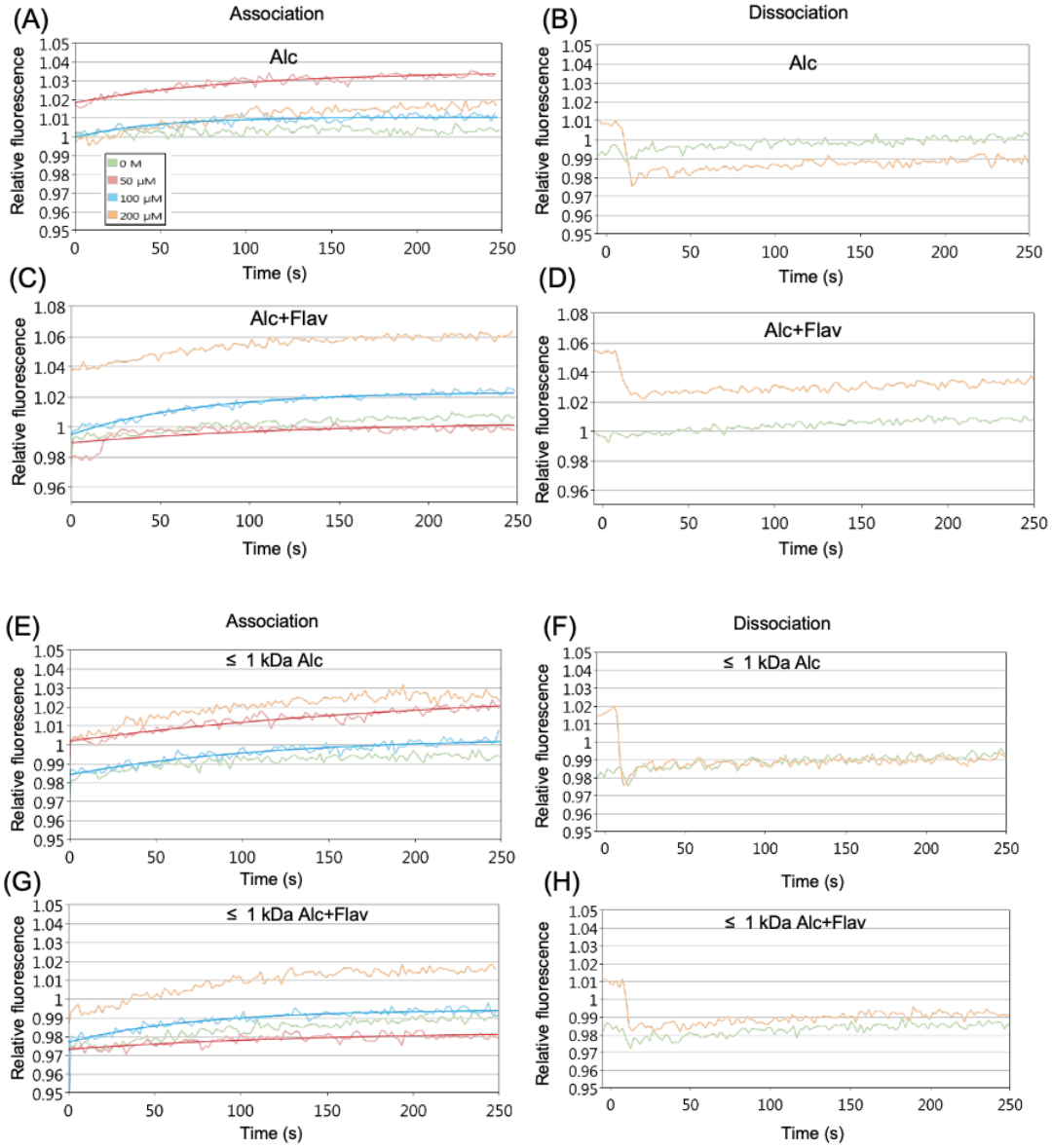

Figure 3.3. Kinetic study between metal-chelating peptides present in TSG hydrolysates and nickel ions using switchSENSE® technology. A, C, E, G**)** association rate (k_{on}) of binding kinetic studies of metal-chelating peptides of Alc, Alc+Flav, ≤ 1 kDa Alc, ≤ 1 kDa Alc+Flav gelatin hydrolysates interacting with Ni^{2+}, respectively. B, D, F and H) dissociation rate (k_{off}) of binding kinetic studies of metal-chelating peptides of Alc, Alc+Flav, ≤ 1 kDa Alc, ≤ 1 kDa Alc+Flav gelatin hydrolysates interacting with Ni^{2+}, respectively. Alc: Alcalase® hydrolysate, Alc+Flav: Alcalase® followed by Flavourzyme®; ≤ 1 kDa: ultrafiltrated hydrolysate.

Besides, for a more accurate assessment of the Ni^{2+} binding capacity of the hydrolysates and to subtract the effect of potential unspecific binding onto the DNA nanolevers, relative changes in fluorescence (**ΔF**) were measured on sample spots (spots functionalized with NTA-Ni^{2+}) compared to the reference (**REF**) spots in the absence of NTA-Ni^{2+} upon injection of the hydrolysates. These results are shown in **Figure 3.4B**, where Alc+Flav hydrolysates (both whole and ≤1 kDa fraction) exhibit the highest shift ΔF compared with the REF, indicating the highest metal-binding properties, especially on the ≤ 1 kDa fraction (**Figure 3.4B**). This might be associated to a higher number of small-sized peptides in this ≤ 1 kDa Alc+Flav hydrolysate.

3.3.2.2 Dynamic mode

Usually, dynamic mode measurements enable to determine the hydrodynamic diameter (D_H) of proteins immobilized on the nanolevers. However, in our study, where no protein was employed as a ligand, the observed D_H variation for all studied hydrolysates rather corresponds to a size index variation (ΔSI) since the Lollipop mathematical model for D_H determination is not appropriate for peptides. However, this dynamic analysis allows one to unveil the binding of MCPs present in TSG hydrolysates onto Ni^{2+} ions.

As shown in **Figure 3.4C** the ΔSI values for the empty NTA and NTA-Ni^{2+} groups remain low, consistent with the expected absence of immobilized MCPs. In contrast, when TSG hydrolysates were injected, a marked and statistically significant increase in ΔSI values was observed (*p-value* < 0.05). This clearly indicates the presence of peptides able to coordinate Ni^{2+} ions. MCPs present in TSG hydrolysates display relatively low ΔSI variation (approximately 2 nm), which shows only a few effects on the motion of the nanolevers. Additionally, between hydrolysates there is not statistically significant difference observed (*p-value* ≥ 0.05), which might be indeed associated with the presence of high number of small-sized MCPs in TSG hydrolysates as discussed earlier in SEC analysis. Considering the high ΔF shift for the ultrafiltrate ≤ 1 kDa Alc+Flav (by comparison with REF; **Figure 3.4C**), this sample is the most enriched fraction in MCPs.

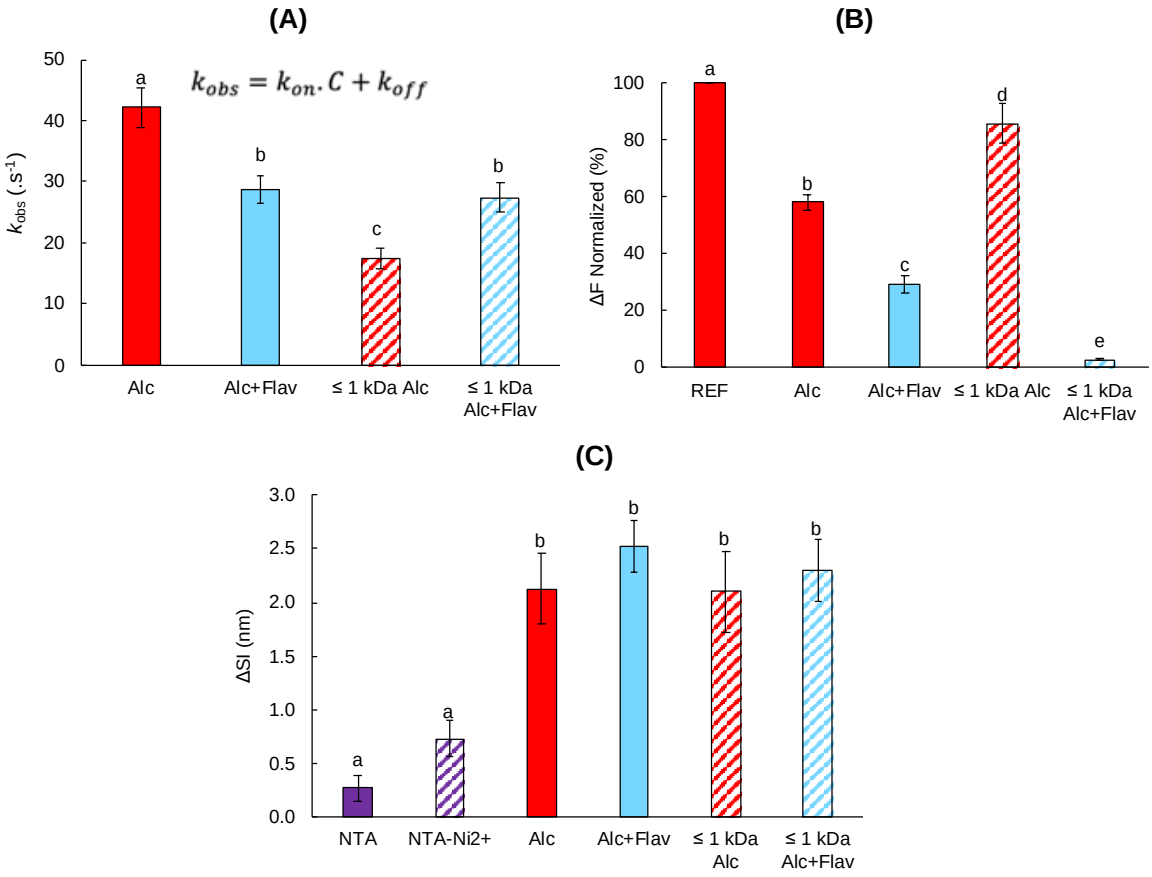

Figure 3.4. SwitchSENSE® measurements in static and dynamic modes of TSG hydrolysates. (A) average observed constant rate (k_{obs}) of TSG hydrolysates with respective standard deviations. (B) changes in the local fluorophore environment (ΔF) of free-nickel references spots and samples spots for Alc, Alc+Flav, ≤ 1 kDa Alc and ≤ 1 kDa Alc+Flav TSG hydrolysates, respectively (static mode). (C) size index changes (ΔSI) of NTA, NTA-Ni^{2+} and NTA-Ni^{2+}-MCPs present in TSG hydrolysates determined by sizing analysis (dynamic mode).

Alc: Alcalase® hydrolysate, Alc+Flav: Alcalase® followed by Flavourzyme®; ≤ 1 kDa: ultrafiltrated hydrolysate.

3.3.3 Biofunctional characterization of Tilapia hydrolysates

3.3.3.1 Antioxidant tests

Metal-chelating activity. ROS production generated *via* the Fenton and Haber Weiss reactions can be delayed by transition metal ions chelation such as Fe^{2+} and Cu^{2+} (Viji et al., 2019). Therefore, it is likely that Alc and Alc+Flav hydrolysates could also be endowed with antioxidant ability. To study the effect of various enzymatic treatments on bioactive properties of hydrolysates obtained from Tilapia scale gelatin, several *in vitro* biological tests

were performed (**Appendix 3.9, Table 3.3**)**.** The metal-chelating property, the first functional activity investigated, can be related to other biofunctional properties as explained later.

Table 3.3. Biofunctional properties of Tilapia scale gelatin hydrolysates and positive controls.

Sample	Iron (Fe^{2+})	ABTS		Reducing power	ACE inhibition
	EC_{50} (mg/mL)	EC_{50} (mg/mL)	µmol TE/g	µmol AAE/g	IC_{50} (mg/mL)
Alc	0.23 ± 0.02[a]	0.17 ± 0.005[a]	71.90 ± 2.60[a]	8.31 ± 0.66[a]	0.43 ± 0.06[a]
Alc+Flav	1.77 ± 0.01[b]	0.16 ± 0.004[b]	74.79 ± 2.10[b]	10.61 ± 1.46[b]	0.57 ± 0.07[b]
≤ 1 kDa Alc	0.07 ± 0.02[c]	0.14 ± 0.003[c]	83.58 ±1.84[c]	2.99 ± 0.28[c]	0.69 ± 0.06[c]
≤ 1 kDa Alc+Flav	0.63 ± 0.02[d]	0.13 ± 0.003[d]	83.40 ±1.26[c]	22.51 ± 1.85[d]	0.58 ± 0.07[b]
Carnosine	0.07 ± 0.003[c]	0.41 ± 0.010[e]	28.38 ± 2.46[d]	8.60 ± 0.96[a]	0.30 ± 0.04[d]
EDTA	0.01 ± 0.001[f]				0.001 ± 0.003[e]
Trolox		0.05 ± 0.001[f]			

Alc: Alcalase® hydrolysate, Alc+Flav: Alcalase® followed by Flavourzyme®; ≤ 1 kDa: ultrafiltrated hydrolysate. Values are mean ± SD (n = 5). Values with different letters within the same column indicate significant differences (*p* -value< 0.05). gray box: not studied; AAE: ascorbic acid equivalent; TEAC: trolox equivalent antioxidant capacity; ACE: angiotensin converting enzyme.

The iron (Fe^{2+})-chelating activities of whole and ≤ 1 kDa hydrolysates were investigated as a function of their concentration, in reference to EDTA and carnosine (**Appendix 3.9**). Indeed, carnosine dipeptide (β -Ala-His) is reported for its high iron- and copper-chelating activity due to the presence of histidine, one main AA able to chelate metal ions (Canabady-Rochelle et al., 2018).

The iron-chelating activity of whole hydrolysates increases sharply from 0.1 to 1 mg/mL, and 0.1 to 5 mg/mL for Alc, and Alc+Flav, respectively (**Appendix 3.9A**). From **Appendix 3.9A**, the EC_{50} values of iron-chelating activities were calculated for all hydrolysates and presented in **Table 3.3**. The EC_{50} value of the whole Alc hydrolysate is lower (*i.e.,* meaning higher activity) than EC_{50} of the whole Alc+Flav hydrolysate (*p-value* < 0.05), signifying a loss of iron-chelating activity upon sequential hydrolysis.

Whatever the enzymatic treatment, looking the ≤ 1 kDa hydrolysates, their EC_{50} values are much lower (*i.e.,* a higher activity) than those of their corresponding whole hydrolysates (*p-value* < 0.05). Thus, the 1 kDa ultrafiltration enhances the iron-chelating activity of TSG

hydrolysates. Indeed, with smaller-sized peptides, the ≤ 1 kDa fractions should logically content a higher proportion of amino and carboxyl terminal groups compared to the whole hydrolysates.

Alcalase® is the best enzymatic treatment to obtain iron-chelating peptides from TSG, showing no significant difference (*p-value* ≥ 0.05) of EC_{50} values when comparing the ≤ 1 kDa ultrafiltrate with carnosine (**Table 3.3**). The iron-chelating properties of hydrolysates can be explained by their DH and their AA content. However, despite the higher DH of Alc+Flav compared to Alc hydrolysate, the iron-chelating activity is higher for Alc one. According to the literature (Guo et al., 2014; Xia et al., 2012), metal-chelating activity is associated to amino or carboxyl group available at each terminus part of a peptide, but also to other amino and carboxyl groups present in the radical side chain of other AA (*i.e.,* acid AA: aspartic acid, glutamic acid*;* basic AA: lysine, arginine, and histidine). Compared to Alc+Flav hydrolysates, Alc hydrolysates contain higher values of such AA as previously discussed in the AA composition results (**Table 3.2**), which may explain its better activity. In addition to the presence of acid and basic AA, metal-chelating activity can be influenced by other AA such as tryptophan, tyrosine and phenylalanine (involving their aromatic side chains) or cysteine through its thiol group (Wen et al., 2020).

Radical scavenging activity. ROS are responsible of radical chain reactions, inducing biomolecules damages and thus, many diseases (*i.e.,* degenerative, neurological, cardiovascular, cancer, Xia et al., 2012). The various produced hydrolysates were evaluated for their antioxidant activity using ABTS radical scavenging activity, based on the ability of antioxidants to donate a hydrogen atom. ABTS results were investigated in reference to Trolox® (**Appendix 3.9B**), from which the EC_{50} values were determined for each sample (**Table 3.3).** Trolox® has the lowest EC_{50} (0.05 mg/mL) due to its high capacity to scavenge ABTS radicals. Carnosine exhibits a EC_{50} value of 0.41 mg/mL (1.18 mM), similar to that reported by Aljawish et al., (2016) (1.8 mM). Both whole and 1 kDa hydrolysates show EC_{50} values lower than carnosine and thus, better ABTS radical scavenging ability than carnosine. Although carnosine is known as a good radical scavenger due to its imidazole group, which can donate protons or electrons for scavenging free radicals, TSG hydrolysates, in addition to histidine, can present others AA residues such as tryptophan, that contains indoyl group. Yet, indoyl

group is also known to stabilize the radicals thanks to a hydrogen donating mechanism (Wen et al., 2020).

On the other hand, for both whole and ≤ 1 kDa fraction hydrolysates, Alc+Flav is slightly but significantly better than Alc (*p-value* < 0.05), indeed, the EC_{50} values of the ≤ 1 kDa fractions are significantly lower than those of whole hydrolysates (*p*-value < 0.05), meaning that the radical scavenging ability is enhanced after both the sequential treatment and ultrafiltration. Thus, small-sized peptides have the highest radical scavenging activity, since they could interact more easily with free radicals due to lower steric hindrance, which is in agreement with the literature (Qiu et al., 2019; Wen et al., 2020). The ≤ 1 kDa Alc and ≤ 1 kDa Alc+Flav hydrolysates from TSG have a high potential for producing metal-chelating peptides endowed with antioxidant properties. Indeed, a high radical scavenging effect can be related to a high metal-chelating activity (Xia et al., 2012).

For comparing with the literature, the EC_{50} values were converted in Trolox® equivalent antioxidant capacity (**TEAC**) and results were expressed as µmol Trolox® equivalent per gram of sample (µmol TE/g sample) (**Table 3.3**). TEAC values (the higher, the greater ABTS scavenging activity) vary between 71 and 74 µmol TE/g for whole hydrolysates, while upon ultrafiltration, such values improve up to 83 µmol TE/g with no significative differences for the two ≤ 1 kDa fraction hydrolysates (*p-value* ≥ 0.05). TSG hydrolysates obtained in our study from different enzymatic treatments present all high TEAC values (71.90 to 83.58 µmol TE/g) compared to that of carnosine (28.38 µmol TE/g), which underlines a very interesting antioxidant capacity. Compared to our samples, the obtained TEAC values were better than those found in milkfish scale gelatin hydrolysate (56.8 ± 0.8 µmol TE/g; Huang et al., 2018) but not as good as spotted golden goatfish scale hydrolysates (102.99 µmol TE/g; Chuaychan et al., 2016).

Reducing power. The various gelatin hydrolysates obtained were investigated for their reducing power in comparison to carnosine and expressed as micromoles of ascorbic acid equivalent per gram of sample (µmol AAE/g), knowing that the higher the values µmol AAE/g the greater the reducing power (**Table 3.3).** Whatever the hydrolysates (whole or ultrafiltrated), Alc+Flav hydrolysates notably exhibit superior reducing power compared to Alc ones. The reducing power for whole Alc+Flav hydrolysates reaches 10.61 µmol AAE/g, further increased after ultrafiltration to 22.51 µmol AAE/g. In contrast, the Alc treatment

shows a decrease in reducing power specifically for the ≤ 1 kDa fraction (2.99 µmol AAE/g). In agreement with the literature, higher DH, associated to smaller-sized peptides (29.7 %, whole Alc+Flav) is correlated to a higher reducing power in various hydrolysates. Also, the reducing power of TSG hydrolysates is mainly associated to the presence of electron-dense side-chain group of AA residues, such as charged (Asp, Glu, Lys, Arg, and His) or polar ones (Ser, Thr, Tyr), present in TSG and its hydrolysates (**Table 3.2**).

Hence, the ≤ 1 kDa Alc+Flav hydrolysate could present higher chemical groups able to donate electron than the ≤ 1 kDa Alc hydrolysate as previously reported (Wen et al., 2020). Our results on Alc+Flav treatment are in agreement with former work on gelatin hydrolysate obtained from skin and scale of sole fish (Viji et al., 2019), which evidence a positive correlation between reducing power and small-sized peptide in hydrolysates. These hydrolysates containing small-sized peptides might possess some easily accessible AA residues (*i.e.*, hydrophobic and aromatic AA) exhibiting a high reducing power. Regarding the ≤ 1 kDa Alc results, peptides able to donate electron atoms may be retained in the higher MW fraction, which was not investigated in our study.

3.3.3.2 ACE inhibitory activity

The ACE inhibition, associated to antihypertensive activity, can occur by non-competitive manner, where peptides can bind to Zn^{2+} ions, and cause a conformational modification of catalytic site structure, leading to ACE inactivation (Cushman & Cheung, 1971; Lin et al., 2023). The ACE inhibitory activity of TSG hydrolysates, carnosine and EDTA were investigated using the FAPGG peptide as substrate (**Appendix 3.9C, Table 3.3**), where the lower IC_{50} values, the better ACE inhibition activity. The highest ACE inhibitory activity is found for the positive controls (EDTA and carnosine) as reported in the literature. Indeed, chelating compounds can inhibit ACE as reported in Cushman & Cheung (1971), EDTA being the most effective inhibitors in these group.

Concerning the ACE inhibitory activity of whole hydrolysates, Alc presents the highest one (IC_{50}: 0.43 mg/mL), followed by Alc+Flav (IC_{50}: 0.57 mg/mL) (**Table 3.3**). The ≤ 1 kDa Alc hydrolysate shows lower ACE inhibition (higher IC_{50}: 0.69 mg/mL) than whole hydrolysate (0.43 mg/mL), meaning that the ultrafiltration process could negatively impact this activity;

however, similar values (*p-value* ≥ 0.05) were obtained for whole Alc+Flav hydrolysate (0.57 mg/mL) and ≤ 1 kDa Alc+Flav (0.58 mg/mL). Hence, 1 kDa ultrafiltration does not enhance ACE inhibitory activity. Both whole hydrolysates (Alc and Alc+Flav), show an ACE inhibitory activity of interest, since their IC_{50} values are comprised within the range of values reported for ACE inhibitory molecules extracted from grass carp fish scale hydrolysates, 0.021 to 1.73 mg/mL (Zhang et al., 2009). Indeed, the whole Alc+Flav hydrolysate shows the highest DH (29.74 % for an IC_{50} of 0.57 mg/mL) compared to whole Alc hydrolysate (DH: 19.70 % for an IC_{50} of 0.43 mg/mL). Our result is in agreement with Theodore & Kristinsson (2007), who evidenced a loss of ACE inhibition activity for small-sized peptide fractions obtained from catfish protein hydrolysate (≤ 1 kDa). Yet, in our study, the higher ACE inhibition activity is not correlated to the higher DH contrarily to Huang et al., (2018). Our results are quite similar to the IC_{50} for ACE inhibition of milkfish (*chanos chanos*) scale gelatin hydrolysates prepared using Alcalase® with values comprised between 0.4-0.7 mg/mL (Huang et al., 2018). In Lassoued et al., (2015), Alcalase hydrolysate from thornback ray gelatin had a IC_{50} around 1 mg/mL. Thus, gelatin extracted from red Tilapia scale could lead to a hydrolysate endowed with better ACE inhibitory activity (lower IC_{50}) compared to other gelatin source from fish.

According to the former AA composition of TSG hydrolysates, whole Alcalase® hydrolysates present a high amount of AA residues associated with metal-chelating properties for complexing zinc ions, which could potentially be responsible of the great ACE inhibition observed (Lin et al., 2023). Also, aromatic AA residues present in TSG hydrolysates (Tyr, Phe) might interact with the active site of ACE, since Alcalase® enzyme has broad specificity, hydrolyzing most peptide bonds, and preferentially those containing aromatic AA residues (Alemán et al., 2011).

In addition to antioxidant and ACE inhibition activities, we also studied the antimicrobial activity of the four gelatin hydrolysates. However, no significant antimicrobial activity was observed against all the tested bacteria (*Staphylococcus aureus* ATCC 29213, *Enterococcus faecalis* ATCC 29212, *Pseudomonas aeruginosa* ATCC 27853, *Escherichia coli* ATCC 25922, *Klebsiella pneumoniae* ATCC 700603) at the highest concentration (MIC > 25 g/mL) (**Appendix 3.10-3.11**).

3.3.4 Peptide identification by LC-MS/MS

Peptides in whole Tilapia scale gelatin hydrolysates and their corresponding ≤ 1 kDa fractions were analyzed by LC-MS/MS. A total of 22, 45, 56 and 45 peptides were identified for Alc, Alc+Flav, ≤ 1 kDa Alc and ≤ 1 kDa Alc+Flav, respectively (**Figure 3.5A**, **Appendix 3.12**). As shown in **Figure 3.5B**, the peptide length of the identified peptides ranges from 3 to 15 AA.

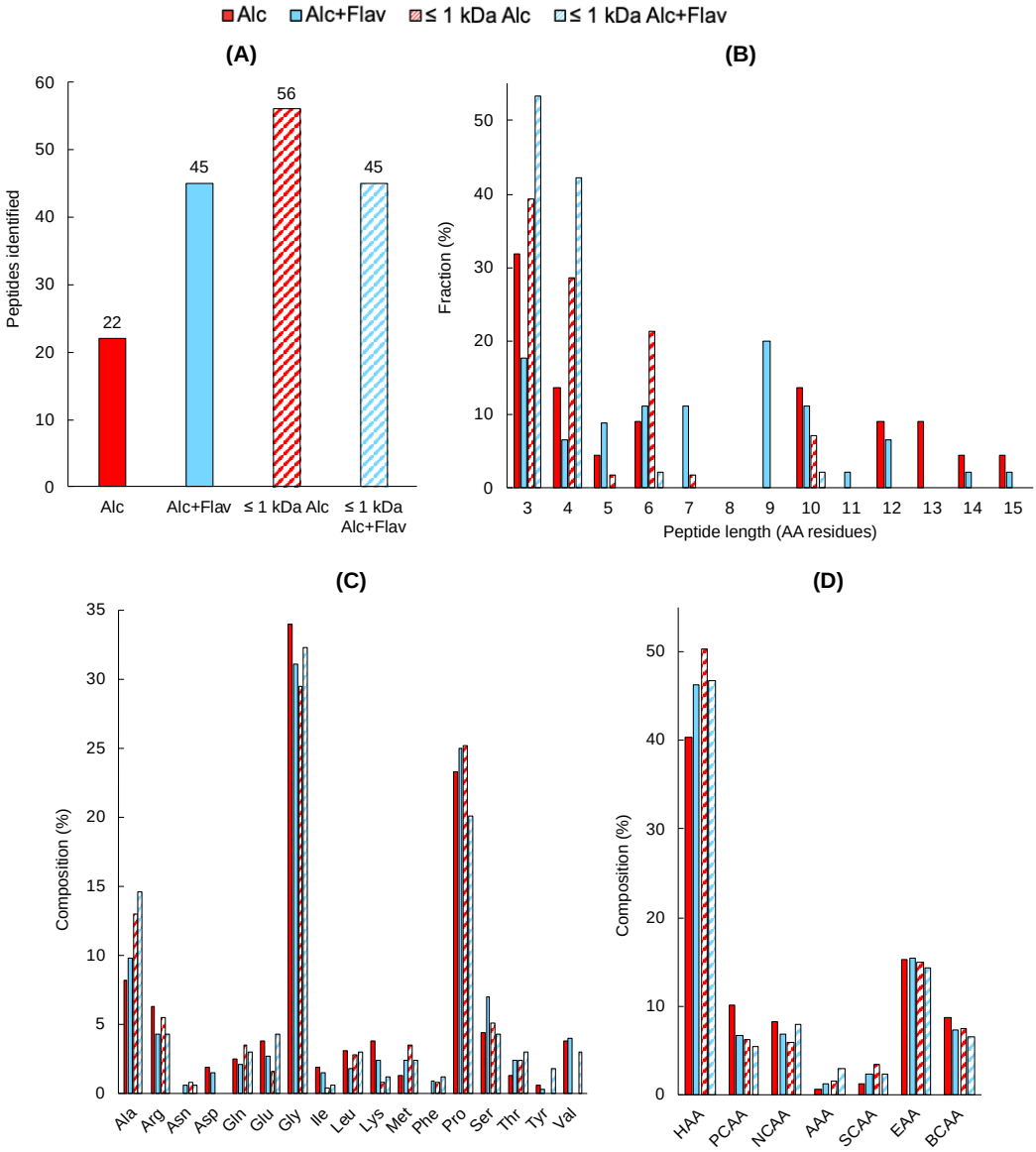

Figure 3.5. Results obtained from the LC-MS/MS identification of peptides present in Tilapia scale hydrolysates. (A) number of peptides identified (B) peptide length distribution, (C-D) AA composition. Alc: Alcalase® hydrolysate, Alc+Flav: Alcalase® followed by Flavourzyme®; ≤ 1 kDa: ultrafiltrated hydrolysate. AAA: Aromatic amino acids= Phe, Trp, Tyr; NCAA: Negatively charged amino acids= Asp, Glu, Asn, Gln; PCAA: Positively charged amino acids= Arg, His, Lys; HAA: Total Hydrophobic amino acids= Ala, Val, Ile, Leu, Tyr, Phe, Trp, Pro, Met and Cys; SCAA: Sulphur containing amino acids= Met and Cys; EAA: Essential amino acids= Trp, Lys, His, Phe, Leu, Ile, Met, Val, Thr; BCAA: Branched chain amino acids= Ile; Leu, Val.

In agreement with the MW distribution determined by SEC, ≤ 1 kDa hydrolysates fraction contain the highest peptide fraction between 3 and 6 AA (200-600 Da). In our study, peptide sequences identified in the ≤ 1 kDa fractions contain the peptides with the highest potential for iron-chelating and antioxidant activities. Similar to our results, Chi et al., (2015) reported that peptides with 4 to 6 AA were characterized by their strong antioxidant activities in fish skin hydrolysate.

In addition to their size, the AA composition of the peptide sequences plays a pivotal role on their bioactivities. Therefore, AA composition of all the peptide hydrolysates obtained in **Appendix 3.12** were computed using the free-accessed ProtParam tool (https://web.expasy.org/protparam/). **Figure 3.5C** shows Gly, Pro and Ala as the three major AA present in the peptide sequences. Indeed, these AA have widely been related with antioxidant properties (Sierra et al., 2021). Besides, identified peptides present high fraction of Hydrophobic AA (HAA), Essential (EAA), Negatively Charged (NCAA) and Branched chain (BCAA) (**Figure 3.5D**), which could be associated with their metal-chelating and ACE-inhibition activities as previously reported (Chen et al., 2018; Guo et al., 2015). Moreover, the higher number of aromatic AA (AAA) in the ≤ 1 kDa fraction hydrolysates could be regarded as main AA to enhance the ABTS radical scavenging and reducing power properties.

From **Appendix 3.12**, the sequences of the 10 most intense ions for each hydrolysate are displayed in **Table 3.4**, while the MS/MS spectra of two of the most intense peptide sequences for each hydrolysate were loaded into the MaxQuant Viewer and are shown in **Figure 3.6A-H**. These peptide sequences display a partial sequence homology with several bioactive peptide sequences previously identified from fish by-product gelatin hydrolysates. For instance, peptide sequences containing motif such as GPL (Chi et al., 2015), GPP (Qiu et al., 2019) and GPP, PGA (Chen et al., 2018) were reported by their antioxidant and ACE inhibition activities in gelatin peptides from bluefin leatherjacket (*Navodon septentrionalis*) skin, skipjack tuna (*Katsuwonus pelamis*) scales and lizardfish (*Synodus macrops*) scales, respectively.

Besides, after ultrafiltration, the ≤ 1 kDa Alc hydrolysate exhibited the highest Fe^{2+}-chelating activity. This property might also be associated with the ACE inhibition activity. More, LC-ESI-MS/MS analysis confirmed the presence of peptide sequences with Asp, Glu, Ser, Lys and Arg, which might offer potentially metal-chelating and antioxidant properties. Furthermore, in

comparison with other studies, the ≤ 1 kDa Alc in our study, contains similarities in terms of Gly, Prol, Ala, Glu and Arg with other peptide sequences which have previously been reported for their high antioxidant properties in protein hydrolysates from Alaska pollock skin gelatin (AGPAGPR, GPAGPR, GPAGPHGPPG Guo et al., 2015), Pacidic cod skin (AGPAGPAGAR, Wu et al., 2017) and Tilapia skin collagen (GPAGPAGEK, Lin et al., 2021).

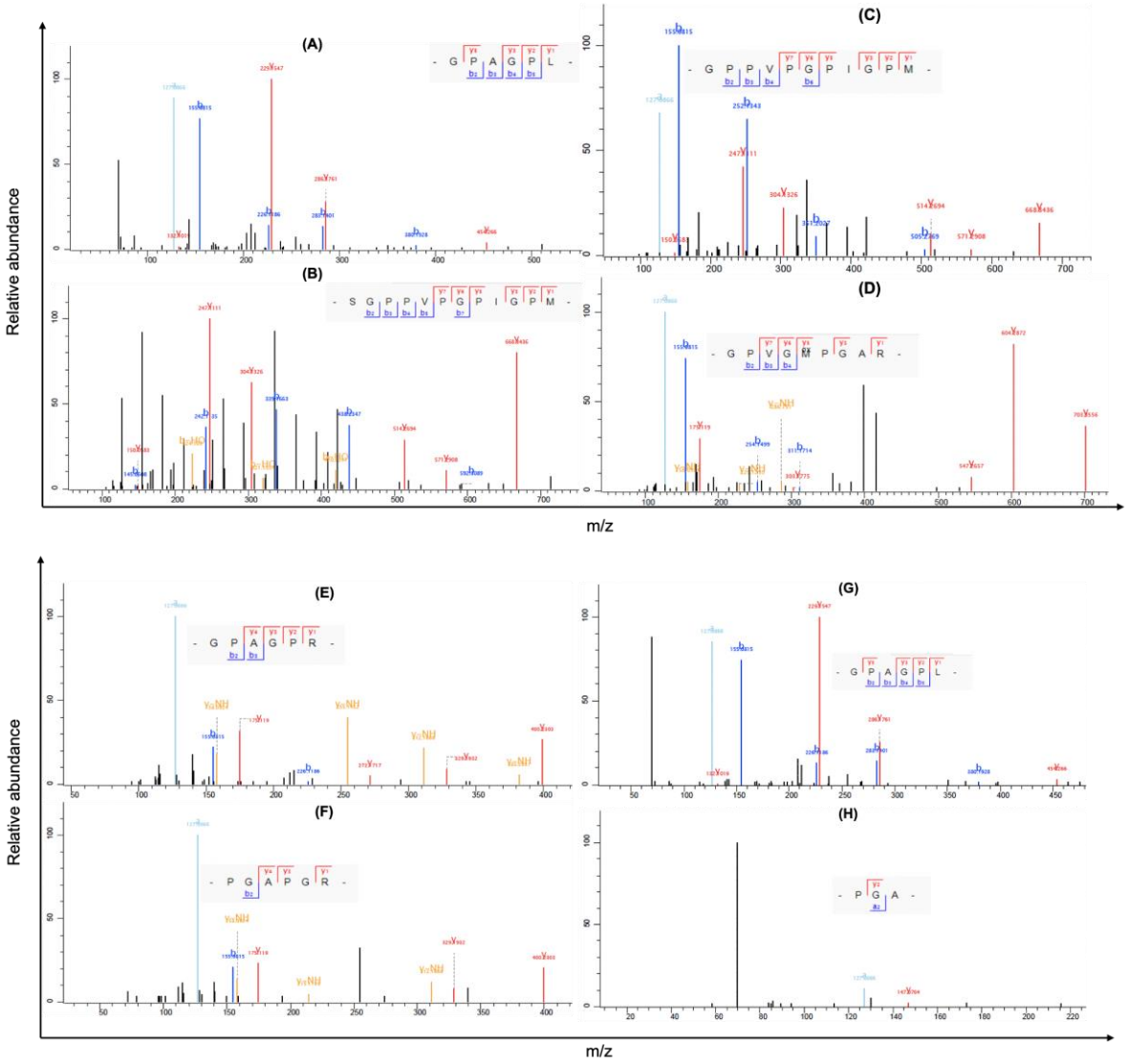

Figure 3.6. MS/MS spectra for the parent ions of peptides present in Tilapia scale hydrolysates. Alc: (A) GPAGPL, (B) SGPPVPGPIGPM; Alc+Flav: (C) GPPVPGPIGPM, (D) GPVGMPGAR; ≤ 1 kDa Alc: (E) GPAGPR, (F) PGAPGR; ≤ 1 kDa Alc+Flav: (G) GPAGPL, (H) PGA.

Alc: Alcalase® hydrolysate, Alc+Flav: Alcalase® followed by Flavourzyme®; ≤ 1 kDa: ultrafiltrated hydrolysate.

3.4 Conclusions

In this work, we hypothesised that a sequential treatment using Alcalase® followed by Flavourzyme® could enhance the biofunctional properties of red Tilapia scale gelatin hydrolysates. Based on our findings, sequential enzymatic treatment shows higher DH than Alcalase® treatment alone. Yet, the biofunctional properties were not all enhanced by the sequential treatment. Indeed, sequential hydrolysis seems to improve the Ni^{2+}-binding capacity, ABTS radical scavenging activity and reducing power. Yet, after UF, ≤ 1 kDa gelatin hydrolysates prepared from TSG using Alcalase® exhibit highest Fe^{2+}-chelating properties, which is also associated with the ACE inhibition activity.

Overall, 1 kDa membrane ultrafiltration enhanced the metal-chelating ability, ABTS radical scavenging and reducing power activities of gelatin hydrolysates prepared from red Tilapia scale but not the ACE-inhibitory activity, which yet remains into an acceptable range for food protein hydrolysates. Therefore, TSG hydrolysates prepared using Alc and Alc+Flav at 1-kDa cutoff ultrafiltration offer an effective strategy for obtaining MCPs endowed with antioxidant and ACE inhibitory activities from Tilapia processing by-products. Such hydrolysates show a high potential to act as bioactive molecule. Finally, further research is needed to explore the use of gelatin hydrolysates as functional ingredients in food industry, and as nutraceutical products.

Chapter 4. Identification of Ni^{2+}-binding Peptides in Sunflower Meal Protein Hydrolysate for Deeper Understanding of Peptide-Metal Interactions

To further develop the concepts introduced earlier for the production of biologically active biomolecules from by-product-derived protein hydrolysates, we will now explore the valorization of sunflower meal (SM) by-product as potential protein source for the production of MCPs from protein hydrolysates. Although literature data has shown the ability of SM hydrolysates to chelate metal ions, there is a limited understanding of the peptide sequences involved and how the metal complexation mechanism by peptide occurs. While **Chapters 2** and **3** focused on the extraction of Tilapia scale gelatin and its subsequent use for the production of MCPs, respectively, this **Chapter 4** directly delves deeper into the screening of MCPs from sunflower meal protein isolate (SMPI) hydrolysates. Indeed, numerous studies previously focused on the optimization of the protein extraction from sunflower meal. In this context, we focused on Nickel-chelating peptides. With many physiological effects on living organisms, nickel can induce oxidative stress due to the participation of the Ni^{2+}/Ni^{3+} redox couple in Fenton/Haber–Weiss reactions. Thus, by complexing Ni^{2+}, MCPs could prevent chronic diseases associated with oxidative damage. In this **Chapter 4**, The SMPI was hydrolyzed by single and sequential enzymatic treatments using Protamex® and Protamex® followed by Flavourzyme®, respectively, and the metal-chelating profile was characterized by IMAC followed by LC-MS/MS and switchSENSE® techniques, for separation and identification, and for a better understanding of peptide-metal ion interactions, respectively. In addition, the interaction between pure peptides (potentially encrypted in SM protein sequences) with Ni^{2+} was studied using UV-vis and CD spectroscopies in order to describe the coordination modes and possible binding sites.

This Chapter will be submitted to the *Journal of Inorganic Biochemistry* as:

Camaño, J.A., Selmeczi*, K., Mathe, C., Girardat, J.M., Paris, C., Udenigwe, C., Canabady-Rochelle*, L. Identification of Ni^{2+}-binding Peptides in Sunflower Meal Protein Hydrolysate for Deeper Understanding of Peptide-Metal Interactions.

4.1 Introduction

Sunflower (*Helianthus annus* L.) is one of the most important oil crops in the world, being the third-largest oilseed globally, following soybean and rapeseed, with a production of 53.5 million tons in 2019 (Náthia-Neves & Alonso, 2022). Once oil extracted, sunflower meal by-product is considered as a potential raw material to be used in food application thanks to its chemical composition, including an abundant protein content (30-50 % w/w) (De Oliveira Filho & Egea, 2021). Sunflower meal by-product has widely been used to produce bioactive peptides. Naturally encrypted within protein sequence under an inactive form, these bioactive peptides are released upon proteolysis. Recently, sunflower meal-derived peptides have gained significant attention due to their wide-ranging health benefits such as immunomodulators (Velliquette et al., 2020), angiotensin-converting inhibitors (Sentís-Moré et al., 2022), antioxidants, anti-inflammatory (Tonolo et al., 2024) and metal-binding compounds (Bao et al., 2021).

Metal-binding peptides can be powerful ligands to complex several transition metal ions such as Ni^{2+}, Cu^{2+}, Zn^{2+} and $Fe^{2+/3+}$. These peptides have been proposed as a powerful substitute for metals-related diseases (Camaño Echavarría et al., 2024). For instance, through the complexation of Fe^{2+} and Cu^{2+}, they may effectively delay oxidative damage linked to chronic diseases (Canabady-Rochelle et al., 2018). Besides, metal-binding peptide can promote better stability, absorption, and bioavailability of minerals and are endowed with important biological functions (El Hajj, *et al.*, 2021; Guo et al., 2015). Metal-binding peptides can be released from various protein sources such as milk, eggs, and fish (Camaño Echavarría et al., 2024). Nonetheless, from the standpoint of sustainable development and the utilization of biological resources, numerous studies have explored the potential of agro-industrial by-products, given their substantial protein content and their added value once hydrolyzed (Tonolo et al., 2024). Although several metal-binding peptides have been reported from agro-industrial by-product-derived proteins (walnut flake, Lv et al., 2017; chia seed, Latha et al., 2021), the evaluation of sunflower meal by-product remains scarce (Bao et al., 2021; Dabbour et al., 2019; Megías et al., 2008).

Nickel is important for many microorganisms and is a component of several metalloenzymes (Balogh et al., 2021). Although it is not an essential metal for human life, nickel can serve as a probe to better understand the peptide-metal interactions along with other metal ions (*e.g.*,

Cu^{2+}). Indeed, many similarities have already been described between Ni^{2+} and Cu^{2+} ion complexing processes (Kastal et al., 2024). Besides, immobilized metal ion affinity chromatography (**IMAC**) is a purification technique based on the affinity of some peculiar amino acids (**AA**) residues present in peptides for some transition metal ions such as Ni^{2+} immobilized onto the chromatographic phase. Thus, IMAC-Ni^{2+} can be used both to separate and purify metal-binding peptides containing potential metal-binding AA, especially histidine residue, known to be an excellent anchoring site for Ni^{2+} and Cu^{2+} ions (Witkowska et al., 2012), and to study the Ni^{2+}-binding ability of His-containing peptides (Irankunda et al., 2024). However, only few information is available on the degree of affinity between the His-containing peptides and the immobilized Ni^{2+} ions. Recently, the switchSENSE® technology has been developed and successfully used to study in real-time peptide interactions with immobilized Ni^{2+} ions strongly bound to the tetradentate nitrilotriacetic acid (**NTA**), while providing complementary and deeper information about the peptide-Ni^{2+} complex (El Hajj et al., 2021). Despite all the advantages of IMAC and switchSENSE® technology to study the Ni^{2+} binding ability of food-derived peptides, the conformational geometry and binding modes of the peptide-Ni^{2+} complexes should be further characterized to better understand this specific interaction. Spectroscopic techniques such as UV-visible (**UV-vis**) and circular dichroism (**CD**) provide some information on the coordination characteristics of peptides with Ni^{2+} ions, revealing significant data about the molecular basis of the peptide-metal interaction such as binding sites and geometry of the metal ion environment in the formed complexes (Balogh et al., 2021).

To the authors' knowledge, there is no report on Ni^{2+}-binding properties of His-containing peptides from sunflower meal by-product and the influence of the amino acid sequence on such biofunctionality. Here, single and sequential enzymatic hydrolysates were produced from sunflower meal protein isolate (**SMPI**) hydrolysed using either Protamex® (**Prot**) or Protamex followed by Flavourzyme® (**Prot+Flav**), respectively in order to study their Ni^{2+}-binding properties using IMAC, switchSENSE®, UV-visible and CD techniques. Additionally, ten pure peptide sequences theoretically present in sunflower proteins were investigated to better understand the formation of peptide-Ni^{2+} complex. This paper focuses on how sunflower meal by-product may be used in the production of food-derived metal-binding peptides. Such knowledge (i) will be an important input to understand the interaction

between the peptide sequences present in SMPI hydrolysates and Ni^{2+} ions, (ii) and will explain the bioinorganic chemistry of the metal-binding mechanism of the formed sunflower peptide-Ni^{2+} complexes.

4.2 Materials and methods

4.2.1 Chemicals

Sunflower meal (**SM**) was provided by SAS IMPROVE (Dury, France). Protamex® (**Prot**, protease from *Bacillus* sp., ≥ 1.5 U/g), Flavourzyme® (**Flav**, protease from *Aspergillus oryzae*, ≥ 500 U/g), hydrochloric acid (37 %, **HCl**), ammonium bicarbonate, ethylenediaminetetraacetic acid (Na_2**EDTA**·$2H_2O$), nickel (Ni^{2+}) sulfate ($NiSO_4$·xH_2O) and imidazole were purchased from Sigma–Aldrich (St Louis, MO, USA). All the other reagents were analytical grade and purchased from VWR International (Atlanta, USA): sodium phosphate monobasic NaH_2PO_4, sodium phosphate dibasic Na_2HPO_4·$12H_2O$, sodium chloride, sodium hydroxide, HEPES (99%, $C_8H_{18}N_2O_4S$).

4.2.2 Synthetic peptides investigated

Ten small-sized peptides (≤ 10 AA residues, **Figure 4.1**), naturally encrypted in the major sunflower protein (11S globulin seed elastic protein G3, P19084, 11S3_HELAN) were selected; the sequence of this former protein was found in UniProt protein data base (https://www.uniprot.org/uniprotkb/P19084/entry) (**Appendix 4.1**). The peptides sequences were chosen according to their particular structures, which could confer them different affinity for Ni^{2+} ions based on the presence of His, Trp, Cys, Glu, Asp and Pro residues (according to the HSAB theory and Porath's triad, *vide infra*) and their position within the sequence. The peptides were classified into 3 groups: group (I) His or Trp-containing peptides without proline (Pep1-4), and it is divided into two subgroups: IA is composed by His-containing peptides (1.**W**L**H**NDGN, 2.**W**L**H**NDGNTE, 3.FATCIAR**H**), while the second one IB is composed by a Trp-containing peptide (4.**W**VSFKTN); group (II) His-containing peptides with proline (5.AIPTGTA**H**, 6.KFPILE**H**, 7.KFPILE**H**L and 8.KFPILE**H**LR); and group (III) peptides without His or Trp (9.GNPQ, 10.LLAF).

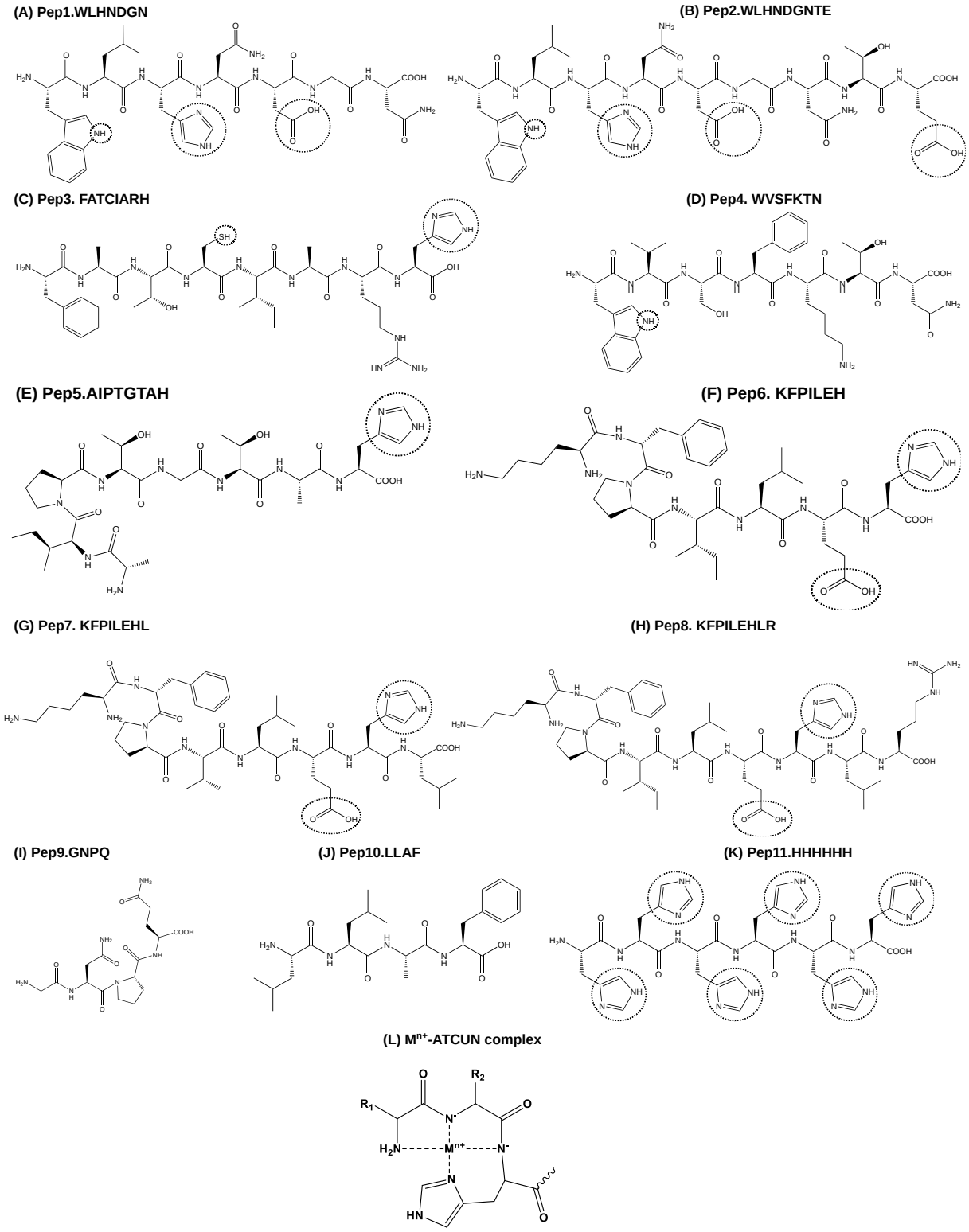

Figure 4.1. Chemical structures of pure peptides studied by IMAC, switchSENSE®, UV-visible spectroscopy, and CD techniques. (A, B, C) His-containing peptides without proline (group I), (E, F, G, H) His-containing peptides with proline (group II), (D, I, J) No His-containing peptides, and (K) positive Ni^{2+}-binding peptide (6His peptide). (L) schematic representation of ATCUN peptide-metal (M^{n+}) complex.

Imidazole, indole and thiol groups could play a role in the Ni^{2+}-binding properties (circle).

The 6His peptide (11.**HHHHHH**) was also investigated as positive control. The peptide sequences selected were synthetized by Genecust (Dudelange, Luxemburg) and characterized by their molecular weight (**MW**), isoelectric point (**pI**, calculated from PepCalc free software, https://pepcalc.com) and their percentage of global charge at pH 7.4 using ACD/Percepta Software version 14.0 (ACD/Labs, https://www.acdlabs.com/). The chemical structures of the 11 synthetic peptides are presented in **Figure 4.1**, while **Table 4.1** shows their physico-chemical properties.

Table 4.1. Ni^{2+}-binding peptides identified from the F2 (elution phase) SMPI hydrolysates using IMAC-Ni^{2+} separation followed by LC-MS/MS analysis.

Protein code	Protein name	Name	Peptide sequence	AA length	Molecular mass (g/mol)	Isoelectric point (pI)	% of global charge at pH 7.4
P19084	11S globulin seed storage protein G3	Pep1	**W**L**H**NDGN	7	854.35	4.87	0% +, 86% -
		Pep2	**W**L**H**NDGNTE	9	1084.44	3.92	0% +, 100%-
		Pep3	FATCIAR**H**	8	918.08	8.62	75% +, 2% -
		Pep4	**W**VSFKTN	7	880.99	10.01	43% +, 0% -
		Pep5	AIPTGTA**H**	8	766.38	7.88	45% +, 11% -
		Pep6	KFPILE**H**	7	882.48	7.6	26% +, 20% -
		Pep7	KFPILE**HL**	8	995.57	7.6	18% +, 33% -
		Pep8	KFPILE**H**LR	9	1151.67	9.9	64% +, 0% -
		Pep9	GNPQ	4	414.17	3.7	0% +, 34% -
		Pep10	LLAF	4	462.27	3.7	0% +, 28% -
		Pep11	**HHHHHH**	6	840.85	7.97	70% +, 3% -

SMPI: sunflower meal protein isolate; Prot: Protamex® hydrolysate; Prot+Flav: Protamex® followed by Flavourzyme®; ≤ 1kDa: 1 kDa ultrafiltrated.

4.2.3 Metal-binding peptides investigated in hydrolysate

4.2.3.1 Hydrolysate production

4.2.3.1.1 Sunflower protein isolate

Sunflower meal protein isolate (**SMPI**) was obtained using the method reported by Kalpana et al., (2020) based on NaCl extraction to solubilize the majority of globulins proteins. Sunflower meal (30 g) was dissolved in a 10 % (w/v) meal-to-ultrapure water ratio, added with 10 % (w/v) of NaCl. Then, this solution was stirred on a magnetic stirrer plate (60 min, 40 °C, pH adjusted at 6). After solubilization, the sample was cloth filtrated to remove solid fibrous residues. The resulting solution was centrifuged (Centrifuge Universal 320, Hettich, Tuttlingen, Germany) at 3 300 g, for 10 min, at 20 °C. Afterward, the resulting supernatant

composed of solubilized proteins was recovered and filtrated by vacuum filtration to remove the residues remaining from solubilization. The filtrated supernatant was precipitated within 10 min by adjusting pH to 4.5, corresponding to the isoelectric point of sunflower proteins (Dabbour et al., 2019). This suspension was rested for 30 min at room temperature (25 °C), and then centrifuged again (3300 g, 10 min, 20°C). The pellet was finally dried using a convective oven (Thermo Scientific™, USA) at 55 °C overnight. SMPI was stored at -20 °C until further use.

4.2.3.1.2 Proteolysis

Sunflower meal protein isolate (SMPI) was then hydrolysed as previously described with some modifications (El Hajj et al., 2023). First, 5 g of SMPI were dissolved in 250 mL of 50 mM ammonium bicarbonate buffer solution. Then, SMPI was hydrolysed either with Protamex® (**Prot**) or Protamex® followed by Flavourzyme® (**Prot+Flav**). The hydrolysis parameters were as follows: 2 % (w/v) SMPI concentration, 1 % (w/w) enzyme/substrate ratio, for 2 h, at pH 8 and 55 °C with Protamex® and for 2 h, pH 7 and 55 °C with Flavourzyme®, which correspond to their respective optimal conditions. Upon hydrolysis, the pH was maintained at the desired values by adding 1 M NaOH solution. After each hydrolysis step, each protease was heat inactivated (95 °C, 15 min). In the sequential treatment, Protamex® was inactivated just before Flavourzyme® treatment. Then, hydrolysates were centrifuged (10 000 g, 15 min, 25 °C) in order to remove the enzymes, and the whole hydrolysates fractions were freeze-dried (Labconco, Kansas City, USA) and stored at −20 °C for further analysis.

These two hydrolysate powders were further dissolved (quantity sufficient for (**qsf**) 250 mL; 2 % (w/v) in ultrapure water) and submitted to ultrafiltration under magnetic stirring and 5 bars of nitrogen pressure (El Hajj et al., 2023). The ultrafiltration unit (UF stirred cell 47 mm system XFUF04701; Millipore, Molsheim, France) was initially equipped with a 10 kDa molecular weight cut-off (**MWCO**) membrane, followed by a 1 kDa MWCO membrane (Millipore, Billerica, USA), conditioned according to their specification, before ultrafiltration. The ultrafiltrated fractions of hydrolysates (the so-called ≤ 1 kDa Prot and ≤ 1 kDa Prot+Flav) were freeze-dried and kept at −20 °C until further analysis. On total, four hydrolysates were investigated (whole hydrolysates: Prot and Prot+Flav, and ≤ 1 kDa fraction hydrolysates: ≤ 1 kDa Prot and ≤ 1 kDa Prot+Flav).

4.2.3.2 Immobilized metal ion affinity chromatography

The eleven synthetic peptides and the Ni^{2+}-binding peptides present in whole hydrolysates and their ≤ 1 kDa fractions were investigated by IMAC-Ni^{2+} using a HPLC system (LC-20AD, Shimadzu, Japan) at 1 mL/min flow rate, an oven temperature set at 25 °C and a diode array detector (SPD-M20A, Shimadzu, Japan). The Ni^{2+}-binding peptides were separated on a 1 mL HisTrap^{TM}HP column (7×250 mm) prepacked with Ni Sepharose High Performance (Cytiva, Marlborough, MA, USA). Experiments were carried out according to Irankunda et al., (2024) with some modifications. The method included five steps: nickel(II) regeneration, equilibration, injection followed by unbound compounds removal, elution and washing. First, 10 column volumes (**CV**) of ultrapure water were used to remove the ethanol remaining in the column (storage conditions). Then, the column was stripped using 50 mM EDTA solution, followed by nickel (Ni^{2+}) regeneration step using a 100 mM nickel (Ni^{2+}) sulfate ($NiSO_4$) solution. Then, 20 CV of equilibration buffer (PBS 1X pH 7.4: Na_2HPO_4 6.7 mM; KH_2PO_4 1.25 mM; NaCl 300 mM) were used to remove the unbound nickel ions and equilibrate the column. Finally, 50 µL of either synthetic peptides (20 mM) or hydrolysates (20 mM eq. NH_2 according to OPA analysis, **Appendix 4.2**) were loaded onto the IMAC-Ni^{2+} column (dead time of the column and the whole HPLC system: 1.2 min (Irankunda et al., 2024). The first fraction (**F1**) corresponding to the non-nickel-binding peptides was eluted with the equilibration buffer after 5 min (retention time (**RT**) comprised between 0 and 5 min), then the Ni^{2+}-binding peptides fractions (**F2**) were eluted with an imidazole gradient (0-300 mM, prepared in PBS 1X pH 7.4) from 5 to 65 min (RT comprised between 5 and 65 min). Finally, 5 CV (5 min) of a 600 mM imidazole solution was used to wash the columns before the next run. Due to imidazole absorption at 214 nm, which is also the wavelength used for monitoring peptide bonds, the peptides were followed at 232 nm. For hydrolysates, the F1 and F2 fractions were collected using a fraction collector (FRC-10A, Shimadzu, Japan) for further LC-MS/MS identification of peptide sequences. The retention time RT and the Imidazole concentration at which elution occurs (**IMC**) was determined for peptides and hydrolysates.

4.2.3.3 Peptide sequence identification by LC-MS/MS

4.2.3.3.1 LC-MS/MS analysis

To identify the peptide sequences present in the produced hydrolysates, the IMAC-Ni^{2+} collected fractions (F1, F2) were evaluated on a Thermo Scientific UHPLC-HRMS system composed of a Vanquish™ liquid chromatography unit coupled to a photodiode array detector and an Orbitrap ID-X™ Tribrid™ high-resolution mass spectrometer operating in positive electrospray ionization mode (**ESI^+**) as previously reported (Dos Santos Morais et al., 2020).

4.2.3.3.2 Peptide sequence identification

The Thermo XCalibur raw LC-MS/MS data files resulting from the collected fractions (F1, F2) from the hydrolysates in IMAC-Ni^{2+} were processed in the Andromeda search engine of the commonly used proteomic software tools MaxQuant™ (version 2.4.13.0) (Boachie et al., 2022). The peptide sequences were searched against a restricted sunflower seed proteins data base (*Helianthus annuus*) containing 30 entries obtained from UniProtKB (https://www.uniprot.org/, accessed on 27 January 2024, **Appendix 4.3**). The peptides identification was achieved by comparing the experimental fragment-ion mass value of the precursor ions with the theoretical fragment masses obtained from the protein sequences data base, obtained by the unspecified digestion rule with a mass tolerance of 10 ppm. The parameters of database searches were set up according to Boachie et al., (2022) (**Appendix 4.4**). Note that before searching peptides sequences from the collected fraction of hydrolysates, this method was first validated using a synthetic peptides hydrolysate composed of 8 pure peptides at 1 mM each (Pep1-8, section 4.2.2). All these 8 peptides were clearly identified (**Appendix 4.5**). Finally, the AA composition of identified Ni^{2+}-binding peptides present in SMPI hydrolysates (F2) were computed through ExPASy ProtParam server (https://web.expasy.org/protparam/).

4.2.4 Peptide-metal interaction

4.2.4.1 switchSENSE® technology

The study of the interaction between Ni^{2+} ions and peptides (either present in synthetic peptides or SMPI hydrolysates) was carried out with a biosensor analyzer DRX using an

electrically switchable DNA chip designated as MPC-48-2-R1-S, incorporated NTA and Cy5 dye was used as a fluorescent probe (switchSENSE® technology; Dynamic Biosensors GmbH, Munich, Germany). This technology can be used both in static and in dynamic modes. The principles of these modes are reported in Muller-Landau & Varela, (2021). Experiments were conducted according to the method initiated by El Hajj et al., (2021) with some modifications. Briefly. the synthetic peptides (at 100 µM), the whole hydrolysates and their ≤ 1 kDa ultrafiltrates (at 200 µM eq. NH_2) were prepared using T40 buffer (*i.e.,* 10 mM Tris-HCl, 40 mM NaCl, and 0.05 % v/v Tween 20 at pH 7.4). Then, the former sample solutions were injected into the microfluidic device at a flow rate of 30 µL/min for a 4 min association phase, followed by the injection of T40 buffer at 50 µL/min for a 4 min dissociation phase to release the analytes. After each investigated concentration, Ni^{2+} ions were removed using a 100 mM EDTA solution, followed by a Ni^{2+} rebinding phase before launching another run. A buffer blank was also investigated to correct all kinetic experiments for non-specific interactions (static mode measurements).

The flow was paused between the association and the dissociation phases in static mode measurements in order to perform the dynamic mode measurement. This dynamic analysis enabled to evaluate the specificity of the peptide-metal ion interaction. The analysis of the different kinetic curves was performed using the switchANALYSIS® software from Dynamic Biosensors using non-linear fitting of single exponential functions. Each kinetic experiment was performed twice with different sample preparations and the changes in fluorescence (**ΔF**) and the change in the dynamic response (**ΔDR**). Unspecific binding was removed by subtracting the results obtained with the reference electrode (No NTA-Ni^{2+}) and ΔF and ΔDR values, corresponding only to specific binding, were presented as the average of eight measurements.

4.2.4.2 UV-visible spectroscopy

The determination of the UV-visible (**UV-vis**) spectrum of Ni^{2+} ions and peptide-Ni^{2+} complexes formed by synthetic peptides and SMPI hydrolysates (whole and ≤ 1 kDa fraction) was carried out at the PhotoNS Platform of the L2CM Laboratory, Université de Lorraine. The samples were prepared by mixing 1.5 mL of 50 mM HEPES buffer at pH 7.4 with 250 µL of 10 mM sample solution (hydrolysates: eq. NH_2) and 250 µL of 10 mM nickel (Ni^{2+}) sulfate solution

in order to have a 1:1 metal-to-ligand molar ratio. The UV-vis spectra were recorded on a Perkin Elmer Lambda1050 UV-vis-NIR spectrophotometer (Perkin Elmer Corp, Massachusetts, USA) in a quartz cuvette with 1.0 cm path length in a range of wavelengths varying from 350 to 800 nm at room temperature (25 °C).

4.2.4.3 Circular dichroism spectroscopy

The circular dichroism (**CD**) spectra of the synthetic peptides and the SMPI hydrolysates (whole and ≤ 1 kDa fractions) with and without Ni^{2+} ions were performed at the PhotoNS Platform of the L2CM Laboratory, Université de Lorraine. The CD spectra were recorded from 250 to 800 nm at 0.5 nm intervals using a MOS-450 CD spectrometer (Bio-Logic Science Instruments, France) in a quartz cuvette with 1.0 cm path length. Solutions of synthetic peptides and hydrolysates were prepared at 10 mM (hydrolysates: mM eq. NH_2) in 50 mM HEPES buffer at pH 7.4 and mixed with 10 mM Ni^{2+} solution to reach 1:1 metal-to-ligand molar ratio. Then, sample solutions (with and without Ni^{2+} ions) were transferred into a 1 cm-pathlength cuvette for analysis at 25 °C as reported in Csire et al., (2022).

4.2.5 Statistical analysis

To evaluate the effect of enzymatic treatments, 1 kDa ultrafiltration process and the AA composition and sequences on the Ni^{2+}-binding ability of synthetic peptides and SMPI hydrolysates (whole and ≤ 1 kDa fractions), results were statistically analyzed by one-way analysis of variance (ANOVA). All the measurements of IMAC-Ni^{2+} and switchSENSE® techniques were triplicated for synthetic peptides and SMPI hydrolysates and data were presented as means ± standard deviation. Differences between means of samples were determined by Fisher's multiple range test where differences at *p-value* < 0.05 were considered significant. Statistical calculations were conducted using the software Statgraphics centurion XVI version 16.1.03 (Statgraphics Technologies Inc, Virginia, USA).

4.3 Results and discussions

4.3.1 Investigation of Ni^{2+}-binding peptides in IMAC-Ni^{2+}

4.3.1.1 Retention time of synthetic peptides

In order to study the ability of the different synthetic peptides to bind to Ni^{2+} ions, samples were initially investigated on IMAC-Ni^{2+}. This method, based on peptides-Ni^{2+} interaction, provides several advantages due to its high-binding capacity and high recovery. The Ni^{2+}-binding peptides were eluted using imidazole gradient (0-300 mM, in 60 min). The **Figure 4.2** shows the retention time (**RT**) of the peptides in the column (the red dash line indicates the beginning of imidazole gradient from 0-300 mM); the higher the RT (min) or IMC (mM of imidazole), the stronger the Ni^{2+}-binding ability of the investigated peptide. The Pep11.**HHHHHH**, well-known for its strong Ni^{2+}-binding ability in IMAC, was used as positive control. It exhibits the highest RT (42.6 min; IMC: 187.9 mM, fraction 2: RT > 5 min), which is associated with its His residues as previously reported (Irankunda et al., 2024). Regarding the sunflower peptides, they were theoretically classified into three groups (see section 4.2.1): group I: His or Trp-containing peptides without proline, which is divided into two subgroups IA (His-containing peptides, Pep1-3) and IB (Trp-containing peptide, Pep4); group II: His-containing peptides with proline (Pep5-8), and group III: peptides without His nor Trp (Pep9-10). In agreement with the theoretical classification, both His-containing peptides groups IA and II without/with proline, respectively 1.**W**L**H**NDGN, 2.**W**L**H**NDGNTE, 3.FAT**C**IAR**H**, 5.AIPTGTA**H**, 6.KFPILE**H**, 17.KFPILE**H**L and 18.KFPILE**H**LR exhibit the highest RT with no significant statistical differences (*p-value* ≥ 0.05). Indeed, these peptides are observed in the elution phase (RT > 5 min; IMC: 22.2-25.2 mM, fraction F2) where imidazole is required for peptide elution.

Our results agree with the hard and soft acid and base theory (the so-called **HSAB** theory), which states that to form a bound between two atoms, one atom behaves like a Lewis base (i.e., imidazole group of histidine) while the other one behaves like a Lewis acid (i.e., Ni^{2+}). The observed interaction between histidine residue and Ni^{2+} ions is governed by both borderline Lewis acid and base groups which confers the strongest interaction (Irankunda et al., 2022). Meanwhile, group III of peptides, those without His (9.GN**P**Q, 10.LLAF), were eluted before applying the imidazole gradient (RT < 5 min, fraction F1). In comparison to peptide Pep9.GNPQ and Pep10.LLAF, which have no affinity for Ni^{2+} ions, the Pep4.**W**VSFKTN (group

IB) has a slightly higher affinity (*p-value* < 0.05, RT: 4.19 min, fraction F1). Note that, the presence of a Trp residue in the sequence of Pep4.**W**VSFKTN, may induce only a weak interaction with Ni^{2+}. However, Trp with Cys and His have been proposed by Porath as a specific triad in the IMAC technique as primary electron-pair donors for protein retention (Porath et al., 1975). Yet, the presence of a Trp residue is not enough to exhibit a good Ni^{2+}-binding ability compared to His residue that has the most significant role in Ni^{2+}-binding ability according to the HSAB theory and as reported for sunflower peptides in this study. Besides, the IMAC-Ni^{2+} results suggest that the affinity of peptides for immobilized Ni^{2+} ions is rather governed by the presence of His residue than by its position within their sequence.

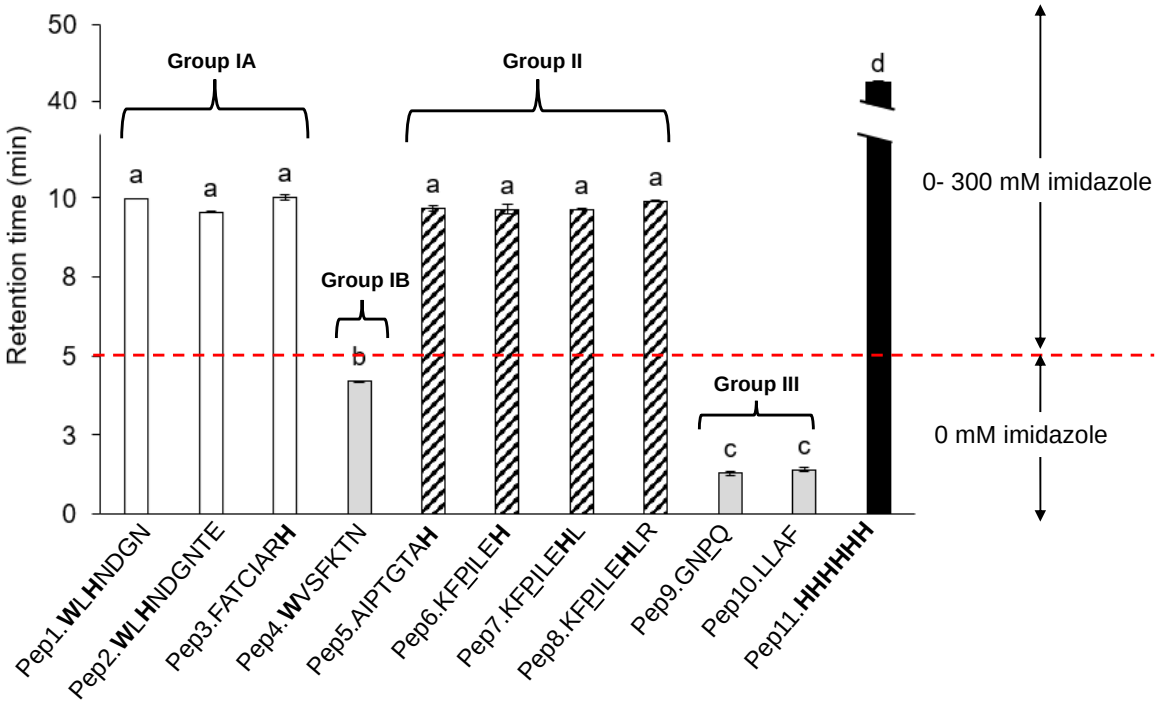

Figure 4.2. Retention times (min) of pure peptides studied with HisTrap IMAC-Ni^{2+}. Values are expresses as the mean ± standard deviation of three independent determination. Different letters indicate significant differences (*p-value* < 0.05).

4.3.1.2 Separation of Ni^{2+}-binding peptides present in hydrolysates

Similar to synthetic peptides, the Ni^{2+}-binding ability of SMPI hydrolysates was investigated using IMAC- Ni^{2+}. The IMAC- Ni^{2+} chromatograms (**Figure 4.3A-D**) show the injection phase (0-5 min) and elution phase (fraction 2: 5-65 min) of whole hydrolysates and their corresponding

≤ 1 kDa fractions (the red dash line indicates the beginning of imidazole gradient from 0-300 mM). Upon elution phase using an imidazole gradient (0-300 mM, 60 min from 5 to 65 min RT), Ni^{2+}-binding peptides bound onto IMAC-Ni^{2+} phase were eluted in one peak, *i.e.,* only one F2 the fraction. For all the four studied hydrolysates, a Ni^{2+}-binding peptides fraction is observed (F2). Thus, SMPI hydrolysates contain metal-binding peptides.

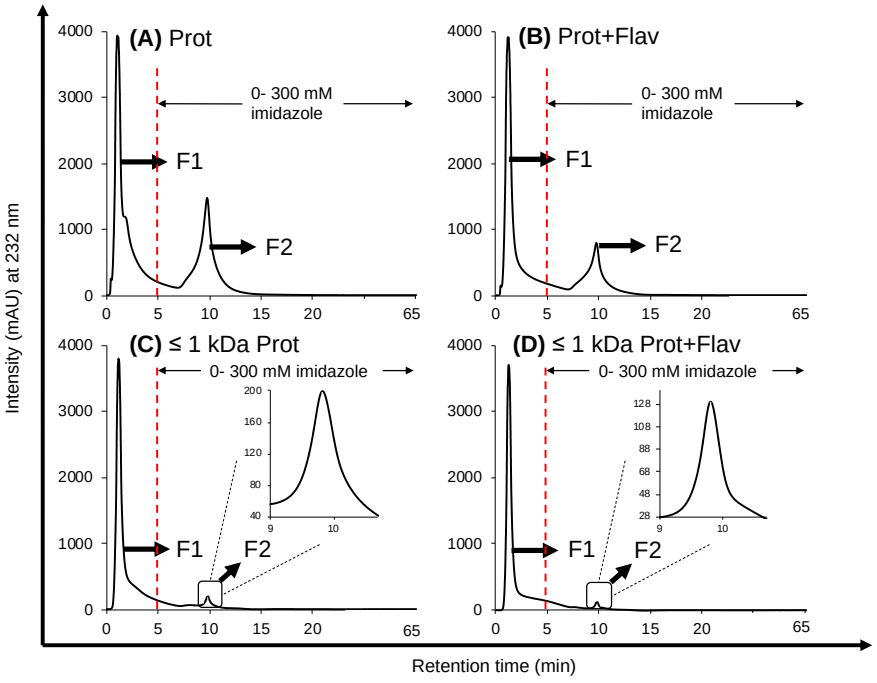

Figure 4.3. Study of peptide-Ni^{2+} interaction in SMPI hydrolysates using immobilized metal ion affinity chromatography (IMAC). (A-D) The isolation of Ni^{2+}-binding peptides of SMPI hydrolysates.

The unbounding peptides (F1) were eluted by 5 min of equilibrating buffer PBS1X pH 7.4. Elution profile of Ni^{2+}-binding peptides (F2) was obtained after imidazole gradient (5-65 min, 0-300 mM). Values are expresses as the mean ± standard deviation of three independent determination. Different letters indicate significant differences (*p-value* < 0.05). SMPI: sunflower meal protein isolate; Prot: Protamex® hydrolysate; Prot+Flav: Protamex® followed by Flavourzyme®; ≤ 1kDa: 1 kDa ultrafiltrated.

We hypothesize that these potential metal-binding peptides may contain histidine, tryptophane or cysteine (three AA residues called Porath's triad, Porath et al., 1975), as well as aspartic and glutamic acids, AA well-known for their transition metal ions binding properties due to their imidazole, indole, thiol and carboxylate groups present on their side chain, respectively (Camaño Echavarría et al., 2024; Irankunda et al., 2024). Indeed, at physiological pH (7.4), imidazole group of His and COOH group of Asp and Glu are

deprotonated, since their side chain group p*K* values are 6, 3.9 and 4.2, respectively, which enable to bind to Ni^{2+} ions (Żamojć et al., 2021). Note that among the hydrolysates, the retention time (**RT**) of the Ni^{2+}-chelating peptides fractions ranged between 9.7 and 10.1 min (IMC: 23.8-25.5 mM), which means that the mechanism of peptide-Ni^{2+} interaction in IMAC-Ni^{2+} column may be similar in the four hydrolysates and their difference in chelation capacity may rather be explained by the concentration of chelating peptides which is related with the absorbance intensity (**Figure 4.3A-D**). Regarding the intensity, the result suggests that Prot hydrolysate contains the highest amount of Ni^{2+}-binding peptides (F2) followed by Prot+Flav, ≤ 1 kDa Prot and ≤ 1 kDa Prot+Flav hydrolysates.

4.3.1.3 Ni^{2+}-binding peptides identified in hydrolysates by LC-MS/MS

The fractions F1 (containing the unbound peptides) and F2 (enriched in Ni^{2+}-binding peptides) collected from previous chromatographic experiments were subjected to LC-MS/MS analysis in order to identify the peptide sequences present in SMPI hydrolysates. The peptide sequences identified in the enriched Ni^{2+}-binding peptides fractions (F2) are shown in **Table 4.2**. Interestingly, all the peptide sequences identified in F2 fractions, contain at least one His or one Trp residue (**Table 4.2**, H or W residues highlighted in bold), which could play a pivotal role in the Ni^{2+}-binding ability of peptides present in hydrolysates due to its imidazole and indole groups, respectively. In comparison, among the 175 peptides identified in the unbound peptides fractions F1, only 1 peptide contains His (DFIR**H**) and 5 peptides contain Trp (i.e., EI**W**DANDQ, E**W**VAF, REEQE**W**E, SL**W**N, **W**TVN; **Appendix 4.6**). This finding agrees with the low Ni^{2+}-binding ability of the synthetic peptide Pep4.**W**VSFKTN (Trp-containing peptide), which was also eluted before applying the imidazole gradient (RT < 5 min).

The **Table 4.2** reveals a total number of 22, 10, 21 and 8 Ni^{2+}-binding peptides identified in Prot, Prot+Flav, ≤ 1 kDa Prot and ≤ 1 kDa Prot+Flav, respectively. From **Table 2**, **Figure 4.A** illustrates the effect of the sequential enzymatic treatment using Flav on the generation of Ni^{2+}-binding peptides. Upon the Flav sequential hydrolysis, 15 Ni^{2+}-binding peptides already produced in Prot hydrolysate are hydrolysed (thus disappearing; represented by a cross (†) in **Table 4.2**), whilst 3 additional peptides are generated (i.e., G**H**LQPN, **H**NDGNTELVVVVF and SFLAGGISSE**H**IQGQQQ, marked by an asterisk (*) in **Table 4.2**). Moreover, **Figure 4.4B** shows the effect of ≤ 1 kDa ultrafiltration on the appearance of peptides that might not be identified

in the whole hydrolysates due to their concentration below the limit of detection of MS/MS analysis. After ultrafiltration, in ≤ 1 kDa Prot fraction, one big-sized peptide (AIQSP**HW**TIN with MW > 1.1 kDa) disappeared, while no additional peptides were identified. Besides, three big-sized peptides (AIQSP**H**WTIN, **H**NDGNTELVVVVF and SFLAGGISSE**H**IQGQQQ, with MW > 1.1 kDa) disappeared upon ultrafiltration in ≤ 1 kDa Prot+Flav (which is coherent with the MWCO of the UF process), while an additional peptide was identified (SEVF**H**) probably related by a better relative detection in the ultrafiltrated hydrolysate (**Table 4.2**).

Table 4.2. Ni^{2+}-binding peptides identified from the F2 (elution phase) SMPI hydrolysates using IMAC-Ni^{2+} separation followed by LC-MS/MS analysis.

Sequence	Peptides identified in F2 fraction				Length	Mass (g/mol)	Score	Entry
	Prot	Prot+Flav	≤ 1 k Da Prot	≤ 1 kDa Prot+Flav				
AHNLL†	x	n.i.	x	n.i.	5	566.32	1.94	
AHNLLY†	x	n.i.	x	n.i.	6	729.38	4.12	A0A251TKL9
AIQSPHWT†	x	n.i.	x	n.i.	8	938.46	5.76	
AIQSPHWTIN	x	x	n.i.	n.i.	10	1165.59	6.72	
ALFSPH†	x	n.i.	x	n.i.	6	670.34	9.64	A0A251UYX1
AVLAPH†	x	n.i.	x	n.i.	6	606.35	9.64	A0A251T566
DFIRH	x	x	x	x	5	686.35	16.21	A0A251TKL9
FSPH†	x	n.i.	x	n.i.	4	486.22	8.08	A0A251UYX1
GAAHW†	x	n.i.	x	n.i.	5	540.24	1.94	A0A251TUS1
GAVHW†	x	n.i.	x	n.i.	5	568.28	6.05	A0A251T566
GHLQPN*	n.i.	x	n.i.	x	6	664.33	9.64	A0A251UYX1
GIVSPH	x	x	x	x	6	608.33	9.64	A0A251TUS1
GSRWVSF†	x	n.i.	x	n.i.	7	837.41	2.89	
GVDFIRH	x	x	x	x	7	842.44	17.09	A0A251TKL9
GVDFIRHR	x	x	x	x	8	998.54	3.60	
HAW†	x	n.i.	x	n.i.	3	412.19	3.98	A0A251VMR6
HNDGNTELVVVVF*	n.i.	x	n.i.	n.i.	13	1441.72	1.46	A0A251TKL9
LLHVT†	x	n.i.	x	n.i.	5	581.35	5.30	A0A9K3NGE6
SEVFH	n.i.	n.i.	n.i.	x	5	617.28	1.94	A0A9K3HVJ0
SFLAGGISSEHIQGQQQ*	n.i.	x	n.i.	n.i.	17	1785.86	0.35	A0A251UYX1
SHTVVY†	x	n.i.	x	n.i.	6	704.35	20.22	
SPH†	x	n.i.	x	n.i.	3	339.15	3.98	
SPHWT	x	x	x	x	5	626.28	1.65	A0A251TKL9
SPHWTIN	x	x	x	x	7	853.41	11.11	
VSPH†	x	n.i.	x	n.i.	4	438.22	8.08	A0A251TUS1
WLH†	x	n.i.	x	n.i.	3	454.23	3.98	A0A251TKL9
Total peptides	22	10	21	8				

SMPI: sunflower meal protein isolate; Prot: Protamex® hydrolysate; Prot+Flav: Protamex® followed by Flavourzyme®; ≤ 1kDa: 1 kDa ultrafiltrated. n.i. in grey cell: peptide not identified; x: peptide identified in the F2 fraction; †: 15 peptides disappeared upon sequential treatment; *: 3 peptides produced upon sequential treatment; Score: measure of how well the observed MS/MS spectrum matches to the stated peptide.

In addition to the presence of His residue in the peptide sequence, the size and the AA composition of Ni^{2+}-binding peptides constituting the fraction F2 plays a pivotal role on the

Ni^{2+}-binding ability. From **Table 4.2** data, the **Figure 4.4C** displays the fraction of Ni^{2+}-binding peptides (%) calculated for different peptide lengths (number of AA residues). The length of the identified Ni^{2+}-binding peptides ranges between 3 and 17 AA residues. For whole hydrolysates and ≤ 1 kDa fractions, the majority of peptide fraction comprises between 5 and 7 AA (> 50 % peptides). Besides, both Prot hydrolysates (whole and ≤ 1 kDa fraction) were the only ones, which present small-sized Ni^{2+}-binding peptides constituted between 3 and 4 AA in the fraction F2. This suggests that although the sequential hydrolysate (Prot+Flav) exhibits higher overall production of small-sized peptides compared to Prot hydrolysate (higher degree of hydrolysis, **Appendix 4.2**), sequential treatment does not favor the production of small-sized Ni^{2+}-binding peptides (3- 4 AA residues).

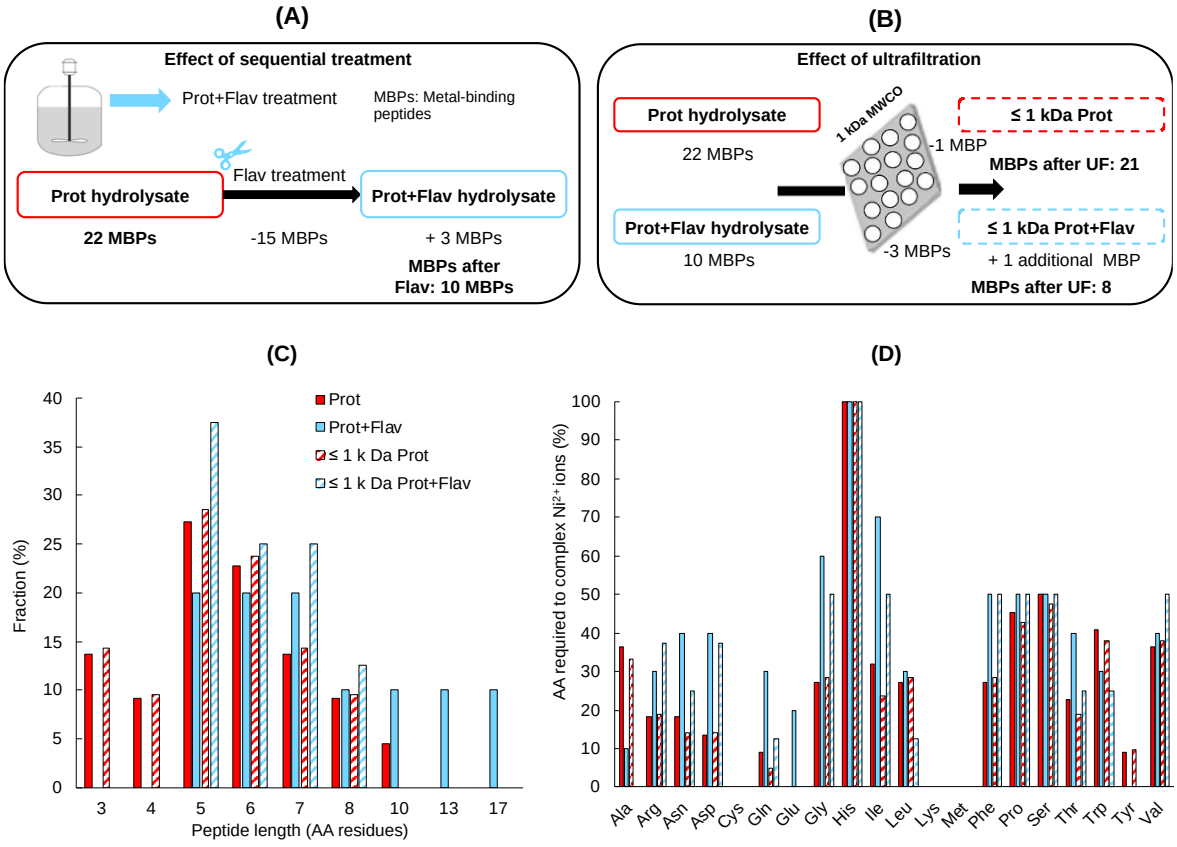

Figure 4.4. Ni^{2+}-binding peptides present in SMPI hydrolysates identified by the LC-MS/MS. (A-B) Effect of sequential enzymatic treatment and 1 kDa ultrafiltration on the number of Ni^{2+}-binding peptides identified in F2 fractions. (C) Peptide length profile of identified peptides. (D) AA frequency of Ni^{2+}-binding peptides identified.

Prot: Protamex® hydrolysate; Prot+Flav: Protamex® followed by Flavourzyme®; ≤ 1kDa: 1 kDa ultrafiltrated.

The AA frencuency of Ni^{2+}-binding peptides (fraction F2) was analysed by the free-accessed ProtParam tool (https://web.expasy.org/protparam/) (**Figure 4.4D**). It evidences that all the hydrolysates contain His residue as the major amino acid in their sequences (100 %), histidine being the main AA residue, responsible of their Ni^{2+}-binding properties. In addition, other AA residues such as Ala, Ser, and Ile in high percentages along the peptide sequences, are necessary to complex Ni^{2+} ions, although they are able to chalate metal ions.

Moreover, **Figure 4.5A-L** illustrates the sequenced mass spectra of the most interesting sequences of Ni^{2+}-binding peptides from SMPI hydrolysates loaded into the MaxQuant Viewer. The mass spectra of sequences with His residue at third position from N-terminus, second and first position from both termini are shown in **Figure 4.5 A-D**, **Figure 4.5 E-H**, and **Figure 4.5 I-L**, respectively. In our study, due to the presence of His residue as well as its position within the sequence, the identified sequences could be endowed with the highest metal-binding properties. Indeed, the Ni^{2+}-binding peptides found in SMPI hydrolysates with His residue at first, second and third position from the N-terminus could possess suitable Ni^{2+}-binding ability and stability in the formed peptide-M^{2+} complex as previously reported (Sóvágó et al., 2012).

The Prot hydrolysates (whole and ≤ 1 kDa fraction) shows high peptide sequences with His residue placed near the N-terminus while there are only four in the case of Prot+Flav hydrolysates (**Table 4.2**). Interestingly, these hydrolysates contain LL**H**VT and WL**H** sequences (**Figure 4.5A-B**), which are the most interesting ones due to the presence of their so-called "amino terminal Cu(II) and Ni(II)-binding (**ATCUN**) motif. This ATCUN motif is structurally characterized by (i) a free N-terminal amino nitrogen (NH_2) of the first residue, (ii) two deprotonated amide nitrogens of the peptide backbone, and (iii) an imidazole nitrogen of the third His residue from N-terminus (Miyamoto et al., 2016) (**Figure 4.1L**). This ATCUN motif has been highly used to design Ni^{2+}-binding peptides due to its high Ni^{2+}-binding ability, specificity and stability (Harford & Sarkar, 1997; Hureau et al., 2011; Lefevre et al., 2022; Maiti et al., 2020). Additionally, apart from this ATCUN motif, several sequences identified by mass analysis contain the His residue at the second position from N-terminus (*i.e.,* A**H**NLLY, A**H**NLL, S**H**TVVY for Prot hydrolysates; G**H**LQPN for Prot+Flav hydrolysates, **Table 4.2**), which could also offer interesting Ni^{2+}-binding ability. Indeed, (Conato et al., 2004) reported that a Ni^{2+}-chelating peptide with such a structural feature (i.e., His residue in second position, G**H**K)

possess strong Ni^{2+}-binding affinity. Besides, for peptides with His residue at first and second position from C-terminus (i.e. GVDFIR**H**, GAA**HW**), both terminal amino and imidazole side chains can take part in the Ni^{2+} complexation; however, these sites could act as independent metal binding sites when they are far apart in the sequence (Sóvágó et al., 2012).

On the other hand, there are many Ni^{2+}-binding peptide sequences identified that, in addition to the His residue, contain proline as well (**Table 4.2**). Yet, the Ni^{2+}-binding properties of these particular identified peptides might be lower compared to others. Indeed, according to the literature, proline could usually work as a break-point for amide coordination since it cannot be deprotonated, affecting the stability of the formed peptide-metal complex (Kastal et al., 2024). Former authors demonstrated that the effect of proline on the formation of peptide-Ni^{2+} complex depends on its position from N-terminus, the highest effect of proline on the complexation can be found when it precedes directly the His residue (Kastal et al., 2024). Some of the Ni^{2+}-binding peptides identified in **Table 4.2** (e.g. VS**PH**, S**PH**WT) may exhibit this behaviour. Similar to the synthetic peptides, hydrolysates investigated by IMAC-Ni^{2+} do not show potential differences between the Ni^{2+}-binding ability of His-containing peptides when proline is present, therefore, other technologies involving immobilized Ni^{2+} ions are required.

Overall, in our study, data obtained from IMAC-Ni^{2+} separation (fraction F2) followed by peptide sequence identification by LC-MS/MS analysis are used to better understand the metal binding behaviour of peptides present in whole SMPI hydrolysates and their ≤ 1 kDa fractions determined by other techniques such as switchSENSE® technology, UV-visible and circular dichroism spectroscopies. While the investigation by these techniques provides information on metal-binding constant rates, coordination geometry as well as potential binding sites of specific peptides, understanding the peptide sequence composition of the Ni^{2+}-binding fractions in IMAC (F2 fraction) can be essential to decipher the Ni^{2+}-binding ability and complexation mechanisms involved in a mixture of peptides such as SMPI hydrolysates

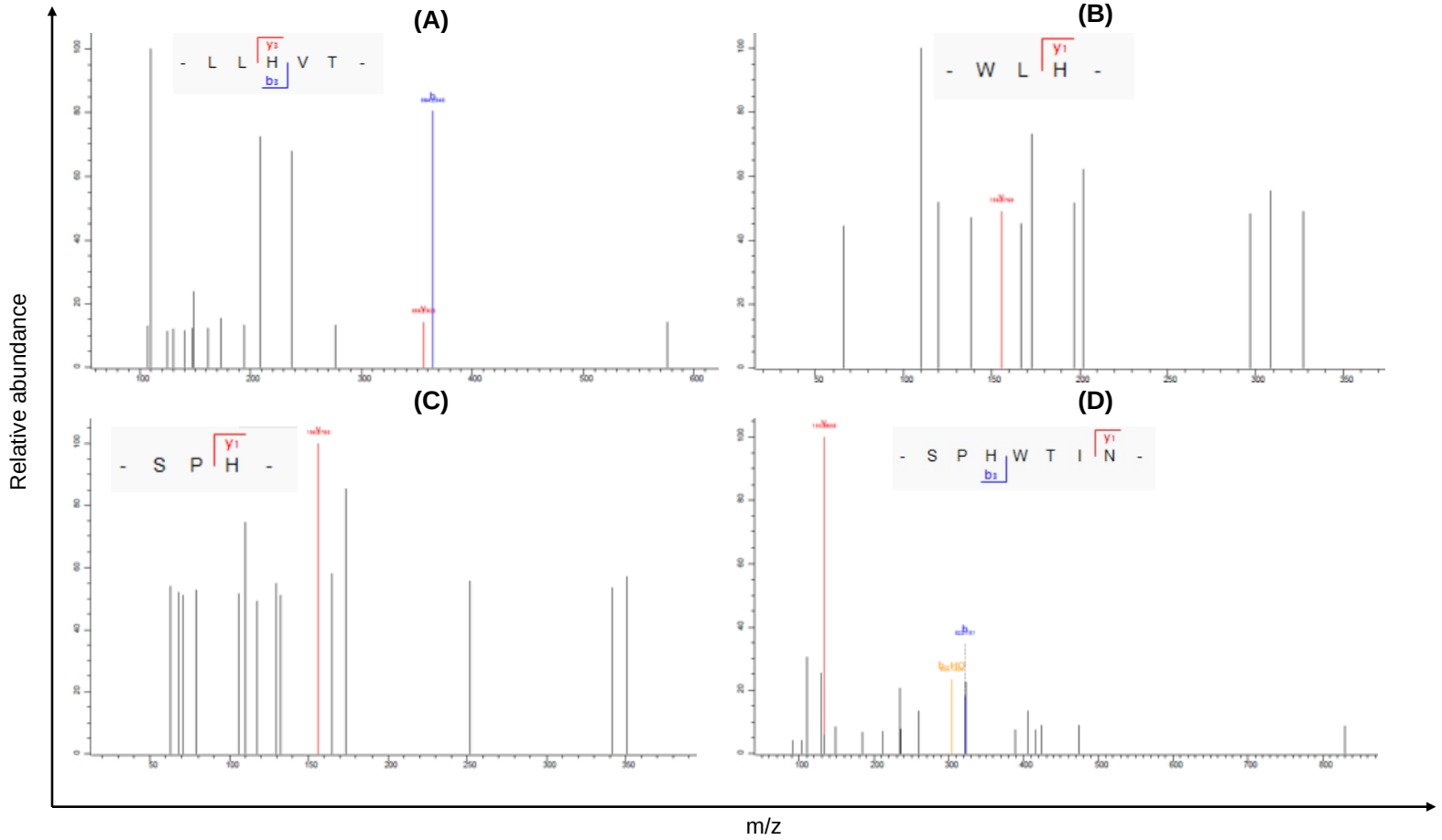

Figure 4.5. Part I. Sequenced mass spectra of twelve different Ni^{2+}-binding peptides structures obtained from SMPI hydrolysates and processes by MaxQuant software. ATCUN motif-containing peptides identified: (A) LL**H**VT, (B) WL**H**, (C) SP**H** and (D) SP**HW**TIN

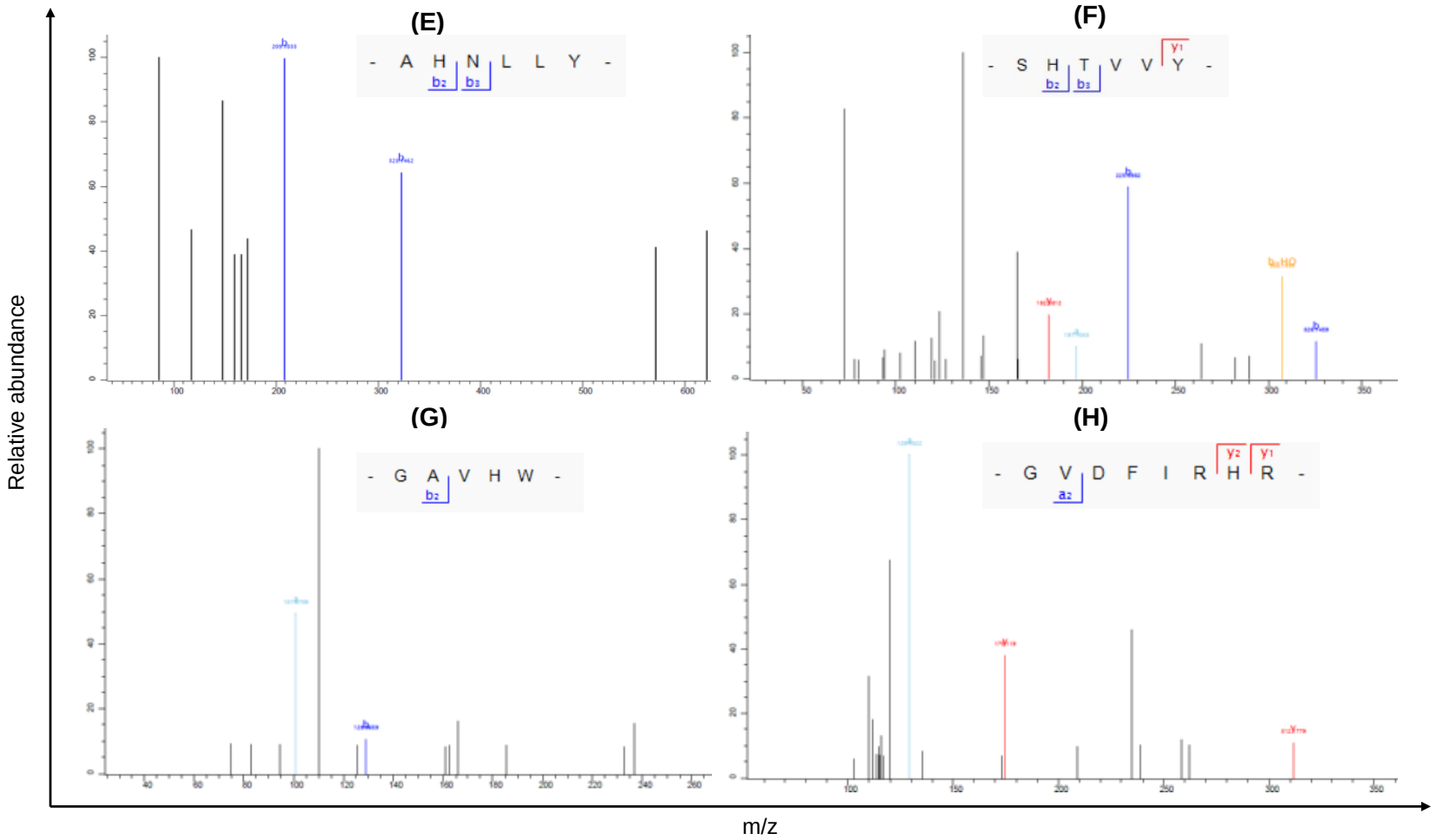

Figure 4.5. Part II. Sequenced mass spectra of twelve different Ni^{2+}-binding peptides structures obtained from SMPI hydrolysates and processes by MaxQuant software. His-containing peptide with His residue placed at second position from N and C-termini: (E) A**H**NLLY, (F) S**H**TVVY, (G) GAV**HW**, (H) GVDFIR**H**R.

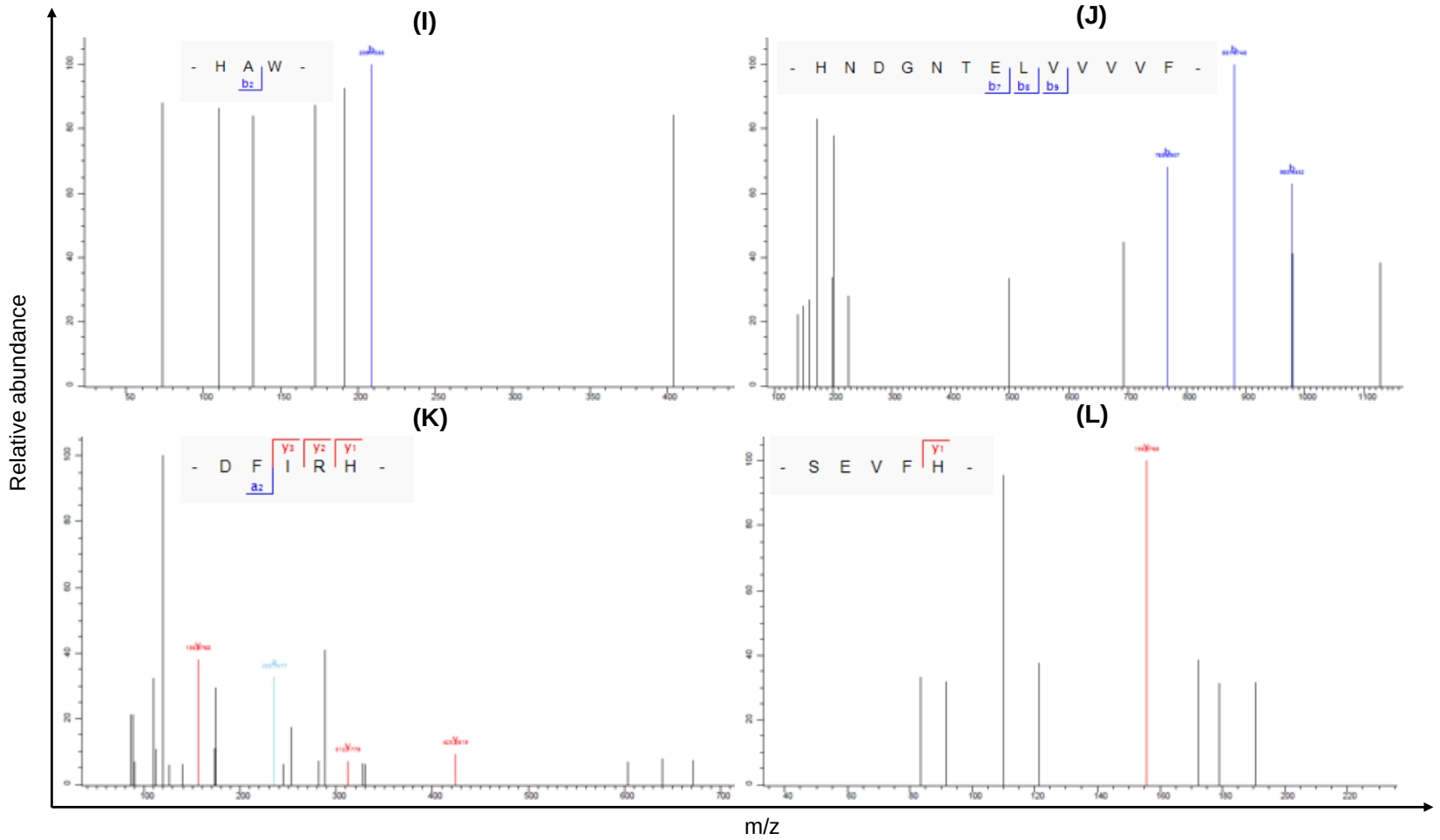

Figure 4.5. Part III. Sequenced mass spectra of twelve different Ni^{2+}-binding peptides structures obtained from SMPI hydrolysates and processes by MaxQuant software. His-containing peptide with His residue placed at first position from N and C-termini: (I) **H**A**W**, (J) **H**NDGNTELVVVVF, (K) DFIR**H**, (L) SEVF**H**.

4.3.2 Peptide-metal interaction

4.3.2.1 Affinity parameter determination by switchSENSE® technology

4.3.2.1.1 Static measurement

Ni^{2+}-binding ability of synthetic peptides and SMPI hydrolysates was also evaluated by real-time molecular interaction analysis using the switchSENSE® technology. Similar to IMAC- Ni^{2+}, this technology studies the interaction between peptides and immobilized Ni^{2+} ions, allowing to unveil potential differences of the degree of Ni^{2+}-binding affinity of sunflower peptides (synthetic peptides or hydrolysates).

The kinetic study of the interaction between synthetic peptides and Ni^{2+} reveals that peptides are bound onto the immobilized Ni^{2+} ions with different binding rate (k_{on}) (**Appendix 4.7A-K**), while no dissociation rate (k_{off} constants) could be observed (maybe the result of rapid metal ion unbinding); thus, the K_D values (K_D= k_{off}/k_{on}) could not be determined as previously reported (El Hajj et al., 2021). Instead, the global fitting of the resulting association rates (k_{on}) allowed to determine the observed rate constant (k_{obs}= k_{on}×C + k_{off}), which depends on the peptide concentration (C) (**Figure 4.6A**). The k_{obs} values obtained provide information about how fast the binding reaction between peptide and metal ion occurs. Upon the Ni^{2+} binding, several behaviors are observed as described hereafter. First and as expected, Pep11.**HHHHHH** exhibits the highest Ni^{2+}-binding association rate (k_{obs}= 6.72 x 10^{-2} s^{-1}) as positive control. Secondly, the Pep1.**W**L**H**NDGN, 2.**W**L**H**NDGNTE, 3.FAT**C**IAR**H** and 4.**W**VSFKTN (initially classified as the group I according to HSAB theory) present the highest association rate among synthetic peptides (3.04-3.54 10^{-2} s^{-1}), with no significant statistical differences (*p-value* ≥ 0.05). Thirdly, the Pep5.AIPTGTA**H,** Pep6.KFPILE**H**, 7.KFPILE**H**L and 8.KFPILE**H**LR binds to Ni^{2+} ions with lower binding rate than Pep1-4 (*p-value* < 0.05). Note that these latter group II peptides bind Ni^{2+} ions with similar binding rate (k_{obs}= 1.59-2.45 x 10^{-2} s^{-1}) which is the lowest association rate for His-containing peptides. Finally, Pep9.GNPQ and 10.LLAF (group III peptides), which do not contain any His nor Trp residue in their sequence, show the lowest k_{obs} values, demonstrating they have hardly any affinity for immobilized Ni^{2+} ions.

Concerning the hydrolysates (whole and ultrafiltrated), the kinetic study of the interaction between peptides contained in SMPI hydrolysates and Ni^{2+} notably shows an increase in fluorescence as a result of the steric hindrance caused by the Ni^{2+}-binding peptides upon the binding process (association phase, **Appendix 4.8A-D**). Thus, these results confirm the

presence of Ni^{2+}-binding peptides in all the SMPI hydrolysates and their respective ≤ 1 kDa fractions. Similar to the synthetic peptides, the global fitting of the resulting association rates (k_{on}) of the investigated hydrolysates allowed to determine their observed rate constant (k_{obs}, **Figure 4.6B**). The Ni^{2+}-binding peptides present in Prot hydrolysate bind to Ni^{2+} ions much faster (31.28 x 10^{-2} s^{-1}, *p-value* < 0.05) than those present in Prot+Flav one (k_{obs}= 0.15 x 10^{-2} s^{-1})), whereas among their respective ≤ 1 kDa fractions, the k_{obs} values decrease and are not statistically different (*p-value* ≥ 0.05). This observation clearly shows that the high Ni^{2+}-binding properties of Prot hydrolysate is strongly associated with its higher concentration of Ni^{2+}-binding peptides compared to other hydrolysates, which agrees with the above-mentioned results found in IMAC-Ni^{2+}.

Besides, for a more accurate assessment of the Ni^{2+} binding ability of the peptides/hydrolysates, relative changes in fluorescence (ΔF) were measured on sample spots (i.e., spots functionalized with NTA-Ni^{2+}) compared to reference spots (i.e., REF: spots in the absence of NTA-Ni^{2+}) upon injection of the peptide/hydrolysates (**Figure 4.6C-D**). Overall, all the studied peptides present a shift of delta of fluorescence when compared with REF. Nevertheless, the His or Trp-containing peptides of group I and II (Pep1.**W**L**H**NDGN, 2.**W**L**H**NDGNTE, 3.FAT**C**IAR**H**, Pep4.**W**VSFKTN, 5.AIPTGTA**H**, 6.KFPILE**H**, 7.KFPILE**H**L and 8.KFPILE**H**LR), and the positive control (Pep11.**HHHHHH**) evidence much higher shift of delta of fluorescence compared with REF values than peptides without His nor Trp (group III peptides: Pep9.GNPQ and 10.LLAF). This validates the affinity of His or Trp-containing peptide (group I and II) for Ni^{2+} ions compared to peptides without these specific AA. Regarding hydrolysates (whole or ultrafiltrated), all the samples show significant differences compared with the REF (*p-value* < 0.05), confirming the present of Ni^{2+}-binding peptides.

4.3.2.1.2 Dynamic measurement

Dynamic mode measurements enable to analyze the Ni^{2+}-binding ability of MBPs based on a decrease of the switching speed of nanolever upon the Ni^{2+} binding through peptides. The measurements were carried out, between the association and dissociation phase of the static mode while applying a current voltage. In this dynamic mode, the switching speed decreases upon the peptide binding onto Ni^{2+} since the nanolevers becomes heavier and its hydrodynamic friction is increased.

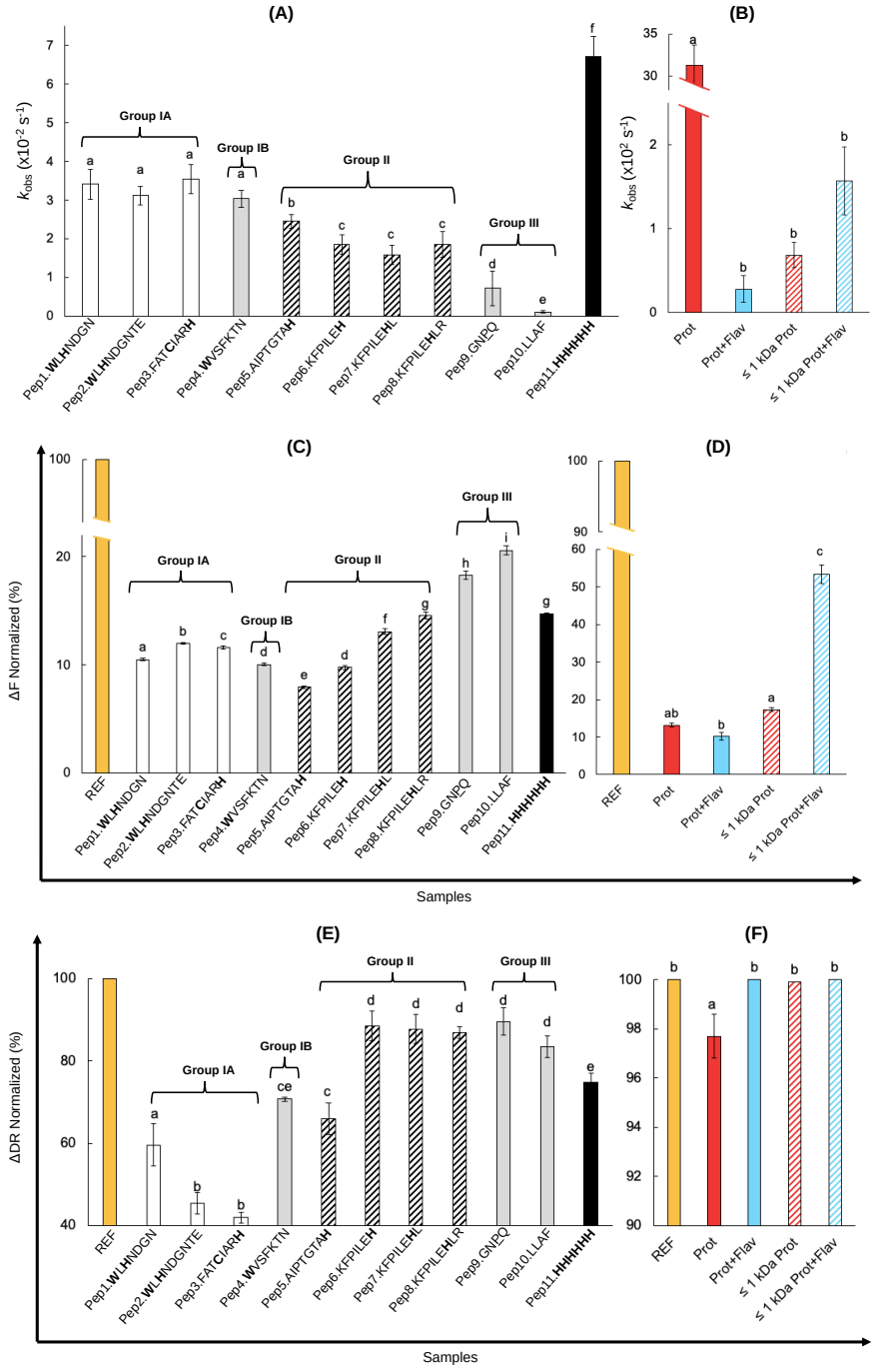

Figure 4.6. Study of the interaction of synthetic peptides and SMPI hydrolysates with nickel ions using switchSENSE® technology.

switchSENSE® measurements static mode: (A-B) average observed rate constant (k_{obs}) of synthetic peptides and SMPI obtained from kinetic study. (C-D) Changes in the local fluorophore environment (ΔF) of free-nickel references spots and samples spots for synthetic peptides and SMPI hydrolysates. switchSENSE® measurements dynamic mode: (E-F) changes in the switching speed (ΔDR) of nanolevers upon peptides binding into Ni^{2+} ions for synthetic peptides and SMPI hydrolysates. Values are expresses as the mean ± standard deviation. Different letters indicate significant differences (*p-value* < 0.05). SMPI: sunflower meal protein isolate; Prot: Protamex® hydrolysate; Prot+Flav: Protamex® followed by Flavourzyme®; ≤ 1kDa: 1 kDa ultrafiltrated

As shown in **Figure 4.6E**, Pep1.**W**L**H**NDGN, 2.**W**L**H**NDGNTE and 3.FAT**C**IAR**H** exhibit the highest change of switching speed (ΔDR comparted to REF) on the motion of nanolevers upon the Ni^{2+} binding, followed by Pep4-10 (4.**W**VSFKTN, 5.AIPTGTA**H** 6.KFPILE**H**, 7.KFPILE**H**L and 8.KFPILE**H**LR, 9.GNPQ and 10.LLAF) with the lowest variation, associated with their low affinity for Ni^{2+} ions showed in static mode (the lowest k_{obs} values). In addition to their His residue, Pep1.**W**L**H**NDGN, 2.**W**L**H**NDGNTE and 3.FAT**C**IAR**H** are characterized by the presence of Trp or Cys residues, respectively. These three amino acids (His, Cys and Trp,) constitute the so-called Porath's triad; due to their respective presence of imidazole (His), thiol (Cys) and indole (Trp) groups, they can form coordination bonds with metal ions at nearby neutral pH (Porath et al., 1975), thus, they could also be excellent anchoring sites for transition metal ions (Rowinska-Zyrek et al., 2011).

Regarding SMPI hydrolysates, **Figure 4.6F** reveals that, compared to other hydrolysates, the Ni^{2+}-binding peptides present in Prot hydrolysate show some effect on the motion of nanolevers, since the dynamic response (ΔDR) for sample spot compared to REF is less than 100 % upon the Ni^{2+} binding (97 %, *p-value* < 0.05). Indeed, Prot hydrolysate, characterized by lower degree of hydrolysis (DH) than Prot+Flav hydrolysate (**Appendix 4.2**), may contain higher concentration of bigger-sized Ni^{2+}-binding peptides causing higher hydrodynamic friction.In agreement with static mode measurement, Prot hydrolysates shows the most interesting Ni^{2+}-binding ability, whereas sequential Prot + Flav hydrolysate and the ≤ 1 kDa fractions evidence a negligeable effect (*p-value* ≥ 0.05) on the motion of nanolevers upon the binding which is related to both their low K_{obs} values observed and also the small-sized Ni^{2+}-binding peptides identified.

Taken together, all the findings of switchSENSE® technology on synthetic peptides clearly show that group I peptides (Pep1.**W**L**H**NDGN, 2.**W**L**H**NDGNTE, 3.FAT**C**IAR**H** and 4.**W**VSFKTN**,** His or Trp-containing peptides without Pro residue) have stronger interaction with the Ni^{2+}-binding sites than group II peptides (Pep5.AIPTGTA**H**, 6.KFPILE**H**, 7.KFPILE**H**L and 8.KFPILE**H**LR, His-containing peptides with Pro residue) and group III (9.GNPQ and 10.LLAF, peptides without His or Trp residue). Although group I and II peptides contain the same number of His Ni^{2+}-binding ligand (one His residue in their sequence), the interaction towards Ni^{2+} ion is lower in this last group (group II containing His and Pro residue). To explain this observation, one can mention the position of the effective anchoring site for metal ion coordination, which

is located at the C-terminus in group II peptides. They can therefore only form a (COO^-, N_{His}) chelate ring or (NH_2, N_{His}) macrochelate which are thermodynamically less stable than those formed by the group I peptide (NH_2, N_{His}) where His is at the N-terminal end. Pep.3 from group I could be an exception with its C-term His. Here, a 7-membered chelate ring could be formed between COO^- and N_{His} reinforced by the second AA Cys thus providing additional stability to this complex. Another point should be mentioned to explain the difference in chelating behaviour between Pep.3 and group II, is the (NH_2, N_{His}) macrochelate formation which can be sterically blocked by the presence of rigid Proline.

Additionally, but to lesser extent in the case of ternary complex formation between NTA-Ni^{2+} and peptides, it was hypothesized that the presence of Pro residue in Pep5 to 8 (Pep5.AI**P**TGTA**H**, 6.KF**P**ILE**H**, 7.KF**P**ILE**H**L and 8.KF**P**ILE**H**LR) could attenuate their Ni^{2+}-binding mechanism. Since Pro is a secondary amine AA, which after its involvement in peptide bond cannot be deprotonated, and therefore cannot take part in metal binding as observed for the ATCUN-motif (Kastal et al., 2024).

These findings suggest that, in our study, the Ni^{2+}-binding ability and the strength of binding of the peptides to Ni^{2+} ions might not depend only on the number of His residues, but also to their position within the peptide sequence, which influences their structural conformation. Indeed, the arrangement of His residue, the adjacent amino acids and the type of amino acid at the termini of Ni^{2+}-binding peptides play a key role on Ni^{2+} complexation.

Finally, interesting conclusions from the switchSENSE® data of synthetic peptides can also be drawn in SMPI hydrolysates: (i) the Ni^{2+} binding ability of peptide sequences identified in sunflower hydrolysates (**Table 4.2**), which could be classified in peptides from the group I (His or Trp-containing peptides without proline; e.g. A**H**NLL, LL**H**VT, **W**L**H**) and group II (His-containing peptides with proline; e.g. AIQS**P****HW**TIN, G**H**LQ**P**N, S**P****HW**T), would vary depending on the presence of His and Pro residue as well as on their position within the peptide sequence. Besides, the ATCUN motif-containing peptides identified in Prot hydrolysates, particularly LL**H**VT and WL**H** (present in Pep1.**WLH**NDGN, 2.**WLH**NDGNTE) as well as all the other His-containing peptides without proline present in SMPI hydrolysates (**Table 4.2**), could have the best Ni^{2+}-binding properties among the identified Ni^{2+}-binding peptides in SMPI hydrolysates.

4.3.2.2 UV-visible and CD spectroscopy measurements

UV-visible spectroscopy (**UV-vis**) and circular dichroism (**CD**) were used to study the coordination characteristics of the resulting complex of synthetic peptides or SMPI hydrolysates with Ni^{2+} ions in solution at physiological pH (7.4). The coordination modes of peptide-Ni^{2+} complexes were investigated by comparing the shifts of absorption/CD bands of peptides alone with those of the corresponding peptide-Ni^{2+} complex using the same concentration. Thanks to UV-vis and CD measurements, different electronic transitions commonly found in metal coordination complexes can be observed (d-d and CT transitions). So, among these specific electronic transitions, the d-d transition refers to electron excitation of the metal ion (i.e., Ni^{2+}) from one d level to another d level. In comparison, the charge-transfer (CT) transition which involves the excitation of an electron from the peptide ligand to the metal ion is characterized by stronger intensities and lower wavelength in the spectrum than the d-d transition. As example, **Figure 4.7A-F** and **Figure 4.8A-H** shows the UV-vis absorption and CD behaviour of peptide-Ni^{2+} complex for three synthetic peptides (i.e., 2.**W**L**H**NDGNTE, 3.FAT**C**IAR**H** and 11.**HHHHHH**) and SMPI hydrolysates, respectively. From such spectra, spectroscopic data (absorption maxima and sign of + or – Cotton effect on CD) were summarized in **Table 4.3** for all investigated peptides and hydrolysates.

Peptides. Among the synthetic peptides, only the Pep11.**HHHHHH** (positive control) and the His or Trp-containing peptides belonging to the group IA (Pep1.**W**L**H**NDGN not shown, 2.**W**L**H**NDGNTE, and 3.FAT**C**IAR**H**) evidence measurable changes in the absorption behaviour of peptide upon their Ni^{2+} complexation. They are characterized by a redshifted d-d band at around 420 nm relative to the band of Ni^{2+} alone found in water solution at 390 nm (blue line; **Figure 4.7**). Indeed, these peptides exhibit the most interesting Ni^{2+}-binding ability as previously observed in IMAC-Ni^{2+} and switchSENSE® techniques. Yet, for the group II peptides (Pep5.AIPTGTA**H**, 6.KFPILE**H**, 7.KFPILE**H**L and 8.KFPILE**H**LR), no measurable changes in UV-vis/CD spectra were detected at pH 7.4 (data not shown), although the Ni^{2+} ion is complexed. A possible explanation is that under physiological conditions (pH: 7.4) only macrochelates (NH_2, N_{im}) are formed for this peptide group, which do not cause significant changes in the UV-vis spectra.

Table 4.3. Spectroscopic data for the peptide-Ni^{2+} complexes at 1:1 metal-to-ligand ratio at pH 7.4.

Sample	UV-vis (nm)						CD (nm)					
Ni^{2+}	390				652	713	N.A					
Pep1.**W**LH**H**NDGN, 2.**W**LH**H**NDGNTE		418						300 (+)	418 (+)		485 (-)	
Pep3.FATCIAR**H**			426	545			280 (-)	337 (+)		462 (-)		553 (+)
Pep4-10*	--											
Pep11.**HHHHHH**		420			622		274 (+)		420 (+)		486 (-)	
Prot	387				678						485 (-)	
Prot+Flav	385				668				420 (+)			497 (-)
≤ 1 kDa Prot	388				688						484 (-)	
≤ 1 kDa Prot+Flav	388				677							500 (-)

Pep4: **W**VSFKTN, Pep5: AIPTGTA**H**, Pep6: KFPILE**H**, Pep7: KFPILE**H**L, Pep8: KFPILE**H**LR, Pep9: GNPQ, Pep10: LLAF; N.A: not applicable; -- not significant changes upon the addition of NI^{2+} ions.

Pep1.**W**L**H**NDGN and Pep2.**W**L**H**NDGNTE contain the same AA motif (WL**H**NDGN) with a slight difference in C-terminus in Pep2 (the **TE** motif). However, the UV-vis and CD data are similar for both peptides, suggesting that these additional amino acids residues (i.e., threonine and glutamic acid) do not have any important effects on the Ni^{2+} coordination mode at pH 7.4 (**Table 4.3**). Therefore, in order to study the complex geometry and the binding modes of WL**H** motif present in Pep1 and 2, only the UV-vis and CD data of 2.**W**L**H**NDGNTE were used.

The analysis of spectroscopic data presented in **Table 4.3** reveals that Pep11.**HHHHHH** and 2.**W**L**H**NDGNTE show similar behaviour upon Ni^{2+} complexation at pH 7.4 (λ_{max} = 420 nm, CD bands in the visible range at 420 nm (+) and 485 nm (-), and agree well with earlier results published on hexahistidine-Ni^{2+} complex (Valenti et al., 2006). This UV-vis/CD behavior (**Figure 4.7A-B** and **Figure 4.7E-F**) is consistent with a square-planar environment, and strongly supports a 4N-binding mode with {NH_2, $2N^-_{amide}$, $N_{imidazole}$} donor set in the formed peptide-Ni^{2+} complex.

Turi et al., (2013) reported the Ni^{2+}-complex formation process of His-containing peptide (NH_2-MK**H**M-NH_2 and NH_2-GT**H**S-NH_2 and octapeptides NH_2-GTHSMKHM-NH_2, NH_2-MKHMGTHS-NH_2) with His residue at third position from N-terminus as Pep2.**W**L**H**NDGNTE in our study. Authors suggested this 4N {NH_2, $2N^-_{amide}$, $N_{imidazole}$} coordination mode where imidazole and terminal NH_2 groups are the primary Ni^{2+} binding sites followed by the deprotonation and coordination of two amide nitrogen atoms in a cooperative manner forming a (5,5,6)-membered fused chelates rings at physiological pH. The CD spectral pattern of Pep2.**W**L**H**NDGNTE investigated in our study (containing the WL**H** ATCUN motif) is similar to that of [MLH_{-2}] species proposed.

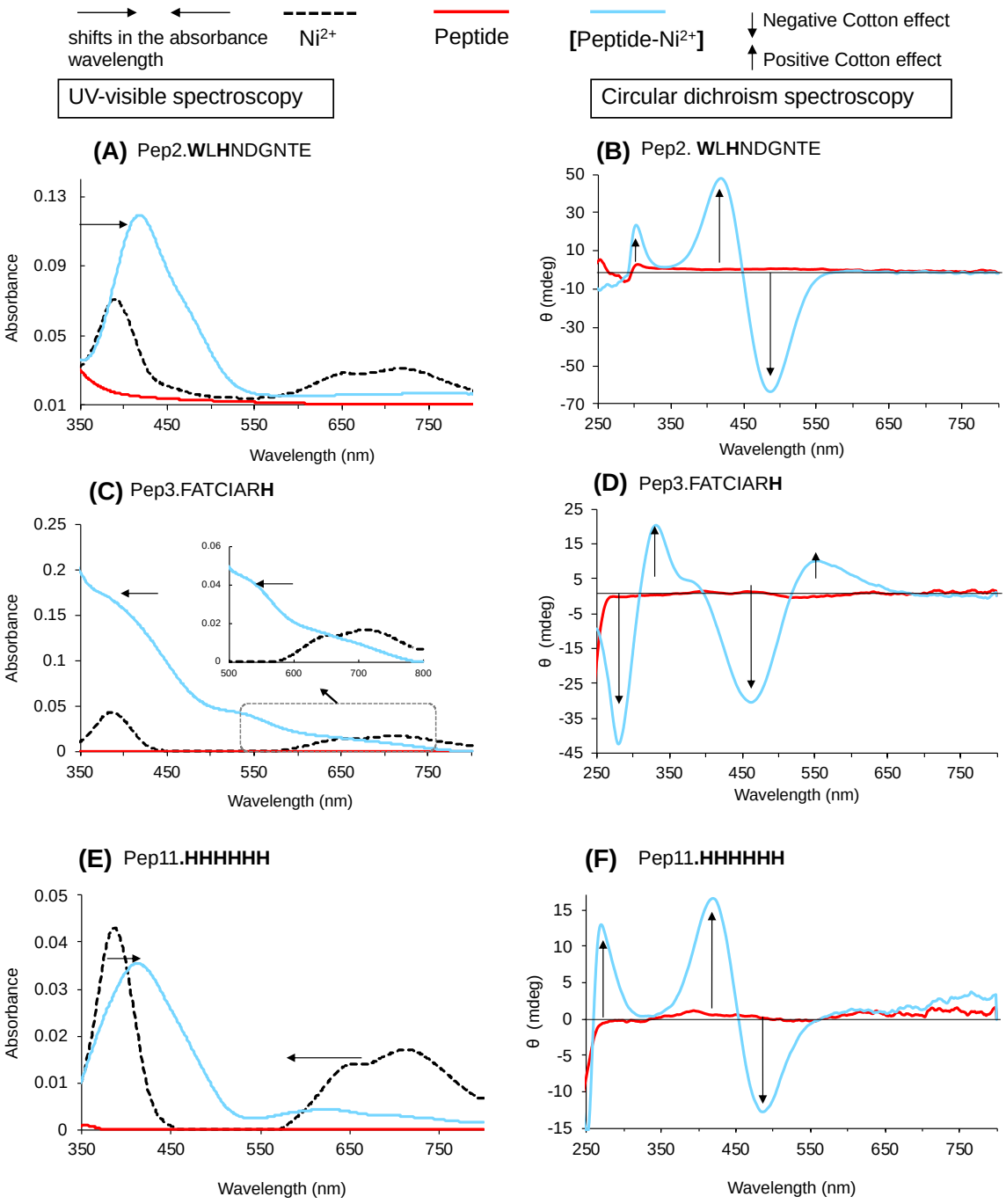

Figure 4.7. UV-visible and CD measurements of the peptide-Ni^{2+} interaction of pure peptides. (A-B) Pep11.**W**L**H**NDTE; (C-D) Pep13.FATCIAR**H**; (E-F) Pep21.**HHHHHH**.

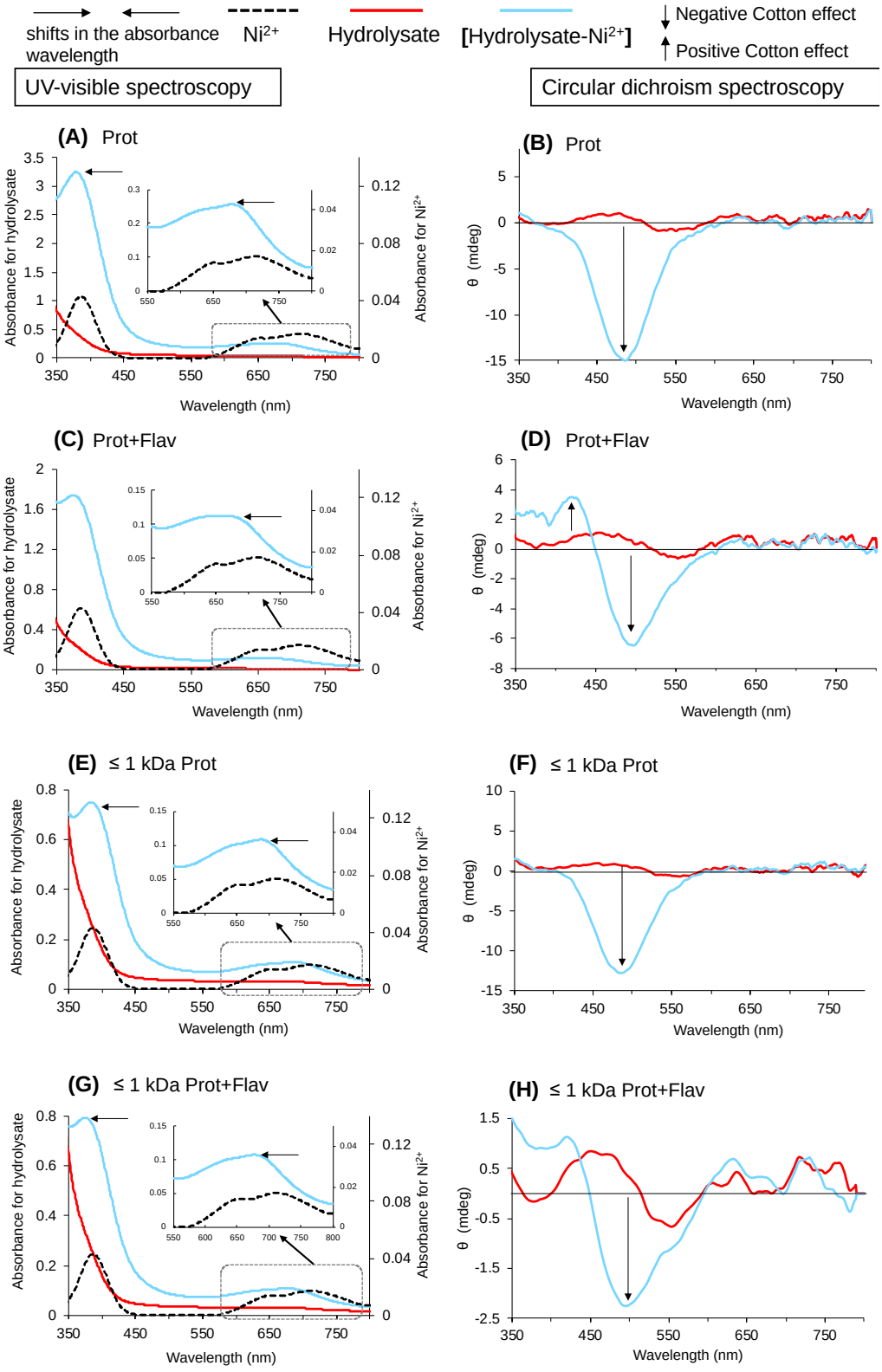

Figure 4.8. UV-visible and CD measurements of the SMPI hydrolysates (A-B) Prot; (C-D) Prot+Flav; (E-F) ≤ 1 kDa Prot; (G-H) ≤ 1 kDa Prot+Flav.

SMPI: sunflower meal protein isolate; Prot: Protamex® hydrolysate; Prot+Flav: Protamex® followed by Flavourzyme®; ≤ 1kDa: 1 kDa ultrafiltrated. Horizontal arrow indicates shift in wavelength after formation of peptide-Ni^{2+} complex.

Besides, the CD profile of Pep3.FATCIAR**H**, characterized by its His residue at first position from C-terminus, shows two bands at 280 nm (- Cotton effect) and 337 nm (+ Cotton effect), and also two distinct bands in the visible region at 462 nm (- Cotton effect) and 553 nm (+ Cotton effect), suggesting a different binding mode compared to Pep11 and 2 (**Figure 4.7D**). In the case of this oligopeptide containing only a single histidyl residue, the simultaneous coordination of Ni(II) ion by the N-terminus and the imidazole-N donor atom in C-terminal location provides the possibility of macrochelation. At physiological pH the amide deprotonation can start from both termini forming 3N ({NH_2, $2N^-_{amide}$} or {$N_{imidazole}$, $2N^-_{amide}$}) or 4N ({NH_2, $3N^-_{amide}$} or {$N_{imidazole}$, $3N^-_{amide}$}) species characterized by this specific CD profile. Since for group II peptides (Pep5.AIPTGTA**H**, 6.KFPILE**H**, 7.KFPILE**H**L and 8.KFPILE**H**LR) where the presence of proline in the 3rd position from N-term does not allow the successive amide deprotonation, no measurable CD spectral was observed, confirming the hypothesis that for Pep3.FATCIAR**H** this deprotonation can only occur at the N-term. However, we cannot completely exclude the coordination of imidazole because for Pep10.LLAF of group III also no modification was observed on the CD spectrum demonstrating that no amide deprotonation occurs from the N-term.

Hydrolysates. As shown in **Figure 4.8A-H** and **Table 4.3**, upon the Ni^{2+} complexation through peptides present in SMPI hydrolysates and their ≤ 1 kDa fractions, the formation of peptide-Ni^{2+} complex results in a very slight blue shift of the d-d transition band centred at 390 nm. Additionally, some variation is evidenced on the two initial bands at 652 and 713 nm from Ni^{2+} alone to a single broad band around 668-688 nm (Figure **4.8A, C, E, F**). This finding agrees with the observation reported by Matys et al., (2022), who found two d-d transition bands shifts between 370 and 690 nm upon the formation of CNAK**H**HPRCGGG- Ni^{2+} complex in the UV-vis spectrum.

Our spectral data shows that the formation of peptide-Ni^{2+} complex could occur in a similar manner for all the four studied hydrolysates. These UV-vis profiles can be attributed to an octahedral geometry coordination (absorbance around 370-390 and 600-700nm, Conato et al., 2001; Krezel et al., 2006), but in a mixture containing several Ni^{2+} coordinating peptides, it is difficult to identify a single coordination type. The measured spectrum is the addition of different individual spectra probably representing different type of coordination mode at physiological pH. However, CD data analysis (**Figure 4.8B, D, F, H**) can provide more

information of the binding properties in these peptides mixture. One main band is observed with a negative Cotton effect around 484-500 nm and a weak positive band at 420 nm only for Prot+Flav hydrolysate.

Comparing these spectra with the CD profiles of synthetic Pep11.**HHHHHH**, Pep2.**W**L**H**NDGNTE and Pep3.FATCIAR**H**, we can conclude that in all hydrolysate the presence of {NH_2, $2N^-_{amide}$, $N_{imidazole}$} coordination observed for Pep11.**HHHHHH** and Pep2.**W**L**H**NDGNTE (**Figure 4.9**, WLH-Ni^{2+} 4N complex), as well as the Pep3.FATCIAR**H**-type coordination mode are presents but this latter is more predominant in Prot hydrolysate as the observed maximum is slightly blue shifted (**Table 4.3**). This hypothesis can be supported by the identified Ni^{2+}-binding peptides found in the F2 (elution phase) of SMPI hydrolysates (IMAC-Ni^{2+} separation followed by LC-MS/MS analysis, **Table 4.2**). Based on these data, the Prot hydrolysate contains more peptide having the sequence with histidine at the C-terminal, such as GAA**H**W, GAV**H**W or AIQSP**H**WT which are disappeared upon sequential treatment.

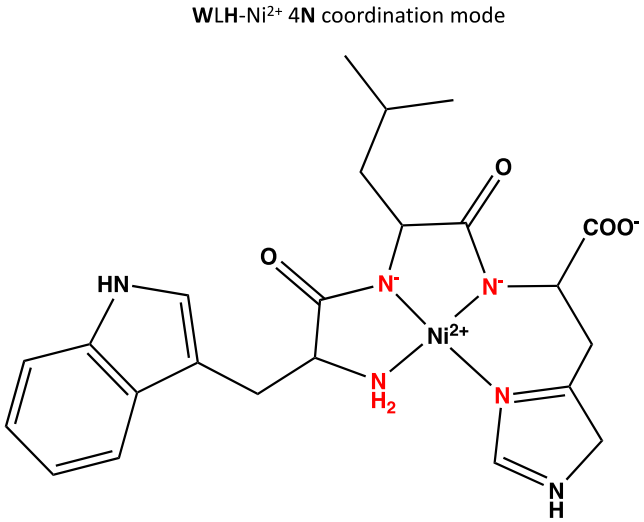

Figure 4.9. Schematic representation of the 4N coordination mode of ATCUN peptide identified in Prot hydrolysates (WL**H**). This peptide motif WL**H** is present in two synthetic studied in the present work (Pep1.**WLH**NDGN, 2.**WLH**NDGNTE).

4.4 Conclusions

Due to the efficiency and selectivity of IMAC technique, SMPI hydrolysates were enriched in Ni^{2+}-binding peptides. All peptide fractions eluted (with imidazole gradient) from the Ni^{2+}-IMAC column contained His residue, which could offer a high promising Ni^{2+}-binding ability. In all the hydrolysates, several peptide sequences identified using LC-MS/MS analysis evidenced the presence of His residue at different position from C and N-termini; nevertheless, the most interesting Ni^{2+}-binding sequences were characterized by their "ATCUN" motif (*i.e.,* WL**H** and LL**H**VT). Indeed, these latter sequences were only found in Prot hydrolysates (whole and <1 kDa), suggesting that Prot+Flav sequential treatment could negatively impact the production of potential metal-binding peptides. Moreover, although IMAC technique provided overall view of Ni^{2+}-binding ability of peptides, no statistically significant difference was found between His-containing synthetic peptides by this separation technique. Therefore, thanks to the complementary information about the Ni^{2+}-binding ability of peptides provided by switchSENSE® technology in static and dynamic modes, we concluded that Pep1.**W**L**H**NDGN, 2.**W**L**H**NDGNTE and 3.FAT**C**IAR**H** showed better Ni^{2+}-binding than Pep5.AIPTGTA**H**, 6.KFPILE**H**, 7.KFPILE**H**L and 8.KFPILE**H**LR, where Pro residue could attenuate such ability. Furthermore, the combined application of UV-vis and CD spectroscopic techniques allowed to describe the coordination geometry as well as the binding modes of formed pepide-Ni^{2+} complex, which varied according to the nature of the coordinating donor atoms. Overall, the results show that sunflower peptides produced either by hydrolysis or by synthesis, formed peptide-Ni^{2+} complexes characterized by both octahedral and square-planar geometries. These conformations can be given through nitrogen atoms donor from deprotonated amide and imidazole as well as through the terminal NH_2. Finally, this study provided clear evidence that sunflower meal by-product is a valuable food-derived protein source for the production of Ni^{2+}-binding peptides. Peptide sequences highlighted in our study could exhibit a high potential to be used as Cu^{2+}-target drug candidates, thus further studies using *in vivo* system should be carried out to validate their potential.

Chapter 5. Sunflower Metal-Chelating Peptides derived from Sunflower Meal Protein: Preparation, Isolation and Antioxidant Properties

After demonstrating the potential of sunflower meal (SM) by-product to produce Ni^{2+}-chelating peptides with interesting amino acid sequences from food-derived protein hydrolysates and understanding the coordination geometry and binding modes of the SM-derived peptide-Ni^{2+} complexes described in **Chapter 4**, the **Chapter 5** now describes the physico-chemical properties and the wide range of metal-related antioxidant activities of SMPI hydrolysates using OPA quantification, SDS-PAGE, SEC, ascorbate tests (Cu^{2+}/Fe^{3+}), Fe^{2+}-chelating, ABTS radical scavenging and reducing power assays. Besides, based on many similarities already described between Ni^{2+} and Cu^{2+} ions complexing processes, Cu^{2+}-chelating peptides present in SMP hydrolysates were fractionated using IMAC-Cu^{2+} and then identified by LC-MS/MS in order to better understand the peptide sequence and metal-related antioxidant property relationship.

This Chapter will be submitted to the *Journal of Agricultural and Food Chemistry* as:

Camaño*, J.A., Mathe, C., Arnoux, P., Stefan, L., Paris, C., Selmeczi, K., Udenigwe, C., Canabady-Rochelle*, L. Metal-Chelating Peptides Derived from Sunflower Meal Protein: Preparation, Isolation, Identification and Antioxidant Properties.

5.1 Introduction

Sunflower (*Helianthus annuus* L.) is the 3rd ranking oilseed after soybean and rapeseed in terms of volumes with a worldwide production of 53.5 million tons in 2019 (Náthia-Neves & Alonso, 2022). Obtained after sunflower seed oil extraction, the meal residue contains approximately 30-50 % proteins. Due to its high protein content and bioavailability, sunflower meal is a potential source of biomaterials for a broad range of food applications, particularly for bioactive peptides production. Initially encrypted within primary protein sequence under an inactive form, bioactive peptides (BAPs) can be released by proteolysis. They have gained considerable attention owing to their diverse health benefits. Sunflower meal protein produced hydrolysates were reported to possess immune-modulating (Velliquette et al., 2020), angiotensin-converting inhibiting (Sentís-Moré et al., 2022), antioxidant and anti-inflammatory activities (Tonolo et al., 2024).

In food protein hydrolysates, metal-chelating peptides (MCPs) can be generated from a variety of protein sources, such as milk, eggs and fish (Camaño Echavarría et al., 2024). Based on a sustainable development perspective and utilization of biological resources, many studies have focused on by-product and plant proteins. This presents tremendous potential for the production of MCPs due to their high protein content and their potential high-added value after proteolysis (Tonolo et al., 2024). Several plant-based proteins such as rapeseed (Xie et al., 2015), defatted walnut flake (Lv et al., 2017) and chia seed (Latha et al., 2021) were reported for producing zinc, iron and copper-chelating peptides, respectively. Meanwhile, MCPs were rarely investigated in sunflower protein hydrolysate (Bao et al., 2021; Dabbour et al., 2019; Megías et al., 2008).

MCPs are characterized by their capacity to form coordination complexes with metals such as Ca^{2+}, Zn^{2+}, $Fe^{2+/3+}$ and Cu^{2+}. These biofunctional peptides have widely been proposed as potent alternatives to combat metal-related diseases (Camaño Echavarría et al., 2024). Indeed, MCPs can be used as delivery agents for enhancing the stability, absorption, and bioavailability of minerals (Guo et al., 2015). Additionally, by complexing Fe^{2+} and Cu^{2+}, MCPs could efficiently mitigate oxidative damage associated with chronic diseases. Indeed, iron and copper ions have the potential to catalyze the production of ROS *via* the Fenton and Haber Weiss reactions, triggering radical chain reactions that can damage biomolecules and thus, induce

various diseases (degenerative, neurological, cardiovascular and cancer) (Canabady-Rochelle et al., 2018).

MCPs can be separated using immobilized metal ion affinity chromatography (IMAC). This separation technique is based on the affinity of some peculiar amino acids (AA) residues present in peptides for some transition metal ions (*e.g.,* Cu^{2+}, Ni^{2+} or Co^{2+}) immobilized onto the chromatographic phase. Due to its high selectivity, high binding capacity and high recovery, IMAC is a powerful purification methodology for MCPs in food-derived protein hydrolysates (Xie et al., 2015). Zhu et al., (2015) and Xie et al., (2015) purified and identified zinc-chelating peptides from wheat germ and rapeseed hydrolysates, respectively, using Zn^{2+}-IMAC. More recently, Bao et al., (2021) used IMAC-Ca^{2+} to purify calcium-binding peptides from sunflower meal hydrolysates, whereas Latha et al., (2021) separated IMAC-Cu^{2+} and identified metal-chelating peptides from chia seed proteins.

To the best our knowledge, there are only a few reports on the use of sunflower meal for producing MCPs (Bao et al., 2021; Dabbour et al., 2019; Megías et al., 2008). Although Cu^{2+}-chelating peptides were produced from sunflower meal protein hydrolysate (Megías et al., 2008), the peptide sequences or their metal-related antioxidant activities were not identified. Besides, there are no reports on purification and identification of Cu^{2+}-chelating peptides from sunflower meal protein hydrolysate generated from sequential enzymatic treatment.

Thus, this study aims to evaluate sunflower meal as a source of protein to produce Cu^{2+}-chelating peptides in hydrolysates obtained by single and sequential enzymatic treatments. This study focused on protein extraction, hydrolysis, physico-chemical and biofunctional characterization of the resulting hydrolysates, as well as peptide fractionation and sequence identification using IMAC- Cu^{2+} followed by LC-MS/MS analysis.

5.2 Materials and methods

5.2.1 Chemicals and equipments

Sunflower meal (**SM**) was provided by SAS IMPROVE (Dury, France). Protamex® (Prot, protease from *Bacillus* sp., ≥ 1.5 U/g), Flavourzyme® (Flav, protease from *Aspergillus oryzae*, ≥ 500 U/g), 37 % hydrochloric acid (HCl), 97 % sulfuric acid (H_2SO_4), nitric acid (HNO_3), ammonium bicarbonate, *o*-Phthalaldehyde (**OPA**), N,N-dimethyl-2-mercaptoethyl

ammonium, sodium tetraborate, sodium dodecyl sulfate, glycine, monobasic potassium phosphate, and all the antioxidant testing chemicals, including ethylenediaminetetraacetic acid (Na_2**EDTA**, $\cdot 2H_2O$), carnosine, 3-(2-Pyridyl)-5,6-diphenyl-1,2,4-triazine-p,p'-disulfonic acid monosodium salt hydrate 97% (ferrozine), ferrous chloride solution ($FeCl_2$) 2,2'-azinobis (3-ethylbenzothiazoline-6-sulfonic acid) diammonium salt (**ABTS**), 6-hydroxy-2,5,7,8-tetramethylchroman-2-carboxylic acid (**Trolox**®), potassium persulfate, potassium ferricyanide, trichloroacetic acid (**TCA**), ferric chloride ($FeCl_3$), iron(III) ferrocyanide $Fe_4[Fe(CN)_6]_3$ (Prussian blue), ascorbic acid were purchased from Sigma–Aldrich (St Louis, MO, USA). All the other reagents were analytical grade and purchased from VWR International (Atlanta, USA): copper (Cu^{2+}) sulfate pentahydrate, potassium sulfate, sodium phosphate monobasic-NaH_2PO_4, sodium phosphate dibasic-Na_2HPO_4, $Na_2HPO_4 12H_2O$, sodium chloride, 99% HEPES ($C_8H_{18}N_2O_4S$), and copper (Cu^{2+}) chloride hydrate. The PolyEthylenGlycol molecular standards (PEG: 200, 600, 1000, 3000 and 8000 Da) were purchased from Sigma–Aldrich (St Louis, MO, USA).

All the spectrophotometric measurements were performed using a MRX Multiskan Go microplate reader (ThermoFicher Scientific, Vantaa, Finland) and 96-well microplates NunclonTM delta surface (Thermo scientific, Roskilde, Denmark).

5.2.2 Production of sunflower meal protein isolate

Sunflower meal protein isolate (**SMPI**) was obtained using the method reported by Kalpana et al., (2020) based on NaCl extraction to solubilize the majority of globulins proteins, and avoid undesirable colour change of the extract due to the oxidation of phenolic compounds. Sunflower meal (30 g) was dissolved into a 1:10 (g/ mL) meal-to-ultra-pure water ratio, added with 10 % (w/v) of NaCl. Then, this former solution was stirred (60 min, 40 °C, and pH 6). After solubilization, the samples were cloth filtrated in order to remove solidified residual fibrous. The resulting solution was centrifuged (Centrifuge Universal 320, Hettich, Tuttlingen, Germany) for 10 min, at 20 °C and 3300 g. Afterward, the resulting supernatant composed of solubilised proteins was recovered and filtrated by vacuum filtration to remove the solid residues remaining from solubilisation. The filtrated supernatant was precipitated by adjusting the pH at 4.5 within 10 min, corresponding to the isoelectric point of sunflower proteins (Dabbour et al., 2019). This suspension was kept for 30 min at room temperature (25

°C), and then centrifuged (3300 g, 10 min, 20 °C). The pellet was finally dried using a convective oven (Thermo ScientificTM, USA) at 55 °C overnight. SMPI was stored at -20 °C until further use.

5.2.3 Enzymatic hydrolysis

Sunflower meal protein isolate hydrolysates were obtained as previously described with some modification (El Hajj et al., 2023). First, SMPI was dissolved in 250 mL of 50 mM ammonium bicarbonate buffer solution, and then hydrolysed with Protamex® (**Prot**), Flavourzyme® (**Flav**), and Protamex® followed by Flavourzyme® (**Prot+Flav**) using their optimal conditions, respectively. Hydrolysis parameters were as follows: 2 % (w/v) SMPI concentration, 1 % (w/w) enzyme/substrate ratio, pH 8, 2 h, and 55 °C for Protamex® while pH 7, 2 h, and 55 °C were used for Flavourzyme®. Upon hydrolysis, pH was maintained at the desired values by adding 1 M NaOH. After each hydrolysis step, each protease was heat inactivated (95 °C, 15 min). In sequential treatment, Protamex® was inactivated just before Flavourzyme® treatment. Then, hydrolysates were centrifuged (10 000 g, 15 min, 25 °C) and the whole hydrolysates fractions were freeze-dried (LABCONCO, Kansas City, USA) and stored at −20 °C for further analysis.

Considering our initial results, the two hydrolysates with the highest degree of hydrolysis (Prot and Prot+Flav) were further dissolved (250 mL; 20 mg/mL in ultrapure water) and submitted to ultrafiltration under magnetic stirring and 5 bar of nitrogen pressure (El Hajj et al., 2023). The ultrafiltration unit (UF stirred cell 47-mm system XFUF04701; Millipore, Molsheim, France) was initially equipped with a 10-kDa molecular weight cut-off membrane (MWCO), followed by a 1-kDa cut-off membrane (Millipore, Billerica, USA), conditioned according to the manufacturer's specification, before ultrafiltration. The ultrafiltrated fractions of hydrolysates (≤ 1 kDa Prot and ≤ 1 kDa Prot+Flav fractions) were freeze-dried and kept at −20 °C until further analysis.

5.2.4 Physico-chemical characterization

5.2.4.1 OPA quantification and degree of hydrolysis

The peptide concentration expressed as mmol equivalent of primary amine groups per gram of hydrolysate (mmol eq. NH_2/g) was evaluated by *o*-Phthalaldehyde (**OPA**) quantification

according to Canabady-Rochelle et al., (2018). The degree of hydrolysis (**DH**) was determined exclusively for the whole hydrolysates (non-ultrafiltrated ones) through OPA quantification and expressed as the ratio of free amino groups present in the hydrolysate to the total amino groups present in the sample. The latter was derived from the complete hydrolysis of sunflower protein (6 N HCl, ratio 1:1 w/v, 130 °C, 24 h), with the assumption that all peptide bonds of the protein were cleaved during acid digestion (El Hajj et al., 2023). The DH was determined by the Equation 1.

$$\text{Degree of hydrolysis } (\%) = \left[\frac{\text{NH}_2\,\text{x} - \text{NH}_2\,0}{\text{NH}_2\,\text{T} - \text{NH}_2 0}\right] \text{X } 100 \qquad (1)$$

Where: NH_2 X is number of free-NH_2 groups at final time of enzymatic hydrolysis, NH_2 0 is number of free-NH_2 groups before hydrolysis, and NH_2 T is NH_2 after complete hydrolysis.

5.2.4.2 Molecular weight distribution

5.2.4.2.1 SDS-PAGE profile

The molecular weight profile of SM, SMPI and SMPI hydrolysates were studied using sodium dodecyl sulphate polyacrylamide gel electrophoresis (**SDS-PAGE**), following the procedure described by Zilic et al., (2010) in a Mini-Protean tetra cell electrophoresis system (Bio-Rad Laboratories, Hercules, USA). Samples were prepared at 20 mg/mL in ultrapure water and the solubilized protein solutions were mixed at a 1:4 (v/v) ratio with sample buffer. This sample buffer consisted of 0.5 M Tris-HCl, pH 6.8, with 10% (w/v) SDS, 50% (v/v) glycerol, and 0.05% (w/v) bromophenol blue along with 0.5% (w/v) 2-mercaptoethanol as a reducing agent. These mixtures were heated at 100 °C for 5 min. Subsequently, 10 µL of each sample (equivalent to 40 µg of protein) or molecular weight markers (Catalog No: 26619, Thermo Scientific™, Vilnius, Lithuania; range: 10–250 kDa) were loaded onto the polyacrylamide gel, consisting in a 7.5 % separation gel and a 5 % stacking gel (Zilic et al., 2010). Electrophoresis was carried out at a voltage of 120 V for 15 min, followed by 180 V for 1 hour. After electrophoresis, the gel was stained for 1 hour using a solution containing 0.16% (w/v) Coomassie blue R-250, 7.5% (v/v) acetic acid, and 5% (v/v) ethanol. Then, the gel was destained for 1 hour using a solution of 30% (v/v) ethanol and 7.5% (v/v) acetic acid.

5.2.4.2.2 Size exclusion chromatography

The molecular weight (**MW**) distribution of the whole hydrolysates (Prot and Prot+Flav) and their ≤ 1 kDa ultrafiltrates (**≤ 1 kDa Prot** and **≤ 1 kDa Prot+Flav**) was analyzed using size-exclusion chromatography (**SEC**) with a 515 HPLC pump (Waters, Milford, MA, USA), a degasser, and a RID 10-A Shimadzu detector, as previously described (El Hajj et al., 2023). The system featured a Phenomenex PolySep-GPC-P 2000 column (300 × 7.8 mm - 8 µm – 200 A - separation range 100 Da – 10 kDa) safeguarded by a guard column (35 × 7.8 mm) linked to a Phenomenex PolySep-GPC-P 1000 column (300 × 7.8 mm - 8 µm – 100 A - separation range 20 Da – 3 kDa). The four previous hydrolysates (5 mg/mL) were loaded (200 µL) and eluted using an aqueous buffer containing 0.1 M sodium nitrate ($NaNO_3$) and 0.2 % (w/v) sodium azide at a flow rate of 0.7 mL/min at room temperature (25 °C). The PEG standard solutions (200, 600, 1000, 3000, and 8000 Da) were similarly injected for SEC calibration. The chromatograms were analyzed using ASTRA® software (Wyatt Technology, Goleta, USA).

5.2.5 Metal-chelating peptide characterization

5.2.5.1 Antioxidant activities

5.2.5.1.1 Ascorbate tests

The ability of hydrolysates to inhibit the ROS generation catalyzed by transition metals (*i.e.,* Cu^{2+}, Fe^{3+}) was investigated by the ascorbate test. In the presence of oxygen, these metals are able to catalyze the ascorbate oxidation and the metal-catalyzed Fenton-type reaction to produce ROS ($O_2^{\bullet-}$, H_2O_2 and $OH^{\bullet}$, Csire et al., 2022). In this assay, Cu^{2+} and Fe^{3+} are reduced into Cu^{+} and Fe^{2+} by ascorbate, respectively; yet, the resulting metal species are unstable and easily oxidized back to Cu^{2+} and Fe^{3+} forms, following the redox cycle of the metal ions (Pradhan et al., 2020). Ascorbate (**$AscH^-$**) solution was prepared at 5 mM using 50 mM HEPES buffer at pH 7.4. Stock solution of Cu^{2+} and Fe^{3+} were prepared at 2 mM using $CuCl_2$ (in ultrapure water) and $FeCl_3$ (in 0.1 M HNO_3 acidic solution to maintain the Fe^{3+} in solution). EDTA (positive control in Cu^{2+} assay, and negative control in Fe^{3+} assay), and desferrioxamine (**DFO**, positive control in Fe^{3+} assay) were prepared at 2 mM in order to reach a final concentration of the components at 100 µM, with 1: 1: 1 $AscH^-$: ligand: Cu^{2+}/Fe^{3+} ratio, whereas, SMPI hydrolysates were prepared at 5 mM (eq NH_2 according to OPA assay), with 1: 5: 1 $AscH^-$: ligand: Cu^{2+}/Fe^{3+} ratio. The reaction was initiated by the introduction of

ascorbate, and the kinetic study of the ascorbate concentration was carried out by following the absorbance at 265 nm (Csire et al., 2022). The results were reported as ascorbate consumed after 2 and 10 min for Cu^{2+} and Fe^{3+}, respectively (ε = 14 500 M^{-1} cm^{-1}). Indeed, ascorbate consumption has a direct correlation with the levels of Cu^{2+} and Fe^{3+} in solution, which can be complexed in the presence of hydrolysates/positive controls. Note that all the measurements were carried out in triplicate.

5.2.5.1.2 Fe^{2+}-chelating activity

The Fe^{2+}-chelating ability of hydrolysates was determined by ferrozine test as described in Canabady-Rochelle et al., (2015) using EDTA (0-0.04 mg/mL) as positive control. Briefly, 7.5 µL of $FeCl_2$ (2 mM) was mixed with 277.5 µL of control or hydrolysate solution (0 to 1 mg/mL in ultrapure water), followed by the addition of 15 µL of ferrozine solution (5 mM) after a 3-minute incubation at room temperature (25 °C). The mixture was allowed to stand for 10 min after shaking. The absorbance of the solution was measured at 562 nm. The iron-chelating activity of the hydrolysates was determined by the Equation 2.

$$\text{Iron chelating activity } (\%) = \left[\frac{A_0 - A_s}{A_o}\right] X\ 100 \qquad (2)$$

A_o is the absorbance of the blank (sample volume replaced by ultrapure water), and A_s is the absorbance of the sample (control/hydrolysates). The half-maximal effective concentration (**EC_{50}**) was determined as the hydrolysate concentration required for 50 % iron chelation activity.

5.2.5.1.3 ABTS scavenging activity

The ABTS radical scavenging activity was determined as described by Canabady-Rochelle et al., (2015) with modifications. 7 mM ABTS stock solution was prepared in phosphate buffer (4 mM, pH 7.4). The solution was maintained in total darkness at room temperature for 16 h before use. Then, an aliquot of the ABTS stock solution was diluted with the buffer to obtain an initial absorbance value of 0.70 ± 0.02 at 734 nm. 150 µL hydrolysate (0-0.4 mg/mL) or Trolox® (0-0.03 mg/mL used as positive control) were mixed with 150 µL ABTS radical, shaking

for 10 s. After 10 min of incubation at 25 °C, the absorbance of the reaction was measured at 734 nm. The ABTS radical scavenging activity was calculated with the Equation 3.

$$\text{ABTS Radical scavenging (\%)} = \left[\frac{A_0 - A_s}{A_o}\right] X\ 100 \quad (3)$$

Where A_0 represents the initial absorbance of ABTS radical solution (sample volume replaced by buffer), and A_s indicates the absorbance of the remaining radical (with samples).

The EC_{50} was determined as hydrolysate/control concentration required for scavenging 50 % of ABTS radical. In addition, the **TEAC** index (Trolox® Equivalent Antioxidant Capacity) was determined from the calibration curve and results were expressed as µmol Trolox® equivalent per gram of sample (µmol TE/g sample).

5.2.5.1.4 Reducing power

The reducing power was measured as reported in Canabady-Rochelle et al., (2015). Hydrolysates (0-3 mg/mL) and positive control (ascorbic acid, 0-1 mg/mL) were prepared in phosphate buffer (0.2 M, pH 6.6). An aliquot of each former dilution (70 µL) was mixed with 35 µL of 1%(w/v) potassium ferricyanide solution and, incubated at 50 °C for 20 min. Then, 135 µL of distilled water, 33 µL of 10% (v/v) trichloroacetic acid solution and 27 µL of 0.1 (w/v) $FeCl_3$ were added. The reduction product, *i.e.,* ferrocyanide, was further stabilized with ferric ions in order to produce Prussian blue. The absorbance was determined at 700 nm after 10 min of incubation at 25 °C. The ability of hydrolysates to reduce Fe^{3+} was expressed in percentage (%) and calculated following Equation 4.

$$\text{Reducing capacity (\%)} = 100 - \left[\frac{A_0 - A_s}{A_o}\right] X\ 100 \quad (4)$$

Where A_o is absorbance of a 66 µM Prussian blue solution in the same reaction medium, and A_s is sample absorbance.

Results were expressed as effective concentration of hydrolysates able to reach 50 % the maximal reducing power capacity (EC_{50}).

5.2.5.2 IMAC-Cu^{2+} experiments

The Cu^{2+}-chelating peptides present in whole and ≤ 1 kDa fractions of hydrolysates were fractionated by IMAC-Cu^{2+} using a HPLC system (LC-20AD, Shimadzu, Japan) at 1 mL/min flow rate, an oven temperature set at 25 °C and a Diode Array Detector (SPD-M20A, Shimadzu, Japan). MCPs were separated on a 1 mL HisTrap™HP column (7 x 250 mm) prepacked with Ni Sepharose High Performance (Cytiva, Marlborough, MA, USA). Experiments were carried out according to Irankunda et al., (2024) with modifications. The method included five steps described below in details: (i) Cu^{2+} regeneration (*i.e.,* Ni^{2+} ions were removed and replaced by Cu^{2+} ions), (ii) equilibration, (iii) injection followed by unbound compounds removal, (iv) elution, and (v) washing.

First, 10 column volumes (**CV**) of ultrapure water were used to remove the ethanol remaining in the column (storage conditions). Then, the column was stripped using 50 mM EDTA solution to remove Ni^{2+} immobilized ions, followed by Cu^{2+} regeneration step using 10 CV of a 0.1 M $CuSO_4.5H_2O$ solution. Then, 20 CV of equilibration buffer (PBS 1X pH 7.4: $Na_2HPO_4.12H_2O$ 6.7 mM; KH_2PO_4 1.25 mM; NaCl 300 mM) were used to remove the unbound copper ions and equilibrate the column. Finally, 50 µL of hydrolysates (20 mM eq NH_2 according to OPA assay) were loaded onto IMAC-Cu^{2+} column. The first fraction (F1) labeled non-copper-chelating peptides was eluted with the equilibration buffer after 5 min in order to remove peptides without metal-chelating properties, then the Cu^{2+}-chelating peptides (F2-F4) were eluted with an imidazole gradient (0-50 mM, prepared in PBS 1X pH 7.4) for 60 min. Finally, a 300 mM imidazole solution was used to wash the columns before the next run. The absorbance of the eluate was monitored at 280 nm. The F1-F4 fractions were collected using a fraction collector (FRC-10A, Shimadzu, Japan) for further LC-MS/MS identification analysis of Cu^{2+}-chelating peptides in hydrolysates.

5.2.5.3 Mass spectrometry identification and sequence analysis

5.2.5.3.1 LC-MS/MS analysis

To identify the peptide sequences present in the produced hydrolysates, the IMAC-Cu^{2+} collected fractions (F1-F4) were analysed on a Thermo Scientific UHPLC-HRMS system composed of a Vanquish™ liquid chromatography unit coupled to a photodiode array detector (PDA) and an Orbitrap ID-X™ Tribrid™ high-resolution mass spectrometer operating

in electrospray positive ionization mode (**ESI$^+$**) as previously reported (Dos Santos Morais et al., 2020).

5.2.5.3.2 Peptide sequences identification

The Thermo Xcalibur raw LC-MS/MS data files resulting from the fractions (F1-F4) collected from the hydrolysates separated in IMAC-Cu^{2+} were processed in the Andromeda search engine of a commonly used proteomic software tools MaxQuant™ (version 2.4.13.0) (Boachie et al., 2022). The peptides sequences were searched against a restricted sunflower seed proteins database (*Helianthus annuus*) containing 30 entries obtained from UniProtKB (https://www.uniprot.org/, accessed on 27 January 2024, **Appendix 4.3**). The peptides identification was achieved by comparing the experimental fragment-ion mass value of the precursor ions with the theoretical fragment masses obtained from the protein sequences data base, obtained by the unspecified digestion rule with a mass tolerance of 10 ppm. The parameters of database searches were set up as previously described (Boachie et al., 2022) (**Appendix 4.4**). Before searching peptides sequences from the collected fraction of hydrolysates, this method was first validated using a synthetic peptides hydrolysate, mixing 8 pure peptides at 1 mM each. These metal-chelating peptides (*i.e.*, AIPTGTA**H**, FATCIAR**H**, KFPILE**H**, KFPILE**H**L, KFPILE**H**LR, WL**H**NDGN, WL**H**NDGNTE, **W**VSFKTN) were obtained from 11S globulin seed storage protein G3 (P19084, 11S3_HELAN) present in sunflower seed. All the 8 peptides were identified (**Appendix 4.5**). Finally, the AA composition of identified MCPs present in SMPI hydrolysates were computed through ExPASy ProtParam server (https://web.expasy.org/protparam/).

5.2.6 Statistical analysis

To evaluate the effect of enzymatic treatments and 1-kDa ultrafiltration process on physical-chemical and biofunctional properties of SMPI hydrolysates, results were statistically analyzed by one-way analysis of variance (ANOVA). All the measurements of OPA quantification and biofunctional properties (Cu^{2+}/Fe^{3+} ascorbate test, Fe^{2+}-chelating, radical scavenging, reduction power and Cu^{2+}-binding abilities) were obtained in triplicate and data presented as means ± standard deviation. Significant differences between means of samples were determined by Fisher's multiple range test. Differences at *p-value* < 0.05 were

considered significant. Statistical calculations were conducted using the software Statgraphics centurion XVI version 16.1.03 (Statgraphics Technologies Inc, Virginia, USA).

5.3 Results and discussions

5.3.1 Physico-chemical characterization of protein hydrolysates

5.3.1.1 Protein content of sunflower meal protein isolate

The sunflower meal (SM) proteins were extracted using a NaCl extraction at pH 6, followed by isoelectric precipitation. The protein content initially present in SM (46.10 ± 0.9 %) increased up to 90.90 ± 2.7 % in SMPI, fulfilling the requirements of protein isolates (> 85 % of protein). Helianthinin *(i.e.,* 11S globulin) is the main storage protein in sunflower meal. The extractability of such protein increases by using NaCl, and upon the isoelectric precipitation at pH 4.5, the 11S globulin can be isolated, resulting in a protein content increase. SMPI obtained has a suitable protein content, and should be further considered as an alternative to obtain hydrolysates. Indeed, the SMPI produced in this study exhibits a similar protein content (90.90 ± 2.7 %) compared to that reported by Alexandrino et al., (2017) (92.08 %-98.6 %).

5.3.1.2 Peptide quantification and degree of hydrolysis

The degree of hydrolysis (**DH**), defined as the percent of peptide bonds cleaved in a protein hydrolysate, is the first parameter used to characterize a hydrolysate. It provides primary information about the peptide size. In our study, we are interested in small-sized peptides, which are commonly reported for their bioactivity.

Hydrolysates were prepared with Protamex® and Flavourzyme®, *i.e.,* complex mixtures of endo-peptidases and endo/exopeptidases, respectively. Due to their low cost, these enzymes are commonly used in the food industry to produce food-derived bioactive peptides. To enhance the hydrolysis of SMPI, a sequential enzymatic treatment was applied (Prot+Flav). After 2 h of hydrolysis, SMPI hydrolysates obtained using Protamex® and Flavourzyme® alone had a DH of 31 and 23 %, respectively (**Table 5.1**). This demonstrates that the endopeptidases contained in Protamex® can hydrolyze more SMPI compared with Flavourzyme®. As endopeptidase, Protamex® is an enzyme widely used in agro-industrial by-products

hydrolysis, with an extensively broad specificity in peptide bond cleavage. Flavourzyme® cleavages peptide bonds between L and P or between two P residues (Bing et al., 2024). Similar trend was reported in other studies, where the DH values of SMPI hydrolysates hydrolysed with Protamex® and Flavourzyme® alone were 10.37-20.05 % (Sentís-Moré et al., 2022) and 5.93- 10.55 % (Bao et al., 2021), respectively.

Table 5.1. The degree of hydrolysis (DH) and peptide concentration of hydrolysates prepared by different enzymatic treatments determined by OPA assay.

Samples	mmol eq. NH_2/g	DH (%)
SMPI	0.39 ± 0.11^{a}	--
Prot	0.89 ± 0.04^{b}	30.96 ± 1.34^{a}
Flav	0.67 ± 0.04^{c}	23.33 ± 1.69^{b}
Prot+Flav	1.23 ± 0.02^{d}	38.80 ± 0.87^{c}
≤ 1 kDa Prot	1.16 ± 0.03^{b}	--
≤ 1 kDa Prot + Flav	3.33 ± 0.01^{e}	--

Different letters indicate in the same column indicate the significant difference between the hydrolysates and their ≤ 1 kDa fractions (*p-value* < 0.05). n=5. Prot: Protamex® hydrolysate; Prot+Flav: Protamex® followed by Flavourzyme® hydrolysate; ≤ 1 kDa: 1 kDa ultrafiltrated hydrolysate

Moreover, considering the specificity of each enzyme, the Flav treatment as endo/exopeptidases was carried out sequentially after the Prot treatment as endopeptidase only to improve the DH. The DH of Prot+Flav hydrolysate increased up to 38 %, significantly higher than that of single enzymatic treatments. Thus, the number of N-terminal sites available for the activity of exopeptidases present in Flavourzyme® was increased by the first hydrolysis step with Protamex®.

Among the produced hydrolysates, Prot and Prot+Flav hydrolysates exhibit the highest DH values and were, therefore, selected for further analysis with their respective ≤ 1 kDa fractions.

The peptide molar concentration expressed as mmol eq. NH_2/g of whole Prot, Prot+Flav hydrolysates and their respective ≤ 1 kDa fractions was studied by OPA assay. The peptide molar concentration increased from 0.39 to 0.89, 0.67 and 1.23 mmol eq. NH_2/g with hydrolysis of the SMPI by Prot, Flav, and Prot+Flav, respectively (**Table 5.1**), indicating the

release of free amino groups from peptides. The peptide molar concentration notably increased in both ≤ 1 kDa fractions up to 1.16 and 3.33 for Prot and Prot+Flav, respectively; however, the most important difference was found in the sequential treatment, where Prot+Flav hydrolysate exhibits the highest amount of small-sized peptides.

5.3.1.3 Molecular weight distribution of peptides

5.3.1.3.1 SDS-PAGE profile

The MW distribution of protein constituents of the SM, SMPI and hydrolysates (Prot and Prot+Flav) was characterized by SDS-PAGE between 10-250 kDa (**Figure 5.1A**). First, the SM electrophoretic pattern shows four major, high-intensity band regions at approximately 35, 25, 20 and 10-15 kDa, corresponding to the 11S globulin subunits (α, α', β) and 2S albumins, respectively. The polypeptide composition of sunflower meal proteins presents a similar pattern to those reported in the literature (Velliquette et al., 2020). Compared to sunflower meal (lane SM), notable changes in MW distribution of the protein isolate (lane SMPI) are observed, especially for the 2S albumins region. This band, representing residual 2S albumins, is of lower intensity due to the protein extraction process used, as 11S globulins are isolated from 2S albumins at their isoelectric point (pH 4.5) (Zilic et al., 2010). Finally, the SDS-PAGE profile of Prot and Prot+Flav hydrolysates shows that the band intensity of 11S globulin subunits decreased, related to their partial Prot hydrolysis, producing peptides with MW range of 10-25 kDa (lane Prot). Finally, for the sequential treatment (lane Prot+Flav), bands with MW higher than 10 kDa disappeared while the bands corresponding to a high number of oligopeptides (< 10 kDa) increased, due to the high proteolytic activity of exopeptidases in Flavourzyme®. These results are in line with those previously discussed for DH.

5.3.1.3.2 Size exclusion chromatography

The size exclusion chromatography (SEC) was used to estimate the molecular MW of the hydrolysates (Prot and Prot+Flav) and their ≤ 1 kDa fractions between 0 and 10 kDa (**Figure 5.1B, C**). Indeed, the peptides MW distribution plays a crucial role in their metal-chelating and antioxidant properties. The enzymatic treatments hydrolyzed the high MW protein of sunflower meal (above 20 kDa) into lower MW peptides (< 10 kDa). The whole hydrolysates

Prot and Prot+Flav exhibit the highest MW distribution in the range of > 3 kDa (45 %) and 0.2-0.6 kDa (64 %), respectively.

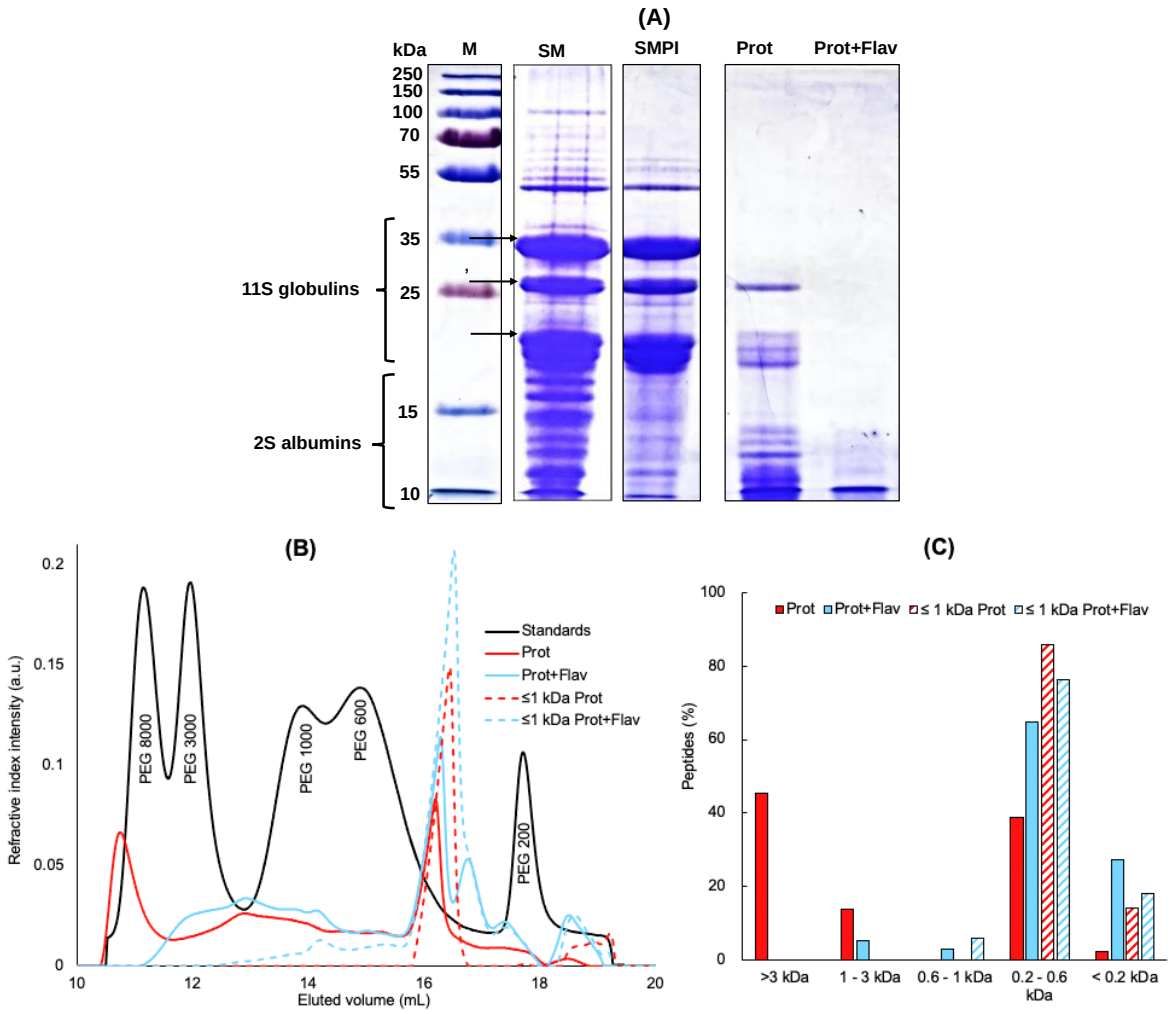

Figure 5.1. Molecular weight distribution of protein and peptides hydrolysates from SMPI. (A) SDS-PAGE profile (12.5 %) of sunflower meal, sunflower meal protein isolate, and whole protein hydrolysates (Prot and Pro). (B) and (C) size exclusion chromatographic profile of sunflower meal protein isolate hydrolysates and their ≤ 1 kDa fractions.

M: Marker; SM: sunflower meal; SMPI: sunflower meal protein isolate; Prot: Protamex® hydrolysate; Prot+Flav: Protamex® followed by Flavourzyme® hydrolysate; ≤ 1 kDa: 1 kDa ultrafiltrated hydrolysate; PEG: Polyethylene glycol.

This finding can be explained by a higher production of small-sized peptides in Prot+Flav hydrolysate (DH: 38.80 %) compared to Prot one (DH: 30.96 %). Besides, in regard to the ≤ 1 kDa MWCO membrane ultrafiltration applied, the highest MW distribution was found from

0.2 to 0.6 kDa, with 76 and 86 % for ≤ 1 kDa Prot and ≤ 1 kDa Prot+Flav, respectively. Thus, it is possible to obtain protein hydrolysates from sunflower meal, enriched with small-sized peptides. Moreover, the SEC analysis is consistent with the DH and SDS-PAGE results. Our findings are in accordance with Sentís-Moré et al., (2022), who reported a Protamex® sunflower hydrolysates, with MW distribution from 0.5 Da to 5 kDa. In contrast, Velliquette et al., (2020) reported sunflower peptides with MW distribution ranging from 10 to 25 kDa after Flavourzyme® only.

5.3.2 Characterization of MCPs in SMPI hydrolysates

5.3.2.1 Antioxidant activities

5.3.2.1.1 Inhibition of Cu^{2+}-induced ROS production

Ascorbate test was used to evaluate the effect of Cu^{2+}/Fe^{3+} complexation by MCPs present in hydrolysates on the inhibition of ROS production (*i.e.,* $O_2^{\bullet-}$, $HO^{\bullet}$) generated through Fenton-type reaction at physiological pH 7.4 (**Figure 5.2A**) (Csire et al., 2022; Pradhan et al., 2020).

The ascorbate test results for the inhibition of Cu^{2+}-induced ROS production are presented for all the obtained hydrolysates and expressed as ascorbate consumed after 3 min (**Figure 5.2B**). The negative control (buffer) displays the highest ascorbate consumption, associated with its oxidation into dehydroascorbic acid, with a value of 46.5 µM, indicating the maximal ROS production. In the same test, the positive control, *i.e.,* EDTA, clearly showed the lowest ascorbate consumption, which is related with its strong Cu^{2+}-chelating ability. Compared to the negative control, all the whole and ≤ 1 kDa fraction samples significantly (*p-value* < 0.05) decreased the absorbate consumption. This indicates that, after Cu^{2+} complexation by peptides present in hydrolysates, Cu^{2+} was unable to catalyze the Fenton-type reaction to produce ROS in the redox cycle. The differences observed between hydrolysates can be attributed to the differences in peptide composition (peptide length, amino acid sequences). Interestingly, Prot hydrolysates (whole and ≤ 1 kDa fraction) present the most potent Cu^{2+}-chelating peptides. Copper-chelating ability could be associated with various amino acid residues such as His, Cys and Arg, as reported in sunflower protein (Megías et al., 2007; Megías et al., 2008) and rice-bran-derived albumin hydrolysates (Kubglomsong et al., 2018). Interestingly, the DH increase in the Prot+Flav sequential treatment does not enhance the Cu^{2+}-chelating ability, suggesting that Cu^{2+}-chelating sites have been destroyed upon

sequential hydrolysis. Similar results were reported by Carrasco-Castilla et al., (2012) who produced lectin hydrolysates, whose Cu^{2+}-chelating activity decreased after extensive hydrolysis. Yet, Peng et al., (2010) reported that Cu^{2+}-chelating activity of whey protein hydrolysates increased with increasing DH (from 19.3 to 38.5 %). Moreover, small-sized peptides obtained after the 1 kDa MWCO ultrafiltration possessed a poor ROS inhibition associated with a lower Cu^{2+}-chelating ability (higher ascorbate consumed).

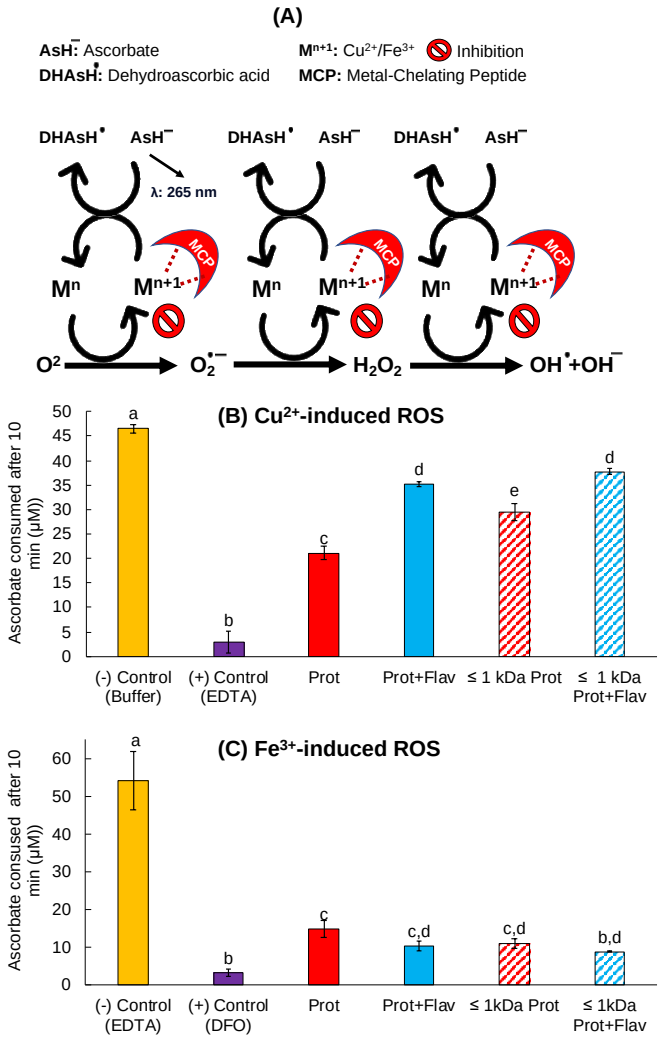

Figure 5.2. (A) The process for generating reactive oxygen species (ROS) *via* the Fenton reaction cycle involves molecular oxygen and ascorbate in the presence of copper and iron ions. (B-C) The inhibition of Cu^{2+}/Fe^{3+}-induced ROS production by chelating copper assessed by measuring ascorbate absorbance intensity at 265 nm.

Error bar corresponds to the standard deviation. Different letters indicate the significant difference between samples (*p-value* < 0.05). n=3. $AscH^-$: ascorbate; DFO: Deferoxamine; Prot: Protamex® hydrolysate; Prot+Flav: Protamex® followed by Flavourzyme® hydrolysate; ≤ 1 kDa: 1 kDa ultrafiltrated hydrolysate.

5.3.2.1.2 Inhibition of Fe^{3+}-induced ROS production

The Fe^{3+}-induced ROS production of all hydrolysates expressed as ascorbate consumed after 10 min (**Figure 5.2C**) was different from the Cu^{2+}-induced ROS production. Here, EDTA, used as negative control agent, showed the maximum ascorbate consumption (54 µM) while the ascorbate consumption decreased drastically to 3 µM (lowest value) for DFO, a positive control highly recognized as a Fe^{3+}-chelating agent. Regarding the hydrolysates, the ascorbate consumption decreased notably to the range 8-14 µM, suggesting that all the produced hydrolysates and their ≤ 1 kDa fractions contain Fe^{3+}-chelating peptides. The ability to complex Fe^{3+} to prevent ROS production is notably associated with the abundance of small-sized peptides in the hydrolysates. For instance, the whole Prot+Flav and both ≤ 1 kDa fractions hydrolysates, all characterized by their high concentration of peptide expressed as mmol eq. NH_2/g of powder (OPA assay, **Table 5.1**) and correlated with their higher small-sized peptide (**Figure 5.1C**) compared to Prot hydrolysate, showed greater potential to prevent Fe^{3+}-induced ROS production than the whole Prot hydrolysate. Yet, this observed difference is only significant for the ≤ 1kDa Prot+ Flav hydrolysate. The Fe^{3+}-chelating ability is mostly influenced by factors such as MW, AA composition and their position within the sequence. Peptide sequences with abundance of negatively charged polar residues (Asp and Glu) can complex Fe^{3+} through carboxylate groups (Csire et al., 2022). Additionally, the MW of peptides with Fe^{3+}-chelating properties usually ranges from 300-1500 Da, associated with a higher amount of carboxyl group available at each terminus of a peptide compared to larger-sized peptides. Verma et al., (2017) reported a range of highest to lowest extent of Fe^{3+}-AA interaction as follows: Glu > Asp > His > Cys > Tyr > Gln > Lys > Asn > Ser > Trp, Leu, Arg, Ala. These AA residues have been reported in the literature for sunflower meal and sunflower meal protein hydrolysate (Dabbour et al., 2019; Ugolini et al., 2015). Based on our results, MCPs present in hydrolysates can complex Cu^{2+}/Fe^{3+} in solution, leading to the inhibition of metal-induced ROS generation.

5.3.2.1.3 Fe^{2+}-chelating activity

The ferrous state of iron (Fe^{2+}), one of the most important pro-oxidant agents, catalyzes ROS production through the Fenton reaction. Therefore, food-derived peptides endowed with iron-chelating properties may contribute to delay peroxidation and subsequently prevent cells and tissues damages (Wang et al., 2021). The Fe^{2+}-chelating activity of the hydrolysates

and their ≤ 1 kDa fractions was assessed by ferrozine test and expressed as EC_{50} (mg/mL) (**Figure 5.3A-B**). The lower the EC_{50} value, the higher the Fe^{2+}-chelating activity. For the whole hydrolysates, Prot hydrolysate showed higher Fe^{2+}-chelating activity than Prot+Flav ones. Indeed, the EC_{50} value increased significatively from 0.09 (Prot) to 0.82 mg/mL (Prot+Flav) after the sequential enzymatic treatment, meaning lower Fe^{2+}-chelating activity of the hydrolysate. Also, this suggests that sequential treatment using Flavourzyme® hydrolyzed a high number of MCPs peptides already produced by Prot. Regarding the two ≤ 1 kDa fractions, the same trend was found for both enzymatic treatments. Indeed, the EC_{50} value of ≤ 1 kDa Prot+Flav could not be determined, as the activity was lower than 7 % in the range of concentration investigated (0-1 mg/mL). The Fe^{2+}-chelating activity was related with the presence of specific AA residues in the peptide sequence, such as negatively charged amino acids (Asp, Glu) and neutral polar amino acids (His, Cys) (Verma et al., 2017). Indeed, these AA were widely reported in sunflower meal and sunflower meal hydrolysates (Dabbour et al., 2019; Ugolini et al., 2015).

Our results demonstrate that the Fe^{2+}-chelating ability of hydrolysates is notably influenced by the MW distribution of peptides, where small-sized peptides (≤ 1 kDa) may not have enhanced this property. The high Fe^{2+}-chelating activity of Prot hydrolysate would be rather associated with the higher content of large-sized peptides than in Prot+Flav hydrolysate, where the enzymes can expose more efficient sites available for Fe^{2+}-chelation. Tang et al., (2009) found that the Fe^{2+}-chelating activity was affected negatively by significant decreases in peptide chain length due to extended hydrolysis in hemp (*Cannabis sativa L.*) protein isolate. Similarly, in He et al., (2013), the whole hydrolysates and its 5-10 kDa fraction obtained from rapeseed protein exhibited the highest Fe^{2+}-chelating activity (lower EC_{50} values).

In our study, Prot hydrolysates (whole and ≤ 1 kDa fraction) exhibited a stronger Fe^{2+}-chelating properties (lower EC_{50} values, EC_{50}: 0.09-0.10 mg/mL) compared to those reported in the literature for other hydrolysates from vegetable-derived proteins, including rapeseed protein (EC_{50} values > 3 mg/mL; He et al., 2013), tree peony seed protein hydrolyzed by Alcalase®, Neutrase® and Papain enzymes (EC_{50}: 0.99-1.18 mg/mL; Wang et al., 2021), mung bean protein (EC_{50}: 0.22-0.55 mg/mL; Liu et al., 2022), and *Lentinus edodes* protein (EC_{50}: 0.99-2.7 mg/mL; Bing et al., 2024). Taken together, these findings suggest that Prot

hydrolysates could be good metal-chelating agents to prevent the oxidative damages caused by ferrous ion in food and biological systems.

5.3.2.1.4 ABTS scavenging activity

The ability of hydrolysates to donate a hydrogen atom or an electron to scavenge free radicals was determined by measurement of ABTS radical scavenging activity (**Figure 5.3C-D**). The hydrolysates and their ≤ 1 kDa fractions exhibited dose-dependent ABTS radical scavenging activity from 0.02-0.4 mg/mL. The highest activity was reached at 0.4 mg/mL (> 87 %) (**Figure 5.3C**). With extended hydrolysis in Prot+Flav, a slight increase (*p-value* < 0.05) in EC_{50} value is observed, meaning a loss of ABTS radical activity (**Figure 5.3D**). Thus, during the sequential use of Flavourzyme®, some ABTS radical scavenging peptides produced in Prot may be cleaved further, leading to the decrease of this antioxidant property. Additionally, among the ≤ 1 kDa fractions, no significant difference was observed (*p-value* > 0.05), suggesting that neither sequential treatment nor ≤ 1 kDa ultrafiltration enhanced the ABTS radical scavenging ability of the hydrolysates.

The ABTS radical scavenging activity of hydrolysates could be attributed to peptides containing Phe, Tyr, Trp, Cys and His, with their benzyl, phenolic, indoyl, sulfhydryl, and imidazole groups, respectively (Wen et al., 2020). In our study, the EC_{50} values of all the studied hydrolysates were lower (better activity) than those of peptides from vegetable-derived proteins hydrolysed by Protamex® (tree peony seed protein, EC_{50}: 1.81 mg/mL; Wang et al., 2021); mung bean proteins, EC_{50}: 0.24 mg/mL; Liu et al., 2022).

Furthermore, data were also reported as µM Trolox equivalent per gram of sample (µmol TE/g) to compare our results with other studies (**Figure 5.3D**). In TEAC analysis, the higher the value, the higher the ABTS radical scavenging activity. Overall, SMPI hydrolysates and their ≤ 1 kDa fractions scavenged the ABTS radical effectively resulting in antioxidant activity. The TEAC value of Prot hydrolysate, which displays the highest radical scavenging activity, is higher than those of peptides from hydrolysate of hemp seeds (124-240 µM TE/g; Yoon et al., 2023), and similar to those of colocynth seeds (290-525 µM TE/g; Alblooshi et al., 2023). In contrast, higher values were reported for canola proteins (5.45 mM TE/g; Bermejo-Cruz et al., 2023).

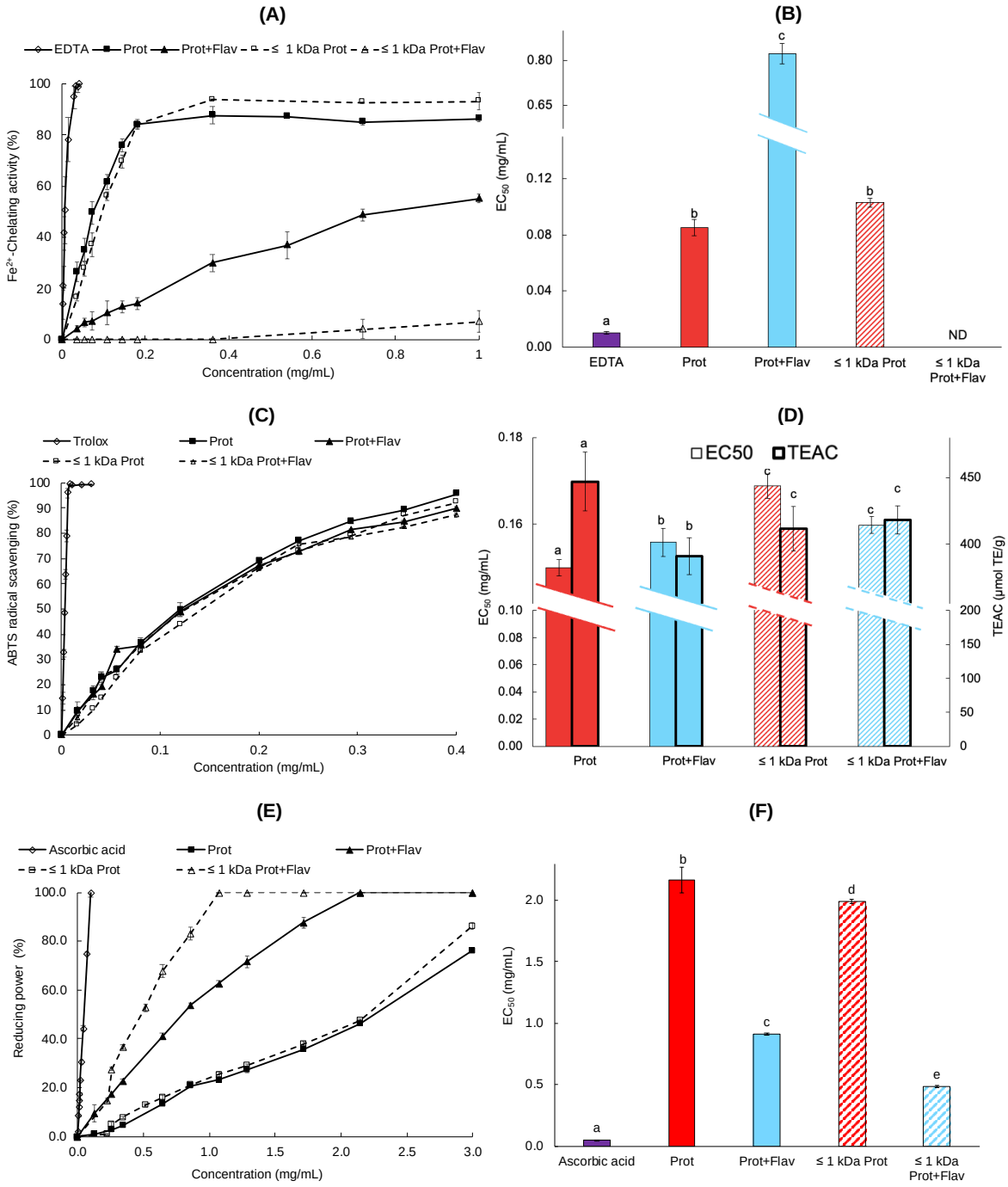

Figure 5.3. Antioxidant activities of Prot, Prot+Flav, ≤ 1 kDa Prot and ≤ 1 kDa Prot+Flav hydrolysates. Fe^{2+}-chelating activity (A), ABTS radical scavenging activity (C), and reducing power ability (E) as a function of hydrolysate concentration. Half efficient concentration EC_{50} (mg/mL) values determined for Fe^{2+}-chelating (B), ABTS radical scavenging (D), and reducing power activities (F).

Error bar corresponds to the standard deviation. Different letters indicate significant difference between samples (*p-value* < 0.05). n=5. TEAC: Trolox equivalent antioxidant capacity; Prot: Protamex® hydrolysate; Prot+Flav: Protamex® followed by Flavourzyme® hydrolysate; ≤ 1 kDa Prot: Protamex® hydrolysate; Prot+Flav: Protamex® followed by Flavourzyme® hydrolysate; ≤ 1 kDa: 1 kDa ultrafiltrated hydrolysate.

5.3.2.1.5 Reducing power

The ability of hydrolysates to reduce ferric ions (Fe^{3+}) into ferrous ions (Fe^{2+}) was evaluated using the Fe^{3+}/ferricyanide assay, commonly used for measuring the antioxidant properties of food protein hydrolysates in reference to ascorbic acid as positive control. The lower the EC_{50}, the higher the reducing power. All the hydrolysates and their ≤ 1 kDa fractions exhibited reducing power in a concentration-dependent manner (**Figure 5.3E-F**). Indeed, peptides present in hydrolysates could present AA residues that act as an extra source of electrons and protons (Phe, Try, Trp, Asp, and Gln; Wang et al., 2021). Compared to Prot hydrolysates, the reducing power of Prot+Flav hydrolysates increased markedly with increasing DH (low EC_{50}, **Figure 5.3F**). This may be attributed, in part, to their higher number of small-sized peptides, which contain abundance of hydrogen ions (protons and electron), after hydrolysis (Guan et al., 2018).

Moreover, upon ≤ 1 kDa ultrafiltration, the EC_{50} values of ≤ 1 kDa Prot and ≤ 1 kDa Prot+Flav were significantly (*p-value* < 0.05) lower than their corresponding whole hydrolysates, meaning that the reducing power was enhanced in both 1 kDa hydrolysate fractions. Irrespective of the hydrolysate, the strongest reducing power was observed in ≤ 1 kDa Prot+Flav, related to its highest peptide concentration (meaning smaller-sized peptides, **Table 5.1**). Similarly, the reducing power of several protein hydrolysates were reported to increase when the number of small-sized peptides or the DH increased (tree peony seed protein, Wang et al., 2021; mung bean protein, Liu et al., 2022; sunflower meal, Dabbour et al., 2023).

5.3.2.2 Cu^{2+}-chelating peptides separation by IMAC

The Cu^{2+}-chelating peptides present in the hydrolysates and their corresponding ≤ 1 kDa fractions were separated/fractionated using IMAC-Cu^{2+}. This method, based on peptides-Cu^{2+} interaction, provides several advantages due to its high-binding capacity and high recovery. The Cu^{2+}-chelating peptides were eluted using imidazole gradient. Yet, due to imidazole absorbing at 214 nm, which is also the wavelength used for monitoring peptide bonds, the peptides were followed at 280 nm. The IMAC-Cu^{2+} chromatogram shows the injection phase (0-5 min) and elution phase (5-65 min) of the hydrolysates (**Figure 5.4A-D**).

The imidazole gradient was applied (0-50 mM, 60 min, elution phase **Figure 5.4**) and Cu^{2+}-chelating peptides bound onto IMAC-Cu^{2+} phase were eluted in several peaks, *i.e.,* the fractions F2, F3, and even the fraction F4 for ≤ 1 kDa Prot+Flav only. Among the hydrolysates, the retention time (**RT**) of the Cu^{2+}-chelating peptides fractions were not significantly different for F2 (RT: ~11 min) and F3 (RT: ~14 min) (*p-value* ≥ 0.05). Thus, the mechanism of peptide-Cu^{2+} interaction in IMAC-Cu^{2+} column may be similar in the four hydrolysates and their difference in chelation capacity may rather be explained by the number of chelating peptides.

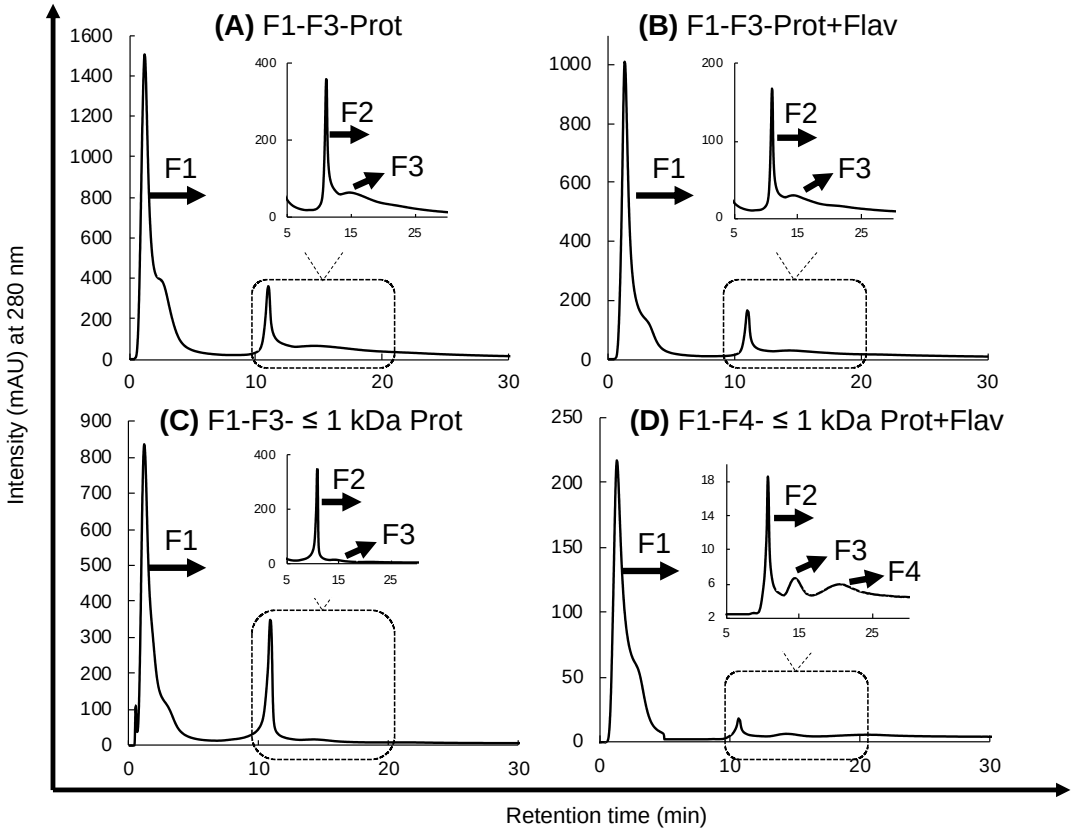

Figure 5.4. The fractionation of Cu^{2+}-chelating peptides of sunflower meal protein isolate hydrolysates obtained by different enzymatic treatments. The unbounding (injection phase) and bound peptides (elution phase) present in Prot (A), Prot+Flav (B), ≤ 1 kDa Prot (C) and ≤ 1 kDa Prot+Flav (D).

Prot: Protamex® hydrolysate; Prot+Flav: Protamex® followed by Flavourzyme® hydrolysate; ≤ 1 kDa Prot: Protamex® hydrolysate; Prot+Flav: Protamex® followed by Flavourzyme® hydrolysate; ≤ 1 kDa: 1 kDa ultrafiltrated hydrolysate.

5.3.2.3 Cu^{2+}-chelating peptides identification by LC-MS/MS

The various fractions F1, F2, F3 and F4 were collected and subjected to LC-MS/MS analysis to identify the Cu^{2+}-chelating peptides sequences present in the hydrolysates. **Figure 5.5A** shows the total number of identified peptides in each fraction, with the highest number of Cu^{2+}-chelating peptides identified in Prot, followed by Prot+Flav and ≤ 1 kDa fractions. This observation strongly supports the high Cu^{2+}-chelating ability of Prot hydrolysate. The peptides sequences identified in the unbound peptides fraction F1 and in the enriched MCPs fractions F2-F4 are displayed in **Appendix 5.1** and **Table 5.2**, respectively.

Table 5.2. Cu^{2+}-chelating peptides identified from the F2-F3 sunflower meal protein isolate hydrolysates fractions using IMAC- Cu^{2+} separation followed by LC-MS/MS analysis.

Sequence	Intensity (x 10^4)				Length	Mass (g/mol)	Score	Entry
	Prot	Prot+Flav	≤ 1 k Da Prot	≤ 1 kDa Prot+Flav				
Fraction 2 (RT ≈ 11 min)								
AGGISSE**H**IQGQQQ		1553.80			14	1438.68	12.87	A0A251UYX1
AIQSP**H**	61.49		30.21		6	651.33	4.66	P19084
AVLAP**H**	49.70		26.83		6	606.35	1.42	A0A251T566
DFIR**H**	432.36	165.68	231.62		5	686.35	10.80	A0A251TKL9
FPILE**H**		37.99		72.46	6	754.40	1.42	P19084
FPILE**H**L		253.26		124.96	7	867.49	3.24	P19084
FSP**H**	163.85		103.38		4	486.22	8.08	A0A251UYX1
FVTPEEEQQQM**H**	76.69				12	1501.65	1.19	
GENDQRG**H**IIF	36.28	507.19			11	1284.62	0.51	A0A251TUS1
GENDQRG**H**IIFVQ		130.80			13	1511.75	1.52	
GIVSP**H**	93.97		58.57	12.87	6	608.33	4.66	A0A251TUS1
GVDFIR**H**	252.44	78.13	118.11	79.36	7	842.44	12.16	A0A251TKL9
HNDGNTELVVVVF		239.82			13	1441.72	4.72	
HVDQETASKL	94.04				10	1126.56	1.84	A0A9K3HVJ0
NIDNPS**H**ADFVNPQ	216.29				14	1566.71	1.74	A0A9K3NGE6
P**H**YA	99.76				4	486.22	2.71	A0A9K3JEW0
RGENDQRG**H**IIF	674.32				12	1440.72	2.73	A0A251TUS1
SEVF**H**				45.03	5	617.28	1.94	A0A9K3HVJ0
SEVF**H**VD	161.31	155.86			7	831.38	3.24	
SFLAGGISSE**H**IQGQQQ		395.13			17	1785.86	2.25	A0A251UYX1
SP**H**WTIN	25.57	121.55	28.07	49.29	7	853.41	11.11	P19084
WV**H**NDGNAE	21.03				9	1040.43	0.52	A0A9K3NGE6
YANQLDPN**H**RRF		54.97			12	1529.75	1.19	A0A251TUS1
Fraction 3 (RT ≈ 14 min)								
ALFSP**H**	304.06		72.077		6	670.34	14.67	A0A251UYX1
DFIR**H**R	151.10		45.85	6.16	6	842.45	4.12	A0A251TKL9
GTA**H**WL	60.17				6	683.34	1.42	P19084
GVDFIR**H**R	484.99	22.71	161.79	24.31	8	998.54	3.60	A0A251TKL9
NPS**H**ADFV				16.08	8	885.40	0.60	A0A9K3NGE6

Prot: Protamex® hydrolysate; Prot+Flav: Protamex® followed by Flavourzyme® hydrolysate; ≤ 1 kDa: 1 kDa ultrafiltrated hydrolysate; grey cell: not identified.

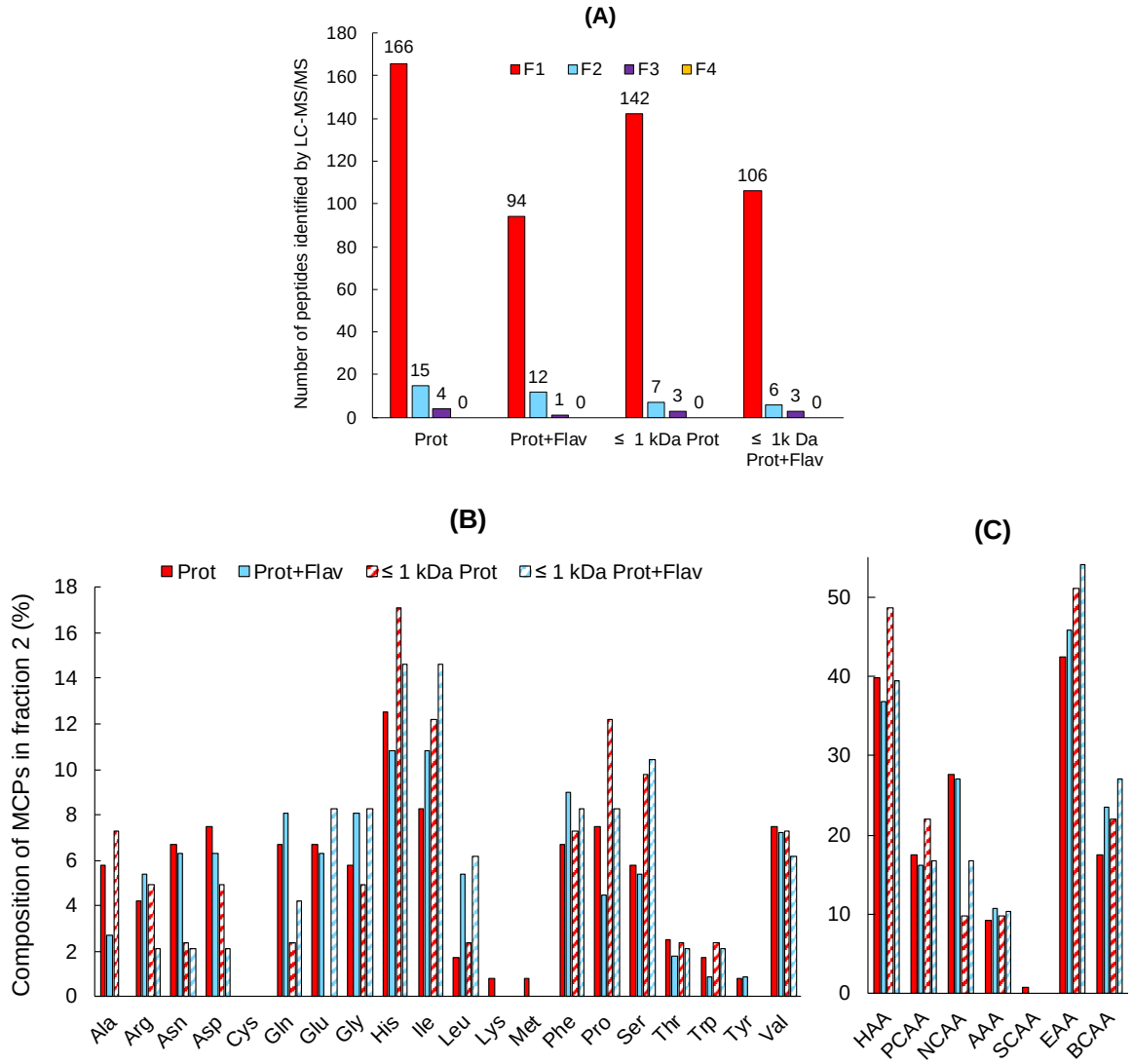

Figure 5.5. Results obtained from the MS/MS identification of peptides present in sunflower meal protein isolate hydrolysates. (A) Number of peptides identified in F1, F2 and F3 fraction in whole and ≤ 1 kDa fraction hydrolysates. (B) and (C) amino acid composition of Cu^{2+}-chelating peptides identified in the F2 fractions of all the hydrolysates.

Prot: Protamex® hydrolysate; Prot+Flav: Protamex® followed by Flavourzyme® hydrolysate; ≤ 1 kDa Prot: Protamex® hydrolysate; Prot+Flav: Protamex® followed by Flavourzyme® hydrolysate; ≤ 1 kDa: 1 kDa ultrafiltrated hydrolysate. AAA: Aromatic amino acids= Phe, Trp, Tyr; NCAA: Negatively charged amino acids= Asp, Glu, Asn, Gln; PCAA: Positively charged amino acids= Arg, His, Lys; HAA: Total Hydrophobic amino acids= Ala, Val, Ile, Leu, Tyr, Phe, Trp, Pro, Met and Cys; SCAA: Sulphur containing amino acids= Met and Cys; EAA: Essential amino acids= Trp, Lys, His, Phe, Leu, Ile, Met, Val, Thr; BCAA: Branched chain amino acids= Ile; Leu, Val.

Interestingly, all the peptide sequences identified in F2 and F3 contain at least one His residue (**Table 5.2**), which plays a pivotal role in the Cu^{2+}-binding ability of hydrolysates due to its

imidazole ring (Camaño Echavarría et al., 2024). In comparison, His-containing peptides were not identified in the unbounding peptides fractions F1 (**Appendix 5.1**). On the contrary, there may be other His-containing MCPs present in the F4 of ≤ 1 kDa Prot+Flav fraction, but they were not identified due to their low concentration compared to the whole hydrolysates and the sensitivity of analysis. Furthermore, the sequential treatment (Prot+Flav) does not show a better Cu^{2+}-chelating activity than the single treatment (Prot). Indeed, MS/MS analysis of fraction 2 indicates that 7 new MCPs were generated in Prot+Flav after Flav treatment. However, 10 MCPs already present in Prot were hydrolysed, resulting in a lower total number (Prot+Flav: 12) of MCPs available to bind Cu^{2+} ions compared to Prot hydrolysate (Prot: 15) (**Table 5.2**).

To better understand the Cu^{2+}-chelating profile of the identified sequences, the AA composition of peptide sequences in F2 (fraction with the highest number of sequences) of all the hydrolysates were determined by the free-accessed ProtParam tool (https://web.expasy.org/protparam/). All the four hydrolysates contain His residue as the major amino acid in their sequences (>10 %), being the main AA responsible for Cu^{2+}-binding properties of the hydrolysates (**Figure 5.5B**). In Prot hydrolysate, the peptide sequences contain higher His content than the Prot+Flav hydrolysate, which could explain its high Cu^{2+}-chelating properties (see **Figure 5.2B** inhibition of Cu^{2+}-induced ROS production). Negatively charged (Asp and Glu) and positively charged amino acids (Arg, His) are the major potential metal-binding amino acid residues present in the identified sequences (**Figure 5.5B**). Also, the peptide sequences contain high amount of Glu, an important AA residue for Fe^{3+}-chelating properties, explaining the results of the inhibition of Fe^{3+}-induced ROS production by the hydrolysates. Our results are similar to the study of Latha et al., (2021), who separated and identified Cu^{2+}-chelating peptides from chia seed protein hydrolysates, reporting His, Glu and Asp as main AA involved in metal-chelating properties. Besides, **Figure 5.5C** reveals high amount of EAA, HAA, NCAA, and PCAA in the identified MCPs, which have highly been associated with the antioxidant properties of food protein hydrolysates (Wen et al., 2020). Furthermore, **Figure 5.6A-D** displays the sequenced mass spectra of four of the most interesting sequences of Cu^{2+}-chelating peptides from SMPI hydrolysates loaded into the MaxQuant Viewer.

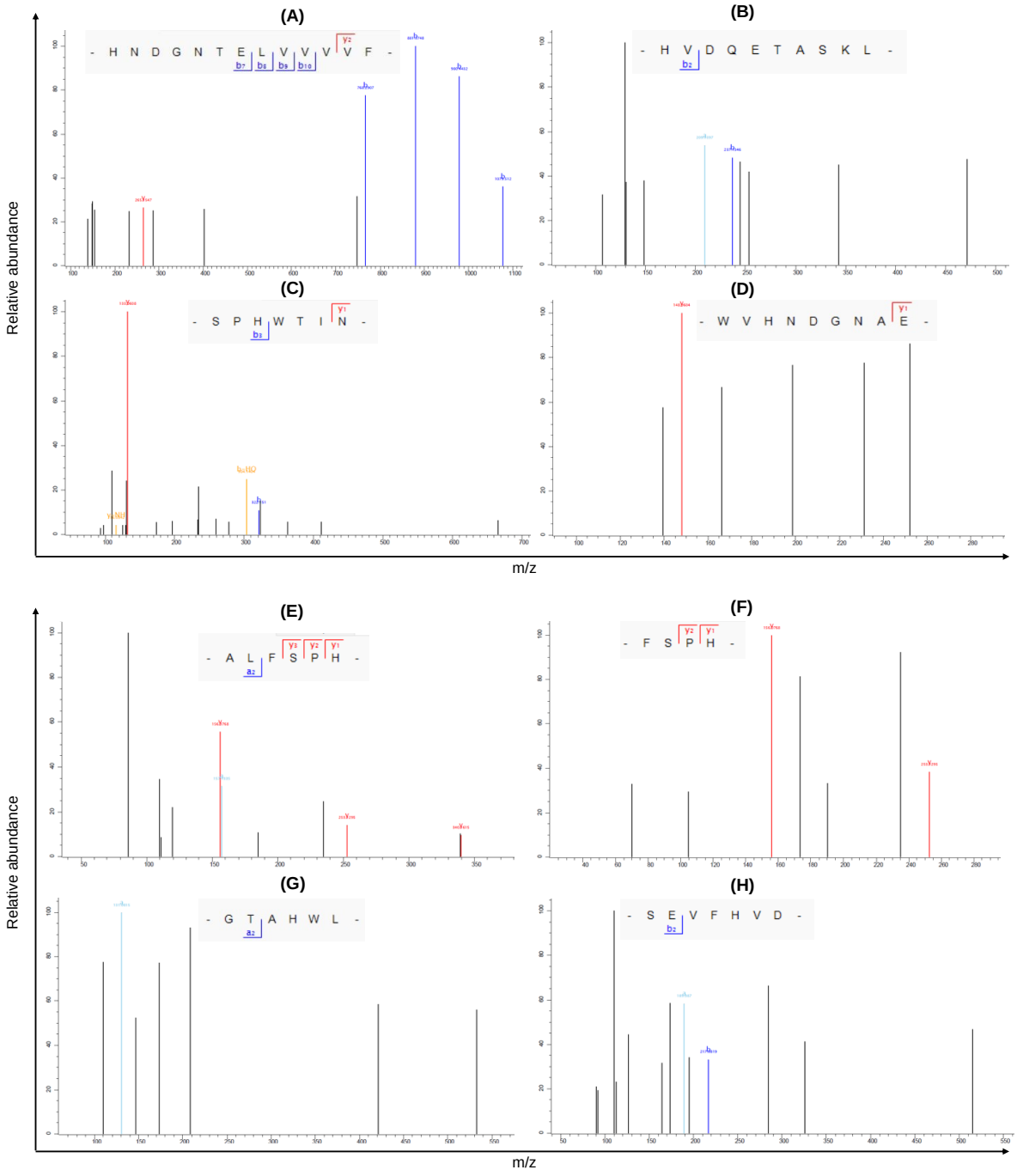

Figure 5.6. Sequenced mass spectra of eight different Cu^{2+}-chelating peptides structures obtained from sunflower meal protein isolate hydrolysates and processes by MaxQuant software. (A) **H**NDGNTELVVVVF (F2: Prot+Flav), (B) **H**VDQETASKL (F2: Prot), (C) SP**H**WTIN (F2: all the hydrolysates), (D) WV**H**NDGNAE (Prot) containing His residue in the first and third position from amino terminus. (E) ALFSP**H** (F3: Prot and ≤ 1 kDa Prot) (F) FSP**H** (F2: Prot+Flav) (G) GTA**H**WL (F3: Prot), (H) SEVF**H**VD (F2: Prot and Prot+Flav) containing His residue in the first and third position from carboxylate terminus.

The different positions of His residue in the structure of MCPs may define the stability of the formed peptide-Cu^{2+} complex. In our study, His residues were mostly found in the first, second and third positions from the amino terminus (**H**NDGNTELVVVVF, **H**VDQETASKL: **Figure 5.6A-B**, P**H**YA, SP**H**WTIN and WV**H**NDGNAE: **Figure 5.6 C-D**) and the first, second and third positions from carboxylate terminus (ALFSP**H**, FSP**H**: **Figure 5.6E-F**, DFIR**H**R, GTA**H**WL and SEVF**H**VD: **Figure 5.6G-H**). For instance, MCPs with His residue in the third position from the amino terminus could possess better stability in the formed peptide-Cu^{2+} complex (Sóvágó et al., 2012). In other studies, Guo et al., (2015) and Latha et al., (2021) reported copper-chelating peptide that contained His residue in the first and second position of carboxylate terminus from hydrolysates obtained from fish skin gelatin (SGSTG**H)** and chia seed proteins (KP**H**K), respectively. Finally, we identify a Cu^{2+}-chelating peptide (FVTPEEEQQQM**H**) in F2 Prot hydrolysate. This sequence was structurally close (85 % similarity) to a metal-binding peptide (FVTPEEEQQQMH**QR**) previously identified by Bao et al., (2021).

5.4 Conclusions

This study reported the physico-chemical properties, metal-chelating and antioxidant activities of SMPI hydrolysate obtained by single (Prot) and sequential (Prot+Flav) enzymatic treatments and their ≤ 1 kDa fractions. For the first time, Cu^{2+}-chelating peptides were identified from SMPI hydrolysate using IMAC-Cu^{2+} and their metal-chelating and metal-related antioxidant activities characterized. Upon sequential treatment, large number of peptide bonds were cleaved effectively, releasing mainly small-sized peptides. Prot hydrolysates contained higher number of larger-sized peptides compared to Prot+Flav. Some similarities were observed between the Fe^{2+}-chelating, inhibition of Cu^{2+}-induced ROS production and ABTS radical scavenging data. Indeed, the Prot hydrolysate and its corresponding ≤ 1 kDa fraction exhibited the highest activities in these assays while the Prot+Flav and its ≤ 1 kDa fraction enhanced the Fe^{3+}-induced ROS and the reducing power. Moreover, both MW distribution and AA residues of the sequences play a key role in metal-chelating and antioxidant properties of peptides from SMPI. The molecular weight of Cu^{2+}-identified peptides ranged from 0.8-1.7 kDa, with the larger-sized peptides (> 1 kDa) presenting the most effective bioactive properties. Besides, the presence of His, Glu, Asp, and Arg in the peptide sequences identified improved the metal-chelating and antioxidant

properties. Taken together, sunflower meal by-product is an interesting protein source to generate protein hydrolysates endowed with metal-chelating and antioxidant agents. According to the structural characteristics of the sequences, the peptides identified in our study could serve as antioxidant and MCPs candidates to be used as food or pharmaceutical active agents to prevent metal-induced oxidation and diseases. Further works should deeply investigate the properties of the hydrolysates and identified Cu^{2+}-chelating peptides *in vivo* as well as molecular basis of the peptide-metal interaction, to validate their high potential.

Considering the great capacity of both TSG and SMPI hydrolysates to chelate metal ions demonstrated in the previous **Chapters 3, 4** and **5**, in the next and last **Chapter 6** (TSG hydrolysates) and **Chapert 7** (SMPI hydrolysates), we finally investigated the potential of these hydrolysates in the production of food-derived peptide-based biomaterials. These experiments were mainly carried out at School of Nutrition Science (University of Ottawa, Ottawa, Canada; 2.5 months), under the supervision of **Pr. Chibuike C. Udenigwe.** This internship was funded by an international mobility grant from the Doctor Explore and Achieve More (**DrEAM9** LUE) project.

Chapter 6. Tuning Peptide Self-Assembly Patterns in Tilapia Scale Gelatin Hydrolysates through Cu^{2+} Coordination: Characterization, Identification and Antioxidant Evaluation

In addition to their biofunctional properties, food-derived peptides could self-assemble into organized nanostructures through a spontaneous and reversible process, giving them great potential to be used in a wide range of nutraceutical, cosmetic and biomedical applications. Nowadays, the combination of bioactivity and self-assembly properties of food-derived peptides has become a research hotspot for the development of novel functional nanomaterials. In particular, metal ion coordination constitutes a potential approach to tune the peptide self-assembly pattern in order to produce peptide-based biomaterials with potential biological functions. However, to date, this approach has not been exploited in food-derived protein hydrolysates. Therefore, following the findings of **Chapter 3**, which demonstrated the great potential of peptides present in gelatin (**TSG**) hydrolysates from Tilapia scales to coordinate metal ions, this **Chapter 6** explores the effect of metal ion coordination on the peptide self-assembly pattern and *in vivo* antioxidant properties using Cu^{2+}-induced oxidative stress in *Caenorhabditis elegans* as a model organism.

This Chapter will be submitted to the journal *Food Chemistry* as:

Camaño*, J.A., Abioye, R.O., Reyes, S., Selmeczi, K., Canabady-Rochelle, L., Udenigwe*, C. Tuning Peptide Self-Assembly Patterns in Tilapia Scale Gelatin Hydrolysates through Cu^{2+} Coordination: Characterization, Identification and Antioxidant Evaluation.

6.1 Introduction

Over the past decade, aquaculture has experienced significant growth, driven by the rapid increase in the world's human population. In 2022, production had reached 223.2 million tons, with 62.6 % coming from capture fisheries (FAO, 2024). Approximately 50-70 % of the total weight of fresh fish ends up as waste, which has a significant negative impact on the environment (Sierra-Lopera & Zapata-Montoya, 2021). Tilapia is the third largest fish production in the world and the global market is growing at 10-12 % annually: with 6 million tons in 2020, its production is expected to reach 7.3 million tons by 2030 (Munguti et al., 2022). The production of red Tilapia generates significant waste, particularly scales, which are typically discarded during the filleting process. Fish scales, consisting of 30-50 % collagen and mainly hydroxyapatite ($Ca_5(PO_4)_3OH$) (30-40 %), are highly valuable for gelatin production. Gelatin, a fibrous protein derived from the thermal degradation of collagen, is widely used in the food, pharmaceutical and cosmetic industries due to its excellent functional and biological properties (Viji et al., 2019).

Encrypted within the primary sequence of parent proteins, bioactive peptides released during the protein hydrolysis have been reported for their antioxidant, antihypertensive, anticancer, anti-inflammatory, antimicrobial, antidiabetic and metal-chelating activities (Wen et al., 2020). The past two decades, there has been a surge of research into the discovery of bioactive peptides derived from food processing by-products. For example, numerous studies have used enzymatic hydrolysis to release encrypted bioactive peptides from fish gelatin as one of the effective strategies to increase the added value of fish waste (Viji et al., 2019; Zhang et al., 2019).

Beside their capability to stimulate positive health effects in the body, food-derived bioactive peptides are capable of forming ordered self-assembled nanostructures that can be arranged and combined in various architectures and functions using 20 natural amino acids (Li et al., 2023). Importantly, combining bioactivity and self-assembly properties of food-derived peptides has become a research hotspot for the development of novel functional nanomaterials in biomedicine, food and cosmetics (Chen et al., 2022). During the peptide assembly process, the molecular arrangement of peptides can vary due to reversible noncovalent interactions such as hydrogen bonding, electrostatic interactions, hydrophobic interactions, etc. (Vahedifar & Wu, 2022). The chemical structure and functional properties

of self-assembled peptides can be modulated by controlling internal (i.e., number of amino acids, the amino acid side chain properties, and the peptide sequence) and external (i.e., changes in the pH, ionic strength, temperature, protein concentration, and metal ion coordination) stimuli (Li et al., 2023). Metal ion coordination is a promising strategy to modify the self-assembly pattern of peptides, enabling the development of peptide-based biomaterials with potential biological applications (Sharma et al., 2019). Nowadays, a large number of studies concerning the induction of peptide self-assembly phenomena through metal ion coordination in synthetic peptides have been reported (Fortunato & Mba, 2021; Rammal et al., 2023; Shao et al., 2020). However, to the best of authors' knowledge, there are no studies using this approach in fish protein hydrolysate. Moreover, there is no existing research on how Cu^{2+} coordination affects the physico-chemical, mechanical, and *in vivo* antioxidant properties of self-assembled bioactive peptides derived from enzymatically digested fish gelatin hydrolysates. Therefore, the aim of the present study was to evaluate the effect of Cu^{2+} coordination on both the self-assembly patterns of peptides and the *in vivo* antioxidant potential of Tilapia scale by-product hydrolysates, using *Caenorhabditis elegans* as a model to assess Cu^{2+}-induced oxidative stress.

6.2 Materials and methods

6.2.1 Chemicals and reagents

Red Tilapia (*Oreochromis* spp.) scales were supplied by El Gaitero SAS (Sopetrán, Colombia). Alcalase® (≥ 2.4 Alcalase® Units (AU)/g, Flavourzyme® (≥ 500 U/g), 37 % hydrochloric acid (HCl), ammonium bicarbonate, ethylenediaminetetraacetic acid (Na_2·**EDTA** $2H_2O$), copper (Cu^{2+}) sulphate pentahydrate, sodium acetate, thioflavin T (**ThT**), 8-anilino-1-naphthalenenesulfonic acid (**ANS**), 5-fluoro-2'-deoxyuridine, 2',7'-dichlorofluorescein diacetate (**DCF**), and sodium azide (NaN_3) were purchased from Sigma–Aldrich (St Louis, MO, USA). All the other reagents, including disodium phosphate (Na_2HPO_4), potassium dihydrogen phosphate (KH_2PO_4), sodium chloride, magnesium(II) sulfate heptahydrate ($MgSO_4$·$7H_2O$), sodium hydroxide and sodium hypochlorite, were of analytical grade (≥ 95 %) and used without further purification.

6.2.2 Preparation of protein hydrolysate from Tilapia scale

*6.2.2.1 **Preparation** of Tilapia scale gelatin*

The Tilapia scale flour (**TSF**) was prepared according to the literature (Chen et al., 2019). Once produced, the TSF was submitted to bromatological analysis according to the AOAC specifications (AOAC, 2000). The TSF used contained 39.58 ± 0.56 % crud proteins, 3.42 ± 0.07 % fat, and 51.69 ± 1.87 % ash (mineral fraction, mainly hydroxyapatite) in the dry matter (d.m.). Thus, the protein extraction process first involved a demineralization of Tilapia scales flour followed by a hydrothermal extraction using ultrapure water. The demineralization process was performed similarly to Chen et al., (2019) using 0.4 M HCl solution at a 1:15 (w/v) ratio of TSF for HCl solution, under stirring for 90 min at room temperature (25 °C ± 2 °C) using a magnetic stirrer plate (Corning, Mexico City, Mexico). The demineralized scales flour was washed with ultrapure water (resistivity of 18.2 MΩ.cm at 25 °C) until reaching pH 7. Then, the gelatin protein was extracted from demineralized TSF at 50 % (w/v) using ultrapure water under stirring for 3 h at 65 °C (Wangtueai & Noomhorm, 2009). After protein extraction, the Tilapia scale gelatin (**TSG**) containing 98.8 % of protein was stored at – 20 °C until further use.

6.2.2.2 Protein hydrolysis

The TSG Hydrolysates were obtained as previously described with some modification (El Hajj et al., 2023). The gelatin protein extracted from Tilapia scales was hydrolyzed using two different enzymatic treatments: Alcalase® alone (**Alc**) and a sequential treatment using Alcalase® followed by Flavourzyme® (**Alc+Flav**). For each proteolysis experiment, the TSG powder (5 g) was dissolved in 250 mL of ammonium bicarbonate buffer solution (50 mM) using a 1 % (w/w) enzyme-to-substrate ratio (E:S) with the following conditions: 55 °C, pH 8 and pH 7 for Alcalase® and Flavourzyme®, respectively. After 2 h of proteolysis, the corresponding protease was heat inactivated (95 °C, 15 min). In the sequential treatment, Alcalase® was heat inactivated just before Flavourzyme® treatment. Then, the solutions were centrifuged (10000 g, 15 min, 25 °C) for removing enzymes. Finally, the supernatants were lyophilized (LABCONCO, Kansas City, USA) and stored at −20 °C for further analysis.

The two TSG hydrolysates were further fractionated by membrane ultrafiltration using an ultrafiltration stirred cell 47-mm system (XFUF04701; Millipore, Molsheim, France) under magnetic stirring and pressure of 5 bar of nitrogen. The ultrafiltration unit was first equipped

with a molecular weight cut-off membrane of 10 kDa (Millipore, Billerica, USA), conditioned according to the specification, before ultrafiltration. Each hydrolysate (200 mL; 20 mg/mL in ultrapure water) was passed through the membrane; then, the permeate was ultrafiltrated onto a 1-kDa cutoff membrane (Millipore, Billerica, USA). The resulting ultrafiltrates (≤ 1 kDa fractions) were lyophilized and stored at −20 °C until further use. The degree of hydrolysis (**DH**) of the whole hydrolysates only and the peptide concentration of the four hydrolysates (2 whole and 2 ultrafiltrated ones) and TSG, were expressed as mM eq. NH_2 (*o*-phthalaldehyde analysis) and displayed in **Appendix 6.1**.

6.2.3 Investigation of peptide-Cu^{2+} interaction

All the spectroscopic measurements were performed at the PhotoNS Platform of the L2CM Laboratory, Université de Lorraine.

6.2.3.1 UV-visible spectroscopy

6.2.3.1.1 UV-visible spectra

The UV-visible (**UV-vis**) spectra of Cu^{2+} ions and peptide-Cu^{2+}complexes formed by peptides present in TSG hydrolysates were recorded on a PerkinElmer Lambda1050 UV-vis-NIR spectrophotometer (Perkin Elmer Corp, Massachusetts, USA) in a quartz cuvette with 1.0 cm path length, in a range of wavelengths varying from 300 to 800 nm at room temperature (25 °C). The samples were prepared by mixing 1500 µL of 50 mM HEPES buffer at pH 7.4 with 500 µL of 5 mM sample solution (expressed as mM eq. NH_2 for hydrolysates) and 62.5 µL of 10 mM $CuSO_4$ solution in order to have a 1:4 Cu^{2+}-to-peptide molar ratio. The coordination modes of peptide-Cu^{2+} complexes were investigated by comparing the shifts in the absorption/UV-vis peaks of Cu^{2+}-binding peptides alone with those of the corresponding peptide-Cu^{2+} complex using the same concentration.

6.2.3.1.2 Pyrocatechol violet assay

The Cu^{2+}-chelating ability of the TSG hydrolysates was determined using the pyrocatechol violet (**PV**) spectrophotometric assay according to Latha et al., (2021), with EDTA as positive control. A 1 mM copper (Cu^{2+}) sulphate solution ($CuSO_4$) was prepared in a 50 mM sodium acetate buffer, at pH 6.0 (using a 1 N HCl solution). The hydrolysate solutions were prepared

in a range of concentrations (0-1 mg/mL) in the former sodium acetate buffer. Then, 237 µL of hydrolysate solution, 50 µL of a 1 mM $CuSO_4$ solution and 13 µL of 2 mM PV solution prepared in the same buffer were mixed and incubated for 3 min at room temperature. The absorbance was measured at a wavelength of 632 nm corresponding to the PV-copper complex using a spectrophotometer MRX Multiskan Go (ThermoFicher Scientific, Vantaa, Finland) equipped with a microplate reader and 96-well microplates Nunclon™ delta surface (Thermo scientific, Roskilde, Denmark). The Cu^{2+}-chelating ability was calculated using the Equation (1).

$$Cu^{2+}\ \text{chelating ability}\ (\%)\ = \left[\frac{A_0 - A_s}{A_o}\right] X\ 100 \qquad (1)$$

where A_0 is the absorbance of the control (without sample, sample volume replaced by sodium acetate buffer), and A_s is the absorbance of either the sample or the positive control (EDTA).

The results were expressed as the half maximal effective concentration (**EC_{50}**), *i.e.,* the hydrolysate concentration required for 50 % copper (Cu^{2+}) chelation.

6.2.3.2 Circular dichroism spectroscopy

The circular dichroism (**CD**) spectral analysis of the four TSG hydrolysates (whole and 1 kDa fractions) in the presence and absence of Cu^{2+} ions was performed using a MOS-450 CD spectrometer (Bio-Logic Science Instruments, France) in a quartz cuvette with 1.0 cm path length in a range of wavelengths varying from 260 to 800 nm at room temperature (25 °C). The sample solutions were prepared at 5 mM (expressed as mM eq. NH_2 for hydrolysates) in 50 mM HEPES buffer at pH 7.4 and mixed with 10 mM Cu^{2+} (at 1:4 metal-to-ligand molar ratios, as UV-vis experiment), as previously reported (Csire et al., 2022). The coordination modes of peptide-Cu^{2+} complexes were investigated by comparing the shifts in the absorption/CD peaks of peptides alone with those of the corresponding peptide-Cu^{2+} complex using the same concentration.

6.2.3.3 Nano-LC-MS/MS identification análisis

To better understand the effect of sequential enzymatic treatment on the production of self-assembled peptide structures and also the effect of Cu^{2+} coordination on the peptide self-assembly, the peptide sequences of TSG hydrolysates were identified using the nano-LC-MS/MS bioinformatic analysis. Only the ≤ 1 kDa hydrolysate fractions (≤ 1 kDa Alc and ≤ 1 kDa Alc+Flav) were studied since they contained lower number of peptide sequences compared to whole hydrolysates, which facilitates the understanding of the peptide self-assembly of TSG hydrolysates and their chelating properties. The mass analysis was carried out by nano-LC-MS/MS on a Orbitrap Fusin mass spectrometer (Thermo Fisher Scientific, Waltham, MA, USA) coupled to an UltiMate 3000 nanoRSLC (Dionex, Thermo Fisher Scientific, Waltham, MA, USA) as previously reported (Risha et al., 2020).

Then, the raw Thermo data files resulting from the two ≤ 1 kDa fractions were processed in the Andromeda search engine of MaxQuant™ (version 2.4.13.0), a commonly used proteomic software tool (Boachie et al., 2022). The peptide sequences were searched against a restricted Tilapia proteins database (*Oreochromis niloticus*) containing 30 entries obtained from UniProtKB (https://www.uniprot.org/, accessed on 27th April 2024, **Appendix 3.6**). The peptides identification was achieved by comparing the experimental fragment-ion mass value of the precursor ions with the theoretical fragment masses; these latter ones were obtained from the protein sequences database and determined from the unspecified digestion rule with a mass tolerance of 10 ppm. The parameters of database searches were set up as previously reported (Boachie et al., 2022) (**Appendix 3.7**).

In order to compute the physico-chemical properties of peptide sequences identified previously (e.g., length, amino acids composition with both individual and groups of AA, isoelectric point (pI) and grand average of hydropathicity (**GRAVY**) index), the MaxQuant™ output tables containing the identified peptide sequences were then loaded in the R software, version 4.0.2 (R Foundation for Statistical Computing, Viena, Austria) using a Peptides R package (Osorio et al., 2015).

6.2.4 Peptide self-assembly characterization

6.2.4.1 Thioflavin T binding assay

The effect of Cu^{2+} coordination on the amyloid fibril structures was investigated in the presence of TSG hydrolysates using the thioflavin T (**ThT**) analysis (Abioye et al., 2022). This analysis was conducted at 1:4 Cu^{2+}-to-peptide (hydrolysate) molar ratio. The TSG hydrolysate solution (60 µL, 4 mM eq. NH_2) investigated in the absence (60 µL of ultrapure water) or presence of copper ions (60 µL, 1 mM $CuSO_4$) was mixed with 10 µL ThT solution (10 µM in ultrapure water) and stirred for 3 min. The fluorescence intensity of ThT alone, ThT with Cu^{2+} ions, ThT with hydrolysates and hydrolysates mixed with Cu^{2+} was measured in a black 96-well microplates with clear bottoms (6005570, PerkinElmer, Waltham, MA, USA), at a final volume of 200 µL. Samples were evaluated in triplicates and fluorescence intensity measurements (emission at 480 nm, at 25 °C) were recorded from the bottom of the plate with excitation at 430 nm using the Spark multimode microplate reader (Tecan, Stockholm, Sweden).

6.2.4.2 ANS binding assay

The variation in surface hydrophobicity of the TSG hydrolysates was measured using 8-anilino-1-naphthalenenesulfonic acid (**ANS**) as a fluorescent probe as previously reported (Hayakawa & Nakai, 1985). The TSG hydrolysate samples were investigated in the absence (60 µL of hydrolysate solution, copper solution replaced by ultrapure water) and presence of copper ions (1:4 metal-to-ligand molar ratio using a 1 mM $CuSO_4$ solution in ultrapure water; vol: 60 µL) and were diluted in series with phosphate buffer (0.1 M, pH 7) to obtain hydrolysate concentrations ranging from 5 to 0.1 mM (eq. NH_2). Then, 200 µL of each sample solution were reacted with 10 µL of ANS solution (8 mM ANS in 0.1 M phosphate buffer, pH 7). The fluorescence intensity was measured at 470 nm in a black 96-well microplates with clear bottoms (6005570, PerkinElmer, Waltham, MA, USA) at the excitation wavelength of 390 nm using the Spark multimode microplate reader (Tecan, Stockholm, Sweden). The index of surface hydrophobicity ($\mathbf{S_o}$ indicates a relative tendency of sample to prefer a nonaqueous environment over an aqueous one) was determined as the slope the value of the plot of fluorescence intensity vs. hydrolysate concentration using linear regression.

6.2.4.3 Dynamic light scattering measurements

The TSG hydrolysates were investigated by dynamic light scattering (**DLS**) for their particle size distribution and polydispersity index (**PDI**) in the absence and presence of copper ions at 1:4 metal-to-ligand molar ratio. Experiments were carried out at 25 °C using a Zetasizer Nano ZS (Malvern Instruments Ltd., Worcestershire, UK) according to the method described by Abioye et al., (2022). The samples were prepared at 4 mM eq. NH_2 with ultrapure water (pH 7, refractive index 1.33, viscosity 0.88 cP and dielectric constant 78.5), similarly as in section 6.2.4.1 with a final volume of 1 mL (500 µL of hydrolysate, 500 µL of Cu^{2+} solution), in the absence of Cu^{2+}, 500 µL of ultrapure water were added. Subsequently, the resulting solution were transferred into a plastic disposable cuvette (Malvern Instruments Ltd., Worcestershire, UK) for DLS measurements. The DLS effect was analyzed with the Smoluchowski model at F(ka) 1.50 (term of Henry's equation) and backscattered angle of 173 °.

6.2.4.4 Mechanical measurements

To evaluate the effect of Cu^{2+} coordination on the mechanical properties (i.e., G′ elastic and G′′ loss moduli) of the TSG hydrolysates, rheometry experiments were carried out. The amplitude sweeps and frequency sweeps analyses were conducted using the Discovery Hybrid Rheometer HR-2 (TA Instruments Ltd., New Castle, USA). This equipment contained a cone (2 °, 40 mm diameter, 50 µm truncation gap) and a Peltier plate steel measuring system, separated with a gap height set to 1 mm, according to the method of Abioye et al., (2022). The solution of TSG hydrolysates in the presence and absence of Cu^{2+} ions (at 1:4 metal-to-ligand molar ratio, prepared as in section 6.2.4.3) were delicately loaded onto the lower testing plate and equilibrated for 5 s at 25 °C. The amplitude sweeps and frequency sweeps were recorded as a function of mechanical strain (0.001-5000 %, at a fixed frequency of 10 rad/s) and with an angular frequency (0.1- 100 rad/s, at a fixed strain of 1 %), respectively. Before starting a test, the excess of sample was removed with a Kimwipe to ensure a clear and smooth interface.

6.2.4.5 Transmission electron microscopy

To gain further information about the particular structures of the self-assembled peptides present in the TSG hydrolysates, the morphology of only two hydrolysates (the Alc+Flav and ≤ 1 kDa Alc, the most interesting ones based on former mechanical properties analysis) was studied by transmission electron microscopy (**TEM**) as formerly described (Abioye et al., 2022; Schindelin et al., 2012). Briefly, a 10 µL aliquot of TSG hydrolysate solutions (4 mM eq. NH_2 in water) in the presence and absence of copper ions at 1:4 metal-to-ligand molar ratio (prepared in the same way as in section 6.2.4.1) was placed on 300-mesh Formvar-carbon coated copper grid and incubated for 5 min for absorption. The sample in excess was blotted with a Kimwipe, and the grids were finally counterstained with TEM staining solution (Micro To Nano©, Haarlem, Netherlands) for 1 min in the dark. The excess stain was blotted again, and the loaded grids were examined using the JEM-1400 Flash Electron Microscope (JEOL, Tokyo, Japan) at an accelerating voltage of 120 kV. Imaging was performed using ImageJ 1.53c software (NIH, Bethesda, MD, USA) under standard operating conditions (Abioye et al., 2022).

6.2.5 Assessment of antioxidant activity in *C. elegans in vivo* model

6.2.5.1 Handling and synchronization

The *in vivo* antioxidant assay was carried out by the method of Sangha et al., (2013) with some modifications. Briefly, the wild-type *C. elegans* strain (isolate N2 from Bristol, UK) was maintained at 22 ± 2 °C on nematode growth medium (**NGM,** Mt. Prospect, IL, USA). This medium contained 200 µL of *Escherichia coli* (**OP50**) (Caenorhabditis Genetics Center, University of Minnesota, Minneapolis, MN, USA) as food for the *C. elegans*. To synchronize the nematodes at a consistent larval stage for further assays, the *C. elegans* eggs were collected. The nematodes pass through four larval life stages (L1, L2, L3, and L4), primarily characterized by increasing worm size (Mudd & Liceaga, 2022). On the third day of growth, the L4 stage adult nematodes were washed 2 times with M9 buffer solution pH 7 (6 g/L Na_2HPO_4, 3 g/L KH_2PO_4, 5 g/L NaCl, 0.215 g/L $MgSO_4 \cdot 7H_2O$) to remove both contaminants and remaining *E. coli* OP50. Then, the samples were centrifuged at 2602 *g* at 4 ± 1 °C for 3 min using a Lynx 4000 Centrifuge (ThermoFisher, Canada). After two rounds of washing, a first one with M9 buffer containing 0.1 M NaOH and a second one with M9 buffer containing both 0.1 M NaOH and 5 % NaClO to lyse them, the eggs were washed 2 more times with M9 buffer

solution only. Thereafter, the eggs were placed on fresh NGM plates supplemented with 200 µL *E. coli* OP50 and incubated at 22 °C ± 2 °C until further experiments.

6.2.5.2 Mean life and survival assay

The oxidative stress resistance assay was performed as previously described (Sangha et al., 2013) with slight modifications. The synchronized nematodes were divided into distinct groups: a negative control group (without hydrolysate sample, 200 µL of water), a positive control group (EDTA at 0.5 mM, 200 µL), and the sample group (200 µL of each investigated TSG hydrolysate at 2 mM eq. NH_2). Approximately 60 ± 5 L2 *C. elegans* nematodes were exposed to each group treatment and then transferred to fresh NGM plates containing 100 µL of 1 mM copper (Cu^{2+}) solution, a standard dose to induce oxidative stress. For each group (i.e., negative control, positive control and sample group), the nematodes were counted every hour for 8 hours, assessing their viability by pricking them with a platinum wire. Adult L4 stage nematodes from the same group (corresponding to the same plates) were synchronized, and the eggs obtained were transferred to fresh NGM plates containing *E. coli* in order to repeat the above-mentioned process (G1). The plates were incubated at 22 °C ± 2 °C until the nematodes reached the L4 stage again. On total, this sequence (egg, larval L1 to larval L4, adult) was repeated to evaluate the oxidative stress resistance over three consecutive generations (G1 to G3). The *C. elegans* survival and lifespan curves were analyzed by Kaplan-Meier method and log-rank test using GraphPad Prism version 8.0, GraphPad Software (La Jolla, California, United States, www.graphpad.com). All experiments were conducted in triplicate.

6.2.5.3 Reactive oxygen species production by fluorometry

The ability of TSG hydrolysates to reduce the reactive oxygen species (**ROS**) production in *C. elegans* model was carried out using fluorometry. The G1 synchronized populations of worms were harvested and washed before being resuspended in M9 buffer. The eggs were placed on new NGM plates with 200 µL *E. coli* OP50 bacteria and 200 µL of samples (ultrapure water, 0.5 mM EDTA and hydrolysates at 2 mM eq. NH_2: Alc, Alc+Flav, ≤ 1 kDa Alc and ≤ 1 kDa Alc+Flav) and incubated at 22 ± 2 °C until reaching the L3 stage. The ROS production was stimulated by exposure to a mixed solution of 200 µL of 1 mM copper (Cu^{2+}) sulfate. A 250

µM 2',7'-dichlorofluorescein diacetate (**DCF**) stock solution was prepared in DMSO and diluted in the assay buffer to achieve the final concentration of 100 µM for the detection of general oxidative stress. The worms were then incubated at 22 ± 2 °C for 2 h with the DCF solution, allowing its penetration into *C. elegans* and its reaction with ROS. The fluorescence intensity was measured using a Spark multimode spectrophotometer (Tecan, Stockholm, Sweden) with an excitation and an emission wavelength set at around 485 nm and 535 nm, respectively (Yoon et al., 2018).

6.2.5.4 Reactive oxygen species production by fluorescence microscopy

In order to measure the ROS production in *C. elegans* model, fluorescence microscopy analysis were carried out in generation 1 G1 using the method reported by Yoon et al.,(2018) with some modifications. The eggs of adult nematodes synchronized were placed on new NGM plates with 200 µL *E. coli* OP50 bacteria and 200 µL of samples (ultrapure water, 0.5 mM EDTA and hydrolysates at 2 mM eq. NH_2: Alc, Alc+Flav, ≤ 1 kDa Alc and ≤ 1 kDa Alc+Flav), followed by incubation at 22 ± 2 °C until reaching the L3 stage (24-36 h). Then, about 15 nematodes were transferred to new NGM plates added with 50 µL of 100 µM 5-fluoro-2'-deoxyuridine (to prevent offspring production) and 100 µL of 1 mM copper (Cu^{2+}) sulfate to induce oxidative stress. The nematodes were incubated at 22 °C ± 2 °C for 12 more hours. Upon reaching L3 stage, the nematodes were transferred to a new NGM plates supplemented with 200 µL of DCF (100 µM) -containing M9 solution and incubated in the dark at room temperature for 1.5 h. Thereafter, 50 µL of M9 solution containing 10 mM sodium azide (NaN_3 used as an anesthetic) was added, and after 1 h of incubation the nematodes were transferred to new NGM plates. The plates were placed on a fluorescence microscope using the Axio Imager 2 microscope equipped with an Axiocam 506 camera. Zen 2.3 pro software in order to capture the fluorescence of the oxidized DCF product.

6.2.6 Statistical analysis

The analyses of PV spectrophotometry, ThT, DLS, ANS and mechanical properties were conducted at least three times, and all the data were presented as means ± standard deviation. The statistical analyses were one-way analysis of variance (ANOVA), and significant differences between means of samples were determined by Fisher's multiple range test. The differences at *p-value* < 0.05 were considered significant. The statistical calculations were

conducted using the software Statgraphics centurion XVI version 16.1.03 (Statgraphics Technologies Inc, Virginia, USA).

6.3 Results and discussion

6.3.1 Cu^{2+} coordination properties

6.3.1.1 Peptide-Cu^{2+} complex formation by UV-vis and CD

UV-visible spectroscopy (**UV-vis**) and circular dichroism spectroscopy (**CD**) were employed to study the metal ion coordination sphere in the complexes formed between peptides present in TSG hydrolysates and Cu^{2+} ions in solution at physiological pH (7.4). Changes in λ_{max} values and absorption/CD band shapes of hydrolysates in the absence and presence of copper (Cu^{2+}) were analysed using the same hydrolysate concentration.

These UV-vis and CD measurements can reveal different electronic transitions commonly observed in metal coordination complexes, such as the d-d and the charge transfer (**CT**) transitions. The UV-vis spectroscopy data shows that upon the Cu^{2+} complexation through peptides present in TSG hydrolysates and their ≤ 1 kDa fractions, the formation of peptide-Cu^{2+} complex results in a significant shift (horizontal arrow) of the initially d-d transition band centred from 805 to 580-607 nm (**Figure 6.1A, C, E, G**, and **Table 6.1**) in all the hydrolysates, consistent with the coordination of three nitrogen donor atoms (3N-coordinated complex) (Mital et al., 2020).

Moreover, in addition to the d-d transition (560- 580 nm in UV-vis), the CD data (Figure **6.1B, D, F, F** and **Table 6.1**) reveal the presence of CT transitions with negative (280 nm) and positive (320 nm) Cotton effects which are characteristic of the involvement of imidazole nitrogen ($N_{imidazole} \rightarrow Cu^{2+}$) and amide nitrogen ($N^{-}_{amide} \rightarrow Cu^{2+}$) in the 3N coordination mode (Mital et al., 2020 and Sóvágó et al., 2012). More, the CT at 320 (positive Cotton effects) could also confirme the involvement of methionyl residues $S \rightarrow Cu^{2+}$ (Osz et al., 2002). Note that in a mixture containing several Cu^{2+} coordinating peptides, it is difficult to identify a single coordination mode, thus, in our study, the Cu^{2+} binding site in all hydrolysates can be described either by the 3N coordination mode [NH_2, N^{-}_{amide},$N_{imidazole}$] (**Figure 6.1I,** Sóvágó et al., 2012) in the case of the peptides containing His, the [NH_2, N^{-}, N^{-}, COO^{-}]-coordination mode in the case of the peptides containing N-terminal and/or internal Met residues, or [NH_2,

N^-, N^-, S^-]-coordination mode for peptides containing C-terminal Met residues(S→Cu^{2+}) as previously reported (**Figure 6.1J**, Osz et al., 2002).

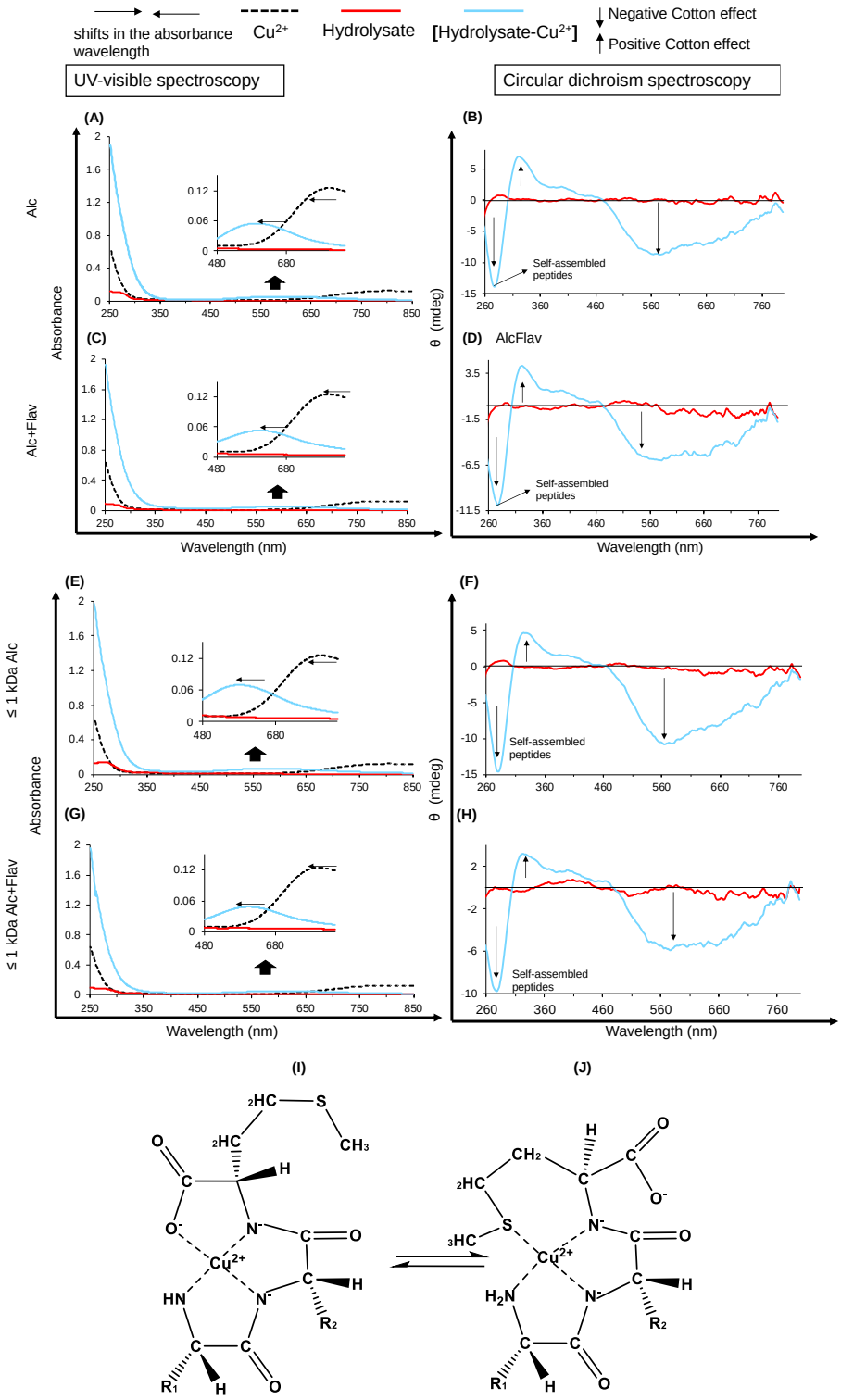

Figure 6.1. Uv-visible and CD measurements of the peptide-Cu^{2+} interaction of different TSG hydrolysates. (A-B) Alc, (C-D) Alc+Flav, (E-F) ≤ 1 kDa Alc, (G-H) ≤ 1 kDa Alc+Flav. (I-J) Proposed modes of coordination for the copper chelating peptides present in the TSG hydrolysates based on CD data (adapted from Osz et al., 2002 and Sóvágó et al., 2012).

Table 6.1. Spectroscopic data for the peptide-Cu^{2+} complexes at 1:1 metal-to-ligand ratio at physiological pH 7.4.

Sample	UV-vis (nm)		CD (nm)	
	d-d transition	CT transition	d-d transition	CT transition
Cu^{2+}	805			
[Alc-Cu^{2+}]	592	n.o	576 (-)	277 (-), 320 (+)
[Alc+Flav-Cu^{2+}]	602	n.o	580 (-)	278 (-), 323 (+)
[≤ 1 kDa Alc-Cu^{2+}]	580	n.o	565 (-)	280 (-), 323 (+)
[≤ 1 kDa Alc+Flav-Cu^{2+}]	607	n.o	575 (-)	278 (-), 323 (+)

Alc: Alcalase® hydrolysate; Alc+Flav: Alcalase® followed by Flavourzyme®; ≤ 1 kDa: 1 kDa ultrafiltrated hydrolysate.; n.o: not observed; grey cell: not investigated.

Beyond the insights provided by CD spectra into the coordination modes of peptide-Cu^{2+} complexes in TSG hydrolysates, further interpretations can be made regarding peptide self-assembly or aggregation. Notably, a negative band located between 270 and 300 nm appears in all four TSG hydrolysates upon Cu^{2+} coordination (**Figure 6.1B, D, F, H**). This band strongly suggests the existence of supramolecular assembly (self-assembled peptides), as previously documented (Fortunato & Mba, 2021). Therefore, additional techniques are needed to gain a deeper understanding of the effect of Cu^{2+} coordination on self-assembled peptides present in TSG hydrolysates.

6.3.1.2 Cu^{2+}-chelating ability

The Cu^{2+}-chelating curves of TSG hydrolysates illustrate a concentration-dependent equilibrium reaction, with a final Cu^{2+}-chelating ability of 82, 75, 73 and 70 % for ≤ 1 kDa Alc+Flav, Alc+Flav, ≤ 1 kDa Prot and Alc hydrolysates, respectively (**Figure 6.2A**). From **Figure 6.2A**, the EC_{50} values of Cu^{2+}-chelating ability were calculated for all hydrolysates and presented in **Figure 6.2B**. According to the EC_{50} values (*i.e.,* lower values mean higher chelating ability), the Cu^{2+}-chelating peptides are released from TSG in the single hydrolysis by Alcalase® (Alc). Yet, after sequential hydrolysis by Flavourzyme® (Alc+Flav), the Cu^{2+}-chelating peptide production seems to be significatively (*p-value* < 0.05) higher, suggesting

that small-sized peptides are more likely to be Cu^{2+} chelators. The Cu^{2+}-chelating ability of TSG hydrolysates correlates positively with their DH and the peptide concentration expressed as mM eq. NH_2 (**Appendix 6.1**). Note that the EC_{50} values of ≤ 1 kDa hydrolysates are lower (higher chelating ability) than those of their corresponding whole hydrolysates (*p-value* < 0.05), indicating that both sequential treatment and ultrafiltration process at 1 kDa enhance the Cu^{2+}-chelating ability of TSG hydrolysates. This ability can be explained by the DH and also by their amino acid content. Both the amino or carboxyl group available at each terminal part of a peptide as well as other amino and carboxyl groups present in other amino acids (*i.e.,* acidic amino acids: aspartate, glutamate*;* basic amino acids: lysine, arginine, and histidine, and sulfur amino acids: methionine and cysteine) can explain such ability. Similar to the literature, our results again demonstrate that peptides with low MW (≤ 1 kDa) have the highest metal-chelating ability. This trend was previously observed in various protein hydrolysates derived from Pacific cod skin gelatin (Wu et al., 2017), mung bean protein (Budseekoad et al., 2018) and casein (Miao et al., 2019).

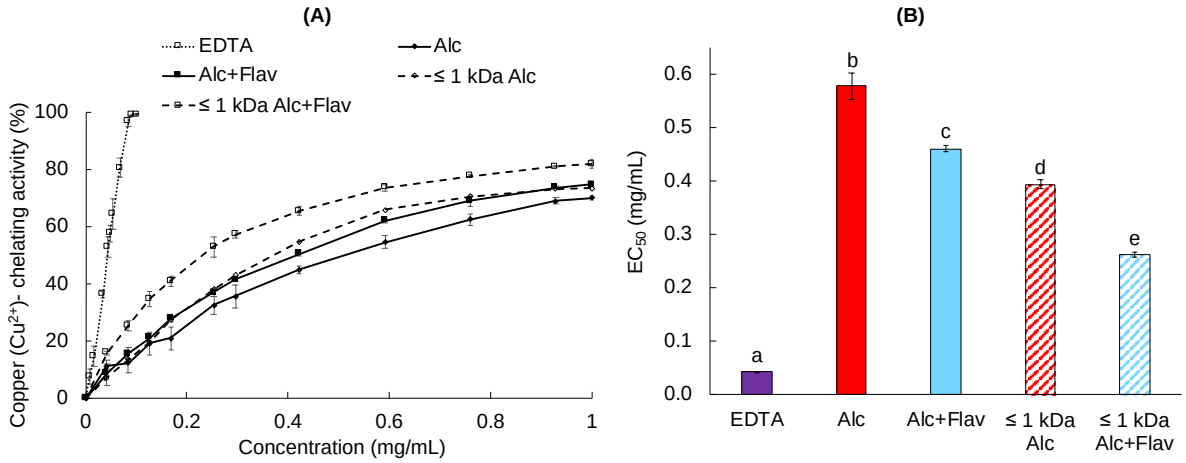

Figure 6.2. Cu^{2+}-chelating ability of different TSG hydrolysates determined with pyrocatechol violet assay. (A) Chelating ability as function of hydrolysate concentration. (B) EC_{50} values expressed as the quantity (mg/mL) of hydrolysate that is required to chelated 50 % of Cu^{2+}.

Different letters indicate significant differences (*p-value* < 0.05). Alc: Alcalase® hydrolysate; Alc+Flav: Alcalase® followed by Flavourzyme®; ≤ 1 kDa: 1 kDa ultrafiltrated hydrolysate.

6.3.1.3 Nano-LC-MS/MS bioinformatic analysis

To better understand how sequential enzymatic treatment influences the formation of self-assembled peptide structures and to gain further insight into the role of Cu^{2+} coordination in peptide self-assembly, the peptide sequences in TSG hydrolysates were identified using nano-LC-MS/MS bioinformatics analysis. Only the ≤ 1 kDa hydrolysate fractions (≤ 1 kDa Alc and ≤ 1 kDa Alc+Flav) were evaluated since they contain fewer peptide sequences than the whole hydrolysates, making it easier to understand their self-assembly pattern and their chelating properties. In addition, these ≤ 1 kDa hydrolysate fractions showed the highest Cu^{2+}-chelating ability.

The peptide sequences identified in ≤ 1 kDa Alc and ≤ 1 kDa Alc+Flav hydrolysates are shown in **Appendix 6.2**. A total of 88 peptides were identified from the single treatment (≤ 1 kDa Alc) and 34 peptides from the sequential treatment (≤ 1 kDa Alc+Flav), with 17 % (15 peptides) of the peptide sequences overlapping (**Figure 6.3A, Appendix 6.2**). On all identified peptides, 11 peptides in ≤ 1 kDa Alc and 5 peptides in ≤ 1 kDa Alc+Flav contain His or Met residues (**Table 6.2**). These peptides could serve as potential Cu^{2+} chelating candidates because they contain imidazole (His) or thioether (Met) groups, respectively, which are known for their ability to complex Cu^{2+} ions (Sóvágó et al., 2012).

Moreover, in our study, the ≤ 1 kDa fractions, with the highest Cu^{2+}-chelating ability, have 34 % and 41 % of peptide sequences containing the GPA motif over the total peptide sequences identified for ≤ 1 kDa Alc and ≤ 1 kDa Alc+Flav hydrolysates, respectively (**Appendix 6.2**). However, several His-containing peptides as well as peptides with such a GPA motif have been previously reported for their high metal-chelating properties in protein hydrolysates produced from Alaska pollock skin gelatin (A**GPA**GPR, **GPA**GPR, **GPA**GP**H**GPPG, Guo et al., 2015), Pacific cod skin (**GPA**GP**H**GPPGKDGR, AGP**H**GPPGKDGR, A**GPAGPA**GAR, Wu et al., 2017) and Tilapia skin collagen (**GPA**GPAGEK, Lin et al., 2021). Altogether, the presence of His or Met-containing peptides and peptides with GPA motif supports the high Cu^{2+}-chelating ability of ≤ 1 kDa TSG hydrolysate fractions determined in the PV assay (**Figure 6.2**).

Various intrinsic factors, such as peptide length, amino acid composition and physico-chemical properties of peptide sequences, can influence copper-induced peptide self-assembly (Abioye et al., 2024). Therefore, the size, amino acid composition, isoelectric point (**pI**) and grand average of hydropathicity (**GRAVY**) index were also determined for all

identified peptides (based on the peptide list in **Appendix 6.2**). As shown in **Figure 6.3B**, more than 50 % of the peptide sequences have between 7 and 11 amino acid residues. Meanwhile, the AA composition (**Figure 6.3C**) of ≤ 1 kDa fractions reveals that the identified peptides are rich in glycine, proline and alanine, which is similar to the study of Zhang et al., (2019) in hydrolysates obtained from Tilapia scales (*Oreochromis niloticus)*. Besides, in terms of residue types (Osorio et al., 2015), a high content of tiny (Ala, Cys, Gly, Ser, Thr), small (Ala, Cys, Asp, Gly, Asn, Pro, Ser, Thr and Val) and nonpolar (Ala, Cys, Phe, Gly, Ile, Leu, Met, Pro, Val, Trp, Tyr) AA resides is demonstrated in both hydrolysates (**Figures 6.3D**).

Table 6.2. Potential Cu^{2+}-chelating peptides containing either His or Met residues obtained from nano-LC-MS/MS analysis.

Sequence	Intensity (x 10^7)		Length	Mass (Da)	Score	Entry
	≤ 1 k Da Alc	≤ 1 kDa Alc+Flav				
APDPGPGP**M**	1.62		9	837.37	76.85	I3JXH5
DLGF**M**	10.48		5	581.25	52.86	G9M6I5
GAPGNIGLPG**M**	3.51	2.67	11	982.49	120.62	A0A668V4P2
GF**M**VQPQ	4.83		7	805.38	130.01	G9M6I5
GPPVPGPIGP**M**	6.62		11	1017.53	60.29	I3JMB4
GPSGPRGPAGP**H**	20.22	160.12	12	1085.54	120.63	I3JXH5
KSPA**M**PVPGP**M**	17.44		11	1110.56	88.18	G9M6I5
MPVPGP**M**	1.55	2.39	7	727.34	110.20	G9M6I5
NIGLPG**M**TGPQ	4.93		11	1083.54	89.03	A0A668V4P2
PFR**M**Y	64.08		5	712.34	62.09	G9M6I5
SGPRGPAGP**H**	4.58	7.85	10	931.46	95.82	I3JXH5
SPA**M**PVPGP**M**		22.25	10	982.46	102.77	G9M6I5

Peptide self-assembly can be driven by noncovalent intermolecular interactions, especially those involving hydrophobic amino acid residues such as the nonpolar AA (Leu and Ala), π–π stacking with aromatic AA (Phe, Trp, and Tyr), hydrogen bonding (via amide, amino, and carboxyl groups), and electrostatic interactions involving both acidic (Asp and Glu) and basic AA (His, Lys, and Arg) (Li et al., 2023). Therefore, TSG hydrolysates may exhibit interesting peptide self-assembly properties.

Regarding the physico-chemical properties calculated from the sequences listed in **Appendix 6.2** (all peptide sequences identified), **Figure 6.3E** illustrates that in both hydrolysates, most of the peptides have a pI value comprised between 3.7 and 6.4 (more than 50%). Therefore, at neutral pH 7 (as in our study), the peptides exhibit an increase in negative charge due to the complete deprotonation of histidine, aspartic acid and glutamic acid residues. This increase in negative charge could promote the formation of self-assembled peptide structures through electrostatic interactions with positively charged amino acid residues.

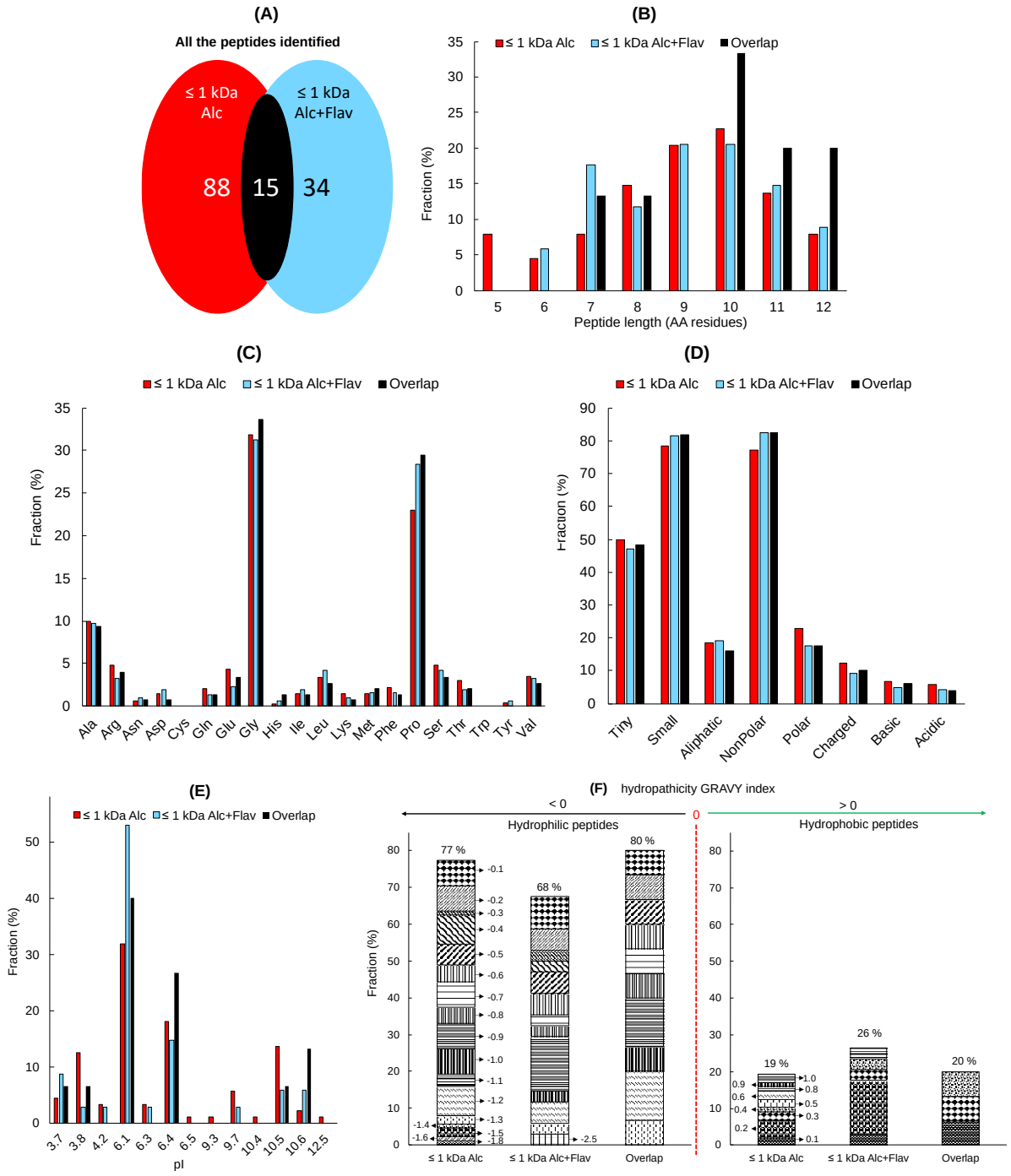

Figure 6.3. Nano-LC-MS/MS identification of peptide sequences present in different TSG hydrolysates. (A) number of peptides identified, (B) percentage of lengths of identified peptides, (C) distribution of amino acid (AA) residues of identified peptides, (D) percentage of AA residue group types, (E) distribution of peptides isoelectric point (pI), and (F) distribution of hydropathicity GRAVY index.

Alc: Alcalase® hydrolysate; Alc+Flav: Alcalase® followed by Flavourzyme®; ≤ 1 kDa: 1 kDa ultrafiltrated hydrolysate. tiny: Ala, Cys, Gly, Ser, Thr; small: Ala, Cys, Asp, Gly, Asn, Pro, Ser, Thr and Val; aliphatic: Ala, Ile, Leu and Val; aromatic: Phe, His, Trp and Tyr; non-polar: Ala, Cys, Phe, Gly, Ile, Leu, Met, Pro, Val, Trp and Tyr; polar: Asp, Glu, His, Lys, Asn, Gln, Arg, Ser and Thr; charged: Asp, Glu, His, Lys and Arg; basic: His, Lys and Arg; acidic: Asp and Glu.

Furthermore, as shown in **Figure 6.3F**, the hydrophobicity of the identified peptides was assessed using the grand average of hydropathicity (**GRAVY**) index (values below 0 indicate hydrophilicity and values above 0 indicate hydrophobicity, Boachie et al., 2022). In our study, the GRAVY index value reveals that although both hydrolysates (≤ 1 kDa Alc and ≤ 1 kDa Alc+Flav) contain a mixture of hydrophilic and hydrophobic peptides (GRAVY index ranging from -1.8 to 1), there is a noticeable tendency towards negative GRAVY index values in both hydrolysates, indicating low hydrophobicity. High hydrophobicity promotes attractive hydrophobic interactions between peptides, leading to the formation of stable, ordered nanoarchitectures from food hydrolysates. At the same time, peptides in TSG hydrolysates that contain hydrophilic regions in their sequences could be excellent candidates for the design of peptide-based self-assembled nanostructures, which are commonly used in drug delivery applications (Vahedifar & Wu, 2022).

Taken together, a comprehensive understanding of the relationship between the size, AA composition, charge of peptides and their hydrophobicity profile with Cu^{2+} coordination in peptide self-assembly of TSG hydrolysates will be based on the present study (section 6.3.2).

6.3.2 Physico-chemical characterization of self-assembled peptides

To decipher the actual role of Cu^{2+} coordination through TSG hydrolysates on the formation of self-assembled peptide structures, a wide range of analytical techniques such as ThT fluorescence, ANS, DLS, rheology and TEM were studied in the presence and absence of Cu^{2+} ions.

Fluorescence. The ThT fluorescence was performed to observe the presence of amyloid-like fibrils in TSG hydrolysates. **The Figure 6.4A** reveals the variation of ThT fluorescence as a function of hydrolysate. Irrespective of the hydrolysate, maximum fluorescence intensities are obtained for hydrolysates treated with a single enzyme (Alc and ≤ 1 kDa Alc), suggesting that sequential hydrolysis with Flav reduces the formation of amyloid-like fibrils (β-sheet fibrils). Interestingly, the presence of these β-sheet fibrils is reduced upon Cu^{2+} coordination, confirming the formation of other types of self-assembled structures such as amorphous aggregates.

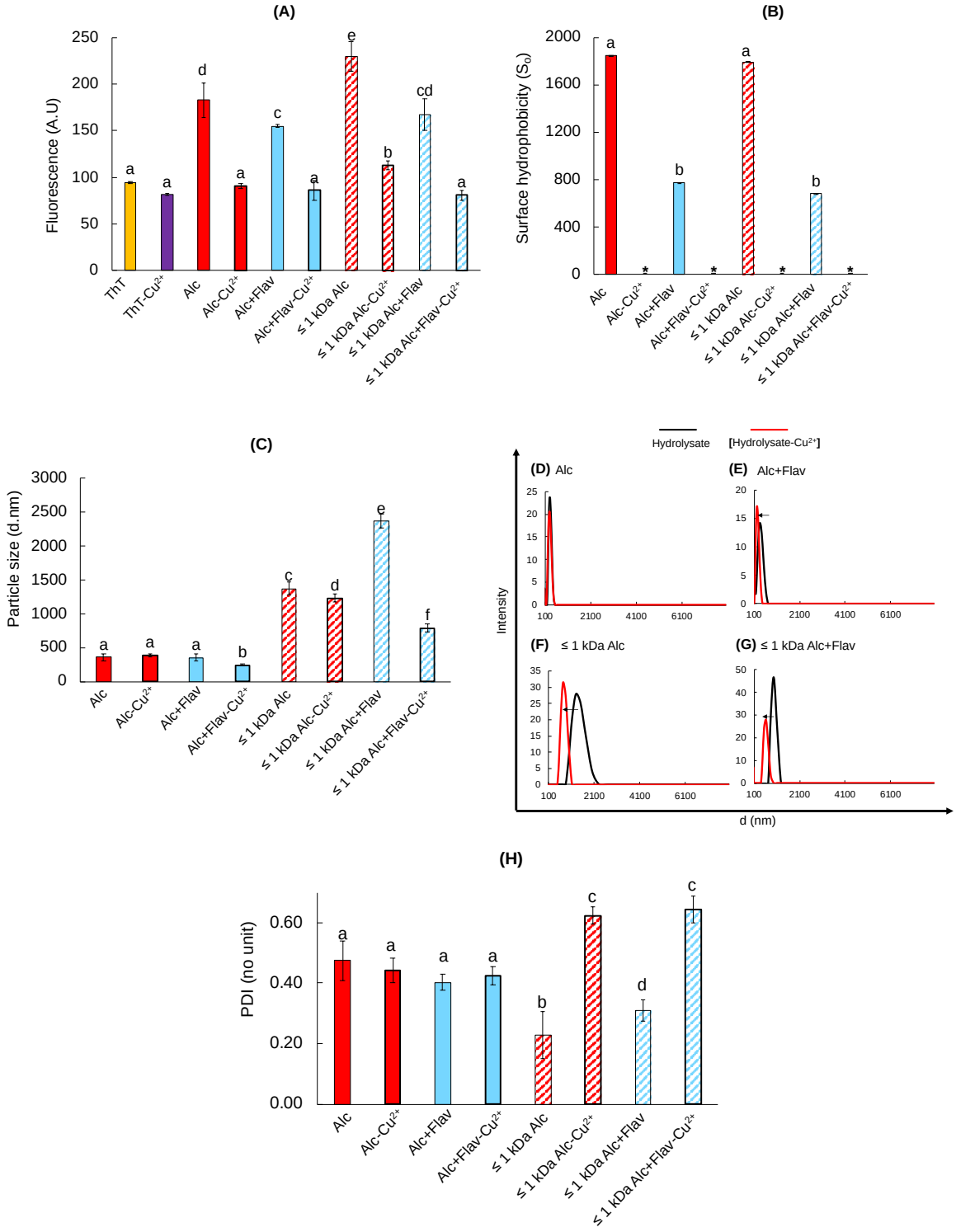

Figure 6.4. Thioflavin T (ThT) intensity, surface hydrophobicity (S_o), particle size, polydispersity index (PDI) and particle size distribution of different TSG hydrolysates upon the Cu^{2+} complexation. (A) Thioflavin T (ThT) assay, (B) Surface hydrophobicity (S_o), (C) average particle size, (D-G) particle size distribution and (H) PDI values.

Different letters indicate significant differences (*p-value* < 0.05). Alc: Alcalase® hydrolysate; Alc+Flav: Alcalase® followed by Flavourzyme®; ≤ 1 kDa: 1 kDa ultrafiltrated hydrolysate. * means surface hydrophobicity S_o: 0. Horizontal arrow indicates shift in particle size of peptides upon the Cu^{2+} coordination.

Similar to the ThT assay, the hydrophobicity of TSG hydrolysates and their complexes with Cu^{2+} was evaluated by the ANS probe assay (**Figure 6.4B**). Note that the sequential enzymatic hydrolysates (Alc+Flav and ≤ 1 kDa Alc+Flav) have lower surface hydrophobicity (S_0) than the single enzymatic hydrolysates (Alc and ≤ 1 kDa Alc), implying that small-sized peptides have higher solubility than larger-sized peptides in TSG hydrolysates. Meanwhile, in the present study, the involvement of Cu^{2+} coordination corresponds to a significant decrease in surface hydrophobicity (S_o of peptide-Cu^{2+} complex= 0), suggesting the presence of highly soluble complexes between peptides in TSG hydrolysates and Cu^{2+}. This observation confirms a trend observed throughout the ThT and ANS analysis, indeed, higher surface hydrophobicity may lead to a greater tendency to form amyloid aggregates (Es-Haghi et al., 2012). Besides, ANS data are consistent with the physico-chemical properties of the peptides identified in the 1 kDa fractions by nano-LC-MS/MS and bioinformatic analysis, where the single enzymatic hydrolysate (Alc) showed a higher hydrophobicity profile (lower solubility) than the sequential hydrolysate (Alc+Flav) (**Figure 6.3F**).

DLS. The average particle size (d, nm), the particle size distribution and the polydispersity index (PDI) were investigated for TSG hydrolysates and their formed complexes with Cu^{2+} ions by DLS analysis (Figure **6.4C-H**). The average particle size of Alc, Alc+Flav, ≤ 1 kDa Alc and ≤ 1 kDa Alc+Flav (**Figure 6.4C**) appeared at 350, 352, 1300 and 2300 nm, respectively, with a unimodal particle size distribution (Figure **6.4D to 4G**). Cu^{2+} coordination does not affect the particle size distribution of the Alc hydrolysate (**Figure 6.4D**). However, for Alc+Flav (**Figure 6.4E**), ≤ 1 kDa Alc (**Figure 6.4F**), and ≤ 1 kDa Alc+Flav (**Figure 6.4G**), a significant reduction in particle size is observed after Cu^{2+} coordination, with peaks shifting to 200, 700, and 500 nm, respectively (as indicated by horizontal arrows). Moreover, the PDI reflects the uniformity of the particle size distribution, with higher values indicating a greater degree of heterogeneity among the particles present in the system. As shown in **Figure 6.4H**, ≤ 1 kDa fractions exhibit lower PDI values than the corresponding whole hydrolysates in the absence of Cu^{2+} ions, indeed, the TSG hydrolysate with the lowest PDI (i.e., ≤ 1 kDa Alc and ≤ 1 kDa Alc+Flav) values also had the lowest surface hydrophobicity (**Figure 6.4B**), probably due to formation of aggregates that buried hydrophobic sites as previously reported (Jung et al., 2005). After the interaction between the peptides and Cu^{2+} ions, no significant difference is observed in the PDI values of the whole TSG hydrolysates. However, Cu^{2+} coordination significantly increases

the PDI values of ≤ 1 kDa fractions, suggesting that the sizes of peptide-Cu^{2+} complexes become less uniformly dispersed, probably due to the intermolecular forces between Cu^{2+} ions and peptides, resulting in the formation of amorphous aggregates of various sizes. Similar to our results, Zhang et al., (2021) reported that collagen-derived peptides (MW ≤ 1 kDa) had a wide size range upon the formation peptide-metal (Ca^{2+}) complexes.

Rheology. The dynamic mechanical properties of TSG hydrolysates and their complexes with Cu^{2+} were studied using dynamic shear rheology. Amplitude sweep measurements show that in all cases the elastic modulus (G') of the peptide-Cu^{2+} complexes is higher than that of the corresponding hydrolysate (**Figure 6.5A-D**). Note that the G' modulus is related to the stiffness: indeed, as the G' modulus of a material increases, the stiffness of the material also increases.

This behaviour confirms that the stiffness properties of TSG hydrolysates can be enhanced by Cu^{2+} coordination due to an increase in supramolecular interactions between peptides and Cu^{2+} ions. Moreover, to assess the structural strength of the gel-like materials, both the elastic (G') and loss (G'') moduli were plotted against the range of deformations (strain %) in the presence and absence of Cu^{2+} ions. The crossover point (**cp**), which represents the percentage of strain required to break down the formed gel (where G' > G''), was then calculated (**Figure 6.5A-D**). In all the cases, the crossover points are higher in the presence of Cu^{2+}, indicating an increase in gel strength as well. However, Alc+Flav and ≤ 1 kDa Alc and ≤ 1 kDa Alc+Flav hydrolysates show the highest enhancement of this property upon Cu^{2+} coordination, with an increase of 324, 310 and 442 % of strain, respectively. This behaviour indicates that these latter hydrolysates are more likely to be mechanically quite robust than the Alc hydrolysates (Δcp: 251, 259 and 303 %, respectively).

The mechanical properties of the TSG hydrolysates and their complexes with Cu^{2+} ions were further characterized by frequency sweep analysis (**Figure 6.5F-I**). Note that when G' > G'', the sample behaves as a gel-like structure; on the contrary, when G'' > G', the sample behaves as a fluid-like structure (Herrada-Manchon et al., 2023). The results show that in the presence of Cu^{2+} ions, the G' (elastic modulus) of all TSG hydrolysates tends to be greater than G'' (loss modulus) over almost the entire frequency range, indicating a gel-like structure rather than a fluid-like structure of the material.

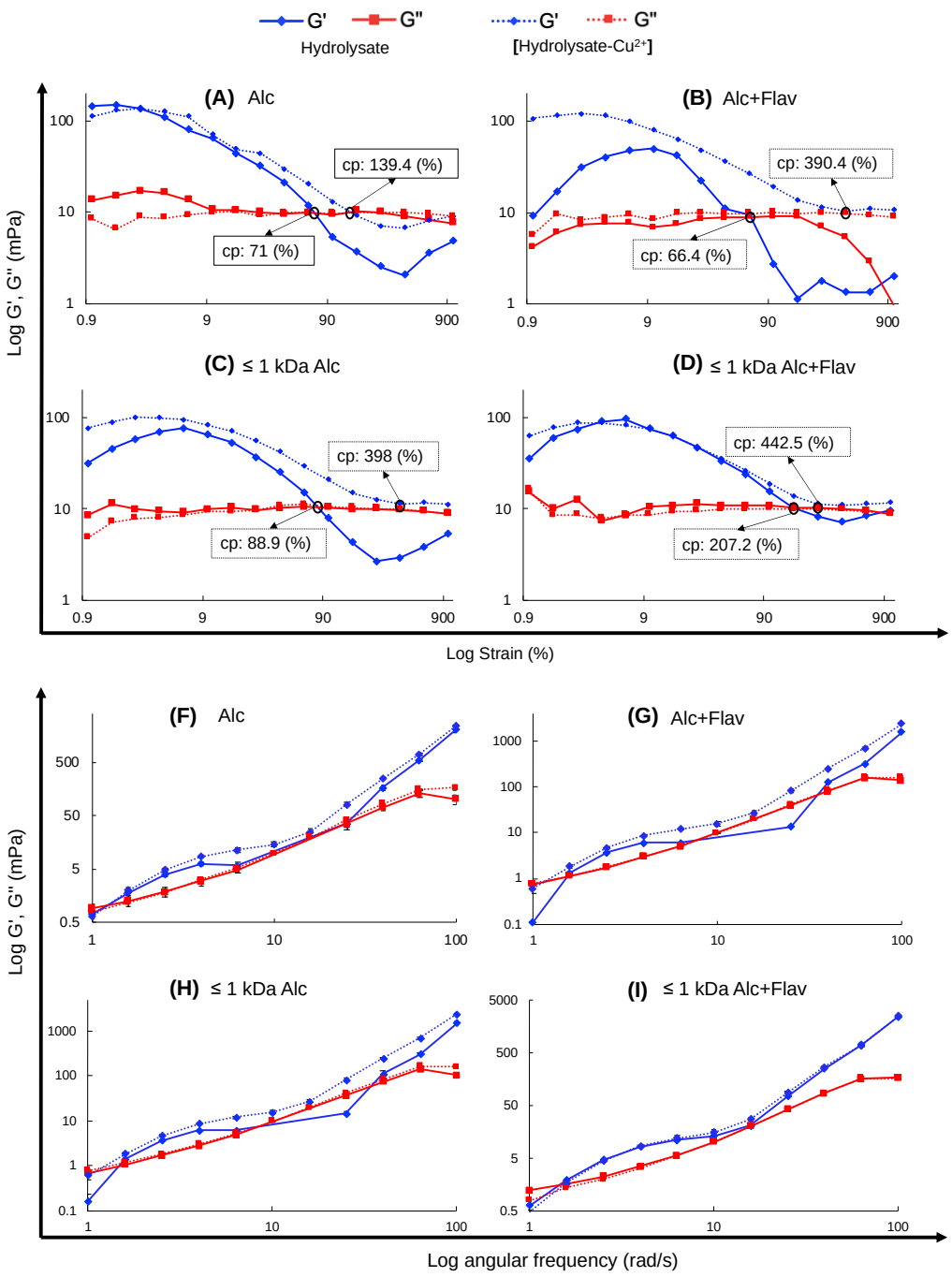

Figure 6.5. Effect of Cu^{2+} complexation on mechanical strength and viscoelastic behaviour study by amplitude sweeps and frequency sweeps measurements of different TSG hydrolysates. (A-D) amplitude sweeps, (E-H) frequency sweeps. G' and G'' are the elastic modulus and loss modulus, respectively.

Mechanical strength indicated by the cross-over point (cp, G' = G''), while gel formation indicated by G'> G'' (blue above red and dashed blue above dashed red without and with Cu^{2+} ions respectively. Alc: Alcalase® hydrolysate; Alc+Flav: Alcalase® followed by Flavourzyme®; ≤ 1 kDa: 1 kDa ultrafiltrated hydrolysate. Blue lines represent the elastic modulus (G') and red lines represent the loss modulus (G'').

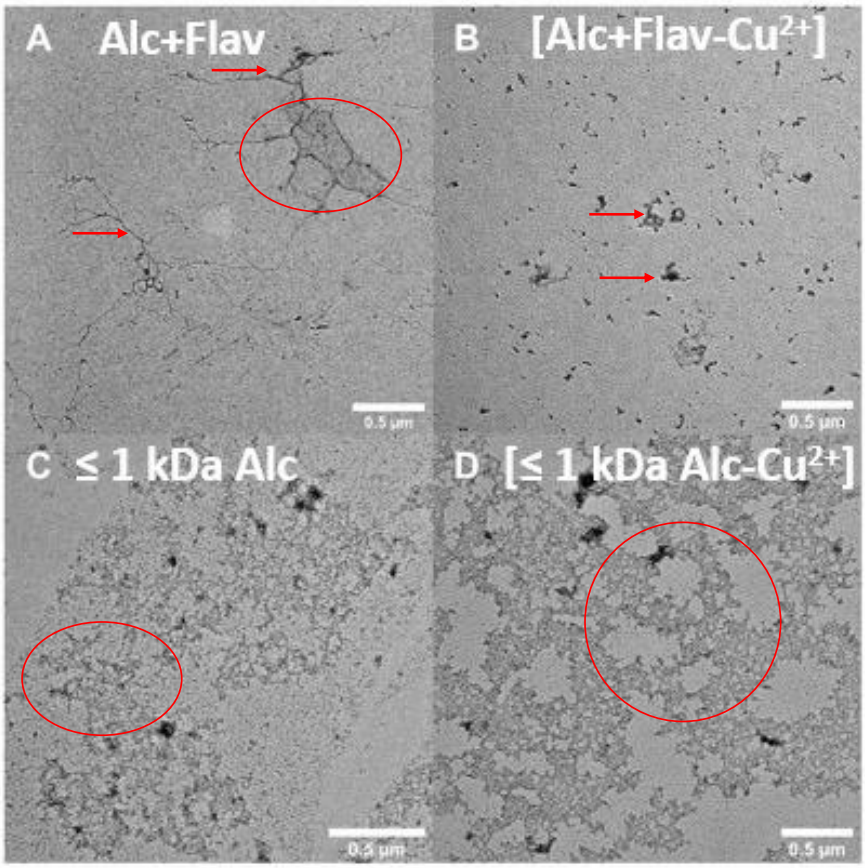

Figure 6.6. Transmission electron microscopy (TEM) of TSG hydrolysates (only Alc+Flav and ≤ 1 kDa Alc) with and without Cu^{2+} ions.

Scale bars represent 0.5 µM. Alc: Alcalase® hydrolysate; Alc+Flav: Alcalase® followed by Flavourzyme®; ≤ 1 kDa: 1 kDa ultrafiltrated hydrolysate.

TEM. To gain further information on the structures of the self-assembled peptides present in the TSG hydrolysates, the morphology of only Alc+Flav and ≤ 1 kDa Alc in the presence and absence of Cu^{2+} ions was studied by TEM (**Figure 6.6A-D**). Indeed, these two latter hydrolysates show the most remarkable self-assembly patterns based on ThT, ANS, DLS and rheological data. TEM images show that the Alc+Flav assemblies consist of thin, but highly networked fibrils, but, upon Cu^{2+} coordination, the formation of heterogeneous shorter assemblies is observed for a same scale (**Figure 6.6A-B**). On the other hand, ≤ 1 kDa Alc shows entangled fibrillar networks, while a higher density of cross-linked fibril fragments is observed in the presence of Cu^{2+} ions for a same scale (**Figure 6.6C-D).** This demonstrates the potential structural reconfiguration of self- and co-assemblies of peptides present in TSG hydrolysates.

In addition, the fine-tuning effects of Cu^{2+} coordination can be correlated to the physico-chemical and mechanical properties observed in ThT, ANS, DLS and rheological analyses.

Altogether, the results discussed herein highlight the ability of peptides present in TSG hydrolysates to coordinate Cu^{2+} ions to modulate and fine-tune the physico-chemical and mechanical and properties of TSG hydrolysate-derived supramolecular materials. In this study, Cu^{2+} coordination leads to the formation of stiffer structures; besides, it increases crosslinking in TSG hydrolysates (rheology data), while limiting growth through β-sheet hydrogen bonding (ThT and ANS data), which explains the formation of shorter supramolecular structures with heterogeneous particle size distribution (DLS and TEM data). This approach provides new opportunities to adapt and fit supramolecular materials from food-derived peptides to their intended applications, highlighting the use of injectable drug delivery systems, coatings and scaffold materials for tissue engineering (Herrada-Manchon et al., 2023).

6.3.3 Antioxidant activity in C. elegans *in vivo* model

6.3.3.1 Effect of Cu^{2+} coordination on lifespan of C. elegans

The effect of Cu^{2+} coordination by peptides present in TSG hydrolysates on the lifespan of *C. elegans* was investigated. *C. elegans* serves as a valuable model organism to study the antioxidant capacity of bioactive compounds *in vivo*. The survival of the worms was evaluated under oxidative stress induced by 1 mM copper (Cu^{2+}) sulphate, a known generator of reactive oxygen species (**ROS**). Excessive ROS at the cellular level leads to oxidative stress and aging, which impairs cellular functions. Therefore, minimizing ROS levels is a key strategy to mitigate oxidative stress and associated free radical damage. In our study, *C. elegans* were exposed to Cu^{2+} ions for three consecutive generations from G1 to G3 and the average lifespan was calculated from the survival curves (**Appendrix 6.3**, **Table 6.3**). In the first generation G1, the average lifespan of *C. elegans* of EDTA (positive control, 25.6 h) and Alc hydrolysate (26.7 h) were higher than that of the Cu^{2+} group (negative control, 23.2 h), suggesting that the use of a Alc hydrolysate significantly can help to retard the aging of *C. elegans* by 15 %. On the contrary, in the second generation G2, no hydrolysate improved the survival rate compared with the negative control. Interestingly, in the third generation, in addition to EDTA and Alc, the average lifespan of *C. elegans* co-treated with Alc+Flav was 11 % (26.7 h) longer than the

negative control (24.1 h), which means that the protective effect of this sequential hydrolysate may be observed only in later generations. Similar to our results, Guo et al., (2020) and Chen et al., (2023) recently found that the average lifespan of *C. elegans* treated with *japonicus* protein and sea cucumber protein hydrolysates was extended by 18.5 % and 57.8 %, respectively in the first generation.

Table 6.3. Effects of Cu^{2+} coordination by EDTA and peptides present in TSG hydrolysates on the lifespan-extension of Cu^{2+}-exposed nematodes.

Sample	Mean life (h)					
	G1	%	G2	%	G3	%
(- control) Cu^{2+}	23.25 ± 0.06^{c}		23.16 ± 0.05^{b}		24.1 ± 0.01^{d}	
(+ control) [EDTA-Cu^{2+}]	25.68 ± 0.26^{b}	10.45	26.78 ± 0.01^{a}	15.63	25.68 ± 0.02^{b}	10.88
[Alc-Cu^{2+}]	26.77 ± 0.01^{a}	15.13	21.47 ± 0.03^{c}	-7.46	25.06 ± 0.03^{c}	8.2
[Alc+Flav-Cu^{2+}]	20.72 ± 0.01^{e}	-10.88	20.96 ± 0.01^{d}	-9.49	26.78 ± 0.01^{a}	15.63
[≤ 1 kDa Alc-Cu^{2+}]	21.45 ± 0.06^{d}	-7.74	23.3 ± 0.18^{b}	0.6	23.38 ± 0.02^{e}	-0.94
[≤ 1 kDa Alc+Flav-Cu^{2+}]	23.18 ± 0.01^{c}	-0.30	19.41 ± 0.15^{e}	-16.19	22.75 ± 0.06^{f}	-1.77

6.3.3.2 Effect of of Cu^{2+} coordination on ROS generation

Fluorescence intensity can measure the level of intracellular ROS in *C. elegans*, which can accordingly damage cellular structure and function, leading to aging and diseases in worms (Wang et al., 2016). The higher the fluorescence intensity, the higher the ROS intracellular level. Therefore, the effect of Cu^{2+} coordination on ROS level was investigated by fluorescence spectroscopy and microscopy (**Figure 6.7**). As shown in **Figure 6.7A** and **Figure 6.7B-G**, due to high copper-chelating ability of EDTA, which was used as a positive control, there is a significant decrease (13 %) in the ROS level of the worm group co-treated with EDTA, whereas, among the TSG hydrolysates, only the worm group co-treated with Alc hydrolysate shows a 7 % decrease in the ROS level in oxidation-damaged *C. elegans*.

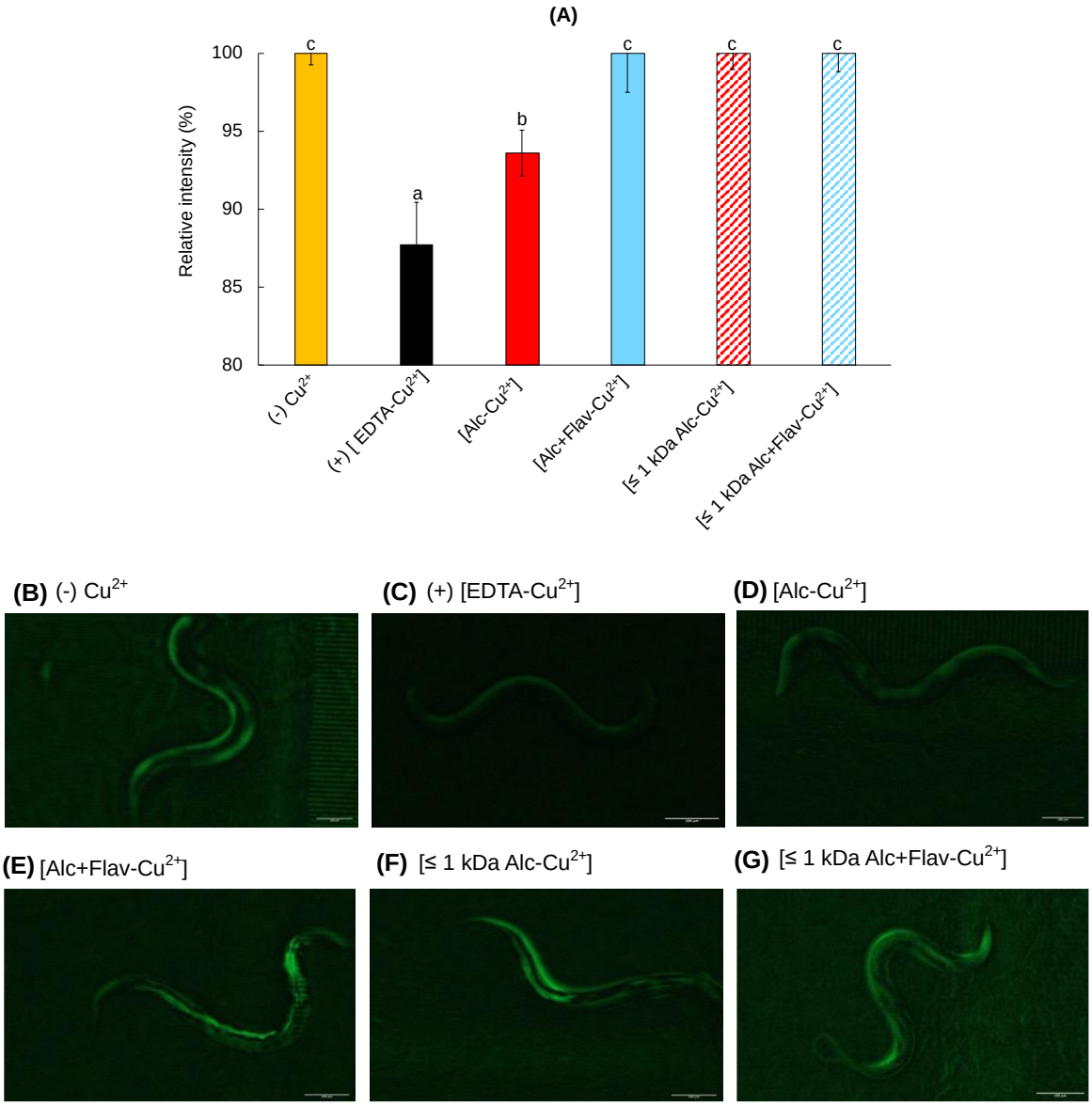

Figure 6.7. Alleviation of oxidative stress by EDTA, Alc, Alc+Flav, ≤ 1 kDa Alc and ≤ 1 kDa Alc+Flav hydrolysates in oxidation-damaged *C. elegans.* (A) Effects of Cu^{2+} coordination by EDTA and peptides present in TSG hydrolysates on ROS level in Cu^{2+}-exposed nematodes. L3-stage nematodes were treated with and without samples treatment (negative control nematodes) for 24 h at 22 ± 2 °C, and then exposed to 1 mM Cu^{2+} sulphate for another 12 h. (B)-(G) Representative images of Cu^{2+}-exposed L3-stage nematodes untreated control (only with Cu^{2+}), EDTA, Alc, Alc+Flav, ≤ 1 kDa Alc and ≤ 1 kDa Alc+Flav-treated groups captured by an Axiocam 506 camera.

Data are expressed as ROS level mean obtained from three independent experiments with approximately 15 worms in each experimental group. Different letters indicate significant differences (*p-value* < 0.05)

Although small-sized peptides present in Alc+Flav hydrolysate and 1 kDa fractions exhibited higher Cu^{2+}-binding properties than Alc hydrolysate (section 6.3.1.2), their Cu^{2+} coordination did not affect the ROS level of *C. elegans* (**Figure 6.7B-G**). This phenomenon could be due to a weak interaction between peptides and Cu^{2+} ions in these hydrolysates (i.e., Alc+Flav hydrolysate and its 1kDa fraction). Taken together, these results interestingly confirm that the antioxidant properties of Alc hydrolysate associated with its Cu^{2+}-binding ability, are relevant to prolonging the lifespan of worms by reducing ROS levels. Indeed, in agreement with our results, Chen et al., (2023), Shi et al., (2021) and Guo et al., (2020) found that the intracellular ROS level of *C. elegans* was negatively correlated with the lifespan of the worm co-treated with sea cucumber protein, marine protein (*Arca subcrenata*) and fish protein (*Decapterus maraudsi*) hydrolysates, respectively; this is due to the accumulation of oxidative damage that affects the aging of *C. elegans*.

6.4 Conclusions

In this study, the peptides from TSG hydrolysates prepared with Alcalase® and Alcalase® followed by Flavourzyme®, respectively, were characterized and identified for their Cu^{2+}-chelating, self-assembly and *in vivo* antioxidant properties. For the first time, to the author's knowledge, we carried out a physico-chemical characterization of self-assembled peptides in TSG hydrolysates tuned through Cu^{2+} coordination. We found that Cu^{2+} coordination by His and Met-containing peptides present in TSG hydrolysates contributes to the formation of tunable supramolecular assemblies. In this work, we demonstrated that the stiffness of supramolecular materials from TSG hydrolysate can be greatly enhanced by using Cu^{2+} coordination approach. The formation of multiple metal coordination bonds in each cross-linking ligand (peptide-Cu^{2+}) compared to the single bond cross-linkers (hydrolysate), allows them to exhibit greater structural strength. Moreover, the study revealed the *in vivo* antioxidant properties based on Cu^{2+}-induced oxidative stress of TSG hydrolysates using the nematode *C. elegans* as a model organism. Peptides present in TSG hydrolysate produced with Alcalase® were found to significantly reduce endogenous ROS levels through Cu^{2+} coordination, which prolonged the lifespan of *C. elegans*. The results of this study suggest that red Tilapia scale gelatin can be used to prepare Cu^{2+}-chelating peptides endowed with tuned self-assembly and antioxidant properties through a single enzymatic treatment with

Alcalase®. These peptides can serve as theoretical models for the development of innovative food-derived functional nanomaterials in the fields of biomedicine, food, and cosmetics. Looking to the future, a better understanding of self-assembly triggered by peptide to Cu^{2+} molar ratio in TSG peptides is needed to design novel food-derived self-assembled peptides under the most suitable conditions.

Chapter 7. Effect of Cu^{2+} Coordination on Peptide Self-Assembly, Mechanical Properties, and Bioactivity of Peptide Hydrolysates Obtained from Sunflower Meal Protein Isolate

Following up on our discussion of the great potential of sunflower meal (SM) by-products for the production of MCPs, as demonstrated in **Chapters 4** and **5,** and following up on the previous **Chapter 6** on bioactive self-assembled peptides from food protein hydrolysates, we now investigate the effect of Cu^{2+} coordination on peptide self-assembly and *in vivo* antioxidant properties of sunflower meal by-product hydrolysates using Cu^{2+}-induced oxidative stress in *Caenorhabditis elegans* as a model organism. This approach may provide a promising strategy to modify the self-assembly pattern of SM-derived peptides, enabling the development of food peptide-based biomaterials with potential biological applications.

This chapter will be submitted to the journal *Food chemistry*:

Camaño*, J.A., Abioye, R.O., Reyes, S., Selmeczi, K., Canabady-Rochelle, L., Udenigwe*, C. Effect of Cu^{2+} Coordination on Peptide Self-Assembly, Mechanical Properties, and Bioactivity of Peptide Hydrolysates Obtained from Sunflower Meal Protein Isolate.

7.1 Introduction

Sunflower (*Helianthus annus* L.) seed is one of the most important consumed oil crops in the world, with a global production estimated by the United States Department of Agriculture (USDA) at 47 million metric tons by 2023 (Li et al., 2024). Owing to their high oil content, sunflower seed is used to produce high quality oil, mostly for food applications. However, the residual meal by-product generated after oil extraction has attracted much attention due to its high protein content (30-50 % w/w), high nutritional value and amino acid composition, making it a high-quality protein resource (De Oliveira Filho & Egea, 2021).

Bioactive peptides are biological compounds naturally encrypted within protein sequence under their inactive form and released upon proteolysis (Liu et al., 2020). Recently, the production of by-products-derived bioactive peptides from hydrolysates has gained strong interest as one of the strategies to promote the valorization of food wastes. In this aspect, several researchers have focused on the enzymatic hydrolysates due to their good biological activities, low cost and high efficiency. For instance, sunflower meal by-product has been reported to produce hydrolysates with immune-modulating (Velliquette et al., 2020), angiotensin I-converting enzyme inhibition (Sentís-Moré et al., 2022), antioxidant and anti-inflammatory activities (Tonolo et al., 2024). Besides, our group reported that sunflower meal by-product provides an excellent protein alternative for producing metal-chelating peptides **Chapters 4** and **5**.

In addition to their biological activity, food protein-derived hydrolysates are highly interesting building blocks for designing and fabricating peptides-based nanomaterials through a spontaneous and reversible process, known as self-assembly (Abioye et al., 2024). Due to the diversity of their primary sequence, enzymatically digested peptides can form organized self-assembled nanostructures endowed with excellent functionality through non-covalent interactions (Vahedifar & Wu, 2022). Thus, the combination of bioactivity and self-assembly of peptides has emerged as a new approach for the design and development of novel functional nanomaterials in biomedicine, food and cosmetics (Chen et al., 2022). Both intrinsic factors (such as hydrophobicity, net charge, polarity, size, amino acid side chains) and extrinsic factors (such as, pH, ionic strength, temperature, and metal ion coordination) can trigger peptide self-assembly (Abioye et al., 2024). Particularly, metal ion coordination is a potential approach to tune the peptide self-assembly pattern in order to produce peptide-

based biomaterials with potential biological functions. Indeed, all the peptides do not follow the same self-assembly pathway. For example, Mohammed et al., (2022) demonstrated that the self-assembly of pentapeptide (FFRGD) formed different nanostructures with improved mechanical properties upon the addition of divalent metal ions (e.g., Mg^{2+}, Ca^{2+} and Ba^{2+}). Likewise, Abul-Haija et al., (2017) reported that after coordination with copper ions, the co-assembly of FFD/GHK peptides formed networks of nanofibers, resulting in hydrogel formation. In contrast, the Cu^{2+} coordination through a pyrene–peptide conjugate was unfavourable to the formation of hydrogels based on an effective crosslinking of a Cu^{2+} triggered peptide; instead, spherical assemblies with a weaker 3D network are formed Fortunato & Mba, (2021). Despite the success in enhancing the physico-chemical and mechanical properties of peptide-based biomaterials through metal ion coordination, the full potential of Cu^{2+} coordination to generate supramolecular assemblies from food-derived self-assembled peptides has not yet been exploited. Therefore, a thorough knowledge of the effect of Cu^{2+} coordination on the self-assembly of peptides present in food protein hydrolysates could provide insights into the ability of food-derived Cu^{2+}-chelating peptides to form metal ion-triggered self-assembled peptide supramolecular structures, thus advancing progress on novel functional nanomaterials. Additionally, there is no literature on the influence of Cu^{2+} coordination on the physico-chemical, mechanical and *in vivo* antioxidant properties of enzymatically digested self-assembled bioactive peptides from food protein hydrolysates. Thus, the present study aimed to provide an understanding of the effect of Cu^{2+} coordination both on the peptide self-assembly pattern and *in vivo* antioxidant ability of sunflower meal by-product hydrolysates, based on Cu^{2+}-induced oxidative stress using the nematode *Caenorhabditis elegans* as a model organism.

7.2 Materials and methods

7.2.1 Chemicals and reagents

Sunflower meal (**SM**) was provided by SAS IMPROVE (Dury, France). Protamex® (**Prot**, protease from *Bacillus* sp., ≥ 1.5 U/g), Flavourzyme® (**Flav**, protease from *Aspergillus oryzae*, ≥ 500 U/g), 37 % hydrochloric acid (HCl), ammonium bicarbonate, ethylenediaminetetraacetic acid (Na_2**EDTA**, $Na_2{\cdot}2H_2O$), copper (Cu^{2+}) sulfate pentahydrate, sodium acetate, thioflavin T (**ThT**), 8-anilino-1-naphthalenenesulfonic acid (**ANS**), 5-fluoro-2'-deoxyuridine, 2',7'-

dichlorofluorescein diacetate, and sodium azide (NaN_3) were purchased from Sigma–Aldrich (St Louis, MO, USA). All the other reagents, including disodium phosphate (Na_2HPO_4), potassium dihydrogen phosphate (KH_2PO_4), sodium chloride, magnesium(II) sulfate heptahydrate ($MgSO_4 \cdot 7H_2O$), sodium hydroxide (NaOH) and sodium hypochlorite (NaClO), were of analytical grade (≥ 95 %) and used without further purification.

7.2.2 Preparation of protein hydrolysate from sunflower meal

*7.2.2.1 **Preparation** of sunflower meal protein isolate*

The sunflower meal protein isolate (SMPI) was obtained using the method reported by Kalpana et al., (2020) based on NaCl extraction to solubilize the majority of globulins proteins. The sunflower meal (30 g) was dissolved in a 10 % (w/v) meal-to-ultrapure water ratio, added to 10 % (w/v) of NaCl. Then, the former solution was stirred on a magnetic stirrer plate (60 min, 40 °C, at pH 6). After solubilization, the sample was cloth filtrated to remove solidified residues. The resulting solution was centrifuged (Centrifuge Universal 320, Hettich, Tuttlingen, Germany) at 3300 g, for 10 min, at 20 °C. Afterwards, the resulting supernatant composed of solubilized proteins was recovered and filtrated with a Whatman No. 4 filter paper (Whatman International, Maidstone, England). The filtrated supernatant was precipitated within 10 min by adjusting the pH at 4.5, corresponding to the isoelectric point of sunflower proteins (Dabbour et al., 2019). This suspension was let at rest for 30 min at room temperature (25 °C), and then centrifuged again (3300 g, 10 min, 20 °C). The pellet was finally dried using a convective oven (Thermo ScientificTM, USA) at 55 °C overnight. SMPI was stored at -20 °C until further use.

7.2.2.2 Protein hydrolysis

Hydrolysates from SMPI were obtained as previously described with some modification (El Hajj et al., 2023). First, SMPI was dissolved at 2 % (w/v) in 50 mM ammonium bicarbonate buffer solution. Then, SMPI was hydrolysed either with Protamex® (**Prot**) or Protamex® followed by Flavourzyme® (**Prot+Flav**). Hydrolysis parameters were as follows: 1 % (w/w) enzyme/substrate ratio, for 2 h, at pH 8 and 55 °C with Protamex® and for 2 h, at pH 7 and 55 °C with Flavourzyme®, which correspond to the optimal enzyme conditions. Upon hydrolysis, pH was maintained at the desired values by adding 1 M NaOH solution. After each hydrolysis

step, the protease was heat inactivated (95 °C, 15 min). In sequential treatment, Protamex® was inactivated before Flavourzyme® treatment. Then, the hydrolysates were centrifuged (10 000 g, 15 min, 25 °C) and the supernatants were freeze-dried (LABCONCO, Kansas City, USA) and stored at −20 °C for further analysis.

The two hydrolysate powders were further dissolved (2 % (w/v) in ultrapure water; quantity sufficient for qsf 250 mL) and subjected to ultrafiltration under magnetic stirring and 5 bar of nitrogen pressure (El Hajj et al., 2023). The ultrafiltration unit (UF stirred cell 47-mm system XFUF04701; Millipore, Molsheim, France) was initially equipped with a 10-kDa molecular weight cut-off (MWCO) membrane, followed by a 1-kDa MWCO membrane (Millipore, Billerica, USA), conditioned according to the manufacturer's specification, before ultrafiltration. The ultrafiltrated fractions of the hydrolysates (≤ 1 kDa Prot and ≤ 1 kDa Prot+Flav) were freeze-dried and kept at −20 °C until further analysis. In total, four hydrolysates were investigated. The degree of hydrolysis (DH) of the whole hydrolysates only and the peptide concentration of the four hydrolysates and SMPI expressed as mM eq. NH_2 (*o*-Phthalaldehyde analysis) are displayed in **Appendix 4.2**.

7.2.3 Investigation of peptide-Cu^{2+} interaction

All the spectroscopic measurements were performed at the PhotoNS Platform of the L2CM Laboratory, Université de Lorraine.

7.2.3.1 UV-visible spectroscopy

7.2.3.1.1 UV-visible spectra

The determination of the UV-visible (UV-vis) spectra of Cu^{2+} ions and peptide-Cu^{2+}complexes formed by peptides present in SMPI hydrolysates were recorded on a PerkinElmer Lambda1050 UV-vis-NIR spectrophotometer (Perkin Elmer Corp, Massachusetts, USA) in a quartz cuvette with 1.0 cm path length in a range of wavelengths varying from 300 to 800 nm at room temperature (25 he coordination modes of peptide-Cu^{2+} complexes were investigated by comparing the shifts in the absorption/UV-vis peaks of Cu^{2+}-binding peptides alone with those of the corresponding peptide-Cu^{2+} complex using the same concentration.). The samples were prepared mixing 1500 µL of 50 mM HEPES buffer at pH 7.4 with 500 µL of 5 mM sample solution (expressed as mM eq. NH_2 for hydrolysates) and 62.5 µL of 10 mM

$CuSO_4$ solution in order to have a 1:4 Cu^{2+}-to-peptide molar ratio. The coordination modes of peptide-Cu^{2+} complexes were investigated by comparing the shifts in the absorption/UV-vis peaks of Cu^{2+}-binding peptides alone with those of the corresponding peptide-Cu^{2+} complex using the same concentration.

7.2.3.1.2 Pyrocatechol violet assay

The Cu^{2+}-chelating ability of SPMI hydrolysates was determined using the pyrocatechol violet (PV) assay according to Latha et al., (2021), using EDTA as positive control. A 1 mM copper (Cu^{2+}) sulfate solution ($CuSO_4$) was prepared in a 50 mM sodium acetate buffer, at pH 6.0 (using a 1 N HCl solution). The hydrolysate solutions were prepared in a range of concentrations (0-1 mg/mL) in the former buffer. Then, 237 µL of hydrolysate solution, 50 µL of a 1 mM $CuSO_4$ solution and 13 µL of 2 mM PV solution prepared in the same buffer were mixed and incubated for 3 min at room temperature. The absorbance was measured at a wavelength of 632 nm corresponding to the PV-copper complex using a spectrophotometer MRX Multiskan Go (ThermoFicher Scientific, Vantaa, Finland) equipped with a microplate reader and 96-well microplates Nunclon™ delta surface (Thermo scientific, Roskilde, Denmark). The Cu^{2+}-chelating ability was calculated using the Equation (1).

$$Cu^{2+}\ \text{chelating ability}\ (\%) = \left[\frac{A_0 - A_s}{A_o}\right] X\ 100 \qquad (1)$$

where A_0 is the absorbance of the control (without sample, sample volume replaced by sodium acetate buffer, and A_s is the absorbance either of the sample or of the positive control (EDTA).

The results were expressed as the half maximal effective concentration (EC_{50}), *i.e.,* the hydrolysate concentration required for 50 % copper (Cu^{2+}) chelation.

7.2.3.2 Circular dichroism spectroscopy

The circular dichroism (CD) spectral analysis of the SMPI hydrolysates (whole and 1 kDa fractions) in the presence and absence of Cu^{2+} ions was performed using a MOS-450 CD spectrometer (Bio-Logic Science Instruments, France) in a quartz cuvette with 1.0 cm path length in a range of wavelengths varying from 260 to 800 nm at room temperature (25 °C).

The samples were prepared at 5 mM (expressed as mM eq. NH_2 for hydrolysates) in 50 mM HEPES buffer at pH 7.4 and mixed with 10 mM Cu^{2+} (at 1:4 metal-to-ligand molar ratios, as UV-vis experiment), as previously reported (Csire et al., 2022). The coordination modes of peptide-Cu^{2+} complexes were investigated by comparing the shifts in the absorption/CD peaks of peptides alone with those of the corresponding peptide-Cu^{2+} complex using the same concentration.

7.2.3.3 Nano-LC-MS/MS identification análisis

To gain a deeper understanding of the effect of sequential enzymatic treatment of the production of self-assembled peptide structures and more insight into the effect of Cu^{2+} coordination on the peptide self-assembly, the peptide sequences of SMPI hydrolysates were identified using the nano-LC-MS/MS bioinformatic analysis. Note that the ≤ 1 kDa hydrolysate fractions (≤ 1 kDa Prot and ≤ 1 kDa Prot+Flav) only were studied since they contain lower number of peptide sequences compared to whole hydrolysates, which facilitates the understanding of the peptide self-assembly of SMPI hydrolysates and their chelating properties. Besides, these ≤ 1 kDa hydrolysate fractions exhibited the highest Cu^{2+}-chelating ability. The SMPI hydrolysates were analyzed by nano-LC-MS/MS on a Orbitrap Fusin mass spectrometer (Thermo Fisher Scientific, Waltham, MA, USA) coupled to an UltiMate 3000 nanoRSLC (Dionex, Thermo Fisher Scientific, Waltham, MA, USA) as previously reported (Risha et al., 2020).

The raw Thermo data files resulting from the two ≤ 1 kDa fractions were then processed in the Andromeda search engine of MaxQuant™ (version 2.4.13.0), a commonly used proteomic software tool (Boachie et al., 2022). The peptide sequences were searched against a restricted sunflower seed proteins database (*Helianthus annuus*) containing 30 entries obtained from UniProtKB (https://www.uniprot.org/, accessed on 27 January 2024, **Appendix 4.3**). The peptides identification was achieved by comparing the experimental fragment-ion mass value of the precursor ions with the theoretical fragment masses obtained from the protein sequences database by the unspecified digestion rule with a mass tolerance of 10 ppm. The parameters of database searches were set up as previously reported (Boachie et al., 2022) (**Appendix 4.4**).

In order to compute the physico-chemical properties of peptide sequences identified previously (e.g., length, amino acids composition (individual and groups of AA), isoelectric point (pI) and the grand average of hydropathicity GRAVY index, the MaxQuant^{TM} output tables containing peptide sequences were then loaded in the R programming environment using a Peptides R package (Osorio et al., 2015).

7.2.4 Peptide self-assembly characterization

7.2.4.1 Thioflavin T binding assay

The effect of Cu^{2+} coordination on the presence of amyloid fibril structures in SMPI hydrolysates was assessed using the thioflavin T (ThT) analysis (Abioye et al., 2022). The analysis was conducted at 1:4 Cu^{2+}-to-peptide (hydrolysate) molar ratio. SMPI hydrolysate solution (60 µL, 4 mM eq. NH_2) in the presence and absence (ultrapure water) of copper ions (60 µL, 1 mM $CuSO_4$) was mixed with 10 µL ThT solution (10 µM in ultrapure water) and stirred for 3 min. The fluorescence intensity of ThT in the presence of sample was measured in a black 96-well microplates with clear bottoms (6005570, PerkinElmer, Waltham, MA, USA), at a final volume of 200 µL. Samples were evaluated in triplicates and fluorescence intensity measurements (emission at 480 nm, at 25 °C) were recorded from the bottom of the plate with excitation at 430 nm using the Spark multimode microplate reader (Tecan, Stockholm, Sweden).

7.2.4.2 ANS binding assay

The variation in surface hydrophobicity of SMPI hydrolysates was measured using 8-anilino-1-naphthalenenesulfonic acid (ANS) as a fluorescent probe as previously reported (Hayakawa & Nakai, 1985). The SMPI hydrolysate samples in the presence and absence of copper ions (1:4 metal-to-ligand molar ratio using a 1 mM $CuSO_4$ solution in ultrapure water) were serially diluted with phosphate buffer (0.1 M, pH 7) to obtain hydrolysate concentrations ranging from 0.1 to 5 mM eq. NH_2. Then, 200 µL of sample solution were reacted with 10 µL of ANS solution (8 mM in 0.1 M phosphate buffer, pH 7). The fluorescence intensity was measured at 470 nm in a black 96-well microplates with clear bottoms (6005570, PerkinElmer, Waltham, MA, USA) at the excitation wavelength of 390 nm using the Spark multimode microplate reader (Tecan, Stockholm, Sweden). The index of surface hydrophobicity ($\mathbf{S_o}$ indicates a

relative tendency of sample to prefer a nonaqueous environment over an aqueous one) was determined as the slope the value of the plot of fluorescence intensity vs. hydrolysate concentration using linear regression.

7.2.4.3 Dynamic light scattering measurements

The particle size distribution and polydispersity index (PDI) of SMPI hydrolysates in the presence and absence of copper ions at 1:4 metal-to-ligand molar ratio (prepared similarly as in section 7.2.4.1) were determined by dynamic light scattering (DLS) using a Zetasizer Nano ZS (Malvern Instruments Ltd., Worcestershire, UK) at 25 °C, according to the method described by Abioye et al., (2022). The samples were diluted with Milli-Q water (pH 7, refractive index 1.33, viscosity 0.88 cP and dielectric constant 78.5) with a concentration of 4 mM eq. NH_2, and subsequently transferred into a plastic disposable cuvette (Malvern Instruments Ltd., Worcestershire, UK) for DLS measurements. The dynamic light scattering effect was analyzed with Smoluchowski model at F(ka) 1.50 (term of Henry's equation) and backscattered angle of 173 °.

7.2.4.4 Transmission electron microscopy

To gain further information about the particular structures of the self-assembled peptides present in the SMPI hydrolysates, the morphology of only the whole hydrolysates was studied by transmission electron microscopy (TEM) (based on ThT, ANS and DLS analysis) as described by Abioye et al., (2022) and Schindelin et al., (2012) and. Briefly, a 10 µL aliquot of SMPI whole hydrolysate solutions (4 mM eq. NH_2 in water, Prot and Prot+Flav) in the presence and absence of copper ions at 1:4 metal-to-ligand molar ratio (prepared in the same way as section 7.2.4.1) was placed on 300-mesh Formvar-carbon coated copper grid and incubated for 5 min for absorption. Excess sample was blotted with a Kimwipe, and the grids were finally counterstained with TEM staining solution (Micro To Nano, Haarlem, Netherlands) for 1 min in the dark. Excess stain was blotted again, and the loaded grids were examined using the JEM-1400 Flash Electron Microscope (JEOL, Tokyo, Japan) at an accelerating voltage of 120 kV. Imaging was performed using ImageJ 1.53c software (NIH, Bethesda, MD, USA) under standard operating conditions (Abioye et al., 2022).

7.2.4.5 Mechanical measurements

To evaluate the effect of Cu^{2+} coordination on the mechanical properties (i.e., G' elastic and G'' loss moduli) of SMPI hydrolysates, amplitude sweeps and frequency sweeps analyses were conducted using the Discovery Hybrid Rheometer HR-2 (TA Instruments Ltd., New Castle, USA) containing a cone (2 °, 40 mm diameter, 50 µm truncation gap) and a Peltier plate steel measuring system with a gap height set to 1 mm, according to the method of Abioye et al., (2022). The solution of SMPI hydrolysates in the presence and absence of Cu^{2+} ions (at 1:4 metal-to-ligand molar ratio, prepared as in section 7.2.4.1) were delicately loaded onto the lower testing plate and equilibrated for 5 s at 25 °C. The amplitude sweeps and frequency sweeps analyses were recorded as a function of mechanical strain (0.001-5000 %, at a fixed frequency of 10 rad/s) and angular frequency (0.1- 100 rad/s, at a fixed strain of 1 %), respectively. Before starting a test, the excess of sample was removed to ensure a clear and smooth interface.

7.2.5 Assessment of antioxidant activity in *C. elegans in vivo* model

7.2.5.1 Handling and synchronization

The *in vivo* antioxidant assay was carried out by the method of Sangha et al., (2013) with some modifications. Briefly, the wild-type *C. elegans* strain (isolate N2 from Bristol, UK) was maintained at 23 ± 2 °C on nematode growth medium (NGM**,** Mt. Prospect, IL, USA) containing 200 µL of *Escherichia coli* (OP50) (Caenorhabditis Genetics Center, University of Minnesota, Minneapolis, MN, USA) as food for the *C. elegans*. To synchronize the nematodes at a consistent larval stage for future assays, the *C. elegans* eggs were collected. Nematodes pass through four larval life stages (L1, L2, L3, and L4), characterized primarily by increasing worm size (Mudd & Liceaga, 2022). On the third day of growth, L4 stage adult nematodes were washed 2 times with M9 buffer solution pH 7 (6 g/L Na_2HPO_4, 3 g/L KH_2PO_4, 5 g/L NaCl, 0.215 g/L $MgSO_4 \cdot 7H_2O$) to remove contamination and *E. coli* OP50. The samples were then centrifuged at 2602 g at 4 °C ± 1 °C for 3 min using a Lynx 4000 Centrifuge (ThermoFisher, Canada). After two rounds of washing, a first one with M9 buffer containing 0.1 M NaOH and a second one with M9 buffer containing 0.1 M NaOH and 5 % NaClO to lyse them, the eggs were washed 2 more times with M9 buffer solution. Thereafter, the eggs were placed on fresh

NGM plates with 200 µL *E. coli* OP50 and incubated at 22 °C ± 2 °C until used in the subsequent experiments.

7.2.5.2 Mean life and survival assay

The oxidative stress resistance assay was performed as previously described (Sangha et al., 2013) with slight modifications. The synchronized nematodes were divided into distinct groups: a negative control group (without hydrolysate sample, 200 µL of water), a positive control group (EDTA at 0.5 mM, 200 µL), and the sample group (200 µL of each investigated SMPI hydrolysate at 2 mM eq. NH_2). Approximately 60 ± 5 L2 *C. elegans* nematodes were exposed to each group treatment and then transferred to fresh NGM plates containing 100 µL of 1 mM copper (Cu^{2+}) sulphate solution, a standard dose to induce oxidative stress. For each group (i.e., negative control, positive control and sample group), the nematodes were counted every hour for 8 hours, assessing their viability by pricking them with a platinum wire. Adult L4 stage nematodes from the same group (corresponding to the same plates) were synchronized, and the eggs obtained were transferred to fresh NGM plates containing *E. coli* in order to repeat the above-mentioned process (G1). The plates were incubated at 22 ± 2 °C °C until the nematodes reached the L4 stage again. On total, this sequence (egg, larval L1 to larval L4, adult) was repeated to evaluate the oxidative stress resistance over three consecutive generations (G1 to G3). The *C. elegans* survival and lifespan curves were analyzed by Kaplan-Meier method and log-rank test using GraphPad Prism version 8.0, GraphPad Software (La Jolla, California, United States, www.graphpad.com). All experiments were conducted in triplicate.

7.2.5.3 Reactive oxygen species production by fluorometry

The ability of SMPI hydrolysates to reduce the reactive oxygen species (ROS) production in *C. elegans* model was carried out using fluorometry (Yoon et al., 2018). The G1 synchronized populations of worms were harvested and washed before being resuspended in M9 buffer. The eggs were placed on new NGM plates with 200 µL *E. coli* OP50 bacteria and 200 µL of samples (ultrapure water, 0.5 mM EDTA and hydrolysates at 2 mM eq. NH_2: Prot, Prot+Flav, ≤ 1 kDa Prot and ≤ 1 kDa Prot+Flav) and incubated at 22 ± 2 °C until reaching the L3 stage. The ROS production was stimulated by exposure to a mixed solution of 200 µL of 1 mM copper

(Cu^{2+}) sulfate. A 250 µM 2',7'-dichlorofluorescin diacetate (DCF) stock solution was prepared in DMSO and diluted in the assay buffer to achieve the final concentration of 100 µM for the detection of general oxidative stress. The worms were then incubated at 22 ± 2 °C for 2 h with the DCF solution, allowing its penetration into *C. elegans* and its reaction with ROS. The fluorescence intensity was measured using a Spark multimode spectrophotometer (Tecan, Stockholm, Sweden) with an excitation and an emission wavelength set at around 485 nm and 535 nm, respectively.

7.2.5.4 Reactive oxygen species production by fluorescence microscopy

In order to measure the ROS production in *C. elegans* model, fluorescence microscopy analysis were carried out in generation 1 G1 using the method reported by Yoon et al., (2018) with some modifications. The eggs of adult nematodes synchronized were placed on new NGM plates with 200 µL *E. coli* OP50 bacteria and 200 µL of samples (ultrapure water, 0.5 mM EDTA and hydrolysates at 2 mM eq. NH_2: Prot, Prot+Flav, ≤ 1 kDa Prot and ≤ 1 kDa Prot+Flav), followed by incubation at 22 ± 2 °C until reaching the L3 stage (24-36 h). Then, about 15 nematodes were transferred to new NGM plates added with 50 µL of 100 µM 5-fluoro-2'-deoxyuridine (to prevent offspring production) and 100 µL of 1 mM copper (Cu^{2+}) sulfate to induce oxidative stress. The nematodes were incubated at 22 °C ± 2 °C for 12 more hours. Upon reaching L3 stage, the nematodes were transferred to a new NGM plates supplemented with 200 µL of DCF (100 µM) -containing M9 solution and incubated in the dark at room temperature for 1.5 h. Thereafter, 50 µL of M9 solution containing 10 mM sodium azide (NaN_3 used as an anesthetic) was added, and after 1 h of incubation the nematodes were transferred to new NGM plates. The plates were placed on a fluorescence microscope using the Axio Imager 2 microscope equipped with an Axiocam 506 camera. Zen 2.3 pro software in order to capture the fluorescence of the oxidized DCF product.

7.2.6 Statistical analysis

The analyses were conducted at least three times, and all the data are presented as means ± standard deviation. The statistical analyses were one-way analysis of variance (ANOVA), and significant differences between means of samples were determined by Fisher's multiple

range test. Differences at *p-value* < 0.05 were considered significant. Statistical calculations were conducted using the software Statgraphics centurion XVI version 16.1.03 (Statgraphics Technologies Inc, Virginia, USA).

7.3 Results and discussion

7.3.1 Cu^{2+} coordination properties

7.3.1.1 Peptide-Cu^{2+} complex formation by UV-vis and CD

UV-visible spectroscopy (**UV-vis**) and circular dichroism (**CD**) were used to study the metal ion coordination sphere in the complexes formed between peptides present in SMPI hydrolysates and Cu^{2+} ions in solution at physiological pH (7.4). Changes in λ_{max} values and absorption/CD band shapes of hydrolysates in the absence and presence of copper (Cu^{2+}) were analysed using the same hydrolysate concentration. These UV-vis and CD measurements can reveal different electronic transitions commonly observed in metal coordination complexes, such as the d-d and the charge transfer (**CT**) transitions. **Figure 7.1A-H** show the UV-vis absorption and CD spectra of peptide-Cu^{2+} complex of the different SMPI hydrolysates. **Table 7.1** illustrates the maximum wavelengths and sign of different bands corresponding to the d-d and CT transitions from the UV-Vis and CD spectra. The UV-vis spectra show a significant blue shift of the d-d transition band from 805 nm (Cu^{2+} alone) to 550-612 nm (peptide-Cu^{2+} complexes) associated with the Cu^{2+} complexation through peptides present in SMPI hydrolysates and their ≤ 1 kDa fractions (**Figure 7.1, Table 7.1**).

Moreover, analyzing the CD data, which provides more detailed information of the binding properties and coordination modes, the d-d transition bands are mainly observed with a negative Cotton effect around 560-577 nm. Keeping in mind that in a mixture containing several Cu^{2+} coordinating peptides, it is difficult to identify a single coordination mode, one can attribute these UV-vis and CD profiles to the formation of 3N- and 4N-coordinated complex in all hydrolysates (Watly et al., 2019; Mital et al., 2020; Kastal et al., 2024). Although the four hydrolysates have 3N/4N-coordinated complexes in common (**Figure 7.1I-J**), it is likely that the donor atom sets involved for single and sequential hydrolysates are differently composed of NH_2, N^-_{amide} and $N_{imidazole}$. For instance, the shift from 597 nm (Prot+Flav) to 550 nm (Prot) and from 612 nm (≤ 1 kDa Prot+Flav) to 573 nm (≤ 1 kDa Prot) (**Table 7.1**) could indicate the participation of a second deprotonated amide nitrogen in Cu^{2+} binding, as

previously reported (Kulon et al., 2008). Moreover, the 4N-coordinated ATCUN motif where the copper coordination sphere in square planar geometry is composed of [NH_2, $2N^-_{amide}$,$N_{imidazole}$] donor set exhibits characteristic absorption and CD d-d transition bands at 520 nm and 560 nm (-), respectively (Gonzalez et al., 2018). Meanwhile, the CT transitions in CD spectra observed around 280 nm and 330 nm with negative and positive Cotton effects, respectively, also confirmed the involvement of imidazole nitrogen ($N_{imidazole}\rightarrow Cu^{2+}$) and amide nitrogen ($N^-_{amide}\rightarrow Cu^{2+}$) in the square planar coordination sphere around the Cu^{2+} ion.

In addition to the information about the coordination modes and geometry of peptide-Cu^{2+} complex formed in SMPI hydrolysates provided by the CD spectra, other significant interpretation in terms of peptide self-assembly or aggregation can be drawn. Note that, upon Cu^{2+} coordination, a negative band between 270 and 300 nm appears in all the four SMPI hydrolysates (**Figure 1B, 1D, 1F, 1H**). This band strongly supports the presence of supramolecular assembly (self-assembled peptides) as previously reported (Fortunato & Mba, 2021).

7.3.1.2 Cu^{2+}-chelating ability

The Cu^{2+}-chelating ability of whole SMPI hydrolysates and their ≤ 1 kDa fractions was investigated as a function of their concentration, in reference to EDTA (**Figure 7.2A**.). The Cu^{2+}-chelating ability increases markedly from 0.1 to 1 mg/mL for all hydrolysates, reaching a final activity of 83, 72, 71 and 50 % for ≤ 1 kDa Prot+Flav, ≤ 1 kDa Prot, Prot+Flav and Prot hydrolysates, respectively. This result clearly shows the presence of Cu^{2+}-chelating peptides in SMPI hydrolysates. From **Figure 7.2A**, the EC_{50} values of Cu^{2+}-chelating activities were calculated for all hydrolysates and presented in **Figure 7.2B**. Notably, the EC_{50} value of the Prot+Flav hydrolysates (whole and ≤ 1 kDa fraction) is lower than EC_{50} of Prot hydrolysates (*p-value* < 0.05), indicating an increase of Cu^{2+}-chelating ability upon sequential hydrolysis using Flavourzyme® after Protamex® treatment. Moreover, comparing the ≤ 1 kDa hydrolysates, the EC_{50} values are much lower than in their corresponding whole hydrolysates (*p-value* < 0.05). Thus, both the sequential enzymatic treatment and the 1 kDa ultrafiltration process enhanced the Cu^{2+}-chelating ability of SMPI hydrolysates.

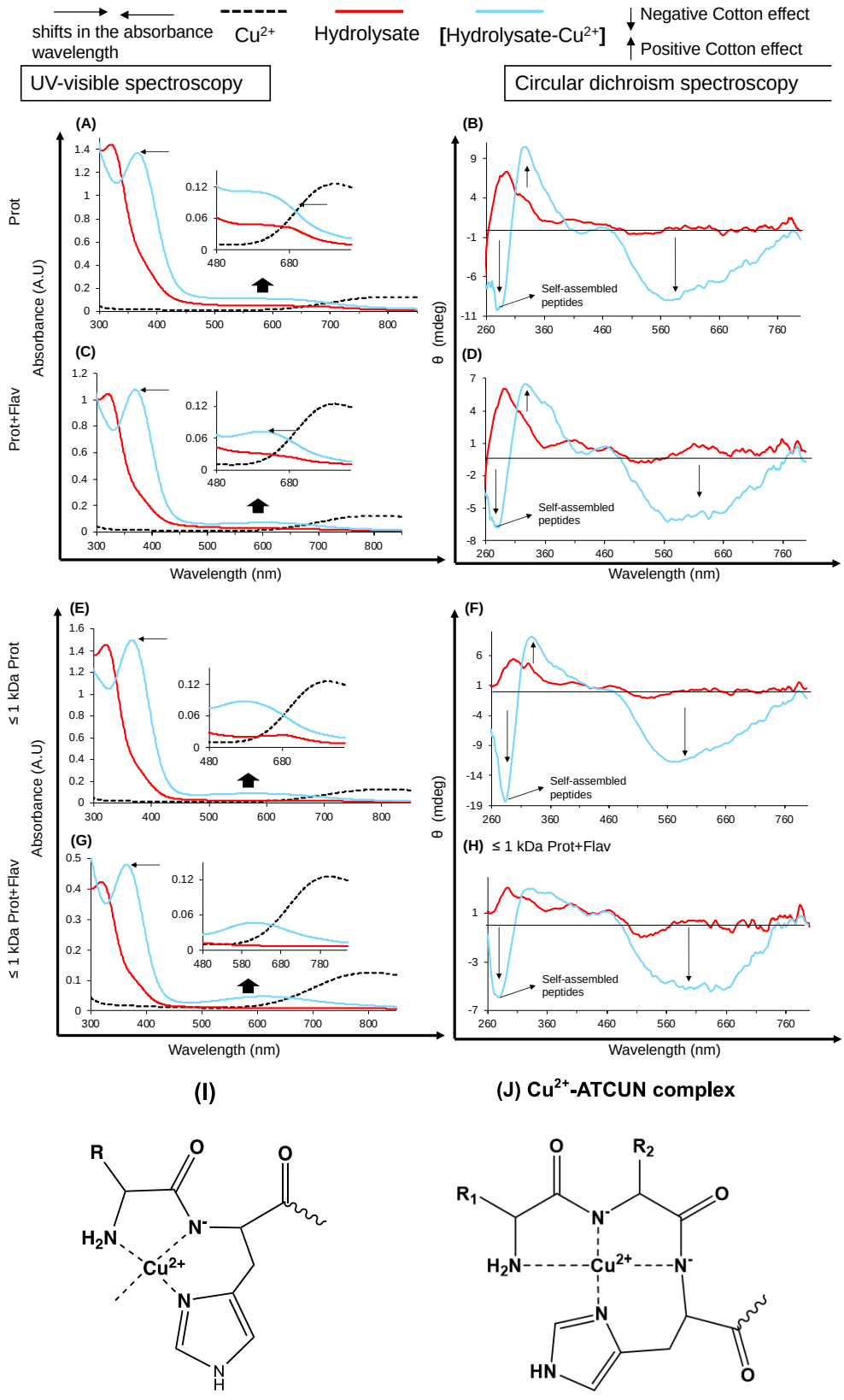

Figure 7.1. UV-visible and CD measurements of the peptide-Cu^{2+} interaction of different SMPI hydrolysates. (A-B) Prot, (C-D) Prot+Flav, (E-F) ≤ 1 kDa Prot, (G-H) ≤ 1 kDa Prot+Flav.

Prot: Protamex® hydrolysate; Prot+Flav: Protamex® followed by Flavourzyme®; ≤ 1 kDa: 1 kDa ultrafiltrated hydrolysate.

Table 7.1. Spectroscopic data for the peptide-Cu^{2+} complexes at 1:4 metal-to-ligand ratio at physiological pH 7.4.

Sample	UV-vis (nm)		CD (nm)	
	d-d transition	CT transition	d-d transition	CT transition
Cu^{2+}	805			
Prot-Cu^{2+}	550	366	577 (-)	278 (-), 327 (+)
[Prot+Flav-Cu^{2+}]	597	369	565 (-)	280 (-), 327 (+)
[≤ 1 kDa Prot-Cu^{2+}]	573	366	577 (-)	284 (-), 329 (+)
[≤ 1 kDa Prot+Flav-Cu^{2+}]	612	364	560 (-)	280 (-)

Prot: Protamex® hydrolysate; Prot+Flav: Protamex® followed by Flavourzyme®; ≤ 1 kDa: 1 kDa ultrafiltrated hydrolysate. Grey cell: not investigated

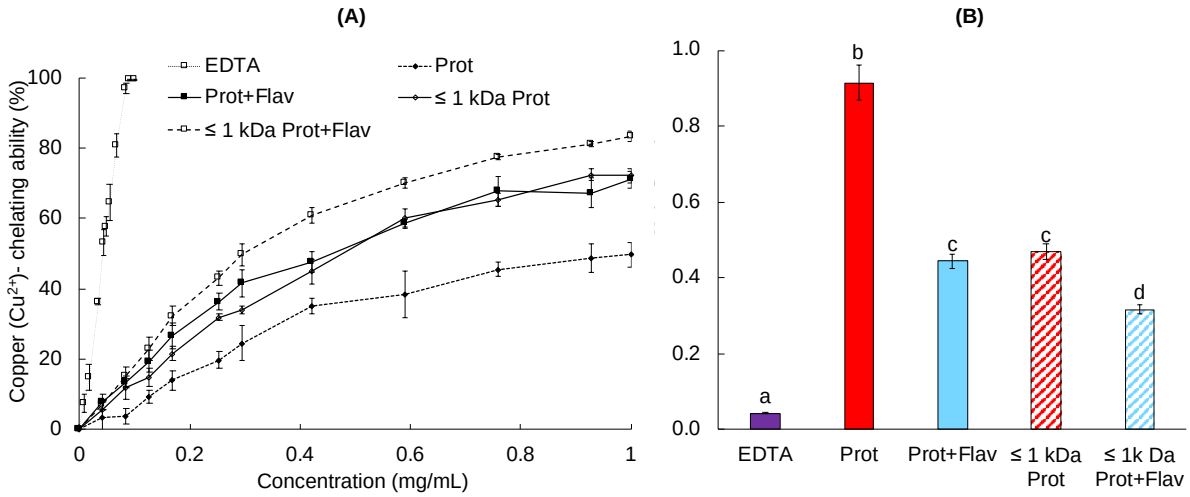

Figure 7.2. Cu^{2+}-chelating ability of different SMPI hydrolysates determined with pyrocatechol violet assay. (A) Chelating ability as function of hydrolysate concentration. (B) EC_{50} values expressed as the quantity (mg/mL) of hydrolysate required to chelate 50 % of Cu^{2+}.

Different letters indicate significant differences (*p-value* < 0.05) by ANOVA. Prot: Protamex® hydrolysate; Prot+Flav: Protamex® followed by Flavourzyme®; ≤ 1 kDa: 1 kDa ultrafiltrated hydrolysate.

SMPI hydrolysates could contain peptides with chelating amino acid (AA) residues such as histidine (His, H) and cysteine (Cys, C), which could form coordination complex with Cu^{2+} ions through their imidazole and thiol groups, respectively (Camaño Echavarría et al., 2024; Sóvágó et al., 2012). In addition to the presence of chelating AA residues, the Cu^{2+}-chelating

activity also depends on the peptide primary structure and its molecular weight. The high Cu^{2+}-chelating ability of Prot+Flav hydrolysates can be attributed to their higher content of small-sized peptides, which are associated with an increased concentration of carboxylic and amino termini groups compared to Prot hydrolysates (lower DH, larger-sized peptide). These termini groups are also known to play a significant role in metal complexation (Bassan & Marchesan, 2022). Similar to our study, Carrasco-Castilla et al., (2012), Vo & Pham, (2020) and Latha et al., (2021) reported small-sized peptides (high DH) as the most effective Cu^{2+} chelators in protein hydrolysates produced from bean (*Phaseolus vulgaris*), salmon by-products and chia seed proteins, respectively.

7.3.1.3 Nano-LC-MS/MS bioinformatic analysis

Peptide sequences identified from ≤ 1 kDa Prot and ≤ 1 kDa Prot+Flav hydrolysate fractions are shown in **Appendix 7.1**. In total, 319 and 389 peptides were identified from the single and sequential treatments, respectively, with 61 % (197) overlapping peptide sequences (**Figure 7.3A**). Among the total identified peptides, 52 and 66 His- or Cys-containing peptides were identified in ≤ 1 kDa Prot and ≤ 1 kDa Prot+Flav, respectively (**Appendix 7.2**), which represent about 16-17 % of all identified peptides. They could be chelating peptide candidates due to their imidazole (His) and thiol groups (Cys), which have been widely reported to complex Cu^{2+} ions (Sóvágó et al., 2012). Interestingly, Prot hydrolysis after ultrafiltration produced one unique Cys-containing peptide while, upon the Flav sequential hydrolysis, 11 additional Cys-containing peptide sequences were generated. This suggests that Prot+Flav hydrolysates contain more metal chelating sites compared to Prot hydrolysates. This finding strongly supports the high Cu^{2+}-chelating ability of ≤ 1 kDa Prot+Flav seen in the PV assay (**Figure 7.2**). Moreover, MS/MS analysis suggests that the Cu^{2+} binding mechanism and their number of binding sites might vary in each hydrolysate.

Thus, the stability, strength and geometry properties of each resulting peptide-Cu^{2+} complex can be different. From **Appendix 7.2**, both ATCUN (highlighted in bold) and Cys-containing peptides are the most interesting peptide sequences because they can highly complex Cu^{2+} ions; these specific identified peptides only are shown in **Table 7.2**. Among the His-containing peptides, both hydrolysates contain peptides with His residue in the third position from the

amino terminus, which induce better stability in the formed peptide-Cu^{2+} complex (Sóvágó et al., 2012).

These peptides contain the so-called "amino terminal Cu(II) and Ni(II)-binding (ATCUN) motif" (**Figure 7.1J**), structurally characterized by (i) a free N-terminal amino nitrogen (NH_2) of the first residue, (ii) two intervening deprotonated amide nitrogen of the peptide backbone, and (iii) an imidazole nitrogen of the third His residue from N-terminus (Miyamoto et al., 2016). The sequenced mass spectra of the most interesting sequences of ATCUN peptides from SMPI hydrolysates loaded into the MaxQuant viewer are illustrated in Appendix data (**Appendix 7.3**). **Figure 7.3B-C** illustrates the 4N coordination mode of peptide-Cu^{2+} complexes of two ATCUN peptide sequences identified in SMPI hydrolysates (AV**H**WTY and KG**H**LPQN).

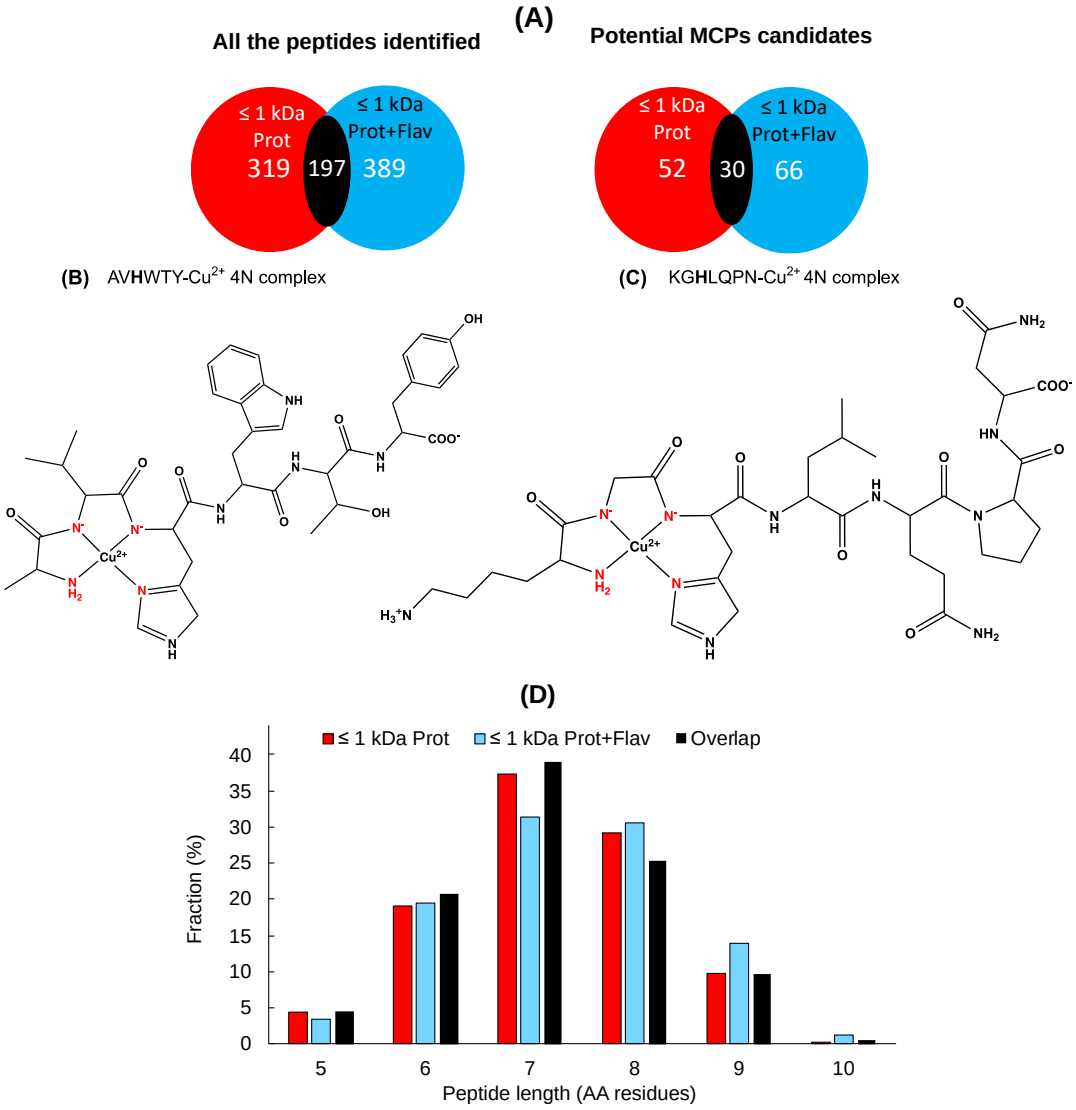

Figure 7.3. Part I. nano-LC-MS/MS identification of peptide sequences present in different SMPI hydrolysates. (A) total number of peptides identified, (B-C) ATCUN peptide sequences identified in complex with Cu^{2+} ions by 4N coordination mode. (D) percentage of lengths of all identified peptides.

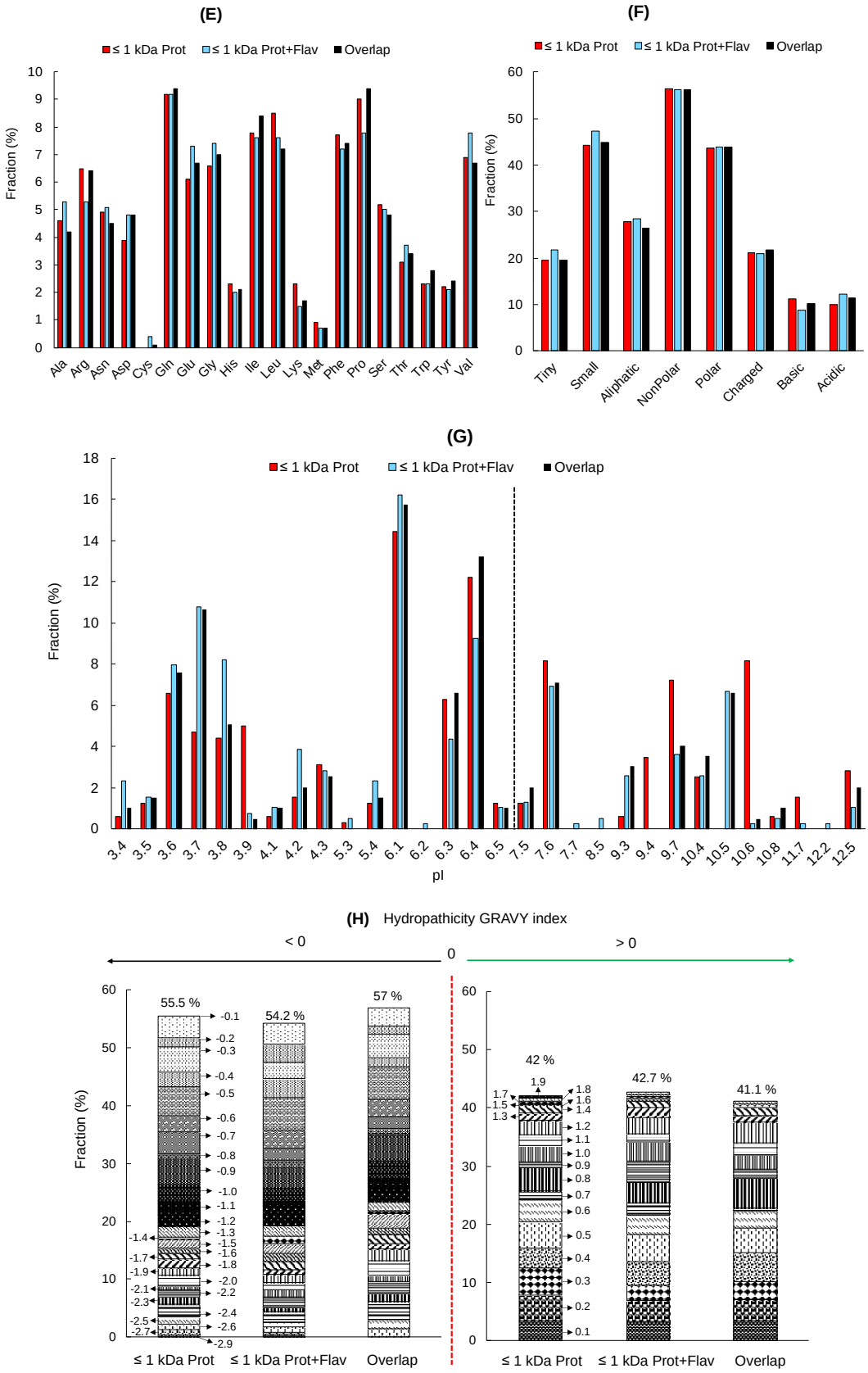

Figure 7.3. Part II, (E) distribution of amino acid (AA) residues of total identified peptides, (F) percentage of AA residue group types, (G) distribution of peptides isoelectric point (pI), and (H) distribution of hydropathicity GRAVY index.

Table 7.2. Potential Cu^{2+}-chelating peptides containing His and Cys residues obtained from nano-LC-MS/MS analysis.

Type of peptide	Sequence	Intensity (x 10^5)		Length	Mass (Da)	Score	Entry
		≤ 1 kDa Prot	≤ 1 kDa Prot+Flav				
ATCUN motif-containing peptides	AV**H**WTY		178.52	6	775.37	63.67	A0A251T566
	KG**H**LQPN	8272.70		7	792.42	85.36	
	KG**H**LQPNA	1722.30		8	863.46	60.97	A0A251UYX1
	NE**H**KLPIL	346.82		8	962.55	60.97	
	QY**H**PGQQ	4250.20	190.36	7	856.38	100.27	A0A251T566
	SE**H**IQGQ	3111.50	2962.40	7	797.37	111.65	A0A251UYX1
	VD**H**ETAE		161.88	7	799.33	74.52	A0A251TUS1
Cys-containing peptides	**C**EPYIVR		76.09	7	935.45	47.92	A0A251UYX1
	CRWISF		782.23	6	867.41	69.09	A0A9K3HVJ0
	G**C**RWISF		1178.50	7	924.43	45.95	
	GIEQT**I**C		49.11	7	819.38	94.01	A0A251T566
	GVEET**I**CS		222.03	8	893.38	106.42	A0A251UCD5
	GVEET**I**CSA		664.64	9	964.42	129.68	A0A251UYX1
	GVILPG**C**PE		86.31	9	940.47	53.35	A0A251TKL9
	LPG**C**VETF		81.31	8	921.43	52.30	A0A251T566
	Q**C**RETE	49.28	181.97	6	821.33	57.45	P15461
	SGPEF**C**NL		641.08	8	922.39	93.20	A0A9K3J8S2
	SPEF**C**NL		608.96	7	865.36	88.64	A0A251UYX1
	VILPG**C**PE		106.76	8	883.45	54.77	A0A251TKL9
Total peptides		6	16				

Prot: Protamex® hydrolysate; Prot+Flav: Protamex® followed by Flavourzyme®; ≤ 1 kDa: 1 kDa ultrafiltrated hydrolysate.

Several intrinsic factors can affect the copper-induced peptide self-assembly, such as peptide length, amino acid composition and physico-chemical properties of the peptide sequences (Abioye et al., 2024). Therefore, the peptide size, amino acid composition, the isoelectric point (pI) and the grand average of hydropathicity GRAVY index of all the peptides identified were also calculated (from peptide list in **Appendix 7.2**). Over 50 % of the peptide sequences have 7-8 amino acid residues (**Figure 7.3D**). Regarding the AA composition (**Figure 7.3E**), Gln, Ile, Leu, Phe and Pro are the most abundant ones in ≤ 1 kDa Prot hydrolysate. Moreover, after Flav hydrolysis, the proportion of Val, Glu, Gly, Asp, Asn, Ala and Cys increased. In terms of residue types (Osorio et al., 2015), only tiny (Ala, Cys, Gly, Ser, Thr), small (Ala, Cys, Asp, Gly, Asn, Pro, Ser, Thr and Val) and acidic AA (Asp and Glu) increased when comparing ≤ 1 kDa Prot and ≤ 1 kDa Prot+Flav hydrolysates (**Figure 7.3F**).

Besides, peptide self-assembly can be governed by noncovalent intermolecular interactions involving notably: hydrophobic AA residues (nonpolar AA, i.e., Leu and Ala), π–π stacking with aromatic AA (Phe, Trp and Tyr), hydrogen-bonding (amide, amino and carboxyl groups), and electrostatic interactions involving both acidic (Asp and Glu) and basic AA (His, Lys and Arg)

(Li et al., 2023). Thus, SMPI hydrolysates could offer interesting peptide self-assembly properties.

Regarding the physico-chemical properties calculated from the sequences displayed in **Appendix 7.2**, **Figure 7.3G** shows that for all hydrolysates the majority of peptides present a pI value between 3.4 and 6.4 (over 50 %). Thus, at neutral pH 7 (as in our study), there is an increase in the negative charge of the peptides partially due to the complete deprotonation of the histidine, aspartic acid and glutamic acid residues; this could lead to the formation of self-assembled peptide structures through electrostatic interactions with positively charged AA.

The hydrophobicity of the identified peptides (**Figure 7.3H**), calculated by the grand average of hydropathicity GRAVY index (the relative hydrophobicity or hydrophilicity of a compound; below 0: hydrophilicity; above 0: hydrophobicity) (Boachie et al., 2022), indicates that, although the two hydrolysates (≤ 1 kDa Prot and ≤ 1 kDa Prot+Flav) contain both hydrophilic and hydrophobic peptides (broad range from -3.4 to 1.8), there is a remarkable trend towards positive GRAVY index values for both hydrolysates, indicating a high hydrophobicity (~40 %). Indeed, high hydrophobicity promotes attractive hydrophobic interactions between peptides, which could lead to the formation of stable ordered nanoarchitectures from food hydrolysates (Vahedifar & Wu, 2022).

7.3.2 Physico-chemical characterization of self-assembled peptides

In order to gain insights into the effect of Cu^{2+} coordination on the supramolecular and global arrangement of self-assembled peptides present in SMPI hydrolysates, several complementary analyses were carried out: ThT fluorescence, ANS, DLS and TEM.

Fluorescence. Firstly, the presence of self-assembled peptides in SMPI hydrolysates was studied by ThT fluorescence assay. In this assay, the ThT probe selectively binds to cross-β structures (amyloid-like fibrils), which are composed of a pair of β-sheets closely packed by interdigitating side chains stabilized by non-covalent interactions (Vahedifar & Wu, 2022). The **Figure 7.4A** shows different degrees of cross-β structures formation for the enzymatic hydrolysates in the absence and presence of copper (Cu^{2+}) ions. Among all the samples, the Prot hydrolysate, characterized by high content of bigger-sized peptides compared to

Prot+Flav one (low DH, **Appendix 4.2**), showed the highest number of cross-β structures, followed by Prot+Flav, ≤ 1 kDa Prot and ≤ 1 kDa Prot+Flav. Thus, the presence of small-sized peptides tends to decrease the formation of cross-β structures in SMPI hydrolysates. In self-assembled peptides derived from food proteins, the cross-β aggregation is a shared characteristics of amyloid-like fibrils and amorphous aggregates, both of which involve non-covalent interactions such as hydrophobic interactions, hydrogen bonds, π–π interactions between aromatic amino acids, and van der Waals interactions (Vahedifar & Wu, 2022).

With the formation of peptide-Cu^{2+} complex in SMPI hydrolysates or fractions, the presence of cross-β structures decreased significantly (*p-value* < 0.05) except for ≤ 1 kDa Prot+Flav. This suggests that the Cu^{2+} coordination with peptide present in hydrolysate induces the formation of other type of self-assembled structures. As previously reported (Shen et al., 2014), the formation of a complex between amyloid-β (Aβ) peptide $Aβ_{19–20}$ and Cu^{2+} ions induced conformational changes from initial well-ordered tubular structures (also called fibrils) into homogeneous micro-vesicles. Furthermore, the histidine-Cu^{2+} interactions could also form aggregated micellar networks due to a competition between copper coordination and peptide self-assembly (Chen et al., 2022). Based on this finding, Cu^{2+}-chelating peptides identified in SMPI hydrolysates could serve as Aβ fibrillation inhibitors since they could capture Cu^{2+} ions from amyloid plaques through their imidazole nitrogen of His-containing motif (Bassan & Marchesan, 2022).

Secondly, the hydrophobicity of SMPI hydrolysates and their peptide-Cu^{2+} complex was investigated by the ANS probe assay. This hydrophobicity property referees to the aggregation phenomenon where molecules of water are repulsed by nonpolar groups, providing information about the number of hydrophobic groups present on the molecular surface as well as the solubility of peptides in aqueous environments (Udechukwu et al., 2018). As shown in **Figure 7.4B**, and similarly to ThT assay, the surface hydrophobicity (S_o) of SMPI hydrolysates decreased significantly *(p-value* < 0.05) after the sequential hydrolysis and the ≤ 1 kDa ultrafiltration process except for ≤ 1 kDa Prot+Flav. This means that small-sized peptides present higher solubility than bigger-sized peptides. Upon Cu^{2+} coordination, the S_o value decreased significantly (*p-value* < 0.05), indicating the formation of a soluble peptide-Cu^{2+} complex. Indeed, due to the high solubility of peptides present in ≤ 1 kDa fraction

hydrolysates in aqueous environments, Cu^{2+} may have better accessibility to their metal ion binding sites.

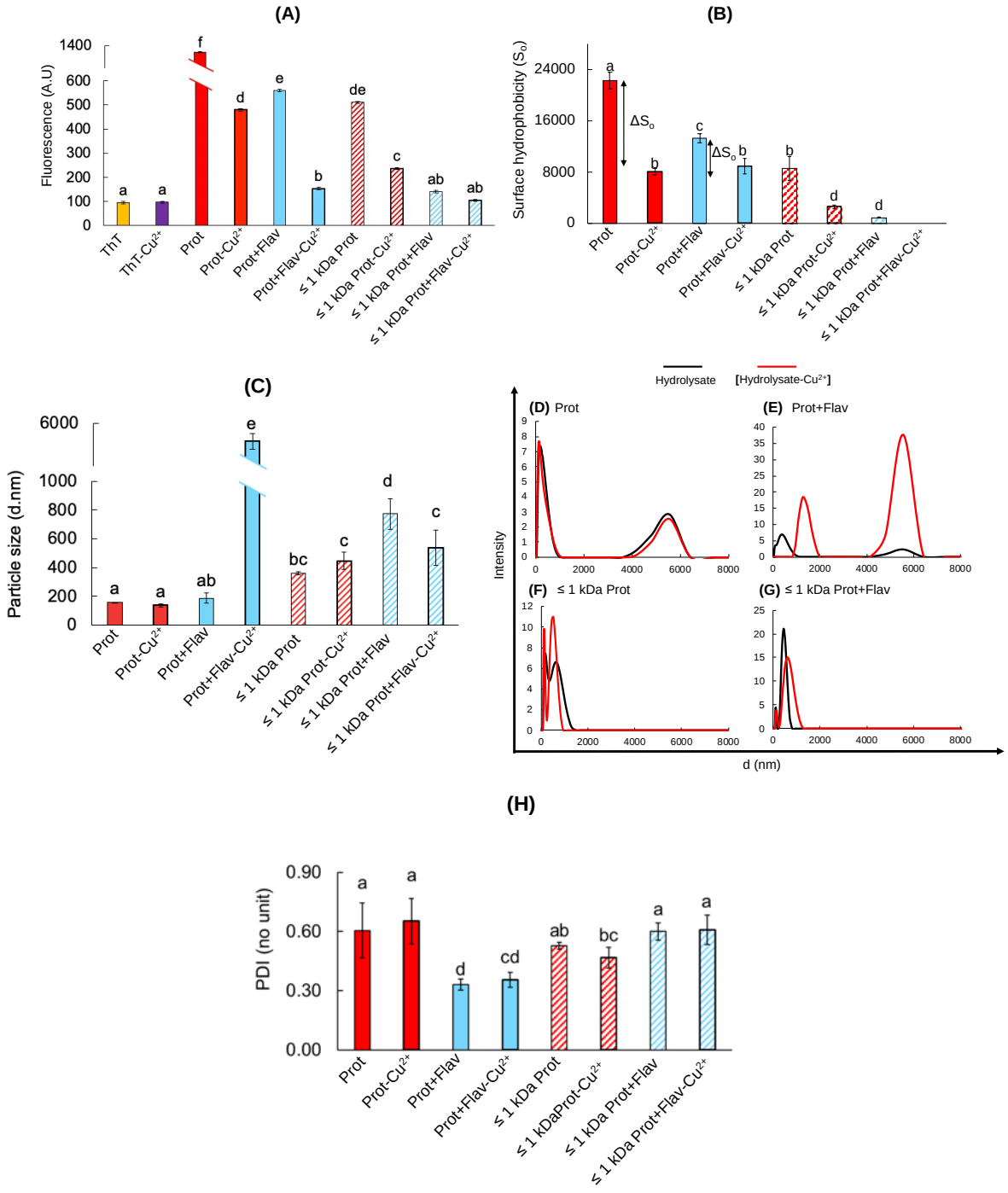

Figure 7.4. Thioflavin T (ThT) intensity, surface hydrophobicity (S_o), particle size, polydispersity index (PDI) and particle size distribution of different SMPI hydrolysates upon the Cu^{2+} complexation. (A) Thioflavin T (ThT) assay, (B) Surface hydrophobicity (S_o), (C) average particle size, (D-G) particle size distribution and (H) PDI values.

Different letters indicate significant differences (*p-value* < 0.05) by ANOVA. Prot: Protamex® hydrolysate; Prot+Flav: Protamex® followed by Flavourzyme®; ≤ 1 kDa: 1 kDa ultrafiltrated hydrolysate.

Furthermore, although Prot+Flav hydrolysate has a lower S_o value than Prot one, the decrease in hydrophobicity of Prot+Flav is less pronounced after Cu^{2+} coordination compared to Prot (ΔS_o, **Figure 7.4B**). This fact can be explained by the presence of different Cu^{2+}-binding interactions, associated with the Cu^{2+}-chelating peptides identified in each hydrolysate (**Table 7.2**). Different from Prot hydrolysate, Prot+Flav sample contains higher number of Cys-containing peptides (after ultrafiltration), which could lead to the formation of peptide self-assemblies through interchain disulfide bond crosslink with different particle diameters and solubility. Indeed, it is likely that with such crosslinking, the copper binding sites are less available, which can also explain the smaller ΔS_o for Prot+Flav relative to Prot hydrolysate.

This finding suggests that the fibrillation process in SMPI hydrolysates (measured by ThT assay) is highly associated with the surface hydrophobicity (S_o) of self-assembled peptides, as previously reported (Es-Haghi et al., 2012). Indeed, ThT and ANS data agree with the physico-chemical properties of peptides identified in the 1 kDa fraction of single and sequential hydrolysates by nano-LC-MS/MS and bioinformatic analysis (**Figure 7.3**).

DLS & TEM. The particle size distribution and polydispersity index (PDI) of the self-assembled peptides of SMPI hydrolysates were investigated by dynamic light scattering (DLS) (**Figure 7.4C-H**). Interestingly, after Cu^{2+} coordination, all hydrolysates have a change in particle size except Prot hydrolysate. Indeed, Prot+Flav hydrolysates (both whole and ≤ 1 kDa fraction) show the most significative change in the average particle size (**Figure 7.4C**). This suggests that the self-assembly properties of SMPI hydrolysates is notably affected by the sequential hydrolysis, where peptides with different structural properties are produced (**Table 7.2**). Particularly, the peptide-Cu^{2+} complex of whole Prot+Flav hydrolysate evidences the most noticeable and significant change in the average particle size. Indeed, for the corresponding 1kDa fraction, the change is slight in the presence/absence of Cu^{2+}. Note that the particle size distribution of this Prot+ Flav hydrolysate is mainly bimodal, with a small peak at 5500 nm and the main peak at 400 nm (**Figure 7.4.E**, black line). However, upon the formation of peptide-Cu^{2+} complex (red line), the main peak appeared at 5400 nm, resulting in an average particle size of 5390 nm for Prot+Flav hydrolysates. Thus, Cu^{2+} coordination changed the spatial structure of the peptide chain, leading to the formation of larger peptide particles in Prot+Flav hydrolysate.

Similar to our results, Ji et al., (2019) reported that the presence of Cu^{2+} ions increased the average particle size of nanofibrils in a dipeptide (FF). Moreover, no significant difference was observed in the PDI values (**Figure 7.4.H**) of the SMPI hydrolysates and their corresponding peptide-Cu^{2+} complex (*p-value* < 0.05), with all the samples presenting a moderately heterogenous particle size distribution (0.3 < PDI < 0.6). Indeed, the nanoparticles found in whole Prot+Flav hydrolysate and its peptide-Cu^{2+} complex appear mainly as the most homogeneous nanoparticle (PDI values ~0.3).

Taken altogether, our data confirms the self-assembly of peptides present in SMPI hydrolysates and fractions with a characteristic amyloid-like fibrillar structure, which notably decreases upon Cu^{2+} coordination. This effect is clearly apparent in whole hydrolysates (Prot and Prot+Flav) based on ThT, ANS and DLS assays. Thus, to gain further information about the particular structures of the self-assembled peptides present in SMPI hydrolysates, the morphology of only the whole hydrolysates with and without Cu^{2+} was studied by TEM (**Figure 7.5A-D**). The microstructure of Prot hydrolysate consisted of the formation of a few thin, single stranded microstructures with fragmented fibrils (red arrows, **Figure 7.5A**). After Cu^{2+} complexation (red arrow and circle, **Figure 7.5B**), the presence of fragmented fibrils and denser globular structures is enhanced while a decrease in the longer fibrils is observed. Similarly, Fortunato & Mba, (2021) showed by TEM the coexistence of spherical structures, fibrils, and worm-like micelles after Cu^{2+} ions coordination by a pyrene–peptide conjugate (peptide coupled with a fluorescent pyrene chromophore). In other studies, Ji et al., (2019) and Wang et al., (2020) observed the presence of spherical structures in dipeptide (FF)-Cu^{2+} and pentapeptide (DHTEK)-Zn^{2+} complexes, respectively.

On the other hand, Prot+Flav hydrolysate shows a more enhanced fibrillation pattern than Prot hydrolysate, with the appearance of smaller amorphous aggregates intercalated within the fibrils (red arrows, **Figure 7.5C**). However, Cu^{2+} coordination enhanced the formation of larger assemblies, resulting in denser fibrillar networks compared to Prot hydrolysate (**Figure 7.5D)**. Considering both ThT and TEM data, we conclude that the formation of the dense fibrillar network was not associated with cross-β structures, since a fluorescence decrease was observed. The fibrils found in the TEM image of Prot+Flav-Cu^{2+} complex (**Figure 7.5D**), thus, are more likely to be non-amyloid fibrils (Pignataro et al., 2020). In addition to His and Cys residues, Cu^{2+}-chelating peptides in Prot+Flav hydrolysates contain aromatic amino acids

(Phe, Tyr and Trp, i.e., AV**HW**T**Y**, SP**HW**TINA and G**C**R**W**IS**F**, section 7.3.1.3 **Table 7.2**), which could actively participate to the stability of the formed complexed through several weak interactions. Hence, π–π interactions, van der Waals, among them electrostatic ones, and hydrophobic interactions play a major role in the formation of self-assembled peptide nanostructures (Shimazaki et al., 2015). This result also agrees with the DLS data (**Figure 7.4C**) where such fibrils were characterized by high particle size (5 µm).

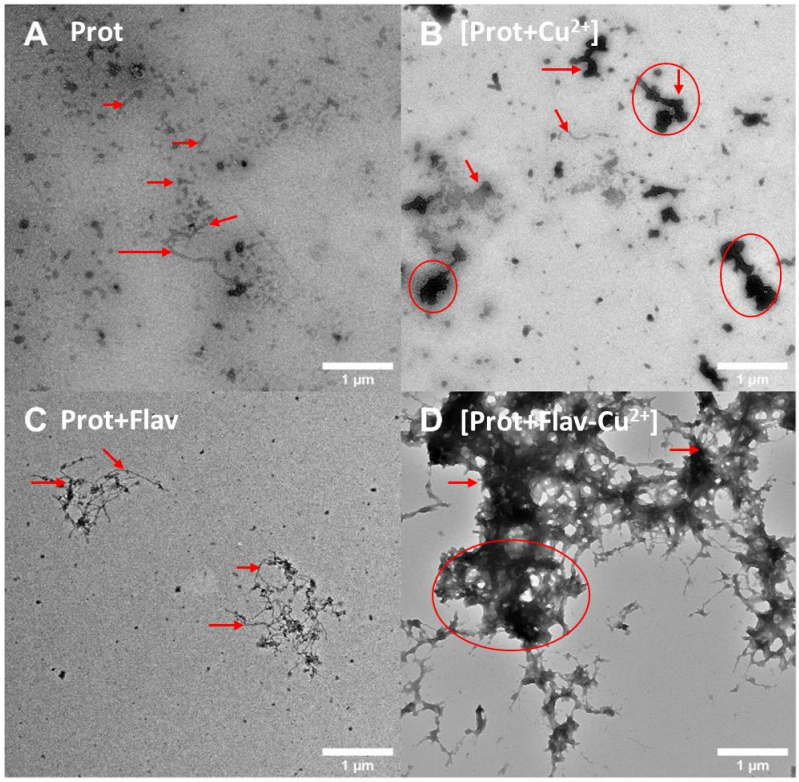

Figure 7.5. Transmission electron microscopy (TEM) of whole SMPI hydrolysates (Prot and Prot+Flav) with and without Cu^{2+} ions.

Scale bars represent 1 µm. Prot: Protamex® hydrolysate; Prot+Flav: Protamex® followed by Flavourzyme®.

Rheology. After confirming the potential effect of Cu^{2+} coordination on the self-assembly of peptides present in SMPI hydrolysates, the mechanical properties of the hydrolysates alone and in complex with Cu^{2+} ions were analyzed *via* oscillatory rheology. First, the amplitude sweeps measurements were used to determine the stiffness and gel strength, and was followed by frequency sweeps measurements. This enabled to better understand the internal

structure of the self-assembled peptides and determine whether the material exhibits gel-like or fluid-like behavior upon Cu^{2+} coordination.

In the amplitude sweeps measurement, samples were subjected to a range of deformation (from 0.1 to 1000 % of strain) at a set frequency (10 rad/s). In this sense, the analysis of the elastic modulus (stiffness: G') indicates the ability of SMPI hydrolysates to store energy elastically (**Figure 7.6A-D**) and describes their stiffness upon Cu^{2+} coordination as well. Stiffness is the ability of a material to return to its original shape after a force is applied. In all the investigated hydrolysates, the G' value of peptide-Cu^{2+} complex is slightly higher than those of hydrolysates alone, which indicates that the Cu^{2+} coordination enhanced slightly the stiffness. This observation can be largely explained by an increased number of supramolecular interactions due to the Cu^{2+} ions coordination by Cu^{2+}-chelating peptides present in SMPI hydrolysates. Similar studies Mohammed et al., (2022) and Rammal et al., (2023) recently reported that, due to the a strong metal–ligand coordination, elastic modulus G' was enhanced upon the coordination of divalent metal ions (Ca^{2+}, Mg^{2+}, Ba^{2+}, Zn^{2+}) with FFRGD peptide and a 25-residue peptide containing five histidine residues, respectively.

Furthermore, to analyze the effect of Cu^{2+} coordination on the structural strength of the gel-like materials, both elastic (G') and loss (G'') moduli were plotted as a function of the deformations range (strain %) in the presence and absence of Cu^{2+} ions and the crossover point (cp), expressed as percentage of strain required to break down the formed gel (G'=G''), was graphically determined from **Figure 7.6A-D**. The results show that the gels break down (cp at G'=G'') at higher strain values (%) when peptide-Cu^{2+} complex is formed in Prot hydrolysate and in ≤ 1 kDa Prot+Flav, indicating an increase in gel strength. On the contrary, although the Cu^{2+} coordination enhances the stiffness in Prot+Flav and ≤ 1 kDa Prot hydrolysates (**Figure 7.6**, higher G' values in the presence of Cu^{2+}), there is a decrease in gel strength (lower cp strain values, **Figure 7.6B-C**). Thus, stiffer structures obtained after Cu^{2+} coordination by the SMPI hydrolysate or fraction may have less strain response leading to gel fracture at lower strain values (weaker network formation). Indeed, the presence of both non-amyloid fibrils and some spherical assemblies after Cu^{2+} coordination as observed in TEM and ThT experiments may not favor effective cross-linking. Similar results were also obtained by Fortunato & Mba, (2021) in several metal cation-triggered peptide hydrogels notably Ca^{2+}, Ni^{2+}, Cu^{2+}, Zn^{2+}, Cd^{2+}.

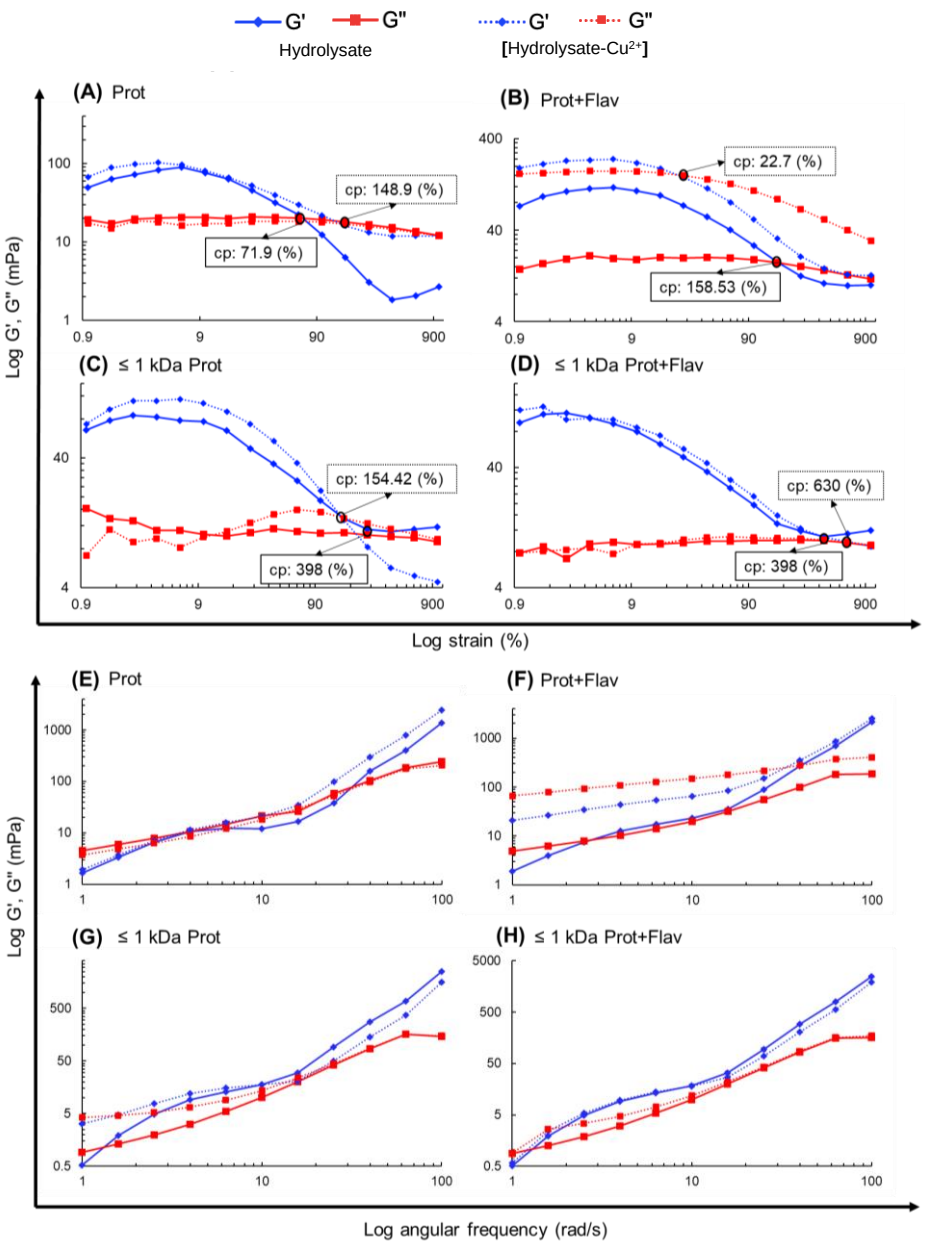

Figure 7.6. Effect of Cu^{2+} complexation on mechanical strength and viscoelastic behaviour study by amplitude sweeps and frequency sweeps measurements of different SMPI hydrolysates. (A-D) amplitude sweeps, (E-H) frequency sweeps. G' and G'' are the elastic modulus and loss modulus, respectively.

The mechanical strength is indicated by the cross-over point (cp, G' = G''), while gel formation is indicated by G' > G'' (blue above red and dashed blue above dashed red without and with Cu^{2+} ions, respectively. Prot: Protamex® hydrolysate; Prot+Flav: Protamex® followed by Flavourzyme®; ≤ 1 kDa: 1 kDa ultrafiltrated hydrolysate. Blue lines represent the elastic modulus (G') and red lines represent the loss modulus (G'').

The frequency sweeps (measurements are made over a range of oscillation frequencies at a constant oscillation amplitude) of SMPI hydrolysates in the presence and absence of Cu^{2+} ions were also investigated (**Figure 7.6E-H**). Note that, when G' > G'', the sample behaves as gel-

like structure, indicating a viscoelastic solid structure. On the contrary, when G'' > G', the sample behaves as fluid-like structure, indicating a viscoelastic liquid structure (Herrada-Manchon et al., 2023). Different behaviors of self-assembled peptides of SMPI hydrolysates are observed at different levels of frequencies. For instance, in the absence of Cu^{2+} ions, the whole hydrolysates (Prot, **Figure 7.6E**; Prot+Flav, **Figure 7.6F**) have a predominance of the fluid-like behaviour (G'' > G') at 6-7 rad/s frequencies and sol-gel transition (G'=G'') at low frequencies (< 10 rad/s). Yet, as the frequency increases (> 40 rad/s), the elastic modulus G' is higher than the loss modulus (G''), indicating a predominance of gel-like behaviour. Once Cu^{2+} is complexed in Prot hydrolysate, the elastic modulus G' surpasses the loss modulus G'' at much lower frequency (5 rad/s) compared to the hydrolysate alone, indicating an enhancement of the gel-like behavior (viscoelastic solid structure). Conversely, Cu^{2+} coordination in Prot+Flav hydrolysate favors the viscous fluid-like behavior (G'' > G') (viscoelastic liquid structure) until 215 rad/s of frequency. Regarding the ≤ 1 kDa fractions, irrespective of the hydrolysate, with or without complexation with Cu^{2+} ions, the elastic modulus G' are higher than loss modulus G'', indicating a predominance of gel-like behaviour across almost the entire frequency range (**Figure 7.6G-H**).

In our study, upon Cu^{2+} coordination by Prot, ≤ 1 kDa Prot and ≤ 1 kDa Prot+Flav hydrolysates, the self-assembled peptides behave as viscoelastic solid structures over wide frequency ranges (G' > G''). This type of supramolecular structures could have potential applications as scaffold materials for tissue engineering where mechanical strength and structural integrity are crucial. On the contrary, due to the prevalence of viscoelastic liquid structures (G'' > G', fluid-like behaviour until 215 rad/s) in Prot+Flav after Cu^{2+} complexation, this sequential hydrolysate is characterized as low-viscosity material, which is more likely to be used in applications where rapid and efficient flow is desired, such as injectable drug delivery systems or coatings (Herrada-Manchon et al., 2023).

Similar to our work, several studies have reported the divalent metal ions (M^{2+}) coordination through His or Cys-containing peptides; these synthetic peptides could be used as templates for the strategy design of peptide-based supramolecular materials (Knerr et al., 2012; Shao et al., 2020). Abul-Haija et al., (2017) reported the role of Cu^{2+} complexation in hydrogelation for a synthetic tripeptide containing histidine (G**H**K) and demonstrated that the Cu^{2+} triggers the peptide self-assembly to form hydrogels. In other studies Zeng et al., (2019) and Knerr et

al., (2012), the mechanical properties of peptide-based hydrogels were improved by His-Zn^{2+} coordination (GG**H** and G**HH**P**H**) and Cys-Zn^{2+}, Cd^{2+}, Hg^{2+}, and Pb^{2+} coordination (**C**GPKE**C**) *via* the histidyl imidazole and cysteinyl thiol groups, respectively.

Taken together, our study suggests that the size, shape, physico-chemical and mechanical properties of the resulting self-assembled structures in SMPI hydrolysates and those derived from their Cu^{2+} coordination depend on the peptide sequences, the number of Cu^{2+} binding ligands, the geometry of the coordination binding, and the Cu^{2+}-ligand binding affinities.

7.3.3 Antioxidant activity in C. elegans *in vivo* model

7.3.3.1 Effect of Cu^{2+} coordination on lifespan of C. elegans

C. elegans is an attractive animal model for evaluating the antioxidant potential of bioactive compounds *in vivo*. This study investigated the effect of Cu^{2+} coordination by SMPI hydrolysates-derived self-assembled peptides in prolonging the lifespan (unequivocal aging index) of *C. elegans,* by assessing the survival rates of the worms under oxidative stress induced by 1 mM copper (Cu^{2+}) solution, which is a reactive oxygen species (ROS) generator. Excessive cellular level of ROS triggers aging and oxidative stress, leading to impaired cell functions. Therefore, preventing excessive ROS accumulation is an effective approach to reduce oxidative stress and its free radical-induced damages (Shi et al., 2021). The worms were co-treated with *E. coli* OP50 bacteria with either SMPI hydrolysates (Prot, Prot+Flav, ≤ 1 kDa Prot and ≤ 1 kDa Prot+Flav) or EDTA used as positive control chelating agent, whereas the negative worm control group was only treated with *E. coli* OP50. Then, Cu^{2+} was added to the negative and positive control worm groups and sample groups to induce oxidative stress. Most studies have used *C. elegans in vivo* model to study the antioxidant property of food-derived peptides using one-generation exposure (G1) and do not consider exposure in subsequent generations (G2, G3, etc.). In our study, *C. elegans* were exposed to Cu^{2+} ions for three consecutive generations from G1 to G3 (**Appendix 7.4** and **Table 7.3**), and lifespan curves were analyzed by Kaplan-Meier method and log-rank test using GraphPad Prism version 8.0, GraphPad Software. In the first generation (G1, **Appendix 7.4, Table 7.3**), the average lifespan of *C. elegans* co-treated with EDTA (positive control: 25 h) and with ≤ 1 kDa Prot hydrolysate (25 h) are significantly higher (10.7 and 8.5 %, respecteviely) than that of negative control group (23 h).

This suggests an improvement of the survival rate of the nematodes by the hydrolysate fraction after Cu^{2+}-induced oxidative damage. Meanwhile, in the second and third generations (G2-G3, **Appendix 7.4, Table 7.3**), in addition to EDTA and ≤ 1 kDa Prot hydrolysates, the mean lifespan of *C. elegans* co-treated with ≤ 1 kDa fraction of the sequential hydrolysate (≤ 1 kDa Prot+Flav) also demonstrates significant improvement of the survival rate compared with the negative control. This indicates that the protective effect of this ≤ 1 kDa Prot+Flav fraction may not be observed until subsequent challenges in later generations. Taken together, the Cu^{2+}-chelating peptides identified (i.e., ATCUN peptides) and present in **Table 7.2** (section 7.3.1.3 for ≤ 1 kDa Prot and ≤ 1 kDa Prot+Flav) show a high potential to extend lifespan and delay the aging process in *C. elegans* through Cu^{2+} complexation over three generations. Similar to our findings, Zhou et al., (2018) and Chen et al., (2023) reported that the mean lifespan of *C. elegans* treated with food-derived protein hydrolysates from marine mussels and sea cucumber protein, respectively was significantly prolonged.

Table 7.3. Effects of Cu^{2+} coordination by EDTA and peptides present in SMPI hydrolysates on the lifespan-extension of Cu^{2+}-exposed nematodes.

Sample	Mean life (h)					
	G1	%	G2	%	G3	%
Cu^{2+}	23.18 ± 0.01^{c}		19.41 ± 0.15^{a}		22.75 ± 0.06^{a}	
[EDTA-Cu^{2+}]	25.68 ± 0.23^{e}	10.78	26.78 ± 0.02^{e}	37.97	25.68 ± 0.02^{c}	12.87
[Prot-Cu^{2+}]	19.68 ± 0.23^{a}	-15.09	19.51 ± 0.02^{a}	0.51	23.32 ± 0.02^{b}	2.5
[Prot+Flav-Cu^{2+}]	20.36 ± 0.04^{b}	-12.16	20.67 ± 0.01^{b}	6.49	22.73 ± 0.01^{a}	-0.08
[≤ 1 kDa Prot-Cu^{2+}]	25.17 ± 0.03^{d}	8.58	24.93 ± 0.01^{d}	28.43	25.72 ± 0.18^{c}	13.05
[≤ 1 kDa Prot+Flav-Cu^{2+}]	23.03 ± 0.02^{c}	-0.6	23.03 ± 0.02^{c}	18.65	26.18 ± 0.09^{d}	15.07

G1: first generation; G2: second generation; G3: third generation; Prot: Protamex® hydrolysate; Prot+Flav: Protamex® followed by Flavourzyme®; ≤ 1 kDa: 1 kDa ultrafiltrated hydrolysate.

7.3.3.2 Effect of of Cu^{2+} coordination on ROS generation

Since Cu^{2+} causes oxidative stress *via* increasing ROS generation, this assay was carried out to observe the potential biological function of the self-assembled peptides present in SMPI hydrolysates and their ≤ 1 kDa fractions to decrease the Cu^{2+}-induced ROS level and therefore

exhibit antioxidant activity in the *C. elegans in vivo* model. The ROS levels were determined by the H_2DCFDA cell permeant tracer method. In this experiment, the greater fluorescence intensity corresponds to higher intracellular ROS level. As shown in **Figure 7.7A**, after treating the worms with Cu^{2+} ions and without samples, the fluorescence signal of the negative control worms group increases reaching the maximum value (relative fluorescence 100 %) after 130 min of incubation. This indicates that Cu^{2+} induces effectively the production of ROS, which triggers oxidative stress on worms (Song et al., 2019). Due to high copper-chelating ability of EDTA, which was used as positive control, there was a significant decrease in the ROS level of the worm group co-treated with EDTA. Regarding the worm groups co-treated with SMPI hydrolysates, the results clearly highlight that (**Figure 7.7A-G**) only Prot+Flav, ≤ 1 kDa Prot, ≤ 1 kDa Prot+Flav significantly (*p-value* < 0.05) decreased the ROS level in the nematodes to 91.6 %, 86 % and 95.5 % relative fluorescence, respectively. In contrast, no antioxidant activity (*p-value* ≥ 0.05) was observed for Prot hydrolysate, although it showed a promising Cu^{2+} chelation activity. This might be related to weaker interaction between peptides and Cu^{2+} ions.

Besides, although smaller-sized peptides present in ≤ 1 kDa Prot+Flav are demonstrated to easily complex Cu^{2+} compared to those of bigger-sized peptides (≤ 1 kDa Prot) according to PV assay (**Figure 7.2**) and its high number of Cu^{2+} binding peptides (MS/MS data **Figure 7.3A**), our results indicate that the ≤ 1 kDa Prot hydrolysate exhibits the highest antioxidant activity in the *C. elegans in vivo* model, similar (*p-value* ≥ 0.05) to the activity of EDTA. Based on this observation, peptides identified in this fraction (full list given in **Appendix 7.1**; specific list presenting ATCUN motif-containing peptides and Cys-containing peptides in **Table 7.2**, section 7.3.1.3), are believed to form the most stable complex with Cu^{2+} ions notably thanks to their ATCUN-motif. Thus, they could be used as Cu^{2+}-chelating peptide-based antioxidant agents to reduce intracellular overproduction of Cu^{2+}-induced ROS and eventually decrease oxidative stress. Taken together, the ability of SMPI hydrolysate to decrease Cu^{2+}-induced oxidative stress in *C. elegans* does not only depend on the number of Cu^{2+} chelating sites but also on the strength and stability of the coordination bound formed in the peptide-Cu^{2+} complex.

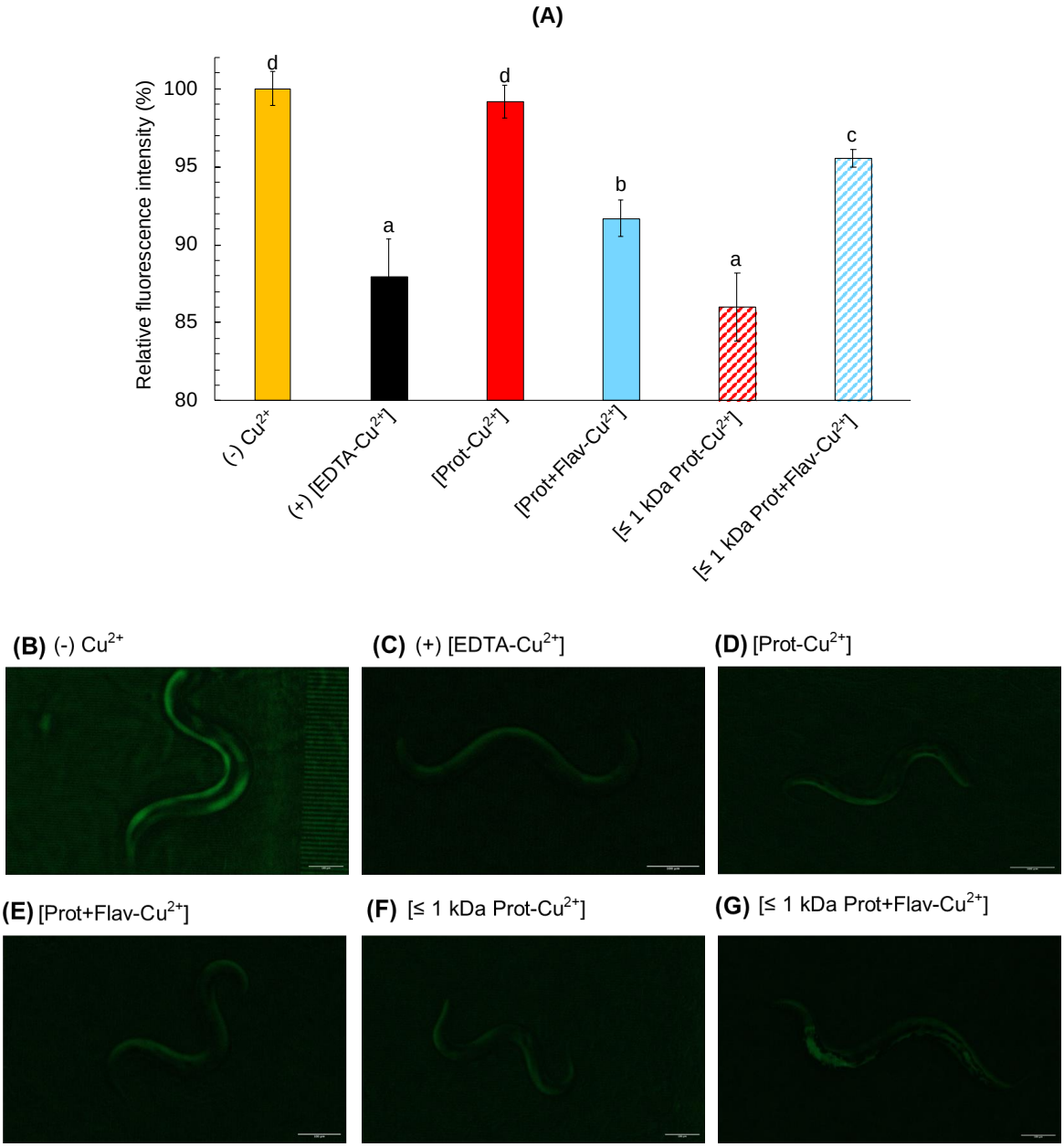

Figure 7.7. Alleviation of oxidative stress by EDTA, Prot, Prot+Flav, ≤ 1 kDa Prot and ≤ 1 kDa Prot+Flav hydrolysates in oxidation-damaged *C. elegans.* (A) ROS level in Cu^{2+}-exposed nematodes. (B-G) L3-stage nematodes were treated with and without samples treatment (control nematodes) for 24 h at 22 ± 2 °C, and then exposed to 1 mM Cu^{2+} (200 µL) for another 12 h.

Representative images of Cu^{2+}-exposed L3-stage nematodes negative control (only with Cu^{2+}), EDTA, Prot, Prot+Flav, ≤ 1 kDa Prot and ≤ 1 kDa Prot+Flav-treated groups captured by an Axiocam 506 camera. Data are expressed as ROS level mean obtained from three independent experiments with approximately 15 worms in each experimental group. Different letters indicate significant differences (*p-value* < 0.05).

7.4 Conclusions

This study revealed for the first time the effect of Cu^{2+} coordination on the peptide self-assembly of single and sequential enzymatic hydrolysates obtained from sunflower meal by-product protein. The use of coordinating Cu^{2+} as a nonconventional approach could generate different tunable self-assembled bioactive peptide-based nanostructures endowed with improved mechanical properties. The results suggested that the size, shape, physico-chemical and mechanical properties of the resulting self-assembled structures do not only depend on the number of Cu^{2+} binding ligands but also on the geometry of the coordination sphere and the Cu^{2+}-ligand binding affinities, which are different among the studied hydrolysates. Moreover, for the first time, *in vivo* characterization of the antioxidant activity of the hydrolysates and fractions was investigated based on Cu^{2+}-induced oxidative stress using the nematode *C. elegans* as model organism. Our findings revealed a distinct biological activity with the ≤ 1 kDa fraction obtained by Protamex® single treatment, containing Cu^{2+}-chelating sequences with ATCUN motif, which exhibited a similar effect as EDTA. Furthermore, our observations clearly demonstrate that owing to the presence of His- and Cys-containing peptides in the hydrolysates, the interaction with Cu^{2+} ions could be used to customize peptide structures and design food-derived self-assembled peptides endowed with physico-chemical, mechanical and bioactive properties of interest for different applications, such as injectable drug delivery systems, scaffold materials for tissue engineering, self-gelling soft materials, therapeutic agents, and functional nutraceutical products. Finally, to further explore the underlying effects of metal coordination on SMPI hydrolysates peptide self-assembly, studies on the effect of Cu^{2+} concentration and metal-to-peptide ratio on the self-assembly pattern are required to determine the suitable conditions to enhance the structures of the supramolecular biomaterials.

General conclusion and perspectives

Conclusions

Metal-Chelating Peptides (MCPs) are biofunctional peptides that interact with metal ions and form peptide-metal complexes (**Chapter 1**). Considering such ability of peptides and the numerous roles of metals in biological processes, many studies in the literature have demonstrated that these MCPs provide positive health outcomes. Thanks to their metal complexation properties, MCPs promote better stability, absorption, and bioavailability of these minerals. More specifically, while complexing divalent metals such as Fe^{2+}, Cu^{2+}, Ni^{2+}, MCPs can also act as indirect antioxidant. In the global context of food protein-derived hydrolysates, MCPs are produced either from animal or vegetable sources. Nevertheless, in recent years, due to the current concern for environmental issues from agro-industrial waste, there is a growing interest to use emerging proteins from agro-industrial by-products. This has inspired many scientists to search for novel alternatives for the production of MCPs. Therefore, in this work, red Tilapia scale and sunflower meal by-products were used as potential protein sources for the production of MCPs, which were extensively investigated by setting up several screening and separation methodologies. For this propose, this PhD thesis has covered a wide variety of research approaches on MCPs production from food proteins, notably by protein extraction, followed by enzymatic proteolysis, screening, separation, identification, up to their physico-chemical and biofunctional characterization. Using both protein hydrolysates and synthetic peptides as model molecules, we have made important contributions in the field of biofunctional and bioactive peptides production from agro-industrial by-products-derived proteins.

Obtaining a protein isolate from agro-industrial by-products is fundamental to our approach. Indeed, the properties of the resulting hydrolysate, potentially containing metal-chelating peptides, will mainly depend on the purity of the native protein and its amino acid sequence. Thus, the proteins were first extracted either from red Tilapia scale or sunflower meal by-products in order to produce protein hydrolysates enzymatically digested with single and sequential treatments. For the Tilapia scale protein extraction (**Chapter 2**), an optimization approach was achieved to produce gelatin with the most suitable properties for further bioactive peptides production or pharmaceutical application. The fractional factorial design methodology applied was proven to be a great tool to evaluate the effects of a relatively large

number of parameters (i.e., solvent-to-solid ratio, extraction time, temperature and ultrasound) on protein content, protein yield and free amino group content, while reducing the number of experiments. The results showed that a solvent-to-solid ratio of 10 mL/g, extraction time of 3 h, and temperature of 85 °C without ultrasounds, provided the maximal responses of free amino group content and protein yield, while crude protein content remained high (> 95 %). Moreover, once Tilapia scale gelatin (**TSG**) was extracted, two protein hydrolysates were produced using single and sequential enzymatic treatment with Alc and Alc+Flav, respectively (**Chapter 3**). The Alc+Flav treatment showed higher DH than a single Alc one. However, the biofunctional properties were not all enhanced by the sequential enzymatic treatment. Indeed, sequential hydrolysis seemed to improve the Ni^{2+}-binding, radical scavenging and reducing power abilities only. Besides, after ultrafiltration, the ≤ 1 kDa Alc hydrolysate exhibited the highest Fe^{2+}-chelating activity. This property might also be associated with the ACE inhibition activity. More, LC-ESI-MS/MS analysis confirmed the presence of peptide sequences with Asp, Glu, Ser, Lys and Arg, which might offer potentially metal-chelating and antioxidant properties.

Meanwhile, in **Chapter 4**, the protein isolate extracted from sunflower meal by-product was subsequently submitted to proteolysis in order to produce protein hydrolysates using single and sequential enzymatic treatment with Prot and Prot+Flav, respectively. Both sunflower-meal protein isolate (**SMPI**) hydrolysates and pure synthetic peptides (potentially encrypted in sunflower proteins) were investigated for their Ni^{2+}-chelating properties using IMAC-Ni^{2+}, switchSENSE®, UV-vis and CD spectroscopies. In all the investigated hydrolysates, several peptide sequences, identified by LC-MS/MS, evidenced the presence of His residue at different position from C- and N-termini. Nevertheless, the most interesting Ni^{2+}-chelating sequences were characterized by their "ATCUN" motif (*i.e.,* WL**H** and LL**H**VT). These results are extremely promising on the production of Ni^{2+}-chelating peptides from sunflower meal by-products.

Therefore, based on many similarities already described between Ni^{2+} and Cu^{2+} ion complexing processes, the **Chapter 5** aimed to investigate metal-related antioxidant activities of the obtained sunflower protein hydrolysates using ascorbate tests (Cu^{2+}/Fe^{3+}), Fe^{2+}-chelating, ABTS radical scavenging and reducing power abilities. Besides, Cu^{2+}-chelating peptides in SMPI hydrolysates were fractionated using IMAC-Cu^{2+} separation and the sequence was identified by LC-MS/MS. The results showed that the Prot hydrolysate and its

corresponding ≤ 1 kDa fraction exhibited the highest activities in Fe^{2+}-chelating, in inhibition of Cu^{2+}-induced ROS production and in ABTS radical scavenging properties, while the Prot+Flav hydrolysate and its ≤ 1 kDa fraction enhanced the inhibition of Fe^{3+}-induced ROS production and the reducing power. The presence of His, Glu, Asp, and Arg in the peptide sequences identified improved the metal-chelating and antioxidant properties. Thus, the Ni^{2+}/Cu^{2+}-chelating peptides identified could serve as antioxidant candidates to be used as food or pharmaceutical active agents to prevent metal-induced oxidation and diseases.

Furthermore, in **Chapter 6** and **7**, we have investigated the bioactivity and self-assembly properties of peptides in order to produce peptide-based biomaterials endowed with potential nutraceutical and biomedical applications. Several strategies have proven to trigger self-assembly of peptides to design supramolecular materials, however, the use of metal coordination approach in food hydrolysate has never been exploited to date. Our work provided for the first time the self-assembly pattern of TSG and SMPI hydrolysates through Cu^{2+} coordination and their *in vivo* antioxidant property by Cu^{2+}-induced oxidative stress using the *Caenorhabditis elegans* as a model organism. The physico-chemical characterization of these self-assembled peptides (SAPs) by various analyses (ThT, ANS, DLS, TEM and rheological data) revealed that upon Cu^{2+} coordination, tunable self-assembled bioactive peptide-based nanostructures endowed with improved mechanical properties were generated in both types of hydrolysates. Moreover, the MCPs present in hydrolysate produced with a single enzymatic treatment (TSG, Alc; SMPI, ≤ 1 kDa Prot) significantly reduced the endogenous ROS levels through Cu^{2+} coordination, which finally extended the lifespan of *C. elegans*. Owing to the presence of His-, Cys- and Met-containing peptides in our study, the interaction with Cu^{2+} could be used to customize the structures of peptides-based biomaterials and design food-derived self-assembled peptides endowed with tunable physico-chemical, mechanical and bioactive properties. According to their properties, different applications such as injectable drug delivery systems, scaffold materials for tissue engineering, self-gelling soft materials, therapeutic agents, and functional and nutraceutical products could be considered.

Perspectives

Based on the results obtained in **Chapters 2** and **3**, the red Tilapia scale by-product has great potential for valorization and stands out as an interesting candidate for the production of metal-chelating peptides. As a short-term perspective, the future research should focus on

the scaling up of both protein extraction and hydrolysate production processes and the effect of the scaling up on the biofunctional properties of the gelatin hydrolysate. First, concerning the scale-up, the optimal conditions for gelatin extraction determined in **Chapter 2**, could be adapted to a larger scale reactor (i.e., pilot scale reactor with 5-10 L capacity) in order to produce gelatin protein in larger volume. Secondly, given the potential of the ≤ 1 kDa Alc gelatin hydrolysate (**Chapter 3**), it would be interesting to scale up the production of this former hydrolysate using a pilot scale reactor followed by a tangential flow ultrafiltration using a 1-kDa MWCO membrane. After the scaling up of the hydrolysis and ultrafiltration processes, the characterization of this hydrolysate would enable to determine whether this former hydrolysate has retained its biofunctional and bioactive properties when scaling up. During the scale up of this process, it will be appropriate to apply and study optimization methods to find the optimal operating conditions (i.e., response surface methodology). Besides, confirming the biofunctional properties of metal-chelating peptide sequences, some metal-chelating peptide sequences identified from gelatin hydrolysates could be synthetized and characterized for their metal-chelating activity and metal-related biofunctional properties.

As a long-term perspective, future work will focus on the introduction of the enzymatic membrane reactor. The enzymatic membrane reactor is based on the coupling of an enzymatic reaction with a membrane separation process. This technology could be an interesting approach to overcome the disadvantages of a classical batch reactor in industrial practice improving both productivity, operating costs, enzymatic activity, etc.

On the other hand, the use of sunflower meal by-product as a protein source to produce Ni^{2+}/Cu^{2+}-chelating peptides (**Chapter 4** and **5**) proved to be an interesting candidate as well. Thus, further investigation into the study of peptide-metal interaction using other techniques such as FTIR and ITC may be useful for in-depth understanding of the coordination mechanisms of pure peptides with metal ions. Besides, the use of molecular dynamic simulation and molecular docking of peptide-metal complexes as theoretical approaches should be performed to gain a better insight into the interaction of peptides with different metal ions before *in vitro* evaluations of peptides. The combination of all these analyses will provide information about molecular scale description of the interaction, structural conformation, docking energies, chelating sites and possible chelating mechanisms. Interestingly, due to the presence of the ATCUN motif, the Ni^{2+}/Cu^{2+}-chelating peptides

identified from SMP hydrolysates with the His residue in the third position from the amino terminus (i.e., LL**H**VT and WL**H**) might have better stability in the formed peptide-Cu^{2+} complex. Thus, they could have both health-promoting effect and some interesting nutritional value of food products by enhancing the mineral bioavailability. These peptide sequences could be synthesized in order to evaluate their ability to extend the shelf life of food formulations by retarding the metal-induced oxidative degradation in emulsion system for instance. Also, the bioavailability and stability of the metal-chelating peptides could be studied both in animal and human model in order to validate their high potential *in vivo*.

Finally, as described in **Chapter 6** and **7**, the use of Cu^{2+} coordination as a nonconventional approach to trigger peptides self-assembly, generated various tunable self-assembled bioactive peptide-based nanostructures, either from Tilapia scale or sunflower meal-derived peptide hydrolysate with enhanced mechanical properties. However, to better understand how the number of Cu^{2+}-binding ligands, the geometry of the coordination bond, and the peptide-Cu^{2+}-binding affinities affect the self-assembly pattern of the resulting nanostructures, the most interesting identified peptides (i.e., AV**HW**TY, **C**R**W**ISF, and GPSGPRGPAGP**H**) should be further investigated. Hence, the effect of the metal-to-peptide ratio could be investigated on the self-assembly pattern in order to determine the appropriate conditions for improving the structures of the supramolecular biomaterials according to the properties required. Lastly, further studies could be devoted to the investigation of the biostability and biocompatibility of food-derived self-assembled peptides in cellular models as well as to their final applications as injectable drug delivery systems, scaffold materials for tissue engineering, self-gelling soft materials, therapeutic agents, and functional nutraceutical products.

PhD outcomes

Scientific publications accepted and in progress

* Corresponding author

- As first author

(1) **Camaño***, **J. A.**, El Hajj, S., Irankunda, R., Selmeczi, K., Paris, C., Udenigwe, C. C., & Canabady-Rochelle*, L. L. S. Screening, Separation and Identification of Metal-Chelating Peptides for Nutrition, Cosmetic and Pharmaceutical Applications. *Food & Function*, 2024, 15, 3300-3326. https://doi.org/10.1039/d3fo05765h

(2) **Camaño*, J.A.,** Nekka, A., Arnoux, P., Mathe, C., Cakir-Kiefer, C., Stefan, L., Paris, C., Selmeczi, K., Zapata, J.E., Canabady-Rochelle*, L. Optimization of Gelatin Extraction from Red Tilapia Scales and Evaluation of its Physico-chemical and Viscoelastic Properties. To submit at *Foods*.

(3) **Camaño*, J.A.,** Irankunda, R., Arnoux, P., Girardet, J.M., Cakir-Kiefer, C., Risler, A., Stefan, L., Paris, C., Zapata, J.E., Selmeczi, K., Canabady-Rochelle*, L. Gelatin Hydrolysates of Red Tilapia (Oreochromis spp.) Scale By-products: Investigation of Metal-Chelating Properties and their related Bioactivities. Submitted at *Journal of Agriculture and Food Chemistry.*

(4) **Camaño, J.A.,** Selmeczi*, K., Mathe, C., Girardet, J.M., Paris, C., Udenigwe, C., Canabady-Rochelle*, L. Identification of Ni^{2+}-binding Peptides in Sunflower Meal Protein Hydrolysate for Deeper Understanding of Peptide-Metal Interactions. To submit at *Journal of Inorganic Biochemistry.*

(5) **Camaño*, J.A.,** Mathe, C., Arnoux, P., Stefan, L., Paris, C., Selmeczi, K., Udenigwe, C., Canabady-Rochelle*, L. Metal-Chelating Peptides Derived from Sunflower Meal Protein: Preparation, Isolation, Identification and Antioxidant Properties. To submit at *Journal of Agriculture and Food Chemistry.*

(6) **Camaño*, J.A.,** Abioye, R.O., Reyes, S., Selmeczi, K., Canabady-Rochelle, L., Udenigwe*, C. Effect of Cu^{2+} Coordination on Peptide Self-Assembly, Mechanical Properties, and Bioactivity of Peptide Hydrolysates Obtained from Sunflower Meal Protein Isolate. To submit at *Food Chemistry.*

(7) **Camaño*, J.A.,** Abioye, R.O., Reyes, S., Selmeczi, K., Canabady-Rochelle, L., Udenigwe*, C. Effect of Cu^{2+} Coordination on Peptide Self-Assembly, Mechanical Properties, and Bioactivity of Peptide Hydrolysates Obtained from Sunflower Meal Protein Isolate. To submit at *Journal of Agriculture and Food Chemistry.*

- As co-author

(1) Irankunda, R., **Camaño Echavarría**, J. A., Paris, C., Stefan, L., Desobry, S., Selmeczi, K., Muhr, L., & Canabady-Rochelle, L. (2022). Metal-Chelating Peptides Separation Using Immobilized Metal Ion Affinity Chromatography: Experimental Methodology and Simulation. *Separations*, *9*(11), 370. https://doi.org/10.3390/separations9110370

(2) Hajj, S., Irankunda, R., **Camaño EchavarrÍa**, J. A., Arnoux, P., Paris, C., Stefan, L., Gaucher, C., Boschi-Muller, S., & Canabady-Rochelle, L. (2023). Metal-chelating activity of soy and pea protein hydrolysates obtained after different enzymatic treatments from protein isolates. *Food Chem*, *405*(Pt A), 134788. https://doi.org/10.1016/j.foodchem.2022.134788

(3) Irankunda, R., **Camaño Echavarría**, J. A., Paris, C., Selmeczi, K., Stefan, L., Boschi-Muller, S., Muhr, L., & Canabady-Rochelle, L. (2024). Deciphering Interactions Involved in Immobilized Metal Ion Affinity Chromatography and Surface Plasmon Resonance for Validating the Analogy between Both Technologies. *Inorganics*, *12*(1), 31. https://doi.org/10.3390/inorganics12010031

(4) Irankunda, R., Jambon, P., Marc, A., **Camaño Echavarría**, J. A., Muhr, L., & Canabady-Rochelle, L. (2024). Simulation of Ni^{2+} Chelating Peptides Separation in IMAC: Prediction of Langmuir Isotherm Parameters from SPR Affinity Data. *Processes*, *12*(3). https://doi.org/10.3390/pr12030592

(5) Abioye, R. O., **Camaño Echavarría**, J. A., Obeme-Nmom, J. I., Yiridoe, M. S., Ogunrinola, O. A., Ezema, M. D., & Udenigwe, C. C. (2024). Self-Assembled Food Peptides: Recent Advances and Perspectives in Food and Health Applications. *J Agric Food Chem*, *72*(15), 8372-8379. https://doi.org/10.1021/acs.jafc.4c01385

Participation to national and international conferences

Presenting author

- Oral communication

(1) **Camaño Echavarría JA.**, R. Irankunda, P. Arnoux, C. Cakir-Kiefer, A. Risler, L. Stefan, J. Zapata, L. Canabady-Rochelle. Metal-Chelating Peptides obtained from Enzymatic Hydrolysis of Protein Extracted from Fish Tilapia Scales (Oreochromis spp.). MBP2022-1st International Conference on Metal-Binding Peptides, from July 5th to 8th, 2022. Nancy, France.

(2) **Camaño Echavarría JA.**, R. Irankunda, P. Arnoux, L. Stefan, J. Zapata, L. Canabady-Rochelle. Protein extraction from agro-industrial byproducts as alternative for animal-derived proteins in bioactive peptides production. 9th International Conference on Food Chemistry & Technology. from November 27th to 29th, 2023. Paris, France

(3) **Camaño Echavarría JA.**, R. Irankunda, P. Arnoux, J-M. Girardet, C. Mathé, Stefan, Selmeczi, K, L. Canabady-Rochelle. Screening of Metal-Chelating Peptides in Protein Hydrolysates from Agro-industrial by-products using switchSENSE® Technology. MBP2024-2nd International Conference on Metal-Binding Peptides, from July 10th to 12th, 2024. Toulouse, France.

- Poster communication

(1) **Camaño Echavarría JA.**, A. Nekkaa, A-A. Balland, P. Arnoux, C. Cakir-Kiefer, L. Stefan, J. Zapata, L. Canabady-Rochelle. Optimization of Gelatin Extraction from Tilapia Scale Using Fractional Factorial Experimental Design. Joint Meeting on Peptides and Proteins GFPP22 & BPGM5", from May 29th- June 3rd, 2022. Port-Leucate, France.

(2) **Camaño Echavarría JA.**, R. Irankunda, P. Arnoux, C. Cakir-Kiefer, A. Risler, L. Stefan, J. Zapata, L. Canabady-Rochelle. Physicochemical and Antioxidant Properties of Gelatin Hydrolysates obtained from Red Tilapia (Oreochromis spp.) scales. Joint Meeting on Peptides and Proteins GFPP22 & BPGM5", from May 29th- June 3rd, 2022. Port-Leucate, France.

(3) **Camaño Echavarría JA.**, R Bounaceur, P, J. Zapata, K. Selmeczi, L. Canabady-Rochelle. In Silico Screening of Metal-Chelating Peptides present in Tilapia Scale

Protein Hydrolysates. MBP2022-1st International Conference on Metal-Binding Peptides, from July 5th to 8 th, 2022. Nancy, France.

(4) **Camaño Echavarría JA.**, R. Irankunda, P. Arnoux, P., J-M. Girardet, J. Zapata, L. Stefan, K. Selmeczi, L. Canabady-Rochelle. Production of Metal-Chelating Peptide Hydrolysates from Gelatin Protein Extracted from Red Tilapia (Oreochromis spp.) Scales and Evaluation of their bioactivities. International Symposium on Bioactive Peptides from September 27th to 29th, 2023. Niagara Falls, Canada. **Poster & Flash talk communication**.

(5) **Camaño Echavarría JA.**, R. Irankunda, P. Arnoux, C. Mathé, L. Stefan, K. Selmeczi, L. Canabady-Rochelle. Metal-Chelating Peptides Hydrolysates from Sunflower Meal Protein Isolate: Enzymatic Preparation and Characterization of their Bioactivities. MBP2024-2nd International Conference on Metal-Binding Peptides, from July 10th to 12th, 2024. Toulouse, France.

Workshop and other scientific days

Presenting author

- **Flash talk communication**

(1) **Camaño Echavarría JA.**, R. Irankunda, P. Arnoux, C. Cakir-Kiefer, A. Risler, L. Stefan, J.E. Zapata, L. Canabady-Rochelle. Metal-Chelating Peptides obtained from Enzymatic Hydrolysis of Protein Extracted from Red Tilapia Scales (Oreochromis spp.). LabEx PhD candidates and PhD day 2022 - October, 11th 2022 - INRAE center, Champenoux, France.

- **Poster communication**

(1) **Camaño Echavarría JA.**, A. Nekkaa, A.A Balland, P. Arnoux, C. Cakir-Kiefer, L. Stefan, J.E Zapata, L. Canabady-Rochelle. “Progrès dans l'extraction des protéines d'écailles de Tilapia : Perspective d'optimisation, de la recherche à l'industrie”. Doctoral scientific day: SIMPPÉ, De la recherche à l'innovation et à l'entreprenariat, 20th June 2022, Nancy, France.

International mobility and Grant obtained

Grant obtained by the PhD student: DrEAM9 LUE financial support (4434 €)

Project intittled "Study of the effect of Cu^{2+} coordination on the self-assembly and *in vivo* antioxidant properties of protein hydrolysates from and red Tilapia scale and sunflower meal by-products".

International mobility at School of Nutrition Science (University of Ottawa, Ottawa, Canada; 2.5 months), under the supervision of **Pr. Chibuike Udenigwe.**

Participation to the organization of scientific events

(1) **International Conference on Metal-Binding Peptides: Methodologies and Applications, 5th-8th July 2022, ENSIC, Nancy.**

Chair(wo)men: Laetitia Canabady-Rochelle and Peter Faller (Université de Strasbourg).

Member of the local team of MBP'2022.

http://mbp2022-nancy.com/committees/

Scientific mediation

(1) General public conference - Honoring the Bioprocesses-Biomolecules axis. **Camaño Echavarría JA**, R. Irankunda, P. Arnoux, C. Cakir-Kiefer, A. Risler, L. Stefan, J. Zapata, L. Canabady-Rochelle. Presentation entitled "Physicochemical and Antioxidant Properties of Gelatin Hydrolysates obtained from Red Tilapia (Oreochromis spp.) scales". 11th May 2023.

(2) Presentation of research activities at welcome day of ENSIC engineering school students (2022, 2023).

References

Ahmad, J., Ali, A. A., Baig, M. A., Iqbal, M., Haq, I., & Irfan Qureshi, M. (**2019**). Chapter 8 - Role of Phytochelatins in Cadmium Stress Tolerance in Plants. In Hasanuzzaman Mirza, M. N. Vara Prasad, & M. Fujita (Eds.), *Cadmium Toxicity and Tolerance in Plants* (pp. 185-212). Academic Press. https://doi.org/10.1016/b978-0-12-814864-8.00008-5

Ajibola, C. F., Fashakin, J. B., Fagbemi, T. N., & Aluko, R. E. (**2011**). Effect of peptide size on antioxidant properties of African yam bean seed (Sphenostylis stenocarpa) protein hydrolysate fractions. *Int J Mol Sci*, *12*(10), 6685-6702. https://doi.org/10.3390/ijms12106685

Al-Nimry, S., Dayah, A. A., Hasan, I., & Daghmash, R. (**2021**). Cosmetic, Biomedical and Pharmaceutical Applications of Fish Gelatin/Hydrolysates. *Mar Drugs*, *19*(3). https://doi.org/10.3390/md19030145

Alexander, B. R. D., Buisson, D. H., Dudeney, W. L., & Irving, R. J. (**1977**). Spectrophotometric Investigations of Aqueous Solutions at Elevated Temperature. *J. Chem. Soc., Faraday trans.*, *6*, 1081-1088.

Alipal, J., Mohd Pu'ad, N. A. S., Lee, T. C., Nayan, N. H. M., Sahari, N., Basri, H., Idris, M. I., & Abdullah, H. Z. (**2021**). A review of gelatin: Properties, sources, process, applications, and commercialisation. *Materials Today: Proceedings*, *42*, 240-250. https://doi.org/10.1016/j.matpr.2020.12.922

Andjelković, U., Giacometti, J., & Josić, D. (**2017**). Chapter 5 - Protein and peptide separations. In S. Fanali, P. R. Haddad, C. F. Poole, & M.-L. Riekkola (Eds.), *Liquid Chromatography (Second Edition)* (pp. 107-157). Elsevier. https://doi.org/10.1016/B978-0-12-805392-8.00005-0

Anekthanakul, K., Hongsthong, A., Senachak, J., & Ruengjitchatchawalya, M. (**2018**). SpirPep: an in silico digestion-based platform to assist bioactive peptides discovery from a genome-wide database. *BMC Bioinform.*, *19*(1), 149. https://doi.org/10.1186/s12859-018-2143-0

AOAC. (**2000**). Official Methods Of Analysis Of AOAC International. *AOAC, international, Washington, DC.*(17th ed.).

Apone, F., Barbulova, A., & Colucci, M. G. (**2019**). Plant and Microalgae Derived Peptides Are Advantageously Employed as Bioactive Compounds in Cosmetics. *Front Plant Sci*, *10*, 756. https://doi.org/10.3389/fpls.2019.00756

Argade, A., & Ahlawat, S. S. (**2021**). Standardization of optimum conditions for hydrolyses of goat milk whey protein with alcalase enzyme. *J. Pharm. Innov.*, *10*(11), 169-173.

Aroua, M. K., Leong, S. P., Teo, L. Y., Yin, C. Y., & Daud, W. M. (**2008**). Real-time determination of kinetics of adsorption of lead(II) onto palm shell-based activated carbon using ion selective electrode. *Bioresour Technol*, *99*(13), 5786-5792. https://doi.org/10.1016/j.biortech.2007.10.010

Athira, S., Mann, B., Sharma, R., Pothuraju, R., & Bajaj, R. K. (**2021**). Preparation and characterization of iron-chelating peptides from whey protein: An alternative approach for chemical iron fortification. *Food Res Int*, *141*, 110133. https://doi.org/10.1016/j.foodres.2021.110133

Auwal, S. M., Zainal Abidin, N., Zarei, M., Tan, C. P., & Saari, N. (**2019**). Identification, structure-activity relationship and in silico molecular docking analyses of five novel angiotensin I-converting enzyme (ACE)-inhibitory peptides from stone fish (Actinopyga lecanora) hydrolysates. *PLoS One*, *14*(5), e0197644. https://doi.org/10.1371/journal.pone.0197644

Bamdad, F., Wu, J., & Chen, L. (**2011**). Effects of enzymatic hydrolysis on molecular structure and antioxidant activity of barley hordein. *J. Cereal Sci.*, *54*(1), 20-28. https://doi.org/10.1016/j.jcs.2011.01.006

Bao, X. L., Lv, Y., Yang, B. C., Ren, C. G., & Guo, S. T. (**2008**). A study of the soluble complexes formed during calcium binding by soybean protein hydrolysates. *J Food Sci*, *73*(3), C117-121. https://doi.org/10.1111/j.1750-3841.2008.00673.x

Barge, A., Cravotto, G., Gianolio, E., & Fedeli, F. (**2006**). How to determine free Gd and free ligand in solution of Gd chelates. A technical note. *Contrast Media Mol Imaging*, *1*(5), 184-188. https://doi.org/10.1002/cmmi.110

Barth, A. (**2000**). The infrared absorption of amino acid side chains. *Prog. Biophys. Mol. Biol.*, *74*, 141-173.

Barth, A. (**2007**). Infrared spectroscopy of proteins. *Biochim Biophys Acta*, *1767*(9), 1073-1101. https://doi.org/10.1016/j.bbabio.2007.06.004

Bassan, G. A., & Marchesan, S. (**2023**). Peptide-Based Materials That Exploit Metal Coordination. *Int J Mol Sci*, *24*(1), 456. https://doi.org/10.3390/ijms24010456

Bing, S. J., Chen, X. S., Zhong, X., Li, Y. Q., Sun, G. J., Wang, C. Y., Liang, Y., Zhao, X. Z., Hua, D. L., Chen, L., & Mo, H. Z. (**2024**). Structural, functional and antioxidant properties of Lentinus edodes protein hydrolysates prepared by five enzymes. *Food Chem*, *437*(Pt 1), 137805. https://doi.org/10.1016/j.foodchem.2023.137805

Biosensors, D. (**2021**). *switchSENSE® technology*. Retrieved 01/03/2022 from https://www.dynamic-biosensors.com/switchsense/

Block, H., Maertens, B., Spriestersbach, A., Brinker, N., Kubicek, J., Fabis, R., Labahn, J., & Schafer, F. (**2009**). Immobilized-metal affinity chromatography (IMAC): a review. *Methods Enzymol*, *463*, 439-473. https://doi.org/10.1016/S0076-6879(09)63027-5

Borch, J., & Roepstorff, P. (**2010**). Surface Plasmon Resonance, Methods and Protocol. In N. J. d. Mol & M. J. E. Fischer (Eds.), *Methods in Molecular Biology* (pp. 225). Humana Press. https://doi.org/10.1007/978-1-60761-670-2

Boukil, A., Suwal, S., Chamberland, J., Pouliot, Y., & Doyen, A. (**2018**). Ultrafiltration performance and recovery of bioactive peptides after fractionation of tryptic hydrolysate generated from pressure-treated β-lactoglobulin. *J. Membr. Sci*, *556*, 42-53. https://doi.org/10.1016/j.memsci.2018.03.079

Brini, M., Cali, T., Ottolini, D., & Carafoli, E. (**2013**). The plasma membrane calcium pump in health and disease. *FEBS J*, *280*(21), 5385-5397. https://doi.org/10.1111/febs.12193

Bucher, J. R., Hailey, J. R., Roycroft, J. R., Haseman, J. K., Sils, R. C., Grumbein, S. L., Mellick, P. W., & Chou, B. J. (**1999**). Inhalation toxicity and carcinoigenicity studies of cobalt sulfate. *Toxicol. Sci.*, *49*, 56-67.

Budseekoad, S., Yupanqui, C. T., Sirinupong, N., Alashi, A. M., Aluko, R. E., & Youravong, W. (**2018**). Structural and functional characterization of calcium and iron-binding peptides from mung bean protein hydrolysate. *J. Funct. Foods*, *49*, 333-341. https://doi.org/10.1016/j.jff.2018.07.041

Burgot, J.-L. (**2012**). Complexometry II: Titrations with EDTA. In Springer (Ed.), *Ionic Equilibria in Analytical Chemistry*. https://doi.org/10.1007/978-1-4419-8382-4

Caetano-Silva, M. E., Alves, R. C., Lucena, G. N., Frem, R. C. G., Bertoldo-Pacheco, M. T., Lima-Pallone, J. A., & Netto, F. M. (**2017**). Synthesis of whey peptide-iron complexes:

Influence of using different iron precursor compounds. *Food Res Int*, *101*, 73-81. https://doi.org/10.1016/j.foodres.2017.08.056

Caetano-Silva, M. E., Netto, F. M., Bertoldo-Pacheco, M. T., Alegria, A., & Cilla, A. (**2021**). Peptide-metal complexes: obtention and role in increasing bioavailability and decreasing the pro-oxidant effect of minerals. *Crit Rev Food Sci Nutr*, *61*(9), 1470-1489. https://doi.org/10.1080/10408398.2020.1761770

Cammarota, M., Lamberti, M., Masella, L., Galletti, P., De Rosa, M., Sannolo, N., & Giuliano, M. (**2006**). Matrix metalloproteinases and their inhibitors as biomarkers for metal toxicity in vitro. *Toxicol In Vitro*, *20*(7), 1125-1132. https://doi.org/10.1016/j.tiv.2006.02.004

Canabady-Rochelle, L. L., Harscoat-Schiavo, C., Kessler, V., Aymes, A., Fournier, F., & Girardet, J. M. (**2015**). Determination of reducing power and metal chelating ability of antioxidant peptides: revisited methods. *Food Chem*, *183*, 129-135. https://doi.org/10.1016/j.foodchem.2015.02.147

Canabady-Rochelle, L. L. S., Selmeczi, K., Collin, S., Pasc, A., Muhr, L., & Boschi-Muller, S. (**2018**). SPR screening of metal chelating peptides in a hydrolysate for their antioxidant properties. *Food Chem*, *239*, 478-485. https://doi.org/10.1016/j.foodchem.2017.06.116

Canabady-Rochelle, L. S., Sanchez, C., Mellema, M., & Banon, S. (**2009**). Study of calcium-soy protein interactions by isothermal titration calorimetry and pH cycle. *J Agric Food Chem*, *57*(13), 5939-5947. https://doi.org/10.1021/jf900424b

Canabady-Rochelle, L. S., Sanchez, C., Mellema, M., & Banon, S. (**2010**). Calcium carbonate-hydrolyzed soy protein complexation in the presence of citric acid. *J Colloid Interface Sci*, *345*(1), 88-95. https://doi.org/10.1016/j.jcis.2010.01.037

Canabady-Rochelle, L. S., Sanchez, C., Mellema, M., Bot, A., Desobry, S., & Banon, S. (**2007**). Influence of calcium salt supplementation on calcium equilibrium in skim milk during pH cycle. *J Dairy Sci*, *90*(5), 2155-2162. https://doi.org/10.3168/jds.2006-665

Canette, A., & Briandet, R. (**2014**). Confocal Laser Scanning Microscopy. In Carl A. Batt & M. L. Tortorello (Eds.), *Encyclopedia of Food Microbiology (Second Edition)* (pp. 676-683). Academic Press. https://doi.org/10.1016/b978-0-12-384730-0.00214-7

Carrasco-Castilla, J., Hernández-Álvarez, A. J., Jiménez-Martínez, C., Jacinto-Hernández, C., Alaiz, M., Girón-Calle, J., Vioque, J., & Dávila-Ortiz, G. (**2012**). Antioxidant and metal

chelating activities of Phaseolus vulgaris L. var. Jamapa protein isolates, phaseolin and lectin hydrolysates. *Food Chem*, *131*(4), 1157-1164. https://doi.org/10.1016/j.foodchem.2011.09.084

Carter, P. (**1971**). Spectrophotometric Determination of Serum Iron at the Submicrogram Level with a New Reagent (Ferrozine). *Anal. Biochem.*, *40*, 450-458.

Caruso, G., Floris, R., Serangeli, C., & Di Paola, L. (**2020**). Fishery Wastes as a Yet Undiscovered Treasure from the Sea: Biomolecules Sources, Extraction Methods and Valorization. *Mar Drugs*, *18*(12). https://doi.org/10.3390/md18120622

Chai, T. T., Tong, S. R., Law, Y. C., Ismail, N. I. N., Manan, F. A., & Wong, F. C. (**2015**). Anti-oxidative, metal chelating and radical scavenging effects of protein hydrolysates from blue-spotted stingray. *Trop. J. Pharm. Res.*, *14*(8), 1349-1355. https://doi.org/10.4314/tjpr.v14i8.5

Chalamaiah, M., Keskin Ulug, S., Hong, H., & Wu, J. (**2019**). Regulatory requirements of bioactive peptides (protein hydrolysates) from food proteins. *J. Funct. Foods*, *58*, 123-129. https://doi.org/10.1016/j.jff.2019.04.050

Chandrapala, J., Zisu, B., Palmer, M., Kentish, S., & Ashokkumar, M. (**2011**). Effects of ultrasound on the thermal and structural characteristics of proteins in reconstituted whey protein concentrate. *Ultrason Sonochem*, *18*(5), 951-957. https://doi.org/10.1016/j.ultsonch.2010.12.016

Charoenphun, N., Cheirsilp, B., Sirinupong, N., & Youravong, W. (**2012**). Calcium-binding peptides derived from tilapia (Oreochromis niloticus) protein hydrolysate. *Eur. Food Res. Technol.*, *236*(1), 57-63. https://doi.org/10.1007/s00217-012-1860-2

Chen, D., Liu, Z., Huang, W., Zhao, Y., Dong, S., & Zeng, M. (**2013**). Purification and characterisation of a zinc-binding peptide from oyster protein hydrolysate. *J. Funct. Foods*, *5*(2), 689-697. https://doi.org/10.1016/j.jff.2013.01.012

Chen, D., Mu, X., Huang, H., Nie, R., Liu, Z., & Zeng, M. (**2014**). Isolation of a calcium-binding peptide from tilapia scale protein hydrolysate and its calcium bioavailability in rats. *J. Funct. Foods*, *6*, 575-584. https://doi.org/10.1016/j.jff.2013.12.001

Chen, K., Yang, X., Huang, Z., Jia, S., Zhang, Y., Shi, J., Hong, H., Feng, L., & Luo, Y. (**2019**). Modification of gelatin hydrolysates from grass carp (Ctenopharyngodon idellus) scales by Maillard reaction: Antioxidant activity and volatile compounds. *Food Chem*, *295*, 569-578. https://doi.org/10.1016/j.foodchem.2019.05.156

Chen, M., Ji, H., Zhang, Z., Zeng, X., Su, W., & Liu, S. (**2019**). A novel calcium-chelating peptide purified from Auxis thazard protien hydrolysate and its binding properties with calcium. *J. Funct. Foods*, *60*. https://doi.org/10.1016/j.jff.2019.103447

Chen, Q. Y., DesMarais, T., & Costa, M. (**2019**). Metals and Mechanisms of Carcinogenesis. *Annu. Rev. Pharmacol. Toxicol.*, *59*, 537-554. https://doi.org/https://doi.org/10.1146/annurev-pharmtox-010818-021031

Chen, S., Tang, L., Hao, G., Weng, W., Osako, K., & Tanaka, M. (**2016**). Effects of α1/α2 ratios and drying temperatures on the properties of gelatin films prepared from tilapia (Tilapia zillii) skins. *Food Hydrocolloids*, *52*, 573-580. https://doi.org/10.1016/j.foodhyd.2015.07.026

Chen, T., Song, Z., Liu, H., Zhou, C., Hong, P., & Deng, C. (**2022**). Physicochemical properties of gelatin produced from Nile tilapia skin using chemical and fermentation pretreatments. *Food Bioscience*, *47*. https://doi.org/10.1016/j.fbio.2022.101650

Chesters, B. J. K., & Will, M. (**1981**). Zinc transport proteins in plasma. *Br. J. Nutr*, *46*, 111-118.

Chikha, G. G., Lia, W. M., Schutze-Redelmeiera, M.-P., Meunierb, J.-C., & Ballya, M. B. (**2002**). Attaching histidine-tagged peptides and proteins to lipid-based carriers through use of metal-ion-chelating lipids. *Biochim. Biophys. Acta*, *1567*, 204-212.

Choi, D.-W., Lee, J.-H., Chun, H.-H., & Song, K. B. (**2012**). Isolation of a calcium-binding peptide from bovine serum protein hydrolysates. *Food Sci. Biotechnol.*, *21*(6), 1663-1667. https://doi.org/10.1007/s10068-012-0221-z

Clery, A., Sohier, T. J. M., Welte, T., Langer, A., & Allain, F. H. T. (**2017**). switchSENSE: A new technology to study protein-RNA interactions. *Methods*, *118-119*, 137-145. https://doi.org/10.1016/j.ymeth.2017.03.004

Crichton, R. R., & Ward, R. J. (**2003**). An Overview of Iron Metabolism: Molecular and Cellular Criteria for the Selection of Iron Chelators. *Curr. Med. Chem.*, *10*(12), 997-1004.

Cui, P., Lin, S., Jin, Z., Zhu, B., Song, L., & Sun, N. (**2018**). In vitro digestion profile and calcium absorption studies of a sea cucumber ovum derived heptapeptide-calcium complex. *Food Funct*, *9*(9), 4582-4592. https://doi.org/10.1039/c8fo00910d

Daniyal, W. M. E. M. M., Saleviter, S., & Fen, Y. W. (**2018**). Development of Surface Plasmon Resonance Spectroscopy for Metal Ion Detection. *Sens. Mater.*, *30*(9). https://doi.org/10.18494/sam.2018.1952

Daroit, D. J., & Brandelli, A. (**2021**). In vivo bioactivities of food protein-derived peptides – a current review. *Curr. Opin. Food Sci.*, *39*, 120-129. https://doi.org/10.1016/j.cofs.2021.01.002

Das, D., Jaiswal, M., Khan, F. N., Ahamad, S., & Kumar, S. (**2020**). PlantPepDB: A manually curated plant peptide database. *Sci Rep*, *10*(1), 2194. https://doi.org/10.1038/s41598-020-59165-2

De la Hoz, L., Ponezi, A. N., Milani, R. F., Nunes da Silva, V. S., Sonia de Souza, A., & Bertoldo-Pacheco, M. T. (**2014**). Iron-binding properties of sugar cane yeast peptides. *Food Chem*, *142*, 166-169. https://doi.org/10.1016/j.foodchem.2013.06.133

De Marco, R., Clarke, G., & Pejcic, B. (**2007**). Ion-Selective Electrode Potentiometry in Environmental Analysis. *Electroanalysis*, *19*(19-20), 1987-2001. https://doi.org/10.1002/elan.200703916

Dean, K. M., Qin, Y., & Palmer, A. E. (**2012**). Visualizing metal ions in cells: an overview of analytical techniques, approaches, and probes. *Biochim Biophys Acta*, *1823*(9), 1406-1415. https://doi.org/10.1016/j.bbamcr.2012.04.001

Drescher, D. G., Selvakumar, D., & Drescher, M. J. (**2018**). Analysis of Protein Interactions by Surface Plasmon Resonance. *Adv Protein Chem Struct Biol*, *110*, 1-30. https://doi.org/10.1016/bs.apcsb.2017.07.003

Dunbar, W. S. (**2017**). Biotechnology and the Mine of Tomorrow. *Trends Biotechnol*, *35*(1), 79-89. https://doi.org/10.1016/j.tibtech.2016.07.004

Eckert, E., Lu, L., Unsworth, L. D., Chen, L., Xie, J., & Xu, R. (**2016**). Biophysical and in vitro absorption studies of iron chelating peptide from barley proteins. *J. Funct. Foods*, *25*, 291-301. https://doi.org/10.1016/j.jff.2016.06.011

El Hajj, S., Irankunda, R., Camano Echavarria, J. A., Arnoux, P., Paris, C., Stefan, L., Gaucher, C., Boschi-Muller, S., & Canabady-Rochelle, L. (**2023**). Metal-chelating activity of soy and pea protein hydrolysates obtained after different enzymatic treatments from protein isolates. *Food Chem*, *405*(Pt A), 134788. https://doi.org/10.1016/j.foodchem.2022.134788

El Hajj, S., Sepulveda Rincon, C. T., Girardet, J. M., Cakir-Kiefer, C., Stefan, L., Zapata Montoya, J. E., Boschi-Muller, S., Gaucher, C., & Canabady-Rochelle, L. (**2021**). Electrically Switchable Nanolever Technology for the Screening of Metal-Chelating Peptides in

Hydrolysates. *J Agric Food Chem*, *69*(31), 8819-8827. https://doi.org/10.1021/acs.jafc.1c02199

El Hajj, S., Sepulveda-Rincon, T., Paris, C., Giraud, T., Csire, G., Stefan, L., Selmeczi, K., Girardet, J.-M., Desobry, S., Bouhallab, S., Muhr, L., Gaucher, C., & Canabady-Rochelle, L. (**2021**). Chapter 19 - Application in nutrition: mineral binding. In F. W. J. Toldra (Ed.), *Biologically Active Peptides From Basic Science to Application for Human Health* (pp. 455-483). Andre Gerhard Wolff. https://doi.org/10.1016/B978-0-12-821389-6.00016-9

Errante, F., Ledwon, P., Latajka, R., Rovero, P., & Papini, A. M. (**2020**). Cosmeceutical Peptides in the Framework of Sustainable Wellness Economy. *Front Chem*, *8*, 572923. https://doi.org/10.3389/fchem.2020.572923

Fan, C., Ge, X., Hao, J., Wu, T., Liu, R., Sui, W., Geng, J., & Zhang, M. (**2023**). Identification of high iron-chelating peptides with unusual antioxidant effect from sea cucumbers and the possible binding mode. *Food Chem*, *399*, 133912. https://doi.org/10.1016/j.foodchem.2022.133912

Fan**,** C., Wang, X., Song, X., Sun, R., Liu, R., Sui, W., Jin, Y., Wu, T., & Zhang, M. (**2023**). Identification of a Novel Walnut Iron Chelating Peptide with Potential High Antioxidant Activity and Analysis of Its Possible Binding Sites. *Foods*, *12*(1). https://doi.org/10.3390/foods12010226

FAO. (**2022**). *The State of World Fisheries and Aquaculture. Towards blue transformation*. Food and Agriculture Organization of the United Nations. https://doi.org/10.4060/cc0461en

Fortunato, A., & Mba, M. (**2021**). Metal Cation Triggered Peptide Hydrogels and Their Application in Food Freshness Monitoring and Dye Adsorption. *Gels*, *7*(3), 85. https://doi.org/10.3390/gels7030085

Forzani, E. S., Zhang, H., Chen, W., & Tao, N. (**2005**). Detection of Heavy Metal Ions in Drinking Water Using a High-Resolution Differential Surface Plasmon Resonance Sensor. *Eviron. Sci. Technol.* , *39*, 1257-1262. https://doi.org/10.1021/es049234z CCC: $30.25

Fraga, C. G. (**2005**). Relevance, essentiality and toxicity of trace elements in human health. *Mol Aspects Med*, *26*(4-5), 235-244. https://doi.org/10.1016/j.mam.2005.07.013

Fu, T., Zhang, S., Sheng, Y., Feng, Y., Jiang, Y., Zhang, Y., Yu, M., & Wang, C. (**2019**). Isolation and characterization of zinc-binding peptides from mung bean protein hydrolysates.

Eur. Food Res. Technol., *246*(1), 113-124. https://doi.org/10.1007/s00217-019-03397-8

Gaetke, L. M., & Chow, C. K. (**2003**). Copper toxicity, oxidative stress, and antioxidant nutrients. *Toxicology*, *189*(1-2), 147-163. https://doi.org/10.1016/s0300-483x(03)00159-8

Gilbert, J. A., Jansson, J. K., & Knight, R. (**2014**). The Earth Microbiome project: Successes and aspirations. *BMC Biol.*, *12*(1), 1-4. https://doi.org/https://doi.org/10.1186/s12915-014-0069-1

Giraud, T., Bouguet-Bonnet, S., Marchal, P., Pickaert, G., Averlant-Petit, M. C., & Stefan, L. (**2020**). Improving and fine-tuning the properties of peptide-based hydrogels via incorporation of peptide nucleic acids. *Nanoscale*, *12*(38), 19905-19917. https://doi.org/10.1039/d0nr03483e

Gitelman, H. J. (**1967**). An improved automated procedure for the determination of calcium in biological specimens. *Anal. Biochem.*, *18*, 521.

Gómez-Guillén, M., López-Caballero, M., Alemán, A., López de Lacey, A., Giménez, B., & Montero, P. (**2010**). 7. Antioxidant and antimicrobial peptide fractions from squid and tuna skin gelatin. In E. L. Bihan (Ed.), *Sea By-Products as Real Material: New Ways of Application* (pp. 89-115).

Gómez-Guillen, M. C., Turnay, J., Fernández-Díaz , Ulmo , N., Lizarbe , M. A., & Montero, P. (**2002**). structural and physical properties of gelatin extracted from different marine species: a comparative stud. *Food Hydrocolloids 16 ?*(2002), 25-34.

Gonzalez, P., Bossak, K., Stefaniak, E., Hureau, C., Raibaut, L., Bal, W., & Faller, P. (**2018**). N-Terminal Cu-Binding Motifs (Xxx-Zzz-His, Xxx-His) and Their Derivatives: Chemistry, Biology and Medicinal Applications. *Chem. Eur. J*, *24*(32), 8029-8041. https://doi.org/10.1002/chem.201705398

Gunalan, S., Somarathinam, K., Bhattacharya, J., Srinivasan, S., Jaimohan, S. M., Manoharan, R., Ramachandran, S., Kanagaraj, S., & Kothandan, G. (2020). Understanding the dual mechanism of bioactive peptides targeting the enzymes involved in Renin Angiotensin System (RAS): An in-silico approach. *J Biomol Struct Dyn*, *38*(17), 5044-5061. https://doi.org/10.1080/07391102.2019.1695668

Guo, L., Harnedy, P. A., Li, B., Hou, H., Zhang, Z., Zhao, X., & FitzGerald, R. J. (**2014**). Food protein-derived chelating peptides: Biofunctional ingredients for dietary mineral

bioavailability enhancement. *Trends Food Sci Technol*, *37*(2), 92-105. https://doi.org/10.1016/j.tifs.2014.02.007

Guo, L., Harnedy, P. A., O'Keeffe, M. B., Zhang, L., Li, B., Hou, H., & FitzGerald, R. J. (**2015**). Fractionation and identification of Alaska pollock skin collagen-derived mineral chelating peptides. *Food Chem*, *173*, 536-542. https://doi.org/10.1016/j.foodchem.2014.10.055

Guo, L., Hou, H., Li, B., Zhang, Z., Wang, S., & Zhao, X. (**2013**). Preparation, isolation and identification of iron-chelating peptides derived from Alaska pollock skin. *Process Biochem*, *48*(5-6), 988-993. https://doi.org/10.1016/j.procbio.2013.04.013

Gupta, S., Kapoor, P., Chaudhary, K., Gautam, A., Kumar, R., Open Source Drug Discovery, C., & Raghava, G. P. (**2013**). In silico approach for predicting toxicity of peptides and proteins. *PLoS One*, *8*(9), e73957. https://doi.org/10.1371/journal.pone.0073957

Hadnadjev, M., Dapcevic-Hadnadjev, T., Pojic, M., Saric, B., Misan, A., Jovanov, P., & Sakac, M. (**2017**). Progress in vegetable proteins isolation techniques: A review. *Food Feed Res.*, *44*(1), 11-21. https://doi.org/10.5937/ffr1701011h

Hao, L., Li, J., Kappler, A., & Obst, M. (**2013**). Mapping of heavy metal ion sorption to cell-extracellular polymeric substance-mineral aggregates by using metal-selective fluorescent probes and confocal laser scanning microscopy. *Appl Environ Microbiol*, *79*(21), 6524-6534. https://doi.org/10.1128/AEM.02454-13

Heiberger, R. M., & Holland, B. (**2015**). Statistical Analysis and Data Display, An Intermediate Course with Examples in R. In Springer Texts in Statistics. In I. S. T. i. Statistics (Ed.), (Second Edi Vol. 168, Issue 2 ed.). Journal of the Royal Statistical Society Series A (Statistics in Society) https://doi.org/https://doi.org/10.1007/978-1-4939-2122-5

Hill, S. J., & Fisher, A. S. (**2017**). Atomic Absorption, Methods and Instrumentation. In John C. Lindon, George E. Tranter, & D. W. Koppenaal (Eds.), *Encyclopedia of Spectroscopy and Spectrometry (Third Edition)* (pp. 37-43). Academic Press. https://doi.org/10.1016/b978-0-12-803224-4.00099-6

Hou, H., Wang, S., Zhu, X., Li, Q., Fan, Y., Cheng, D., & Li, B. (**2018**). A novel calcium-binding peptide from Antarctic krill protein hydrolysates and identification of binding sites of calcium-peptide complex. *Food Chem*, *243*, 389-395. https://doi.org/10.1016/j.foodchem.2017.09.152

Hou, Y., Wu, Z., Dai, Z., Wang, G., & Wu, G. (**2017**). Protein hydrolysates in animal nutrition: Industrial production, bioactive peptides, and functional significance. *J Anim Sci Biotechnol*, *8*, 24. https://doi.org/10.1186/s40104-017-0153-9

Huang, C. Y., Kuo, J. M., Wu, S. J., & Tsai, H. T. (**2016**). Isolation and characterization of fish scale collagen from tilapia (Oreochromis sp.) by a novel extrusion-hydro-extraction process. *Food Chem*, *190*, 997-1006. https://doi.org/10.1016/j.foodchem.2015.06.066

Huang, C. Y., Wu, T. C., Hong, Y. H., Hsieh, S. L., Guo, H. R., & Huang, R. H. (**2018**). Enhancement of Cell Adhesion, Cell Growth, Wound Healing, and Oxidative Protection by Gelatins Extracted from Extrusion-Pretreated Tilapia (Oreochromis sp.) Fish Scale. *Molecules*, *23*(10). https://doi.org/10.3390/molecules23102406

Huang, G., Ren, L., & Jiang, J. (**2010**). Purification of a histidine-containing peptide with calcium binding activity from shrimp processing byproducts hydrolysate. *Eur. Food Res. Technol.*, *232*(2), 281-287. https://doi.org/10.1007/s00217-010-1388-2

Huang, G., Ren, Z., & Jiang, J. (**2011**). Separation of Iron-Binding Peptides from Shrimp Processing By-products Hydrolysates. *Food Bioproc Tech*, *4*(8), 1527-1532. https://doi.org/10.1007/s11947-010-0416-3

Huang, S. L., Zhao, L. N., Cai, X., Wang, S. Y., Huang, Y. F., Hong, J., & Rao, P. F. (**2015**). Purification and characterisation of a glutamic acid-containing peptide with calcium-binding capacity from whey protein hydrolysate. *J Dairy Res*, *82*(1), 29-35. https://doi.org/10.1017/S0022029914000715

Huebner, A., Kind, B., & Koehler, K. (**2013**). Chaper - 16- Molecular Biology and Molecular Genetics in Paediatric Endocrinology. In M. Zacharin (Ed.), *Practical Pediatric Endocrinology in a Limited Resource Setting* (pp. 355-378). Academic Press. https://doi.org/10.1016/b978-0-12-407822-2.00016-5

Inamuddin, & Alam, M. M. (**2008**). Studies on the Preparation and Analytical Applications of Various Metal Ion-Selective Membrane Electrodes Based on Polymeric, Inorganic and Composite Materials—A Review. *J. Macromol. Sci. A*, *45*(12), 1084-1101. https://doi.org/10.1080/10601320802458178

Irankunda, R., Camaño Echavarría, J. A., Paris, C., Selmeczi, K., Stefan, L., Boschi-Muller, S., Muhr, L., & Canabady-Rochelle, L. (**2024**). Deciphering Interactions Involved in Immobilized Metal Ion Affinity Chromatography and Surface Plasmon Resonance for

Validating the Analogy between Both Technologies. *Inorganics*, *12*(1), 31. https://doi.org/10.3390/inorganics12010031

Irankunda, R., Camaño Echavarría, J. A., Paris, C., Stefan, L., Desobry, S., Selmeczi, K., Muhr, L., & Canabady-Rochelle, L. (**2022**). Metal-Chelating Peptides Separation Using Immobilized Metal Ion Affinity Chromatography: Experimental Methodology and Simulation. *Separations*, *9*(11), 370. https://doi.org/10.3390/separations9110370

Jai ganesh, R., Nazeer, R. A., & Sampath Kumar, N. S. (**2011**). Purification and identification of antioxidant peptide from black pomfret, Parastromateus niger (Bloch, 1975) viscera protein hydrolysate. *Food Sci. Biotechnol.*, *20*(4), 1087-1094. https://doi.org/10.1007/s10068-011-0147-x

Jekle, M., & Becker, T. (**2015**). Wheat dough microstructure: the relation between visual structure and mechanical behavior. *Crit Rev Food Sci Nutr*, *55*(3), 369-382. https://doi.org/10.1080/10408398.2012.656476

Ji, G., & Silver, S. (**1995**). Bacterial resistance mechanisms for heavy metals of environmental concern. *J. Ind. Microbiol.*, *14*(2), 61-75. https://doi.org/https://doi.org/10.1007/BF01569887

Jia, J., Wu, Q., Yan, H., & Gui, Z. (**2015**). Purification and molecular docking study of a novel angiotensin-I converting enzyme (ACE) inhibitory peptide from alcalase hydrolysate of ultrasonic-pretreated silkworm pupa (Bombyx mori) protein. *Process Biochem*, *50*(5), 876-883. https://doi.org/10.1016/j.procbio.2014.12.030

Jiang, H., Zhang, W., Chen, F., Zou, J., Chen, W., & Huang, G. (**2019**). Purification of an iron-binding peptide from scad (Decapterus maruadsi) processing by-products and its effects on iron absorption by Caco-2 cells. *J Food Biochem*, *43*(7), e12876. https://doi.org/10.1111/jfbc.12876

Jimsheena, V. K., & Gowda, L. R. (**2011**). Angiotensin I-converting enzyme (ACE) inhibitory peptides derived from arachin by simulated gastric digestion. *Food Chem*, *125*(2), 561-569. https://doi.org/10.1016/j.foodchem.2010.09.048

Johnson, C. R., Shrout, J. D., & Fein, J. B. (**2018**). Visualization and quantification of Cd sorption to bacteria using confocal laser scanning microscopy and Cd-specific fluorescent probes. *Chem. Geol.*, *483*, 21-30. https://doi.org/10.1016/j.chemgeo.2018.02.020

Jozefczak, M., Remans, T., Vangronsveld, J., & Cuypers, A. (**2012**). Glutathione is a key player in metal-induced oxidative stress defenses. *Int J Mol Sci*, *13*(3), 3145-3175. https://doi.org/10.3390/ijms13033145

Jungbauer, A., & Hahn, R. (**2009**). Ion-exchange chromatography. *Methods Enzymol*, *463*, 349-371. https://doi.org/10.1016/S0076-6879(09)63022-6

Karim, A. A., & Bhat, R. (**2009**). Fish gelatin: properties, challenges, and prospects as an alternative to mammalian gelatins. *Food Hydrocolloids*, *23*(3), 563-576. https://doi.org/10.1016/j.foodhyd.2008.07.002

Kasankala, L. M., Xue, Y., Weilong, Y., Hong, S. D., & He, Q. (**2007**). Optimization of gelatine extraction from grass carp (Catenopharyngodon idella) fish skin by response surface methodology. *Bioresour Technol*, *98*(17), 3338-3343. https://doi.org/10.1016/j.biortech.2006.03.019

Katsoulos, P. D., Athanasiou, L. V., Dedousi, A., & Polizopoulou, Z. S. (**2020**). Serum calcium determination with atomic absorption spectrophotometry and colorimetric method: association and predictive equations between them in cattle and sheep samples. *Comp. Clin. Path.*, *30*(1), 11-15. https://doi.org/10.1007/s00580-020-03183-z

Kim, E. J., Chung, B. H., & Lee, H. J. (**2012**). Parts per trillion detection of Ni(II) ions by nanoparticle-enhanced surface plasmon resonance. *Anal Chem*, *84*(22), 10091-10096. https://doi.org/10.1021/ac302584d

Knecht, S., Ricklin, D., Eberle, A. N., & Ernst, B. (**2009**). Oligohis-tags: mechanisms of binding to Ni2+-NTA surfaces. *J Mol Recognit*, *22*(4), 270-279. https://doi.org/10.1002/jmr.941

Kong, X., Bao, S., Song, W., Hua, Y., Zhang, C., Chen, Y., & Li, X. (**2021**). Contributions of ethanol fractionation on the properties of vegetable protein hydrolysates and differences in the characteristics of metal (Ca, Zn, Fe)-chelating peptides. *Lwt*, *146*, 111482. https://doi.org/10.1016/j.lwt.2021.111482

Kowdley, K. V. (**2004**). Iron, hemochromatosis, and hepatocellular carcinoma. *Gastroenterology*, *127*(5 Suppl 1), S79-86. https://doi.org/10.1016/j.gastro.2004.09.019

Kroll, R. D. (**1984**). Effect of pH on the bindiong of calcium ions by soybean proteins. *Cereal Chem.*, *61*(6), 490-495.

Kubglomsong, S., Theerakulkait, C., Reed, R. L., Yang, L., Maier, C. S., & Stevens, J. F. (**2018**). Isolation and Identification of Tyrosinase-Inhibitory and Copper-Chelating Peptides from Hydrolyzed Rice-Bran-Derived Albumin. *J Agric Food Chem*, *66*(31), 8346-8354. https://doi.org/10.1021/acs.jafc.8b01849

Kula, E., Kocadag Kocazorbaz, E., Moulahoum, H., Alpat, S., & Zihnioglu, F. (**2020**). Extraction and characterization of novel multifunctional peptides from Trachinus Draco (greater weever) myofibrillar proteins with ACE/DPP4 inhibitory, antioxidant, and metal chelating activities. *J Food Biochem*, *44*(5), e13179. https://doi.org/10.1111/jfbc.13179

Kumar, V., & Gill, K. D. (**2018**). Chapter 21 - Estimation of Total Calcium in Serum and Urine. In *Basic Concepts in Clinical Biochemistry: A Practical Guide* (pp. 85-88). Springer, Singapore. https://doi.org/10.1007/978-981-10-8186-6_21

Ladbury, J. E., & Chowdhry, B. Z. (**1996**). Sensing the heat: the application of isothermal titration calorimetry to thermodynamic studies of biomolecular nteractions. *Chem. Biol.*, *3*(10), 791-801.

Latha, B. V., Likhitha, R., & Kumar, M. (**2021**). Copper chelating protein hydrolysate from Salvia hispanica L. by pepsin-pancreatin treatment. *Curr Res Food Sci*, *4*, 829-839. https://doi.org/10.1016/j.crfs.2021.11.007

Le Gouic, A. V., Harnedy, P. A., & FitzGerald, R. J. (**2018**). Bioactive Peptides From Fish Protein By-Products. In J. Mérillon, Ramawat, K. (Ed.), *Bioactive Molecules in Food. Reference Series in Phytochemistry* (pp. 1-35). Springer, Cham. https://doi.org/10.1007/978-3-319-54528-8_29-1

Ledwon, P., Errante, F., Papini, A. M., Rovero, P., & Latajka, R. (**2021**). Peptides as Active Ingredients: A Challenge for Cosmeceutical Industry. *Chem Biodivers*, *18*(2), e2000833. https://doi.org/10.1002/cbdv.202000833

Lee, S.-H., & Song, K. B. (**2009**). Purification of an iron-binding nona-peptide from hydrolysates of porcine blood plasma protein. *Process Biochem*, *44*(3), 378-381. https://doi.org/10.1016/j.procbio.2008.12.001

León, C., Cifuentes, A., & Valdés, A. (**2018**). Foodomics Applications. In Joaquim Jaumot, Carmen Bedia, & R. Tauler (Eds.), *Comprehensive Analytical Chemistry* (Vol. 82, pp. 643-685). Elsevier. https://doi.org/10.1016/bs.coac.2018.06.008

Li, B., He, H., Shi, W., & Hou, T. (**2019**). Effect of duck egg white peptide-ferrous chelate on iron bioavailability in vivo and structure characterization. *J Sci Food Agric*, *99*(4), 1834-1841. https://doi.org/10.1002/jsfa.9377

Li, R. H., Liu, G. B., Wang, H., & Zheng, Y. Z. (**2013**). Effects of Fe3+ and Zn2+ on the structural and thermodynamic properties of a soybean ASR protein. *Biosci Biotechnol Biochem*, *77*(3), 475-481. https://doi.org/10.1271/bbb.120666

Li, Y., Jiang, H., & Huang, G. (**2017**). Protein Hydrolysates as Promoters of Non-Haem Iron Absorption. *Nutrients*, *9*, 609. https://doi.org/10.3390/nu9060609

Li-Chan, E. C. Y. (**2015**). Bioactive peptides and protein hydrolysates: research trends and challenges for application as nutraceuticals and functional food ingredients. *Curr. Opin. Food Sci.*, *1*, 28-37. https://doi.org/10.1016/j.cofs.2014.09.005

Liao, W., Chen, H., Jin, W., Yang, Z., Cao, Y., & Miao, J. (**2020**). Three Newly Isolated Calcium-Chelating Peptides from Tilapia Bone Collagen Hydrolysate Enhance Calcium Absorption Activity in Intestinal Caco-2 Cells. *J Agric Food Chem*, *68*(7), 2091-2098. https://doi.org/10.1021/acs.jafc.9b07602

Liao, W., Liu, S., Liu, X., Duan, S., Xiao, S., Yang, Z., Cao, Y., & Miao, J. (**2019**). The purification, identification and bioactivity study of a novel calcium-binding peptide from casein hydrolysate. *Food Funct*, *10*(12), 7724-7732. https://doi.org/10.1039/c9fo01383k

Lin, S., Hu, X., Li, L., Yang, X., Chen, S., Wu, Y., & Yang, S. (**2021**). Preparation, purification and identification of iron-chelating peptides derived from tilapia (Oreochromis niloticus) skin collagen and characterization of the peptide-iron complexes. *Lwt*, *149*, 111796. https://doi.org/10.1016/j.lwt.2021.111796

Lin, Y., Cai, X., Wu, X., Lin, S., & Wang, S. (**2020**). Fabrication of snapper fish scales protein hydrolysate-calcium complex and the promotion in calcium cellular uptake. *Journal of Functional Foods*, *65*. https://doi.org/10.1016/j.jff.2019.103717

Liu, F. F., Li, Y. Q., Wang, C. Y., Liang, Y., Zhao, X. Z., He, J. X., & Mo, H. Z. (**2022**). Physicochemical, functional and antioxidant properties of mung bean protein enzymatic hydrolysates. *Food Chem*, *393*, 133397. https://doi.org/10.1016/j.foodchem.2022.133397

Liu, F. R., Wang, L., Wang, R., & Chen, Z. X. (**2013**). Calcium-binding capacity of wheat germ protein hydrolysate and characterization of Peptide-calcium complex. *J Agric Food Chem*, *61*(31), 7537-7544. https://doi.org/10.1021/jf401868z

Liu, L., Li, S., Zheng, J., Bu, T., He, G., & Wu, J. (**2020**). Safety considerations on food protein-derived bioactive peptides. *Trends Food Sci Technol*, *96*, 199-207. https://doi.org/10.1016/j.tifs.2019.12.022

Liu, X., Wang, Z., Yin, F., Liu, Y., Qin, N., Nakamura, Y., Shahidi, F., Yu, C., Zhou, D., & Zhu, B. (**2019**). Zinc-Chelating Mechanism of Sea Cucumber (Stichopus japonicus)-Derived Synthetic Peptides. *Mar Drugs*, *17*(8), 438. https://doi.org/10.3390/md17080438

Lorenzo, J. M., Munekata, P. E. S., Gómez, B., Barba, F. J., Mora, L., Pérez-Santaescolástica, C., & Toldrá, F. (**2018**). Bioactive peptides as natural antioxidants in food products – A review. *Trends Food Sci Technol*, *79*, 136-147. https://doi.org/10.1016/j.tifs.2018.07.003

Lu, C. H., Lin, Y. F., Lin, J. J., & Yu, C. S. (**2012**). Prediction of metal ion-binding sites in proteins using the fragment transformation method. *PLoS One*, *7*(6), e39252. https://doi.org/10.1371/journal.pone.0039252

Luza, S. C., & C, S. H. (**1996**). Liver copper storage and transport during development: implications for cytotoxicity. *Am J Clin Nutr*, *63*, 812S-820S.

Lv, Y., Bao, X., Liu, H., Ren, J., & Guo, S. (**2013**). Purification and characterization of calcium-binding soybean protein hydrolysates by Ca2+/Fe3+ immobilized metal affinity chromatography (IMAC). *Food Chem*, *141*(3), 1645-1650. https://doi.org/10.1016/j.foodchem.2013.04.113

Lv, Y., Wei, K., Meng, X., Huang, Y., Zhang, T., & Li, Z. (**2017**). Separation and identification of iron-chelating peptides from defatted walnut flake by nanoLC-ESI–MS/MS and de novo sequencing. *Process Biochem*, *59*, 223-228. https://doi.org/10.1016/j.procbio.2017.05.010

Makowska, J., Wyrzykowski, D., Pilarski, B., Neubauer, D., Kamysz, E., Tesmar, A., & Chmurzyński, L. (**2019**). Copper(II) coordination properties of GxG peptides: Key role of side chains of central residues on coordination of formed systems; combined potentiometric and ITC studies. *J. Chem. Thermodyn.*, *128*, 336-343. https://doi.org/10.1016/j.jct.2018.08.040

Malerich, S., & Berson, D. (**2014**). Next generation cosmeceuticals: the latest in peptides, growth factors, cytokines, and stem cells. *Dermatol Clin*, *32*(1), 13-21. https://doi.org/10.1016/j.det.2013.09.003

Malison, A., Arpanutud, P., & Keeratipibul, S. (**2021**). Chicken foot broth byproduct: A new source for highly effective peptide-calcium chelate. *Food Chem*, *345*, 128713. https://doi.org/10.1016/j.foodchem.2020.128713

Maret, W. (**2013**). Zinc biochemistry: from a single zinc enzyme to a key element of life. *Adv Nutr*, *4*(1), 82-91. https://doi.org/10.3945/an.112.003038

Martínez-Alvarez, O., Chamorro, S., & Brenes, A. (**2015**). Protein hydrolysates from animal processing by-products as a source of bioactive molecules with interest in animal feeding: A review. *Food Research International*, *73*, 204-212. https://doi.org/10.1016/j.foodres.2015.04.005

May May, L., & Russell, D. A. (**2003**). Novel determination of cadmium ions using an enzyme self-assembled monolayer with surface plasmon resonance. *Anal. Chim. Acta*, *500*(1-2), 119-125. https://doi.org/10.1016/s0003-2670(03)00943-7

Megías, C., Pedroche, J., Yust, M. M., Girón-Calle, J., Alaiz, M., Millán, F., & Vioque, J. (**2008**). Production of copper-chelating peptides after hydrolysis of sunflower proteins with pepsin and pancreatin. *Lwt*, *41*(10), 1973-1977. https://doi.org/10.1016/j.lwt.2007.11.010

Mejáre, M., & Bülow, L. (**2001**). Metal-binding proteins and peptides in bioremediation and phytoremediation of heavy metals. *Trends Biotechnol.*, *19*(2), 67-73. https://doi.org/https://doi.org/10.1016/S0167-7799(00)01534-1

Meng, K., Chen, L., Xia, G., & Shen, X. (**2021**). Effects of zinc sulfate and zinc lactate on the properties of tilapia (Oreochromis Niloticus) skin collagen peptide chelate zinc. *Food Chem*, *347*, 129043. https://doi.org/10.1016/j.foodchem.2021.129043

Merlos, M. A., Michálek, P., Kryštofová, O., Zítka, O., Adam, V., & Kizek, R. (**2014**). The role of phytochelatins in plant and animals: A review. *J. Metallomics Nanotechnol.*, *1*(4), 22-77.

Miao, J., Liao, W., Pan, Z., Wang, Q., Duan, S., Xiao, S., Yang, Z., & Cao, Y. (**2019**). Isolation and identification of iron-chelating peptides from casein hydrolysates. *Food Funct*, *10*(5), 2372-2381. https://doi.org/10.1039/c8fo02414f

Michaelis, M., Fayyaz, A., Parambath, M., Koeppen, S., Ciacchi, L. C., Hanley, Q. S., & Perry, C. C. (**2019**). Platform for Screening Abiotic/Biotic Interactions Using Indicator Displacement Assays. *Langmuir*, *35*(44), 14230-14237. https://doi.org/10.1021/acs.langmuir.9b03085

Minkiewicz, P., Iwaniak, A., & Darewicz, M. (**2019**). BIOPEP-UWM Database of Bioactive Peptides: Current Opportunities. *Int J Mol Sci*, *20*(23), 5978. https://doi.org/10.3390/ijms20235978

Montero, M., & Acosta, Ó. G. (**2020**). Tuna skin gelatin production: optimization of extraction steps and process scale-up. *CyTA - Journal of Food*, *18*(1), 580-590. https://doi.org/10.1080/19476337.2020.1801849

Mooney, C., Haslam, N. J., Holton, T. A., Pollastri, G., & Shields, D. C. (**2013**). PeptideLocator: prediction of bioactive peptides in protein sequences. *Bioinform.*, *29*(9), 1120-1126. https://doi.org/10.1093/bioinformatics/btt103

Mooney, J. T., Fredericks, D., & Hearn, M. T. (**2011**). Use of phage display methods to identify heptapeptide sequences for use as affinity purification 'tags' with novel chelating ligands in immobilized metal ion affinity chromatography. *J Chromatogr A*, *1218*(1), 92-99. https://doi.org/10.1016/j.chroma.2010.10.113

Muhr, L., Pontvianne, S., Selmeczi, K., Paris, C., Boschi-Muller, S., & Canabady-Rochelle, L. (**2020**). Chromatographic separation simulation of metal-chelating peptides from surface plasmon resonance binding parameters. *J Sep Sci*, *43*(11), 2031-2041. https://doi.org/10.1002/jssc.201900882

Muller, L. K., Duznovic, I., Tietze, D., Weber, W., Ali, M., Stein, V., Ensinger, W., & Tietze, A. A. (**2020**). Ultrasensitive and Selective Copper(II) Detection: Introducing a Bioinspired and Robust Sensor. *Chemistry*, *26*(39), 8511-8517. https://doi.org/10.1002/chem.202001160

Nagai, T., Izumi, M., & Ishii, M. (**2004**). Fish scale collagen. Preparation and partial characterization. *International Journal of Food Science & Technology*, *39*(3), 239-244. https://doi.org/10.1111/j.1365-2621.2004.00777.x

Nagarajan, M., Benjakul, S., Prodpran, T., Songtipya, P., & Kishimura, H. (**2012**). Characteristics and functional properties of gelatin from splendid squid (Loligo formosana) skin as affected by extraction temperatures. *Food Hydrocolloids*, *29*(2), 389-397. https://doi.org/10.1016/j.foodhyd.2012.04.001

Ng, C. K., Osuna-Sanchez, H., Valery, E., Sorensen, E., & Bracewell, D. G. (**2012**). Design of high productivity antibody capture by protein A chromatography using an integrated experimental and modeling approach. *J Chromatogr B Analyt Technol Biomed Life Sci*, *899*, 116-126. https://doi.org/10.1016/j.jchromb.2012.05.010

Ngo, D.-H., Qian, Z.-J., Ryu, B., Park, J. W., & Kim, S.-K. (**2010**). In vitro antioxidant activity of a peptide isolated from Nile tilapia (Oreochromis niloticus) scale gelatin in free radical-mediated oxidative systems. *Journal of Functional Foods*, *2*(2), 107-117. https://doi.org/10.1016/j.jff.2010.02.001

Ni, H., Li, L., Liu, G., & Hu, S. Q. (**2012**). Inhibition mechanism and model of an angiotensin I-converting enzyme (ACE)-inhibitory hexapeptide from yeast (Saccharomyces cerevisiae). *PLoS One*, *7*(5), e37077. https://doi.org/10.1371/journal.pone.0037077

Nie, R., Liu, Y., & Liu, Z. (**2014**). The calcium-binding activity of fish scale protein hydrolysates. *JACEN*, *03*(01), 11-15. https://doi.org/10.4236/jacen.2014.31B003

Nielsen, A. D., Fuglsang, C. C., & Westh, P. (**2003**). Isothermal titration calorimetric procedure to determine protein-metal ion binding parameters in the presence of excess metal ion or chelator. *Anal Biochem*, *314*(2), 227-234. https://doi.org/10.1016/s0003-2697(02)00655-3

Nielsen, S. D., Beverly, R. L., Qu, Y., & Dallas, D. C. (**2017**). Milk bioactive peptide database: A comprehensive database of milk protein-derived bioactive peptides and novel visualization. *Food Chem*, *232*, 673-682. https://doi.org/10.1016/j.foodchem.2017.04.056

Ninan, G., Jose, J., & Abubacker, Z. (**2011**). Preparation and Characterization of Gelatin Extracted from the Skins of Rohu (Labeo Rohita) and Common Carp (Cyprinus Carpio). *Journal of Food Processing and Preservation*, *35*(2), 143-161. https://doi.org/10.1111/j.1745-4549.2009.00467.x

Nuwaysir, L. M., & T., S. J. (**1993**). Electrospray Ionization Mass Spectrometry of Phosphopeptides Isolated by On-Line Immobilized Metal-Ion Affinity Chromatography. *J. Am. Soc. Mass Spectrom.*, *4*, 662-669.

Nwachukwu, I. D., & Aluko, R. E. (**2019**). Structural and functional properties of food protein-derived antioxidant peptides. *J Food Biochem*, *43*(1), e12761. https://doi.org/10.1111/jfbc.12761

O'Fagain, C., Cummins, P. M., & O'Connor, B. F. (**2011**). Gel-filtration chromatography. *Methods Mol Biol*, *681*, 25-33. https://doi.org/10.1007/978-1-60761-913-0_2

Ocka, K., Janga, G., Rohb, Y., Kimc, S., Kimd, J., & Kohe, K. (**2001**). Optical detection of Cu2+ ion using a SQ-dye containing polymeric thin-film on Au surface. *Microchem. J.*, *70*(2001), 301-305.

Olalere, O. A., Yap, P.-G., & Gan, C.-Y. (**2023**). Comprehensive review on some food-derived bioactive peptides with anti-hypertension therapeutic potential for angiotensin-converting enzyme (ACE) inhibition. *J. protein proteomics*, *14*(2), 129-161. https://doi.org/10.1007/s42485-023-00106-8

Palika, R., Mashurabad, P. C., Nair, M. K., Reddy, G. B., & Pullakhandam, R. (**2015**). Characterization of iron-binding phosphopeptide released by gastrointestinal digestion of egg white. *Food Res. Int.*, *67*, 308-314. https://doi.org/10.1016/j.foodres.2014.11.049

Pan, D., Lu, H., & Zeng, X. (**2013**). A Newly Isolated Ca Binding Peptide from Whey Protein. *Int. J. Food Prop.*, *16*(5), 1127-1134. https://doi.org/10.1080/10942912.2011.576361

Panyayai, T., Ngamphiw, C., Tongsima, S., Mhuantong, W., Limsripraphan, W., Choowongkomon, K., & Sawatdichaikul, O. (**2019**). FeptideDB: A web application for new bioactive peptides from food protein. *Heliyon*, *5*(7), e02076. https://doi.org/10.1016/j.heliyon.2019.e02076

Paris, C., Selmeczi, K., Ebel, B., Stefan, L., Csire, G., Cakir-Kiefer, C., Desobry, S., Canabady-Rochelle, L., & Chaimbault, P. (**2021**). Metabolomics approach based on LC-HRMS for the fast screening of iron(II)-chelating peptides in protein hydrolysates. *Anal Bioanal Chem*, *413*(2), 315-329. https://doi.org/10.1007/s00216-020-03037-1

Pokusa, M., & Kralova Trancikova, A. (**2017**). The Central Role of Biometals Maintains Oxidative Balance in the Context of Metabolic and Neurodegenerative Disorders. *Oxid Med Cell Longev*, *2017*, 8210734. https://doi.org/10.1155/2017/8210734

Ponzo, I., Moller, F. M., Daub, H., & Matscheko, N. (**2019**). A DNA-Based Biosensor Assay for the Kinetic Characterization of Ion-Dependent Aptamer Folding and Protein Binding. *Molecules*, *24*(16), 2877. https://doi.org/10.3390/molecules24162877

Prasad M, N., V (**2004**). Chapter 3 - Metallothioneins, Metal Binding Complexes and Metal Sequestration in plants. In M. N. V. Prasad (Ed.), *Heavy Metal Stress in Plants* (pp. 47-83). Springer-Verlag https://doi.org/10.1007/978-3-662-07745-0_3

Prohaska, J. R., & Gybina, A. A. (**2004**). Intracellular Copper Transport in Mammals. *J. Nutr.* , *134*, 1003-1006.

Qi, Z. D., Lin, Y., Zhou, B., Ren, X. D., Pang, D. W., & Liu, Y. (**2008**). Characterization of the mechanism of the Staphylococcus aureus cell envelope by bacitracin and bacitracin-

metal ions. *J Membr Biol*, *225*(1-3), 27-37. https://doi.org/10.1007/s00232-008-9130-8

Qu, J. H., Dillen, A., Saeys, W., Lammertyn, J., & Spasic, D. (**2020**). Advancements in SPR biosensing technology: An overview of recent trends in smart layers design, multiplexing concepts, continuous monitoring and in vivo sensing. *Anal Chim Acta*, *1104*, 10-27. https://doi.org/10.1016/j.aca.2019.12.067

Rauser, W. E. (**1999**). Structure and function of metal chelators produced by plants: The case for organic acids, amino acids, phytin, and metallothioneins. *Cell Biochem. Biophys.*, *31*(1), 19-48. https://doi.org/https://doi.org/10.1007/BF02738153

Remko, M., Fitz, D., Broer, R., & Rode, B. M. (**2011**). Effect of metal Ions (Ni(2)(+), Cu(2)(+) and Zn(2)(+)) and water coordination on the structure of L-phenylalanine, L-tyrosine, L-tryptophan and their zwitterionic forms. *J Mol Model*, *17*(12), 3117-3128. https://doi.org/10.1007/s00894-011-1000-0

Ren, L. K., Fan, J., Yang, Y., Liu, X. F., Wang, B., Bian, X., Wang, D. F., Xu, Y., Liu, B. X., Zhu, P. Y., & Zhang, N. (**2023**). Identification, in silico selection, and mechanism study of novel antioxidant peptides derived from the rice bran protein hydrolysates. *Food Chem*, *408*, 135230. https://doi.org/10.1016/j.foodchem.2022.135230

Rezende, C. A., Atta, B. W., Breitkreitz, M. C., Simister, R., Gomez, L. D., & McQueen-Mason, S. J. (**2018**). Optimization of biomass pretreatments using fractional factorial experimental design. *Biotechnol Biofuels*, *11*, 206. https://doi.org/10.1186/s13068-018-1200-2

Roy, K., Kar, S., & Das, R. N. (**2015**). Chapter 10 - Other Related Techniques. In Kunal Roy, Supratik Kar, & D. Rudra Narayan (Eds.), *Understanding the Basics of QSAR for Applications in Pharmaceutical Sciences and Risk Assessment* (pp. 357-425). Academic Press. https://doi.org/10.1016/b978-0-12-801505-6.00010-7

Salleh, E. M., Zuhailawati, H., Ramakrishnan, S., & Gepreel, M. A.-H. (**2015**). A statistical prediction of density and hardness of biodegradable mechanically alloyed Mg–Zn alloy using fractional factorial design. *Journal of Alloys and Compounds*, *644*, 476-484. https://doi.org/10.1016/j.jallcom.2015.04.090

Sarbon, N. M., Badii, F., & Howell, N. K. (**2018**). Purification and characterization of antioxidative peptides derived from chicken skin gelatin hydrolysate. *Food Hydrocoll.*, *85*, 311-320. https://doi.org/10.1016/j.foodhyd.2018.06.048

Schonberger, N., Taylor, C., Schrader, M., Drobot, B., Matys, S., Lederer, F. L., & Pollmann, K. (**2021**). Gallium-binding peptides as a tool for the sustainable treatment of industrial waste streams. *J Hazard Mater*, *414*, 125366. https://doi.org/10.1016/j.jhazmat.2021.125366

Seidel-Morgenstern, A. (**2004**). Experimental determination of single solute and competitive adsorption isotherms. *J Chromatogr A*, *1037*(1-2), 255-272. https://doi.org/10.1016/j.chroma.2003.11.108

Sepian, A., Raihana, N., Yasin, M., & Norazwina, Z. (**2019**). Evaluation of factors for cells growth of immobilized Chlorella vulgaris via factorial design approach. *Chemical Engineering Communications*, *208*(5), 601-612. https://doi.org/10.1080/00986445.2019.1680372

Seung, H. L., & Kyung, B. S. (**2009**). Isolation of a Calcium-binding Peptide from Enzymatic Hydrolysates of Porcine Blood Plasma Protein. *J. Korean Soc. Appl. Biol. Chem*, *52*(3), 290-294. https://doi.org/doi:10.3839/jksabc.2009.051

Shamsipur, M., Esmaeili, A., & Kazem, M. (**1989**). Formation of cobalt, nickel and copper complexes with murexide in ethanol-water mixtures. *Talanta*, *36*(12), 1300-1302.

Sharma, P., Pandey, A. K., Udayan, A., & Kumar, S. (**2021**). Role of microbial community and metal-binding proteins in phytoremediation of heavy metals from industrial wastewater. *Bioresour Technol*, *326*, 124750. https://doi.org/10.1016/j.biortech.2021.124750

Shenkin, A. (**2008**). Basics in clinical nutrition: Physiological function and deficiency states of trace elements. *E Spen Eur E J Clin Nutr Metab*, *3*(6), e255-e258. https://doi.org/10.1016/j.eclnm.2008.06.003

Sierra-Lopera, L. M., & Zapata-Montoya, J. E. (**2021**). Optimization of enzymatic hydrolysis of red tilapia scales (Oreochromis sp.) to obtain bioactive peptides. *Biotechnol Rep (Amst)*, *30*, e00611. https://doi.org/10.1016/j.btre.2021.e00611

Silverstein, R. M., Webster, F. X., & Kimemble, D. (**2005**). *Spectrometric identification of organic compounds* (D. Brennan, Ed. Seventh ed.). State University of New york.

Singh, P. P., Gupta, V., & Prakash, B. (**2023**). Recent advancement in functional properties and toxicity assessment of plant-derived bioactive peptides using bioinformatic approaches. *Crit Rev Food Sci Nutr*, *63*(20), 4503-4521. https://doi.org/10.1080/10408398.2021.2002807

Sinthusamran, S., Benjakul, S., & Kishimura, H. (**2014**). Characteristics and gel properties of gelatin from skin of seabass (Lates calcarifer) as influenced by extraction conditions. *Food Chem*, *152*, 276-284. https://doi.org/10.1016/j.foodchem.2013.11.109

Smith, G. L., Reutovich, A. A., Srivastava, A. K., Reichard, R. E., Welsh, C. H., Melman, A., & Bou-Abdallah, F. (**2021**). Complexation of ferrous ions by ferrozine, 2,2'-bipyridine and 1,10-phenanthroline: Implication for the quantification of iron in biological systems. *J Inorg Biochem*, *220*, 111460. https://doi.org/10.1016/j.jinorgbio.2021.111460

Song, Y., Li, J., Tian, H., Xiang, H., Chen, S., Li, L., & Hu, X. (**2023**). Copper chelating peptides derived from tilapia (Oreochromis niloticus) skin as tyrosinase inhibitor: Biological evaluation, in silico investigation and in vivo effects. *Food Res Int*, *163*, 112307. https://doi.org/10.1016/j.foodres.2022.112307

Sun, N., Cui, P., Jin, Z., Wu, H., Wang, Y., & Lin, S. (**2017**). Contributions of molecular size, charge distribution, and specific amino acids to the iron-binding capacity of sea cucumber (Stichopus japonicus) ovum hydrolysates. *Food Chem*, *230*, 627-636. https://doi.org/10.1016/j.foodchem.2017.03.077

Sun, N., Cui, P., Li, D., Jin, Z., Zhang, S., & Lin, S. (**2017**). Formation of crystalline nanoparticles by iron binding to pentapeptide (Asp-His-Thr-Lys-Glu) from egg white hydrolysates. *Food Funct*, *8*(9), 3297-3305. https://doi.org/10.1039/c7fo00843k

Sun, N., Wu, H., Du, M., Tang, Y., Liu, H., Fu, Y., & Zhu, B. (**2016**). Food protein-derived calcium chelating peptides: A review. *Trends Food Sci Technol*, *58*, 140-148. https://doi.org/10.1016/j.tifs.2016.10.004

Sun, X., Sarteshnizi, R. A., Boachie, R. T., Okagu, O. D., Abioye, R. O., Pfeilsticker Neves, R., Ohanenye, I. C., & Udenigwe, C. C. (**2020**). Peptide-Mineral Complexes: Understanding Their Chemical Interactions, Bioavailability, and Potential Application in Mitigating Micronutrient Deficiency. *Foods*, *9*(10). https://doi.org/10.3390/foods9101402

Tacias-Pascacio, V. G., Morellon-Sterling, R., Siar, E. H., Tavano, O., Berenguer-Murcia, A., & Fernandez-Lafuente, R. (**2020**). Use of Alcalase in the production of bioactive peptides: A review. *Int J Biol Macromol*, *165*(Pt B), 2143-2196. https://doi.org/10.1016/j.ijbiomac.2020.10.060

Tan, Y., & Chang, S. K. C. (**2018**). Isolation and characterization of collagen extracted from channel catfish (Ictalurus punctatus) skin. *Food Chem*, *242*, 147-155. https://doi.org/10.1016/j.foodchem.2017.09.013

Tang, X., Wang, P.-Y., & Buchter, G. (**2018**). Ion-Selective Electrodes for Detection of Lead (II) in Drinking Water: A Mini-Review. *Environments*, *5*(9), 95. https://doi.org/10.3390/environments5090095

Thuy, L. T. M., Okazaki, E., & Osako, K. (**2014**). Isolation and characterization of acid-soluble collagen from the scales of marine fishes from Japan and Vietnam. *Food Chem*, *149*, 264-270. https://doi.org/10.1016/j.foodchem.2013.10.094

Timon, M. L., Andres, A. I., Otte, J., & Petron, M. J. (**2019**). Antioxidant peptides (<3 kDa) identified on hard cow milk cheese with rennet from different origin. *Food Res Int*, *120*, 643-649. https://doi.org/10.1016/j.foodres.2018.11.019

Tito, A., Carola, A., Bimonte, M., Barbulova, A., Arciello, S., de Laurentiis, F., Monoli, I., Hill, J., Gibertoni, S., Colucci, G., & Apone, F. (**2011**). A tomato stem cell extract, containing antioxidant compounds and metal chelating factors, protects skin cells from heavy metal-induced damages. *Int J Cosmet Sci*, *33*(6), 543-552. https://doi.org/10.1111/j.1468-2494.2011.00668.x

Tobin, D. J. (**2006**). Biochemistry of human skin--our brain on the outside. *Chem Soc Rev*, *35*(1), 52-67. https://doi.org/10.1039/b505793k

Tok, K., Moulahoum, H., Kocadag Kocazorbaz, E., & Zihnioglu, F. (**2020**). Bioactive peptides with multiple activities extracted from Barley (Hordeum vulgare L.) grain protein hydrolysates: Biochemical analysis and computational identification. *J. Food Process. Preserv.*, *45*(1), e15024. https://doi.org/10.1111/jfpp.15024

Torres-Fuentes, C., Alaiz, M., & Vioque, J. (**2011**). Affinity purification and characterisation of chelating peptides from chickpea protein hydrolysates. *Food Chem*, *129*(2), 485-490. https://doi.org/10.1016/j.foodchem.2011.04.103

Tu, M., Cheng, S., Lu, W., & Du, M. (**2018**). Advancement and prospects of bioinformatics analysis for studying bioactive peptides from food-derived protein: Sequence, structure, and functions. *Trends Analyt Chem*, *105*, 7-17. https://doi.org/10.1016/j.trac.2018.04.005

Tu, Z. C., Huang, T., Wang, H., Sha, X. M., Shi, Y., Huang, X. Q., Man, Z. Z., & Li, D. J. (**2015**). Physico-chemical properties of gelatin from bighead carp (Hypophthalmichthys nobilis) scales by ultrasound-assisted extraction. *J Food Sci Technol*, *52*(4), 2166-2174. https://doi.org/10.1007/s13197-013-1239-9

Udechukwu, M. C., Collins, S. A., & Udenigwe, C. C. (**2016**). Prospects of enhancing dietary zinc bioavailability with food-derived zinc-chelating peptides. *Food Funct*, *7*(10), 4137-4144. https://doi.org/10.1039/c6fo00706f

Udechukwu, M. C., Dang, C., & Udenigwe, C. C. (**2021**). Identification of zinc-binding peptides in ADAM17-inhibiting whey protein hydrolysates using IMAC-Zn2+ coupled with shotgun peptidomics. *FPPN*, *3*(1), 3:5. https://doi.org/10.1186/s43014-020-00048-4

Udechukwu, M. C., Downey, B., & Udenigwe, C. C. (**2018**). Influence of structural and surface properties of whey-derived peptides on zinc-chelating capacity, and in vitro gastric stability and bioaccessibility of the zinc-peptide complexes. *Food Chem*, *240*, 1227-1232. https://doi.org/10.1016/j.foodchem.2017.08.063

Udechukwu, M. C., Tsopmo, A., Mawhinney, H., He, R., Kienesberger, P. C., & Udenigwe, C. C. (**2017**). Inhibition of ADAM17/TACE activity by zinc-chelating rye secalin-derived tripeptides and analogues. *RSC Adv.*, *7*(42), 26361-26369. https://doi.org/10.1039/c6ra26678a

Udenigwe, C. C., & Aluko, R. E. (**2012**). Food protein-derived bioactive peptides: production, processing, and potential health benefits. *J Food Sci*, *77*(1), R11-24. https://doi.org/10.1111/j.1750-3841.2011.02455.x

Upasen, S., Naeramitmarnsuk, K., Antonio, C., Roces, S., Morillas, H., & Wattanachai, P. (**2019**). Acid-Pepsin Soluble Collagen from Saltwater and Freshwater Fish Scales. *Engineering Journal*, *23*(5), 183-195. https://doi.org/10.4186/ej.2019.23.5.183

Valko, M., Rhodes, C. J., Moncol, J., Izakovic, M., & Mazur, M. (**2006**). Free radicals, metals and antioxidants in oxidative stress-induced cancer. *Chem Biol Interact*, *160*(1), 1-40. https://doi.org/10.1016/j.cbi.2005.12.009

Viji, P., Phannendra, T. S., Jesmi, D., Madhusudana Rao, B., Dhiju Das, P. H., & George, N. (**2019**). Functional and Antioxidant Properties of Gelatin Hydrolysates Prepared from Skin and Scale of Sole Fish. *Journal of Aquatic Food Product Technology*, *28*(10), 976-986. https://doi.org/10.1080/10498850.2019.1672845

Villamil, O., Vaquiro, H., & Solanilla, J. F. (**2017**). Fish viscera protein hydrolysates: Production, potential applications and functional and bioactive properties. *Food Chem*, *224*, 160-171. https://doi.org/10.1016/j.foodchem.2016.12.057

Vo, T. D. L., & Pham, K. T. (**2020**). Copper-chelating peptide from salmon by-product proteolysate. *Int. J. Food Eng.*, *16*(4). https://doi.org/10.1515/ijfe-2019-0280

Vo, T. D. L., Pham, K. T., Le, V. M. V., Lam, H. H., Huynh, O. N., & Vo, B. C. (**2020**). Evaluation of iron-binding capacity, amino acid composition, functional properties of Acetes japonicus proteolysate and identification of iron-binding peptides. *Process Biochem*, *91*, 374-386. https://doi.org/10.1016/j.procbio.2020.01.007

Walters, M. E., Esfandi, R., & Tsopmo, A. (**2018**). Potential of Food Hydrolyzed Proteins and Peptides to Chelate Iron or Calcium and Enhance their Absorption. *Foods*, *7*(10). https://doi.org/10.3390/foods7100172

Wang, C., Li, B., & Ao, J. (**2012**). Separation and identification of zinc-chelating peptides from sesame protein hydrolysate using IMAC-Zn(2)(+) and LC-MS/MS. *Food Chem*, *134*(2), 1231-1238. https://doi.org/10.1016/j.foodchem.2012.02.204

Wang, C., Wang, C., Li, B., & Li, H. (**2014**). Zn(II) chelating with peptides found in sesame protein hydrolysates: identification of the binding sites of complexes. *Food Chem*, *165*, 594-602. https://doi.org/10.1016/j.foodchem.2014.05.146

Wang, J., Yin, T., Xiao, X., He, D., Xue, Z., Jiang, X., & Wang, Y. (**2018**). StraPep: a structure database of bioactive peptides. *Database (Oxford)*, *2018*, 1-7. https://doi.org/10.1093/database/bay038

Wang, J., Zhang, Y., Jiang, H., Cai, Y., & Qian, X. (**2006**). Phosphopeptide detection using automated online IMAC-capillary LC-ESI-MS/MS. *Proteomics*, *6*(2), 404-411. https://doi.org/10.1002/pmic.200500223

Wang, L., Ding, Y., Zhang, X., Li, Y., Wang, R., Luo, X., Li, Y., Li, J., & Chen, Z. (**2018**). Isolation of a novel calcium-binding peptide from wheat germ protein hydrolysates and the prediction for its mechanism of combination. *Food Chem*, *239*, 416-426. https://doi.org/10.1016/j.foodchem.2017.06.090

Wang, L., Li, T., Du, Y., Chen, C., Li, B., Zhou, M., & Dong, S. (**2010**). Au NPs-enhanced surface plasmon resonance for sensitive detection of mercury(II) ions. *Biosens. Bioelectron.*, *25*(12), 2622-2626. https://doi.org/10.1016/j.bios.2010.04.027

Wang, W. Y., Zhao, Y. Q., Zhao, G. X., Chi, C. F., & Wang, B. (**2020**). Antioxidant Peptides from Collagen Hydrolysate of Redlip Croaker (Pseudosciaena polyactis) Scales: Preparation, Characterization, and Cytoprotective Effects on H(2)O(2)-Damaged HepG2 Cells. *Mar Drugs*, *18*(3). https://doi.org/10.3390/md18030156

Wang, X., & Zhou, F. (**2018**). Dual-Valve and Counter-Flow Surface Plasmon Resonance. *Anal Chem*, *90*(8), 4972-4977. https://doi.org/10.1021/acs.analchem.8b00277

Wang, X., Zhou, J., Tong, P. S., & Mao, X. Y. (**2011**). Zinc-binding capacity of yak casein hydrolysate and the zinc-releasing characteristics of casein hydrolysate-zinc complexes. *J Dairy Sci*, *94*(6), 2731-2740. https://doi.org/10.3168/jds.2010-3900

Wang, Y. Y., Wang, C. Y., Wang, S. T., Li, Y. Q., Mo, H. Z., & He, J. X. (**2021**). Physicochemical properties and antioxidant activities of tree peony (Paeonia suffruticosa Andr.) seed protein hydrolysates obtained with different proteases. *Food Chem*, *345*, 128765. https://doi.org/10.1016/j.foodchem.2020.128765

Wang, Z., Cheng, S., Wu, D., Xu, Z., Xu, S., Chen, H., & Du, M. (**2021**). Hydrophobic peptides from oyster protein hydrolysates show better zinc-chelating ability. *Food Biosci.*, *41*. https://doi.org/10.1016/j.fbio.2021.100985

Wangtueai, S., & Noomhorm, A. (**2009**). Processing optimization and characterization of gelatin from lizardfish (Saurida spp.) scales. *LWT - Food Science and Technology*, *42*(4), 825-834. https://doi.org/10.1016/j.lwt.2008.11.014

Wen, C., Zhang, J., Zhang, H., Duan, Y., & Ma, H. (**2020**). Plant protein-derived antioxidant peptides: Isolation, identification, mechanism of action and application in food systems: A review. *Trends Food Sci Technol*, *105*, 308-322. https://doi.org/10.1016/j.tifs.2020.09.019

Weng, W., & Wu, F. (**2015**). Water resistance and mechanical property improvement of tilapia (Tilapia zillii) scale gelatin films by dehydrated thermal treatment. *J Food Sci Technol*, *52*(6), 3358-3366. https://doi.org/10.1007/s13197-014-1401-z

Wu, C.-M., & Lin, L.-Y. (**2005**). Utilization of albumin-based sensor chips for the detection of metal content and characterization of metal–protein interaction by surface plasmon resonance. *Sens. Actuators B Chem.*, *110*(2), 231-238. https://doi.org/10.1016/j.snb.2005.01.047

Wu, W., Li, B., Hou, H., Zhang, H., & Zhao, X. (**2017**). Identification of iron-chelating peptides from Pacific cod skin gelatin and the possible binding mode. *J. Funct. Foods*, *35*, 418-427. https://doi.org/10.1016/j.jff.2017.06.013

Wu, W., Yang, Y., Sun, N., Bao, Z., & Lin, S. (**2020**). Food protein-derived iron-chelating peptides: The binding mode and promotive effects of iron bioavailability. *Food Res Int*, *131*, 108976. https://doi.org/10.1016/j.foodres.2020.108976

Xie, N., Huang, J., Li, B., Cheng, J., Wang, Z., Yin, J., & Yan, X. (**2015**). Affinity purification and characterisation of zinc chelating peptides from rapeseed protein hydrolysates:

possible contribution of characteristic amino acid residues. *Food Chem*, *173*, 210-217. https://doi.org/10.1016/j.foodchem.2014.10.030

Xue, Y., Liu, H., Chen, S., Dichtl, N., Dai, X., & Li, N. (**2015**). Effects of thermal hydrolysis on organic matter solubilization and anaerobic digestion of high solid sludge. *Chemical Engineering Journal*, *264*, 174-180. https://doi.org/10.1016/j.cej.2014.11.005

Yadav, P., & Zelder, F. (**2021**). Detection of glyphosate with a copper(II)-pyrocatechol violet based GlyPKit. *Anal Methods*, *13*(38), 4354-4360. https://doi.org/10.1039/d1ay01168e

Yiannikouris, A., Connolly, C., Power, R., & Lobinski, R. (**2009**). Characterization of metal-peptide complexes in feed supplements of essential trace elements. *Metallomics*, *1*(3), 235-248. https://doi.org/10.1039/b901406c

Zeng, Y. B., Yang, N., & Sun, H. (**2011**). Metal-binding properties of an Hpn-like histidine-rich protein. *Chemistry*, *17*(21), 5852-5860. https://doi.org/10.1002/chem.201100279

Zhang, F., Qu, J., Thakur, K., Zhang, J. G., Mocan, A., & Wei, Z. J. (**2019**). Purification and identification of an antioxidative peptide from peony (Paeonia suffruticosa Andr.) seed dreg. *Food Chem*, *285*, 266-274. https://doi.org/10.1016/j.foodchem.2019.01.168

Zhang, J. F., Zhou, Y., Yoon, J., & Kim, J. S. (**2011**). Recent progress in fluorescent and colorimetric chemosensors for detection of precious metal ions (silver, gold and platinum ions). *Chem Soc Rev*, *40*(7), 3416-3429. https://doi.org/10.1039/c1cs15028f

Zhang, K., Li, J., Hou, H., Zhang, H., & Li, B. (**2019**). Purification and characterization of a novel calcium-biding decapeptide from Pacific cod (Gadus Macrocephalus) bone: Molecular properties and calcium chelating modes. *J. Funct. Foods*, *52*, 670-679. https://doi.org/10.1016/j.jff.2018.11.042

Zhang, M.-n., Huang, G.-r., & Jiang, J.-x. (**2012**). Effects of Chemical Modification and Molecular Weight Distribution on Iron Binding Ability of Phytate-Removal Soybean Protein Isolate Hydrolysate. *Adv J Food Sci Technol*, *4*(2), 78-83.

Zhang, T., Sun, R., Ding, M., Li, L., Tao, N., Wang, X., & Zhong, J. (**2020**). Commercial cold-water fish skin gelatin and bovine bone gelatin: Structural, functional, and emulsion stability differences. *Lwt*, *125*. https://doi.org/10.1016/j.lwt.2020.109207

Zhang, X., Jia, Q., Li, M., Liu, H., Wang, Q., Wu, Y., Niu, L., & Liu, Z. (**2021**). Isolation of a novel calcium-binding peptide from phosvitin hydrolysates and the study of its calcium

chelation mechanism. *Food Res Int*, *141*, 110169. https://doi.org/10.1016/j.foodres.2021.110169

Zhang, Y., Ding, X., & Li, M. (**2021**). Preparation, characterization and in vitro stability of iron-chelating peptides from mung beans. *Food Chem*, *349*, 129101. https://doi.org/10.1016/j.foodchem.2021.129101

Zhang, Y., Tu, D., Shen, Q., & Dai, Z. (**2019**). Fish Scale Valorization by Hydrothermal Pretreatment Followed by Enzymatic Hydrolysis for Gelatin Hydrolysate Production. *Molecules*, *24*(16). https://doi.org/10.3390/molecules24162998

Zhao, L., Huang, S., Cai, X., Hong, J., & Wang, S. (**2014**). A specific peptide with calcium chelating capacity isolated from whey protein hydrolysate. *J. Funct. Foods*, *10*, 46-53. https://doi.org/10.1016/j.jff.2014.05.013

Zhao, Q., Xiong, H., Selomulya, C., Chen, X. D., Zhong, H., Wang, S., Sun, W., & Zhou, Q. (**2012**). Enzymatic hydrolysis of rice dreg protein: effects of enzyme type on the functional properties and antioxidant activities of recovered proteins. *Food Chem*, *134*(3), 1360-1367. https://doi.org/10.1016/j.foodchem.2012.03.033

Zhao, X., Zhang, X., & Liu, D. (**2021**). Collagen peptides and the related synthetic peptides: A review on improving skin health. *J. Funct. Foods*, *86*, 104680. https://doi.org/10.1016/j.jff.2021.104680

Zheng, Y., Guo, M., Cheng, C., Li, J., Li, Y., Hou, Z., & Ai, Y. (**2023**). Structural and physicochemical characteristics, stability, toxicity and antioxidant activity of peptide-zinc chelate from coconut cake globulin hydrolysates. *Lwt*, *173*. https://doi.org/10.1016/j.lwt.2022.114367

Zhou, J., Qi, Q., Wang, C., Qian, Y., Liu, G., Wang, Y., & Fu, L. (**2019**). Surface plasmon resonance (SPR) biosensors for food allergen detection in food matrices. *Biosens Bioelectron*, *142*, 111449. https://doi.org/10.1016/j.bios.2019.111449

Zhou, J., Wang, X., Ai, T., Cheng, X., Guo, H. Y., Teng, G. X., & Mao, X. Y. (**2012**). Preparation and characterization of beta-lactoglobulin hydrolysate-iron complexes. *J Dairy Sci*, *95*(8), 4230-4236. https://doi.org/10.3168/jds.2011-5282

Zhu, K.-X., Wang, X.-P., & Guo, X.-N. (**2015**). Isolation and characterization of zinc-chelating peptides from wheat germ protein hydrolysates. *J. Funct. Foods*, *12*, 23-32. https://doi.org/10.1016/j.jff.2014.10.030

Zidane, F., Mateos, A., Cakir-Kiefer, C., Miclo, L., Rahuel-Clermont, S., Girardet, J. M., & Corbier, C. (**2012**). Binding of divalent metal ions to 1-25 beta-caseinophosphopeptide: an isothermal titration calorimetry study. *Food Chem*, *132*(1), 391-398. https://doi.org/10.1016/j.foodchem.2011.11.006

Zoroddu, M. A., Aaseth, J., Crisponi, G., Medici, S., Peana, M., & Nurchi, V. M. (**2019**). The essential metals for humans: a brief overview. *J Inorg Biochem*, *195*, 120-129. https://doi.org/10.1016/j.jinorgbio.2019.03.013

Appendices

Appendix 2.1. The employed design (FFD 2^{4-1}) fits a first-order polynomial model (Sepian et al., 2019) (Equation. (1)).

$$Y = \beta_0 + \sum_{i=1}^{n} \beta_i X_i + \sum_{1<i<j}^{n} \beta_{ij} X_i + \varepsilon \quad (1)$$

Where: Y is the predicted response (CPC, FAG or PEY), X_i are the uncoded values of the factors (A, B, C, D), β_0 is a constant, β_i are the coefficients of the main effects for each factor, β_{ij} are the coefficients of the effect of the interactions, and ε is the error.

For each investigated response Y, a statistical model was obtained, whose adequacy was assessed using the coefficient of correlation (R^2), the adjusted R^2, the lack of fit, and adequate precision (Adeq precision). This approach enabled to better understand how the change in the studied factor levels does affect each response Y.

Appendix 2.2. Steps carried out in rheology experiments with their respective conditions

Number	Analysis	Experimental condition
I	Time sweep	Constant shearing strain: 0.1 %
		Angular frequency: 1 rad.s^{-1}
		Time: 15 min
		Temperature: 60 °C
II	Temperature sweep	Temperature range: 60 °C to 10 °C
		Ramp: 0.5 °C/min
		Strain amplitude: 0.1 %
		Angular frequency: 1 rad.s^{-1}
III	Time sweep	Constant shearing strain: 0.1 %
		Angular frequency: 1 rad.s^{-1}
		Time: 60 min
		Temperature: 10 °C
IV	Temperature sweep	Temperature range: 10 °C to 60 °C
		Ramp: 0.5 °C/min
		Strain amplitude: 0.1 %
		Angular frequency: 1 rad.s^{-1}
V	Temperature sweep	Temperature range: 60 °C to 10 °C
		Ramp: 0.5 °C/min
		Strain amplitude: 0.1 %
		Angular frequency: 1 rad.s^{-1}
VI	Time sweep	Constant shearing strain: 0.1 %
		Angular frequency: 1 rad.s^{-1}
		Time: 60 min
		Temperature: 10 °C
VII	Frequency sweep	Constant shearing strain: 0.1 %
		Frequency range: 0.1-100 rad.s^{-1}

Note: steps I, II and III are preconditioning steps to ensure reliability between samples.

Appendix 2.3. Pareto charts for CPC (A), FAG content (B) and PEY (C). A: Solvent-to-solid ratio; B: extraction time; C: temperature; D: ultrasound time; FAG: free amino groups; PEY: protein extraction yield. CPC: crude protein content. Orange bars: positive effects. Blue bars: negative effects. Higher bars: higher impact on the response

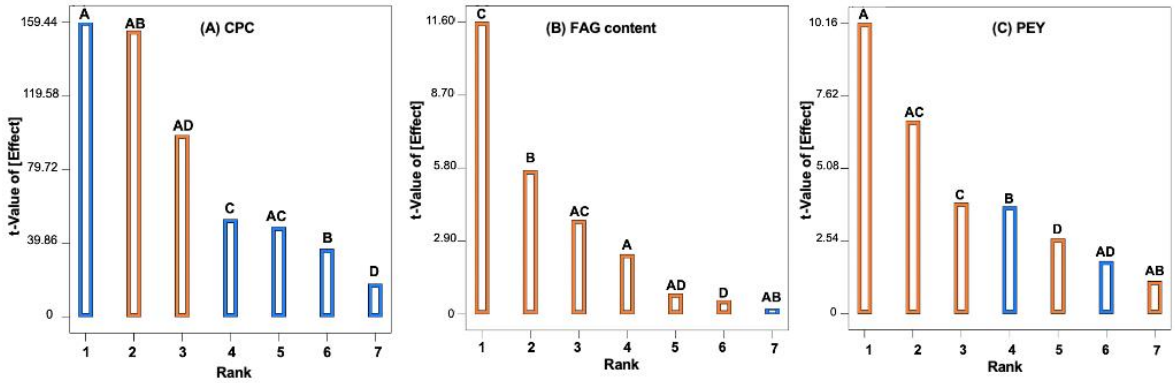

In a Pareto chart, individual values of each effect are plotted in descending order by bars; as observed, an order of priorities is assigned with positive (increasing levels of factor, response increases) and negative effects (increasing levels of factor, response decreases) on responses (Gutierrez Pulido & De Vara Salazar, 2008).

The Pareto charts were plotted for the crude protein content. From Pareto charts, the investigated factors show both positive (orange) and negative (blue) effects on the studied responses. The Pareto chart plotted for the CPC response evidences a positive effect of the interactions solvent-to-solid ratio with extraction time (AB) and the ultrasound time (AD). On the other hand, a negative effect is observed for the solvent-to-solid ratio (A), temperature (C), their interaction (AC), the extraction time (B) and the ultrasound time (D).

Concerning the FAG response, the Pareto chart evidences that the four single factors (solvent-to-solid ratio, extraction time, temperature and ultrasound time) in addition to the two interaction (solvent-to-solid ratio with temperature (AC) and solvent-to-solid ratio with ultrasound time (AD)) show a positive effect. The extraction temperature (C) and time (B) particularly improve the release of a high content of amino groups. Indeed, this latter variable (C) is positively and directly correlated to the degree of hydrolysis of Tilapia scales collagen into gelatin.

According to the Pareto chart, the PEY response is positively affected by the solvent-to-solid ratio (A, 54 %), the interaction of solvent-to-solid ratio with temperature (AC, 23.7 %), the temperature (C, 7.9 %), the ultrasound time (D, 3.6 %), and the interaction solvent-to-solid ratio with extraction time (AB, 0.7 %). On the contrary, the extraction time (B, 7.3 %), and the interactions solvent-to-solid ratio with ultrasound time (AD, 1.7 %) negatively affect the protein extraction yield.

Appendix 2.4. ANOVA analysis of fractional experimental design of gelatin protein extraction on the three investigated responses.

Factor	Response variable					
	CPC		FAG content		PEY	
	***p*-value**	**Coefficient**	***p*-value**	**Coefficient**	***p*-value**	**Coefficient**
Model	**0.02**	--	**2.50×10^{-5}**	--	**1.36×10^{-3}**	--
Constant	--	97.07	--	0.26	--	40.12
A	**0.02**	-0.65	**0.02**	4.47×10^{-3}	**5.16×10^{-4}**	3.75
B	--	--	**3.02×10^{-4}**	0.01	0.05	-1.38
C	0.31	-0.22	**5.21×10^{-6}**	0.02	**0.04**	1.43
D	--	--	--	--	--	--
AB	**0.02**	0.63	--	--	--	--
AC	--	--	**2.82×10^{-3}**	7.04×10^{-3}	**4.20×10^{-3}**	2.49
AD	0.09	0.40	--	--	--	--
Lack of fit	2.88E-04	--	0.81	--	0.27	--
Pure error	2.67×10^{-4}		5.72×10^{-5}		2.18	
R^2	**0.82**		**0.98**		**0.93**	
Adjusted R^2	0.69		0.97		0.88	
Adeq Precision	10.14		28.80		14.38	

A: Solvent-to solid ratio; B: Extraction time; C: Temperature; D: Ultrasound time. CPC: Crude protein content. FAG: Free amino group. PEY: Protein extraction yield. Adeq precision: Adequate precision.

ANOVA analysis

From pareto chart results, we focused our attention on single factors and two-factor interactions, which have the greatest impact on responses, to determine the statistically significant effects carried out by ANOVA. Thus, whatever positive or negative, effects with the three lowest contribution percentages for each investigated response (last three ones shown in Data S3A, B, and C) are neglected similar to Sepian et al., (2019). Main results of the ANOVA are shown in Table above.

Appendix 2.5. Multiple regression modelling

The multiple regression modelling enables to plot the linear relationship between the factors (A, B, C and D) and their interactions with the investigated responses (CPC, FAG, and PEY). It allows to predict responses outcome given the level of factors.

Concerning the lack of fit test, the ANOVA Table (Appendix 2.4) shows that for FAG content and PEY, this value is non-significant (*p-value* ≥ 0.05), confirming a high accuracy and reliability of these models for prediction of responses. Inversely, for the crude protein content, lack of fit is significant (*p-value* < 0.05), suggesting that this mathematical model does not fit experimental values with strong prediction, corroborating the results found with R^2 coefficients.

Besides, the adequate precision is used as secondary check. This signal-to-noise ratio compares the range of the predicted values to the average prediction error at the experimental runs. For the three models (CPC, FAG, and PEY), adequate precisions are higher than 4, satisfying the requirement in terms of signal-to- noise ratio (Portilha-Cunha et al., 2020). Thus, these models can be used to navigate within the design space.

Table of Appendix 2.5. Meaning and interpretation of statistical parameters used in the analysis of experimental design.

Statistical parameter	**Abreviation**	**Meaning**	**Interpretation**
Regression coefficient	R^2	Amount of variation in the data explained by the model	> 0.90
Adjusted regression coefficient	Adjusted R^2	Modified version of R-squared that adjusts for predictors that are not significant in a regression mode	> 0.90 and similar to R^2
Lack of fit	LOF	Determines if there is any other relationship that fits the model better than what is predicted and included in the analysis	*p* value ≥ 0.05, lack of fit no significant. Model fits the data well.
Adequate precision	Adeq precision	Signal-to-noise ratio, compares the range of the predicted values at the experimental runs to the average prediction error	Ratio > 4. Model can be reliable.

Appendix 2.6. CD spectra of gelatin extracts prepared using different extraction conditions.

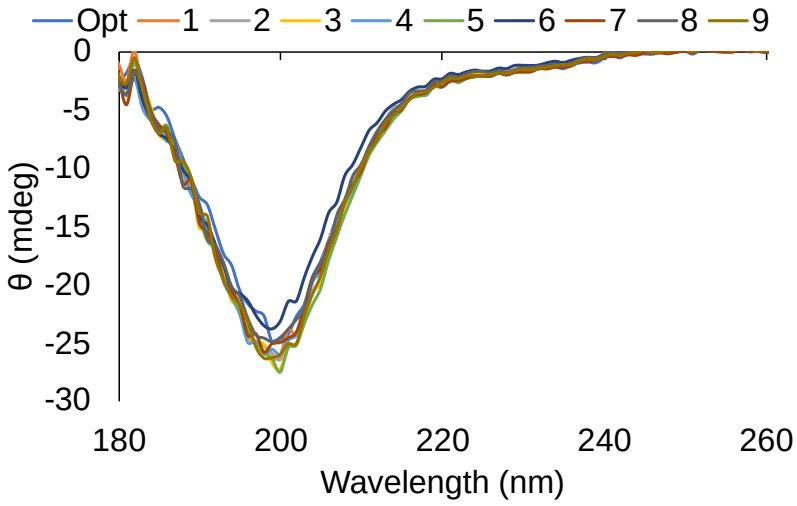

Appendix 2.7. Rheological properties of the most interesting gelatin extracts (Run 1, 8, 9 and optimal run). (a, c, e, g) Changes in the elastic (G') and loss (G'') moduli during cooling (50 to 10 °C) for run 1, run 8, run 9 and optimal one, respectively. (b, d, f, h) Changes in the elastic (G') and loss (G'') moduli during heating (10 to 50 °C) for run 1, run 9, optimal run and run 8, respectively (I and j).

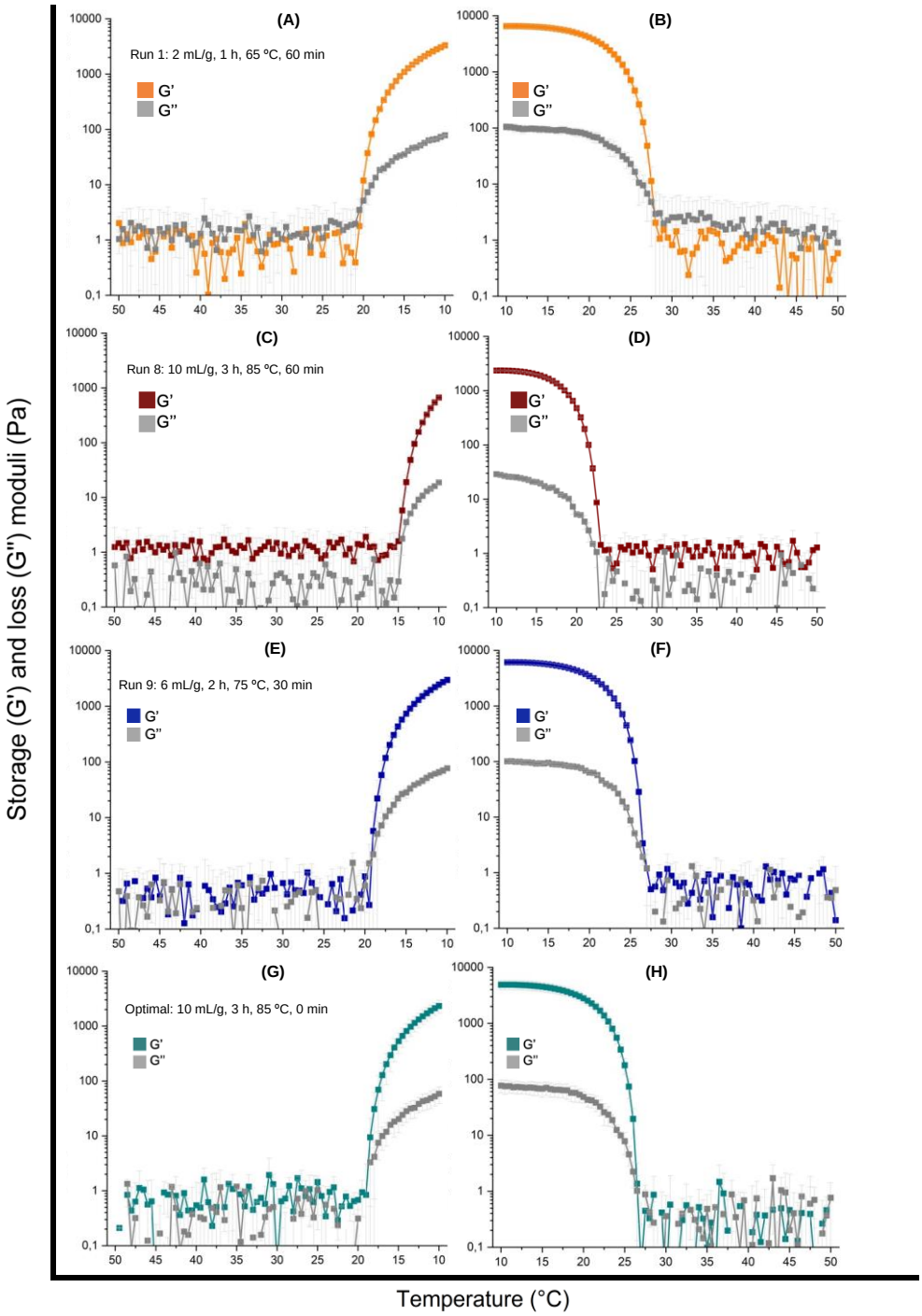

Appendix 2.8. Changes in the phase angle during cooling (50-10 °C) and heating (10-50 °C), respectively.

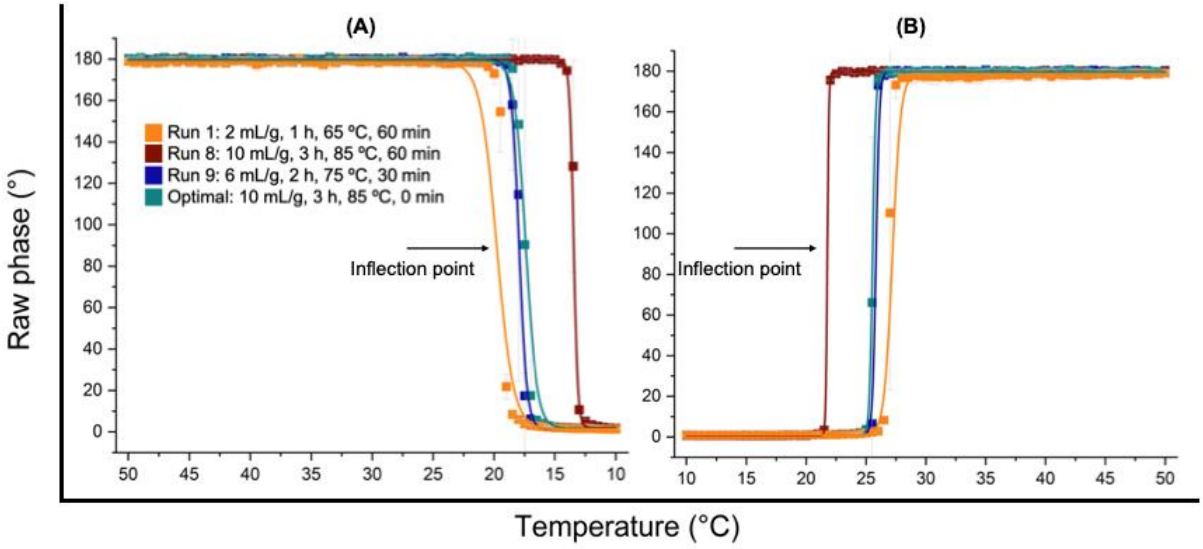

Appendix 3.1. CAS numbers of chemicals and reagents.

Reagent	CAS Number
37% hydrochloric acid	7647010
Sulfuric acid	7664939
Ammonium bicarbonate	1066337
O-Phthalaldehyde	643798
N,N-dimethyl-2-mercaptoethyl ammonium	13242449
Sodium tetraborate	1303964
Sodium dodecyl sulphate	151213
Glycine	56406
Ethylenediaminetetraacetic acid	6381926
Carnosine	305840
Ferrozine	69898459
Ferrous chloride solution	7758943
Murexide	3051090
Copper sulfate	7758998
Hexamine	100970
ABTS	3093167
Trolox®	53188071
Potassium persulfate	7727211
Potassium ferricyanide	13746662
Trichloroacetic acid	76039
Ferric chloride	7705080
Iron(III) ferrocyanide	14038438
Ascorbic acid	51817
N- [3- (2-Furyl) acryloyl] -Phe-Gly-Gly	64967391
Angiotensin converting enzyme	9015821
Alcalase®	9014011
Flavourzyme®	2327522
Tris (2-Amino-2-hydroxymethyl-propane-1,3-diol)	77861
Sodium phosphate monobasic-$NaH_2PO_4.2H_2O$	13472350
Sodium phosphate dibasic-$Na_2HPO_4.2H2O$	10028247

Appendix 3.2. Tilapia scale gelatin extraction process set up in this study.

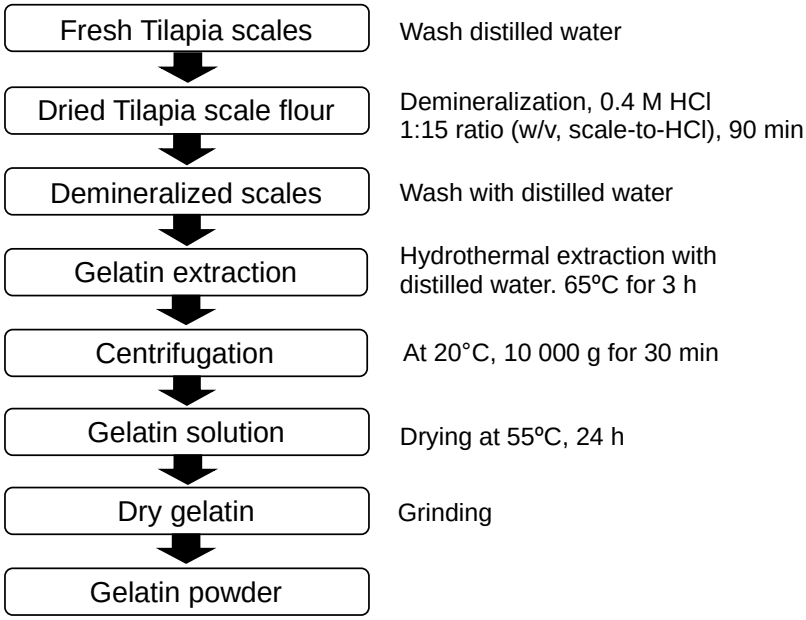

Appendix 3.3. Composition of stacking and separation gels used in SDS-PAGE experiments.

Component	Stacking gel	Separation gel
	Vol (µL)	Vol (µL)
Water	3000	3300
Tris-HCl 1.5 M pH 8.8	0	2000
Tris-HCl 0.5 M pH 6.8	384	0
40 % acrylamide/bisacrylamide 29:1	500	2500
10 % SDS	40	80
50 mg/mL Ammonium persulfate	40	80
TEMED	40	80

Appendix 3.4. Size Exclusion Chromatography

The system consisted of a column Phenomenex PolySep-GPC-P 2000 (300 x 7.8 mm - 8 µm – 200 A - separation range 100 Da – 10 kDa) protected by a guard column (35 x 7.8 mm) connected to a column Phenomenex PolySep-GPC-P 1000 (300 x 7.8 mm - 8 µm – 100 A - separation range 20 Da – 3 kDa). The five hydrolysates and ultrafiltrates (10 mg/mL) were loaded (200 µL) and eluted using an aqueous buffer containing sodium nitrate ($NaNO_3$) at 0.1 M and sodium azide at 0.2 % (w/v) at a flow rate of 0.7 mL/min at room temperature. Polyethylene Glycol (**PEG**) standard solutions (200, 600, 1000, 3000, and 8000 Da) were injected similarly for SEC calibration. The chromatograms were analyzed with ASTRA® software (Wyatt Technology, Goleta, USA).

Appendix 3.5. Amino acid composition

A 20-fold dilution in ultrapure water, samples with a final concentration of 0.05 g/L in total amino acids were injected (5 µL) on a C18 Alltima reverse phase column (150 x 2.1 mm, 5 µm; Grace/Alltech, Darmstadt, Germany) equipped with a C18 Alltima pre-column (7.5 x 2.1 mm, 5 µm) at 10°C. MS data were acquired with the Xcalibur v. 4.3 software (Thermo Scientific), and the results were normalized and reported as gram of amino acid per 100 g of sample.

Appendix 3.6. Protein data base used for peptide identification

Number	Entry	Name	Organism
1	A0A669F9X1	Collagen alpha-1(II) chain	
2	I3KK22	Collagen alpha-1(II) chain	
3	A0A669DZD5	Collagen alpha-1(II) chain	
4	I3JC78	Collagen alpha-1(II) chain	
5	A0A669BIH1	Collagen alpha-2(I) chain	
6	A0A669EAT8	Collagen alpha-2(I) chain	
7	I3JXH5	Collagen alpha-2(I) chain	
8	A0A669BST3	Collagen, type I, alpha 1b	
9	A0A669DNY6	Collagen, type I, alpha 1b	
10	A0A669BAB1	Collagen, type I, alpha 1b	
11	A0A669BRC2	Collagen, type I, alpha 1b	
12	A0A669DPF7	Collagen, type I, alpha 1a	
13	A0A669DWT0	Collagen, type I, alpha 1a	
14	A0A669BKD4	Collagen, type I, alpha 1b	
15	A0A669CCL2	Collagen, type I, alpha 1b	Oreochromis niloticus (Nile
16	I3JGN1	Collagen, type I, alpha 1a	tilapia) (Tilapia nilotica)
17	I3JMB4	Collagen, type I, alpha 1b	
18	G9M6I5	Collagen type I alpha 1	
19	G9M6I6	Collagen type I alpha 2	
20	G9M6I7	Collagen type I alpha 3	
21	A0A669CAJ8	Collagen, type I, alpha 1a	
22	A0A669EA36	Collagen, type I, alpha 1a	
23	A0A669BM68	Collagen, type I, alpha 1a	
24	A0A669D9Z5	Collagen, type I, alpha 1a	
25	A0A669BUY3	Collagen, type I, alpha 1a	
26	A0A668V4P2	Collagen, type I, alpha 2	
27	A0A668RYQ9	Collagen, type I, alpha 1a	
28	A0A668RU29	Collagen, type I, alpha 1b	
29	A0A668S2V1	Collagen, type I, alpha 1b	
30	A0A668SA92	Collagen, type I, alpha 1a	

Appendix 3.7. Parameters of database searches used for peptide identification

Parameter	Condition
Digestion mode	No enzyme and unspecific cleavage
Length	3 to 25 amino acids
Variable modification	N-terminal acetylation and methionine oxidation
Fixed modification	Cysteine carbamidomethylation
Initial precursor-ion mass tolerances	10 ppm
Mass tolerance for fragment ions	10 ppm
False discovery rate (FDR)	0.01
Include contaminants	Disabled
Match between run	Enabled
All the other parameters	Set up as default settings

Appendix 3.8. MaxQuant™ identification successfully carried out on a synthetic mixture containing 8 peptides at 1 mM: MS/MS spectra show y ions (red peak), b ions (blue peaks), and ions resulting from loss of water or ammonia of b and y ions (orange peaks). A) GHR, (B) GHRGFSGL, (C) KGHR, (D) KGHRGF, (E) GHRGF, (F) KHV, (G) RGMKGH, (H) RGMKGHR.

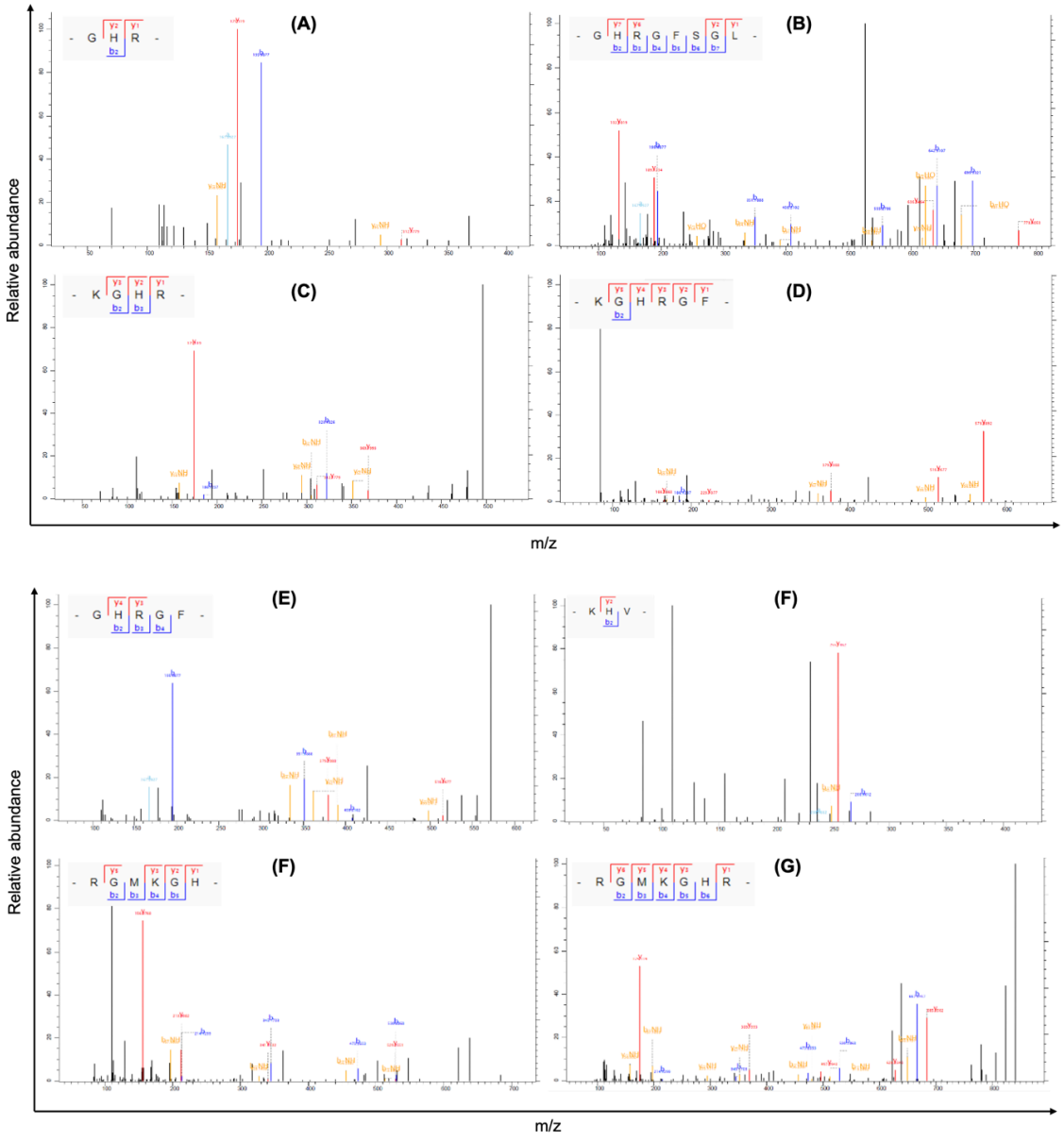

Appendix 3.9. Biofunctional properties of red Tilapia scale gelatin hydrolysates. (A) iron-chelating activity, (B) ABTS scavenging activity, (C) ACE inhibition activity.

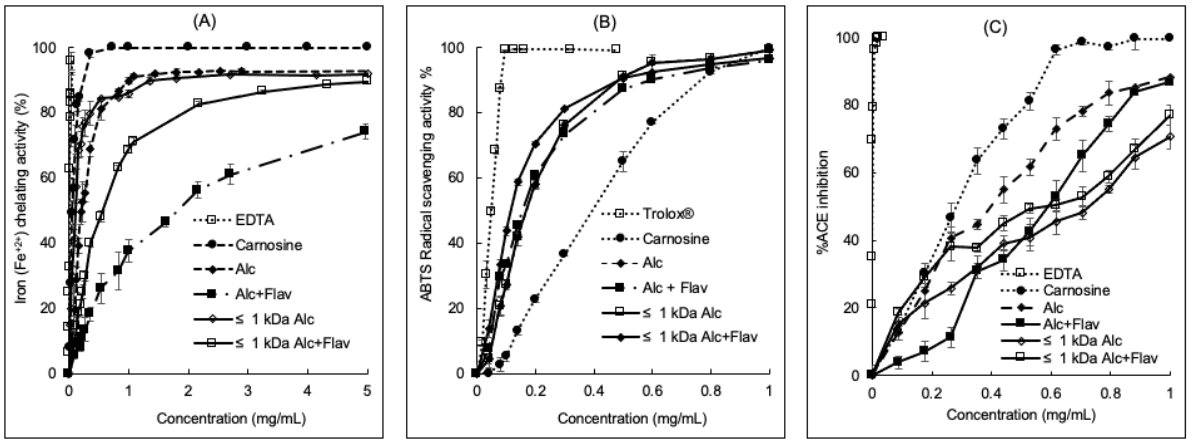

Alc: Alcalase® hydrolysate, Alc+Flav: Alcalase® followed by Flavourzyme® hydrolysate; ≤ 1 kDa Alc: 1 kDa ultrafiltrated Alcalase® hydrolysate; ≤ 1 kDa Alc + Flav: 1 kDa ultrafiltrated Alcalase® followed by Flavourzyme® hydrolysate.

Appendix 3.10. Antimicrobial activity

The antimicrobial activity was evaluated using the broth microdilution method according to the ISO 20776-1:2019 guidelines (International Organization for Standardization, 2019). Five reference strains were tested: 2 gram-positive strains (*Staphylococcus aureus* ATCC 29213, *Enterococcus faecalis* ATCC 29212) and 3 gram-negative strains (*Pseudomonas aeruginosa* ATCC 27853, *Escherichia coli* ATCC 25922, *Klebsiella pneumoniae* ATCC 700603). Fresh cultures (16-20 h) of bacteria grown at 35°C in 5 mL Mueller-Hinton Broth, Cation-Adjusted (MHB-CA, BD 212322) were used for these experiments. Briefly, bacteria were centrifugated (3000 *g*, 5 min) and washed with 0.85% sterile NaCl solution. Then, they were adjusted at a turbidimetry of 0.5 McFarland in MHB-CA, and diluted 1/100 in MHB-CA to reach 1 x 10^6 CFU/mL. Stock solutions of the gelatin hydrolysates (whole hydrolysates and ≤ 1 kDa fractions) prepared in sterile water and sodium benzoate (commercial positive control) were two-fold serial diluted in MHB-CA with concentrations ranging from 0.1 mg/mL to 25 mg/mL to in untreated, round-bottom 96 wells microplates (ref. 82.1582.001, Sarstedt, Numbrecht, Germany). An equal volume (50 µL) of bacterial inoculum was then added to 50 µL sample volume. Final sample concentration ranged then from 0.1 mg/mL to 25 mg/mL, final bacterial concentration was 0.5 x 10^6 CFU/mL for a total volume of 100 µL. Each experiment was performed in triplicate. Bacterial inoculum was checked according to the ISO guidelines. Plates were then incubated 24 h at 37°C and Minimum Inhibitory Concentrations (**MICs**) were assessed as the lowest concentration with no visible bacterial growth.

Appendix 3.11. Antimicrobial activity of sodium benzoate, whole Tilapia scale gelatin hydrolysates, and their 1 kDa fractions.

Bacteria	Samples (MIC, mg/mL)				
	S. aureus	*E.faecalis*	*P.aeruginosa*	*E. coli*	*K. pneumoniae*
Alc	>25	>25	>25	>25	>25
Alc+Flav	>25	>25	>25	>25	>25
≤ 1 kDa Alc	>25	>25	>25	>25*	>25
≤ 1 kDa Alc+Flav	>25	>25	>25	>25	>25
Sodium benzoate	>25	>25	>25	12.5	>25*

Alc: Alcalase®; Alc+Flav: Alcalase® followed by Flavourzyme®; ≤ 1 kDa Alc: ultrafiltrated Alcalase® hydrolysate; ≤1kDa Alc+Flav: ultrafiltrated Alcalase® followed by Flavourzyme® hydrolysate.

Metal ions as Fe^{2+}, Zn^{2+} and Cu^{2+} are essential for the survival and virulence of bacteria and fungi. As cofactors of many enzymes, they play an important role in protein synthesis. While forming coordination complexes with metal ions, antimicrobial peptides prevent the metal ions uptake by microorganisms, inducing the inhibition of nucleic acid biosynthesis, protein biosynthesis, protein folding, proteases, cell division and cell wall biosynthesis and eventually resulting in bacterial cell death (Łoboda et al., 2018).

Broth dilution method was used to evaluate the antimicrobial activity of the whole hydrolysates, ≤ 1 kDa hydrolysates and sodium benzoate (food preservative used as reference) against Gram-positive (*S. aureus* and *E. faecalis*) and Gram-negative (*P. aeruginosa*, *E. coli*, and *K. pneumoniae*) bacteria.

For all investigated TSG hydrolysates, no significant antimicrobial activity is observed against all the tested bacteria even at the highest concentration (MIC > 25 mg/mL), whereas sodium benzoate only presents strong antimicrobial activity against *E. coli* (MIC < 12.5 mg/mL). In contrast, other works on fish protein hydrolysates showed antimicrobial activity at lower concentration but after HPLC purification. The MIC of hydrolysates produced from skin of yellow catfish (Su, 2011) and half-fin anchovy (Song et al., 2011) was respectively determined in the range 2-64 µg/mL and 28.3-56.7 µg/mL for both Gram-positive and Gram-negative bacteria.

Although no TSG hydrolysates show 100 % of growth inhibition against the tested bacteria (prerequisite for determining the MIC), the ≤1 kDa Alc hydrolysate inhibits the *E. coli* growth by 49 % compared to growth control (bacteria growing without sample), being the only hydrolysate that presents any inhibition. Thus, antimicrobial peptides could be present at low concentration in this former ≤ 1 kDa Alc hydrolysate, and their activity could be improved after chromatographic purification.

Thus, ultrafiltration of Alc hydrolysate at 1 kDa MWCO can enhance the antimicrobial activity. Indeed, the peptides interaction with bacterial cytoplasmic membrane does depend on the peptide MW, the lower MW peptides interacting more easily than higher MW peptides (Verma et al., 2017). Similar to our findings, antimicrobial peptides produced from hydrolysates have shown better antimicrobial activity after ultrafiltration. MIC values were reported in the range from 100 to 1200 µg/mL against *S. typhimurium, E. coli and B. cereus* for small-sized peptides fraction (700-3000 Da) obtained from goat whey protein and hen egg white lysozyme (Osman et al., 2016). Contrary to our results concerning the ≤ 1 kDa Alc hydrolysate, no antimicrobial activity was observed against *E. coli* in fish protein hydrolysates (whole and 1 kDa fraction) produced from blackfin pacu and for lower concentrations (5-10 mg/mL; De Quadros et al., 2019). These latter results could be associated to the work of Klompong et al., (2010) on peptides derived from fish protein hydrolysates, used as a growth factor of different microorganisms rather than inhibiting growth.

In addition to peptide size, AA residues present in peptide play a major role in the antimicrobial activity. The main action mechanisms of antimicrobial peptides involve membrane disruption and intracellular targeting, associated with rich-cationic peptides (containing notably positively charged AA: Lys, Arg, His) and anionic peptides (containing notably negatively charged AA: Asp, Glu), respectively. In intracellular targeting mechanism, MCPs can complex metal ions (Fe^{2+}, Zn^{2+} and Cu^{2+}), which are essential for the survival of microorganisms, preventing their uptake, and thus leading to bacterial death (Lei et al., 2019). The ≤ 1 kDa Alc hydrolysate is characterized by a high Fe^{2+}-chelating activity, which could increase the antimicrobial activity of peptides in comparison to other hydrolysates as previously reported (Verma et al., 2017). Similarly to our results, Lin et al., (2013) evidenced that the antimicrobial activity of peptide obtained from hairtail protein hydrolysate was associated to the Fe^{2+}-chelating activity.

References

De Quadros, C. D. C., Lima, K. O., Bueno, C. H. L., Fogaça, F. H. d. S., Da Rocha, M., & Prentice, C. (2019). Evaluation of the Antioxidant and Antimicrobial Activity of Protein Hydrolysates and Peptide Fractions Derived from Colossoma macropomum and Their Effect on Ground Beef Lipid Oxidation. Journal of Aquatic Food Product Technology, 28(6), 677-688. https://doi.org/10.1080/10498850.2019.1628152

Klompong, V., Benjakul, S., Kantachote, D., & Shahidi, F. (2010). Use of Protein Hydrolysate from Yellow Stripe Trevally (Selaroides leptolepis) as Microbial Media. Food and Bioprocess Technology, 5(4), 1317-1327. https://doi.org/10.1007/s11947-010-0402-9

Lei, J., Sun, L., Huang, S., Zhu, C., Li, P., He, J., Mackey, V., Coy, D. H., & He, Q. (2019). The antimicrobial peptides and their potential clinical applications. American Journal of Translational Research, 11(7), 3919–3931.

Lin, H., Zhang, B., Yu, T., & Deng, S. (2013). Preparation of ferrous chelate of hairtail (Trichiurus haumela) protein hydrolysate (Fe(II)-HPH) and its antibacterial activity PIAGENG 2013: Intelligent Information, Control, and Communication Technology for Agricultural Engineering,.

Łoboda, D., Kozłowski, H., & Rowińska-Żyrek, M. (2018). Antimicrobial peptide–metal ion interactions – a potential way of activity enhancement. New Journal of Chemistry, 42(10), 7560-7568. https://doi.org/10.1039/c7nj04709f

Osman, A., Goda, H. A., Abdel-Hamid, M., Badran, S. M., & Otte, J. (2016). Antibacterial peptides generated by Alcalase hydrolysis of goat whey. LWT - Food Science and Technology, 65, 480-486. https://doi.org/10.1016/j.lwt.2015.08.043

Song, R., Wei, R., Zhang, B., & Wang, D. (2011). Optimization of the Antibacterial Activity of Half-Fin Anchovy (Setipinna taty) Hydrolysates. Food and Bioprocess Technology, 5(5), 1979-1989. https://doi.org/10.1007/s11947-010-0505-3

Su, Y. (2011). Isolation and identification of pelteobagrin, a novel antimicrobial peptide from the skin mucus of yellow catfish (Pelteobagrus fulvidraco). Comp Biochem Physiol B Biochem Mol Biol, 158(2), 149-154. https://doi.org/10.1016/j.cbpb.2010.11.002

Verma, A. K., Chatli, M. K., Kumar, P., & Mehta, N. (2017). Antioxidant and antimicrobial activity of protein hydrolysate extracted from porcine liver. The Indian Journal of Animal Sciences, 87(6). https://doi.org/10.56093/ijans.v87i6.71070

Appendix 3.12. MS Peptides sequences identified from Alc, Alc+Flav, ≤ 1 kDa Alc and ≤ 1 kDa Alc+Flav hydrolysates.

Sample	Sequence	Length	Mass (g/mol)	Intensity (x 10^5)	Score	Proteins	Entry
Alc	SGPPVPGPIGPM	12	1104.56	374.90	53.833	Collagen, type I, alpha 1b	A0A669DNY6
	GPAGPL	6	510.28	179.11	73.37	Collagen, type I, alpha 2	A0A668V4P2
	AGPQGPIGPR	10	948.51	132.46	68.081	Collagen, type I, alpha 2	A0A668V4P2
	GPVGPS	6	512.26	102.93	48.674	Collagen type I alpha 1	G9M6I5
	GGRGPEGPAGAR	12	1080.54	92.33	16.838	Collagen type I alpha 1	G9M6I5
	PGPSGDSGPGGPA	13	1051.46	77.68	10.8	Collagen alpha-1(II) chain	I3KK22
	GPSGA	5	387.18	76.30	41.193	Collagen type I alpha 1	G9M6I5
	AGPVGEPGKQ	10	938.48	64.26	24.021	Collagen type I alpha 1	G9M6I5
	GVDGAPGKDGPRGL	14	1294.66	60.07	11.025	Collagen, type I, alpha 1b	A0A669DNY6
	EGR	3	360.18	57.96	47.27	Collagen, type I, alpha 2	A0A668V4P2
	GEEGKRGPTGEIG	13	1285.63	55.39	12.873	Collagen, type I, alpha 2	A0A668V4P2
	AGPTGPAGPL	10	836.44	49.60	23.148	Collagen alpha-2(I) chain	I3JXH5
	GPRGPPGPPGSSGPQ	15	1343.66	44.44	26.121	Collagen type I alpha 1	G9M6I5
	PGR	3	328.19	39.05	9.4904	Collagen type I alpha 1	G9M6I5
	KGP	3	300.18	29.86	3.9761	Collagen alpha-1(II) chain	I3KK22
	VGPK	4	399.25	27.02	18	Collagen type I alpha 1	G9M6I5
	GGGY	4	352.14	20.49	15.834	Collagen, type I, alpha 2	A0A668V4P2
	VGR	3	330.20	14.25	3.9761	Collagen alpha-1(II) chain	I3KK22
	PGK	3	300.18	10.34	11.355	Collagen type I alpha 1	G9M6I5
	GAM	3	277.11	6.06	11.355	Collagen type I alpha 1	G9M6I5
	AGQR	4	430.23	5.58	20.123	Collagen type I alpha 1	G9M6I5
	LLA	3	315.22	4.80	3.9761	Collagen, type I, alpha 2	A0A668V4P2
Alc+Flav	GPVGMPGAR	9	840.43	192.71	50.855	Collagen alpha-2(I) chain	A0A669EAT8
	GPPVPGPIGPM	11	1017.53	182.95	53.576	Collagen, type I, alpha 1b	A0A669DNY6
	GPAGPA	6	468.23	152.98	45.108	Collagen, type I, alpha 1b	A0A669DNY6
	PSGAA	5	401.19	143.43	52.958	Collagen type I alpha 1	G9M6I5
	GPAGPL	6	510.28	132.07	58.112	Collagen alpha-2(I) chain	A0A669EAT8
	SGPPVPGPIGPM	12	1104.56	121.22	41.84	Collagen, type I, alpha 1b	A0A669DNY6
	GPSGE	5	445.18	119.11	41.193	Collagen, type I, alpha 1b	A0A669DNY6
	GPTGPR	6	583.31	105.36	48.848	Collagen, type I, alpha 1b	A0A669DNY6
	GPPGLA	6	510.28	98.63	58.112	Collagen alpha-2(I) chain	A0A669EAT8
	PGSAGPR	7	640.33	94.16	56.048	Collagen alpha-1(II) chain	I3JC78
	SGPAGPR	7	640.33	94.16	26.341	Collagen, type I, alpha 1b	A0A669DNY6
	PGAQ	4	371.18	90.68	22.701	Collagen, type I, alpha 1b	A0A669DNY6
	AGPQGPIGPR	10	948.51	79.83	61.357	Collagen alpha-2(I) chain	A0A669EAT8
	GPAGPRGPS	9	794.40	71.85	22.736	Collagen, type I, alpha 1b	A0A669DNY6
	GKTGDRGETGPA	12	1144.55	67.64	12.873	Collagen type I alpha 1	G9M6I5
	GPTGEIG	7	629.30	62.39	48.848	Collagen alpha-2(I) chain	A0A669EAT8

	GPSGLAGPA	9	725.37	59.67	28.487	Collagen alpha-2(I) chain	A0A669EAT8
	GESGDSGPK	9	832.36	58.11	17.113	Collagen, type I, alpha 1b	A0A669DNY6
	GDSGPAGPK	9	784.37	57.10	27.629	Collagen, type I, alpha 1b	A0A669DNY6
	GPQGPIGPR	9	877.48	52.62	28.487	Collagen alpha-2(I) chain	A0A669EAT8
	SGPSGPAGPA	10	796.37	52.06	28.487	Collagen, type I, alpha 1b	A0A669DNY6
	GPPGPGGSR	9	780.39	51.33	11.64	Collagen, type I, alpha 1b	A0A669DNY6
	SGPVGER	7	700.35	50.26	32.117	Collagen, type I, alpha 1b	A0A669DNY6
	GPVGN	5	442.22	47.17	33.905	Collagen type I alpha 1	G9M6I5
	GPAGPK	6	525.29	46.90	41.817	Collagen, type I, alpha 1b	A0A669DNY6
	TGM	3	307.12	45.63	30.281	Collagen type I alpha 1	G9M6I5
	SPAMPVPGPM	10	982.46	42.82	15.847	Collagen type I alpha 1	G9M6I5
	GPRGPPGPPGSSGPQ	15	1343.66	42.46	26.121	Collagen type I alpha 1	G9M6I5
	GAVGPVGPS	9	739.39	40.69	28.487	Collagen alpha-2(I) chain	A0A669EAT8
	EGR	3	360.18	37.11	25.946	Collagen alpha-2(I) chain	A0A669EAT8
	GPAGPRGPSGAA	12	993.50	31.02	9.544	Collagen type I alpha 1	G9M6I5
	AGPVGEPGKQ	10	938.48	26.35	13.906	Collagen type I alpha 1	G9M6I5
	GVDGAPGKDGPRGL	14	1294.66	26.05	9.2438	Collagen, type I, alpha 1b	A0A669DNY6
	AGPTGPAGPL	10	836.44	25.86	12.532	Collagen alpha-2(I) chain	A0A669EAT8
	VAS	3	275.15	23.86	3.9761	Collagen alpha-1(II) chain	I3JC78
	GPVGNTGPK	9	825.43	23.75	18.146	Collagen type I alpha 1	G9M6I5
	GGGY	4	352.14	21.93	25.946	Collagen alpha-2(I) chain	A0A669EAT8
	SPGFQ	5	534.24	16.19	22.116	Collagen, type I, alpha 1b	A0A669DNY6
	QPL	3	356.21	15.24	11.355	Collagen, type I, alpha 1b	A0A669DNY6
	GFM	3	353.14	13.75	11.355	Collagen type I alpha 1	G9M6I5
	GEE	3	333.12	11.59	3.9761	Collagen, type I, alpha 1b	A0A669DNY6
	SGPAGPA	7	555.27	10.38	12.157	Collagen, type I, alpha 1b	A0A669DNY6
	TGF	3	323.15	5.17	11.355	Collagen, type I, alpha 1b	A0A669DNY6
	KGSP	4	387.21	4.60	12.162	Collagen type I alpha 1	G9M6I5
	VAM	3	319.16	4.55	3.9761	Collagen alpha-1(II) chain	I3JC78
≤ 1 kDa Alc	GPA	3	243.12	1905.90	36.83	Collagen, type I, alpha 1b	A0A668S2V1
	GPAGPR	6	553.30	626.41	77.20	Collagen, type I, alpha 1b	A0A668S2V1
	PGAPGR	6	553.30	626.41	34.99	Collagen alpha-1(II) chain	I3KK22
	SGAP	4	330.15	544.13	33.73	Collagen type I alpha 1	G9M6I5
	SGPA	4	330.15	544.13	13.81	Collagen, type I, alpha 1b	A0A668S2V1
	QSP	3	330.15	544.13	3.26	Collagen, type I, alpha 1b	A0A668S2V1
	GPVGN	5	442.22	354.11	33.91	Collagen type I alpha 1	G9M6I5
	GPAGPL	6	510.28	335.71	58.11	Collagen alpha-2(I) chain	I3JXH5
	PGR	3	328.19	326.22	30.28	Collagen, type I, alpha 1b	A0A668S2V1
	VGPA	4	342.19	321.19	38.72	Collagen type I alpha 1	G9M6I5
	GAR	3	302.17	303.95	55.25	Collagen, type I, alpha 1b	A0A668S2V1
	AGPA	4	314.16	250.10	38.72	Collagen, type I, alpha 1b	A0A668S2V1
	GFM	3	353.14	192.41	11.36	Collagen type I alpha 1	G9M6I5
	VGPS	4	358.19	178.22	49.86	Collagen, type I, alpha 1b	A0A669BKD4
	VGSP	4	358.19	178.22	41.72	Collagen, type I, alpha 1b	A0A669BKD4
	GPAGPA	6	468.23	170.33	45.11	Collagen, type I, alpha 1b	A0A668S2V1

	GLAGPA	6	484.26	155.85	33.91	Collagen alpha-2(I) chain	I3JXH5
	TGAP	4	344.17	144.75	33.73	Collagen, type I, alpha 1b	A0A668S2V1
	SGPAGPR	7	640.33	142.39	59.80	Collagen, type I, alpha 1b	A0A668S2V1
	MGPA	4	374.16	139.05	38.72	Collagen, type I, alpha 1b	A0A668S2V1
	AGPQGPIGPR	10	948.51	138.94	61.36	Collagen alpha-2(I) chain	I3JXH5
	GPPGLA	6	510.28	133.90	58.11	Collagen type I alpha 1	G9M6I5
	GPVGPS	6	512.26	131.66	45.01	Collagen type I alpha 1	G9M6I5
	GPTGPR	6	583.31	116.38	45.01	Collagen, type I, alpha 1b	A0A668S2V1
	RGF	3	378.20	110.44	30.28	Collagen, type I, alpha 1b	A0A668S2V1
	AGPQ	4	371.18	108.93	64.61	Collagen, type I, alpha 1b	A0A669DNY6
	QPGA	4	371.18	108.93	29.93	Collagen, type I, alpha 1b	A0A669BKD4
	GPSGPQ	6	541.25	108.76	71.96	Collagen type I alpha 1	G9M6I5
	GPT	3	273.13	108.33	30.28	Collagen, type I, alpha 1b	A0A668S2V1
	PGPGPM	6	554.25	95.78	58.11	Collagen alpha-2(I) chain	I3JXH5
	TGM	3	307.12	83.52	30.28	Collagen type I alpha 1	G9M6I5
	PGAR	4	399.22	80.10	22.70	Collagen, type I, alpha 1b	A0A668S2V1
	VQPQ	4	470.25	76.74	37.42	Collagen type I alpha 1	G9M6I5
	SGPSGPAGPA	10	796.37	75.78	42.10	Collagen, type I, alpha 1b	A0A669BKD4
	SGPAGPSGAP	10	796.37	75.78	39.96	Collagen, type I, alpha 1b	A0A669F9X1
	EGR	3	360.18	75.26	47.27	Collagen alpha-2(I) chain	I3JXH5
	GER	3	360.18	75.26	3.26	Collagen, type I, alpha 1b	A0A668S2V1
	GPL	3	285.17	70.99	22.01	Collagen, type I, alpha 1b	A0A669BKD4
	VGPK	4	399.25	66.35	18.00	Collagen type I alpha 1	G9M6I5
	GPM	3	303.13	61.93	22.01	Collagen, type I, alpha 1b	A0A669DNY6
	PGM	3	303.13	61.93	11.36	Collagen, type I, alpha 1b	A0A668S2V1
	GGGY	4	352.14	52.15	38.72	Collagen alpha-2(I) chain	I3JXH5
	NGY	3	352.14	52.15	3.98	Collagen alpha-2(I) chain	I3JXH5
	GPS	3	259.12	47.56	18.44	Collagen, type I, alpha 1b	A0A668S2V1
	AGAR	4	373.21	46.50	41.72	Collagen, type I, alpha 1b	A0A669DNY6
	VGR	3	330.20	41.87	18.44	Collagen alpha-1(II) chain	I3KK22
	AGPTGPAGPL	10	836.44	38.42	36.04	Collagen alpha-2(I) chain	I3JXH5
	GLMGPR	6	629.33	37.74	18.56	Collagen alpha-2(I) chain	I3JXH5
	GEE	3	333.12	34.58	18.44	Collagen, type I, alpha 1b	A0A668S2V1
	TGPK	4	401.23	28.85	18.00	Collagen, type I, alpha 1b	A0A669DNY6
	VAM	3	319.16	28.45	11.36	Collagen alpha-1(II) chain	A0A669F9X1
	VPQ	3	342.19	24.70	3.98	Collagen, type I, alpha 1b	A0A669BKD4
	QPL	3	356.21	15.89	3.98	Collagen, type I, alpha 1b	A0A668S2V1
	GPPGPA	6	494.25	14.85	45.11	Collagen, type I, alpha 1b	A0A668S2V1
	GAM	3	277.11	10.99	11.36	Collagen type I alpha 1	G9M6I5
	GPV	3	271.15	6.69	22.01	Collagen, type I, alpha 1b	A0A668S2V1
	PGA	3	243.12	1514.30	11.355	Collagen alpha-2(I) chain	A0A669EAT8
	GPA	3	243.12	1477.50	36.833	Collagen alpha-2(I) chain	A0A669EAT8
≤ 1 kDa Alc+Flav	GPAGPL	6	510.28	246.65	73.37	Collagen alpha-2(I) chain	A0A669EAT8
	AGAP	4	314.16	214.15	38.717	Collagen alpha-2(I) chain	A0A669EAT8
	AGPA	4	314.16	214.15	38.717	Collagen alpha-2(I) chain	A0A669EAT8

PGAA	4	314.16	214.15	8.0791	Collagen alpha-2(I) chain	A0A669EAT8
SGPA	4	330.15	210.65	8.0791	Collagen alpha-2(I) chain	A0A669EAT8
PGEK	4	429.22	120.31	8.0791	Collagen alpha-2(I) chain	A0A669EAT8
GAR	3	302.17	114.15	30.281	Collagen alpha-2(I) chain	A0A669EAT8
GPL	3	285.17	108.17	22.014	Collagen alpha-2(I) chain	A0A669EAT8
GPT	3	273.13	100.04	18.441	Collagen alpha-2(I) chain	A0A669EAT8
GTP	3	273.13	100.04	9.4904	Collagen alpha-2(I) chain	A0A669EAT8
TGP	3	273.13	100.04	3.9761	Collagen alpha-2(I) chain	A0A669EAT8
AGPQ	4	371.18	81.90	49.857	Collagen alpha-2(I) chain	A0A669EAT8
PGQA	4	371.18	81.90	8.0791	Collagen alpha-2(I) chain	I3JXH5
VGA	3	245.14	67.68	11.355	Collagen alpha-2(I) chain	A0A669EAT8
SPGL	4	372.20	50.87	22.701	Collagen alpha-2(I) chain	I3JXH5
PGAR	4	399.22	45.51	13.805	Collagen alpha-2(I) chain	A0A669EAT8
AGPQGPIGPR	10	948.51	43.55	37.974	Collagen alpha-2(I) chain	A0A669EAT8
GPM	3	303.13	40.84	22.014	Collagen alpha-2(I) chain	I3JXH5
PGM	3	303.13	40.84	11.355	Collagen alpha-2(I) chain	A0A669EAT8
PGVA	4	342.19	30.94	8.0791	Collagen alpha-2(I) chain	A0A669EAT8
EGR	3	360.18	29.94	38.717	Collagen alpha-2(I) chain	A0A669EAT8
GER	3	360.18	29.94	9.4904	Collagen alpha-2(I) chain	A0A669EAT8
GPK	3	300.18	27.37	38.717	Collagen alpha-2(I) chain	A0A669EAT8
GGGY	4	352.14	27.36	25.946	Collagen alpha-2(I) chain	A0A669EAT8
NGY	3	352.14	27.36	3.9761	Collagen alpha-2(I) chain	A0A669EAT8
GPV	3	271.15	26.97	22.014	Collagen alpha-2(I) chain	A0A669EAT8
GPS	3	259.12	19.82	9.4904	Collagen alpha-2(I) chain	A0A669EAT8
PGS	3	259.12	19.82	3.9761	Collagen alpha-2(I) chain	A0A669EAT8
SGPL	4	372.20	16.43	8.0791	Collagen alpha-2(I) chain	A0A669EAT8
TGF	3	323.15	13.64	11.355	Collagen alpha-2(I) chain	A0A669EAT8
PGPS	4	356.17	13.19	8.0791	Collagen alpha-2(I) chain	A0A669EAT8
GEE	3	333.12	12.51	18.441	Collagen alpha-2(I) chain	A0A669EAT8
VGPA	4	342.19	11.08	2.7116	Collagen alpha-2(I) chain	A0A669EAT8
TGA	3	247.12	10.35	3.9761	Collagen alpha-2(I) chain	A0A669EAT8
GAE	3	275.11	8.46	9.4904	Collagen alpha-2(I) chain	A0A669EAT8
PGR	3	328.19	8.42	9.4904	Collagen alpha-2(I) chain	A0A669EAT8
PGLQ	4	413.23	8.30	22.701	Collagen alpha-2(I) chain	A0A669EAT8
GGSF	4	366.15	7.62	8.0791	Collagen alpha-2(I) chain	I3JXH5
VAGA	4	316.17	6.54	8.0791	Collagen alpha-2(I) chain	A0A669EAT8
RAGE	4	431.21	5.49	2.2817	Collagen alpha-2(I) chain	A0A669EAT8
AGGM	4	334.13	4.17	8.0791	Collagen alpha-2(I) chain	A0A669EAT8
QGM	3	334.13	4.17	3.9761	Collagen alpha-2(I) chain	A0A669EAT8
GGY	3	295.12	3.25	11.355	Collagen alpha-2(I) chain	A0A669EAT8

Alc: Alcalase® hydrolysate, Alc+Flav: Alcalase® followed by Flavourzyme® hydrolysate; ≤ 1 kDa: 1 kDa ultrafiltrated hydrolysate.

Appendix 4.1. 11S globulin seed storage protein G3, 55.687 kDa, 493 amino acids.

MASKATLLLAFTLLFATCIARHQQRQQQQNQCQLQNIEALEPIEVIQAEAGVTEIWDAYDQ
QFQCAWSILFDTGFNLVAFSCLPTSTPLFWPSSREGVILPGCRRTYEYSQEQQFSGEGG
RRGGGEGTFRTVIRKLENLKEGDVVAIPTGTAHWLHNDGNTELVVVFLDTQNHENQLDE
NQRRFFLAGNPQAQAQSQQQQQRQPRQQSPQRQRQRQRQGQGQNAGNIFNGFTPELI
AQSFNVDQETAQKLQGQNDQRGHIVNVGQDLQIVRPPQDRRSPRQQQEQATSPRQQQ
EQQQGRRGGWSNGVEETICSMKFKVNIDNPSQADFVNPQAGSIANLNSFKFPILEHLRLS
VERGELRPNAIQSPHWTINAHNLLYVTEGALRVQIVDNQGNSVFDNELREGQVVVIPQNF
AVIKRANEQGSRWVSFKTNDNAMIANLAGRVSASAASPLTLWANRYQLSREEAQQLKFS
QRETVLFAPSFSRGQGIRASR

Letters highlighted in yellow indicate the amino acid sequences used for the selection of synthetic peptides.

Appendix 4.2. The peptide concentration and degree of hydrolysis (DH) of hydrolysates prepared by different enzymatic treatments determined by OPA assay.

Samples	mM eq. NH_2	Degree of hydrolysis (DH, %)
SMPI	0.39 ± 0.11[a]	--
Prot	0.89 ± 0.04[b]	30.96 ± 1.34[a]
Prot+Flav	1.23 ± 0.02[d]	38.80 ± 0.87[b]
≤ 1 kDa Prot	1.16 ± 0.03[b]	--
≤ 1 kDa Prot + Flav	3.33 ± 0.01[e]	--

Different letters in the same column indicate the significant difference between the hydrolysates and their ≤ 1 kDa fractions (*p-value* <0.05). n=5. Prot: Protamex® hydrolysate; Prot+Flav: Protamex® followed by Flavourzyme® hydrolysate; ≤ 1 kDa: 1 kDa ultrafiltrated hydrolysate

Appendix 4.3. Protein data base used for peptide identification from *Helianthus annuus* (Common sunflower).

Number	Entry	Name
1	P19084	11S globulin seed storage protein G3
2	P23110	Albumin-8
3	P15461	2S seed storage protein
4	A0A9K3N4U5	
5	A0A9K3J848	11-S seed storage protein, plant
6	A0A251TLE7	
7	A0A251TKL9	
8	A0A251UYX1	Putative 11-S seed storage protein
9	A0A251THI6	Putative 11-S seed storage protein
10	A0A251TMX5	Seed storage 2S albumin superfamily protein
11	A0A251UCD5	Putative 11S globulin subunit beta
12	A0A161CKQ7	Seed storage albumin 2
13	A0A9K3J4X3	
14	A0A9K3JE69	
15	A0A9K3JEW0	
16	A0A9K3HYV6	
17	A0A9K3NGE6	
18	A0A9K3J8S2	
19	A0A9K3HVJ0	
20	A0A251VQB6	11-S seed storage protein, plant
21	A0A251T566	
22	A0A251V6R8	
23	A0A251V6N9	
24	A0A251TVT1	
25	A0A251TUS1	
26	A0A251TAA6	
27	A0A251VMR6	
28	A0A251TKL9	
29	T1WKB1	11S globulin
30	Q39928	2S albumin

Appendix 4.4. Parameters of database searches used for peptide identification.

Parameter	Condition
Digestion mode	No enzyme and unspecific cleavage
Length	3 to 25 amino acids
Variable modification	N-terminal acetylation and methionine oxidation
Fixed modification	Cysteine carbamidomethylation
Initial precursor-ion mass tolerances	10 ppm
Mass tolerance for fragment ions	10 ppm
False discovery rate (FDR)	0.01
Include contaminants	Disabled
Match between run	Enabled
All the other parameters	Set up as default settings

Appendix 4.5. Sequenced mass spectra of metal-binding peptides structures from a synthetic peptides hydrolysate composed of 8 pure peptides obtained from 11S globulin seed storage protein G3 (P19084) and processes by MaxQuant software. (A) AIPTGTA**H,** (B) FATCIAR**H**, (C) KFPILE**H**, (D) KFPILE**H**L, (E) KFPILE**H**LR, (F) WL**H**NDGN, (G) WL**H**NDGNTE and (H) **W**VSFKTN.

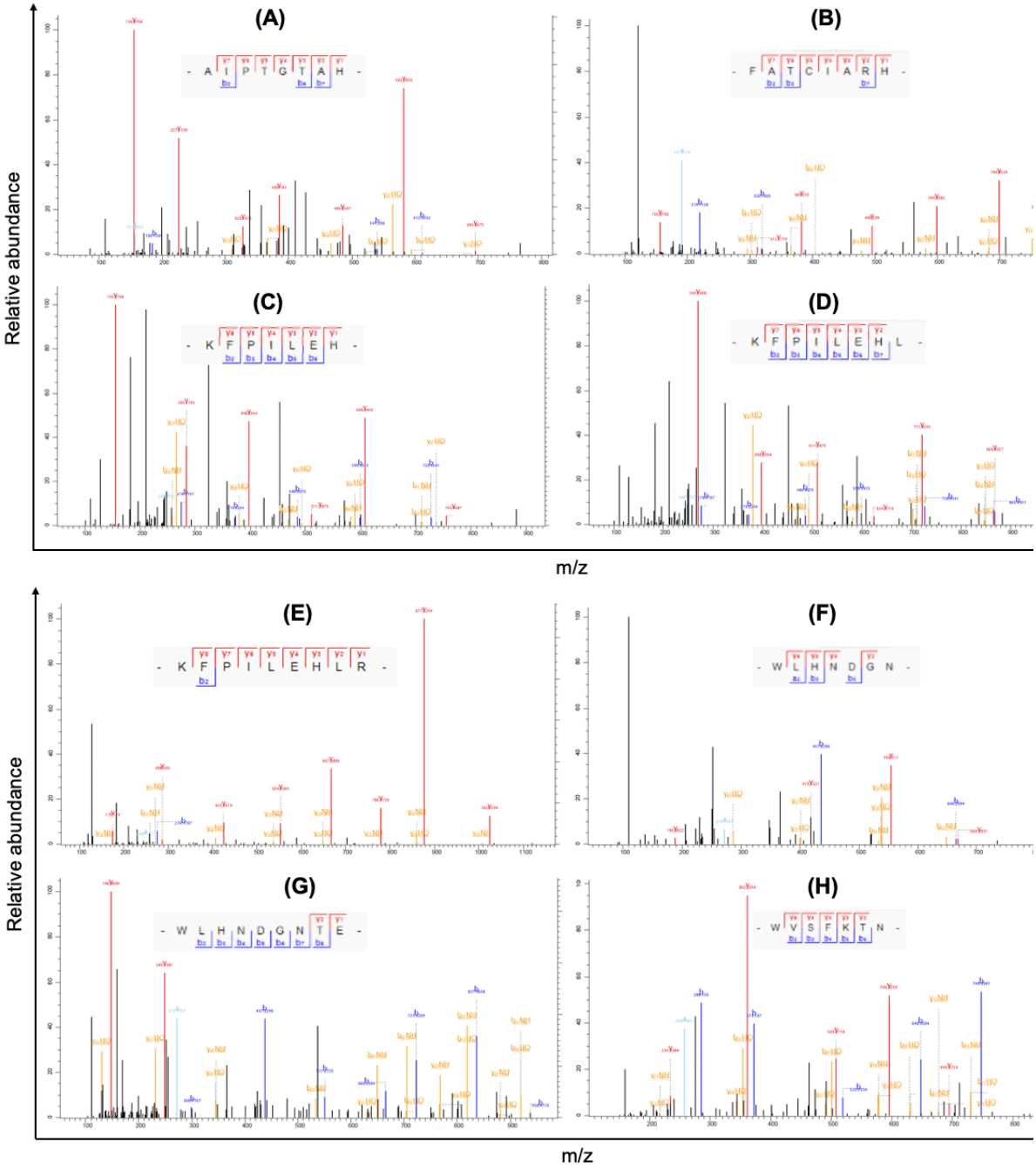

Appendix 4.6. Unbound peptides sequences identified from Prot, Prot+Flav, ≤ 1 kDa Prot and ≤ 1 kDa Prot+Flav hydrolysates.

Sequence	Intensity (x 10^5)				Length	Mass	Score	Entry
	Prot	Prot+Flav	≤ 1 k Da Prot	≤ 1 kDa Prot+Flav				
ADVF	59.77	13.33	67.30	33.59	4	450.21	22.70	A0A251UYX1
AEAF	33.75	16.47	42.96	16.78	4	436.20	15.83	A0A251TUS1
AGFDDEILQ		9.21		0.59	9	1006.46	4.33	A0A251T566
AIIVDDVNNPANQL		73.64			14	1494.77	6.63	A0A251UYX1
ALEPIE	116.78		30.11		6	670.35	26.18	A0A251TKL9
ALEPIEVIQA	17.55	2.23	1.03		10	1081.60	7.29	
ALEPNERVE	13.01	4.51			9	1055.52	6.72	A0A9K3HVJ0
ALEPNERVEAE	22.96	5.37			11	1255.60	5.30	
ALNVT	17.14		18.92		5	516.29	10.80	A0A251V6N9
ALQESRNRGVIVQVQQ		105.38		1.15	16	1824.00	2.42	A0A251UYX1
APLKSPLAGY		19.42		5.56	10	1015.57	4.33	
APSF		10.78		25.11	4	420.20	22.70	
AYQL	10.95		18.47		4	493.25	15.83	A0A251TKL9
DFIR**H**				0.20	5	686.35	16.21	
DIVMQ		3.01			5	604.29	9.64	A0A251T566
DNQREADVF	21.64	28.51	4.38	3.71	9	1092.48	6.72	A0A251UYX1
DTELL	47.83	4.25	23.54	3.59	5	589.30	45.11	
EAF			1.67	2.07	3	365.16	3.98	A0A251TUS1
EAGVT	18.15	4.96	21.73	3.57	5	475.23	22.12	A0A251TKL9
EI**W**DANDQ	11.82	8.61	1.98	1.92	8	989.41	5.76	A0A9K3NGE6
EQVSRGDIFPVPQ	43.23	26.04			13	1470.75	4.72	A0A251UYX1
ESFQ	8.05				4	509.21	6.96	
ETVL	56.32	31.32	55.86	45.67	4	460.25	33.73	A0A251TKL9
EVITN	13.96	6.07	14.72	3.79	5	574.30	34.99	A0A251UYX1
E**W**VAF	1.47	3.70	3.12	3.53	5	650.31	18.00	
FAPS	22.11		40.53		4	420.20	13.81	A0A251TKL9
FDTQ	8.05	2.60	11.91	2.74	4	509.21	18.00	A0A9K3NGE6
FDTQNNENQLDEYQRR	4.28	56.33			16	2068.92	4.96	
FFAA	22.29		40.74		4	454.22	15.83	A0A251UYX1
FFDSGDQQFQ	17.41		4.49		10	1217.50	3.94	A0A9K3HVJ0
FFLA	29.30		30.87		4	496.27	15.83	A0A251TKL9
FIEQ	20.70		12.26		4	535.26	22.70	A0A251UYX1
FIEQGEGLVGI	16.12		1.95		11	1160.61	3.60	
FLA	31.25		41.50	1.46	3	349.20	11.36	
FPIL		22.01	2.22	39.51	4	488.30	25.95	A0A251TKL9
FPILE		41.05	1.22	32.76	5	617.34	18.00	

FQGQ	42.57		68.41		4	478.22	45.11	A0A251UYX1
FREGDIIAIPA	72.22	1.30			11	1200.65	13.62	
FTPE	5.72		6.80		4	492.22	6.96	A0A251TKL9
FTPELIAQS		10.98			9	1004.52	4.33	
GAF			1.88	4.97	3	293.14	3.98	A0A251TUS1
GAL	5.85	6.23	18.28	20.49	3	259.15	11.36	A0A251TKL9
GDIFPVPQ	1.75	23.13	2.91	0.71	8	871.44	5.23	
GEAVLN	17.65	9.90	9.82	4.35	6	601.31	11.11	A0A251UYX1
GEGLVGI	17.25	3.86	17.48	4.85	7	643.35	11.11	
GFE			4.39	4.76	3	351.14	9.49	
GLEE	4.44	2.32	5.13	2.93	4	446.20	2.71	A0A9K3HVJ0
GNSVFDNELRE	26.69	11.41			11	1278.58	8.98	
GQVVVIPQ	10.81	1.07	7.17		8	838.49	5.23	A0A251TKL9
GVEE	19.16	6.77	22.41	11.05	4	432.19	22.70	
IDIPFRDRP	98.28	12.14			9	1127.61	7.61	A0A161CKQ7
IDIPFRDRPFGRS	164.26	42.54			13	1574.83	3.60	
IDIPFRDRPFGT	47.49	8.24			12	1432.75	4.33	P15461
IDIPFRDRPFGTG	77.62	20.02			13	1489.77	7.43	P15461
IDQETAQKL	2.38	29.42			9	1044.55	6.72	A0A9K3NGE6
IPLSAGV	18.54		15.82		7	655.39	3.65	A0A9K3JEW0
IPQ		3.80		8.99	3	356.21	15.83	A0A251TKL9
IQPGGL	42.16		67.88		6	583.33	30.95	
IVAIVM	4.46		7.18		6	644.39	9.64	A0A9K3HVJ0
IVNDL	32.22		29.29		5	572.32	18.00	A0A251TUS1
KEGDVVAIPT	131.07	82.50	18.97	11.83	10	1027.56	22.66	A0A251TKL9
LAGY	6.52		7.59		4	422.22	25.95	A0A251UYX1
LAS	4.04		12.70	4.52	3	289.16	3.98	A0A251TMX5
LDEY		4.07			4	538.23	6.96	A0A9K3NGE6
LDTQ	11.72	2.05	13.49		4	475.23	18.00	A0A251TKL9
LEFE	5.17		2.25		4	536.25	6.96	A0A251UYX1
LEL	9.06	2.87	11.77	7.82	3	373.22	11.36	A0A251TMX5
LEPIE	10.07	51.33	2.68	15.47	5	599.32	20.22	A0A251TKL9
LFIEQ	7.85		6.24		5	648.35	10.80	
LFLPS	24.81		34.93		5	575.33	10.80	A0A251UYX1
LFSPQ	16.66		25.07		5	590.31	37.87	
LGA	0.00	10.01		29.52	3	259.15	3.98	A0A251VMR6
LLAE	7.58		6.22		4	444.26	6.96	A0A251UYX1
LLAQ	23.73		44.66		4	443.27	29.93	A0A9K3NGE6
LLLPS	3.70	14.19	6.02	14.92	5	541.35	10.80	A0A251TKL9
LLPS	25.73		39.06	1.25	4	428.26	6.96	
LLQ	4.55		8.86		3	372.24	3.26	A0A161CKQ7
LNSF	23.95		33.65		4	479.24	41.72	A0A251TKL9
LPIL		68.98	4.34	116.60	4	454.32	38.72	A0A251UYX1

LPN				4.37	3	342.19	3.26	A0A251TVT1
LPVLE		8.29		8.24	5	569.34	10.80	A0A251T566
LSREDAQQL	18.58		3.96		9	1058.54	5.73	A0A9K3NGE6
LTRDNVYAGF	86.15				10	1154.57	16.57	A0A251UYX1
LVVV	93.55		171.82	2.00	4	428.30	25.95	A0A251TKL9
LVVVPQ	20.80		6.71		6	653.41	20.22	A0A251TUS1
LVVVVF	8.70	3.12	3.28		6	674.44	9.64	
LYVT	2.59		4.10		4	494.27	2.71	A0A251TKL9
LYVTE	16.21		9.20		5	623.32	16.21	
NAGNIF	14.14		24.94		6	634.31	7.78	
NALEPIE	23.32		3.69		7	784.40	26.34	A0A251TUS1
NALEPIERVQSEAG		19.73			14	1511.76	3.07	
NDDRGLIVL	21.67	5.38	7.35	1.35	9	1013.55	3.60	A0A251T566
NEGDVVAIPT	32.85	21.85	3.02	2.01	10	1013.50	3.28	A0A9K3NGE6
NFAVIK	99.39		105.72	2.61	6	690.41	17.09	A0A251TKL9
NFAVVK	54.31		36.17		6	676.39	7.78	A0A251TUS1
NIDQETAQKL	29.69	4.46			10	1158.59	3.60	A0A9K3NGE6
NLDNQREADVF	20.74	4.64			11	1319.61	3.00	A0A251UYX1
NLQ	2.83		7.55		3	373.20	18.44	A0A251TVT1
NVDQETAQKL	29.97	7.33			10	1144.57	3.60	
NVGQDL	67.66		44.20	1.04	6	644.31	26.18	A0A251TKL9
NVGQDLQ	8.82		1.91		7	772.37	7.02	
PILQYL	43.91		40.54		6	745.44	9.64	A0A251TVT1
QESRNRGVIVQVQ	6.32	35.37			13	1511.82	3.19	
QESRNRGVIVQVQQ		77.06			14	1639.88	4.28	A0A251UYX1
QEVFNDEVQ	23.62				9	1106.49	11.64	A0A251TUS1
QFL	10.12		25.36		3	406.22	11.36	
QGDI		13.77		23.46	4	431.20	6.96	A0A251UYX1
QLVVVPQ	30.02		24.70		7	781.47	28.17	A0A251TUS1
QQL			11.31	5.83	3	387.21	3.98	A0A251TKL9
QVVVIPQ	23.92		11.74		7	781.47	22.45	
RALPVDVL	92.85		24.82		8	881.53	38.15	A0A251TUS1
RDNVYAGF	0.00	34.99	1.63	22.37	8	940.44	13.91	A0A251UYX1
REDAKIL	23.74	16.65	6.25	3.37	7	843.48	12.53	A0A251T566
REDAQQL	10.83	34.79	6.68	13.39	7	858.42	7.91	A0A9K3NGE6
REEAQQL	3.95	14.05	2.36	4.37	7	872.44	7.91	A0A251TKL9
REEQE**W**E	41.06	18.65	2.95	1.08	7	1004.42	23.15	
REGDILALPA	187.88	165.02			10	1053.58	23.79	A0A251T566
REGDILALPAG	1.86	29.49			11	1110.60	4.19	
REGDMIIIPA	12.15	28.18			10	1113.59	4.90	A0A9K3HVJ0
RFREGDIIAIPA	38.44				12	1356.75	2.38	A0A251UYX1
RGELRPN	55.05		54.76		7	840.46	12.53	A0A251TKL9
RIQPGGL	29.21		26.95	0.77	7	739.43	11.11	

RIQPGGLLLP		45.37			10	1062.66	6.21	
RQGDIIAIPA	11.96				10	1052.60	3.00	A0A251UYX1
RQGDVVAIPT	61.69		20.05		10	1054.58	12.87	A0A251TUS1
SEVF	22.65	8.16	27.90	13.74	4	480.22	22.70	A0A9K3HVJ0
SFKFPILE	25.09	1.08	0.67		8	979.54	12.53	A0A251TKL9
SLLFSP	9.71		11.49		6	662.36	7.78	A0A251UYX1
SL**W**N	8.47				4	518.25	6.05	A0A251V6N9
SPEQARSL	4.09	17.19	1.51	2.96	8	886.45	4.76	A0A9K3HVJ0
SPFGGQEELTRD		41.62			12	1334.61	3.88	A0A251UYX1
SPLA				4.76	4	386.22	2.71	
SREDAQQL	24.67		11.34		8	945.45	4.33	A0A9K3NGE6
SVFDNELRE	11.81				9	1107.52	3.60	A0A251TKL9
SYQVSPN	6.97		3.93		7	793.36	3.24	A0A251UYX1
SYVNTPILA		14.25		6.32	9	976.52	4.76	A0A251TKL9
TELL		27.59		16.63	4	474.27	22.70	A0A251UYX1
TELV		31.32	55.86		4	460.25	22.70	A0A251TKL9
TETL		7.65		3.43	4	462.23	13.81	A0A251TUS1
TNPI		7.67		4.53	4	443.24	2.71	A0A251TMX5
TPELIAQ		7.85		3.50	7	770.42	10.18	
TPELIAQS		20.08		8.16	8	857.45	8.59	A0A251TKL9
TPILA		37.56	3.24	86.68	5	513.32	33.91	
TPILAF		14.07	1.07	11.68	6	660.38	7.78	
TPILF		9.82	1.60	21.93	5	589.35	16.21	A0A251TUS1
TPLL	3.33	39.37	8.06	91.96	4	442.28	41.72	A0A9K3JEW0
TSF	8.57	13.93	14.58	11.33	3	353.16	18.44	A0A251UYX1
TTETL	13.75		4.87		5	563.28	18.00	A0A251TUS1
TVDLL	39.10		39.66		5	559.32	16.21	A0A9K3NGE6
VAF	7.85	8.46	13.77	5.75	3	335.18	11.36	A0A251UYX1
VDLL	1.81	26.05	2.28	24.29	4	458.27	6.96	A0A9K3NGE6
VDQETAQKL	1.27	39.63		3.08	9	1030.53	6.72	A0A251TKL9
VGE	4.06		8.54	5.49	3	303.14	18.44	A0A251VMR6
VITN	3.61		8.42		4	445.25	6.96	A0A251UYX1
VIVQ	9.11		8.72		4	457.29	20.12	
VLFAPS	9.56		9.95		6	632.35	8.64	A0A251TKL9
VLLL	6.01		10.89		4	456.33	15.83	P23110
VLM			16.83		3	361.20	11.36	A0A251T566
VLQ	3.79		8.02		3	358.22	18.44	A0A251TVT1
VLQA	49.74		108.13		4	429.26	33.73	A0A251VMR6
VNTPIL	18.54				6	655.39	8.64	A0A251TKL9
VPQ		4.07		9.02	3	342.19	15.83	A0A251TUS1
VSF	29.58	23.27	43.54	30.04	3	351.18	18.44	A0A251TKL9
VSRGDIFPVPQ	99.26				11	1213.65	19.63	A0A251UYX1
VSVL	8.90		11.61		4	416.26	6.96	A0A9K3HVJ0

VTE		2.83	11.99	8.57	3	347.17	3.98	A0A251TKL9
VVAIIV	23.44		14.71		6	612.42	16.21	
VVAIIVD	4.59		1.23		7	727.45	3.65	A0A251UYX1
VVAIIVDDVNNPANQL	58.88				16	1692.90	1.35	
VVRPPIRIQ	49.42	5.73			9	1076.68	4.53	A0A9K3HVJ0
VVVIPQ	6.95		9.74		6	653.41	20.22	A0A251TKL9
VVVPQ	7.00		5.41		5	540.33	9.64	A0A251TUS1
WTVN			22.90		4	518.25	12.16	A0A251UYX1
YVNTPIL	77.72		83.71	0.62	7	818.45	18.56	A0A251TKL9
YVTE	3.44		3.89		4	510.23	6.96	

Prot: Protamex® hydrolysate; Prot+Flav: Protamex® followed by Flavourzyme®; ≤ 1kDa Prot: 1kDa ultrafiltrated Protamex® hydrolysate; ≤ 1 kDa Prot+Flav: 1 kDa ultrafiltrated Protamex® followed by Flavourzyme® hydrolysate.

Appendix 4.7. Kinetic study between metal-binding peptides and nickel ions using switchSENSE® technology. (A-K**)** association rate (k_{on}) of binding kinetic studies of pure metal-chelating peptides.

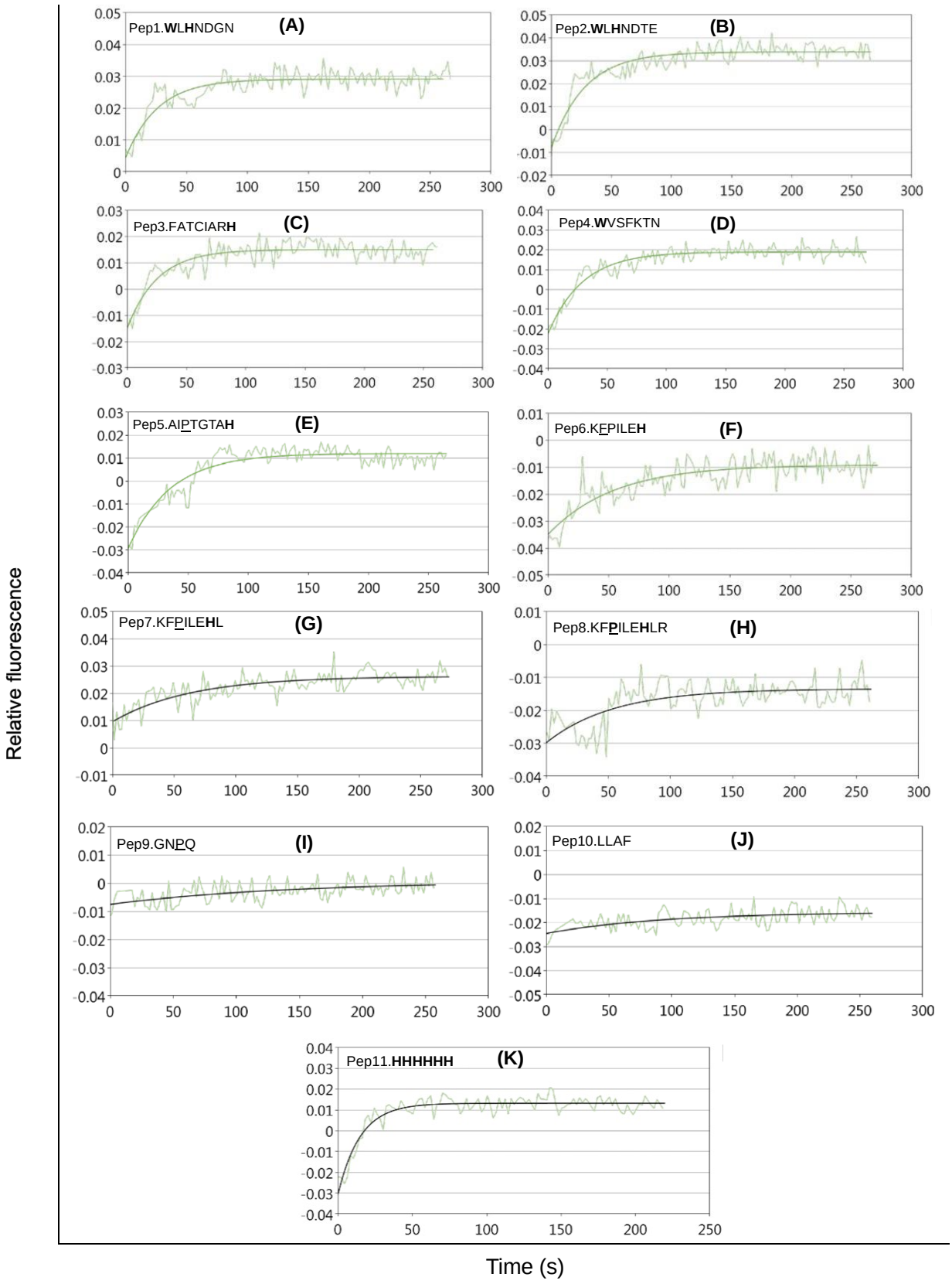

Appendix 4.8. Kinetic study between metal-binding peptides present in SMPI hydrolysates and nickel ions using switchSENSE® technology. (A-D**)** association rate (k_{on}) of binding kinetic studies of metal- binding peptides.

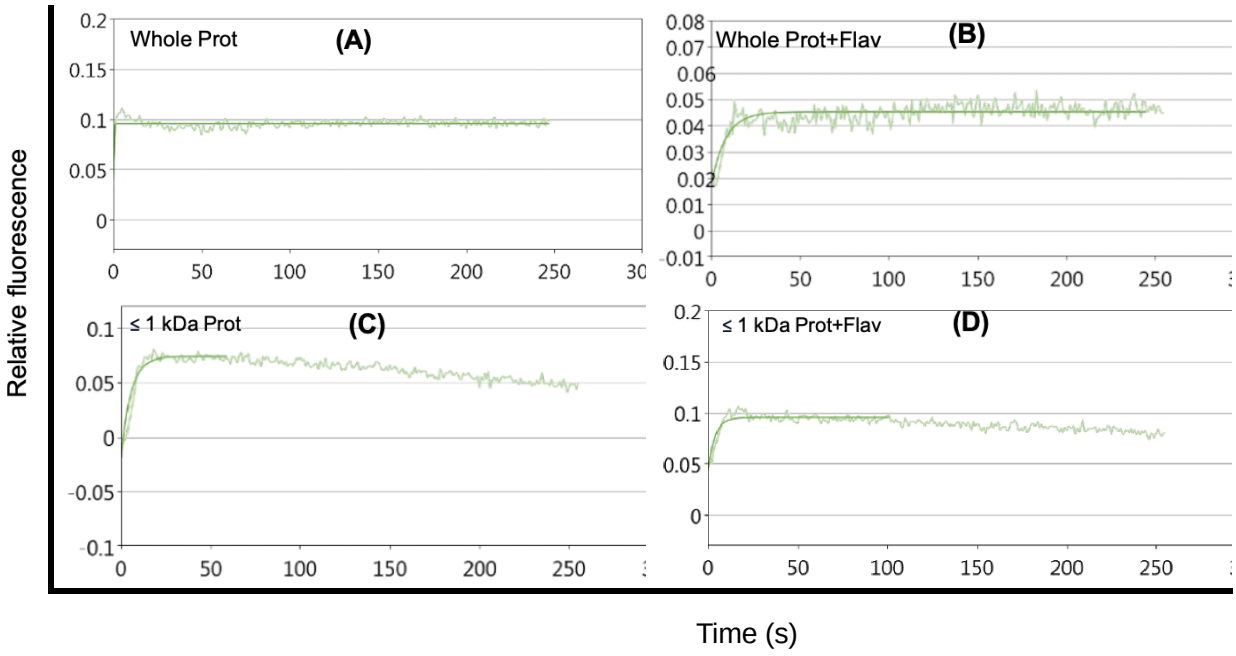

Prot: Protamex® hydrolysate; Prot+Flav: Protamex® followed by Flavourzyme® hydrolysate; ≤ 1kDa Prot: 1kDa ultrafiltrated hydrolysate.

Appendix 5.1. Peptides sequences identified from the F1 fractions (unbounding peptides) of sunflower meal protein hydrolysates fractions using IMAC-Cu-$^{2+}$ separation followed by LC-MS/MS analysis.

Sequence	Intensity (x 10^5)				Length	Mass (g/mol)	Score	Entry
	Prot	Prot+Flav	≤ 1 k Da Prot	≤ 1 kDa Prot+Flav				
ADVF	54.04	15.67	45.20	19.91	4	450.21	13.81	A0A251UYX1
AEAF	37.41	13.69	30.08	18.83	4	436.20	22.70	
AERGVLY	30.11	10.68	13.10	3.90	7	806.43	5.23	A0A251T566
AGFDDEILQQ	14.63	13.80			10	1134.52	1.65	
AIIVDDVNNPANQL	8.92	112.14			14	1494.77	9.54	A0A251UYX1
ALEPIE	100.87		17.63		6	670.35	26.18	A0A251TUS1
ALEPNERVE	12.02	3.12			9	1055.52	4.33	A0A9K3HVJ0
ALEPNERVEAE	21.55	5.36			11	1255.60	3.28	
ALNVT	15.80		19.57		5	516.29	10.80	A0A251V6N9
ALQESRNRGVIVQVQQ		62.54			16	1824.00	1.59	
APL				8.36	3	299.18	11.36	
APLKSPLAGY		51.07		6.41	10	1015.57	15.85	A0A251UYX1
APRLGSPE		28.66		17.11	8	825.43	4.76	
APSF				19.49	4	420.20	22.70	
APSFSRGQ				18.97	8	848.41	4.33	P19084
APSFSRGQG		10.39			9	905.44	1.84	
DDRGLIVL		9.49		4.51	8	899.51	2.30	A0A251T566
DELVII		5.56		1.05	6	700.40	7.78	A0A251TUS1
DFAVIK	52.39	4.86	32.15	3.02	6	691.39	13.33	A0A251T566
DFQAK	29.54		21.44		5	607.30	10.80	A0A251UYX1
DFVNPQ	36.42		20.04		6	718.33	13.33	P19084
DIFPVPQ	3.06		0.97	0.97	7	814.42	2.89	A0A251UYX1
DIPWPFRPS	14.81	17.00			9	1113.56	1.84	Q39928
DNQREADVF	34.36	29.79			9	1092.48	1.84	A0A251UYX1
DTELL	57.17	5.11	12.42	1.21	5	589.30	26.86	
DTQNNENQLDEYQRRF		80.25			16	2068.92	4.71	A0A9K3NGE6
DVSRPDF		6.39		2.60	7	834.39	2.89	A0A9K3HVJ0
DVSRPDFFNPE	38.35	9.30	3.49	0.79	11	1321.59	4.90	
EIWDAY	28.25	6.85	10.35		6	795.34	4.66	P19084
ENPISGQ	9.80	4.31	4.12		7	743.34	3.24	P15461
EQVSRGDIFPVPQ	31.03	17.43			13	1470.75	6.19	A0A251UYX1
ETVL	48.06		32.37	28.40	4	460.25	33.73	P19084
EVITN	18.10	4.89	9.17		5	574.30	20.22	A0A251UYX1
EWVAF	12.64	15.58	7.44	6.47	5	650.31	26.86	
FDDEILQQ		10.92			8	1006.46	2.58	A0A251T566
FDTQNNENQLDEYQRRF		152.48			17	2215.99	16.99	A0A9K3NGE6
FFDSGDQQFQ	18.54				10	1217.50	1.65	A0A9K3HVJ0
FFL	5.16		4.08		3	425.23	3.98	A0A251UYX1

FIEQ	20.10		11.87		4	535.26	13.81	
FIEQGEGLVGI	18.85				11	1160.61	3.60	
FLA			34.76	1.37	3	349.20	11.36	
FLPSFQ	21.93		11.55		6	737.37	4.12	
FPIL		39.55	4.61	51.07	4	488.30	25.95	A0A251TUS1
FPILE		63.39	1.95	24.23	5	617.34	18.00	P19084
FQGQ	36.43		34.94		4	478.22	20.12	
FQSYPRL	18.36		9.56	0.52	7	909.47	2.58	A0A251UYX1
FQSYPRLL	30.98		5.03		8	1022.55	11.64	
FRP				23.92	3	418.23	9.49	Q39928
FTPELIAQS		5.67			9	1004.52	2.06	P19084
GAL				12.12	3	259.15	3.98	P19084
GAVY	19.81		21.13		4	408.20	15.83	
GDIFPVPQ	5.89	24.92	1.47	7.36	8	871.44	8.59	A0A251UYX1
GEAVLN	21.96	6.85	10.51	5.22	6	601.31	17.09	
GEGLVGI	20.34				7	643.35	2.89	
GELRPN		12.02		6.52	6	684.36	4.12	P19084
GFD	9.98	4.67	12.51	11.75	3	337.13	3.98	A0A251UYX1
GFEWVAF	27.24		11.10		7	854.40	12.16	
GFS				1.25	3	309.13	3.98	A0A251VMR6
GGL				5.66	3	245.14	3.98	A0A251TKL9
GGW	2.84			10.10	3	318.13	3.98	P19084
GLLLPS	40.97	8.82	16.28	3.85	6	598.37	14.67	A0A251TUS1
GLVGI	3.31	2.70	6.41	10.84	5	457.29	12.16	A0A251UYX1
GNSVFDNELRE	30.30	13.03			11	1278.58	12.87	
GQVVVIPQ	36.86		12.89		8	838.49	24.67	P19084
GQVVVIPQN	6.03				9	952.53	1.84	
GQVVVVPQ	4.40				8	824.48	4.76	A0A9K3HVJ0
GSRWVSF	7.30		2.13		7	837.41	2.89	P19084
GVAGIVLP		10.00			8	724.45	2.89	A0A251VMR6
GVDFIR	6.87		5.50		6	705.38	4.12	A0A251TKL9
GVEE	17.78	6.07	13.14		4	432.19	13.81	A0A251UYX1
GWDNILR	18.97		13.56		7	872.45	14.58	A0A251TUS1
IALPFGVVTWWYNK	151.71				14	1692.90	2.09	A0A251VMR6
IDIPFRDRP	112.68	1.89			9	1127.61	15.25	P15461
IDIPFRDRPFGR	87.37	18.21			12	1487.80	5.20	A0A161CKQ7
IDIPFRDRPFGRS	56.58	11.21			13	1574.83	2.22	
IDIPFRDRPFGTG	103.68				13	1489.77	3.39	P15461
IEQGEGLVGI	6.17	11.08			10	1013.54	1.84	A0A251UYX1
IERGRGIQGVIL	100.27	18.20			12	1309.78	1.93	A0A9K3NGE6
IPFR	312.13		221.34	3.73	4	531.32	22.70	P15461
IPLSAGV	19.88		9.63		7	655.39	3.65	A0A9K3JEW0
IQGVIL	19.98		13.15		6	641.41	3.65	A0A251TKL9
IQPGGL	44.84		35.09	0.57	6	583.33	30.95	
IQPQ	8.01		8.28		4	484.26	12.16	A0A251TUS1
IVAIVM	8.78		4.70		6	644.39	9.64	A0A9K3HVJ0

KEGDVVAIPT	116.37	74.34			10	1027.56	14.41	P19084
KFPILE	134.76		44.55		6	745.44	32.45	P19084
KLPILQ	32.70		12.94		6	710.47	7.78	A0A9K3HVJ0
KLPVLE	6.85		2.96		6	697.44	4.12	A0A251T566
LALPAG	5.05		4.40		6	540.33	4.66	
LDNQREADVF	9.42	9.20			10	1205.57	1.48	A0A251UYX1
LEL	10.16		9.17	5.63	3	373.22	11.36	A0A251TMX5
LEPIE	7.64	42.77		12.07	5	599.32	14.67	A0A251TUS1
LEPIEVIQA	2.73	9.60			9	1010.56	2.06	P19084
LFA	34.41				3	349.20	3.98	P19084
LFIEQ	14.89		5.25		5	648.35	18.00	
LFLPS	46.81		28.90		5	575.33	10.80	A0A251UYX1
LFSPQ	30.15		15.16		5	590.31	24.30	
LLAE	7.79		3.83		4	444.26	13.81	
LLAQ	32.64		26.28		4	443.27	29.93	A0A9K3NGE6
LLPS	111.68		90.59	1.89	4	428.26	13.81	A0A251TUS1
LLPSY	33.13		18.08		5	591.33	9.64	
LLQ	5.38		6.27		3	372.24	9.49	A0A161CKQ7
LLY	5.74		5.56		3	407.24	3.98	P19084
LNSF	18.26		18.50		4	479.24	13.81	A0A251TUS1
LPIL		133.38	11.05	132.83	4	454.32	25.95	A0A251UYX1
LPILQ		16.72		15.11	5	582.37	33.91	A0A9K3HVJ0
LPVDVL		10.02		7.02	6	654.40	8.64	A0A251TUS1
LPVLE		11.47			5	569.34	12.16	A0A251T566
LQVVRPPIRIQ	43.22				11	1317.82	2.43	A0A9K3HVJ0
LRPF			221.34		4	531.32	20.12	
LTRDNVYAGF	149.04				10	1154.57	30.70	A0A251UYX1
LVVV	142.86		91.39	1.73	4	428.30	25.95	A0A251TUS1
LVVVPQ	22.61		9.25		6	653.41	4.66	A0A251TUS1
LVVVVF	23.94	3.09	1.97		6	674.44	4.66	A0A251TKL9
LYVTE	16.11		7.15		5	623.32	10.80	P19084
MPL				8.43	3	359.19	3.98	A0A251UYX1
MPV				2.70	3	345.17	3.98	A0A251TKL9
NAGNIF	20.75		14.81		6	634.31	7.78	P19084
NALEPIE	14.14				7	784.40	11.11	A0A251TUS1
NALEPIERVQSEAG		18.51			14	1511.76	1.74	
NFAVIK	218.15	2.66	142.37	2.20	6	690.41	24.21	P19084
NFAVVK	92.89		55.17		6	676.39	13.33	A0A251TUS1
NGIF	27.69	19.96	29.51		4	449.23	13.81	A0A251VMR6
NIDDPSNADLYNPQ	11.89	5.75			14	1574.68	1.74	A0A251TUS1
NLAGRVS	25.73		15.08		7	715.40	2.89	P19084
NLDNQREADVF	18.74	3.68			11	1319.61	1.48	A0A251UYX1
NLL	8.16		10.94		3	358.22	3.98	P19084
NLLY	21.25		14.85		4	521.28	20.12	P19084
NLNSF			12.86		5	593.28	10.80	P19084
NPQAGRIA		9.74			8	825.45	2.30	A0A9K3NGE6

NVDQETAQKL	33.40	5.38			10	1144.57	1.65	P19084
NVGQDL	73.45	0.00	31.75	0.78	6	644.31	13.33	P19084
PFDIPWPFRPS	24.55	4.62			11	1357.68	5.30	Q39928
PILQYL	145.91				6	745.44	4.66	A0A251TVT1
PILSL	6.90	17.92	7.04		5	541.35	12.16	A0A251UYX1
QEL	5.18	3.19	5.18	7.96	3	388.20	3.98	P15461
QESRNRGVIVQVQQ		44.30			14	1639.88	1.46	A0A251UYX1
QEVFNDEVQ	20.15				9	1106.49	7.29	A0A251TUS1
QFL	13.20		19.08	1.15	3	406.22	11.36	
QFQG	36.43		34.94		4	478.22	20.12	A0A251UYX1
QGDI				12.34	4	431.20	13.81	A0A251UYX1
QIIRPPQAR	49.03				9	1077.64	7.61	A0A9K3NGE6
QLDENQ	4.11		2.31		6	745.32	4.12	P19084
QLVVVPQ	51.83		11.50		7	781.47	28.17	A0A251TUS1
QVVVIPQ	15.64		6.81		7	781.47	28.17	P19084
RALPVDVL	85.84		14.11		8	881.53	12.53	A0A251TUS1
RDNVYAGF		34.24		12.82	8	940.44	10.82	A0A251UYX1
REDAKIL	20.18	16.16	7.66		7	843.48	2.30	A0A251T566
REDAQQL	11.33	44.09	3.88		7	858.42	7.91	A0A9K3NGE6
REEAQQL	4.77	13.85			7	872.44	2.30	P19084
REEQEWE	36.71	15.56			7	1004.42	11.64	
REGDIL	6.92	4.35	3.00	1.20	6	701.37	3.65	A0A251T566
REGDILALPA	200.56	164.63			10	1053.58	20.42	
REGDILALPAG		29.27			11	1110.60	4.19	
REGDMIIIPA	40.35	0.56			10	1113.59	1.48	A0A9K3HVJ0
REGVIL	6.38		3.06		6	685.41	3.65	P19084
RETVLF		24.49		7.34	6	763.42	3.65	P19084
RFREGDIIAIPA	54.17	2.85			12	1356.75	1.65	A0A251UYX1
RGELRPN	57.76		32.79		7	840.46	13.51	P19084
RGFDLQ	7.12		4.07		6	734.37	7.02	A0A9K3HVJ0
RIQPGGL	51.25		30.36	0.84	7	739.43	32.45	A0A251TKL9
RIQPGGLLLP		66.03			10	1062.66	1.65	
RLPF	26.99		14.56		4	531.32	13.81	A0A9K3NGE6
RPF			27.16	23.92	3	418.23	18.44	P15461
RPSWE				10.96	5	673.32	9.64	A0A251T566
RQGDVVAIPT	58.31				10	1054.58	14.41	A0A251TUS1
RVQSEAGFTE	12.77				10	1122.53	1.48	
SEVF			17.71	9.62	4	480.22	13.81	A0A9K3HVJ0
SFK	4.11				3	380.21	3.98	A0A251TUS1
SFKFPIL	83.61		20.94		7	850.50	17.09	
SFKFPILE	110.43	1.86	21.00	1.21	8	979.54	2.58	P19084
SFKLPILQ	27.90		4.82		8	944.57	18.14	A0A9K3HVJ0
SFNVDQETAQKL	18.68	6.94			12	1378.67	2.50	P19084
SLFLPS	40.52		28.73	1.05	6	662.36	12.16	A0A251UYX1
SLLFSP	49.73		21.48		6	662.36	7.78	
SLWN	31.56				4	518.25	12.16	A0A251V6N9

SPLAGY		10.50	3.41	5.61	6	606.30	7.78	A0A251UYX1
SPQIT				14.65	5	544.29	20.22	A0A9K3NGE6
SPY				6.85	3	365.16	3.98	Q39928
SREDAQQL	30.73		6.76		8	945.45	4.33	A0A9K3NGE6
SVFDNELRE	12.93				9	1107.52	1.84	P19084
SYPRLL	61.67		21.45		6	747.43	13.33	A0A251UYX1
SYQVSPN	17.35		9.82		7	793.36	11.11	
SYVNTPILA		19.31			9	976.52	2.30	A0A251TKL9
TEF		3.72		15.40	3	395.17	11.36	A0A251TUS1
TELL		23.36		14.09	4	474.27	13.81	A0A251UYX1
TELV				28.40	4	460.25	13.81	P19084
TLNVTP	20.34	4.44	10.46		6	643.35	3.65	A0A9K3JEW0
TNPI		6.81		5.53	4	443.24	2.71	A0A251TMX5
TPELIAQS		13.91		1.61	8	857.45	2.30	P19084
TPILA		33.72	2.41	70.05	5	513.32	30.95	A0A251TKL9
TPILAF		29.17		17.84	6	660.38	26.18	
TPILF		19.50	1.91	30.67	5	589.35	24.30	A0A251TUS1
TPL				9.03	3	329.20	3.98	
TPLL	5.24	49.04	8.76	74.67	4	442.28	13.81	A0A9K3JEW0
TSF	15.18	12.61	19.78	15.41	3	353.16	18.44	A0A251UYX1
TTRAPRLGSPE	75.48				11	1183.63	7.04	A0A251UYX1
TVDLL	63.54		22.72		5	559.32	9.64	A0A9K3NGE6
TVL				1.23	3	331.21	3.98	
TVVY	12.86		12.44		4	480.26	13.81	A0A251UYX1
VAF	6.94	6.58	9.62	3.69	3	335.18	11.36	
VAR			5.85	11.32	3	344.22	18.44	P15461
VDL				9.74	3	345.19	11.36	A0A9K3NGE6
VDQETAQKL		32.88		4.26	9	1030.53	4.33	P19084
VFRAMPL	21.12		10.44		7	832.46	3.24	
VIVQ	12.85		9.90		4	457.29	29.93	A0A251UYX1
VLF	8.47	8.23	13.09	10.28	3	377.23	3.98	
VLFAPS	15.81		9.05		6	632.35	8.64	P19084
VLFTPG	15.81				6	632.35	9.64	A0A251TUS1
VLK	2.68	3.62	3.09	0.99	3	358.26	3.98	A0A251T566
VLL	6.77		7.98	1.51	3	343.25	3.98	A0A9K3JEW0
VLQ	4.09		3.91		3	358.22	9.49	A0A251TVT1
VLQA	64.10		60.37		4	429.26	33.73	A0A251V6N9
VLY	8.81		7.02		3	393.23	3.98	A0A251T566
VPQ		3.93		5.98	3	342.19	8.08	A0A251UYX1
VQN	10.07		15.84		3	359.18	9.49	A0A251TUS1
VSF	22.64	21.46	32.52	27.59	3	351.18	18.44	P19084
VSL	7.86	5.03	9.73	6.72	3	317.20	3.98	A0A251TUS1
VSRGDIFPVPQ	122.49				11	1213.65	28.23	
VSRGDIFPVPQF	27.54				12	1360.71	3.88	A0A251UYX1
VTE	7.75		6.64	4.52	3	347.17	3.98	
VVAII	11.26		7.57		5	513.35	12.16	

VVAIIV	26.40		10.89		6	612.42	16.21	
VVF				4.04	3	363.22	3.98	P19084
VVRPPIRIQ	161.43				9	1076.68	49.55	A0A9K3HVJ0
VVVIPQ	8.50		6.08		6	653.41	4.66	P19084
VVVVF	9.12		6.85		5	561.35	12.16	A0A251TKL9
VVY		8.43		5.24	3	379.21	3.98	
WTVN			28.66		4	518.25	12.16	A0A251UYX1
WTY	12.17	4.67	10.86		3	468.20	3.98	
YINTPL	42.69		18.53		6	719.39	9.64	A0A9K3HVJ0
YQPSFQ	11.72		8.53		6	768.34	7.78	A0A251TUS1
YSP				2.08	3	365.16	3.98	A0A9K3NGE6
YTNTPILFY	12.90				9	1130.56	2.30	A0A251TUS1
YTSQPNQRLE	15.46				10	1234.59	1.48	A0A251UYX1
YVNTPIL	49.40		19.22		7	818.45	18.56	A0A251TKL9

Prot: Protamex® hydrolysate; Prot+Flav: Protamex® followed by Flavourzyme® hydrolysate; ≤ 1kDa: 1kDa ultrafiltrated hydrolysate.

Appendix 6.1. The peptide concentration and degree of hydrolysis (DH) of hydrolysates prepared by different enzymatic treatments determined by OPA assay.

Samples	mM eq. NH_2	Degree of hydrolysis (%)
TSG	0.26 ± 0.01^{a}	--
Alc	1.44 ± 0.06^{b}	19.70 ± 1.08^{a}
Alc+Flav	2.02 ± 0.08^{c}	29.74 ± 1.29^{b}
≤ 1kDa Alc	1.79 ± 0.07^{d}	--
≤ 1kDa Alc+Flav	2.93 ± 0.10^{e}	--

Different letters in the same column indicate the significant difference between the hydrolysates and their ≤ 1 kDa fractions (*p-value* < 0.05). n=5. Alc: Alcalase® hydrolysate; Alc+Flav: Alcalase® followed by Flavourzyme® hydrolysate; ≤ 1 kDa: 1 kDa ultrafiltrated hydrolysate.

Appendix 6.2. Peptides sequences identified from ≤ 1 kDa fractions of Tilapia scale gelatin hydrolysates using nano-LC-MS/MS analysis.

Sequence	Intensity (x 10^7)		Length	Mass (g/mol)	Score	Entry
	≤ 1 k Da Alc	≤ 1 kDa Alc+Flav				
AGPAGPPGPT	339.30		10	820.41	79.45	A0A668V4P2
AGPAGPRGPA	7.42		10	849.45	68.79	G9M6I5
AGPQGPIGPR	650.88	2.50	10	948.51	122.18	A0A668V4P2
AGPSGPAGPRG	55.45		11	922.46	61.69	A0A669BAB1
AGPTGPAGPL	24.85	626.15	10	836.44	99.38	I3JXH5
AGPTGPAGPLG	2.17		11	893.46	84.92	I3JXH5
AGPVGEPGKQ	187.39	153.50	10	938.48	129.42	G9M6I5
APDPGPGPM	1.62		9	837.37	76.85	I3JXH5
ATGAAGEAGAP	4.90		11	871.40	93.20	I3JGN1
APGNIGLPG		0.90	9	794.43	68.49	I3JXH5
DAGRAGEPGA		22.81	10	899.41	69.63	I3JXH5
DLGFM	10.48		5	581.25	52.86	G9M6I5
EFVSQPL	251.99		7	818.42	143.02	A0A669BAB1
EKAPDPF	72.65		7	802.39	92.19	G9M6I5
FPGLPGPS		1.76	8	770.40	77.94	I3JMB4
FVSQPL	1914.60		6	689.37	69.09	A0A669BAB1
FVSQPLQ	3.06		7	817.43	128.86	A0A669BAB1
GAAGPAGPR	76.88		9	752.39	63.31	G9M6I5
GAAGPAGPRGPA	2.54		12	977.50	93.14	G9M6I5
GAPGNIGLPG	6.14		10	851.45	60.97	A0A668V4P2
GAPGNIGLPGM	3.51	2.67	11	982.49	120.62	A0A668V4P2
GARGPPGE	24.91		8	739.36	68.79	G9M6I5
GASGPAGPR	79.00		9	768.39	96.19	I3JXH5
GAVGPVGPS	3.29		9	739.39	101.21	A0A668V4P2
GDAGPPGPTGPA	10.22	9.65	12	992.46	85.86	A0A669BAB1
GDRGETGL	39.84		8	803.38	63.31	I3JMB4
GDSGPAGPK	17.07		9	784.37	96.19	A0A669BAB1
GDNGPPGLT		7.94	9	826.38	112.41	I3JXH5
GEAGPTGGR	13.84		9	800.38	76.77	I3KK22
GELGPIGPL	0.18		9	851.48	76.85	I3KK22
GENGIPGALG	42.24		10	883.44	56.72	A0A669BAB1
GERGPSGA	13.58		8	729.34	60.12	A0A668V4P2
GETGPVGAT	0.06		9	787.37	63.31	A0A668V4P2
GFMVQPQ	4.83		7	805.38	130.01	G9M6I5
GFPGLPGPS		0.31	9	827.42	68.49	I3JMB4
GFSGL	218.73		5	479.24	76.27	G9M6I5
GFSGLDGAKG	0.94		10	907.44	56.43	G9M6I5
GFTGA	75.59		5	451.21	66.54	A0A669BAB1
GFTGL	3.09		5	493.25	66.54	A0A669DZD5
GFTGPPGE	99.74		8	760.34	90.78	G9M6I5

GGGYDVSGGY	12.42		10	930.37	76.77	A0A668V4P2
GGVGEPGR	4.69	5.01	8	727.36	58.78	A0A668V4P2
GGVGEPGRL	400.95		9	840.45	77.32	A0A668V4P2
GGVGEPGRLG	8.19		10	897.47	77.32	A0A668V4P2
GKRGPTGEIG	280.48		10	970.52	58.23	A0A668V4P2
GKTGDRGETGPA	30.95		12	1144.55	120.63	G9M6I5
GIVGLPGQR		8.42	9	895.52	68.49	G9M6I5
GLPGPAGPPGE	3.62	40.68	11	947.47	113.41	A0A669BAB1
GLPGPSGE	0.36		8	712.34	57.81	A0A669DZD5
GLQGF	4.51		5	520.26	52.86	A0A668V4P2
GPAGARGEP	8.32		9	810.40	110.12	G9M6I5
GPAGPA	3.13		6	468.23	56.94	A0A668V4P2
GPAGPPGFPGGA	18.13	2.79	12	980.47	114.59	I3JMB4
GPAGPRGPS	2.54		9	794.40	68.79	I3JXH5
GPAGPRGPSGE	100.21	1.89	11	980.47	77.53	I3JXH5
GPAGVRGPA	12.85		9	780.42	71.38	I3JMB4
GPIGVP		22.39	6	538.31	56.94	I3JMB4
GPPGAP		200.53	6	494.25	32.32	G9M6I5
GPPVPGPI		4.16	8	732.42	131.47	I3JMB4
GPSGLAGPA		2.40	9	725.37	68.49	I3JXH5
GPSGPAGPA		0.43	9	709.34	68.49	I3JMB4
GPTGPAGPL		3.53	9	765.40	94.01	I3JXH5
GPPGFPGGA	12.71		9	755.36	100.36	I3JMB4
GPPGLSGPTGE	1.22		11	967.46	87.70	A0A669BAB1
GPPGPA	2.78		6	494.25	56.94	A0A668V4P2
GPPGPPGSGF	2.70	1.60	10	868.41	138.24	A0A669BAB1
GPPGPPGSSGPQ	4.76		12	1033.48	77.53	G9M6I5
GPPVPGPIGPM	6.62		11	1017.53	60.29	I3JMB4
GPSGARGPPGE	0.89		11	980.47	66.92	G9M6I5
GPSGPRGPAGPH	20.22	160.12	12	1085.54	120.63	I3JXH5
GPVGERGAP	0.70		9	838.43	68.79	A0A669BAB1
GPVGNTGPK	58.39		9	825.43	74.26	G9M6I5
GPVGPS	1405.00		6	512.26	58.26	A0A668V4P2
GSSGPVGER	110.60		9	844.40	63.53	A0A669BAB1
GVGEPGRL	22.55		8	783.42	71.30	A0A668V4P2
GVRGPAGP	2.44		8	709.39	62.98	I3JMB4
GVRGPAGPA	458.89		9	780.42	68.49	I3JMB4
GVTGE	19.06		5	461.21	71.48	A0A669BAB1
IAGPTGPR	8.81		8	767.43	68.79	A0A669BAB1
KDGLPGPPGPA		27.83	11	1004.53	67.49	I3JXH5
KPGERGPA	1.94		8	810.43	62.11	I3KK22
KSPAMPVPGPM	17.44		11	1110.56	88.18	G9M6I5
MPVPGPM	1.55	2.39	7	727.34	110.20	G9M6I5
NIGLPGMTGPQ	4.93		11	1083.54	89.03	A0A668V4P2
PFRMY	64.08		5	712.34	62.09	G9M6I5
PGPDGKIGPS	27.81		10	923.47	72.24	G9M6I5

PTGPAGPL	2.68	2.07	8	708.38	86.94	A0A668V4P2
QEKAPDPL	15.35		8	896.46	99.38	A0A669BAB1
QGPSGSPGFQ	6.89		10	960.43	59.93	A0A668V4P2
RGDQGPK		0.10	7	756.39	29.15	G9M6I5
RGEPGGAGPR	11.62		10	952.48	90.60	A0A669BAB1
RGESGPAGA	0.12		9	800.38	66.43	G9M6I5
RGGAGPAGPR	0.96		10	894.48	69.63	A0A668V4P2
SAGPQGPIGPR	20.01		11	1035.55	79.49	A0A668V4P2
SGLPGPAGPPGE	2.35		12	1034.50	81.53	A0A669BAB1
SGPQGPA	6.95		7	612.29	62.98	A0A669BAB1
SGPRGPAGPH	4.58	7.85	10	931.46	95.82	I3JXH5
SGPVGER	7.63	52.42	7	700.35	62.11	A0A669BAB1
SGPAGAP		3.39	7	555.27	72.62	G9M6I5
SGSPGAPGAP	2.69		10	796.37	73.98	A0A669BAB1
SPAMPVPGPM		22.25	10	982.46	102.77	G9M6I5
SPGATGFPGPA		0.70	11	957.46	37.81	I3JMB4
SSGPVGER	7.14		8	787.38	58.23	A0A669BAB1
STPVGPTGPK	8.43		10	939.50	56.72	I3JMB4
VGEPGRL		3.37	7	726.40	68.49	I3JXH5
VGPTGPAGPL	18.06		10	864.47	63.31	A0A668V4P2
YDVSGGY		1.50	7	759.31	62.98	I3JXH5
Total peptides	88	34				

Alc: Alcalase® hydrolysate, Alc+Flav: Alcalase® followed by Flavourzyme® hydrolysate; ≤ 1 kDa: 1 kDa ultrafiltrated hydrolysate.

Appendix 6.3. Effects of Cu^{2+} coordination by EDTA and peptides present in TSG hydrolysates on the lifespan-extension of Cu^{2+}-exposed nematodes.

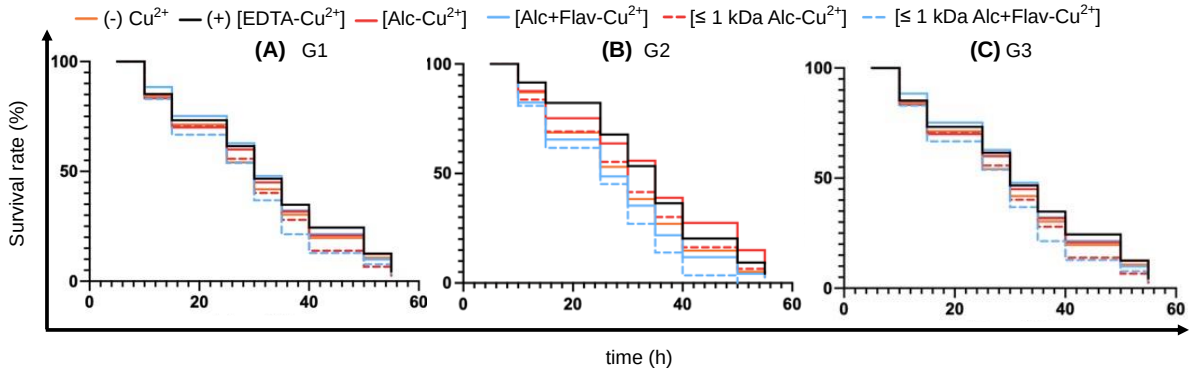

Alc: Alcalase® hydrolysate, Alc+Flav: Alcalase® followed by Flavourzyme® hydrolysate; ≤ 1 kDa: 1 kDa ultrafiltrated hydrolysate.

Appendix 7.1. Peptides sequences identified from ≤ 1 kDa fractios of sunflower meal protein hydrolysates using nano-LC-MS/MS analysis.

Sequence	Intensity (x 10^5)		Length	Mass (g/mol)	Score	Entry
	≤ 1 k Da Prot	≤ 1 kDa Prot+Flav				
ADFVNPQ		80.25	7	789.37	66.43	A0A251UCD5
ADVFNR	2342.80	991.20	6	720.36	100.27	A0A251UYX1
ADVFNRQ	243.75	369.04	7	848.41	79.45	A0A251UYX1
AEDFQVL	633.42		7	820.40	73.98	A0A251T566
AEKGHLQPN	1374.10	793.12	9	992.50	74.26	A0A251UYX1
AERGVLY	31436.00	2792.40	7	806.43	76.85	A0A9K3HVJ0
AGEQGSRW	592.41	410.52	8	889.40	90.37	A0A251UCD5
AGGISSEH		2264.10	8	756.34	79.94	A0A251UYX1
AGGISSEHIQ		536.94	10	997.48	74.17	A0A251UYX1
AGVDFIRH		1199.30	8	913.48	71.88	A0A251UCD5
AGVEVIRH		293.55	8	879.49	54.78	A0A9K3HVJ0
AHEIIHVT	5959.90		8	918.49	82.31	A0A9K3HVJ0
AIIVDDVNN		58.86	9	971.49	134.81	A0A251UYX1
AIQEVAR		102.18	7	785.44	47.66	P15461
AIQEVARR		104.47	8	941.54	56.72	P15461
AIQSPHW	198.95	1713.00	7	837.41	101.21	A0A251UCD5
AIQSPHWT	39422.00	688.84	8	938.46	96.19	A0A251UCD5
AKLVFNL		49.48	7	803.49	88.64	A0A251UYX1
AKTSFLA		729.05	7	736.41	55.50	A0A251UYX1
ALEPIER		543.63	7	826.45	57.81	A0A251TUS1
ALEPIEVI	190.17		8	882.51	68.49	A0A251UCD5
ALPAGAVHW	283.09		9	920.49	100.36	A0A251T566
ALPVDVL	820.21	3051.70	7	725.43	120.06	A0A251TUS1
ALPVDVLA		1475.00	8	796.47	71.38	A0A251TUS1
ALPVDVLAN	69.70	622.26	9	910.51	110.12	A0A251TUS1
ALPVDVLANA		268.18	10	981.55	58.23	A0A251TUS1
ALQESR		212.47	6	702.37	76.85	A0A251UYX1
ALQESRN		252.36	7	816.41	56.72	A0A251UYX1
AMPVSVLM	1102.40		8	846.43	114.60	A0A9K3HVJ0
ANEQGSRW	380.25	81.27	8	946.43	77.32	A0A251TAA6
APHYNLN	317.99		7	827.39	65.90	A0A251T566
APLKSPL	874.89		7	724.45	94.01	A0A251UYX1
APRLGSPE	4721.70		8	825.43	96.19	A0A251UYX1
APSFSRG		305.41	7	720.36	53.35	A0A251UCD5
AQQLKF		1650.30	6	733.41	104.94	A0A251UCD5
AREGFGL	1928.70	181.97	7	748.39	94.01	A0A251UCD5
ASAREGFG	3110.30	235.95	8	793.37	93.20	A0A251UCD5

ASAREGFGL	331.64		9	906.46	53.09	A0A251UCD5
AVFDDMIQ	66.10		8	937.42	58.78	A0A9K3HVJ0
AVHWTY		178.52	6	775.37	63.67	A0A251T566
AVYWTY		38.22	6	801.37	81.00	A0A251UYX1
AVYWTYN		28.79	7	915.41	49.21	A0A251UYX1
CEPYIVR		76.09	7	935.45	47.92	A0A251UYX1
CRWISF		782.23	6	867.41	69.09	A0A9K3HVJ0
DDRGLIVL	123.90	5039.40	8	899.51	65.80	A0A251T566
DDWVQE		47.16	6	790.31	96.05	A0A251T566
DFAVIK	23156.00	1902.80	6	691.39	95.38	A0A251T566
DFIRHR		1622.70	6	842.45	65.90	A0A251UCD5
DFQAK	229.05	31.32	5	607.30	72.62	A0A251UYX1
DFVNPQ	2684.40		6	718.33	90.94	A0A251UCD5
DFVNPQA		1591.50	7	789.37	82.31	A0A251UCD5
DFVNPQAG		136.03	8	846.39	49.44	A0A251UCD5
DGNTELVVV		579.99	9	944.48	62.11	A0A251TAA6
DGQEEIVAI		66.04	9	972.48	54.78	A0A9K3HVJ0
DIFPVPQ	948.95	805.69	7	814.42	101.21	A0A251UYX1
DIFPVPQF	2288.00	405.09	8	961.49	90.78	A0A251UYX1
DIPWPF	226.23	58.56	6	773.37	71.48	Q39928
DLSAEKGY		49.28	8	881.41	45.97	A0A9K3J8S2
DNILRGF	73.36	707.83	7	833.44	102.77	A0A251TUS1
DQETAQKL		572.35	8	931.46	75.04	A0A251UCD5
DQFHR	1450.20	1824.10	5	701.32	57.45	A0A9K3HVJ0
DQFHRR	8467.70	1199.40	6	857.43	74.52	A0A9K3HVJ0
DRNFKKF	2129.00	42.97	7	953.51	63.31	A0A251T566
DTSNVANQL		149.59	9	960.45	93.14	A0A251T566
DVNNPANQL	1556.40	994.67	9	983.47	115.49	A0A251UYX1
DVSRPDF		5292.60	7	834.39	53.35	A0A9K3HVJ0
DVYNPR	1978.30	1389.30	6	762.37	57.45	A0A251T566
EDAKILKY		130.97	8	978.54	85.36	A0A251T566
EDAQQLKF		2327.00	8	977.48	111.65	A0A251UCD5
EEAQQLKF		688.00	8	991.50	124.59	A0A251TKL9
EEQEWE		195.97	6	848.32	60.40	A0A251T566
EFFDSGDQ		64.39	8	943.36	95.82	A0A9K3HVJ0
EFFNSN	11082.00		6	756.31	88.64	A0A251TUS1
EFWDSF	295.10	44.58	6	829.33	85.91	A0A251T566
EFWDSFE	183.07	27.06	7	958.37	110.34	A0A251T566
EGDILALPAG		46.45	10	954.50	79.45	A0A251T566
EGDMIIIPA		224.93	9	957.48	47.92	A0A9K3HVJ0
EGFGL	8940.50	9142.70	5	521.25	66.54	A0A251UCD5
EGGFIE		1185.00	6	650.29	54.90	A0A9K3J8S2
EGGREQFF		430.43	8	968.44	82.31	A0A251T566

EGQLIVVPQ	326.80	66.23	9	981.55	104.06	A0A251T566
EGQVVVIPQ		479.92	9	967.53	75.04	A0A251UCD5
EGRKGGGAF	330.24	5471.70	9	877.44	131.03	A0A251TUS1
EHKLPIL	29084.00		7	848.51	74.52	A0A251UYX1
EHKLPILS	4144.60	45.90	8	935.54	111.65	A0A251UYX1
EIIHVT		1497.90	6	710.40	77.94	A0A9K3HVJ0
EIPFDMPF	78.49	49.23	8	994.45	109.70	Q39928
EIWDANDQ	12217.00	6572.60	8	989.41	241.30	A0A251UCD5
EIWDAY	3830.20	1739.50	6	795.34	95.38	A0A251TKL9
ELREGQVV		257.69	8	928.50	58.78	A0A251UCD5
ENQLDEY		308.37	7	909.37	96.19	A0A251UCD5
EPIEVIQ		176.34	7	826.44	110.34	A0A251UCD5
EPIEVIQA		2297.60	8	897.48	63.31	A0A251UCD5
EQGSRWVS		443.13	8	947.45	84.92	A0A251UCD5
EQQGEPW	420.55	148.67	7	872.37	62.98	A0A251T566
ERGELRPN		2132.70	8	969.50	62.11	A0A251UCD5
ERGVLY		531.28	6	735.39	63.67	A0A9K3HVJ0
ERGVLYN		64.47	7	849.43	76.85	A0A9K3HVJ0
ETVLF	24966.00	29310.00	5	607.32	66.54	A0A251UCD5
ETVLFA		143.68	6	678.36	67.33	A0A251UCD5
ETVLFAP		51.56	7	775.41	100.36	A0A251UCD5
ETVLFAPS	159.54		8	862.44	82.31	A0A251UCD5
EVFHVD		911.29	6	744.34	63.67	A0A9K3HVJ0
EWVAF		12.29	5	650.31	66.54	A0A251UYX1
EYSQEQ	731.22	428.17	6	782.31	77.94	A0A251UCD5
FDDEILQ		204.66	7	878.40	101.21	A0A251T566
FDIPWP	490.71	654.05	6	773.37	81.00	Q39928
FDLQML		18.89	6	765.37	62.98	A0A9K3HVJ0
FDNELRE		548.13	7	921.42	67.49	A0A251UCD5
FEGGFIE	3942.90	2176.20	7	797.36	68.49	A0A9K3J8S2
FEIPFDMP	18.22	42.72	8	994.45	50.03	Q39928
FEWVAF		58.62	6	797.37	63.67	A0A251UYX1
FFDSGDQQ		55.91	8	942.37	76.77	A0A9K3HVJ0
FFDTQ	3717.90		5	656.28	72.62	A0A251UCD5
FIEQGEGL	282.33		8	891.43	85.16	A0A251UYX1
FIRHR	5800.50	270.66	5	727.42	86.11	A0A251UCD5
FKFPIL	3057.20	20.39	6	763.46	76.55	A0A251UCD5
FKFPILE	1465.40	52.20	7	892.51	68.49	A0A251UCD5
FKKFF	201.72	141.36	5	715.41	58.26	A0A251T566
FKLPILQ	578.52	13.67	7	857.54	88.64	A0A9K3HVJ0
FLAGNPQ	209.10		7	745.38	62.98	A0A251UCD5
FLAGNPQAQ	885.78		9	944.47	124.59	A0A251UCD5
FLPSFQ	3674.00	173.59	6	737.37	109.70	A0A251UYX1

FLPSFQS	57.34	16.06	7	824.41	68.49	A0A251UYX1
FPILE	31.00	26.36	5	617.34	52.86	A0A251UCD5
FPILEH		5731.70	6	754.40	81.00	A0A251UCD5
FPILEHL	3111.30	7487.90	7	867.49	136.44	A0A251UCD5
FPILEHLQ		160.14	8	995.54	74.26	A0A251UCD5
FPILQFL	19.64		7	876.51	69.09	A0A251TUS1
FPVPQF		103.53	6	733.38	81.00	A0A251UYX1
FPVPQFF		89.02	7	880.45	63.67	A0A251UYX1
FQAKTSF		200.22	7	827.42	87.75	A0A251UYX1
FQNSGNIF	2114.70		8	925.43	60.97	A0A251UCD5
FQPFPR	4590.40		6	790.41	86.94	A0A251UYX1
FQPFPRL	3237.60		7	903.50	74.52	A0A251UYX1
FQSYPR	11787.00	221.64	6	796.39	106.42	A0A251UYX1
FQSYPRL	17386.00	33.84	7	909.47	115.46	A0A251UYX1
FREGDII	1368.10		7	848.44	55.50	A0A251UYX1
FREGDIIA	863.70	4765.60	8	919.48	51.34	A0A251UYX1
FRQGDVV	1638.80		7	819.42	114.59	A0A251TUS1
FSPHWT	362.88		6	773.35	65.90	A0A251UYX1
FSPHWTVN	8234.70	63.71	8	986.46	87.70	A0A251UYX1
FSRGQGIR	1136.60		8	919.50	76.77	A0A251TAA6
FTPELIAQ	232.51	69.45	8	917.49	76.77	A0A251TKL9
FTPGGSYTR	22730.00		9	984.47	54.72	A0A251TUS1
FTTETLAEA		256.44	9	981.47	96.19	A0A251TUS1
FTVDL		27.28	5	593.31	58.26	A0A251UCD5
FTVDLL	50462.00	328.44	6	706.39	85.91	A0A251UCD5
FTVDLLAQS		56.83	9	992.52	93.14	A0A251UCD5
GAVHWTY	928.44		7	832.39	69.09	A0A251T566
GCRWISF		1178.50	7	924.43	45.95	A0A9K3HVJ0
GDIFPVPQ	548.74	5102.90	8	871.44	102.77	A0A251UYX1
GDILALPA	403.34	95.17	8	768.44	109.70	A0A251T566
GDMIIIPA	48.58		8	828.44	62.98	A0A9K3HVJ0
GDVVAIPT	578.99	338.74	8	770.42	99.38	A0A251UCD5
GEQGSRW	241.69	1945.50	7	818.37	54.78	A0A251UCD5
GFDDEILQ		603.89	8	935.42	45.95	A0A251T566
GFEWVAF	3855.90	53.25	7	854.40	110.17	A0A251UYX1
GFEWVAFK	2537.60	27.31	8	982.49	68.79	A0A251UYX1
GFQDRH		1101.70	6	758.35	68.49	A0A9K3HVJ0
GFTPELIAQ	220.99	477.52	9	974.51	107.01	A0A251TKL9
GFTVDLLA		25.32	8	834.45	79.94	A0A251UCD5
GGDIFPVPQ		357.01	9	928.47	52.94	T1WKB1
GGGAFTDRH		315.59	9	916.42	77.32	A0A251TUS1
GGISSEHIQG		4119.50	10	983.47	98.58	A0A251UYX1
GGRAPGRGW	10113.00	3636.00	9	912.47	45.95	A0A251TAA6

GHIIFVQN		2079.00	8	926.50	52.30	A0A251TUS1
GHIIFVQNG		4150.90	9	983.52	65.80	A0A251TUS1
GHIVNVGQ		116.41	8	822.43	55.50	A0A251UCD5
GHIVNVGQD		331.19	9	937.46	75.04	A0A251UCD5
GIEQTIC		49.11	7	819.38	94.01	A0A251T566
GIVSPHW	137.04		7	794.41	76.55	A0A251TUS1
GLEWVAF	340.78		7	820.41	69.09	A0A251UYX1
GLEWVAFK	91.90		8	948.51	79.45	A0A251UYX1
GLLLPSY		20.13	7	761.43	95.38	A0A251UCD5
GLMLPSY	98.05		7	779.39	69.09	A0A9K3HVJ0
GNIFNGF	152.69	303.99	7	767.36	140.01	A0A251UCD5
GNIFNGFTP		21.64	9	965.46	54.78	A0A251TKL9
GNMRIQ	1399.70	779.74	6	717.36	95.38	A0A251TUS1
GNSVFDN	6283.30	108.15	7	751.31	71.30	A0A251UCD5
GNSVFDNEL		48.54	9	993.44	78.26	A0A251UCD5
GQDELVII	603.97	159.41	8	885.48	111.65	A0A251TUS1
GQDELVIIA	179.07	75.22	9	956.52	68.79	A0A251TUS1
GQLIVVPQ	1355.80	75.49	8	852.51	111.65	A0A251T566
GQNAGNIF		92.18	8	819.39	85.36	A0A251TKL9
GQVVVIPQ	6220.60	785.88	8	838.49	79.45	A0A251UCD5
GQVVVIPQN	2127.60	516.16	9	952.53	113.41	A0A251UCD5
GQVVVVPQ	893.57		8	824.48	87.75	A0A9K3HVJ0
GRPQQQF	2209.50	3314.00	7	859.43	124.32	A0A251UCD5
GSDNIFKGF	381.57	437.01	9	983.47	69.63	A0A251TVT1
GSGSISPIK	849.42	117.98	9	844.47	80.46	A0A251T566
GSRWVSF	51368.00	797.33	7	837.41	58.78	A0A251UCD5
GTYPSRM	6110.90	99.41	7	810.37	55.50	A0A251UYX1
GTYPSRMT	6385.10	866.70	8	911.42	74.26	A0A251UYX1
GVDFIR	8691.20	1500.20	6	705.38	77.94	A0A251UCD5
GVDFIRH	65397.00	27065.00	7	842.44	96.05	A0A251UCD5
GVDFIRHR	7.39		8	998.54	58.78	A0A251UCD5
GVEETICS		222.03	8	893.38	106.42	A0A251UCD5
GVEETICSA		664.64	9	964.42	129.68	A0A251UYX1
GVEVIRH	4524.30	1334.20	7	808.46	79.94	A0A9K3HVJ0
GVHFIR	1489.80		6	727.41	81.00	A0A251TAA6
GVILPGCPE		86.31	9	940.47	53.35	A0A251TKL9
GVIVQVQ	145.86	3168.80	7	741.44	65.90	A0A251UYX1
GVIVQVQQ		271.33	8	869.50	138.48	A0A251UYX1
GWDNILR	28047.00	964.59	7	872.45	102.77	A0A251TUS1
GWDNILRG	7284.60	615.47	8	929.47	68.79	A0A251TUS1
GYTSVFR		243.29	7	828.41	55.50	A0A251UYX1
HEIIHVT	13.63	3216.90	7	847.46	88.64	A0A9K3HVJ0
HIIFVQ		2081.30	6	755.43	67.33	A0A251TUS1

HIIFVQN	56.91	2351.30	7	869.48	81.72	A0A251TUS1
HIIFVQNG		3736.80	8	926.50	54.77	A0A251TUS1
HIVNVGQD		423.13	8	880.44	45.97	A0A251UCD5
HQKIRHF	547.47		7	964.54	62.98	A0A9K3HVJ0
HRIQPGGL	9794.40		8	876.49	97.47	A0A251UCD5
HYWNF	4975.00	400.49	5	765.32	56.94	A0A251UYX1
IADVYNPR	11805.00	192.18	8	946.49	93.20	A0A251T566
IDNPSHAD	421.63	664.06	8	867.37	67.49	A0A251UCD5
IDNPSQA	17291.00	15079.00	7	743.34	76.77	A0A251TKL9
IDQETAQK		2818.40	8	931.46	117.81	A0A251UCD5
IEALEPIE	132.16	116.42	8	912.48	35.62	A0A251TAA6
IEQGEGLVG		376.49	9	900.46	49.54	A0A251UYX1
IERGRGIQ	16539.00	4982.20	8	927.53	58.78	A0A251UCD5
IERGRGIQG	2318.70	1623.30	9	984.55	87.70	A0A251UCD5
IFPVPQ	7642.60	985.24	6	699.40	123.06	A0A251UYX1
IFPVPQF	2031.50	194.69	7	846.46	57.45	A0A251UYX1
IFPVPQFF		84.32	8	993.53	65.90	A0A251UYX1
IFRGFD	144.24		6	753.38	65.90	A0A9K3HVJ0
IIFVQNG		367.89	7	789.44	95.38	A0A251TUS1
IIRPPQ	961.28	937.23	6	722.44	77.94	A0A251UCD5
IIRPPQA		225.16	7	793.48	62.98	A0A251UCD5
IIRPPQAR	3525.80	776.72	8	949.58	60.29	A0A251UCD5
IIRPPQQ	185.94	374.26	7	850.50	74.52	A0A251TAA6
IIRPPQQH	448.18	123.48	8	987.56	50.03	A0A251TAA6
IPTGAAHW		346.17	8	851.43	86.94	A0A251TUS1
IPWPFRP	89.52	305.60	7	911.50	60.40	Q39928
IPWPFRPS	2852.50	4605.30	8	998.53	99.38	Q39928
IQALEPIE	3296.50		8	911.50	66.43	A0A251UCD5
IQPGGLLLP		353.48	9	906.55	68.49	A0A251UCD5
IQPGGLLLPS	1136.60	41.19	10	993.59	79.71	A0A251UCD5
IQRPVSQ	2904.90		7	826.47	108.09	Q39928
IQSPHWT	9789.40	278.16	7	867.42	120.62	A0A251UCD5
IQSSRPY	577.40		7	849.43	58.78	Q39928
IRALPEE	610.45		7	826.45	85.36	A0A251T566
IRPPQAR	720.50		7	836.50	62.98	A0A251UCD5
ISSEHIQGQ	1256.60		9	997.48	70.82	A0A251UYX1
ITRQGRPQ	548.25		8	954.54	84.92	A0A251UCD5
IVNDL	1288.60		5	572.32	85.91	A0A251TUS1
IVNVGQDL	734.22		8	856.47	106.42	A0A251UCD5
IVNVGQDLQ	507.51	190.66	9	984.52	98.58	A0A251UCD5
IWDANDQ	487.83	129.05	7	860.37	73.98	A0A251UCD5
IWDAYDQ	400.88	63.79	7	909.39	82.31	A0A251TKL9
KAGNIFN	120.33		7	762.40	54.77	A0A251TAA6

KAGNIFNGF	421.00		9	966.49	58.78	A0A251TAA6
KFPILE	22612.00	589.73	6	745.44	110.17	A0A251UCD5
KFPILEHL	2857.00		8	995.58	99.38	A0A251UCD5
KFPILQ	3862.60		6	744.45	95.38	A0A251TUS1
KFPILQF	159.82		7	891.52	74.52	A0A251TUS1
KGHLQPN	8272.70		7	792.42	85.36	A0A251UYX1
KGHLQPNA	1722.30		8	863.46	60.97	A0A251UYX1
KLNRETE	3795.20		7	888.47	87.75	A0A251UYX1
KLPILQ	8626.00	59.31	6	710.47	164.83	A0A9K3HVJ0
KLPILQM	274.00		7	841.51	88.64	A0A9K3HVJ0
KLPILSL	138.93		7	782.53	79.94	A0A251UYX1
KLVFNL	193.09		6	732.45	77.94	A0A251UYX1
KSPLAGY	4556.70	49.63	7	734.40	73.98	A0A251UYX1
KTNDNAMIA	3507.00		9	976.46	85.16	A0A251UCD5
KTNRAPL	1234.50		7	798.47	76.85	A0A251UYX1
LDFQAK		2641.80	6	720.38	114.59	A0A251UYX1
LDFQAKT		212.86	7	821.43	118.74	A0A251UYX1
LDFQAKTS		1006.80	8	908.46	104.06	A0A251UYX1
LDNQRE	323.45	19.53	6	773.37	82.31	A0A251UYX1
LDSTNY	323.95		6	711.31	62.98	A0A251TUS1
LEFEGGSIE		36.19	9	979.45	90.37	A0A251UYX1
LEPIERVQ	239.33	458.22	8	982.54	51.19	A0A251TUS1
LEPIEVI	17.27	73.12	7	811.47	77.94	A0A251UCD5
LEPIEVIQ		132.00	8	939.53	96.19	A0A251UCD5
LFLPSFQ	109.36		7	850.46	88.64	A0A251UYX1
LFSPHW	124.66		6	785.39	96.04	A0A251UYX1
LKSPLAGY	1273.30		8	847.48	111.65	A0A251UYX1
LLFIEQ	183.66		6	761.43	85.91	A0A251UYX1
LLLPSYT		158.87	7	805.46	81.72	A0A251TUS1
LLLPSYTN		48.30	8	919.50	124.59	A0A251TUS1
LLLPSYVN		129.24	8	917.52	94.01	A0A251UCD5
LLLPYYPN	780.97	16.97	8	991.54	109.70	A0A251T566
LLPYYPN	1024.10	16.70	7	878.45	95.38	A0A251T566
LMLPSY	1361.00	55.55	6	722.37	81.00	A0A9K3HVJ0
LNALEPIE	116.42		8	897.48	104.75	A0A251TUS1
LNRETE	590.92		6	760.37	92.19	A0A251UYX1
LNRETESL	836.31		8	960.49	77.32	A0A251UYX1
LPAGAVHW		899.84	8	849.45	81.00	A0A251T566
LPGCVETF		81.31	8	921.43	52.30	A0A251T566
LPILQM		176.52	6	713.41	54.90	A0A9K3HVJ0
LPSFQP	164.54	95.47	6	687.36	60.40	A0A251UYX1
LPVDVLANA		331.92	9	910.51	111.65	A0A251TUS1
LQGQNDQR			8	957.46	67.49	A0A251UCD5

LQIIRPPQ		522.07	8	963.59	60.97	A0A251UCD5
LQVVRPPI	414.73		8	920.58	73.98	A0A9K3HVJ0
LSREEAQQ	87.98	374.11	8	959.47	45.97	A0A251TKL9
LTRDNVYA	4206.70		8	950.48	64.21	A0A251UYX1
LVSPHW	10829.00		6	737.39	81.00	A0A9K3J8S2
MPVDIVAN		1010.70	8	857.43	71.30	A0A251TAA6
MPVDVVAN		3139.20	8	843.42	90.78	A0A251UCD5
MTLQPNSL		149.67	8	902.45	60.12	A0A251UYX1
MVERGLQ	862.14		7	831.43	79.45	A0A9K3HVJ0
NAGNIFN	1215.10		7	748.35	54.77	A0A251TKL9
NALEPIE	445.65	49.76	7	784.40	82.31	A0A251TUS1
NALEPIER		349.26	8	940.50	45.97	A0A251TUS1
NDQRGHIV	12628.00	1091.00	8	937.47	71.88	A0A251UCD5
NDVSRPDF		436.02	8	948.43	112.41	A0A9K3HVJ0
NEHKLPIL	346.82		8	962.55	60.97	A0A251UYX1
NEQGSRW	399.54	289.05	7	875.39	85.16	A0A251TAA6
NEQGSRWV		183.83	8	974.46	87.70	A0A251TAA6
NFAVIKQ	1338.50		7	818.47	57.81	A0A9K3HVJ0
NFAVIKR	1939.90		7	846.51	60.29	A0A251UCD5
NFAVVK		374.84	6	676.39	90.94	A0A251TUS1
NFAVVKQ	2375.30		7	804.45	97.47	A0A251TUS1
NGFEWVAF		21.93	8	968.44	79.45	A0A251UYX1
NGFTVDLLA		26.10	9	948.49	64.21	A0A251UCD5
NGFTVELLA		23.25	9	962.51	71.88	A0A251TAA6
NIFRGFD	68.92	144.35	7	867.42	57.81	A0A9K3HVJ0
NILRGF		2116.20	6	718.41	57.45	A0A251TUS1
NLKEGDVVA		742.42	9	943.50	47.66	A0A251TKL9
NNAVMSPY	173.95		8	894.39	115.46	A0A9K3HVJ0
NQGNSVFDN			9	993.42	72.88	A0A251UCD5
NQLDEY	6127.70	289.16	6	780.33	86.94	A0A251UCD5
NQLDPNHR		1231.20	8	992.48	69.63	A0A251TUS1
NQLDRNF		129.53	7	905.44	53.35	A0A251T566
NQREADVF		497.29	8	977.46	90.37	A0A251UYX1
NRETESL	555.11		7	847.40	55.50	A0A251UYX1
NRGVIVQ	663.64	2102.80	7	784.46	68.49	A0A251UYX1
NRGVIVQV		1535.60	8	883.52	65.80	A0A251UYX1
NSFKFPIL	4081.00		8	964.54	71.88	A0A251UCD5
NSFKLPIL	734.12		8	930.55	71.88	A0A9K3HVJ0
NSGNIFNGF		109.60	9	968.44	93.20	A0A251UCD5
NTPILAF		32.87	7	774.43	79.94	A0A251UCD5
NTPILF		54.81	6	703.39	95.38	A0A251TUS1
NTPILFY	116.32	68.54	7	866.45	71.38	A0A251TUS1
NVDHETAE	260.95	304.58	8	913.38	58.78	A0A251TUS1

NVGQDL	1684.80	71.74	6	644.31	114.59	A0A251UCD5
NVYAGFD		185.66	7	784.34	62.98	A0A251UYX1
PFDIPWP	4388.70	724.79	7	870.43	81.72	Q39928
PISGQ		293.38	5	500.26	54.90	P15461
PSFQPFPR	130.38		8	974.50	66.43	A0A251UYX1
QADFVNPQ	69.61		8	917.42	60.97	A0A251TKL9
QCRETE	49.28	181.97	6	821.33	57.45	P15461
QEQEGYNM		71.88	8	997.38	108.09	A0A251T566
QEQQLL	1024.90		6	757.40	54.77	Q39928
QESVLF		17014.00	6	721.36	90.94	A0A251TUS1
QESVLFTPG		75.21	9	976.49	68.79	A0A251TUS1
QETAQKL	5254.70	293.45	7	816.43	97.47	A0A251UCD5
QETASKL	3984.00	475.00	7	775.41	90.78	A0A9K3HVJ0
QGDVVAIPT	55.77	419.63	9	898.48	74.26	A0A251TUS1
QGQNAGNIF		124.60	9	947.45	60.97	A0A251TKL9
QGQNIPR	947.03	81.44	7	811.43	101.21	P15461
QGRPQQQF	351.49	458.48	8	987.49	53.35	A0A251UCD5
QGRQGQQQ	168.09		8	928.45	94.01	A0A251UYX1
QGSRWVSF		329.14	8	965.47	66.43	A0A251UCD5
QIIRPPQ		651.90	7	850.50	71.38	A0A251UCD5
QIIRPPQQ		232.51	8	978.56	57.81	A0A251TAA6
QIWHQ	857.49		5	710.35	112.70	A0A251UYX1
QLIVVPQ	273.31	62.65	7	795.49	92.19	A0A251T566
QLVVVPQ	46073.00	1348.50	7	781.47	114.59	A0A251TUS1
QNAGNIFNG		1724.60	9	933.43	87.75	A0A251TKL9
QNSGNIFNG		1856.30	9	949.43	98.63	A0A251UCD5
QPGGLLLP	7.91	4741.30	8	793.47	104.94	A0A251UCD5
QPGGLLLPS		2168.60	9	880.50	53.35	A0A251UCD5
QPNQRLE	515.09	2933.40	7	883.45	53.35	A0A251UYX1
QPNSLFLP		792.31	8	914.49	53.35	A0A251UYX1
QPWWE		762.86	5	744.32	67.33	A0A251T566
QPWWET		95.00	6	845.37	90.94	A0A251T566
QPWWETS		9740.40	7	932.40	119.22	A0A251T566
QQGQRGQQ	559.57		8	928.45	79.94	Q39928
QQGRQGQQ		7.77	8	928.45	79.94	A0A251UYX1
QQLVVVPQ	226.84		8	909.53	79.94	A0A251TUS1
QQPWWE	2295.40	402.42	6	872.38	72.62	A0A251T566
QQQFQPR	18624.00		7	930.47	92.19	A0A251TUS1
QQVVAV		127.54	6	642.37	67.33	A0A251UYX1
QREADVF		685.07	7	863.41	47.92	A0A251UYX1
QRETVL	1432.00		6	744.41	77.94	A0A251UCD5
QRETVLF	3749.70	4053.10	7	891.48	65.80	A0A251UCD5
QRLEFE		517.27	6	820.41	83.29	A0A251UYX1

QRPGWE	1996.90		6	771.37	110.17	A0A251T566
QRPSWE	2841.20	2254.90	6	801.38	96.05	A0A251T566
QSPHWTIN	1333.30	4945.90	8	981.47	104.06	A0A251UCD5
QSPYEQR		182.54	7	906.42	56.72	Q39928
QVIQPPMR		179.99	8	967.53	47.92	A0A251TUS1
QVVRPPI		57.12	7	807.50	57.45	A0A9K3HVJ0
QVVVIPQ	2492.80	1275.80	7	781.47	92.19	A0A251UCD5
QVVVIPQN	913.60	593.30	8	895.51	63.31	A0A251UCD5
QYHPGQQ	4250.20	190.36	7	856.38	100.27	A0A251T566
RALPVDVL	23507.00		8	881.53	82.31	A0A251TUS1
RAPLKSPLA	217.33		9	951.59	71.88	A0A251UYX1
RDNVYAGF	1705.70	31846.00	8	940.44	90.78	A0A251UYX1
REDAKIL	8678.50	4019.90	7	843.48	53.35	A0A251T566
REGDILA		2467.40	7	772.41	53.35	A0A251T566
RETEIQ	238.99	1583.80	6	774.39	54.90	P15461
RETVLF	106.75	8678.20	6	763.42	57.45	A0A251UCD5
RGELRPN	47540.00	1833.80	7	840.46	82.24	A0A251UCD5
RGFQDR	11255.00	501.26	6	777.39	52.30	A0A9K3HVJ0
RGVIVQVQ		753.14	8	897.54	51.34	A0A251UYX1
RIQPGGL	37433.00	1296.00	7	739.43	65.90	A0A251UCD5
RNRGVIVQ	3128.10		8	940.56	76.85	A0A251UYX1
RPGWETRP		282.21	8	997.51	54.78	A0A251T566
RPPQDRR		16.97	7	923.50	60.97	A0A251TKL9
RPSWETR	448.42	7987.30	7	930.47	129.68	A0A251T566
RQESVL	1100.10		6	730.40	69.09	A0A251TUS1
RQQYQHQ	48.72		7	986.47	54.77	A0A251UCD5
RVQSEAGFT	1463.40		9	993.49	56.43	A0A251TUS1
RWISF	456.17		5	707.38	67.33	A0A9K3HVJ0
RWVSFK	141.91		6	821.45	69.09	A0A251UCD5
RYGIVSPH	3925.60		8	927.49	85.36	A0A251TUS1
SAREGFG	1737.60	1482.50	7	722.33	94.01	A0A251UCD5
SDNIFKGF	134.90		8	926.45	107.01	A0A251TVT1
SEHIQGQ	3111.50	2962.40	7	797.37	111.65	A0A251UYX1
SEVFHVD	5245.50	11254.00	7	831.38	73.98	A0A9K3HVJ0
SFKFPIL	30473.00	335.82	7	850.50	97.47	A0A251UCD5
SFKFPILE	24773.00		8	979.54	98.58	A0A251UCD5
SFKFPILQ	908.31		8	978.55	101.60	A0A251TUS1
SFKLPIL	6638.80	67.69	7	816.51	110.34	A0A9K3HVJ0
SFKLPILQ	9304.70	41.93	8	944.57	101.60	A0A9K3HVJ0
SFLAGGIS		302.83	8	750.39	71.30	A0A251UYX1
SFNVDQE	1879.60		7	837.35	116.90	A0A251TAA6
SFQSYP		190.65	6	727.32	81.72	A0A251UYX1
SFQSYPR		115.40	7	883.42	62.11	A0A251UYX1

SFQSYPRL	1548.50		8	996.50	87.70	A0A251UYX1
SGPEFCNL		641.08	8	922.39	93.20	A0A9K3J8S2
SHKLPVLE	710.82		8	921.53	60.97	A0A251T566
SKWISF		64.37	6	766.40	57.81	A0A251TVT1
SLFLPSFQ	1935.70	14.03	8	937.49	98.63	A0A251UYX1
SLLFSPQ	260.05		7	790.42	90.78	A0A251UYX1
SMPVDIVAN	2759.90	123.31	9	944.46	110.12	A0A251TAA6
SMPVDVVAN	5280.30	2283.80	9	930.45	110.12	A0A251UCD5
SNNGEAVLN		209.74	9	916.43	120.87	A0A251UYX1
SPEFCNL		608.96	7	865.36	88.64	A0A251UYX1
SPEQARSL	2324.40	6841.60	8	886.45	95.82	A0A9K3HVJ0
SPFGGQ		9961.20	6	591.27	65.90	A0A251UYX1
SPFGGQEE		533.16	8	849.35	111.65	A0A251UYX1
SPHWTI	65.16	733.87	6	739.37	69.09	A0A251UCD5
SPHWTIN	20408.00	35427.00	7	853.41	85.36	A0A251UCD5
SPHWTINA		129.26	8	924.45	49.44	A0A251UCD5
SPLAGYT	4625.60	7202.30	7	707.35	86.94	A0A251UYX1
SPYDRR	701.13	1457.50	6	792.39	71.38	Q39928
SPYEQR	314.72	1795.50	6	778.36	97.47	Q39928
SQPNQRLE	1044.40	834.27	8	970.48	49.54	A0A251UYX1
SQRETVL	1325.90		7	831.45	63.31	A0A251UCD5
SQRETVLF	4326.50	9361.80	8	978.51	71.88	A0A251UCD5
SQRPSWE	103.15	111.96	7	888.41	49.44	A0A251T566
SREDAQQL	3535.00	223.85	8	945.45	79.71	A0A251UCD5
SRWVSF		5567.10	6	780.39	71.38	A0A251UCD5
SRWVSFK		126.11	7	908.49	56.72	A0A251UCD5
STNEVNQL		29.63	8	903.43	47.66	A0A9K3HVJ0
SVFRAMPL	9494.70		8	919.49	60.97	A0A251UYX1
SYINTPL		12.86	7	806.42	82.31	A0A9K3HVJ0
SYPRLL	16303.00		6	747.43	74.52	A0A251UYX1
SYSIS	123.26	140.01	5	555.25	86.11	A0A251T566
SYVNTPILA		827.97	9	976.52	77.32	A0A251UCD5
TEGNMRIQ		253.29	8	947.45	49.44	A0A251TUS1
TEGSLRVQ		2790.80	8	888.47	65.47	A0A251UCD5
TELLAE		389.88	6	674.35	57.45	A0A251UYX1
TEQFEGR	2905.10	521.87	7	865.39	95.82	A0A251TUS1
TETLAEAFN		191.80	9	994.46	45.97	A0A251TUS1
TNDNAMIAN		203.81	9	962.41	98.63	A0A251UCD5
TNTPILFY	189.07	38.55	8	967.50	94.01	A0A251TUS1
TPELIAQ	1889.20	8291.50	7	770.42	54.77	A0A251TKL9
TPELIAQS		2980.00	8	857.45	51.34	A0A251TKL9
TPGGSYTR		3037.80	8	837.40	69.63	A0A251TUS1
TSQPNQRL	3694.60	106.24	8	942.49	84.92	A0A251UYX1

TTETLAEAF	245.55	225.99	9	981.47	124.59	A0A251TUS1
TVDLLAQ	4375.20	162.87	7	758.42	88.64	A0A251UCD5
TVDLLAQS		51.73	8	845.45	138.24	A0A251UCD5
TVELLAQS		26.48	8	859.47	120.62	A0A251TAA6
VDFIRH	2887.70	14486.00	6	785.42	96.05	A0A251UCD5
VDHETAE		161.88	7	799.33	74.52	A0A251TUS1
VDLLAQS		481.01	7	744.40	133.81	A0A251UCD5
VDNQGNSVF		217.51	9	978.44	87.70	A0A251TKL9
VDQETAQK		385.88	8	917.45	176.09	A0A251TAA6
VDQETASKL		2658.60	9	989.50	120.27	A0A9K3HVJ0
VERGLQ	7530.10	561.57	6	700.39	79.94	A0A9K3HVJ0
VERGRGIQG	564.86	467.28	9	970.53	51.34	A0A251TKL9
VERILE	543.01		6	757.43	68.49	Q39928
VEVIRH	84.21	1726.50	6	751.43	83.29	A0A9K3HVJ0
VEVIRHH		577.59	7	888.49	65.80	A0A9K3HVJ0
VFFDTQ	8216.70	115.31	6	755.35	119.22	A0A251UCD5
VFNLDNQ	1538.50		7	848.40	102.77	A0A251UYX1
VFRAMPL	33115.00	338.35	7	832.46	95.38	A0A251UYX1
VFRAMPLE	1490.20		8	961.51	58.78	A0A251UYX1
VILPGCPE		106.76	8	883.45	54.77	A0A251TKL9
VIVQVQQ		860.62	7	812.48	156.93	A0A251UYX1
VLFTPGGSY	784.92		9	939.47	128.86	A0A251TUS1
VNIDNPSHA	477.60		9	965.46	80.46	A0A251TAA6
VNTPILAF	211.20	17.56	8	873.50	123.99	A0A251UCD5
VRPPIR	1896.50	713.27	6	736.47	72.62	A0A9K3HVJ0
VSRGDIF	118.67		7	792.41	57.81	A0A251UYX1
VTEGALR	2124.70		7	744.41	106.42	A0A251TAA6
VTEGSLR	6105.70	108.46	7	760.41	68.49	A0A251UCD5
VTEGSLRVQ	579.11		9	987.53	154.12	A0A251UCD5
VVRPPIR	5309.40		7	835.54	77.94	A0A9K3HVJ0
WEQYHPG	546.61	291.15	7	915.39	88.64	A0A251T566
WETGRQQ	1412.30	702.87	7	903.42	94.01	A0A251T566
WETGRTG	1473.10	263.82	7	805.37	57.81	A0A251T566
WNFNDE	617.48	281.43	6	823.31	92.19	A0A251UYX1
WNFNDEQ	107.46	64.44	7	951.37	54.78	A0A251UYX1
YDIVMQ		57.68	6	767.35	57.45	A0A251T566
YINTPL	769.56	87.25	6	719.39	90.94	A0A9K3HVJ0
YINTPLM	1723.20	26.83	7	850.43	148.21	A0A9K3HVJ0
YLNSF	1636.60		5	642.30	58.26	A0A9K3HVJ0
YPRLLF		245.35	6	807.46	81.00	A0A251UYX1
YQPSFQ	2525.10	143.13	6	768.34	92.19	A0A251TUS1
YTNTPIL	570.06		7	820.43	54.77	A0A251TUS1
YTNTPILF	10377.00	189.45	8	967.50	102.77	A0A251TUS1

YVEQGSGIQ	438.66	190.20	9	979.46	125.71	A0A251TUS1
YVNTPIL	6680.30	265.92	7	818.45	109.70	A0A251UCD5
YVNTPILA	1139.20	305.71	8	889.49	71.30	A0A251UCD5
Total peptides	319	389				

Prot: Protamex® hydrolysate; Prot+Flav: Protamex® followed by Flavourzyme® hydrolysate; ≤ 1kDa: 1kDa ultrafiltrated hydrolysate.

Appendix 7.2. His and Cys-contanig peptides sequences identified from ≤ 1 kDa fractios of sunflower meal protein hydrolysates using nano-LC-MS/MS analysis.

Type of peptide	Sequence	Intensity (x 10^5)		Length	Mass (g/mol)	Score	Entry
		≤ 1 k Da Prot	≤ 1 kDa Prot+Flav				
His-containing peptides	AEKGHLQPN	1374.10	793.12	9	992.50	74.26	A0A251UYX1
	AGGISSEH		2264.10	8	756.34	79.94	A0A251UYX1
	AGGISSEHIQ		536.94	10	997.48	74.17	A0A251UYX1
	AGVDFIRH		1199.30	8	913.48	71.88	A0A251UCD5
	AGVEVIRH		293.55	8	879.49	54.78	A0A9K3HVJ0
	AHEIIHVT	5959.90		8	918.49	82.31	A0A9K3HVJ0
	AIQSPHW	198.95	1713.00	7	837.41	101.21	A0A251UCD5
	AIQSPHWT	39422.00	688.84	8	938.46	96.19	A0A251UCD5
	ALPAGAVHW	283.09		9	920.49	100.36	A0A251T566
	APHYNLN	317.99		7	827.39	65.90	A0A251T566
	AVHWTY		178.52	6	775.37	63.67	A0A251T566
	DFIRHR		1622.70	6	842.45	65.90	A0A251UCD5
	DQFHR	1450.20	1824.10	5	701.32	57.45	A0A9K3HVJ0
	DQFHRR	8467.70	1199.40	6	857.43	74.52	A0A9K3HVJ0
	EHKLPIL	29084.00		7	848.51	74.52	A0A251UYX1
	EHKLPILS	4144.60	45.90	8	935.54	111.65	A0A251UYX1
	EIIHVT		1497.90	6	710.40	77.94	A0A9K3HVJ0
	EVFHVD		911.29	6	744.34	63.67	A0A9K3HVJ0
	FIRHR	5800.50	270.66	5	727.42	86.11	A0A251UCD5
	FPILEH		5731.70	6	754.40	81.00	A0A251UCD5
	FPILEHL	3111.30	7487.90	7	867.49	136.44	A0A251UCD5
	FPILEHLQ		160.14	8	995.54	74.26	A0A251UCD5
	FSPHWT	362.88		6	773.35	65.90	A0A251UYX1
	FSPHWTVN	8234.70	63.71	8	986.46	87.70	A0A251UYX1
	GAVHWTY	928.44		7	832.39	69.09	A0A251T566
	GFQDRH		1101.70	6	758.35	68.49	A0A9K3HVJ0
	GGGAFTDRH		315.59	9	916.42	77.32	A0A251TUS1
	GGISSEHIQG		4119.50	10	983.47	98.58	A0A251UYX1
	GHIIFVQN		2079.00	8	926.50	52.30	A0A251TUS1
	GHIIFVQNG		4150.90	9	983.52	65.80	A0A251TUS1
	GHIVNVGQ		116.41	8	822.43	55.50	A0A251UCD5
	GHIVNVGQD		331.19	9	937.46	75.04	A0A251UCD5
	GIVSPHW	137.04		7	794.41	76.55	A0A251TUS1
	GVDFIRH	65397.00	27065.00	7	842.44	96.05	A0A251UCD5
	GVDFIRHR	7.39		8	998.54	58.78	A0A251UCD5
	GVEVIRH	4524.30	1334.20	7	808.46	79.94	A0A9K3HVJ0

	GVHFIR	1489.80		6	727.41	81.00	A0A251TAA6
	HEIIHVT	13.63	3216.90	7	847.46	88.64	A0A9K3HVJ0
	HIIFVQ		2081.30	6	755.43	67.33	A0A251TUS1
	HIIFVQN	56.91	2351.30	7	869.48	81.72	A0A251TUS1
	HIIFVQNG		3736.80	8	926.50	54.77	A0A251TUS1
	HIVNVGQD		423.13	8	880.44	45.97	A0A251UCD5
	HQKIRHF	547.47		7	964.54	62.98	A0A9K3HVJ0
	HRIQPGGL	9794.40		8	876.49	97.47	A0A251UCD5
	HYWNF	4975.00	400.49	5	765.32	56.94	A0A251UYX1
	IDNPSHAD	421.63	664.06	8	867.37	67.49	A0A251UCD5
	IIRPPQQH	448.18	123.48	8	987.56	50.03	A0A251TAA6
	IPTGAAHW		346.17	8	851.43	86.94	A0A251TUS1
	IQSPHWT	9789.40	278.16	7	867.42	120.62	A0A251UCD5
	ISSEHIQGQ	1256.60		9	997.48	70.82	A0A251UYX1
	KFPILEHL	2857.00		8	995.58	99.38	A0A251UCD5
	KGHLQPN	8272.70		7	792.42	85.36	A0A251UYX1
	KGHLQPNA	1722.30		8	863.46	60.97	A0A251UYX1
	LFSPHW	124.66		6	785.39	96.04	A0A251UYX1
	LPAGAVHW		899.84	8	849.45	81.00	A0A251T566
	LVSPHW	10829.00		6	737.39	81.00	A0A9K3J8S2
	NDQRGHIV	12628.00	1091.00	8	937.47	71.88	A0A251UCD5
	NEHKLPIL	346.82		8	962.55	60.97	A0A251UYX1
	NQLDPNHR		1231.20	8	992.48	69.63	A0A251TUS1
	NVDHETAE	260.95	304.58	8	913.38	58.78	A0A251TUS1
	QIWHQ	857.49		5	710.35	112.70	A0A251UYX1
	QSPHWTIN	1333.30	4945.90	8	981.47	104.06	A0A251UCD5
	QYHPGQQ	4250.20	190.36	7	856.38	100.27	A0A251T566
	RQQYQHQ	48.72		7	986.47	54.77	A0A251UCD5
	RYGIVSPH	3925.60		8	927.49	85.36	A0A251TUS1
	SEHIQGQ	3111.50	2962.40	7	797.37	111.65	A0A251UYX1
	SEVFHVD	5245.50	11254.00	7	831.38	73.98	A0A9K3HVJ0
	SHKLPVLE	710.82		8	921.53	60.97	A0A251T566
	SPHWTI	65.16	733.87	6	739.37	69.09	A0A251UCD5
	SPHWTIN	20408.00	35427.00	7	853.41	85.36	A0A251UCD5
	SPHWTINA		129.26	8	924.45	49.44	A0A251UCD5
	VDFIRH	2887.70	14486.00	6	785.42	96.05	A0A251UCD5
	VDHETAE		161.88	7	799.33	74.52	A0A251TUS1
	VEVIRH	84.21	1726.50	6	751.43	83.29	A0A9K3HVJ0
	VEVIRHH		577.59	7	888.49	65.80	A0A9K3HVJ0
	VNIDNPSHA	477.60		9	965.46	80.46	A0A251TAA6
	WEQYHPG	546.61	291.15	7	915.39	88.64	A0A251T566
	CEPYIVR		76.09	7	935.45	47.92	A0A251UYX1

Cys-containig peptides	**C**RWISF		782.23	6	867.41	69.09	A0A9K3HVJ0
	G**C**RWISF		1178.50	7	924.43	45.95	A0A9K3HVJ0
	GIEQTI**C**		49.11	7	819.38	94.01	A0A251T566
	GVEETI**C**S		222.03	8	893.38	106.42	A0A251UCD5
	GVEETI**C**SA		664.64	9	964.42	129.68	A0A251UYX1
	GVILPG**C**PE		86.31	9	940.47	53.35	A0A251TKL9
	LPG**C**VETF		81.31	8	921.43	52.30	A0A251T566
	Q**C**RETE	49.28	181.97	6	821.33	57.45	P15461
	SGPEF**C**NL		641.08	8	922.39	93.20	A0A9K3J8S2
	SPEF**C**NL		608.96	7	865.36	88.64	A0A251UYX1
	VILPG**C**PE		106.76	8	883.45	54.77	A0A251TKL9
	Total peptides	52	66				

Prot: Protamex® hydrolysate; Prot+Flav: Protamex® followed by Flavourzyme® hydrolysate; ≤ 1kDa: 1kDa ultrafiltrated hydrolysate.

Appendix 7.3. Sequenced mass spectra of six different ATCUN-binding peptides structures obtained from SMPI hydrolysates and processes by MaxQuant software. (A) AV**H**WTY, (B) KG**H**LQPN, (C) NE**H**KLPIL, (D) QY**H**PGQQ, (E) SE**H**IQGQ, (F) VD**H**ETAE.

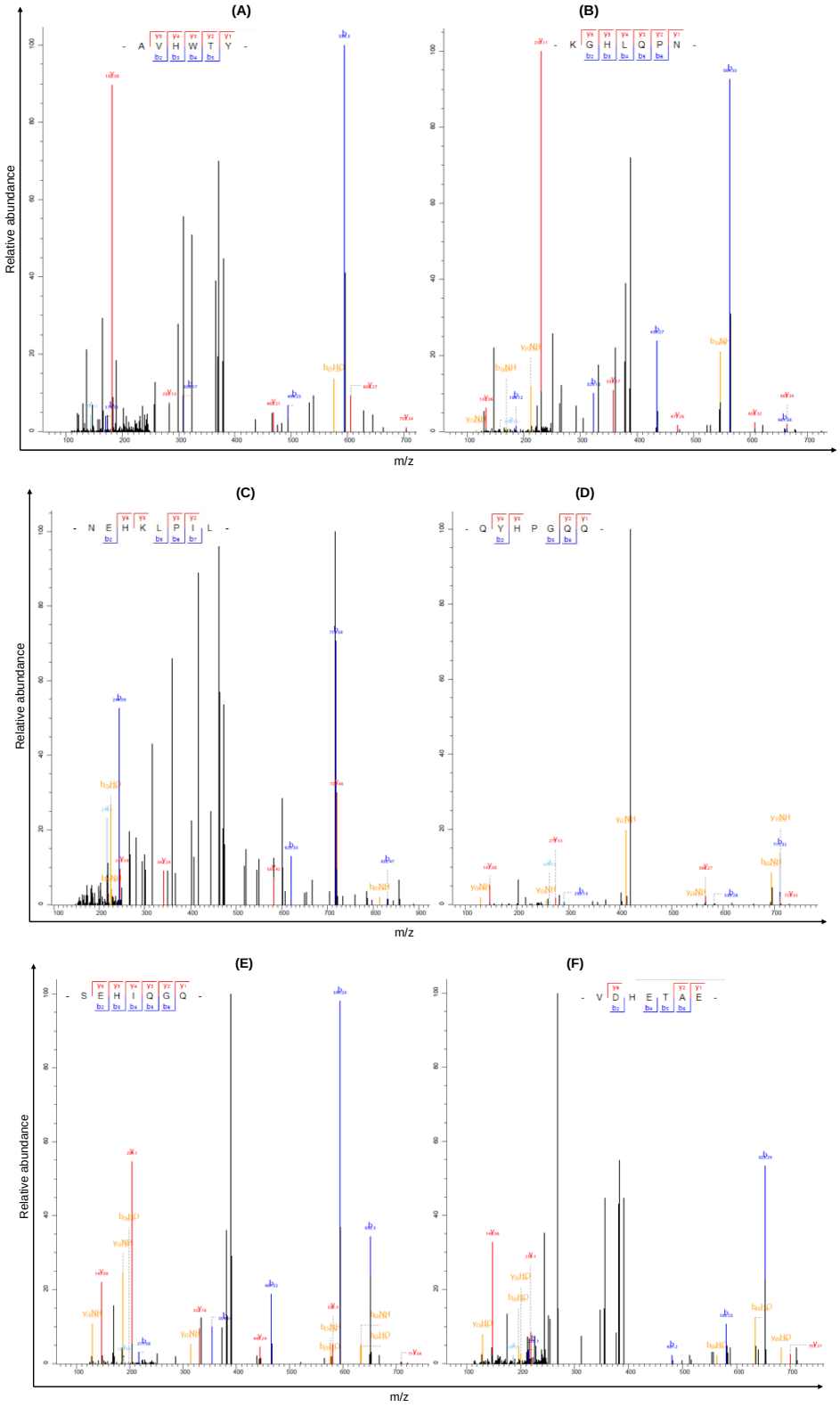

Appendix 7.4. Effects of Cu^{2+} coordination by EDTA and peptides present in SMPI hydrolysates on the lifespan-extension of Cu^{2+}-exposed nematodes.

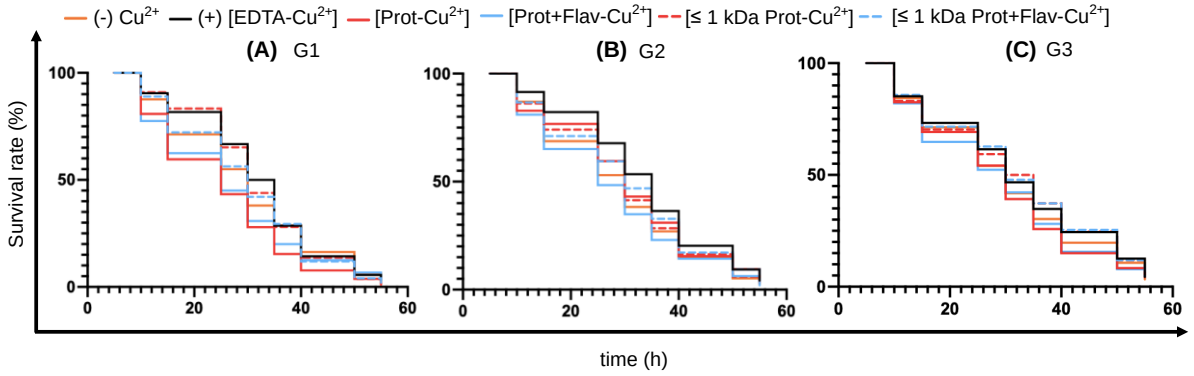

Prot: Protamex® hydrolysate; Prot+Flav: Protamex® followed by Flavourzyme® hydrolysate; ≤ 1 kDa: 1 kDa ultrafiltrated hydrolysate.